

**Modern Technologies for
Engineering, Applied Mechanics
and Material Science**

Edited by
Debnath Sujan and Reddy M. Mohan



TRANS TECH PUBLICATIONS

**Modern Technologies
for Engineering,
Applied Mechanics
and Material Science**

Edited by
Debnath Sujan
Reddy M. Mohan

Modern Technologies for Engineering, Applied Mechanics and Material Science

Selected, peer reviewed papers from the
5th International Conference on
Manufacturing Science and Technology
(ICMST 2014),
June 7-8, 2014, Sarawak, Malaysia

Edited by

Debnath Sujan and Reddy M. Mohan



Copyright © 2014 Trans Tech Publications Ltd, Switzerland

All rights reserved. No part of the contents of this publication may be reproduced or transmitted in any form or by any means without the written permission of the publisher.

Trans Tech Publications Ltd
Churerstrasse 20
CH-8808 Pfaffikon
Switzerland
<http://www.ttp.net>

Volume 980 of
Advanced Materials Research
ISSN print 1022-6680
ISSN cd 1022-6680
ISSN web 1662-8985

Full text available online at <http://www.scientific.net>

Distributed worldwide by

Trans Tech Publications Ltd
Churerstrasse 20
CH-8808 Pfaffikon
Switzerland

Fax: +41 (44) 922 10 33
e-mail: sales@ttp.net

and in the Americas by

Trans Tech Publications Inc.
PO Box 699, May Street
Enfield, NH 03748
USA

Phone: +1 (603) 632-7377
Fax: +1 (603) 632-5611
e-mail: sales-usa@ttp.net

Preface

2014 5th International Conference on Manufacturing Science and Technology (ICMST 2014) was held in Sarawak, Malaysia on 7-8, June, 2014. The conference provides a platform to discuss Manufacturing Science and Technology etc. with participants from all over the world, both from academia and from industry. Its success is reflected in the papers received, with participants coming from several countries, allowing a real multinational multicultural exchange of experiences and ideas.

The present volumes collect accepted papers and represent an interesting output of this conference. This book covers these topics: Acoustics and Noise Control, Aerodynamics, Applied Mechanics, Automation, Mechatronics and Robotics, Automobiles, Automotive Engineering, Ballistics, Biomechanics, Biomedical Engineering, CAD/CAM/CIM, CFD, Composite and Smart Materials, Compressible Flows, Computational Mechanics, Computational Techniques, Dynamics and Vibration, Energy Engineering and Management, Engineering Materials, Fatigue and Fracture, Fluid Dynamics, Fluid Mechanics and Machinery, Fracture, Fuels and Combustion, General mechanics, Geomechanics, Health and Safety, Heat and Mass Transfer, HVAC, Instrumentation and Control, Internal Combustion Engines, Machinery and Machine Design, Manufacturing and Production Processes, Marine System Design, Material Engineering, Material Science and Processing, Mechanical Design, Mechanical Power Engineering, Mechatronics, MEMS and Nano Technology, Multibody Dynamics, Nanomaterial Engineering, New and Renewable Energy, Noise and Vibration, Noise Control, Non-destructive Evaluation, Nonlinear Dynamics, Oil and Gas Exploration, Operations Management, PC guided design and manufacture, Plasticity Mechanics, Pollution and Environmental Engineering, Precision mechanics, Mechatronics, Production Technology, Quality assurance and environment protection, Resistance and Propulsion, Robotic Automation and Control, Solid Mechanics, Structural Dynamics, System Dynamics and Simulation, Textile and Leather Technology, Transport Phenomena, Tribology, Turbulence and Vibrations.

This conference can only succeed as a team effort, so the editors want to thank the international scientific committee and the reviewers for their excellent work in reviewing the papers as well as their invaluable input and advice.

Prof. Dr. Ashutosh Kumar Singh
Department of Computer Application
National Institute of Technology
Kurukshehra, India

Committees

Conference Chairs

Prof. Dr. Ashutosh Kumar Singh, Department of Computer Application, National Institute of Technology, Kurukshetra, India

Program Co-Chairs

Dr. Sujan Debnath, Curtin University, Sarawak, Malaysia

Dr. Moola Mohan Reddy, Curtin University, Sarawak Malaysia

Technical Committee

Prof. Nordin Abu Bakar, Faculty of Computer & Mathematical Sciences, Universiti Teknologi MARA, Malaysia

Prof. P. Sivaprakash, A. S. L. Pauls College of Engineering & Technology, India

Nardinocchi Alessandro, Università Politecnica delle Marche, Ancona, Italy

Dr. Wan Hasrulnizam Wan Mahmood, Universiti Teknikal Malaysia, Malaysia

Dr. Hwa Jen YAP, Faculty of Engineering, University of Malaya, Malaysia

Prof. Yusri Yusof, Universiti Teknologi Tun Hussein Onn, Malaysia

Dr. S. K. Singh, India Gokaraju Rangaraju Institute of Engineering and Technology

Prof. Alexander Gorin, Swinburne University, Sarawak, Malaysia

Prof. Khaled Abou Hossein, Nelson Mandela Metropolitan University, South Africa

Dr. Nazrul Islam, Curtin University, Australia

Dr. Brian Bosewell, Curtin University, Australia

Dr. Rajaram Ganesan, National Engineering Industries Ltd. Jaipur, India

Dr. Rajamohan Ganesan, Curtin University, Sarawak, Malaysia

Dr. Vincent Lee Chieng Chen, Curtin University, Sarawak, Malaysia

Prof. Jamaluddin Mahmud, Universiti Teknologi Mara (UiTM), Malaysia

Sponsors

Curtin University of Technology, Sarawak Campus, Malaysia

Table of Contents

Preface and Committees

Chapter 1: Advanced Materials Engineering and Technological Processes

Properties and Growth Rate of Intermetallic Al-Fe through Hot Dipped Aluminizing Z. Samsu, N.K. Othman, A.R. Daud and M. Daud	3
Performance Evaluations of Carbon/Glass Hybrid Polymer Composites C.L. Tan, A.I. Azmi and N. Mohamad	8
Bioactivity Behavior of YSZ-Al₂O₃/10HAP Bioceramics Composites in Simulated Body Fluid M.R.N. Liyana, N.M.S. Adzali and M.Z.M. Zamzuri	13
Water Absorbency Properties of OPEFB Filled Hydrogels Composites N.E. Rabat, S. Hashim and R.A. Majid	18
Oil Palm Fibre and Nano-Silica Reinforced Epoxy Composite Material N. Samuel, D. Sujan, M.E. Rahman, O. Nabinejad and M.M. Reddy	23
Preparation and Dimensional Stability of Organo-Montmorillonite (O-MMT) Treated Unsaturated Polyester Hybrid Composites Filled with Keratin Fiber K.K. Siong, S.K. Heng, S. Hamdan, M. Mohsin, A. Kakar and M. Hameed	28
A Critical Survey of Ceramics Materials for Production of Automotive Engine Block P.B. Mogaji, T. Jamiru, D. Desai and R. Sadiku	33
Optical Properties of Gallium Nitride Heterostructures Grown on Silicon for Waveguiding Application I. Saraswati, A. Stolz, S. Ko, E. Dogheche, N.R. Poespawati, R. Wigajatri and D. Decoster	41
Effect of Austenizing and Tempering Time on Corrosion Rate of Austenitic Stainless Steel in Oxalic Acid M.A. Gebril, M.S. Aldlemey, F.I. Haider and N. Ali	46
Analysis of Thickness Strain Prediction in Warm Deep Drawing of Ti-6Al-4V Alloy N. Kotkunde, A.D. Deole, A.K. Gupta and S.K. Singh	52
Evaluation of CO₂ Uptake under Mild Accelerated Carbonation Conditions in Cement-Based and Lime-Based Mortars C. Furcas, G. Balletto, S. Naitza and A. Mazzella	57
A Breif Review on Manufacturing of Al-TiC MMC S.K. Josyula and N.S.K. Reddy	62
The Investigation of Microstructures Fabrication on Quartz Substrate Employing Electron Beam Lithography (EBL) and ICP-RIE Process L. Shamsuddin, K. Mohamed and A.R. Maryam	69
Potential of Clay Deposits in Kelantan for Ceramic Production: A Literature Analysis O.F. Enoch, A.A. Shuaib and K.A.B.M. Daud	74

Chapter 2: Applied Mechanics and its Applications in Civil Engineering

Finite Element Prediction of Mechanical Behaviour under Bending of Honeycomb Sandwich Panels K. Sid-Ali, M. Amar, S. Boutaleb and K. Azouaoui	81
The Effect of Alkali Treatment of OPKS Filler on Mechanical Property of Polyester-Composite O. Nabinejad, D. Sujan, M.E. Rahman, M.M. Reddy, W.Y.H. Liew and I.J. Davies	86
Effect of Curing Age on the Compressive Strength of Petrovege Blocks O.A. Johnson, N. Madzlan and I.B. Kamaruddin	91
Evaluation of Spur Gear Pair on Tooth Root Bending Stress in Yawing Misalignment Contact Condition M.R. Lias, M. Awang, T.V.V.L.N. Rao and M. Fadhil	97

The Effect of Morphing Force on Aerodynamic Performances of TM Wing N.I. Ismail, A.H. Zulkifli, M.Z. Abdullah, M.H. Basri and M.M. Mahadzir	102
Analysis of Concurrent Brake Application for Underbone Motorcycle M.H. Basri, A.H. Zulkifli, N.I. Ismail, S. Che Mat and M.M. Mahadzir	107
The Three-Dimensional Unsteady Numerical Analysis of the Internal Flow Field of the New Control Valve D.Y. Qu, J.L. Xu, Y.Y. Huang and X.Z. Xie	112
Determination of Nozzle Angle for Flow Performance in Supersonic Subsea Compact Wet Gas Separator F.M. Mohd Hashim and M.F.A. Ahmad	117
Identification of the Mechanical Properties of High-Strength Steel Using Digital Image Correlation M. Štamborská, M. Kvičala and M. Losertová	122
Comparison of the Stress-Strain Behaviour of Cast TiAl6V4, Porous TiAl6V4 and Cortical Bone during the Mechanical Load Caused by Common Daily Activities M. Kvičala, M. Štamborská and J. Drápala	127
Development of Splice Connections for Precast Concrete Structures A.B.A. Rahman, J.H. Ling, Z.A. Hamid, M.H. Osman, S. Mohammad and A.A. Saim	132
Study of Ultra High Performance Fiber Reinforced Concrete with Expansive and Shrinkage Reducing Agents A. Nardinocchi and V. Corinaldesi	137
Lightweight Aggregate Mortars for Sustainable and Energy-Efficient Building V. Corinaldesi, A. Nardinocchi and J. Donnini	142
Study on Damage Modes of a Sandwich Panel Impacted Repeatedly K. Azouaoui and S. Mouhoubi	147
Micromechanical Model Prediction Overall Young Modulus Nanocomposites Polymer-Clay-Silica by Self Consistent Approach A. Mesbah, K. Azouaoui, S.A. Kaoua and S. Boutaleb	152

Chapter 3: Modern Technologies for Modelling, Simulation and Automation, Instrumentation, Measurement and Control Technologies

A Method of Determining the Direction of Two Dimensional Curves F. Wang, R.K.F. Abdelmaguid and H.M.A. Hussein	159
Implementation of a Voice-Control System for Issuing Commands in a Virtual Manufacturing Simulation Process Y.S. Pai, H.J. Yap and S. Ramesh	165
Non-Zero Multi-Valued Decision Diagram (NZMDD) Based Synthesis of Multi-Valued Logic (MVL) Functions A.K. Chowdhury, N. Raj and A.K. Singh	172
Developing a Solar Calculator System S. Muhammad-Sukki, M.T.K.M.N. Khan, A.M. Zeki, A. Abubakar and F. Muhammad-Sukki	179
ISO 6983 Translator for PC Based CNC Systems Y. Yusof and K. Latif	184
On the Proportionality of Damage Rule in Finite Element Simulations of the Ductile Failure F. Šebek, J. Hůlka, P. Kubík and J. Petruška	189
New Algorithm to Reduce File Size and Bandwidth of Hashed Digital Signature for Image Steganography Using LSB E. Noroozi, S.B.M. Daud, A. Sabouhi and M.R. Salehnamadi	194
Simulation Optimization – Testing Selected Optimization Methods and their Setting of the Parameters P. Raska and U. Zdenek	198
Characterization of Diamond Electrodeposited Tool for Vibration Assisted Grinding Diagnostic M.F. Ismail	203
If-Then Rules for Selection the Die-Set for Sheet Metal Punching and Blanking Dies H.M.A. Hussein, J.A. Qudeiri, U. Umer and R.K. Abdel-Magied	208

Adaptive GA-NN for MDF Prediction Model S.I. Faridah and A.B. Nordin	214
New Model for Knock Factors Optimization in Internal Combustion Engine (SI) A.R.H. Witwit, A. Yasin, H. Gitano and T.K. Yadav	219
RFID Secure Protocol Based on Time-Based Hash Chain C. Lin, S.F. Zhao and S.P. Chen	225
A Novel Manufacturing Chain for Low Cost 3D Textile Reinforced Polymer Composites A. Almansa, M. Fazeli, B. Laurent, P. Padros and M. Hörlesberger	230

Chapter 4: Product Design and Development, Industrial Engineering

Multi-Echelon Production System Planning: Case Study at a Steel Company in Indonesia R. Govindaraju and R.A.R. Hariadi	237
Research – Design & Development of Fast Customized Manufacturing for Prostheses TKR Based on Rapid Prototyping A. Suwandi, G. Kiswanto, W. Kusumaningsih and T.P. Soemardi	243
Manufacturing Execution System Design Using ISA-95 R. Govindaraju, K. Lukman and D.R. Chandra	248
A Vide Survey on Product Development and Commercialization Process R.R. Salman, Y.A.A. Hammouda, S. Monsef and M. Sadeghi	253
Basic Approaches to Green Production of Board Wood Composite Materials V.P. Tishchenko, L.P. Mayorova and O.M. Morina	258
Design and Analysis of Automotive Instrument Panel N.A. Haniffah, M.F. Zakaria and T.K. Sheng	263

CHAPTER 1:

Advanced Materials Engineering and Technological Processes

Properties and Growth Rate of Intermetallic Al-Fe Through Hot Dipped Aluminizing

Zaifol Samsu^{1, 2, a}, Norinsan Kamil Othman^{1, b}, Abd Razak Daud¹,
Muhammad Daud^{2, c},

¹School of Applied Physics, Universiti Kebangsaan Malaysia, 43600 Bangi, Selangor, Malaysia

²Material Technology Group, Industrial Technology Division, Malaysian Nuclear Agency, 43600 Bangi, Selangor, Malaysia

zaifolsamsu@nuclearmalaysia.gov.my^a, insan@ukm.my^b, mdaud@nuclearmalaysia.gov.my^c

Keywords: Hot Dipped Aluminizing. Finger-Like. Hardness.

Abstract. Hot dipped aluminizing is the one of the most famous and effective method of the surface protection. The growth behavior in the intermetallic layer by introducing a different dipping time and various of molten aluminium temperature had been detail investigated. The result showed that the top portion of the coated steel substrate is compose of a thin layer of α -Al₂O₃, followed by thicker Aluminium pure layer, thinner layer of FeAl₃, and then a much thicker of Fe₂Al₅. The intermetallic layer is 'thick' and exhibits a finger-like growth into the steel. The thickness of Al-Fe intermetallic layer on the steel base is increased with the increasing of hot dipping temperature and time. The micro hardness testing result shown that increasing of the aluminizing temperature was increased the hardness of the intermetallic layer.

Introduction

Hot dipped aluminizing process has been widely used for protection of carbon steel in high temperature application. The process involves dipping of steel sheet into molten aluminium or its alloy, at a fixed temperature for a certain period of time. The microstructure of the protective coating on the hot-dipped aluminide steel is composed of an outer aluminum topcoat containing the same composition as the aluminum bath and an Fe–Al intermetallic layer formed by Fe/Al interdiffusion during the hot-dip process. Shigeaki Kobayashi and Takao Yakou [1] showed that the coating layers of hot dip aluminized steel consist mainly of aluminum and Fe₂Al₅. Aluminized steel exhibit excellent oxidation and corrosion resistance [2].

It was reported [3,4,5] that composition of aluminizing metal and carbon content of steel substrate and its dipping time intensely affect the growth rate of the intermetallic layer, but aluminizing temperature [6] of the substrate does not affect it significantly. Since, previously the effect of the aluminizing temperature on the growth rate of the intermetallic layer was examined in a very short range 775–850 °C [6] and most of the researchers conducted hot-dipping tests above 750 °C in pure Al and Al–Si alloys [7]. As a result, they concluded that aluminizing temperature does not affect the growth rate of intermetallic layer.

Then, the study of aluminizing was re examined by extending the temperature range between 675°C and 950°C of was conducted with width range of aluminizing temperature. It was reported that the growth intermetallic layer was increased for the aluminizing temperature in the range 675°C-775°C but the thickness did not increase further when the aluminizing temperature increased in the range 775°C–950°C [8]. However, the results of the present study were found different from the preceding one. This study reveal that the variation in the aluminizing temperature and dipping time have a profound effect on the growth kinetics and hardness of the intermetallic layer

Experimental

Material and Method. A commercial AISI 1005 steel was used as the substrate material in this study. The chemical composition of the adopted steel is Fe-0.047C-0.137Mn-0.035P-0.01S (%wt).

Rectangular specimen with dimension of 20mm x 10mm x 2mm was cut using a water cooled cutting machine. Laboratory grade pure aluminium with a purity of 99.9% was used as the molten aluminium bath. The surfaces of the steel specimens for aluminizing were finished by grinding with a #1000 SiC paper. Then the specimen was degreased in acetone and finally cleaned ultrasonically in acetone. A hole of its diameter approximately 3mm was drilled at one end of the specimen to facilitate its hanging into molten aluminium.

Hot Dipping. The aluminium granular was heated to the temperatures of range between 700°C until 850°C in a graphite crucible using a resistance furnace. The temperature of the molten aluminium bath was controlled to be within $\pm 10^\circ\text{C}$. The specimen was dipped in the molten aluminium for the time period of 3 min until 9 min. These temperatures were maintain throughout the required range of dipping time and were controlled by using a K-type thermocouple. The specimens were gently shaken inside the bath to ensure good wet ability. After dipping for the specified duration, the specimens were withdrawn and cooled in air. These test were conducted to examine the effect of varying aluminizing temperature and dipping time on the growth and morphology of intermetallic layer

Micro Hardness Measurement. Micro-hardness of the aluminised sample was also measured with a Vickers micro hardometer (Shimadzu HMV 2000). The hardness test was performed under an indentation load of 25gf for 10s. Analysis points were spaced so that to eliminate the effect of neighbouring indentations. The sample was separate with the three layers consist of aluminium layer, intermetallic layer and substrate layer. The micro hardness was evaluated by taking ten indentations on each layer and was averaged.

Analysis of Samples. The aluminized specimens were sectioned carefully with a slow water cooled cutting machine. For microstructure observation and analysis, the specimen was carefully mounted, ground and polished to protect the edges. The specimen was etched with a 2% Nital solution to reveal the coating layer microstructure. The thickness of the layer was then measured at least five times at different places on the section.

Analysis of the chemical composition of substrate was performed using spark emission spectroscopy. The microstructures of the aluminized specimens were examined by using an optical microscope. Scanning electron microscope (SEM) attached with EDX (energy dispersive X-ray) facility was employed to analyze elemental concentration of the phases formed in the outer coating and in the intermetallic layer. X-ray diffraction (XRD) technique was also used to identify the phases formed in the outer coating as well as in the intermetallic layer.

Result and Discussion

The Growth of Intermetallic Layer During Hot Dipping. Cross sectional micrograph of mild steel hot dipped in pure Al in Fig. 1. The analysis of the microstructure and composition of the specimen shown that the diffusion layer are divided into three major layer that consist of aluminium layer, intermetallic layer and substrate. The aluminide layer is composed of an outer aluminium topcoat and an inner Fe-Al intermetallic layer. This suggested that the formation of the aluminide layer was mainly due to the outward diffusion of iron, while the inward diffusion of Al contributed to the growth of the aluminide layer.

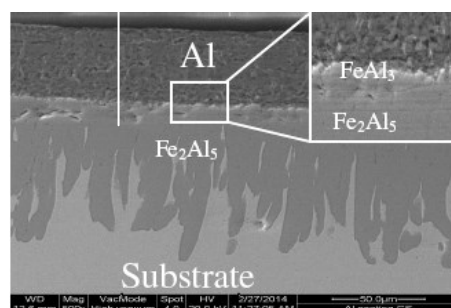


Fig. 1. SEM Micrographs of cross section of specimens after aluminizing

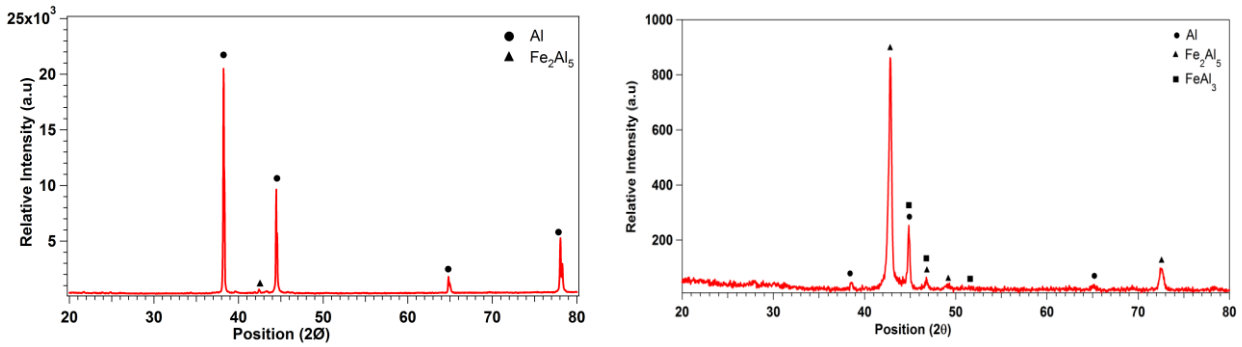


Fig. 2. X ray diffraction pattern of a specimen aluminized in Al pure melt obtained from (a) the outer coating and (b) intermetallic layer

X-ray diffraction analysis confirmed the presence of the phases identified by the scanning electron microscopy in the outer coating as well as in the intermetallic layer. The XRD pattern illustrates the phases formed in the outer coating of the steel specimen aluminized in the Al pure melt as given in Fig. 2(a). The diffraction pattern in the intermetallic layer shows the presence of thin layer of FeAl_3 and thick layer of Fe_2Al_5 layer as shown in Fig 2(b). It means that intermetallic layer of Fe_2Al_5 was a major layer for protection of steel after aluminizing.

Fig. 3 and 4 illustrate the different micrograph of the variation in the aluminizing temperature and dipping time on the growth and the morphology of the intermetallic layer respectively. These depict that with increasing the aluminizing temperature of the specimen in the range 700 – 850, the intermetallic layer increased as shown in graphical Fig. 3. The same situations are happen when the dipping time of the aluminizing increased and as a result the intermetallic layer also increased as shown in graphical Fig. 4. These micrograph shown that the pattern growth was changing when the aluminizing temperature and dipping time were increased.

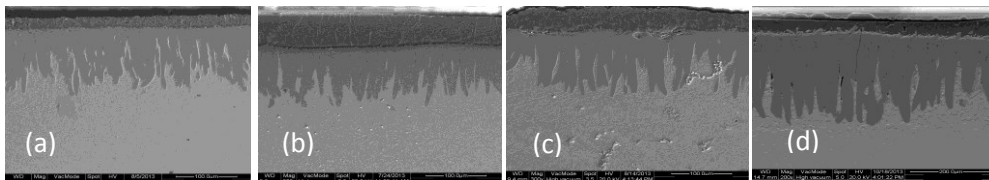


Fig. 3. Cross sectional view of aluminized carbon steel sheets which were hot dipped in melt pure Al at different temperature (a) 700°C (b) 750°C (c) 800°C (d) 850°C

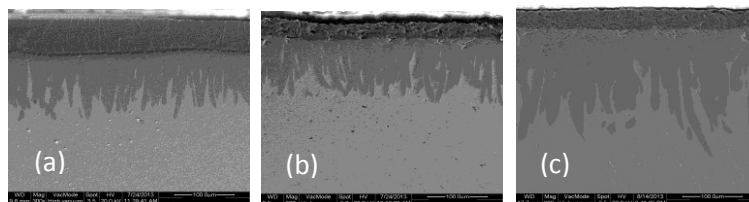


Fig. 4. Cross sectional view of aluminized carbon steel sheets which were hot dipped in melt pure Al at 750°C with various dipping time (a) 3 min (b) 6 min (c) 9 min

Based on the characterization of microstructure (Fig. 1) and phase constitution (Fig 2(b)) in the intermetallic layer, the tongue-like morphology of the Fe_2Al_5 phase is formed by the non-uniform growth of the columnar grains.

In the hot dipping process, the specimen dipped in the molten aluminum bath and the steel substrate started to dissolve into the molten aluminum bath. As a result, molten aluminium was diffused into the steel substrate to form an Fe–Al intermetallic layer. The crystalline defects of Fe_2Al_5 with the orthorhombic structure offered a rapid diffusion path to increase the growth rate of Fe_2Al_5 [7], resulting in columnar Fe_2Al_5 and the corresponding residual steel substrate. As the

immersion time increased, the columnar grains grew at a fast rate toward the steel substrate, whereas they grew at a slow rate in the lateral direction of the columnar grains. Finally, the consumption of the outer residual steel substrate due to the growth of the columnar $\text{FeAl}_3 + \text{Fe}_2\text{Al}_5$ caused the tongue-like morphology. Moreover, the slow lateral growth of the columnar Fe_2Al_5 provided a pathway for the formation of crystal nuclei of Fe_2Al_5 in the lateral direction, resulting in fine grains clustered in a strip-shaped form around the peaks of the serration-like steel substrate, the original locations of the outer residual steel substrate.

The gradual increase in thickness of the intermetallic layer lead to the possibility that the phases of the steel substrate like ferrite, pearlite and austenite might have affected its growth rate. These phases could have appeared at the outer skin of the steel substrate during the hot-dip aluminizing process at a particular temperature or in a range of temperatures.. As a result the increasing of the intermetallic layer at a range of temperature was due to the ferrite phase for the rapid growth of the intermetallic layer, while both the pearlite and the austenite hampered the growth of the intermetallic layer. As long as the ferrite was present with the pearlite or the austenite in the range of temperature, there was some increase in the intermetallic layer positively.

Micro hardness Analysis. Fig. 5 summarize graphically the effect of aluminizing temperature and dipping time to the hardness of the specimens. The trend of the graph shown that the hardness of the intermetallic layer was increase with increasing the aluminizing temperature. the changes of hardness were come after aluminizing temperature reach to the 800°C and above. The gradual increase of intermetallic layer hardness lead to the possibility that the phase have ferrite, pealite and more austenite during aluminizing process. There were no significant effect to the hardness of aluminium and steel layer.

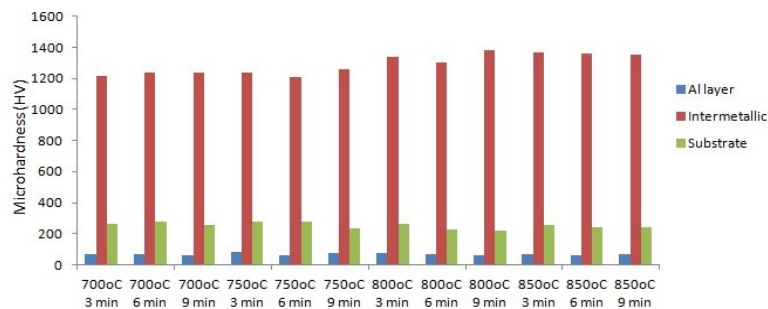


Fig. 5. Microhardness measurement in the cross section of the sample after aluminising at different aluminizing temperature and various of dipping time.

Conclusion

The growth of the intermetallic layer formed in aluminide mild steel by different aluminizing temperature and various of dipping time has been characterized. SEM micrograph shown that the tongue-like morphology of Fe_2Al_5 observed from the cross section of the specimen. The thickness of the intermetallic was increased when increasing the dipping time at various aluminizing temperature. XRD studies shown that the formation of the intermetallic phase for all specimens. The inter metallic layer consisted of thin layer of FeAl_3 and thick layer Fe_2Al_5 layer. The crystalline defects of Fe_2Al_5 along the diffusion direction causing Fe_2Al_5 to grow at a rapid rate, resulting in columnar Fe_2Al_5 and corresponding residual steel substrate. The columnar Fe_2Al_5 had a fast growth rate along the diffusion direction, but it grew slowly in the lateral direction of the columns. Microhardness testing shown that the specimen become more harden and probably brittle when the aluminizing temperature was increased.

Acknowledgement

The author would like to thank to all the colleagues from Universiti Kebangsaan Malaysia and a staff from Malaysian Nuclear Agency for assistance and guideline.

References

- [1] S. Kobayashi, T. Yakou, Control of intermetallic compound layers at interface between steel and aluminum by diffusion-treatment, *Mater Sci Eng A*. 338 (2002) 44.
- [2] O.N. Mohanty, A. Bahadur, Structural studies of calorized coatings on mild steel. *Mater Trans, JIM* 31.11 (1990) 948-953.
- [3] S.H. Hwang, J.H. Song, Y.S. Kim, Effect of carbon content of carbon steel on its dissolution into a molten aluminum alloy, *Mater Science Engineering A* 390.1 (2005) 437-443.
- [4] M. Yousaf, I. Javed, A. Rafiq, I. Amir, The role of Cu additions in Al on the properties of hot-dip-aluminized steel, *J Qual Technol Management* 6 (2010) 149.
- [5] T. Shih, T. Shu Hao, Interaction of steel with the pure Al, Al-7Si and A356 alloy, *Mater Sci Eng A*. 349 (2007) 454-455.
- [6] M.V. Akdeniz, A. Mekhrabov, The effect of substitutional impurities on the evolution of Fe-Al diffusion layer. *Acta Mater.* 46 (1998) 1185.
- [7] M.V. Akdeniz, A. Mekhrabov, T. Yilmaz, The role of Si addition on the interfacial interaction in Fe-Al diffusion layer, *Scr Metall Mater.* 31 (1994) 1723.
- [8] C. Wang, S. Ming Chen, The high temperature oxidation behavior of hot-dipping Al-Si coating on low carbon steel, *Surf Coat Tech.* 200 (2006)6601.

Performance Evaluations of Carbon/Glass Hybrid Polymer Composites

Tan, C.L.^{1, a}, Azmi, A.I.^{1,2, b*} and Mohamad, N.^{1, c}

¹School of Manufacturing Engineering, Universiti Malaysia Perlis (UniMAP), Pauh Putra Campus, 02600 Arau, Perlis, Malaysia

²Faculty of Engineering Technology, Universiti Malaysia Perlis (UniMAP), Pauh Putra Campus, 02600 Arau, Perlis, Malaysia

^achyelih@gmail.com, ^bazwaniskandar@unimap.edu.my, ^cnoorhafiza@unimap.edu.my

Keywords: Carbon fiber; Glass fiber; Hybrid composites; Mechanical properties; Vacuum-assisted resin transfer moulding.

Abstract. In this work, the influence of hybrid effect on carbon and glass fiber reinforced polymer (FRP) on the mechanical performance for structural application was studied. The hybrid fiber reinforced polymer (FRP) composites made from woven E-glass and carbon fibers with epoxy resin. The FRP hybrid composites were fabricated using vacuum-assisted resin transfer moulding process, which is capable of producing constant thickness with high volume fractions of composite panels compared to that of traditional wet hand lay-up method. Mechanical performance of the FRP hybrid composites were evaluated against full carbon or glass fiber reinforced polymer composites. Important properties such as tensile strength, flexural strength and volume fraction of reinforcement were determined according to the ASTM standards. It was found that the mechanical properties of carbon-glass hybrid composites exhibited significant improvement in term of strength and strain respectively compared to that of full glass FRP composites and full carbon FRP composites.

Introduction

With the recent technological advancements, conventional materials such as steel and aluminum no longer play the dominant roles in product design and manufacturing. As the strict environmental concerns and awareness grows, along with different customer needs, lightweight materials are gaining rapid development in the research communities and industries. In fact, lightweight fiber reinforced polymer (FRP) composites are finding importance uses in various applications which include in automobile components (car bodies), for marine parts (e.g. hulls, decks), and for aerospace components (e.g. wing, nose strake, antenna, fuselages).

Fundamentally, FRP composites have different material structure from that of conventional composites such as metal alloys, wood and minerals. The constituent materials in FRP composites usually retain their original form but their final properties are better than the constituent material [1]. However, hybrid composites include at least two different types of matrix or reinforcements either by distinct physical or mechanical properties [2]. Normally, one of the fibers in the hybrid composite is high modulus fiber, which is mainly to provide the stiffness properties to the composite materials. While, the second fiber is usually low modulus fibers, but these fibers are able to retain the composite material high ultimate strain and low in cost. The most commonly used fiber reinforcements for hybrid composites are carbon and glass fibers. It is well known that, carbon fiber composites provide high specific strength and modulus to the composites, whereas their weaknesses are low damage tolerant and high cost. In order to address those issues as well as to widen the applications of FRP composites, low modulus glass fibers are incorporated into the carbon fibers to create the FRP hybrid composites.

In the early study, Sonparote and Lakkad [3] studied the mechanical properties of carbon or glass fiber reinforced hybrid composites. Those composites were fabricated by filament winding process with different volume fraction. However, the hybrid composites showed low effect in tensile strength. In another study, G Kretsis [4] reviewed the mechanical properties for

unidirectional carbon-glass reinforced hybrid composites. The authors reported that mechanical properties such as tensile, compressive and flexural strengths of hybrid composites showed negative hybrid effect as its fall below the rule-of-mixture predictions. In recent years, there are a few reported studies on the mechanical properties of woven carbon-glass reinforced hybrid composites, which were produced by the traditional wet hand lay-up method [5–8]. In the present study, reinforcement of plain woven E-glass fibers and plain woven carbon fibers with epoxy resin matrix were used to produce hybrid composites via vacuum-assisted resin transfer moulding (VARTM). The fabricated carbon-glass hybrid composites, full carbon FRP composites and full glass FRP composites were investigated under the tensile and flexural tests.

Materials, and fabrication methods

The hybrid composites in this study were fabricated using E-glass weave fabric and carbon weave fabric (T300, 3K Tow) with EpoxAmite 100 resin and 103 slow hardener. All of these materials were supplied by Makna Value Sdn. Bhd, Malaysia. Brief specifications of carbon fiber and E-glass fiber are listed in Table 1.

Table 1. Specifications of fiber reinforcements.

Specifications	Carbon fiber	E-glass fiber
Yarn Density (ends/cm)	5	5
Areal weight (g/m ²)	200	200
Thickness (mm)	0.25	0.25
Weave pattern	Plain	Plain

In the early stage of the test panels preparation, woven carbon and glass fibers were cut into 320 mm x 320 mm prior to lay-up of the fiber reinforcements. Mould release agent was applied on the flat glass mould to prevent the final fabricated panel from sticking on the glass mould. Subsequently, the carbon and E-glass fiber were carefully stacked on the flat glass mould with orientations: [CGCG], where C and G are carbon fiber and glass fiber respectively. Once the arrangement of laminates has been completed, air in the vacuum bag was removed by vacuum pressure which was in the range of 11-17 mBar. Then, mixture of epoxy resin and hardener was prepared at the ratio of 4:1 and then infused into the mould cavity under the vacuum pressure. The infused panel was left for 24 hours in room temperature for curing process. The final cured panel was then cut into required specimen sizes for different mechanical tests.

Sample characterizations

Volume fraction test

To ensure consistent percentage of fiber reinforcements and epoxy resin in every batch panels, the fiber volume fraction of the fabricated panels was determined using burn-off test as state in ASTM D3171-09. Five samples of 625 m² were randomly chosen from different batch panels. The mass specimens and crucible were measured by Electronic balance meter (AY220, 0.1mg), while the density of specimen was measured by Densimeter. The samples were burn in the Nabertherm electrical furnace at 500°C for 5 hours [9]. After the burn-off test, the mass of remaining fiber reinforcements were measured. Once all data have been measured, the volume fraction was determined using Eq.1.

$$V_f = M_f/M_i \times 100 \times \rho_c / \rho_f \quad (1)$$

where:

M_i is the initial mass of the specimen;

M_f is the final mass of the left over specimen after combustion;

ρ_c is the density of the specimen;

ρ_f is the density of in the fiber reinforcement;

Tensile and flexural tests

Five rectangular specimens of 250 mm x 25 mm were prepared from different batch of fabrication panels. Tensile tests were performed on Universal Testing Machine (AG-X,250KN-300KN SHIMADZU) with loading rate of 1 mm/min as per the ASTM D3039/D standard. On the other hand, flexural property was determined through three-point bending as specified in ASTM D790 using Universal Testing Machine (AG-X,250KN-300KN SHIMADZU) with loading rate of 6.8 mm/min. Similar to the previous tests, five specimens were tested and the average value was taken for analysis.

Results and discussion

Fiber volume fraction of the hybrid composites

Quantity of reinforcements in FRP hybrid composites is often determined by fiber volume fraction and density, in which the results are shown in Table 2. The average density for carbon-glass FRP hybrid composite was 1.62 g/cm³. This result shows that addition of 50% carbon fiber reinforcement into the FRP hybrid composites reduces the density of pure glass fiber reinforced composites which is 1.88 g/cm² [10]. Low density composite is desirable so that lightweight parts can be made or produced. The calculated fiber volume fractions for the FRP hybrid specimens were found to be consistent and the average value is 55%, as shown in Table 2. Hence, it can be concluded that the VARTM method was able to compact the fiber reinforcement under vacuum pressure so as to produce uniform thickness, lower void and higher volume fraction panel than hand lay-up method.

Table 2. Specifications of fiber reinforcements.

Batch No:	Density (g/cm ³)	Volume Fraction (V _f)
1	1.61	0.56
2	1.60	0.54
3	1.65	0.58
4	1.60	0.52
5	1.62	0.54
Average:	1.62	0.55

Tensile properties of the hybrid composites

Results on the tensile loads response for different batch of FRP hybrid composites are presented in Table 3. Similar to that of volume fraction results, the results for ultimate tensile strength, strain and modulus are consistent and the average value for these properties are 447 MPa, 2.84% and 25.95 GPa, respectively. The tensile results of [CGCG] fiber arrangement in this research were compared with the results from previous study as depicted in Figure. 1. As expected, the [C] which is full carbon FRP composites from reference [6] have the highest tensile strength which is 511 MPa, whereas the average tensile strength of [CGCG] fibers arrangement is 447 MPa. In other words, there is a reduction of approximately 14% for tensile strength compared to that of full carbon FRP composites.

Table 3. Tensile properties for different batch of [CGCG] FRP hybrid specimens.

Batch No:	Tensile strength (MPa)	Ultimate strain (%)	Modulus (GPa)
1	442	2.58	28.55
2	468	2.98	23.93
3	448	2.96	25.25
4	424	2.76	26.21
5	454	2.93	25.82
Average :	447 (±19)	2.84 (±0.20)	25.95(±4.62)

With respect to the ultimate strain, it was found that the ultimate strain for the [CGCG] fiber arrangement is 2.84%, whereas for [C] is 1.36%. This result indicated that, there is a significant increase of tensile strain for hybrid composite [CGCG] compared to that of [C]. This is likely due to high elongation of glass fiber layer in the FRP hybrid composites which alleviate the crack of the low elongation carbon fiber. Hence, this allows the hybrid composites to reach their maximum ultimate strength. As mentioned earlier, VARTM method is capable to produce high volume fraction and low void composite panels than the hand lay-up method. Hence, the tensile strength and ultimate strain of [CGCG] hybrid composites which were fabricated by this process is higher than that of the hand lay-up [C₂G₃] hybrid composites from the previous study [6] as shown in Figure 1. Moreover, alternating stacking sequence for hybrid composites cause bridging effect between carbon and glass fiber in the hybrid composites, thus the [CGCG] fiber arrangement shown higher value in tension and elongation properties [4,11].

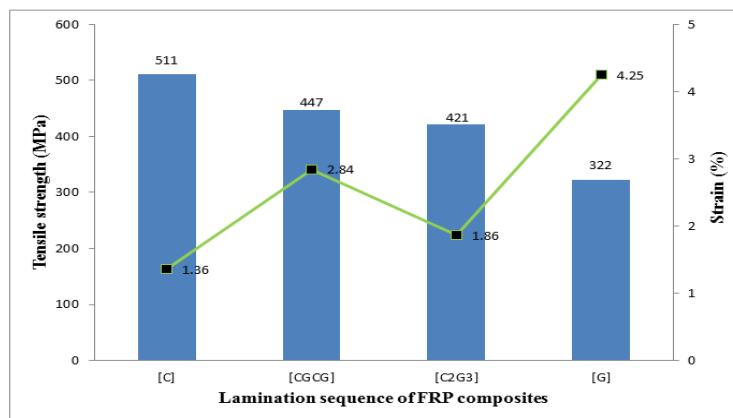


Fig. 1. Tensile responses for different lamination sequence of FRP composites.

Flexural properties of the hybrid composites

Flexural properties for five different batches of [CGCG] arrangements for FRP hybrid composites are shown in Table 4. In addition to that, the comparisons of flexural strength and strain for different lamination sequence are depicted in Figure 3. The average value of flexural strength, ultimate strain and modulus for five different batches of [CGCG] is 443 MPa, 2.03 %, 26.83 GPa, respectively. From Figure 2 shown the flexural results for [CGCG] in this study were higher than [CGCG]* that of previous study by [11] in which the composites were fabricated by hand lay-up method. Dong has concluded that in hybrid composites, high volume fraction of FRP composites will improve the flexural strength and modulus [8].

Table 4. Flexural properties for different batch of [CGCG] FRP hybrid specimens.

Batch No:	Flexural strength (MPa)	Ultimate strain (%)	Modulus (GPa)
1	451	1.98	28.47
2	438	2.12	25.83
3	447	2.03	27.52
4	449	1.93	23.26
5	434	2.09	29.08
Average :	443 (±19)	2.03 (±0.10)	26.83(±1.78)

Meanwhile, as depicted in Figure 2, the [C] composites had the highest flexural strength and lowest ultimate strain, which are 455 MPa and 1.69 % respectively. However, this is contrary to that of [G] composites, which are 218 MPa and 3% respectively. Based on literature review, placing carbon fiber in FRP composites can effectively increase the flexural properties of the material. Nevertheless, the result of this study found that the flexural strength of the [CGCG] was 443 MPa,

accounting a loss of only 2.7% of flexural strength for full carbon fiber [C] composites but gained a 103% of flexural strength for full glass fiber [G] composite.

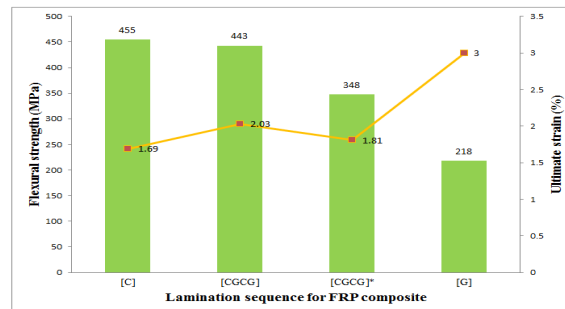


Fig. 2. Flexural responses for different lamination sequence of FRP composites.

Concluding remarks

Mechanical properties of [CGCG] FRP hybrid composite were compared with those of full carbon FRP composite [C], full glass FRP composite [G] and hybrid composites which is fabricated by hand lay-up method. The results shown that, VARTM is able to produce high fiber volume fraction of FRP hybrid composites than the previously employed method of hand lay-up. It is important to note that hybridization of glass and carbon fiber is effective method to increase the tensile and flexural strengths of full glass FRP composites. However, the result of this study also found that there is a loss of the tensile and flexural strain of FRP hybrid composite compare to that of full glass FRP composites. Nevertheless, it should be noted that the percentage gain in the tensile and flexural strengths for hybrid composite is significantly higher than the percentage loss in the ultimate strain.

References

- [1] Sandjay; K. Mazumdar, *COMPOSITES MANUFACTURING :Materials, Product, and Process Engineering*, vol. 92, no. 12. 2002, pp. 1334–6.
- [2] ASTM, “D3878-07 Standard Terminology for composite materials,” vol. 07, no. Reapproved 2013. ASTM International, West Conshohocken, PA, 2013.
- [3] P. W. S. ; S.C.Lakkad;, “Mechanical properties of carbon/glass fibre reinforced hybrids,” 1982.
- [4] G. Kretsis, “A review of the tensile , compress , ve , flexural and shear properties of hybrid fibre- reinforced plastics,” vol. 18, no. 1, pp. 13–23, 1987.
- [5] M. Ansar, W. Xinwei, and Z. Chouwei, “Modeling strategies of 3D woven composites: A review,” *Composite Structures*, vol. 93, no. 8, pp. 1947–1963, Jul. 2011.
- [6] K. S. Pandya, C. Veerajju, and N. K. Naik, “Hybrid composites made of carbon and glass woven fabrics under quasi-static loading,” *Materials & Design*, vol. 32, no. 7, pp. 4094–4099, Aug. 2011.
- [7] K. Palanikumar and R. Karthikeyan, “Optimal Machining Conditions for Turning of Particulate Metal Matrix Composites Using Taguchi and Response Surface Methodologies,” *Machining Science and Technology*, vol. 10, no. 4, pp. 417–433, Dec. 2006.
- [8] C. Dong and I. J. Davies, “Optimal design for the flexural behaviour of glass and carbon fibre reinforced polymer hybrid composites,” *Materials & Design*, vol. 37, pp. 450–457, May 2012.
- [9] T. M. Hermann, J. E. Locke, and K. K. Wetzel, “Fabrication , Testing , and Analysis of Anisotropic Carbon / Glass Hybrid Composites Volume 1 : Technical Report,” 2006.
- [10] A. I. Azmi, “Machinability Study of Fibre- Reinforced Polymer Matrix Composites,” University of Auckland, 2013.
- [11] J. Zhang, K. Chaisombat, S. He, and C. H. Wang, “Hybrid composite laminates reinforced with glass/carbon woven fabrics for lightweight load bearing structures,” *Materials & Design*, vol. 36, pp. 75–80, Apr. 2012.

Bioactivity Behavior of YSZ-Al₂O₃/10HAP Bioceramics Composites in Simulated Body Fluid

M.R.N. Liyana^{1, a*}, NurMaizatulShima Adzali^{2, b}, M.Z.M. Zamzuri^{1, c}

¹Schools of Manufacturing Engineering, University Malaysia Perlis (UNIMAP)

²Schools of Materials Engineering, University Malaysia Perlis (UNIMAP)

^{a*}nurliyana.rosli13@gmail.com, ^bshima@unimap.edu.my, ^cmzamzuri@unimap.edu.my

Keyword: Bioactivity, Bioceramics, Simulated Body Fluid, Apatite

Abstract. Yttria-stabilized zirconia and alumina made significant contributions to the development of health care industry, specifically as orthopedic and dental materials. Both bioceramics are nearly inert ceramics, as they do not allow the interfacial bonding with tissue. Thus, it is necessary to provide bioactive surrounding as to elicit a specific biological response at the interface of material. This research reported the microstructure and bioactivity behavior of YSZ-Al₂O₃/10HAP with 30 wt. % and 60 wt. % of YSZ content. Powders were mixed before being compacted at 225MPa using uni-axial press machine. The composites were sintered at 1200°C with heating rate of 10°C/min. In-vitro bioactivity behavior of the composites were evaluated by immersing the composites into simulated body fluid. Results from x-ray diffraction pattern, confirmed the phase formation of apatite by the presence of Ca₂P₂O₇, and CaO that might be useful on implant cell interaction in a body environment. The apatite formation was observed on the surfaces of the composites by SEM only after 9 days of immersion and subsequently apatite nucleation increased with prolonging immersion time. The dynamic changes in pH, between ion concentration in SBF and bioceramics surfaces corresponded with an immersion time. Up to 30 days of immersion, the pH value of SBF stabilized approximately around pH 7.4 -7.6, similar to the human blood plasma. Formation of apatite on composites surface of prepared YSZ-Al₂O₃/10HAP bioceramics may contribute to the improved biocompatibility and osteoconductivity.

Introduction

Bioceramics have evolved to repair and reconstruct bones and teeth, and to augment both hard and soft tissue [1]. Hydroxyapatite (Ca₁₀(PO₄)₆(OH)₂) (HAP) and calcium phosphate (Ca₂P₂O₇) exhibit excellent bioactivity that induce bone tissue growth after implantation because of its own similar chemical and mineralogical composition structure to apatite human body living bone [2]. Nearly inert ceramics attached to bone growth such as Alumina (Al₂O₃) and Zirconia (ZrO₂) are materials that are essentially stable with little or no tissue reactivity when implanted within the living organism [3]. These bio-inert materials are being deposited on the bioactive hydroxyapatite and used as recovery part of human skeletal system. In contrast, metals possess poor biocompatibility through extremely exposure to corrosion due to chemical reaction with the body enzymes and acids. The substances released may contribute to cytotoxic effect on human body. The weakness of these metal elements in human bodies may cause some diseases. A firm bonding between metal implant and surrounding tissue is a crucial consideration to avoid the aseptic loosening, that result of implant failure which requires secondary operation [4]. As a result, recent developments of bioceramics research are primarily used as alternatives to metals.

Most of the researchers are working on development of excellent bioceramics for hard tissue replacements, with the primary attention on bone bonding ability in human body with the materials. Kokubo and colleagues have established an immersion technique in SBF solution as in-vitro simulations of in-vivo surroundings [5]. The number of animals needed for in-vivo evaluation can be reduced significantly as it will cause an expensive experimental procedure [6]. Thus, the study will focus on improving the bioactivity behavior of HAP by the addition of bio-inert materials

(YSZ-Al₂O₃). The bone bonding mechanism is evaluated by an apatite layer formation on surface of the living body through the simulated body fluid (SBF).

Materials and Experimental

In this research, commercially available 3mol% yttria stabilized zirconia (YSZ), α -alumina (Al₂O₃) and hydroxyapatite (HAP) powders were used as starting materials. The composite was fabricated by blending, pressing and sintering. All powders were mixed up with different weight proportions of YSZ (30 and 60 wt. %) and Al₂O₃, respectively using 3D shaker for 20 minutes at 97 rpm. The green composites had been compacted using uni-axial press machine with 225 MPa compaction pressure to form cylindrical shape in size of 13mm x 13mm. The samples were sintered at 1200°C sintering temperature with the heating rate of 10°C/min. In order to evaluate the bioactivity behavior of YSZ-Al₂O₃/10HAP composites, in-vitro test was carried out in a simulated body fluid (SBF). SBF solutions were prepared accordingly by dissolving an appropriate reagent grade of chemicals in ultra-pure water using the technique established by Kokubo et al. [7]. The entire sample had been submerged in the SBF solutions. After soaking at 37°C on different days within 30 days in SBF, the sample had been taken out from the SBF solution and gently washed with the ultra-pure water. The sample must be dried in a desiccator without heating [8]. The phase analysis of the bioceramics composites after an immersion in SBF for various periods, was determined by Shimadzu 6000 X-ray diffractometer (XRD) to confirm the presence of chemical element of apatite formation. The surface morphologies of composites were observed using Hitachi TM3000 Scanning Electron Microscopy (SEM) in order to capture the apatite formed on the surface after immersion. The changes in pH of SBF medium were measured at pre-determined time intervals using Hanna Checker HI-98103 pH meter. The pH measurement is very important to evaluate chemical stability and biological activity on the basis of pH changes with the time immersion in SBF which was equivalent to the human blood plasma [9].

Results and Discussion

The bioceramics has been examined after immersion in SBF solution for 30 days by x-ray diffraction (XRD). The XRD patterns after immersing in SBF were shown in Figure 1, the diffraction peak of calcium phosphate (Ca₂P₂O₇), acknowledged as an intermediate phase was detected during the formation of apatite [10]. The crystal growth in SBF was attributed to the released calcium ions by dissolution in surrounding area of immersion. Thus, it is obviously seen that all samples released greater amount of calcium ions due to the increasing of calcium oxide (CaO) content and hence deposited an apatite nucleation on the surface of samples. The formation of CaO phase (which had been detected by XRD as shown in Figure 1) would react with H₂O from SBF and formed OH⁻, as shown in Equation 2, which lead to the increased in pH value of SBF.



SEM micrographs of 30 and 60 wt. % YSZ-Al₂O₃/10HAP composites after being immersed in SBF for 9 days and 30 days were displayed as a comparison in Figure 2. The white precipitation or also known as apatite was not clearly revealed by SEM micrographs after 9 days of immersion, as in Figure 2 (a-b). The increased of agglomerated precipitation which was caused by the formation of apatite can be seen on the surface of composite after 30 days of immersion. The observations were similarly reported by some researcher that apatite forming ability take place on the surface with the increasing of immersion time in SBF solution at the ideal body condition around 37°C and pH of 7.4 [10,11]. As a result, the surrounding bone may contact directly with the apatite layer of bioceramics and thus has tight chemical bond with each other [13].

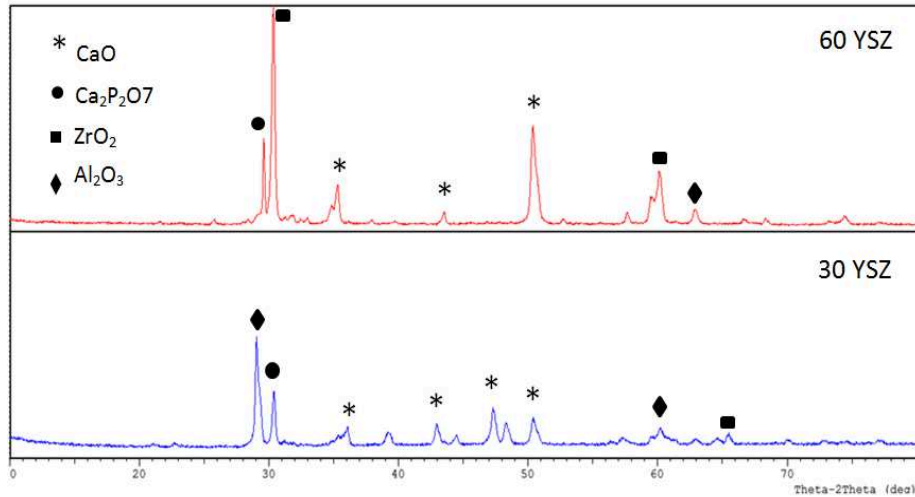


Figure 1: X-ray diffraction patterns of YSZ- Al_2O_3 /10HAP surfaces immersed in 30 days

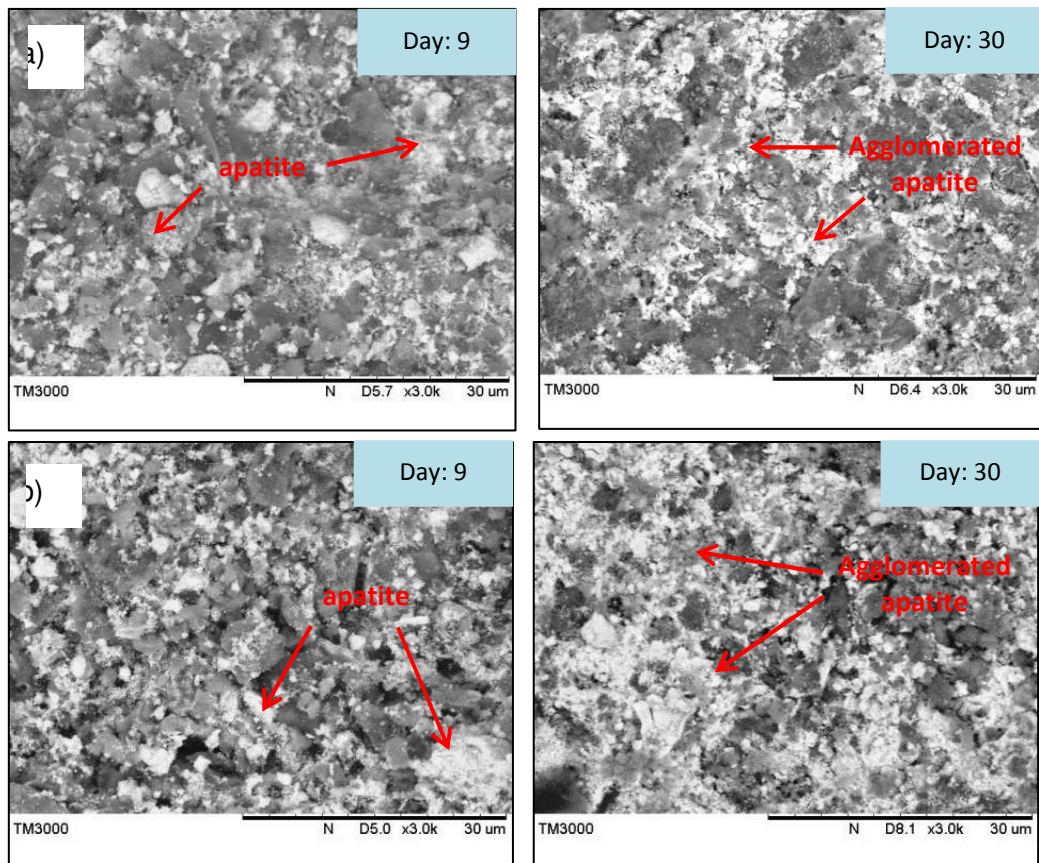


Figure 2: Scanning electron microscope image of YSZ- Al_2O_3 /10HAP composite after immersion of SBF solution on 9th and 30th days of immersion: (a) 30 wt. % YSZ (b) 60 wt. % YSZ

Analysis on pH was evaluated to investigate the chemical stability of atmosphere on composite immersed in SBF solution. Figure 3 showed the influences of the immersion time for (0 day – 30 days) on the pH value of SBF of YSZ- Al_2O_3 /10HAP composites. The data was collected up to 30 days with periodic interval of 3 days. Initially, the pH of prepared SBF solution was 7.4. On the first three days, the pH value of SBF for 30 and 60 wt. % YSZ- Al_2O_3 /10HAP of composites was increased extremely up to pH of 9.94, and 9.68, respectively.

However, with the further prolonging immersion time, the pH decreased gradually. After immersion for 30 days, the observed pH value of SBF solution was stabilized and its value was

approximately around 7.4 - 7.6 which was equivalent to the human blood plasma. Results showed a very strong correlation between the number of days of immersion and pH value. After certain days of immersion, the pH for all samples in SBF solution decrease gradually and stabilized within the timeframe of 14-28 days[2,14].

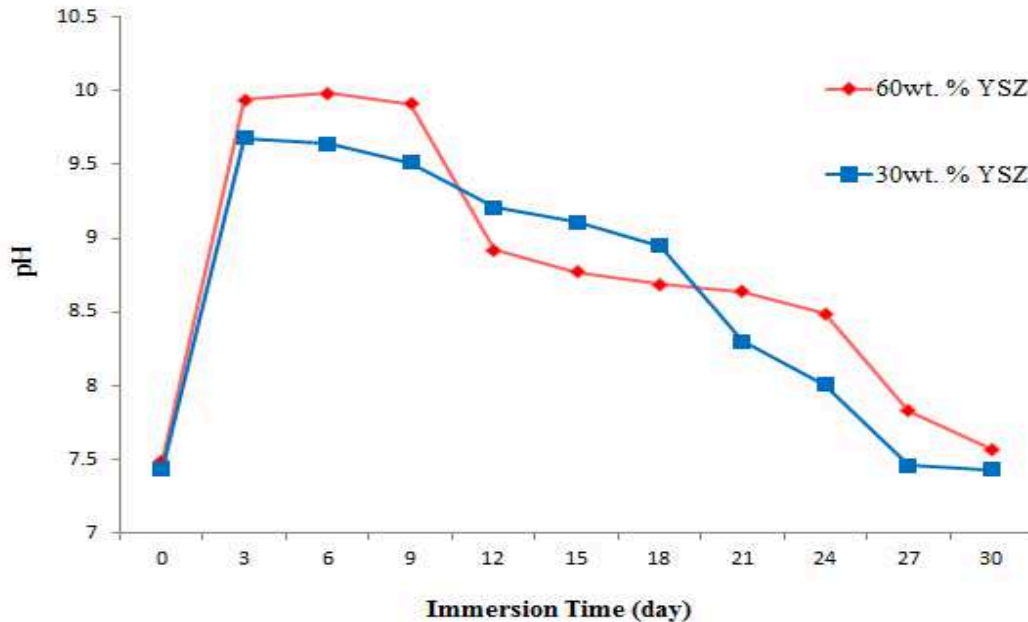


Figure 3: The effect of immersion time of YSZ-Al₂O₃/10HAP composite in SBF on pH value of SBF

Conclusion

The present study of bioactivity behavior of YSZ-Al₂O₃/10HAP composites resulted in high biocompatibility bioceramics. This statement was demonstrated by the formation of apatite recognized by the presence of Ca₂P₂O₇, and CaO that might be useful on implant cell interaction in a body environment. Meanwhile, excellent in-vitro activity of surface YSZ-Al₂O₃/10HAP composites had been observed by SEM micrographs through the formation of apatite nucleation. The change in pH of SBF solution was recorded and it was noticed that the pH of SBF increase correspondingly with the immersion time. After immersion for 30 days, the observed pH value of SBF solution approximately around 7.4 - 7.6 which was equivalent to the human blood plasma.

References

- [1] L. L. Hench and J. Wilson, "An Introduction to Bioceramics," 2013.
- [2] X. Fan, J. Chen, J. Zou, Q. Wan, Z. Zhou, and J. Ruan, "Bone-like apatite formation on HA/316L stainless steel composite surface in simulated body fluid," *Trans. Nonferrous Met. Soc. China*, vol. 19, no. 2, pp. 347–352, Apr. 2009.
- [3] S. Bettuzzi, "Biomaterials," *Adv. Cancer Res.*, vol. 104, pp. 1–8, Jan. 2009.
- [4] K. Y. Ling Ren, "Bio-functional Design for Metal Implants, a New Concept for Development of Metallic Biomaterials," *J. Mater. Sci. Technol.*, 2013.
- [5] T. Kokubo, "Apatite formation on surfaces of ceramics, metals and polymers in body environment," *Acta Mater.*, vol. 46, no. 1, 1998.

-
- [6] C. Wu and Y. Xiao, "Bone and Tissue Regeneration Insights Evaluation of the In Vitro Bioactivity of Bioceramics," *Bone tissue Regen. insights*, pp. 25–29, 2009.
- [7] M. Nakamura, M. Inuzuka, K. Hashimoto, A. Nagai, and K. Yamashita, "Polarized Yttria-Stabilized Zirconia Improves Durability for Degradation and Apatite Formation in Simulated Body Fluid," *Phosphorus Res. Bull.*, vol. 26, pp. 77–80, 2012.
- [8] Tadashi Kokubo & Hiroaki Takadama, "How useful is SBF in predicting in vivo bone bioactivity?," *Biomater.* 27 2907-2915, MAY 2006, 2010.
- [9] A. Sobczak-Kupiec, Z. Wzorek, R. Kijkowska, and Z. Kowalski, "Effect of calcination conditions of pork bone sludge on behaviour of hydroxyapatite in simulated body fluid," *Bull. Mater. Sci.*, vol. 36, no. 4, pp. 755–764, Aug. 2013.
- [10] Y. Cai, S. Zhang, X. Zeng, Y. Wang, M. Qian, and W. Weng, "Improvement of bioactivity with magnesium and fluorine ions incorporated hydroxyapatite coatings via sol–gel deposition on Ti6Al4V alloys," *Thin Solid Films*, vol. 517, no. 17, pp. 5347–5351, Jul. 2009.
- [11] A. Singh, "Hydroxyapatite, a biomaterial: Its chemical synthesis, characterization and study of biocompatibility prepared from shell of garden snail, *Helix aspersa*," *Bull. Mater. Sci.*, vol. 35, no. 6, pp. 1031–1038, Dec. 2012.
- [12] K. Y. Msahiro Inuzuka, Satoshi Nakamura, Shigeki Kishi, Katsumi Yoshida, Kazuaki Hashimoto, Yoshitomo Toda, "Effect of Hydroxyapatite dopant to Yttria Stabilized Zirconia Ceramics for biomedical application," *Phosphorus Research Bulletin*, vol. 16, pp. 75–82, 2003.
- [13] T. Kokubo and H. Takadama, "How useful is SBF in predicting in vivo bone bioactivity?," *Biomaterials*, vol. 27, no. 15, pp. 2907–15, May 2006.
- [14] A. Priya, S. Nath, K. Biswas, and B. Basu, "In vitro dissolution of calcium phosphate-mullite composite in simulated body fluid.," *J. Mater. Sci. Mater. Med.*, vol. 21, no. 6, pp. 1817–28, Jun. 2010.

Water Absorbency Properties of OPEFB Filled Hydrogels Composites

NURUL EKMI RABAT^{1,a}, SHAHRIR HASHIM^{1,b} and Rohah A. Majid^{1,c}

¹Department of Polymer Engineering, Faculty of Chemical Engineering, Universiti Teknologi Malaysia, 81310 Skudai, Johor, Malaysia

^anekmi2@live.utm.my, ^bshahrir@cheme.utm.my, ^crohah@cheme.utm.my

Keywords: hydrogel composite; oil palm empty fruit bunch fiber; scanning electron microscopy; water absorbency properties; in-situ polymerization.

Abstract. For slow release fertilizer application, oil palm empty fruit bunch-*grafted*-poly(acrylic acid-co-acrylamide) [OPEFB-*g*-P(AA-co-AAm)] hydrogel composites were synthesized via two techniques; Two Steps (T1) and *in-situ* (T2). Scanning electron microscopy of hydrogel composite T1 has higher surface area and holes while hydrogel T2 displays smoother and tighter surface. Water absorbency capacity of hydrogel T1 is 42.90 gram/gram (g/g) and hydrogel T2 is 39.96 g/g. WAC of hydrogel T2 has much better re-swelling ability compared to T1 after it went through five cycles of drying-swelling-drying process. Hence, T2 has produced a hydrogel composite that is reusable with great morphology properties.

Introduction

Hydrogel is a loosely crosslinked three dimensional networks of hydrophilic monomer with the ability to absorb great amount of water and retains more than 20% of water within its structure without being dissolve in it [1]. The combination of hydrogel and fertilizer as slow release fertilizer hydrogel (SRFH) has became one of the promising materials to overcome the shortcomings of conventional fertilizer by greatly improving the nutrition of plants, decreasing fertilizer loss rate, alleviating environmental impact from water-soluble fertilizer, supplying nutrients sustainably, lowering frequency of irrigation, and minimizing the potential negative effects associated with unused fertilizer [2-4]. Two series of OPEFB-*g*-P(AA-co-AAm) hydrogel composites were prepared via two different techniques namely Two Steps (T1) and *in-situ* (T2).

T1 was performed by allowing the dry hydrogel to swell in urea liquid at ambient temperature and the swollen hydrogel was dried in an oven at 70°C for the final drying stage after the equilibrium swelling had reached. For T2, all materials including monomer and fertilizer were added into the reaction mixture and polymerized *in-situ* whereby the fertilizer can be entrapped within the gel matrix. In our previous research Rabat *et.al* (2014), agricultural applications have been determined from both samples and *in-situ* technique produced an excellent hydrogel composite as slow release fertilizer [5]. Swelling kinetic of hydrogel composites is greatly influenced by varieties of feature such as the composition of the hydrogel, the particle size, and the surface area.

Experimental

Materials. Acrylamide (AAm), acrylic acid (AA), sodium hydroxide, urea fertilizer (diluted to 1%), ammonium persulphate (APS) and N’N-Methylenebisacrylamide (NMBA) were purchased from Merck (M) Sdn. Bhd. and OPEFB fiber from Sabutek (M) Sdn. Bhd., Perak, Malaysia.

Two Steps Technique (T1). 1.7 wt% NMBA, 0.8 wt% APS and water were added into a flask containing OPEFB and monomer. Dissolved oxygen emerged from the reaction was constantly removed by nitrogen gas. After hydrogel has formed, it was then filtered and washed with distilled water and oven-dried at 70°C. The dried hydrogel composite was submerged into urea solution for 24 hours. The urea-filled OPEFB-*g*-P(AA-co-AAm) hydrogel composite was dried again in oven at 70°C for 24 hours.

In-situ Technique (T2). Urea solution was added into the flask containing OPEFB and monomer. 1.7 wt% NMBA and 0.8 wt% APS were added 30 minutes later. Temperature was strictly controlled to eliminate the possibility of biuret's formation. After the copolymerization process finished, the OPEFB-g-P(AA-co-AAm) hydrogel composite were filtered, washed and dried in oven at 70°C.

Scanning Electron Microscopy (SEM). SEM was employed to study the morphology of hydrogel composites. SEM images were observed using Hitachi SU1510 SEM Acc Voltage: 10kVS instrument. Before the SEM observation, a small amount of sample was placed on the copper stub and sputter-coated with a thin layer of platinum to avoid electrostatic charging during the examination.

Water Absorbency Capacity (WAC). WAC is most crucial property of hydrogel. 2g of dried hydrogel composite sample (W_1) was immersed in 200ml of distilled water. The water and sample were then allowed to mix for 24 hours. After that, the swollen sample (W_2) was filtrated for 15 minutes. The WAC of hydrogel composite can be calculated using Eq.1:

$$WAC = (W_1 - W_2) / W_1 \quad (1)$$

Reswelling Ability of Hydrogel Composite. 2g of hydrogel composite was immersed in 200ml of distilled water for 24 hours. The swollen samples were placed in an oven at 70°C for 24 hours. The weights of dried and swollen samples were taken to calculate the WAC using Eq.1. 200ml of water was added to the dried samples and dried in the oven again. Similar procedure was repeated and then WAC of the sample for five cycles of swell-dry-swallow obtained [6].

Result and Discussion

Scanning Electron Microscopy (SEM). The SEM micrographs of hydrogel composite T1 and hydrogel composite T2 were shown in Fig.1. Hydrogel composite made from T1 has irregular porous structures. These structures caused increment in the surface area of hydrogel composite T1. In water, the fluid easily diffuses into the hydrogel mass through the gaps of the structures led to substantially increasing of water absorbency capacity.

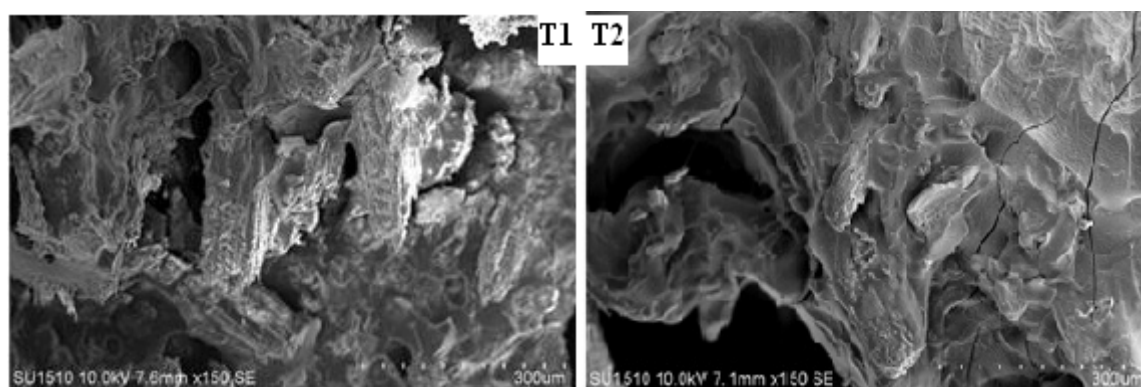


Fig.1: SEM micrographs of OPEFB-g-P(AA-co-AAm) hydrogel composite T1 and T2

The structure porosity is originated from synthesis stages. The structure might be introduced into the hydrogel by two steps of drying process. As a result, some of the crosslinking density was destroyed from the reaction mixture. This coarse surface of hydrogel composite T1 has facilitated the permeation of water into the polymeric network. Comparatively, SEM micrograph of hydrogel composite T2 has less porosity. Besides, it displays a much smoother and tight surface between fiber and hydrogel. This structure prevents water to be diffuse into the hydrogel composite. Although the common method for producing slow release fertilizer hydrogel is T1, these images verify that the graft copolymers made from T2 have also porous structures. The same observations were recorded by

Teodorescu et.al (2009) where slow-release agrochemical based on crosslinked PAA hydrogels was produced via T2 [7].

Water Absorbency Capacity (WAC). The effect of two preparation techniques on WAC of OPEFB-*g*-P(AA-co-AAm) hydrogel composite is shown in Fig.2. The figure shows the WAC of OPEFB-*g*-P(AA-co-AAm) hydrogel prepared via T1 is always higher than OPEFB-*g*-P(AA-co-AAm) hydrogel composite prepared via T2 in tap, distilled and rain water. According to Donnan equilibrium theory, osmotic pressure is the driving force for swelling of the hydrogel composite. In tap water and rain water, the osmotic pressure difference between the polymeric network and the external solution decreases, resulting in the decrease of the water absorbency in hydrogel composite made from both techniques.

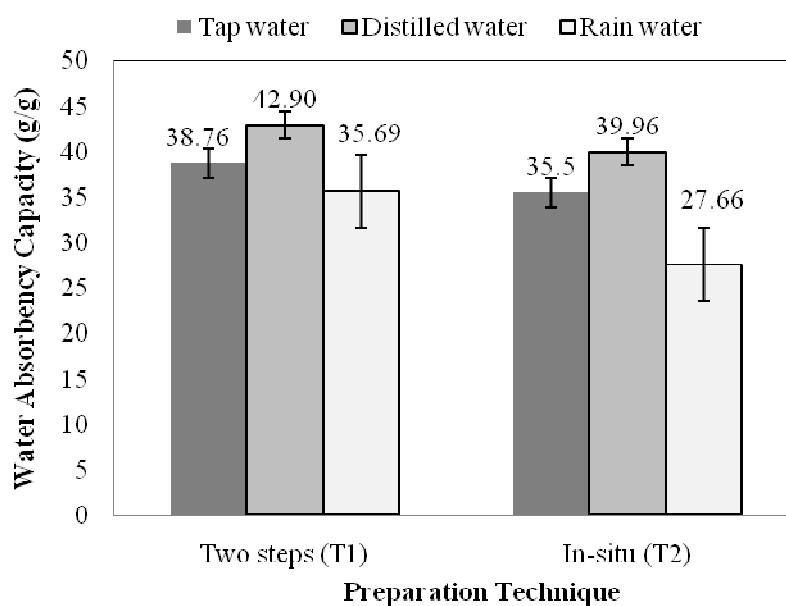


Fig.2: Water absorbency capacity of OPEFB-*g*-P(AA-co-AAm) produced by T1 and T2

Hydrogel composite T1 has better WAC compared to hydrogel composite T2 because of the two swelling processes of T1 has destroyed some crosslinking density inside hydrogel composite's structure. Possibly, some fractions of the hydrogel composite dissolved during swelling in urea and swelling in water. If the polymer network operates only as a barrier against diffusing water, less water molecules will diffuse to the highly crosslinked network. When the hydrogel composite T1 went through swelling, drying, and swelled in urea solution, the crosslinking density was slowly loosen and dissolved in water. On the other hand, a hydrogel composite T2 has only one swelling process and has higher amount of crosslinking density. Noticeable point in hydrogel composite T2 is the swelling of the sample without crosslinker or self-crosslinking that happened when the existence of the large heat evolved from the exothermic polymerization. The active chains of AA end through hydrogen abstraction producing new active centers on the polymer backbones, as a result the newly formed free radicals may recombine either with similar macroradicals or with monomers [8] and imide formation between neighbouring amide units can also caused the self crosslinked networks of AAm [9]. The same result can also be observed by their physical size difference before and after absorbency process as photographed in Fig.3. Hydrogel composite T1 has lighter color corresponding to high extension of gel while in hydrogel composite T2 had darker color indicating the tight crosslinking between gel and fiber.

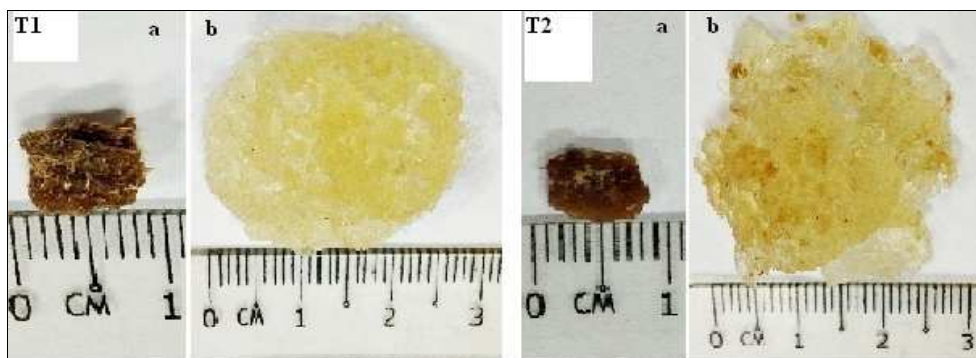


Fig.3: The size difference of OPEFB-g-P(AA-co-AAm) T1: a) dried b) swollen and T2: a) dried b) swollen

Re-swelling Ability of Hydrogel Composite. Reswelling ability is a one of vital features in hydrogel composite together with equilibrium water absorbency and swelling rate. Fig.4 demonstrates the reswelling behaviours of the OPEFFB-g-P(AA-co-AAm) hydrogel composite made using two different techniques in distilled water at ambient temperature as a function of WAC versus reswelling time (cycle). One cycle equals to 24 hours swelling process in distilled water and 24 hours for drying process in 70⁰C in oven. The WAC of hydrogel composite s made using both techniques have increased at 2nd cycle and started to decrease after 3rd cycle. The increasing trend might be related to crosslinking density of hydrogel composite that works as barrier against diffusing water. The crosslink density inside hydrogel composite structure was too high and makes the hydrogel composite network to become close with each other. Hence, there were not enough hydrodynamic free places to accommodate the water molecules uptake. When the crosslinking density has been lessen at 2nd cycle, water uptake started to increase.

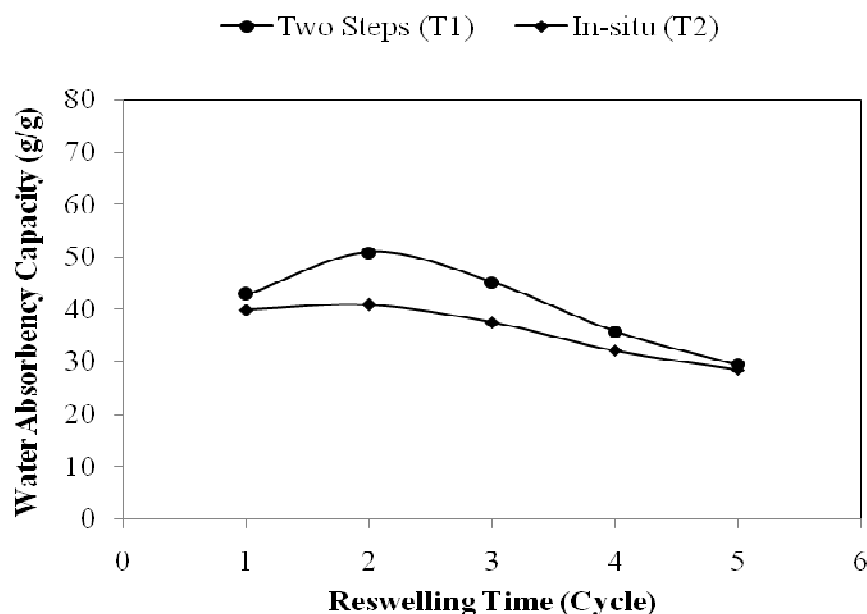


Fig.4: Reswelling ability of hydrogel composites prepared by two techniques

However, after 3rd cycle, the WAC started to decrease. This happened because of the gel content in hydrogel composite was loss during swelling-heating-swelling cycle. Some of the ungrafted OPEFB might also loss during washing process, especially in hydrogel composite T1. As shown in SEM images, the OPEFB fiber was not perfectly attached after going through two steps of drying. While T2 has only one step of drying, the grafting between gel and OPEFB fiber is much stronger hence, preventing OPEFB to be easily removed. Furthermore, WAC of hydrogel composite made from T2 decrease slower than that in T1 as T2's different percentage from 1st cycle to 5th cycle is 28.68% while

hydrogel composite made from T1's different percentage is 31.96%. Thus, T2 has much better reswelling ability compared to T1.

Summary

Two series of OPEFB-*g*-P(AA-co-AAm) hydrogel composite were prepared via Two Steps (T1) and *in-situ* (T2). WAC of hydrogel composite T1 was higher than hydrogel composite T2 possibly because of the two swelling-drying processes of T1 has destroyed some crosslinking density inside hydrogel composite's structure. SEM micrograph showed that hydrogel composite T1 has higher surface area and holes while hydrogel composite T2 displays a much smoother and tight surface, limiting the intake of water. However, after went through five times drying-swelling process in reswelling test for reusability purposes, hydrogel composite T2 has much better reswelling ability compared to hydrogel composite T1.

Acknowledgements

Great appreciations offered to Universiti Teknologi Malaysia (UTM) and Ministry of Higher Education, Malaysia (MOHE) under the research Vot. No. R.J130000.7844.4L143 for the supports and funding.

References

- [1] K. Kabiri, H. Omidian, M.J. Zohuriaan-Mehr and S. Doroudiani, Superabsorbent Hydrogel Composites and Nanocomposites: A Review, *Pol. Comp.* (2011)
- [2] R. Liang, H. Yuan, G. Xi and Q. Zhou, Synthesis of wheat straw-*g*-poly(acrylic acid) superabsorbent composites and release of urea from it, *Carb. Pol.* (2009) 1-7.
- [3] L. Xie, M. Liu, B. Ni, X. Zhang and Y. Wang, Slow-release nitrogen and boron fertilizer from a functional superabsorbent formulation based on wheat straw and attapulgite, *Chem. Eng. J.* 167 (2011) 342–348.
- [4] H.X. Sheng, L.Z. Wen, H.P. Zhao, D.J. Xian, G.R. Shan, L.H. Bo and G.Z. Chao, Characteristics and performance of novel water absorbent slow release nitrogen fertilizers, *Agri. Sci. in China.* 6 (2007) 338-346.
- [5] N.E. Rabat, S. Hashim and R.A. Majid, Effect of oil palm empty fruit bunch-*grafted*-poly(acrylic acid-co-acrylamide) hydrogel preparations on plant growth performance, *Adv. Mat. Eng. and Tech. II.* 236 (2014) 594-595.
- [6] J. Zhang and A. Wang, Study on superabsorbent composites. IX: synthesis, characterization and swelling behaviors of polyacrylamide/clay composites based on various clays, *React. & Func. Pol.* 67 (2007) 737–745.
- [7] M. Teodorescu, A. Lungu, P.O. Stanescu and C. Neamt, Preparation and properties of novel slow-release NPK agrochemical formulations based on poly(acrylic acid) hydrogels and liquid fertilizers, *Ind. & Eng. Chem. Res.* 48 (2009) 6527–6534.
- [8] K. Kabiri, H. Omidian, S.A. Hashemi and M.J. Zohuriaan-Mehr, Synthesis of fast-swelling superabsorbent hydrogels: effect of crosslinker type and concentration on porosity and absorption rate, *Euro. Pol. J.* 29 (2003) 1341–1348.
- [9] N. Bicak, B.F. Senkal and M. Gazi, Hydrogels prepared by crosslinking copolymerization of N-allyl maleamic acid with acrylamide and acrylic acid, *Des. Mono. and Pol.* 7 (2004) 261–267.

Oil Palm Fibre and Nano-Silica Reinforced Epoxy Composite Material

Ng Samuel¹, D. Sujan^{1a*}, M. E. Rahman^{1b}, O. Nabinejad^{1c} and M. M. Reddy^{1d}

¹School of Engineering & Science, Curtin University Sarawak, CDT 250, 98009, Miri, Malaysia

^ad.sujan@curtin.edu.my; ^bmerahman@curtin.edu.my; ^comid.nabinejad@gmail.com;

^dmohan.m@curtin.edu.my

Keywords: Composite material, Epoxy, Nano Silicon Carbide, Oil palm fibres, Tensile strength

Abstract: This paper presents a study on tensile properties of Nano Silicon Carbide (n-SiC) and oil palm fibre (OPF) reinforced epoxy composites. The dosage of n-SiC and OPF are limited to 0%, 1%, 3% & 5% by mass of the total epoxy material. As a part of the research, experimental study is carried out on n-SiC and OPF based epoxy composites to investigate the tensile strength of the composite material. The utilization of 1% n-SiC & 1% treated OPF shows an improvement in tensile strength compared to the pure epoxy. The experimental results are also compared with 3-D finite element analysis results and a good agreement is observed between the experimental and the finite element results.

Introduction

Nowadays, most of the polymer composites are reinforced with synthetic fibres just to enhance its mechanical properties [1, 2]. The most commonly used synthetic fibres are Carbon and Glass fibres [3-8]. Synthetic fibres can be advantageous to improve the properties of polymer composites. However it also has some disadvantages for instance its high energy consumption during the manufacturing process and its non-biodegradable behaviour that can bring negative impacts to the Mother Nature [9]. Synthetic fibres for polymer composite are deliberately manipulated in such a way just to ensure that it possess excellent properties and will not break down easily within a reasonable amount of time [10]. As the demand of plastic has been highly increasing every year, it continues to raise concern on the Carbon footprint that caused by non-biodegradable plastic. Therefore, it is utmost important for engineers take drastic measures and research to address a solution to stop further deterioration of the environment. Such effort has been dedicated to investigating these future materials, with the aim to create environmental friendly material with unique mechanical properties and performance. For example the material has to be low density, low cost and mechanical properties that are comparable to synthetic fibres. Currently, the researchers are interested in the implementation of biopolymers. Biopolymers are the polymers that produced by living organisms [11, 12, 13]. It is biodegradable non-petroleum based polymer that can be decomposed easily in a short amount of time.

In this research, a study is carried out on tensile properties of Nano Silicon Carbide (n-SiC) and oil palm fibre (OPF) reinforced epoxy composites. The role of n-SiC and alkaline treated OPF is to enhance the mechanical properties of the composite material.

Materials and Methods

Materials. Oil palm cellulose fibres were used as reinforcements and general purpose low viscosity epoxy resin (FR-251) was used as the matrix. Oil palm cellulose fibres purchased from the market are normally in packet with loads of dirt such as shell, nuts and stones. Therefore in order to filter out all the unwanted particles, sieve shaker was used in this process. The purpose of Sieve shaker is to filter out all the unwanted particles and also divides the fibres into each different size. The average length of oil palm fibre used in this research is around 15mm. Before sieving, the fibres were pre-dried in the oven for 30 minutes at 50°C to make it dry. After the pre-dried process, the oil palm cellulose fibres were poured into the sieve shaker for sieving process. As for the n-SiC particles, it was pre dried at

60°C for 40 minutes. As for alkaline treated fibres, the fibres were immersed in 5% concentrated Sodium hydroxide (NaOH) solution for 48 hours at room temperature. Subsequently the alkalized oil palm cellulose fibres were washed off with distilled water, followed by neutralization process with 10% concentration of acetic acid solution. Finally the alkalized fibres were heated in a furnace oven at 30°C for around 8 hours for drying. Isophorone Diamine was used as the hardener in this fabrication.

Fabrication.

Epoxy reinforced with oil palm fibre (OPF). 1 wt% of the fibre was first weighted using a weighting disc and placed inside the mold. The required epoxy was then placed in a 25ml beaker. The amount of 10wt% of hardener was weighted and prepared in a 5ml measuring cylinder. The hardener was then mixed with the epoxy inside the beaker. The mixture was gently disturbed to prevent any air bubble trap and placed inside the mold. The mixture was then left for around 24 hours for curing before removing it from the mold. The processes are repeated for 1wt%, 3wt% and 5wt% of the untreated and treated fibres.

Epoxy reinforced Oil Palm Fibre and Nano Silicon Carbide. 5wt% of the treated fibre was first weighted and distributed evenly in the mold. The epoxy was then prepared and placed in the 25ml beaker. 1wt% n-SiC was weighted using weighing paper and mixed comprehensively with epoxy into the beaker. Subsequently 10wt% of the hardener was weighted and mixed inside the content of the beaker gently before pouring it into the mold. Finally the mixture was left for 24 hours for curing before removing it from the mold. The experiment was repeated for 3wt% and 5wt% of n-SiC.

3-D Finite Element Modeling. Three-dimensional finite element models allow the analyst to account accurately for the extent and geometry of each of these constituents in constructing a representative numerical model of a composite material. Finite element software was used to construct the model and three-dimensional eight noded elements were used to replicate the composite material. Linear elastic material parameters were used to represent the composite material properties. The 3-D finite element model is shown in Fig. 1.

Results and Discussions

Effect of EPF Fibre Reinforced in Epoxy Matrix. The experimental results and finite element results are presented in Table 1. Based on the results, the 1% reinforcement of treated OPF in epoxy matrix increased the ultimate tensile strength (UTS) from 16.59MPa to 21.20MPa, a significant increment of 27.79%. However, further addition of oil palm fibre in the matrix reduced the UTS of the composites. This is due to the fibre entanglement or poor distribution of fibres at higher fibre loading condition. Table 1 also shows that the treated fibre by 5% had resulted much lower UTS compared to pure epoxy possibly due to the poor distribution of fibre in the matrix where fibre entanglement occurred which resulted a reduction in the surface area of fibre to epoxy. The similar effect was also reported by [14].

In comparison between treated and untreated oil palm fibre reinforced epoxy composites, it is shown that the treated oil palm fibre showed a significant higher ultimate tensile strength compared to the untreated oil palm fibre. For instance from Table 1, epoxy reinforced with 3% untreated fibres shows an ultimate tensile strength of 14.67MPa while epoxy reinforced with 3% treated fibres yielded an increased ultimate tensile strength of 17.06MPa, a significant improvement by 16.29%. From the microstructure analysis of the composites, it can be observed from Fig.2 that there are fibre pull out for untreated fibres during fracture. This is associated with the fibre debonding caused by the poor adhesion or bonding between the oil palm fibre and the epoxy matrix. As a result the fibre pullout created voids in the matrix. While for the treated fibre reinforced epoxy, the fibres are well within the epoxy matrix.

It can be explained that the alkaline treatment removes a portion of lignin, hemicelluloses, pectin, wax and oil and increases the rough surface topography for better adhesion. Moreover, the alkaline

treatment increases the aspect ratio of oil palm fibre. Aspect ratio, defined as the ratio of length and diameter, significantly contributes to the effectiveness of fibre as reinforcement in composites due to the increasing strength of composites with increasing aspect ratio. The range of diameter of oil palm fibre is 150 μm to 500 μm [33]. Aspect ratios of 20-60 are generally categorized as short fibre while aspect ratios of 200-500 are categorized as long fibres. In this research, aspect ratio of oil palm fibre is calculated to be in the range of 30 to 100 which can be categorized as short fibre or discontinuous fibre. The alkaline treated oil palm fibre is seen to be finer in diameter compared to untreated oil palm fibre due to removal of micro voids that reduces fibre diameter.

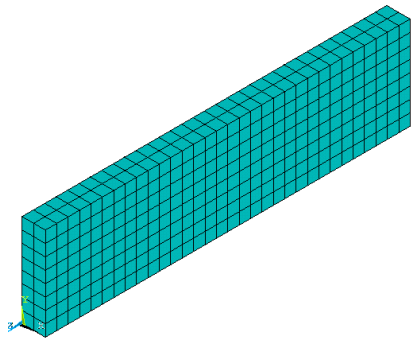


Fig. 1: 3-D Finite Element Model



Fig. 2: Tensile failure of 3% untreated fiber reinforced in the epoxy matrix

Therefore, from the observation, it is agreeable that alkaline treatment can significantly reduce the diameter of oil palm fibre and hence improve the aspect ratio. This subsequently contributes to the improvement of the effective fibre surface area for good adhesion with the matrix. However, usage of alkaline treatment must be monitored carefully as the high concentration of alkali treatment over optimum condition may cause delignification and consequently reduces the strength of fibre. Strain is the ratio of deformation and original length. From Table 1, it shows that the samples with no fibre reinforced show the highest strain of 6.60%. However, the strain subsequently decreases with the increase of fibre contents. It was also observed that for 5% treated fibre reinforced epoxy composite, plastic deformation occurred and this is due to crack and failure of the matrix. Despite that, the specimen did not fail completely as a composite because there are still fibres attaching to both ends of the fractured matrix. This is a possible explanation of phenomena under low tensile stress.

It can also be seen from the Table 1 that there is a good agreement between the experimental results and finite element results which indicates that the composite materials can be analyzed using finite element software.

Effect of nano-Silicon Carbide (n-SiC) in EPF Fibre Reinforced Epoxy Matrix. Table 2 presents the effect of n-SiC in Epoxy composites. n-SiC was varied at four stages (0%, 1%, 3%, and 5%) while a constant weight percentage of 5% alkaline treated oil palm fibre is used across all samples. From Table 2 it is clear that the increase in weight percentage of n-SiC improve the ultimate tensile strength of the polymer composites. For instance, the enhancement of 1% n-SiC increase the ultimate tensile strength up to 101.99% compared to specimen without n-SiC. This can be explained as a good dispersion of n-SiC particles into the epoxy matrix which improve the interaction surface and hence provide excellent stress transfer from matrix to nanofillers. However, above 3% of n-SiC inclusion, the tensile strength has seen to improve insignificantly. The addition of 3% to 5% only contributes to 4.8% improvement in tensile strength. It is predicted that the addition of more n-SiC beyond 5% would reduce the tensile strength. This is due to the increased amount of n-SiC may lead to agglomeration and uneven distribution of the particles in the epoxy matrix. Subsequently, the agglomerated n-SiC acts as a stress concentrators and initiate micro-cracks which promote failure at lower stress and strain.

Table 1: Tensile strength of various fibrewt% in epoxy matrix

Fibre Weightage	Experimental Results		Finite Element Results	
	Ultimate Tensile Strength (MPa)	Strain (%)	Ultimate Tensile Strength (MPa)	Strain (%)
0% Fibre	16.59	6.60	16.59	5.44
1% Treated Fibre	21.20	4.73	21.2	3.44
3% Untreated Fibre	14.67	4.09	14.67	2.7
3% Treated Fibre	17.06	4.06	17	3.1
5% Treated Fibre	2.73	3.35	2.73	1.34

Table 2: Effect of nano-Silicon Carbide (n-SiC) in 5% EPF Fiber Reinforced Epoxy Matrix

n-SiCWeightage	Ultimate Tensile Strength (MPa)	Strain (%)
0% n-SiC	2.73	3.35
1% n-SiC	5.76	5.44
3% n-SiC	13.17	5.34
5% n-SiC	13.80	3.65

Conclusion

A small quantity of oil palm fibre (1%wt) increases the ultimate tensile strength by 27.79% compared to pure epoxy and therefore has the potential to substitute glass fibre as reinforcement in epoxy matrix in condition that the material is applied in low strength application. The addition of more oil palm fibre deteriorates the tensile strength of epoxy matrix. It is also observed that the alkaline treatment can successfully increase the interfacial adhesion of oil palm fibre with epoxy matrix and consequently enhance the mechanical properties. Through the study, it is found that 1wt% of n-SiC and 5wt% treated fibre improves the tensile strength by 110.99% compared to specimen with only 5% treated fibre. In addition, reinforcement of nano-silicon carbide increases the mechanical properties of polymer composites. It is also found that the finite element software can predict the mechanical properties of the composite materials.

Acknowledgment

The Authors are grateful to the R&D Department, Curtin University Sarawak for financial support to conduct this research work under CSCRF scheme (Cost Centre No: 5004)

References

- [1] Matthew, F.L., and Rawlings R.D. 1994. *Composite Materials: Engineering and Science*. Oxford: Chandos Publishing.
- [2] McCauley, A. Ronald. 2004. *Corrosion of Ceramic and Composite Materials* 2nd Ed. New York: Marcel Dekker Inc.
- [3] Askeland, Donald R., and Pradeep P. Phule. 2003. *The Science and Engineering of Materials* 3rd Ed. Canada: Thomson Canada Limited.
- [4] Bahadur, P. and Sastry N.V. 2002. *Principles of Polymer Science*. England: Alpha Science International Ltd.
- [5] Budinski, Kenneth G., and Michael K. Budinski. 2005. *Engineering Materials Properties and Selection* 8th Ed. New Jersey: Pearson Education, Inc.

-
- [6] Budinski, Kenneth G., and Michael K. Budinski. 2005. *Engineering Materials Properties and Selection* 9th Ed. New Jersey: Pearson Education, Inc.
- [7] Callister, W.D. 2003. *Materials Science and Engineering* 6th Ed. New York: John Wiley & Sons Inc.
- [8] Savage, G. 1992. *Carbon-Carbon Composites*. London, United Kingdom: Chapman & Hall.
- [9] Ray, D and J. Rout. 2005. *Thermoset Biocomposites*. New York: Taylor & Francis.
- [10] Zini, Elisa, and Mariastella Scandola. 2011. "Green Composites: An Overview" *Polymer Composites* 2011. 32(12): 1905- 1915. doi:10.1002/pc.21224.
- [11] Taj, Saira, Munawar Ali Munawar, and Shafiullah Khan. 2007. "Natural Fibre-Reinforced Polymer Composites." *Proc. Pakistan Acad. Sci.* 44(2): 129-144.
- [12] Mulinari, D.R., Cioffi M.O.H. and Voorwald H.J.C. 2010. *Review on Natural Fibres/HDPE Composites: Effect of Chemical Modification on the Mechanical and Thermal Properties*. New York: Nova Science Publishers.
- [13] Mohanty, A.K., Misra M. and Drzal L.T. 2005. *Natural Fibres, Biopolymers and Biocomposites*. London: Taylor & Francis.
- [14] Shinoj, S., R. Visvanathan, S. Panigrahi, and M. Kochubabu. 2011. "Oil Palm Fibre (Opf) and Its Composites: A Review." *Industrial Crops and Products* 33 (1): 7-22. doi: 10.1016/j.indcrop.2010.09.009.

Preparation and Dimensional Stability of Organo-Montmorillonite (O-MMT) Treated Unsaturated Polyester Hybrid Composites Filled with Keratin Fiber

Kiew Kwong Siong^{1,a}, Soon Kok Heng^{2,b}, Sinin Hamdan^{1,c}, Moaz Mohsin², Akshay Kakar², Maaz Hameed²

¹Faculty of Engineering, Universiti Malaysia Sarawak, Kota Samarahan, 94300 Kuching, Sarawak, Malaysia

²Faculty of Engineering, Computing and Science, Swinburne University of Technology, 93350 Kuching, Sarawak, Malaysia

^aKiew_ks@hotmail.com, ^bkhsoon@swinburne.edu.my, ^cdrsinin2003@yahoo.com

Keywords: organo-montmorillonite, keratin fiber, unsaturated polyester, dimensional stability, composite

Abstract. O-MMT treated unsaturated polyester based hybrid composites were prepared using keratin fiber obtained from chicken feathers. Fibers of similar dimension were selected to fabricate composites through hand lay-up method. The preparation and dimensional stability properties of keratin fiber as reinforcements in composites is outlined in this paper. Varying O-MMT contents in nanocomposites is performed to investigate the effects on the dimensional stability (water absorption and thickness swelling) of the composites. Results indicated that increasing fiber content deteriorates dimensional stability of the composites and composites. However, improvements in dimensional stability of the keratin fibercomposites were observed with O-MMT. O-MMT treatment reduces the water absorption and thickness swelling, especially at 5wt% of O-MMT concentrationat all range of fiber content. At 5wt% concentration of O-MMt, 10wt% keratin fiber content marks the lowest water absorption and thickness swelling with rate of 0.65% and 1.93%, respectively. Adopting 10wt% of keratin fiber at 5wt% of O-MMT can be utilized for application requiring high dimensional stability.

Introduction

The application of nanomaterials in the manufacturing of composites has been increasing, providing the composites with improved performance in properties [1-3]. The projected market share for composites was US\$920million in 2011 and estimated to grow to more than US\$2.4 billion by 2016 [4].Organo modified montmorillonite (O-MMT) nanoclays account for more than half of the composite market due to the efficiency and low cost [4]. Polymer – clay composites have extensive wide range of applications, such as packaging, automotive, coatings and constructions [3].

The effective and sustainable utilization of natural resources has been negatively influenced by the increasing population of the world. Waste generates are directly proportional with increasing population. The disposals of wastes are not being effective at the time, with choices limited to landfill or open burning. One of the abundantly available wastes is chicken feather. Chicken feathers were subjected to disposals, landfills and open burning, which there is no means of sustainable utilization of this waste material[5].The use of chicken feather in composites as reinforcement provides an environmentally sustainable solution for feather disposal and assists the poultry farm for cost reduction. It is anticipated that agricultural fibers such as chicken feather fiber having lower density than inorganic fiber may not suffer from size reduction during processing [6].

Chicken feathers were generated by the US poultry industry each year [7]. Chicken feathers are made of keratin, which contains ordered alpha-helix or beta-sheet structure [8]. The feather fiber fraction has more alpha-helix over beta-sheet structure [8]. This contributes to a crystalline melting point of ca. 240°C for the feather fiber [8]. Chicken feather keratin has a molecular weight of approximately 10500 g/mol [9] and a cysteine/cystine content of 7% [10] in the amino acid

sequence, which is a sulphur containing amino acid sequence responsible for the sulphur-sulfur bonding in the keratin [6].

There are some studies detailing the incorporation of chicken feather fiber in polymers. Barone and Schmidt [6] introduced chicken feather fiber into polyethylene to obtain a lower density composite with higher elastic modulus and yield stress over the polyethylene alone. Polymer such as polypropylene (PP) was also used to reinforce chicken feather fiber and compared with jute fiber – PP composites, with chicken feather fiber – PP composites has similar flexural properties but higher acoustical properties in noise reduction coefficient [11]. Zhan et al. [5] and Kiew et al. [12] has fabricated composites with epoxy, chicken feather fiber, jute fiber and E-glass fiber to investigate the dielectric properties in application such as printed circuit board. It is found out that the chicken feather fiber yields lower dielectric properties in comparison with other fiber system composites, which can potentially be used for printed circuit board industry in terms of dielectric properties, sustainability and cost. Furthermore, Cheng and coworkers [13] studied the tensile properties of chicken feather fiber reinforced poly lactic acid (PLA) composites through injection molding technique, with findings that the tensile moduli of chicken feather fiber/PLA composites were found to be higher than PLA alone, without causing any substantial weight increment.

There have been limited applications whereby, reinforcing natural fiber composites with nanotechnological approach. Hence, this study focuses on the preparation of keratin fiber reinforced composites. Standard unsaturated polyester resin have been used as matrix material, while organomontmorillonite (C14-C18) have been selected as nanomaterial for the treatment of matrix, to reinforce with keratin fiber for the preparation of composite.

Materials and Methods

Materials

Characterisation of O-MMT

The organo-modified nanoclay (Nanomer 1.44P) was obtained from Sigma Aldrich, which contains about 65% MMT and 35% surfactant – dimethyl dialkyl (C14-C18) amine. It is hereby referred as O-MMT. As reported by the supplier, the particle size was below the range of 10 μ m.

Keratin fiber

The chicken feathers were collected in the raw form from chicken slaughter house located in the mini industrial zone, Kota Samarahan, Kuching. The chicken feathers were subjected to rinse in running water and washed in water soluble ethanol solution before sun-dried for duration of 7 hours. Semiplume feather as depicted in Fig. 1 were specifically chosen for chopping in a range of 3mm to 6mm to be used as keratin fiber.



Fig. 1. Semiplume feather

Specimen preparation

Preparation of O-MMT treated unsaturated polyester resin

Four stocks of unsaturated polyester resin at 1000ml were prepared. Organo modified montmorillonitenanoclay (O-MMT) in powder form at various weight ratio of 0wt% (control), 1wt%, 3wt% and 5wt% were added into the unsaturated polyester resin. The O-MMT based on the desired concentrations were first introduced into the unsaturated polyester resin by mechanical stirring until all nanoclay have been visually dispersed in the resin. These stocks of unsaturated polyester resin introduced with O-MMT were put in the ultrasonic sonication bath at water

temperature of 60°C and frequency of 44kHz for a period of 60 minutes. The stocks of O-MMT treated unsaturated polyester resin were bottled and kept in ambient room environment for at least a week before usage.

Composite preparation

The composites were prepared with keratin fiber loading of 10wt%, 20wt% and 30wt% while a set of composites without any fiber was served as control. The preparation of composite is conducted through hand lay-up method. The mould release agent was spread on the mould surfaces to ensure the finished specimen can be removed easily. The keratin fiber was weighted before mixing with unsaturated polyester resin. The unsaturated polyester-keratin fiber premix was hand-stirred to ensure homogeneous distribution of fiber within the matrix. The premix was mixed with 1wt% of Methyl Ethyl Ketone Peroxide (MEKP) and hand-stirred again for a minute. The resin was poured into the cavity of the mold and closed before subjected for cold-compression for 24 hours in order for the solidification process to complete. The composites were post-cured at 80°C in a convection oven for 3 hours. For each composite fiber loading, five specimens were produced. This procedure repeats for unsaturated polyester resin at various O-MMT concentrations (0wt%, 1wt%, 3wt% and 5wt%).

Characterization

Dimensional stability measurement

Rectangular specimens were prepared from the fiber-matrix composites with the dimension of 39mm x 10mm x 5mm. The specimens were left in the furnace at 80 °C for 1 hour and then left in open air for 1 hour before weighted for original weight. The test specimens were immersed in the distilled water according to ASTM D570-99 standard for 24 hours. After immersion, the specimens were taken out from the water, with the excessive water on the surface was lightly wiped with a soft cloth. The weight of the specimens was recorded again as the final weight of the specimens. For each test sample with specific fiber content, results from three samples were averaged. The increment of the weight in the specimen was calculated based on the following equation in percentage:

$$\text{Water absorption}(\%) = \frac{\text{Final Weight} - \text{Original Weight}}{\text{Original Weight}} \times 100 \quad \text{Eq. 1}$$

Following the immersion test, thickness swelling coefficient can also be obtained with the same samples as water immersion.

$$\text{Thickness swelling coefficient} = \frac{\text{Final thickness} - \text{Initial thickness}}{\text{Initial thickness}} \times 100 \quad \text{Eq. 2}$$

Results and Discussions

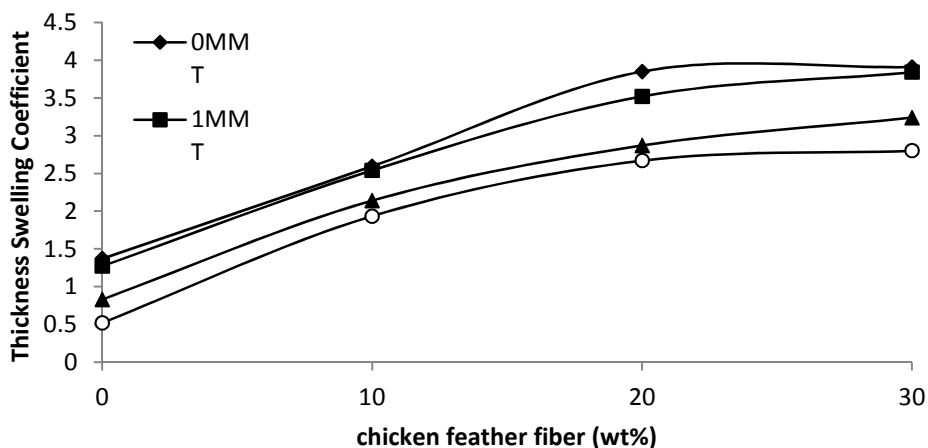


Fig. 2 Thickness swelling coefficient of composites with different concentration of O-MMT

Fig. 2 shows the results of dimensional stability in terms of thickness swelling of various composites. It is evident that the untreated composites, 0MMT system exhibits overall highest thickness swelling coefficient compared to the treated composites. The O-MMT effectively decreases the thickness swelling coefficient of all treated composites. The reduction of thickness swelling coefficient corresponds to the moisture excluding capacity of the treatment [14]. Increasing O-MMT concentration in composites reduced the thickness swelling coefficient. It is suggested that the O-MMT reacted with the keratin chains of fiber and effectively clogged the water molecule movement within the composite structures. The improvement in thickness retention is in accordance of the order from the highest O-MMT content to non within the composites. Increasing chicken feather fiber loading also contributes to the increase of thickness swelling. This is due to characteristics of feather fiber as being hydrophilic. Even though O-MMT effectively reduces the water retention of the composites, the amount of chicken feather fiber is strictly too much for 5wt% of O-MMT to completely hinders the water molecules movement within the composites itself.

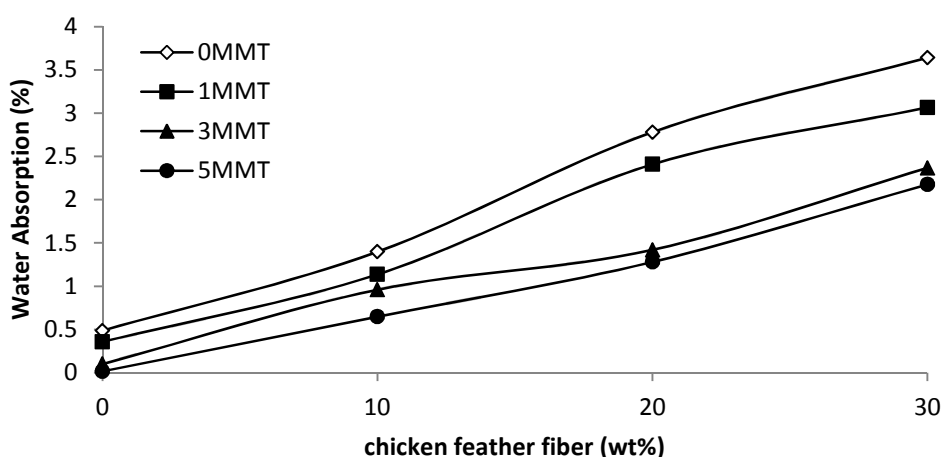


Fig. 3 Water absorption of composites with different concentration of O-MMT

Water absorption for various composites are shown in Fig. 3. It can be observed that the water absorption increased with increasing fiber loading. Fiber loading at 30wt% marks the highest water absorption rate among other fiber loadings. Increasing concentrations of O-MMT has also reduced water absorption in the composites, especially at level of 5wt%. This indicated that O-MMT is effective against reducing water absorption rate in the composites. The keratin fiber is composed mainly of keratin protein. The formation of chemical bonding between keratin proteins and MMT enhances the absorption rate of water. The O-MMT hinders the water penetration into the composites, as indicated with the reduction in water absorption with increasing O-MMT contents. Improved interfacial bonding between treated matrix and keratin fiber has successfully reduced the void formations in the composites. Hence, when immersed in the water, reduced void formations reduce the water uptake within the composites.

Conclusion

In this study, composite materials were developed from O-MMT treated unsaturated polyester at various concentrations with keratin fiber. Increasing keratin fiber up to 30wt% in composites deteriorates the dimensional stability due to the natural characteristics of keratin fiber. Increasing O-MMT to 5wt% reduced the thickness swelling coefficient and water absorption rate of the composites. Overall, the dimensional stability of the keratin fiber composites can be enhanced through hybrid composite approach, as indicated from O-MMT increases the water retention rate of the composites, yielding improved dimensional stability. At 5wt% concentration of O-MMT, 10wt% keratin fiber content marks the lowest water absorption and thickness swelling with rate of 0.65% and 1.93%, respectively. Overall, the 5wt% of O-MMT with 10wt% of keratin fiber is the

best composition of keratin fibercomposites, suitable for application requiring good dimensional stability.

References

- [1] K.Q. Han, M.H. Yu, Study of the preparation and properties of UV-blocking fabrics of a PET/TiO₂ composite prepared by in situ polycondensation, *J Appl Polymer Sci.* 100 (2006) 1588–1593.
- [2] T.V. Duncan, Applications of nanotechnology in food packaging and food safety: barrier materials, antimicrobials and sensors, *J Colloid Interface Sci.* 363 (2011) 1–24.
- [3] X. Yining, M.Rubino, R. Auras, Detection and quantification of montmorillonitenanoclay in water-ethanol solutions by graphite furnace atomic absorption spectrometry, *Food Additives and Contaminants: Part A*, 30 (2013) 2177-2183.
- [4] BCC Research. 2012. Global Markets for Composites, Nanoparticles, Nanoclays, and Nanotubes. Wellesley, MA: BCC Research LLC. Information on <http://www.bccresearch.com/report/composites-global-markets-nan021e.html>
- [5] M.J. Zhan, R.P. Wool, J.Q. Xiao, JQ.,Electrical properties of chicken feather fiber reinforced epoxy composites, *Composites: Part A* 42 (2011) 229-233.
- [6] J.R. Barone, W.F. Schmidt, Polyethylene reinforced with keratin fibers obtained from chicken feathers, *Composites Science and Technology* 65(2004) 173-181.
- [7] G. Parkinson, Chementator: a highly use for lowly chicken feathers, *Chemical Engineering* 105(1998) 21.
- [8] W.F. Schmidt, M.J. Line, Physical and chemical structures of poultry feather fiber fractions in fiber process development, *TAPPI Proceedings: Nonwovens Conference* (1996) 135-140.
- [9] R.D.B. Fraser, T.P. MacRae, G.E. Rogers, *Keratins: their composition, structure and biosynthesis*,Springerfield: Charles C. Thomas Publisher (1972) 31.
- [10] K. Murayama-Arai, R. Takahashi, Y.Yokote, K.Akahane, Amino acid sequence of feather keratin from fowl, *Eur J Biochem*, 132(1983) 501-507.
- [11] S. Huda, Y. Yang, Composites from ground chicken quill and polypropylene, *Composites Science and Technology*, 68 (2008) 790 – 798.
- [12] K.S. Kiew, S. Hamdan, M.R. Rahman, Comparative study of dielectric properties of chicken feather/ kenaffiber reinforced unsaturated polyester composite, *Journal of BioRes*,8 (2013) 1591 – 1603.
- [13] S. Cheng, K. Lau, Y. Zhao, P.M. Lam, Y. Yin, Mechanical and thermal properties of chicken feather fiber/PLA green composites, *Composites: Part B* 40 (2009) 650-654.
- [14] M.S. Islam, S. Hamdan, M.Rusop, M.R. Rahman, A.S. Ahmed, M.A.M.Idrus, Dimensional stability and water repellent efficiency measurement of chemically modified tropical light hardwood, *Bioresources*, 7(2012),1221-1231.

A Critical Survey of Ceramics Materials for Production of Automotive Engine Block

Pius Bamidele Mogaji^a, Tamba Jamiru^b, Dawood Desai^c and Rotimi Sadiku^d

Department of Mechanical Engineering, Tshwane University of Technology, Pretoria, South Africa

^amogajipb@tut.ac.za, ^bjamirut@tut.ac.za, ^cdesaida@tut.ac.za, ^dsadikur@tut.ac.za

Keywords: Ceramic, Materials, Production, Automotive, Engine block, Survey, strengths and weaknesses

Abstract. Efforts at utilizing ceramic materials with their undeniably interesting range of properties in automobile manufacture, has persisted for many years. The corrosion resistance, the resistance to oxidation at high temperatures, the capacity of its resistance to wear and the low relative density of these materials make them especially attractive candidates for use in the automotive engine block production. The limitations of ceramics materials in the area of low fracture toughness can be assuaged by using various methods of grain and boundary size strengthening. This paper presents a critical survey of some of the existing materials used in the production of automotive engine block, the existing methods of toughening and strengthening of ceramic composite materials with emphasis on methodologies, strengths and weaknesses.

Introduction

Ceramics engineering can be defined as the science and the technology of forming objects from non-metallic and inorganic materials. This action can be achieved by using heat, or at lower temperatures, by using precipitation reaction from high purity chemical solutions [1]. Ceramics materials are usually ionic or covalent bonded and can be in crystalline or amorphous phase. They possess several superior properties, such as: high thermal resistance, chemical durability and mechanical strength. A material held together by ionic or covalent bond will tend to fracture before any plastic deformation takes place, which results in poor toughness in these materials [2]. A lot of work has been done in the past on ceramics. Abraham in 1709 was the first person that used coke in to improve the yield of smelting process. In similar manner, Carl in 1888 developed a process to separate alumina from bauxite [3]. Acheson in 1893 heated a mixture of coke and clay and invented Carborundum, or synthetic silicon carbide. Moissan also synthesized SiC and tungsten carbide in his electric arc furnace about the same time as Acheson. Karl in 1923 used liquid-phase sintering to bond Moissan's tungsten carbide particles with cobalt in [3]. Literature cited the use of cemented carbide edges that greatly increase the durability of hardened steel cutting tools [4]. Consequently, Nernst in 1926 developed cubic-stabilized Zirconia. This material is used as an oxygen sensor in the exhaust systems of automobiles. Areas of application of ceramics continue to expand as researchers develop new kinds of ceramics to serve different purposes [1& 5]. Zirconium dioxide ceramics are used in the manufacture of knives, with the blade of the ceramic knife staying sharp for much longer than that of a steel knife. Ceramics, such as: alumina, boron carbide and silicon carbide have been used in bullet proof vest to repel large-calibre rifle fire. Silicon nitride parts are used in ceramic ball bearings. Their high hardness means that they are considerably less susceptible to wear and can offer more than triple lifetimes. Work is on-going in the development of ceramic parts for gas turbine engines [1]. The challenges in ceramic science were fully analysed in a report from a workshop on emerging research areas in ceramic science [6]. These challenges were categorized into six: understanding rare events in ceramic microstructure, understanding the phase-like behaviour of interfaces and predicting and controlling heterogeneous microstructures with unprecedented functionalities [7]. Others are: controlling the properties of oxides electronics and understanding defects in the vicinity of interfaces [8]; controlling ceramics far from equilibrium and accelerating the development of new ceramics [9] and finally, harnessing order within disorder in glasses [10 & 11].

In the early 1980s, Toyota researched the production of an adiabatic ceramic engine which can run at a temperature of over 6000°F (3300°C). Ceramic engines do not require a cooling system and hence allow a major weight reduction and therefore greater fuel efficiency. Despite all of these desirable properties such engine are not in production simply because the manufacturing of ceramics parts in the requisite precision and durability is difficult. Imperfection in ceramics leads to cracks, which can lead to potentially dangerous equipment failure [5].

[18] itemized the traditional ceramic process in this sequence: (1) Milling, (2) Batching, (3) Mixing, (4) Forming, (5) Drying, (6) Firing and (7) Assembly. Ceramics forming techniques include: throwing, slip casting, tape casting, injection moulding, dry pressing, isostatic pressing, hot isostatic pressing (HIP) amongst others (Onoda & Hench, 1979). A material strength is dependent on its microscopic structure. The engineering structure to which a material is subjected can alter this microstructure. The varieties of strengthening mechanisms that alter the strength of a material include the mechanism of grain boundary strengthening [12]. This paper focused on the survey of ceramic materials for the production of automotive engine block. Section 2 discusses some existing materials used in the production of engine block. Section 3 is a summary of some of the existing methods of strengthening of ceramic materials. Sections 4 and 5 present the strength and weaknesses of some existing techniques and the conclusion drawn respectively.

Some Existing Materials for Production of Automotive Engine Block

Since materials play a significant role with regard to quality and cost of a car, correct materials of choice at the earliest possible stage of the development process is of vital importance [13]. Nowadays materials used in vehicles are selected in order optimally fulfil the specific requirements. It is the job of the materials engineer in a car-manufacturing company to ensure that this optimum is reached [14]. Many early engine blocks were manufactured from cast iron alloys, primarily due to its high strength and low cost. But, as engine designs became more complicated, the weight of the engine had increased [15].

Consequently, the desire among manufacturers is to use lighter alloys that were as strong as cast irons arose. One such material that was being used as a substitute was aluminium alloys. It was used sparingly in the 1930's, due to problems with durability [16]. Aluminium alloy usage, in engine blocks, increased during the 1960's and 1970's which undoubtedly increased fuel efficiency and performance. Together, these two metals (iron and aluminium) were used exclusively to fabricate engine blocks. As of late, however, a new material process has made magnesium alloys suitable for use in engines. The alloy, called AMC-SC1, weighs less than cast iron and aluminium alloys and represents new possibilities in engine manufacturing. A new manufacturing process have made compacted graphite cast iron (CGI) a viable alternative to gray cast iron for the manufacture of diesel engine blocks. Like magnesium alloys, this material offers a higher strength and lower weight than gray cast iron [17].

An engine block is the core of the engine which houses nearly all of the components required for the engine to function properly. The block is typically arranged in a "V," inline, or horizontally-opposed configuration and the number of cylinders range from 3 to as many as 16. Figure 1 shows engine blocks with "V" inline, and Figure 2 shows horizontally-opposed configurations.

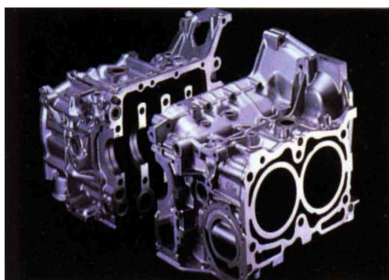


Fig. 1 : Cylinder Block in horizontally-opposed configurations Source: [17]



Fig. 2: Cylinder Block in "V" incline Source: [17]

In order for an engine block to meet the functional requirements, such as: lasting the life of the vehicle, housing internal moving parts and fluids, ease of service and maintenance and withstand pressures created by the combustion process, the engineering material(s) used to manufacture the product must possess high strength, modulus of elasticity, abrasion resistance and corrosion resistance [18]. The material should also have a low density, thermal expansion and thermal conductivity. Good machinability and castability of the metal alloy are also important factors in selecting the appropriate material, as the harder it is to machine the product, the higher the costs of manufacturing. In addition to the previously mentioned properties, the alloys must possess good vibration damping in order to absorb the shuddering of the moving parts [17].

The required mechanical properties for a typical aluminium engine block includes an ultimate tensile strength of ~245 MPa, yield stress of ~215 MPa and fatigue strength of 60 MPa [19]. Discussed below are alloys that are currently being used to cast engine blocks and their mechanical properties.

Gray cast iron alloy (GCI) have been the dominant metal that was used to manufacture conventional gas-powered engine blocks. It contains 2.5-4 wt.% carbon and 1-3 wt.% silicon, 0.2-1.0 wt.% manganese, 0.02-0.25 wt.% sulphur and 0.02-1.0 wt.% phosphorus [16]. GCI has excellent damping capacity, good wear and temperature resistance, easily machinable and is inexpensive to produce. However, gray cast irons are relatively weak and are prone to fracture and deformation. Due to these problems, compacted graphite iron has recently begun to compete with gray cast iron as the choice material to produce diesel engine blocks [20].

Compacted graphite cast iron (CGI), which was accidentally discovered while trying to produce ductile cast iron, possesses higher tensile strength and elastic modulus than gray cast iron due to the compacted graphite found in the microstructure of CGI. Table 1 shows the comparison between the strengths and modulus of elasticity of gray cast iron and CGI. As seen in Table 1, gray cast iron has a lower tensile strength than CGI, despite its higher weight [21].

Table 1: Comparison of the tensile strength and modulus of elasticity of gray cast iron and compacted graphite cast iron

	Gray Cast Iron(GCI)	Compacted Graphite Cast Iron (CGI)
Tensile strength (MPa)	160-320	300-600
Modulus of Elasticity (GPa)	96-110	170-190

Source: [21]

Like gray cast iron, compacted graphite cast iron has good damping capacity and thermal conductivity, but its difficulty to machine has limited the wide-scale use of CGI.

Aluminium alloy usage has gained popularity since the 1960's as a way to reduce the overall weight of the vehicle. There are two practical implications: improved performance-to-weight ratio and increased fuel efficiency. The drawbacks in using aluminium in engine blocks are that they are more expensive to manufacture than cast iron alloys. However, the strength-to-weight ratio of aluminum alloys is hard to ignore and manufacturing processes developed throughout the years have minimized the cost disparity between aluminum and cast iron [22].

Magnesium alloys have been used in engines before, but not for cylinder blocks. Rather, they were used as valve covers, cylinder head covers, intake manifolds, rocker arm covers, air intake adaptors, induction systems and accessory drive brackets [23]. The biggest attraction for manufacturers is that the material is much lighter than cast iron and aluminum alloys and has the same strength as cast iron and aluminum alloys.

Some Existing Methods of Strengthening Ceramics Materials

In order to compensate for the low fracture toughness in ceramics materials, series of methods of strengthening have been adopted by different researchers. [24 & 25] enumerated the methods that have been adopted in the past in order to improve the low fracture toughness of ceramics, thus:

Transformation toughening which is limited in Zirconium oxide (ZrO_2)-based ceramics; dispersed ductile particle toughening and dispersed brittle particle toughening that may decrease the strength of the ceramics; fibre toughening and whisker toughening, which require special forming process, such as: Hot Isostatic Pressing (HIP) and Hot pressing which lead to higher cost; and complex structure toughening.

Method of Toughening of Ceramics Using Piezoelectric. A new approach for the toughening of ceramics, using piezoelectric secondary phase crystal which was incorporated into the ceramics matrix as a toughening phase, which increased the fracture toughness of ceramics to $5.1MPam^{1/2}$ was developed by [26]. The toughening mechanisms for ceramics are all based on the energy dissipation/energy balance approach [4] and the toughness of composite ceramics can be given as:

$$K_{IC} = [E^c (J^m + \Delta J)]^{1/2} \quad (1)$$

where, K_{IC} is the overall toughness of the composite ceramics and E^c is the Young modulus of the composite ceramic and J_m is the energy change associated with crack extension in the matrix, while ΔJ is used to define the energy change increment due to the presence of the secondary phase which may play a role as toughening phase although via different mechanisms, respectively. By extending such energy dissipation consideration, alternative toughening approaches for ceramics can be designed, in which a piezoelectric secondary phase material is incorporated into the ceramic matrix and toughening is performed through energy dissipation due to piezoelectric effect. This part of mechanical energy, that causes a crack extension, may be transformed into electrical energy or dissipated by stress-induced Ferro elastic phase transformation and domain wall motion in such a composite and this subsequently leads to the enhancement of fracture resistance. The fracture toughness of the composite ceramic can be given in the extended form of equation (1).

$$K_{IC} = [E^c (J^m + \Delta J + \Delta J^{piezo})]^{1/2} \quad (2)$$

Where, ΔJ^{piezo} defines the energy dissipated by the piezoelectric effect. Such a unique toughening mechanism can be called the piezoelectric energy dissipation mechanism [5].

Method of Particle- Bridging Mechanism. Particle-bridging mechanism in which a crack-face shielding results when nanosized particles bridge a propagating crack behind the crack tip, as a strengthening mechanism for ceramics nanocomposites was developed by [27]. The toughness increase by crack- shielding, ΔK , is as expressed by [28 & 29].

$$\Delta K = \zeta \sigma_s l_s^{1/2} \quad (3)$$

Where, ζ is a constant of the order of unity, σ_s the shielding stress and l_s is the length of the shielding zone. Transmission Electroscopie Microscope studies (TEM) on alumina-silicon carbide nanocomposites with different volume fractions, reveals that fact that the diameter ratio was well represented by the equation (4) [27].

$$\frac{\lambda}{d} = (\pi |6fp|)^{1/3} \quad (4)$$

Where, d is the particle diameter and f_p is the volume fraction of the dispersed particle. Based on the results from equations (3) and (4), the increase in toughness caused by particle bridging can be estimated using a crack-face shielding concept, generally called the Dugdale-Barenblatt model.

Strengthening of Ceramics Based on Griffith's Energy Equilibrium. Toughening and strengthening mechanisms in ceramic-based nanocomposites were based on the Griffith's energy equilibrium and residual stress around the secondary-phase nanoparticles dispersed in the matrix grains. The residual thermal stresses around a spherically dispersed particle within a concentric sphere of matrix grain were specifically analysed in order to clarify the effects of residual stresses on the toughening in the frontal process zone, involving nano cracking and on the strengthening mechanism caused by nucleation of dislocation. The analytical results reveal that the ratio of thermal expansion coefficients of the particle and matrix has a marked effect on the residual stresses

and the estimated residual stresses were of sufficient magnitude to generate lattice defects, such dislocations around the particle (even in ceramics) and the nanosize particle within a matrix can only create dislocations around the particle [2].

Method of Dislocation Sub-Boundaries. A technique to improve the fracture toughness of sub-surface regions of ceramic materials was developed by [30]. Surface of different ceramic materials (single crystals of Al_2O_3 and Si; sintered poly-crystals of Al_2O_3 and Si_3N_4) were impacted with hard ceramic particles at room temperature using a short blasting technique. The important point is that by causing the appropriate conditions for short blasting and annealing, the fracture toughness K_{IC} can be improved by a factor of about 4. Table 2 summarizes the optimal value of the fracture toughness, K_{IC} , obtained under the condition employed in this method of approach by [31]. The highest value of K_{IC} obtained was $15MPam^{1/2}$ for sintered poly-crystals of Si_3N_4 . This value is a lot higher than those for Zirconia ($\sim 8MPam^{1/2}$) and higher than the K_{IC} for typical brittle metallic materials ($10-12 MPam^{1/2}$) [22 & 35].

Table 2: Summary of Toughening Effect

Sample	Annealing Temp. (K)	Fracture of Toughness, K_{IC} ($MPam^{1/2}$)	Fracture of Toughness, K_{IC} ($MPam^{1/2}$)	Fracture of Toughness, K_{IC} ($MPam^{1/2}$)
		As received condition (a)	After Toughening (b)	Improved Factor (b/a)
Single crystal of Al_2O_3	1673	0.9	3.7	4.0
Single crystal of Si	1673	0.9	1.9	2.1
Sintered poly-crystal of Al_2O_3 (99.99%)	1473	3.0	4.3	1.4
Sintered poly-crystal of Si_3N_4	1573	5.9	15.2	2.6

Source: [35].

Method of Reinforced By In Situ Formation of β -Silicon Carbide. The fabrication and characterization of ceramic matrix composites reinforced by in-situ formation of β -silicon carbide were carried out by [32]. They were able to fabricate yttria-stabilized zirconia-based ceramic matrix composites via in situ formation and dispersion of SiC rather than fine particles and densification by Hot Isostatic Press (HIP) and improved on their mechanical properties. The reinforcement due to the formation of β -SiC, in addition to the densification by HIP, led to an increase in the hardness of the composites. The average fracture of toughness obtained from composites Z30, Z60 and Z90 used for the experiment were 9.39, 10.59 and 10.60 $MPam^{1/2}$, respectively. The yttria-stabilized zirconia has a fracture toughness of $8MPam^{1/2}$. Therefore this approach has improved the fracture toughness of yttria-stabilized zirconia. The improvement in the fracture toughness was due, not only to crack blockage of deflection by uniform dispersion of in situ formed β -SiC particles with high Young's modulus, but also to the phase transformation of t-ZrO₂ to m-ZrO₂, accelerated by the residual stresses resulting from the coefficient of thermal expansion mismatch between TZ-3YS and SiC.

Strength and Weaknesses of Existing Methods

The summary of the methodology, strength and weaknesses of some of the existing methods for strengthening ceramics materials, is presented in Table 3.

Table 3: Summary of some existing methods for strengthening ceramics materials

Researchers	Methodology adopted	Strength	Weakness
He et al, 1997	Inclined Ligament Bridging	Provided Explicit Implication For Property optimization	Rely on the Concept that Resistance behaviour can be Simulated.
Chen and Yang, 1997	Piezoelectric Approach	Significantly Enhanced fracture toughness	Appearance of some phases made the problem Complex.
Ohji et al, 1998	Particle-Bridging Mechanism	Extremely High Shielding stress and steep increase in Fracture Toughness	Difficulty in Evaluating the Initial Flaw Size.
Awaji et al, 2002	Griffith's Energy Equilibrium	Enhance Strength and Fracture Toughness of Nanocomposite	Solely Dependent on generation of dislocation around the second- phase Particles.
Moon et al, 2004	Dislocation Sub-Boundaries	Increased Considerably the Fracture Toughness of the Sub-Surface Region	The Technique is Complex
Chonghai, 2005	Thermal Residual Stress	Produce High Toughening Mechanism in Ceramic Composite	Is only effective when the thermal expansion of dispersed particle is larger than the Matrix Grain.
Sharif et al, 2008	In Situ Formation of β -Silicon Carbide	Greatly Improved Hardness and Fracture Toughness	Tedious and Expensive

Conclusion

This paper presents a review of some of the existing materials for the production of automobile engine block. A detailed documentation of the methods of strengthening of ceramics materials, strengths and weaknesses of some common approaches used for strengthening are also presented. The review established that the existing techniques, although, present strong a improvement in the fracture toughness of ceramic composite materials, there are still a number of problems, including: relying on the concept that resistance behaviour can be simulated, appearance of some phases that made the problem complex, difficulty in evaluating the initial flaw size, solely dependent on the generation of dislocation around the second-phase particles and those that are only effective when the thermal expansion of the dispersed particle is larger than the matrix grain. Future research by this group, therefore aims at developing a technique that integrates some of the existing methods in order to produce a better ceramic composite which will eliminate some of these problems in production of automotive engine block.

References

- [1] W.D, Kingery, H.K, Bowen and D.R.,Uhlmann,Introduction to Ceramics. (Wiley-Interscience, 2nd Edition,)(2006) p. 690
- [2] H.,Awaji, S., Choiand E., Yagi,Mechanism of Toughening and Strengthening in Ceramics-basednanocomposite'. The Journal of Mechanics of Materials..Vol. 34.p 411-422. Elsevier Publication.(2002)
- [3] P.J,Parimal,Transparent ceramics for armor and EM window applications". *Proceedings of SPIE***4102**.p. 1. (2000)
- [4] D.M., Dubbs andI.A Aksay, Self-Assembled Ceramics".*Ann. Rev. Phys. Chem.***51**: (2009) 601–22.
- [5] D.W., Richerson, *Modern Ceramic Engineering*, 2nd Ed., (Marcel Dekker Inc.)(1992)
- [6] G.S., Rohrer, M., Affatigato and R.K., Bordia,Challenges in Ceramic science: A report from the workshop on emerging research areas in ceramics' The Journal of America Ceramic Society. Vol. 95 (12).pp3699-3712(2012)
- [7] Y.M., Chiang and K., Jakus,Fundamental Research Needs in Ceramics: Report from the 1997 NSF Workshop. (2012) Available at: <http://www-unix.ecs>.
- [8] K., Niihara, T., Ohji and Y., Sakka,3rd International Congress on Ceramics (ICC3), IOP Conf. Ser., 18, 012001 pp4-6(2011)
- [9] L.W., Martin, Y.H., Chu and R., Ramesh,Advances in the Growth and Characterization of Magnetic, Ferroelectric, and Multiferroic Oxide Thin Films, *Mater. Sci. Eng., R*, 68 [4–6] 111–333 *Materials and Processes*, vol. 161, issue 8, p. 13.(2010)
- [10] G.A., Gonzons, J.W. McCauleyand I.G., Batyrev,MultiscaleModeling of Armor Ceramics: Focus on AlON; pp. 1–11 in ARL Tech Report, ARLRP- 337. (2011)
- [11] H, Conrad,Space Charge and Grain Boundary Energy in Zirconia (3YTZP), *J. Am. Ceram. Soc.*, 94 [11] 3641–2(2011)
- [12] S., Christopher and T.G., Nieh,Harness and Abrasion Resistance of Nano crystalline Nickel Alloys near the Hall Petch breakdown Regime. (2002)*Mat. Res. Soc. Symp. Proc.*740.
- [13] B.M, Lee, L., Wenger and G., Poschel, *KunststoffeinFahrzeugaufbau – Evolution Statt*(1992).
- [14] M., Wilhelm,Materials used in Automobile manufacture- current state and perspectives. *Journal De physique IV*, Vol.3.(1993)
- [15] C., Schneider and W.,Prange, ThyssenTechnischeBerichte, Heft 1. pp. 97 – 106(1992)
- [16] P.N., Anyalebechi,Essentials of Materials Science &Engineering, p. 94.(2005)
- [17] N., Hieu,Manufacturing Processes and Engineering materials used in Automotive Engine Blocks. Term paper: EGR250- material Science and Engineering Section B.(2005)
- [18] S., Christopher,Cast in foam,Automotive Design & Production, vol. 74.pp 225-269(2003)
- [19] Anonymous, Magnesium alloy resists high temperature in engine blocks, *Advanced materials and processes*. Vol. 161, issue 8, pp. 2.(2003)
- [20] G., George,Iron engines may be in your future,Tooling & Production, Vol. 69, issue 9, p. 26.(2003)
- [21] J., Mortimer,New process widens use of iron-diesels, *Automotive news Europe*

- [22] "MatWeb – Online Material Data Sheet," [Online], 23 March 2005-last update, Available: 115, issue 3, pp. 42-44.(2004)
- [23] S., Lampman, Tuning Up the Metals in Auto Engines, Advanced Materials & manufacturing. (1991) .
- [24] A.G., Evans, Toughening of ceramics. Journal of America ceramics society. Vol. 73. pp 187-206. (1990)
- [25] P.F., Becher, Strengthening of ceramics. Journal of American ceramics society. Vol. 74. pp 225-269(1991)
- [26] X.M., Chen, and B. Yang, A new approach for toughening of ceramics. Journal of materials Letters. Elsevier publication ltd. Vol 33. pp 237-240(1997)
- [27] T., Ohji, K., Niihara, Y., Choa, and K., Jeon, Strengthening and toughening of ceramic nano composites. J. Am. Ceram. Soc. 81 (6).(1998)
- [28] H., Saka, and G., Nagaya, Phil Mag. Lett. 72. Pp 251(1995)
- [29] M., Sakai and R.C., Bradt, The crack growth resistance curve of Non-phase Transformation ceramics J. ceram. Soc. Jpn., 96 (8) 801-809.(1988)
- [30] W.J., Moon and H., Saka, Phil Mag. Lett. 80. Pp 461(2000)
- [31] W., Moon, T., Ito, S., Uchimura and H., Saka, Toughening of ceramics by dislocation sub-boundaries. Journal of Material Science and Engineering, A 387-389. (2004) Elsevier Publication ltd.
- [32] A.M., Sharif and H., Sueyoshi, Fabrication and Characterization of Ceramic Matrix Composites reinforced by In Situ formation of β -silicon carbide. Elsevier Publication Ltd. Scripta Materialia, vol.58 (2008)

Optical Properties of Gallium Nitride Heterostructures Grown on Silicon for Waveguiding Application

Irma Saraswati^{1,2,3a}, Arnaud Stolz^{1,b}, S.Ko^{4,f}, Elhadj Dogheche^{1,b},
NR. Poespawati^{2,c}, Retno Wigajatri P^{2,d}, Didier Decoster^{1,e}

¹IEMN, Institute of Electronics, Microelectronics and Nanotechnology, UMR CNRS8520, Université de Lille 1, 59652 Villeneuve d'Ascq Cedex, France.

²Electrical Engineering Dept., Faculty of Eng., University Indonesia, 42435, Depok, Indonesia

³Electrical Eng. Dept., Faculty of Eng., Univ. of Sultan Ageng Tirtayasa, Banten, 42435, Indonesia

⁴Dept. Of Physics, Korea Advanced Institute of Science and Technology (KAIST), Daejeon, 305-701, Republic of Korea

^airma.saraswati@ui.ac.id, ^belhadj.dogheche@univ-valencienes.fr, ^cpupu@eng.ui.ac.id,
^dretno.wigajatri@eng.ui.ac.id, ^edidier.decoster@univ-lille1.fr

Keywords: gallium nitride, silicon, microstructure, refractive index, optical characterizations

Abstract. Gallium nitride (GaN) on silicon (Si) is governed by the possibility to use this family of semiconductor for novel optoelectronic devices. GaN layers are deposited by MOCVD on silicon Si(111) using AlGa_xN buffer layer. We have studied the microstructure quality of the films. From SEM, TEM and AFM observations, we have observed that the films exhibit a good quality: the films are highly oriented (0001) with a smooth surface morphology (roughness of 12nm). We have completely characterized the optical properties using the prism coupling technique.

Introduction

The III-nitride semiconductors, Aluminium Nitride (AlN), Gallium Nitride (GaN) and their alloy are excellent properties for use in optoelectronics devices [1,2]. This materials are potensial for high performace; high-power operation, high-frequency and high-temperature application due to their wide band gap energy, wurtzite structure, good thermal conductivity and high break down voltage [3-6]. Until now, researcher have studied and interested optical properties characterisation of GaN on Sapphire (Al₂O₃) for many application in electrical and electronic properties (light emitting diode, high frequency varactor diode, photodetector, surface acoustic wave, etc.)[5-10].

Another substrate for GaN is Silicon (Si). Attempts to grow GaN on substrates like Si or quartz, which is available at low cost, and large areas have resulted in highly defective films [11]. The performance of these devices is closely related to the epitaxy quality grown by MOCVD or MBE [11-12]. For electronic application, we need optical and electrical characterisation at materials.

Therefore this paper interest is about the fundamental properties of GaN. Also this paper will discuss the characterization of optical materials at Gallium Nitride on Silicon substrates (GaN/Si). Particularly, we investigated the refractive index, birefringence in relation with film/substrate interface properties, surface roughness of the film, and the evolution refractive index at different temperature. For the comparation sample in this paper using GaN/Al₂O₃.

GaN on Silicon Structure

The samples of GaN are grown on Si (111) by metalorganic chemical vapour deposition (MOCVD) at KAIST. This samples using AlN/AlGa_xN 80nm as buffer layers [13]. Then, an Al_xGa_{1-x}N interlayer was used to reduce the strain due to lattice mismatch between AlN and GaN. Al_yGa_{1-y}N/GaN superlattice is consists 24 periods with a total thickness of around 80 nm and GaN 1µm on top [14-15].

Particularly, we investigated the refractive index and birefringence in relation with film/substrate interface properties.

Microstructure Analysis

Structural properties of GaN/Si have been studied by scanning electron microscopy (SEM), transmission electron microscopy (TEM) and the atomic force microscope (AFM). The microstructure of GaN/Si from SEM plane view and TEM can be seen in Fig. 1a and 1b. The GaN thickness is $1.2\mu\text{m}$ from SEM observation.

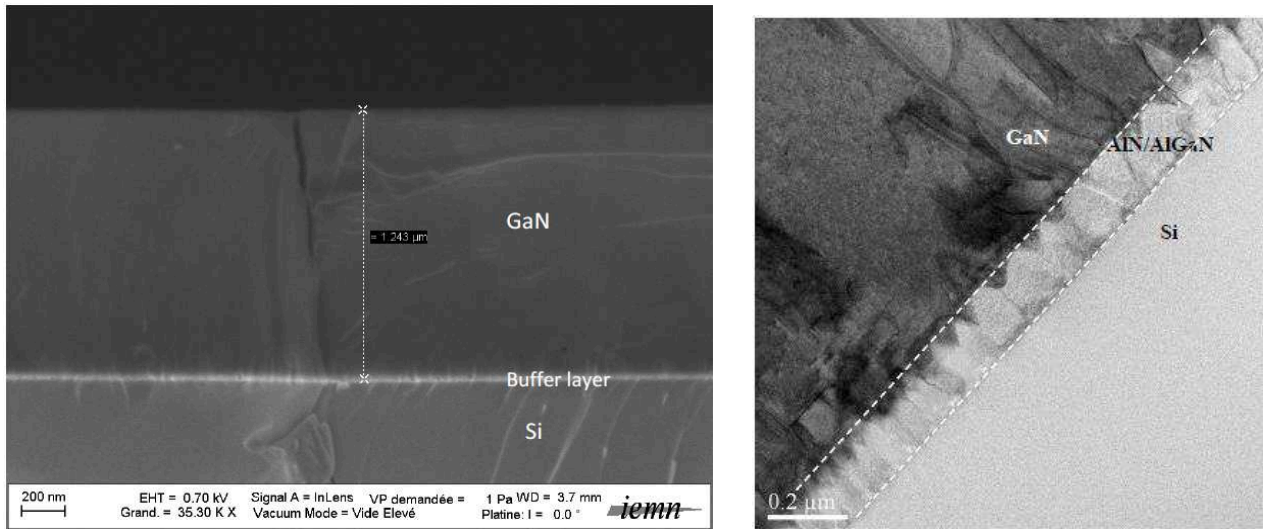


Fig 1.(a). SEM cross-section observation of GaN deposited on Si by MOCVD
(b). Microstructure analysis of GaN/Si sample from TEM observation: dislocations are concentrated in AlN/AlGaN and GaN interface

In order to investigate the microstructure in the film, at the interface and on top surface, TEM analysis by FEI Tecnai G220 (Fig. 1 (b)) was conducted on GaN. Threading dislocations density at the surface are about $4 \times 10^8 \text{cm}^{-2}$. The impact of the dislocation of GaN on optical properties is observed. AlN/AlGaN plays a role of absorption layer for dislocations. TEM analysis permits to calculate the thickness of AlN/AlGaN buffer layer.

AFM analysis is conducted by Nano-Probe Instruments for observations of the threading dislocations. Figure 2 show about AFM analysis at GaN on silicon thin film has many dislocation at surface. This finding correlates well to AFM analysis which shows small root mean square roughness of 1.72nm on a $1\mu\text{m} \times 1\mu\text{m}$ area.

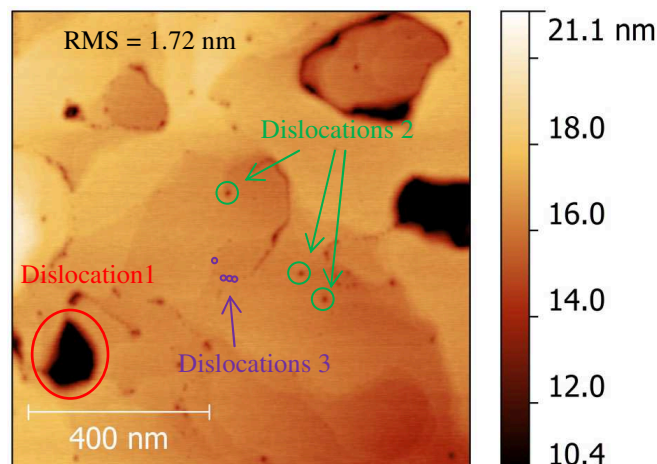


Fig. 2 AFM analysis for threading dislocation density at surface

Optical Characterization

To investigate the effect of GaN epilayer on resulting optical properties, the guided wave technique based on prism coupling has been used [13, 16, 17]: using a rutile prism (TiO_2) on Metricon M2010 setup. The reflectivity dips have been observed at certain angles, corresponding to the excitation and propagation of guided modes in the film structure. Referring to the literature [18,19], the very sharp modes indicate a good film quality of the GaN epilayer.

For GaN/Si films, measurement of the refractive index in Transverse Electric (TE) and Transverse Magnetic (TM) modes were performed for different wavelengths from ultraviolet to near infra red wavelength ranges (450, 532, 633, 975,1539nm) together with the film thickness show at Fig.3. We have compared the optical properties of GaN/ Al_2O_3 [13] and GaN/Si: the refractive index are quite close for TE/TM conditions.

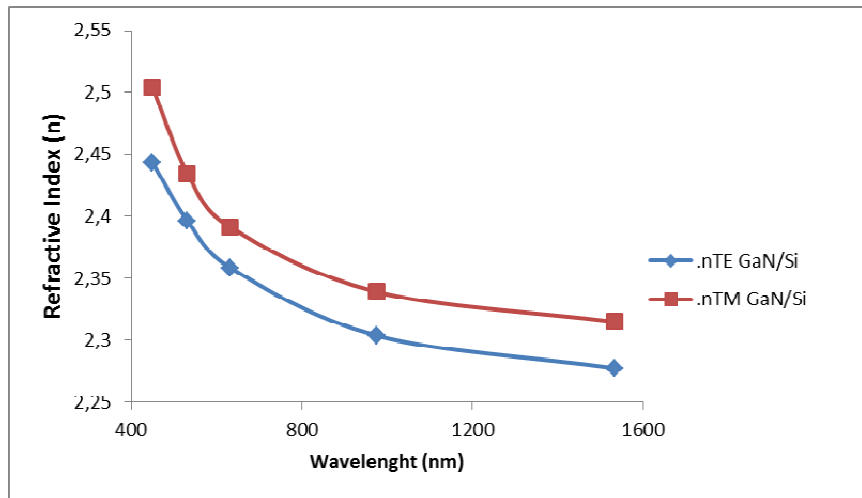


Fig. 3. Dispersion of refractive index TE and TM on GaN/Si

In temperature influence of refractive index TE on two films: GaN/Si and GaN/Sapphire can see at Fig.4. This condition shown GaN/Si have good optical properties like GaN/Sapphire properties [13].

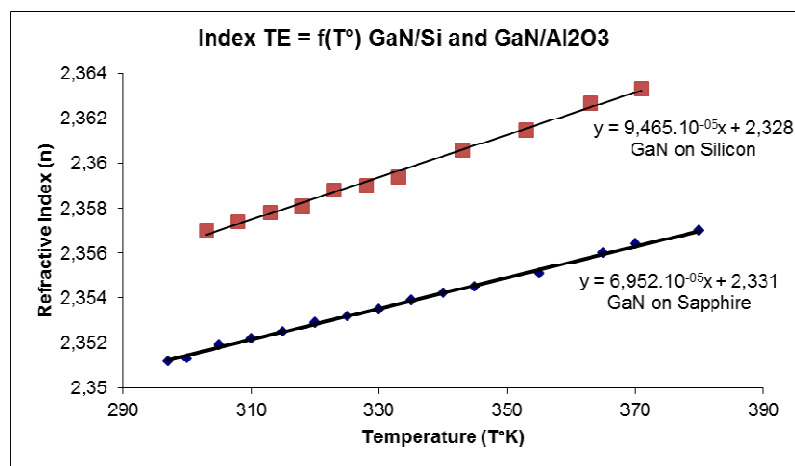


Fig. 4. Temperature influence of the refractive index TE on GaN/sapphire and GaN/Si

The result from measurement of thickness is $1.248 \mu\text{m}$, refractive index TE is 2.357 and TM is 2.392. This result demonstrates the optical waveguiding into GaN/Si structure. It can be observed that the sample exhibits two TE modes (TE₀ and TE₁) with narrow widths. In this work, the ordinary and extraordinary modes are excited by using TE and TM polarized light. From measurement of TE and TM modes are obtained that calculated GaN/Si birefringence (Δn) have value around 0.0373.

Optical characterization at GaN/Si similar with GaN/ Al₂O₃. Referring to the literature [16,18,20], optical characterization at GaN/Si demonstrate excellent waveguide properties like GaN/ Al₂O₃.

Conclusion

The complete analysis of GaN on Silicon structures are presented. GaN structures deposited on silicon have been analyzed using SEM, TEM and AFM. And the optical properties of GaN/Si: the refractive index are quite close with GaN/ Al₂O₃ for TE/TM. Optical measurements demonstrate excellent waveguide properties in terms of index and the dependence versus temperature. This condition shown GaN/Si have good optical properties with very promising characteristics for future optical waveguide devices like GaN/Sapphire properties.

Acknowledgement

This research is supported by Indonesian-French International Joint Research and Dual Degree Indonesia Prancis from Indonesia Ministry of Education and Culture. Also research materials is supported by S. Ko and Prof. Y.H. Cho from Department of Physics (WCU), Korea Advanced Institute of Science and Technology (KAIST), Daejeon, 305-701, Republic of Korea.

References

- [1] Jasprit Singh, Electronic and Optoelectronic Properties of Semiconductor Structures, 1st ed., University of Michigan, Cambridge University Press, New York., 2003.
- [2] Shuji Nakamura, Gerhard Fasol, The Blue Laser Diode: GaN Based Light Emitters and Lasers, Springer-Verlag, Berlin, 1997.
- [3] N. Ikeda , J. Li, H. Takehara, T. Wada, S. Yoshida, High-performance normally off FET using an AlGaIn/GaN heterostructure on Si substrate, J. Crystal Growth 275 (2005) e1019-e1095.
- [4] S. Kato, Y. Satoh, H. Sasaki, I. Masayuki, S. Yoshida, C-doped GaN buffer layers with high breakdown voltages for high-power operation AlGaIn/GaN HFETs on 4-in Si substrates by MOVPE, J. Crystal Growth 298 (2007) 831-834.
- [5] C. Jin, D. Pavlidis, L. Considine, A Novel GaN-Based High Frequency Varactor Diode, Proceedings of the 5th European Microwave IC Conference, Paris, France, 27-28 September (2010).
- [6] A. Cai, Wide band gap semiconductor optical waveguide, Dissertation, Electrical Eng. Dept., North Carolina State University, Raleigh, NC, (2005).
- [7] Z. S. Luo, Y. Cho, V. Loryuenyong, T. Sands, N. W. Cheung, and M. C. Yoo, Enhancement of (In,Ga)N Light-Emitting Diode Performance by Laser Liftoff and Transfer From Sapphire to Silicon, IEEE Phot. Tech. Lett., 14, 10, (2002) 1400.
- [8] Y. Zhang, L. McKnight, E. Engin, I. M. Watson, M. J. Cryan, E. Gu, M. G. Thompson, S. Calvez, J. L. O'Brien, and M. D. Dawson, GaN directional couplers for integrated quantum photonics, Appl. Phys. Lett. 99, (2011) 161119.
- [9] M. Razeghi, P. Sandvik, P. Kung, D. Walker, K. Mi, X. Zhang, V. Kumar, J. Diaz, and F. Shahedipour, Lateral epitaxial overgrowth of GaN on sapphire and silicon substrates for ultraviolet photodetector applications, Materials Science and Engineering B74, (2000) 107–112.
- [10] K. Nishimura, N. Shigekawa, H. Yokoyama and K. Hohkawa, SAW characteristics of GaN with n⁺-GaN IDTs, Electronics Letters Vol. 42 No. 1, 5th January (2006).

-
- [11] W.C. Lan, C.D. Tsai, C.W. Lan, The effects of shower head orientation and substrate position on the uniformity of GaN growth in a HVPE reactor, J. of the Taiwan Institute of Chemical Engineers 40, (2009) 475–478.
- [12] A.T. Winzera, R. Goldhahn, G. Gobsch, A. Dadgar, H. Witte, A. Krtshil, and A. Krost, “Temperature dependence of the built-in electric field strength of AlGaIn/GaN heterostructures on Si(111) substrate”, J. Superlattices and Microstructures 36, 693–700, (2004).
- [13] I. Saraswati, NR. Poepawati, R. Wigajatri P, E. Dogheche, D. Decoster, S. Ko, Y.H. Cho, L. Considine, D. Pavlidis, “Investigation of Structural, Morphological and Optical Properties of GaN/AlGaIn Heterostructures on Si”, Photonic Global Conf. Singapore, (2012)
- [14] M. Wei, X. Wang, X. Pan, H. Xiao, C. Wang, Q. Hou, and Z. Wang, Mater. Sci. Semicond. Process. 14(2), 97–100 (2011).
- [15] A. Stolz, Ph.D. dissertation, Dept. Elect. Eng., Univ. de Valenciennes, French, (2011).
- [16] P.K.Tien, R. Ulrich and R.J. Martin, “Modes of Propagation Light Waves in Thin Deposited Semiconductor Films”, Appl. Phys. Lett. 14, 291 (1969).
- [17] R. Ulrich and R. Torge, “Measurement of Thin Film Parameters with a Prism Coupler”, Applied Opt. 12, 12, 2901, (1973).
- [18] H. P. D. Schenk, E. Feltin, M. Laugt, O. Tottereau, P. Vennegues, and E. Dogheche., Realization of waveguiding epitaxial GaN layers on Si by low-pressure metalorganic vapor phase epitaxy, Appl. Phys. Lett. 83, 5139-5141, (2003).
- [19] E. Dogheche, X. Lansiaux, and D. Rémiens, ” *m*-line spectroscopy for optical analysis of thick LiNbO₃ layers grown on sapphire substrates by radio-frequency multistep sputtering”, J. Appl. Phys. 93, 1165 (2003).
- [20] Arnaud Stolz, Suk-Min Ko, Gilles Patriarche, Elhadj Dogheche, Yong-Hoon Cho and, “Surface plasmon modulation induced by a direct-current electric field into gallium nitride thin film grown on Si(111) substrate”, Appl. Phys. Lett. 102, 021905 (2013).

Effect of Austenizing and Tempering Time on Corrosion Rate of Austenitic Stainless Steel in Oxalic Acid

Mohamed A. Gebril^{1,a}, M. S. Aldlemey^{2,b}, Farag I. Haider^{3,c}, Naji Ali^{4,d}

^{1,3,4} Mechanical Department, Engineering Faculty, Benghazi University, Benghazi-Libya

² Technical Collage of Mechanical Engineering, Benghazi-Libya

^amagebril@yahoo.com, ^bmaldleme@yahoo.com, ^cfah1232003@yahoo.com,
^dal_sahabi@yahoo.com

Keywords: Austenizing time, Tempering, Austenitic stainless steel, Oxalic acid and Corrosion rate.

Abstract. The aim of this work is to study the effect of austenizing time, tempering process and tempering time on corrosion rate of austenitic stainless steel in oxalic acid. The samples of typical 304 stainless steel were heated to 1050°C for 10, 20 and 30 minutes and quenched to room temperature in water, then tempered at 250°C, 400°C and 600°C for 30, 60 minutes for each tempering time. These samples were then immersed in 0.1M of oxalic acid and then their weight losses were measured after 30 days. The result obtained show that corrosion rate of all austenitic stainless steel samples decreased with an increase austenizing time, this behaviour is due to more homogenously of austenite, and the corrosion rate will be increased with increase the tempering temperature and tempering time, this behaviour is due different phases at microstructure below 400°C, and above of 400 to 600°C the corrosion rate will be increased due to formation of carbides which are non-uniform distributed at the grain boundaries and causes intergranular corrosion.

Introduction

Stainless steel are selected as engineering materials mainly because of their excellent corrosion resistance in many environment. Austenitic stainless steel are essentially iron chromium –nickel ternary alloys containing about 16 to 25 percent Cr and 7 to 20 percent Ni. These alloys are called austenitic since their structure remains austenitic (FCC, γ iron type) at all normal heat treating temperatures. The presence of the nickel, which has an FCC crystal structure, enable the FCC structure to be retained at room temperature. The high formability of the austenitic stainless steel is due to their FCC structure. Austenitic stainless steel normally have better corrosion resistance than ferritic and martensitic ones because the carbides can be retained in solid solution by rapid cooling from high temperature [1]. Chromium imparts the stainless properties to these steels by coating the surface with a thin but extremely dense film of chromium oxide [2]. The resistance of stainless steels is determined by its passive nature, alloy chemistry, heat treatment, precipitation morphology, kinetics and specific environment. The intactness of passive film on the surface is dependent on its stability in the medium of exposure [3 – 5]. Even though passive layer is an inexpensive means of corrosion protection, depending on the environment, it sometimes breaks down, causing severe localized corrosion attack, such as pitting, crevice, and stress corrosion cracking, leading to catastrophic failures. Austenitic stainless steels (ASS) offer excellent corrosion resistance in many organic, acidic, industrial and marine environments. The non-magnetic properties combined with exceptionally high toughness at all temperatures make these steels an excellent selection for a wide variety of applications such as in chemical plants, industrial and maritime field [6]. As a result of these, many investigations are being carried out on these types of steels almost on a daily basis [7 – 11]. Heat treatment which involves the application of heat to bring about modification in the microstructure [12] essentially alters mechanical and chemical properties based on the retained austenite, grain size and defects such as dislocation, twinning, vacancies and so on. Microstructure plays an important role in the improvement of corrosion resistance of ASS. The constituents of the microstructure such as grain size, phases, precipitates and inclusions are strongly influenced by

solidification rate or heat treatment. Oxalic acid is a relatively strong organic acid being several times stronger than acetic acid. It is used in etching for metallurgical micro-examination [13] and in the refrigerator which also incorporates stainless steels. Oxalates, which are usually formed when these steels are attacked by oxalic acids, are sparingly soluble salts, hence the manner of their deposition on the steel and the adherence or otherwise of the deposit, are likely to affect considerably the further action of the acid on the steel. The above precipitates the investigation into the effect of different tempering temperatures and time on corrosion behaviour of 304 ASS in this medium.

Experimental Work

Materials used in this study are; Austenitic stainless steel, Water as quenching media. The chemical composition of the 304 austenitic stainless steel is shown in Table 1.

Table.1 Composition of the austenitic stainless steel.

	%C	%Cr	%Mn	%Si	%Ni	%S	%P	%Fe
304 Austenitic stainless steel	0.08	18-20	1.14	0.87	8.86	0.03	0.045	remaining

Equipment used in this research includes: Heat-treatment Furnace, rotary wheel for polishing, oxalic acid (1%M), digital balance.

Hardening process. The samples were initially austenised at 1050⁰ C for 10, 20 and 30 minutes, then quenched in water and tempered at temperatures 250,400 and 600⁰C.

Corrosion rate. The corrosion rate of the samples were determined using weight loss method, samples were immersion in oxalic acid (1M) for 30 days.

Results and Discussion

The corrosion rate of austenitic stainless steel in 1.0 M oxalic acid is presented in Figure 1 in terms of corrosion rate versus austenizing time.

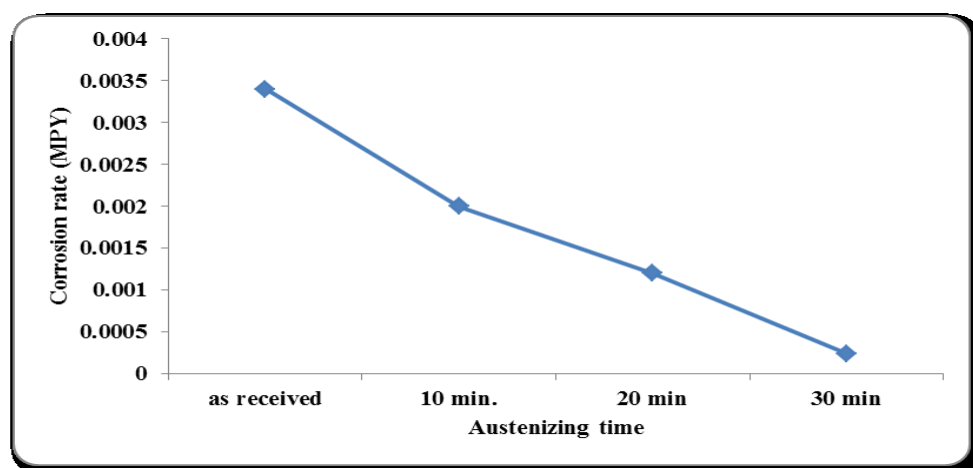


Fig. 1 Effect of austenizing time on corrosion rate

It can be observed from the Figure that the corrosion rate decreases with increase in austenizing temperature. This could be attributed to more austenitic homogenous with increasing the austenizing time to 30 minutes. Oxalic acid attacked the steel samples to form oxalate which is sparingly soluble salt and could not form a protective layer on the steel thereby enable continuous diffusion of the corrosion medium into the steel surface. The normal protective chromium oxide

which was formed on the steel surface is responsible for the little passivation observed during the exposure period. This further explains why this reagent is widely used in etching for micro-examination of austenitic stainless steel [4, 13].

Fig 2, 3 and 4 shows the effect of tempering temperature and tempering time for samples that subjected to austenizing time 10,20 and 30 minutes respectively on the corrosion rate.

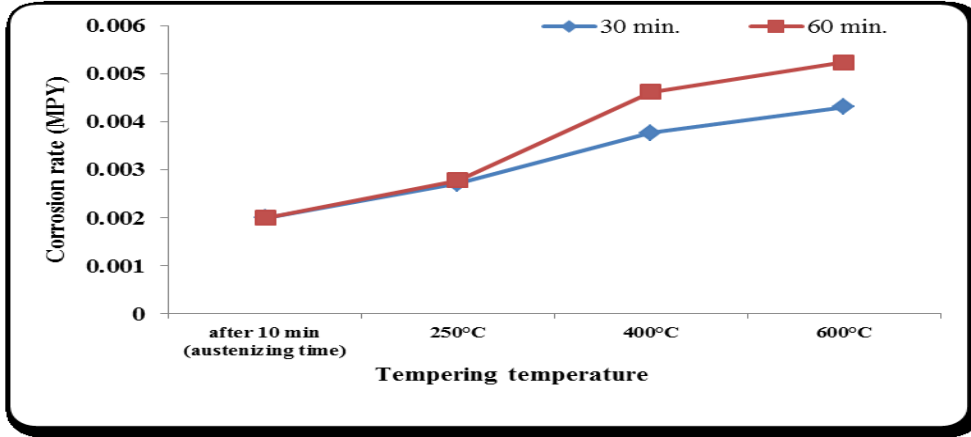


Fig. 2 Effect of tempering temperature on corrosion rate of 10 mintuse austenizing

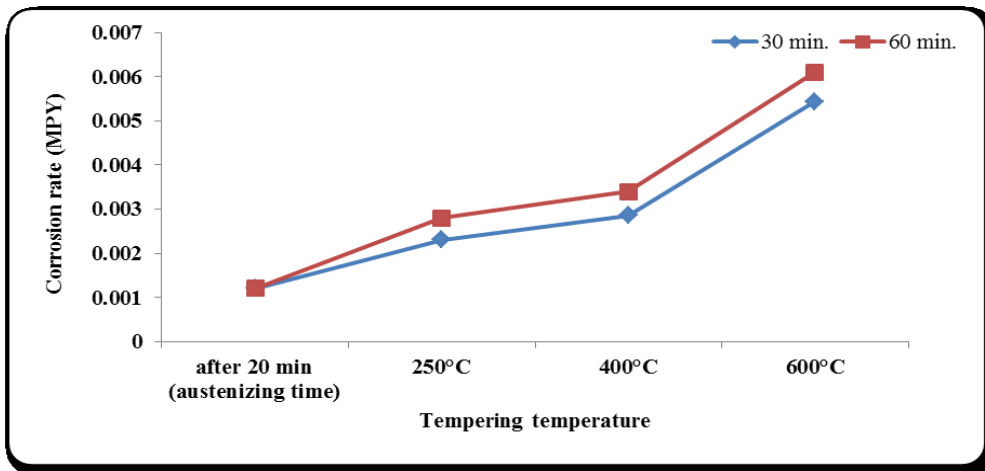


Fig. 3 Effect of tempering temperature on corrosion rate of 20 mintuse austenizing

Fig 4 shows the effect of both tempering temperature and time on the corrosion rate.

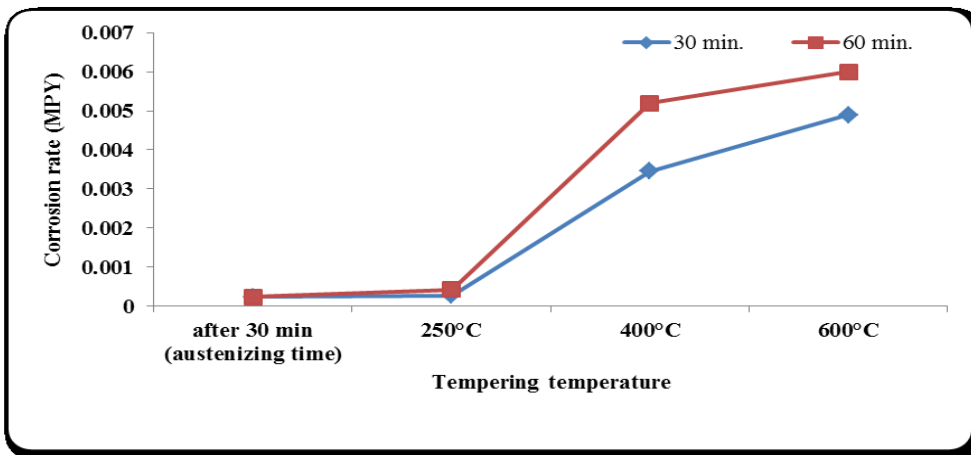


Fig. 4 Effect of tempering temperature on corrosion rate of 30 mintuse austenizing

Fig. 2, 3 and 4 shows the effect of tempering temperature and tempering time on corrosion rate of samples that austenised at 10, 20 and 30 minutes respectively, with increases tempering

temperature and tempering time, the corrosion rate increase due to different phases present (ferrite and retained austenite) which created galvanic corrosion cell at temperature 250°C . The corrosion rate increases clarity starting from 450°C and at 600°C due to precipitation of chromium carbide on the grain boundaries which will be increased with tempering temperature and time in range of 400 to 700°C [14-16]. Chromium carbides could be formed up to 800°C [17]. The higher in tempering temperature lead to more precipitation of chromium carbides and that will enhanced with time increased and leads to intergranular corrosion.

Fig. 5 shows the average of corrosion rate for three tempering temperatures 250, 400 and 600°C versus to austenizing time with considering the tempering time.

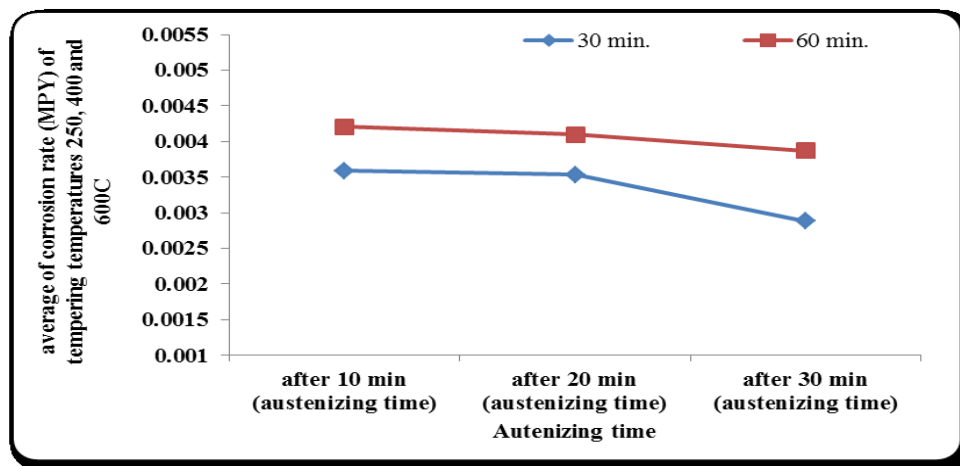


Fig. 5 Average of corrosion rate of tempering temperatures versus the austenizing time

From the Figure it's clearly that with increases tempering time the corrosion rate increases and the average rate of corrosion after 10 minutes is higher than two others time 20 and 30 minutes respectively. Presence of molybdenum in chemical composition of stainless steel will enhance of intergranular corrosion because it has an overall beneficial effect on the general corrosion resistance of stainless steel [18]. This element hinders the breakdown of passivity of pitting. It is also improves the pitting resistance of stainless steel in many environments by forming passive oxide film. Molybdate is insoluble and reduces the amount of free metal ions in the pit solution, thus decreasing the diffusion of metal cations out the pit, this decrease in diffusion reduces the rate of dissolution significantly, resulting in a decrease in size of the pit.

Conclusion

The effect of austenizing time, tempering process and tempering time on corrosion rate of austenitic stainless steel in oxalic acid was investigated by using weight loses method. The results showed that the corrosion rate of the 304 stainless steel samples decreases with increasing austenizing time, this attributable to the more austenite homogenous state. The corrosion rate of the 304 stainless steel samples increases with increasing the tempering temperature and time less than 400°C due to different phases in the microstructure which created galvanic corrosion cells. The corrosion rate of the 304 austenitic stainless steel samples increases with increasing tempering temperature and tempering time, this attributable to precipitation of carbides at the grain boundaries causes intergranular corrosion.

References

- [1] William F. Smith, Foundations of materials science and engineering, McGraw-Hill, Third edition, 1990, pp 494-497.
- [2] Raymond A. Higgins, Material for the engineering technician, The English university press ltd, First published 1972, pp161.
- [3] J. L, Pandey, S. Inder and, M. N. Singh. Electrochemical corrosion behaviour of heat treated AISI 304 austenitic stainless steel in inorganic acid mixture. *Anti –Corrosion Methods and Materials* 1997, Vol. 44, No1, p 6.
- [4] M. Matula, L. Hyspecka, M. Svoboda, V. Vodarek, C. Dagbert, J. Galland, Z. Stonawska, and L. Tuma. Intergranular corrosion of AISI 316L steel. *Materials Characterization* 2001, Vol. 46, pp 203 – 210
- [5] Aydogdu, G. H. and Aydinol, M. K. (2006) Determination of susceptibility to intergranular corrosion and electrochemical reactivation behaviour of AISI 316L type stainless steel. *Corrosion Science* Vol. 48, pp 3565 – 3583.
- [6] L.W., Tsay, S.C., Yu, S. D. Chyou and D.Y. Lin. A comparison of hydrogen embrittlement susceptibility of two austenitic stainless steel welds. *Corrosion Science* 2007, Vol. 49, pp 4028 – 4039.
- [7] M. Matula, C. Dagbert, L. Hyspecka, J. Galland and I. Martinakova. Detection of sensitization to intergranular corrosion in AISI 316L stainless steel: electrochemical potentiokinetic reactivation tests. *ProcInt Conf Euro–corr*, 2000, London.
- [8] I. Betova, M. Bojinov, P. Kinnunen, P. Pohjanne and T. Saario Influence of the electrolyte composition and temperature on the transpassive dissolution of austenitic stainless steels in simulated bleaching solutions. *ElectrochimicaActa* 2002 Vol. 47, pp 3335 – 3349.
- [9] A. Galal, N. F. Atta and M. H. S. Al-Hassan. Effect of some thiophenederivatives on the electrochemical behaviour of AISI 316 austenitic stainless steel in acidic solutions containing chloride ions. I Molecularstructure and inhibition efficiency relationship. *Materials Chemistry and Physics* 2005, Vol. 89, pp 38 – 48.
- [10] S. Girija, U. Kamachi Mudali, H.S. Khatak and B. Raj. The application of electrochemical noise resistance to evaluate the corrosion resistance of AISI type 304 SS in nitric acid. *Corrosion Science* 2007, Vol. 49, pp4051– 4068.
- [11] S. Frangini and S. Loreti. The role of alkaline-earth additives on the molten carbonate corrosion of 316L stainless steel. *Corrosion Science* 2007, Vol. 49, pp 3969 – 3987.
- [12] A. Rajan Heat treatment principles and techniques. Prentice Hall of India, New Delhi. 1998, pp 1-6.
- [13] ASTM A 262 – 90. Standard practices for detecting susceptibility to intergranular attack in austenitic stainless steels. Annual Book of ASTM Standards 1990: Section 3. Metals test methods and analytical procedures: Vol. 03.02. Wear and erosion. Metal corrosion. Philadelphia, PA: ASTM, 1992.
- [14] K. P. Balan, , A. Venugopal Reddy and D. S. Sarma. Austenite precipitation during tempering in 16Cr – 2Ni martensitic stainless steels. *ScriptaMaterialia* 1998, Vol. 39, No 7, pp 901 – 905.
- [15] L. C. Lim, M. O. Lai, and J. Ma, Tempering of AISI 403 stainless steel. *Materials Science and Engineering* 1993, Vol. A171, pp 13 – 19.

-
- [16] B. Qin, Z. Y. Wang, and Q. S. Sun. Effect of tempering temperature on properties of 00Cr16Ni5Mo Stainless steel. *Materials Characterization*.2007, Article in press.
- [17] Husain Baker, Corrosion engineering and metal surface protection, Baghdad, 1989, pp 81.
- [18] G.O. Ilevbare, and G.T. Burstein. The role of alloyed molybdenum in the inhibition of pitting corrosion in stainless steels. *Corrosion Science*2001, Vol. 43, pp 485-513.

Analysis of Thickness Strain Prediction in Warm Deep Drawing of Ti-6Al-4V Alloy

Nitin Kotkunde^{1, a}, Aditya D Deole^{1, b}, Amit Kumar Gupta^{1, c},
Swadesh Kumar Singh^{2, d}

¹Department of Mechanical Engineering, BITS-Pilani, Hyderabad Campus, Hyderabad-500078, Andhra Pradesh, India

²Department of Mechanical Engineering, GRIET, Hyderabad-500072, Andhra Pradesh, India

^anitink@hyderabad.bits-pilani.ac.in, ^bdeoleaditya@gmail.com,
^cakgupta@hyderabad.bits-pilani.ac.in, ^dswadeshsingh@griet.ac.in

Keywords: Ti-6Al-4V, Warm deep drawing, Thickness strain, FEA

Abstract. In this work, deep drawing experiments have been performed in order to study formability of Ti-6Al-4V alloy sheet at temperature ranging from room temperature to 400⁰C. It is found that below 150⁰C, formability of the material is very poor and above 150⁰C till 400⁰C, limiting draw ratio (LDR) is found to be 1.8 which is substantially lesser than other structural alloys such as austenitic stainless steels. In order to understand qualitative aspects of formability, thickness distribution of drawn cup has been evaluated experimentally over a temperature range of 150⁰C - 400⁰C. Additionally, Finite Element (FE) analysis is done using a commercially available code Dynaform version 5.6.1 with LS-Dyna version 971 solver. 3- Parameter Barlat yield model is used for FE analysis. Predicted thickness distribution using FE simulation is in good agreement with experimental results.

Introduction

Over the years, titanium and its alloys have proven themselves to be superior and cost effective materials for a wide range of applications in various industries such as aerospace, automotive, marine and biomedical [1]. Ti-6Al-4V alloy has an attractive combination of characteristics in terms of high specific strength (strength/density), excellent corrosion/erosion resistance which consider it an admirable alternative for various fields of applications [2, 3]. The warm forming is one of the main forming technologies to fabricate titanium components which can not only reduce the cost due to machining but also enhance the performance of the products [4]. However titanium alloys are difficult to form because of their high deformation resistance, low ductility at room and low elevated temperature, anisotropy and strong microstructural sensitivity [5-6].

Deep-drawing process is an important process in assessment of formability of sheet metal. Nowadays, warm deep drawing of Ti-6Al-4V alloy is an extensively used in the aerospace and automotive industries [7]. This process is commonly used in the industry because it eradicates costly operations such as welding, machining and manufactures parts with reduced weight and good mechanical properties with high production rates [8]. Titanium alloy possesses poor formability at room temperature because of certain inimitable characteristics that affect the formability such as ductility of titanium and its alloys is generally less than that of the common structural metals [9].

Few research efforts had been made in sheet metal forming of titanium alloy enlightening many interesting characteristics. Formability depends on material properties, namely strain hardening exponent (n) and strain rate sensitivity (m) [10]. It is observed that the formability of titanium alloy sheets could be significantly enhanced by hot forming process [11]. In addition to that, the experimental investigation of formability for commercially pure titanium sheets at various temperatures was studied [12]. However, very limited research is reported in the field of warm deep drawing of Ti-6Al-4V alloy. Therefore, it is essential to understand effect of variation of temperature

on formability aspect of Ti-6Al-4V alloy. The objective of present work is study the thickness distribution of Ti-6Al-4V alloy sheet at elevated temperature and validates the results with finite element analysis.

Experimental Details

In this work, Ti-6Al-4V alloy sheet of 0.89 mm thickness is used. The composition of the employed material is given in Table 1. The experiments were carried out on the test rig which is shown in Fig.1. This test rig is specifically designed so that deep drawing operations can be performed at elevated temperatures. However, there is tendency in the materials to change dimensions at higher temperatures. Therefore, nickel based super alloy was used for manufacturing die, blank holder and punch. Two sets of furnaces were utilized for 20 ton hydraulic press. One heater was employed to heat the blank and another was used to heat lower die in order to prevent the blank from becoming cold before the actual drawing starts. The setup temperature was controlled and prevented from overheating by means of water circulation from cooling tower.

Table 1 Chemical composition of as received Ti-6Al-4V sheet

Element	Al	V	Fe	C	Ti
Comp [wt. %]	5.56	4.07	0.185	0.022	89.997

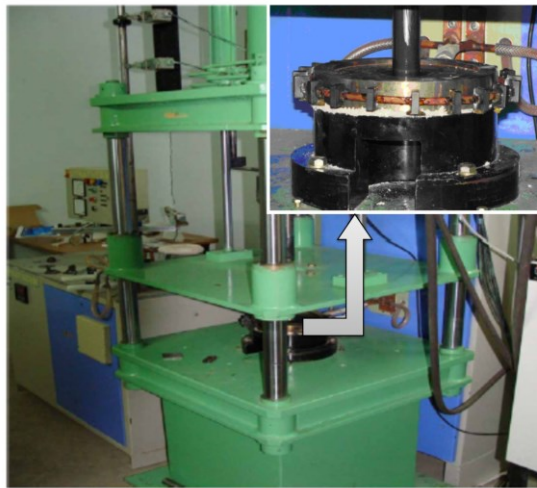


Fig. 1 Experimental test rig of deep drawing setup

A noncontact type pyrometer was used to measure the operating temperature. Circular blanks were machined by using wire-cut electro-discharge machining process for high accuracy and finish. The experiments were performed at 400⁰C and different possible diameters. The maximum limiting drawing ratio (LDR) was obtained 1.8 which is quite lower than other metallic materials. Forming at temperatures higher than 400⁰C increases the oxygen contamination and with oxygen the material becomes more brittle due to formation of α -scale. Therefore, it is preferred to perform warm forming of Ti-6Al-4V alloy in an inert and protective environment for temperature higher than 400⁰ C [13]. Molykote was used as a lubricant for warm forming process [14]. Blanks were kept at particular temperature for certain duration (approximately 3-5 minutes) for uniform heating of sheet. Deep drawing operation was performed when the blank reaches required temperature. All the experiments were performed at 10 mm/min punch speed and uniform 10 bar blank holder pressure which approximately 2% of the yield stress of material.

Finite Element Analysis

The finite element analysis is done using a commercially available code Dynaform version 5.6.1 with LS-Dyna version 971 solver. Finite Element (FE) simulations are comprehensively used for warm

forming which significantly reduced the time consuming, inexact and costly die tryouts. However, the reliability of the numerical simulations depends not only on the models and methods used but also on the accuracy and applicability of the input data.

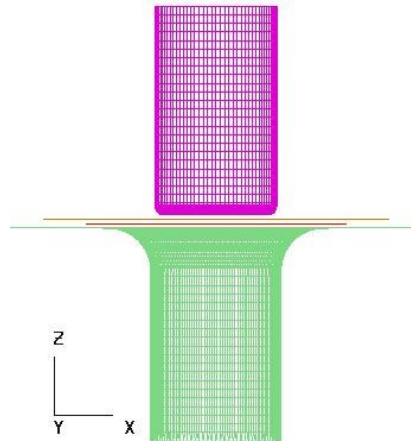


Fig. 2 Finite element model of deep drawing setup

The input models like die, blank, blank holder and punch were constructed in pre-processor. For present investigation, iso-thermal model was used. After surface was generated, fine meshing was done on the surface of the tool components and on the blank. Adaptive meshing was used on the blank to obtain accurate results. The complete model in the pre-processor is shown in Fig. 2. The blank and the tool components were meshed using Belytschko- Tsay shell elements as it takes less computational time, around 30–50% less than others [14]. Material properties were calculated using uniaxial tensile test performed at room temperature to 400⁰C at interval of 50⁰C. The tensile test experimental details are given in our previous work [13]. To avoid the effect of strain rate sensitivity on input material properties for FE simulations, same tensile test velocity was used as a punch speed for deep drawing experiments and simulation. Based on previous literature studies 3- parameter Balart model are chosen for FE simulation. It incorporates the effect of both normal and planar anisotropy in the yielding behavior of the material [14]. The Lankford parameter was calculated for 0⁰, 45⁰ and 90⁰ and used as input for simulations. The coefficient of friction under the forming conditions was calculated by inverse approach. The methodology was adopted by varying the coefficient of friction values and superimposing experimental and simulated plot of maximum punch force [14].

Result and Discussion

Drawn cups were cut using wire cut EDM and the thickness was measured from the center towards the cup wall. Thickness plots at representative setting for 52 mm and 54 mm diameter blank at 150⁰C and 400⁰C are shown in Fig. 3. In order to maintain the uniformity in measured and simulated thickness distribution graph, distance from center of cup to wall are normalized in the scale of 0 to 1. The experimental readings of drawn cups are measured three times and average values are chosen for comparison.

It can be seen from representative thickness distribution plot in Fig.3 that neck formation appeared at the punch corner and increase in thickness was observed in wall region. Similar trend is observed in finite element simulation. Moreover, the predictions are quite accurate and closer to the experimental thickness distribution as shown in Fig.3 which indicates the suitability of 3-paramter Balart model for warm deep drawing simulations. At same temperature (150⁰C) and lower the blank diameter (52 mm) more uniform thickness distribution is observed. The reason behind the non-uniformity is larger the blank diameter it is because more area of flange has to be drawn into the die which require higher punch load. Excessive punch load requirement tend to increase thinning in the punch corner region. However, at higher temperature (400⁰C) and same blank diameter (54mm), more uniform thickness

distribution is observed. The reason for uniform thickness distribution is as temperature increases, the ultimate and yield strength of material decreases which means the mean flow stress of material decreases and material become more flow able to draw. In addition to that, it can be seen from material properties that as temperature increases strain hardening exponent of Ti-6Al-4V alloy consistently increase. Strain hardening exponent (n) signifies the ability of a material to undergo large uniform strains before diffuse necking occur [10]. Therefore, increase in strain hardening exponent tend to decrease the necking tendency in all thickness distribution plots shown in Fig. 3. The similar reduced necking tendency at higher temperature can be seen in the finite element analysis.

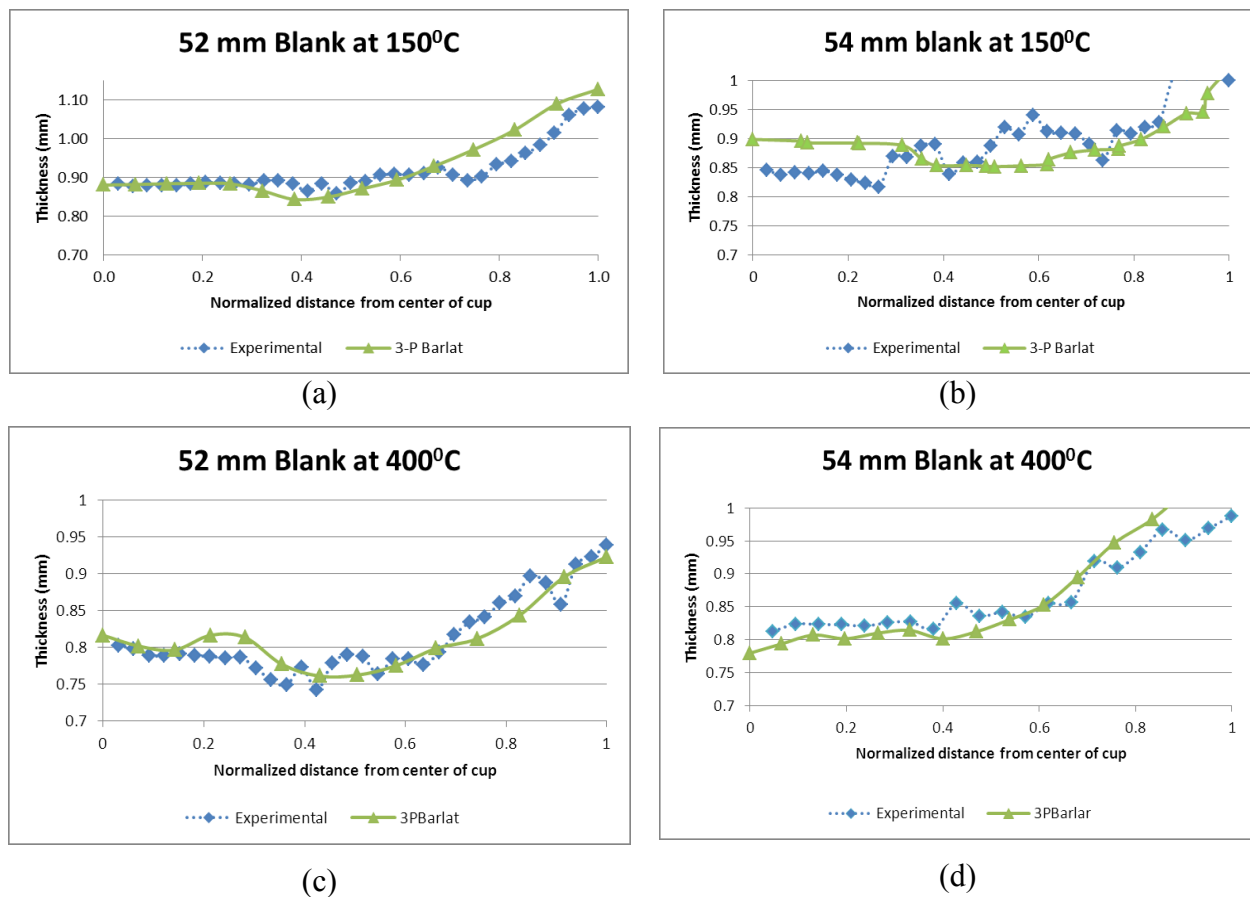


Fig. 3 Thickness distribution of deep drawn cup

Conclusion

This work involves experiments of deep drawing, study of thickness distribution and FE analysis of Ti-6Al-4V alloy at elevated temperatures. Uniformity of thickness distribution is dependent on blank diameter and temperature. However, at higher temperature more uniform thickness distribution is obtained. In addition to that, thickness distribution obtained by FE simulations show good agreement with experimental results.

Future work involves prediction of failure types, formability study and finite element simulations using different anisotropic yield criteria at higher elevated temperatures.

Acknowledgment

The authors would like to acknowledge the financial support given by Department of Science and Technology (DST), Government of India, SERB-DST, SR/FTP/ETA-0056/2011 to carry out the research activities in the institute.

References

- [1] N. Poondla, T.S. Srivatsan, a. Patnaik, M. Petraroli, A study of the microstructure and hardness of two titanium alloys: Commercially pure and Ti-6Al-4V, *J. of Alloys and Compounds*, 486 (2009) 162–167.
- [2] T. Seshacharyulu, S.C. Medeiros, W.G. Frazier, et al. Hot working of commercial Ti-6Al-4V with an equiaxed α - β microstructure: materials modeling considerations, *Material Science and Engineering A* 284 (2000) 184–194.
- [3] M. Vanderhasten, L. Rabet, B. Verlinden, Deformation mechanisms of Ti-6Al-4V during tensile behavior at low strain rate, *Journal of Materials Engineering and Performance* 16 (2007) 208–212.
- [4] F. Chen, K. Chiu, Stamping formability of pure titanium sheets, *Journal of Materials Processing Technology* 170 (2005) 181–186.
- [5] L. Zhang, Q. Lu, Z. Han, et al. Shape distortion of TC1M titanium alloy sheet during drawing process, *Journal of Acta Materialia* 43(8) (2007) 875–878.
- [6] J. Luo, M.Q. Li, H. Li, et al. Effect of the strain on the deformation behavior of isothermally compressed Ti-6Al-4V alloy, *Material Science and Engineering A* 505 (2009) 88–95.
- [7] F. Djavanroodi, A. Derogar, Experimental and numerical evaluation of forming limit diagram for Ti6Al4V titanium and Al6061-T6 aluminum alloys sheets. *Journal of Materials and Design* 31 (2010) 4866–4875.
- [8] I. Hugo, Medellín-Castillo et al. Analysis of the allowable deep drawing height of rectangular steel parts. *International Journal of Advanced Manufacturing Technology* 66 (1-4) (2013) 371–380.
- [9] R. Westman, B. Pederson, M. Wikman, Oldenburg, Numerical and Microstructural Evaluation of Elevated Temperature Compression Tests on Ti- 6Al-4V, Ti-2003 *Science and Technology*, 10th World Conference on Titanium, Hamburg, Germany (2003) Volume III 1461-1468.
- [10] Aly El-Domiaty, The effect of strain, strain rate and temperature on formability of Ti-6Al-4V alloy. *Journal of Materials Processing Technology* 32 (1992) 243-251.
- [11] J. Satoh, M. Gotoh, Y. Maeda, Stretch-drawing of titanium sheets. *Journal of Materials Processing Technology* 139 (2003) 201-207.
- [12] F.K.Chen, K.H. Chiu, Stamping formability of pure titanium sheets. *Journal of Materials Processing Technology* 170 (2005) 181-186.
- [13] N. Kotkunde, N. K. Hansoge, P. Puranik, A.K. Gupta, S.K. Singh, Microstructure study and constitutive modeling of Ti-6Al-4V alloy at elevated temperatures, *Journal of Materials and Design* 54 (2014) 96–103.
- [14] S. K. Singh, K. Mahesh, A. Kumar, M. Swathi, Understanding formability of extra-deep drawing steel at elevated temperature using finite element simulation, *Journal of Materials and Design* 31 (2010) 4478–4484.

Evaluation of CO₂ Uptake under Mild Accelerated Carbonation Conditions in Cement-Based and Lime-Based Mortars

Carla Furcas^{1,a*}, Ginevra Balletto^{2,b}, Stefano Naitza^{2,c}, Alessandro Mazzella^{3,d}

¹University of Cagliari, Interdepart. Center of Environmental Science and Engineering – Italy

²University of Cagliari, Dept. of Civil and Environmental Engineering and Architecture – Italy

³National Research Council, Institute of Environmental Geology and GeoEngineering – Italy

^acarla.furcas@unica.it, ^bballetto@unica.it, ^csnaitza@unica.it, ^damazella@unica.it

Keywords: CaCO₃, Carbonation, Cement, CO₂ uptake, Lime, Mortar.

Abstract. The industrial production of cement-based and lime-based materials such as mortars contributes significantly to the release of greenhouse gases such as CO₂ into the atmosphere. However, a percentage of these emissions is reabsorbed as the mortar hardens, owing to carbonation reactions. This study aims to explore the CO₂ sequestration capacity of a cement-based (CM) and a lime-based mortar (LM) over the first 28 days of curing. The CO₂ uptake of CM and LM was experimentally evaluated in mildly accelerated conditions by using a volumetric approach. This procedure enabled us to assess the CO₂ absorbed after 1, 7 and 28 days from mortar preparation so as to simulate CM and LM behavior during their setting, hardening, and service-life conditions. Through the experimental approach values of 19.1, 25.5 and 26.4 g CO₂/kg for CM and 5.0, 11.0 and 16.1 g CO₂/kg for LM were obtained. These results, which were validated by means of X-ray diffraction along with calcimetry analysis, confirmed that carbon sequestration by common mortars during their curing time is not negligible.

Introduction

Carbon dioxide is a greenhouse gas (GHG) mainly generated by the combustion of fossil fuels (coal, oil, gas) and by industry, notably cement and mortar manufacture. Indeed, cement production is responsible for about 5% of annual CO₂ emissions, accounting for 450 million metric tons of carbon in 2010 [1], which are mainly created by burning fuels and the calcination reaction in the production of clinker (the binder part of cement, primarily composed of limestone and aluminosilicates). Through the calcination reaction (1), calcium carbonate is converted into calcium oxide (i.e. lime) and carbon dioxide.



Furthermore, the lime industry is also involved in this process since calcination occurs in the production of natural hydraulic lime as well. In fact, natural hydraulic limes (NHLs) are produced by calcining argillaceous or siliceous limestone at around 1200°C, whereas cement clinker production requires higher temperatures, namely about 1450°C. Nevertheless, it is widely known that a percentage of emitted CO₂ due to the production of NHLs and cement-based products is reabsorbed during mortar setting and hardening, thanks to carbonation reactions (2) (3) [2], by means of which CO₂ reacts with calcium hydroxide in mortars and precipitates as calcium carbonate.



Although scientific literature concerning accelerated carbonation of coal ashes [3], alkaline industrial waste residues (i.e.: steel slag, fly ash, cement kiln dust, waste cement, etc.) [4], sludge

from urban waste water treatment plants [5], and soils and sludge including numerous metal pollutants [6] is plentiful, few studies have been conducted concerning the positives of the application of carbonation technology on cement- and/or lime-based materials. In fact, the literature on carbonation of cement-based products (i.e. mortars and concrete) has mainly concentrated on degradation [7,8], whilst little research has been developed on positive outcomes of carbonation in cement- and/or lime-based materials (i.e. pastes and mortars) owing to CO₂ uptake [9]. Indeed, these materials, having no structural use, are not subjected to rebar corrosion. Consequently, given that every year the cement and lime industry causes a considerable amount of the world's CO₂ emissions, evaluation of the CO₂ sequestration capacity during setting and hardening in the first 28 days of two selected cement- and lime-based mortars is provided in this experimental work.

Materials and Methods

Mortars. To assess the environmental effects of CO₂ uptake in highly urbanized areas, two of the most common commercial mortars in Sardinia (Italy) were considered. CM is a cement-based mortar suitable for new buildings and reinforced concrete, which was prepared in compliance with EN 998-1:2010. LM is a natural hydraulic lime mortar (NHL 3,5) suitable for historic masonry buildings, and prepared in accordance with EN 459-1:2010. The primary characteristics of CM and LM are reported in Table 1; the carbon dioxide required for the theoretically possible total carbonation of both CM and LM at 1 atm pressure of CO₂ was computed using Steinoor's formula [10].

The mineral composition of the mortars was evaluated by powder X-ray diffraction analysis. The main crystalline phases detected in LM e CM proved to be: CaCO₃ (Calcite) and Ca(OH)₂ (Portlandite).

Table 1.Characterization of CM and LM.

Oxide	CM	LM	Oxide	CM	LM	Calcimetry	CM	LM
Al ₂ O ₃ [%]	0.37	0.71	Na ₂ O [%]	0.03	0.09	CO ₂ [g]	0.139	0.149
Fe ₂ O ₃ [%]	0.12	0.40	TiO ₂ [%]	0.02	0.03	Steinoor theoretical uptake	CM	LM
MnO [%]	0.01	0.02	SiO ₂ [%]	2.46	2.78			
MgO [%]	0.75	1.13	CaO [%]	52.79	53.88	minimum [g/kg]	424	415
K ₂ O [%]	0.07	0.12	LOI [%]	43.59	41.61	maximum [g/kg]	435	422

Experimental Apparatus. CM and LM CO₂ sequestration capacity was experimentally evaluated under standard ambient temperature and pressure conditions (SATAP: pressure = 1 bar, temperature = 25°C) using a modification of the Mavor volumetric approach [11] as described in literature [12]. The Experimental apparatus (Fig. 1) consisted of a double 500 cm³ stainless cell: the Sample Cell hosted the Sample and the Reference Cell served as reservoir for the carbon dioxide, which also allowed evaluation of gas behavior in the same conditions as those of the Sample Cell. In order to keep the temperature constant during each test, the experimental apparatus was immersed in a thermostatic bath. Pressures and temperatures in both cells were independently monitored with high precision transducers within 0.1 bar and 0.1°C. All time-dependent pressure data were collected with a PC at a rate of 1 point per second.

Laboratory Procedure. The experimental procedure was the following: four samples of about 45g each for both CM and LM were cast in four small cylindrical plastic molds and immediately sealed with para-film paper to prevent early carbonation. Of these four samples, three were tested after 1, 7 and 28 days respectively from their preparation in mildly accelerated conditions (1 bar and 25°C) and the fourth sample was kept sealed as an untreated control sample. The experimental measuring procedure was initiated: the experimental apparatus was kept under vacuum (in order to exclude the uptake of atmospheric gases), and the Sample Cell was charged with 1 bar of CO₂ with a percentage by volume of approximately 99%, thus allowing the reaction between CO₂ and the sample for 24 hours.

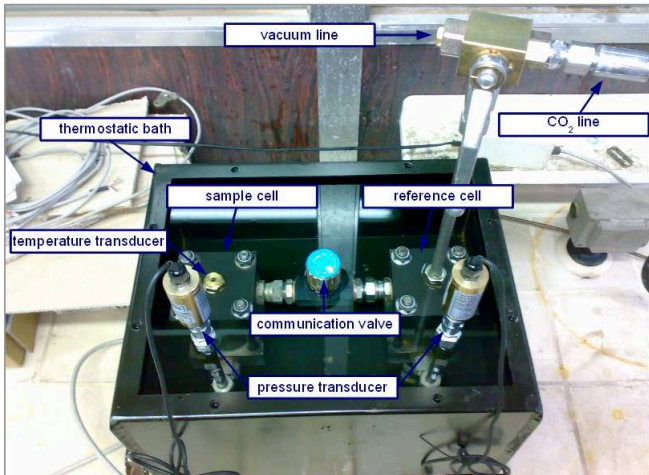


Figure 1. Experimental apparatus.

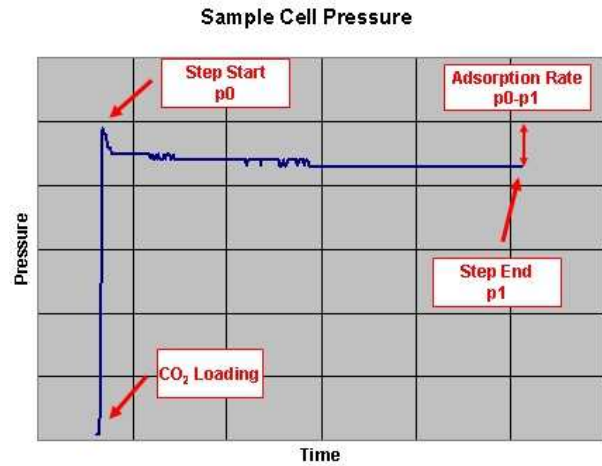


Figure 2. Pressure trend during a 24-hour test.

As a consequence of carbonation, a decrease in the pressure measured within the Sample Cell as compared to the Reference Cell was recorded by pressure transducers (Fig. 2). On the basis of the pressure values measured, the amount of CO₂ at start and end of each test was calculated using the Soave modification of the Redlich-Kwong (RKS) equation of state [13] (4):

$$p = \frac{RT}{(V-b)} - \frac{a\alpha}{V(V-b)} \quad (4)$$

where P is the pressure; T is the temperature; R is the ideal gas constant; V is the molar volume. For each sample, the difference between the moles of CO₂ calculated to be transferred into the Sample Cell and the moles of CO₂ calculated to be present in the Sample Cell after 24 hours were considered to be absorbed moles. At the end of the test, each sample was weighed and analyzed by means of an XRD technique and Dietrich-Fruehling Calcimetry. This procedure was repeated for curing day 1, day 7, and day 28 of both CM and LM.

Results and Discussion

In order to quantify the actual percentage and to confirm RKS values of CO₂-uptake, CO₂ content was determined through Dietrich-Fruehling calcimetry. In Table 2 the experimental results are reported. The values demonstrate that both LM and CM are capable of taking up CO₂. In particular, CM showed higher figures than LM. In comparison with Steinour's theoretical uptake, the carbon sequestration obtained through these 24-hour tests is considerably lower; one possible reason for this could be that the carbonation process starts from the preparation of mortars, lasts for all their service life, and even after their demolition [14].

X-ray diffraction and microscopy analyses on the untreated and treated samples were performed so as to evaluate structural modifications of both CM and LM as a result of CO₂ uptake.

Table 2. Results of the experimental procedure.

Sample ID	Mortar Type	Curing day	RKS CO ₂ -Uptake [g CO ₂ /kg mortar]	Calcimetry CO ₂ variation [g CO ₂ /kg mortar]
1	CM	1	19.1	15.6
2	CM	7	25.5	24.0
3	CM	28	26.4	27.4
4	CM	As such	-	-
7	LM	1	5.0	2.3
8	LM	7	11.0	13.7
9	LM	28	16.1	18.1
10	LM	As such	-	-

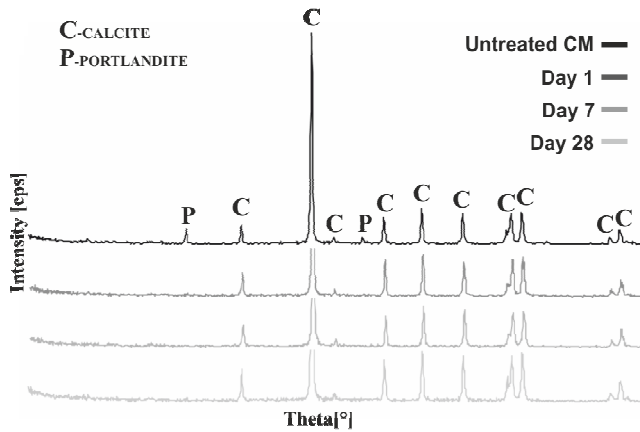


Figure 3. XRD patterns of untreated and treated CM.

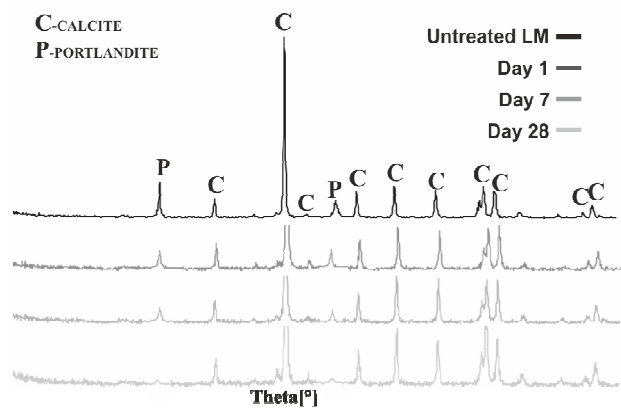


Figure 4. XRD patterns of untreated and treated LM.

XRD pattern analyses (Fig. 3 and 4) were conducted with a Rigaku Geigerflex diffractometer, using $\text{CuK}\alpha$ radiation ($\lambda_{\text{Cu}} = 1.54178 \text{ \AA}$). As expected, these analyses highlighted the fact that whilst Portlandite ($\text{Ca}(\text{OH})_2$) peaks disappeared as a result of the reaction between gaseous CO_2 and the CM and/or LM matrix, an increase in Calcite (CaCO_3) peaks was noted due to its higher concentration in the treated samples.

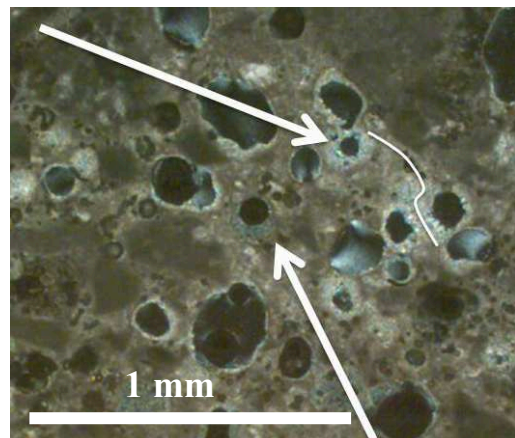
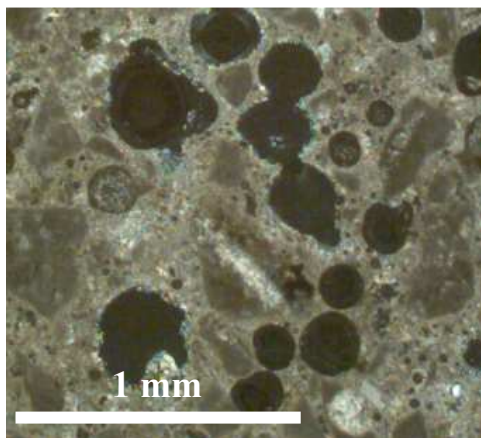


Figure 5 – Comparison between untreated (left) and treated CM (right).

The petrographic study was conducted through the preparation of thin sections, which were analyzed by means of a polarizing microscope in transmitted light. These analyses firstly underlined that for both CM and LM the carbon uptake occurred in the pores, in which calcite crystals consequently precipitated. Moreover, the higher value of porosity for CM than LM, amounting to about 25% and 11% respectively, can provide an explanation for the higher CO_2 absorption capacity of CM. Also, the comparison between the thin sections of untreated and treated samples (Fig. 5) showed that, as a consequence of carbonation, a ring structure of calcite was determined. Once calcite crystals had occluded the pore, CO_2 was allowed to flow through the fractures into the mortar matrix, reacting with calcium hydroxide and silicates, and precipitated as calcium carbonate.

Conclusion

From the experimental results it follows that common mortars are fully capable of taking up carbon dioxide. During the first 28 days of curing, a higher CO_2 sequestration capacity for CM was observed, and afterwards confirmed by X-ray diffraction and microscopy analyses. In particular, the petrographic study showed that for both CM and LM the CO_2 uptake occurred at pore level, CM exhibiting higher uptake figures due to its higher porosity.

Although the CO₂ sequestration values obtained are far from the performance of other materials, such as coal ash and industrial residues, it should be pointed out that mortars have great potential. Indeed, though they may seem low, these amounts could be significant considering the widespread use of mortars, the period of their service life, and afterwards (i.e. after demolition). In fact, the environmental importance of carbonation in mortars emerges from comparison between the CO₂ emitted due to calcination in their production and the evaluation of their CO₂ absorption capacity during their whole lifetime. Thus, the next steps in our research will concentrate on the assessment of the absorbed CO₂ as a result of carbonation as compared to the CO₂ emissions in the production process of mortars.

References

- [1] T.A. Boden, G. Marland, R.J. Andres, Global, Regional, and National Fossil-Fuel CO₂ Emissions. U.S. Department of Energy, Oak Ridge, 2013.
- [2] D. R. Moorehead, Cementation by the carbonation of hydrated lime, *Cement Concrete Res.* 16 (1986) 700-708.
- [3] H. Y. Jo, J. H. Kim, Y. J. Lee, M. Lee, S. Choh, Evaluation of factors affecting mineral carbonation of CO₂ using coal fly ash in aqueous solutions under ambient conditions, *Chem. Eng. J.* 183 (2012) 77– 87.
- [4] S.Y. Pan, E.E. Chang, P.C. Chiang, CO₂ capture by accelerated carbonation of alkaline wastes: a review on its principles and applications, *Aerosol Air Qual. Res.* 12 (2012) 770–791.
- [5] S. Valls, E. Vazquez, Accelerated carbonation of sewage sludge–cement–sand mortars and its environmental impact, *Cem. Concr. Res.* 31 (2001) 1271.
- [6] M. Fernández Bertos, S.J.R. Simons, C.D. Hills, P.J. Carey, A review of accelerated carbonation technology in the treatment of cement-based materials and sequestration of CO₂, *J. Hazard. Mater.* B112 (2004) 193–205.
- [7] S.K. Roy, K.B. Poh, D.O. Northwood, Durability of concrete-accelerated carbonation and weathering studies, *Build. Environ.* 23 (1999) 597-606.
- [8] B. Johannesson, P. Utgenannt, Microstructural changes caused by carbonation of cement mortar, *Cement Concrete Res.* 31 (6) (2001) 925-931.
- [9] Ö. Cizer, K. Van Balen, J. Elsen, D. Van Gemert, Real-time investigation of reaction rate and mineral phase modifications of lime carbonation, *Constr. Build. Mater.* 35 (2012) 741–751.
- [10] H.H. Steinour, Some effects of carbon dioxide on mortars and concrete-discussion, *J. Am. Concrete I* 30 (1959) 905-907.
- [11] M.J. Mavor, Measurement and evaluation of coal sorption isotherm data. In: Society of Petroleum Engineers, Annual Technical Conference and Exhibition, New Orleans, 1990, pp.157-170.
- [12] R. Ciccù, A. Mazzella, C. Tilocca, G. Mei, CO₂ uptake and metal release capacity of carbonated Sulcis Coal Ash, in: Proceedings Sardinia 2011, Thirteenth International Waste Management and Landfill Symposium, CISA Publisher, Padova, 2011.
- [13] G. Soave, Equilibrium constants from a modified Redlich-Kwong equation of state, *Chem. Eng. Sci.*, 27 (1972) 1197-1203.
- [14] R. Andersson, K. Fridh, H. Strippl, M. Häglund, Calculating CO₂ Uptake for Existing Concrete Structures during and after Service Life, *Environ. Sci. Technol.* 47 (2013) 11625–11633.

A Brief Review on Manufacturing of Al-TiC MMC

Sravan Kumar Josyula^{1, a}, Narala Suresh Kumar Reddy^{2, b}

¹Research Scholar, Department of Mechanical Engineering, BITS-Pilani Hyderabad Campus, Hyderabad, AP, 500078. INDIA

²Associate Professor Department of Mechanical Engineering, BITS-Pilani Hyderabad Campus, Hyderabad, AP, 500078. INDIA

^asrbavanty@gmail.com, ^bnskreddy@hyderabad.bits-pilani.ac.in

Keywords: Aluminum, Titanium carbide, Metal Matrix Composites (MMCs), machinability, powder metallurgy.

Abstract. Aluminum based Titanium carbide particulate reinforced metal matrix composite (Al-TiC PMMC) draws attention by many researchers & industries over alloy materials because of its excellent thermo-physical and mechanical characteristics. Despite of its superior properties of Al-TiC MMC, its complexity in manufacturing process and poor machinability has been the main deterrents to its application level. Controlling agglomeration of TiC particles is a challenging task to retain improved microstructure. The hard abrasive nature of carbide particles cause poor machinability and high machining cost. Therefore, in this paper an attempt has been made to study the various manufacturing techniques to achieve uniform distribution of TiC reinforcements in Al matrix. Further, the review follows the secondary manufacturing process of Al-TiC PMMC, which address three topics: machining, forming & welding.

Introduction

MMC are the next generation of materials with good physical, chemical, and mechanical properties. They have potential to be replacement for conventional metal and alloys in various applications due to their low weight and toughness. Interest on MMCs are widely spread all over structural and engineering industries due the availability of relatively inexpensive reinforcements, and improvement of various processing techniques which results in reproducible micro structure & properties[1]. The mechanical and Thermo physical properties of MMCs are mainly depends on the reinforcement size and weight percentage presented in the matrix.

Al based MMC got prominent importance due its excellent wear/stiffness, and good strength-to-weight ratio, where as in reinforcement TiC particles projected significance due its predominant wettability and strong interfacial bonding with matrix in fabrication of composite materials[3 &4]. Al-TiC composite belongs to the new generation of aluminium based particulate reinforced metal matrix composite (PMMC) which is to expected to use in higher commercial & industrial applications due to its low cost, ease of fabrication and improved properties[5].

Even though Al-TiC MMC is considered to be holding superior metallurgical and mechanical properties, its application is undermined due to the complex manufacturing process as well as poor machinability. In this paper, an attempt has been made to review the various manufacturing process techniques to achieve improved microstructure in Al-TiC PMMC. In this paper section 2 gives information about various manufacturing techniques like in-suit, powder metallurgy, stir casting, pressure less infiltration, friction stir process for production of Al-TiC composite. Further section explains about various studies that has been carried on three main secondary manufacturing process: machining, forming & welding to understand the effect of input parameters during the processes.

Past Research on Production of Al-TiC PMMC

Particulate reinforced MMCs(PMMC) are of particular interest because of their easy manufacturing & low production cost[6]. There are several possible methods of producing PMMC's which are primarily depends on type and level of material system and degree of microstructural

integrity desired. For economic reasons near net shape production should be attempted to minimized mechanical finishing operations. In general, Al-TiCPMMC's are produced by In-suit Synthesis process (ISP) [7 - 14] Powder metallurgy (P/M) [21 & 22], Friction stir process (FSP)[15&16], Stir casting (SC) [17] respectively.

In suit synthesis process. In situ techniques involve a chemical reaction resulting in the formation of a very fine and thermodynamically stable reinforcing ceramic phase within a metal matrix. As a result, this provides thermodynamic compatibility at the matrix-reinforcement interface. This procedure can take place in both *solid and liquid phase processes*. Both phases produce very fine reinforcements in the matrices which are clean and semi coherent in some cases.

In solid synthesis processes, high purity titanium and carbon powder and aluminium powder were mixed together, compacting this mixture and heated from top to begin the formation of reinforcements. EL Zhang[7] successfully fabrication of Al-TiC composite using this processes. The whole process of synthesis is started by diffusion of partially molten aluminium around the Ti and C powders. When concentration of Ti powder around aluminium reaches 0.15wt% a precipitate reaction happens and Al_3Ti phase is formed around the Ti powder. *Titanium concentrated around carbon and a Ti-rich layer is high enough, an exothermic reaction to synthesize TiC.* The micro-mechanism of the reaction synthesis TiC is shown in fig 1.

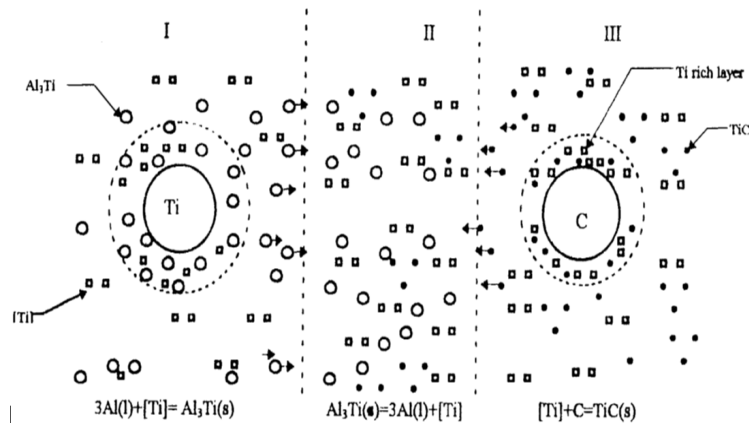
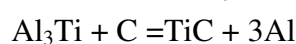
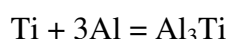
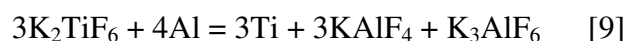


Fig.1 Micro mechanism of reaction synthesis TiC, [7]

In *liquid state synthesis process*, TiC particles are formed by addition of *gaseous phase* [8] (Carbonaceous gas) and *Precipitates phase* [9&10] (K_2TiF_6 or Ti and C) into a *liquid metal/alloy*. R.F. Shyu et al [16] used Al-5.1Cu-6.2Ti was used as a matrix material in this process for fabrication Al-TiC composite. The in-suit reaction was carried out by diffusion of carbonaceous gas in vacuum induction furnace for 4hrs at a constant temperature of 1400K. The diffused C gas reacts with Ti substrate in the molten matrix and forms TiC particles.

Reaction synthesis by precipitate phase, Ti dissolves and wets the graphite particles which leads to the formation of TiC reinforcement. Ranjit Bauri[9] successfully fabricated Al-TiC PMMC by reaction synthesis of K_2TiF_6 and graphite powder in molten Al matrix, the results shows that at lowest temperature there is no sign of formation of TiC and only blocky type Al_3Ti particles are observed. When temperature increased above $900^\circ C$ the blocky Al_3Ti particles become and unstable and Ti dissolves and wets the graphite particles to form TiC according to the following reaction. Effect of temperature on reaction process is showed in fig2. these observations also provide some insights in to the reaction mechanism of TiC formation.



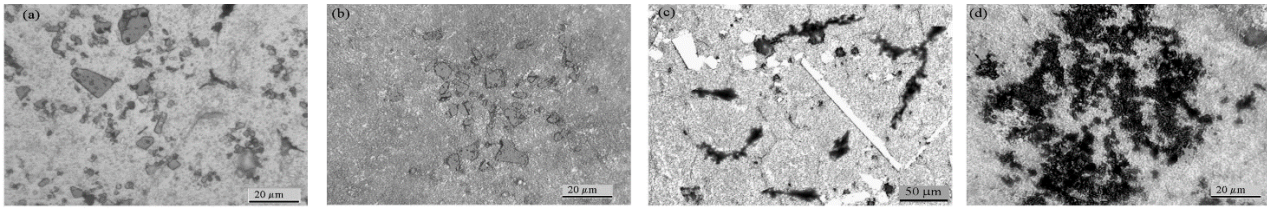


Fig.2 Optical micrographs of powder blends processed at (a) 700°C (b) 800°C (c) 900°C (d) 1000°C.[9]

Composite manufactured from in situ processes are having better properties over the conventional composites. This is due to formation of fine and dispersed TiC particles in the composite. The reaction kinetics for formation of TiC particles in situ in the Al melt depends on various factors like temperature, reaction time, Ti:C ratio. TiC particle formation during process. K.B. LEE et al [11] have observed Al_4C_3 , $Al_{18}Ti_2Mg_3$, Ti_2AlC , Al_3Ti , and $TiAl$ interfacial reaction products in Al-Mg/TiC composite, which was fabricated by the Pressure less infiltration process, whereas Mitra et al.[12] have reported Al_3Ti , Al_4C_3 , Ti_2AlC , and $TiAl$ phases in Al/TiC composite, which was fabricated by the XD process. This interfacial reaction product will cause disturbance in mechanical and thermal properties of composites. Extensive interfacial reaction causes detriment of composite. Therefore, in course of reaction synthesis, system must be carefully screened in order to obtain optimum mechanical properties & appropriate interfacial reaction.

Friction Stir process (FSP). A Thangarasu et al [13] used Friction stir processing (FSP) to fabricate TiC particulate ($\sim 2 \mu m$) reinforced aluminum matrix composite (AMC) as shown in fig. 3. The TiC powders were compacted into a groove of $0.5 mm \times 5.5 mm$. A single pass FSP was carried out using HCHCr steel tool rotational speed of 1600 rpm, processing speed of 60 mm/min and axial force of 10 kN. Friction between the rotating tool and the work piece causes a rise in local temperature till the material can plastically deform. Though FSP has been basically advanced as a grain refinement technique, it is a very attractive process for also fabricating composites.

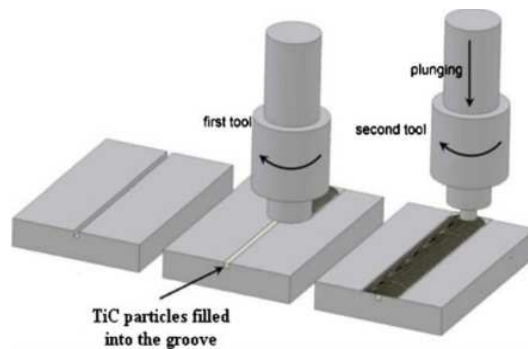


Fig.3 FS Process [13]

Stir casting (SC). In stir casting process, powder form reinforcements are distributed into molten metal by the means of mechanical stirring process. Production of MMC's using this process can be affected by process variables such as holding temperature, stirring speed, size of the impeller, and the position of the impeller in the melt which has an impact on mechanical properties [14]. S. GopalaKrishnan et al [15] used stir casting process to fabricate Al-TiC PMMC under argon atmosphere to prevent reaction of molten aluminium with an atmosphere during casting process. It is observed that wear loss in terms of volume was found to be very less when compared with composite manufacture in in-situ reaction process. Hence it may be concluded that stir casting technique is the best and easiest process for production of Al-TiC PMMC than any other methods.

Powder metallurgy (P/M). Powder metallurgy is a highly evolved method for fabrication of composite to very close dimensional tolerances, with minimum scrap and fewer secondary machining operations. Optimal TiC (sized and wt %) powder [16] and Al powder were mixed for a

longer duration to achieve uniform distribution of TiC particle. The mixed powder was compacted at a pressure of 300-500Mpa with zinc stearate as a lubricant. This compacted product is sintered at 500°C - 550°C with a soaking time of 2-3hr under argon atmosphere and then subjected to furnace cooling. V SenthilKumar et al [17] & M Ali et al [18] has found that mechanical properties like hardness & strength increase with increase in % of TiC content in composite. Also results reveals that with the increase in sintering temperature, the number of pores decreased and the rate of grain growth apparently increased. However, this method requires alloy powders that are generally more expensive than bulk material, and involves complicated processes during the material fabrication. Thus, powder metallurgy may not be an ideal processing technique for mass production.

Past Research on Secondary Manufacturing Process

From the above studies it is understood there are various techniques for production of Al-TiC near to the net shape but in most engineering applications, the need for secondary manufacturing process cannot be completely eliminated to get the desired dimensions accuracy and surface finish.

Machining. In turning, lower percentage of TiC content gives better surface finish, feed is the significant factor which is affecting the surface roughness followed by the interaction between feed rate and depth of cut, quadratic effect of feed rate and interaction effect of speed and depth of cut [19]. In shaping operation discontinuous chips are formed due to micro cracks propagation on chip thickness. This fracture through the chip thickness leads to reduction in cutting force (CF). R N Rai et al [20] observed that CF are less in Al-TiC PMMC than those of Al-TiAl₃, Al-Si and pure Al as shown in fig 4.

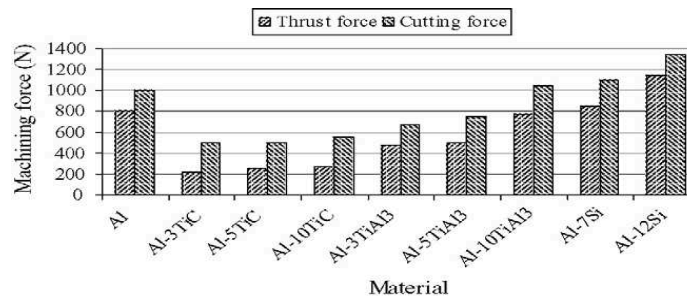


Fig.4 Cutting and thrust forces for different composite materials and alloys [20].

Welding. Welding is a way to make high strength joints between two or more parts. R Garcia et al [21] did a comparative study of the MIG welding of Al/TiC composites using direct and indirect electric arc processes. He observed slight dissolution in DEA process and very little or no dissolution in IEA process. Based on micro structural and mechanical properties he concluded that IEA can be considered an alternative for solving some problems encountered in welding of MMCs. In friction stirrer well (FSW), as the welding speed increased the ultimate tensile strength (UTS) values of taper square tool and square tool decreased as shown in fig 5. Hence it is recognized that the tool pin profile has maximum effect on tensile strength of friction stir welded joints followed by welding speed [22].

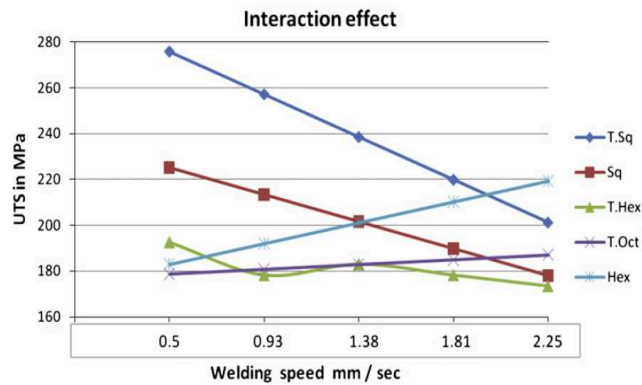


Fig. 5 Effect of tool pin profile and welding speed on ultimate tensile strength (UTS) [22]

Forming. It is well known that a metal takes a desired shape and size during forming by improving the strength of the components, due to plastic deformation. Seksak Asavavisithchai et al [23] observed the composite foam has higher strength and larger energy absorption than the pure Al foam, for a given strain. The yield strength of the foams also increases with increasing particle contents. RN Rai et al, [24] reported that forged and rolled specimens improve uniform distribution of the TiC particles, which are responsible for the enhancement of the tensile strength of the composite. This improvement in mechanical properties are due to the fact that the cohesion of the clustered TiC particles gets weakened and particles are redistributed in the matrix. Size of the TiC clusters decreases continuously with the reduction in cross-section during rolling. In the case of forging, cluster size decreases with increase in forging load through damage/disintegration of TiC clusters.

Future Direction of Research

Al-TiC composite is a new class of MMC materials with distinct properties over the alloy materials. Literature review of open source emphasizes that there are only few reports exist in the area of machinability, welding & forming of composite materials particularly Al-TiC MMC. The complexity in secondary manufacturing process like poor machinability, formability & weldability (convention welding) has been the main deterrents to its application level. The existence of hard TiC particles in aluminium matrix influences rapid abrasive wear and high processing cost. Hence there is a need to understand the fundamentals of machining, forming and welding process. Following is a list summarizing the future research opportunities, Challenges and guidelines in the area of machining, welding, and forming of metal matrix composites.

- Basic understanding of secondary manufacturing process on MMC
- Investigation of machinability characteristics of Al-TiC MMC and the cutting tool performance during machining
- Study the failure behavior and reinforcement distribution of TiC during welding & forming.

Acknowledgment

Author wish to acknowledge the funding support (22(0567)/12/EMR-II) from Council of Scientific and Industrial Research Human Resource Development Group, India.

Reference

- [1] P. M. Ajayan, L. S. Schadler, P. V. Braun, Nanocomposite Science and Technology, Copyright 2003 WILEY-VCH Verlag GmbH Co. KGaA, Weinheim, ISBN: 3-527-30359-6.
- [2] G. B. Veeresh Kumar, C. S. P. Rao, N. Selvaraj, Mechanical and tribological behavior of particulate reinforced aluminum metal matrix composites – A review, *Journal of Minerals & Materials Characterization & Engineering*, 10:1 (2011)59-91.
- [3] H.Persson, Machining guidelines of Al/SiC particulate MMC, MMC-Assess Thematic Network, MMC-Assess Consortium, 6 (2001).
- [4] C. A. Leon, V. H. Lopez, E. Bedolla, Wettability of TiC by commercial aluminum alloys, *Journal Of Materials Science*, 37 (2002) 3509 – 3514.
- [5] Malek Ali, ProjjalBasu, MarwaLiwa, M. I. Fadhel, M. Souiyah, Basem Abu Zien Comparison between the properties of Al–TiC and Al–(TiC+Fe₃C+Fe₂Ti+Fe) composites, *Arabian Journal for Science and Engineering*,38:10 (2013) 2785-2791.
- [6] T. Lucey , R. Wuhner, W. Y. Yeung, A quadrat analysis on particle distribution of cold rolled SiCp/Zn-22 Wt% Al composites, *Materials Forum*.32 (2008).
- [7] El Zhang, B Yang, S Y Zeng, QC Li, M Z Ma, Experimental study on reaction synthesis of TiC in Al-Ti-C system, *ACTA Metallurgic Sinica* 11:4 (1998) 255-260.
- [8] Premkumar, M.K., Chu, M.GAlTiC particulate composite produced by a liquid state in situ process, *Materials Science and Engineering A* 202:1-2, 1 (1995) 172-178.
- [9] Ranjit Bauri, Synthesis of Al -TiC in-situ composites: Effect of processing temperature and Ti:C ratio, *Transactions of The Indian Institute of Metals*, 62: 4-5 (2009) 391-395.
- [10]El Zhang, Zeng Xiaochun, Zeng Songyan, Li Aingchun, Microstructure and properties of Al/TiC composite prepared by reaction synthesis, *Transaction of NFsoc*, 16:1(1996) 114-119.
- [11]K.B. Lee, H.S. Sim, And H. Kwon Reaction Products Of Al/Tic Composites Fabricated By The Pressureless Infiltration Technique, *Metallurgical And Materials Transactions A*, 36a (2005) 2517-2527
- [12]R. Mitra, J.R. Weertman, M.E. Fine, and R.M. Aikin, Jr: Proc. Conf. on the Developments in Ceramic and Metal-Matrix Composites, K.Upadhyaed.,TMS,Warrendale,PA,(1991)125-42.
- [13]A Thangarasu, N Murugan, I Dinaharan, S J Vijay, Microstructure and micro-hardness of AA1050/Tic surface composite fabricated using friction stir processing, *Sadhana*, 37:5 (2012) 579–586.
- [14]J. Hashim, L. Looney, M.S.J. Hashmi Metal matrix composites: production by the stir casting method, *Journal of Materials Processing Technology*, 1:7(1999) 92-93.
- [15]S. Gopalakrishnan, N. Murugan, Production and wear characterisation of AA 6061 matrix titanium carbide particulate reinforced composite by enhanced stir casting method, *Composites: Part B* 43 (2012) 302–308.
- [16]A. T. Alpas, J. Zhang Effect of microstructure (particulate size and volume fraction) and counter face material on the sliding wear resistance of particulate-reinforced aluminum matrix composites,*Metallurgical and Materials Transactions A*, 25:5 (1994) 969-983.
- [17]V. Senthilkumar, A. Balaji, HafeezAhamed, Effect of secondary processing and nanoscale reinforcement on the mechanical properties of Al-TiC composites, *Journal of Minerals & Materials Characterization & Engineering*, 10:14 (2011) 1293-1306.

- [18] Malek Ali, M. I. Fadhel, M. A. Alghoul, A. Zaharim, K. Sopian, Synthesis and characterization of aluminum matrix composites reinforced with various ratio of TiC for light devices, *Models and Methods in Applied Sciences*, 169-174.
- [19] P. R. Patel, B. B. Patel, V. A. Patel, Effect of machining parameters on surface roughness for 6063 Al-TiC (5 & 10 %) metal matrix composite using RSM, *IJRET*, 2:1(2013) 65-71.
- [20] Ram Naresh Rai, G.L. Datta, M. Chakraborty, A.B. Chattopadhyay, A study on the machinability behaviour of Al-TiC composite prepared by in situ technique, *Materials Science and Engineering A*, 428 (2006) 34-40.
- [21] R. Garcia, V. H. Lopez, E. Bedolla A comparative study of the MIG welding of Al/TiC composites using direct and indirect electric arc processes, *Journal of Materials Science* 38 (2003) 2771-2779.
- [22] S.Gopalakrishnan, N.Murugan, Prediction of tensile strength of friction stir welded aluminium matrix TiC particulate reinforced composite, *Materials and Design*, 32(2011) 462-467.
- [23] Seksak Asavavisithchai and Apiyut Opa, Effect of TiC Particles on Foamability and Compressive Properties of Aluminium Foams, *Chiang Mai J. Sci.* 2010; 37(2): 213-221
- [24] Ram Naresh Rai, A.K. Prasada Rao, G.L. Dutta and M. Chakraborty, Forming behaviour of Al-TiC in-situ composites, *Materials Science Forum*, 765 (2013) 418-422.

The Investigation of Microstructures Fabrication on Quartz Substrate Employing Electron Beam Lithography (EBL) and ICP-RIE Process

Liyana Shamsuddin^{1, a}, Khairudin Mohamed^{1, b} and Maryam Alsadat Rad^{3, c}

¹Nanofabrication and Functional Material Research Group, School of Mechanical Engineering, USM Engineering Campus, 14300, Nibong Tebal, Seberang Perai Selatan, Penang, Malaysia.

²Nano-Optoelectronics Research and Technology Laboratory, School of Physics, Universiti Sains Malaysia (USM), 11800 Minden, Penang, Malaysia

^anliyana39@gmail.com, ^bmekhairudin@eng.usm.my, ^cmaryam.s.rad@gmail.com

Keywords: Electron Beam Lithography. Inductively Coupled Plasma Reactive Ion Etching. PMMA. Development Process. Raith ELPHY Quantum.

Abstract. The fabrication of micro or nano-structures on quartz substrate has attracted researchers' attention and interests in recent years due to a wide range of potential applications such as NEMS/MEMS, sensors and biomedical engineering. Various types of next generation lithographic methods have been explored since optical lithography physical limitations has hindered the fabrication of high aspects ratio (HAR) structure on quartz substrates. In this research, the top-down fabrication approach was employed to fabricate microstructures on quartz substrate using Electron Beam Lithography (EBL) system, followed by the pattern transfer process using Inductively Coupled Plasma-Reactive Ion Etching (ICP-RIE) technique. The factors that influenced pattern definition include the type of electron beam (e-beam) photoresist, e-beam exposure parameter such as spot size, working distance, write field, step size, e-beam current, dosage as well as the type of developer and its developing time. The optimum conditions were investigated in achieving micro or nano-structures. Field emission scanning electron microscopy (FESEM) with energy-dispersive X-ray (EDX) and atomic force microscope (AFM) were utilized to characterize the structures profiles.

Introduction

Fabricating of micro/nano structures on quartz would open several new possibilities because of its superior properties in UV transmission, piezoelectricity, can bear high temperature and extremely hard. The structures have many applications such as X-ray diffractive optical elements, microfluidic, light trapping structures for solar cells, and micro/nano-electro-mechanical system (MEMS/NEMS) [1] especially in biomedical engineering, three-dimensional (3D) batteries as well as the interconnection of 3D integrated multiple circuit layers for integrated circuit (IC). However, the fabricating process of micro/nano structures on insulating material is still a challenging due to limited information available for quartz etching. Pseudo Bosch and Cryogenic processes that employed for deep silicon etches are not suitable for quartz [2].

The major fabrication processes involved in this study are pattern definition on an imaging layer using EBL and pattern transferred onto a substrate by ICP-RIE. EBL system based on the scanning electron microscope is a powerful tool for fabricating fine micro/nanostructures pattern, capable of very high resolution and can work with variety of materials. There are two basic methods of pattern definition which are subtractive and additive. The additive pattern transfer method is the most suitable for a HAR fabrication because for etching hard materials such as quartz, it requires mask material that is highly resistant to plasma etch. While, ICP-RIE system can produce high density plasmas thus well suited to achieve directional and HAR structures. RIE with combination of inductively coupled plasma (ICP) employs magnetic fields to enhance the densities of the plasma bring the success on nanostructures creation. In an ICP process, the excitation is again a time-varying RF source but is delivered inductively. For several applications, the use of RIE will remain the best option. However, for specific applications mainly where a HAR is required plasma at low pressures to create fined nanostructures.

Experimental Details

The overall processes of fabricating structures as illustrated in Fig. 1. Quartz wafer was cleaned using Radio Corporation of America (RCA) cleaning method to remove organic contaminations from the wafer surface, any oxide layer that may build up and ionic or heavy metal contaminations [3]. In this work, the PMMA bi-layer photoresist was coated on the quartz surface which are PMMA 120K (2% in Chlorobenzene) followed by PMMA 996K (2% in Chlorobenzene). Both layers were spun coated at speed 4000 rpm for 45 s get the overall thickness about 180 nm were prebaked at a temperature 90 °C for 30 min for each layer. Conductive polymer, PEDOT/PSS was coated on top of the photoresist to suppress the surface changing effects during lithography. Raith-150 ELPHY Quantum EBL based on the SEM system (JEOL JSM-6460LV) was employed to define the pattern. The EBL exposure parameters to define the pattern as listed in Table 1. The exposed PMMA layer was developed in MIBK:IPA 1:3 for 60 s at 23 °C. NiCr thin film was coated on developed pattern on quartz using a thermal evaporator to function as a mask during the etching process. Then, soaked the quartz in acetone to remove the remaining resists and unwanted metal layer. The pattern transfer process was carried out by a PlasmaLab 80 Plus of Oxford Instruments system using CHF₃/Ar etchant gas with flow rate 50 sccm and 30 sccm, respectively. Table 1 show the etching parameter used to transfer the pattern on quartz, where the pressure used is 30 mTorr, RIE RF power 200 W and ICP RF power 20 W for duration 10 min.

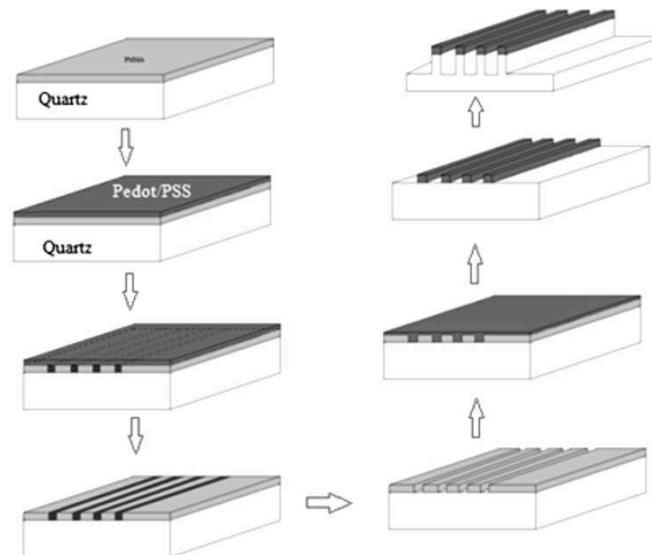


Fig. 1. The fabrication process using conductive polymer method on the quartz substrate.

Table 1 Parameters of EBL to define pattern on PMMA and ICP-RIE etching process.

Exposure Parameters	Setting	ICP-RIE Parameters	Setting
Write fields	100 [μm]	Gases	CHF ₃ /Ar
Voltage acceleration	30 [keV]	Gases flowrate	50/30 [sccm]
Aperture	35 [μm]	Pressure	30 [mTorr]
Beam current	60 [pA]	Temperature	293 [K]
Line step size	10.7 [nm]	ICP/RIE RF power	20/200 [W]
Line dosage	1000 [pAs/cm]	Etching rate	14 [nm/min]

Result & Discussion

The EBL exposure parameters, developing processes, metal deposited and parameter during etching are dependent on feature size of pattern design. Fig. 2 shows AFM image (a) finger pattern shape after developing process and etched pattern on quartz (b) L-shape (c) Line shape and (d) close up of line shape. The main issues during EBL pattern writing on an insulated substrate are surface

changing, electron scattering and proximity effect [4]. Reaction of electrons hit the substrate are more complex although e-beam lithography tools are capable of forming extremely fine probes. Forward scattering occurred when the electron penetrate the resist, which tend to broaden the initial beam diameter. While, the backscattering ensue when the electrons penetrate through the resist into the substrate. According to [5], the backscattered electron caused the proximity effect where the dose that a pattern feature receives is affected by electrons scattering from other feature nearby. The developed pattern was immense compare to the actual pattern design using GDSII through AFM profile measurements. The proximity effect place a limit on the minimum spacing between patterns features due to electron beam probe size where a different effect upon the development of exposed pattern.

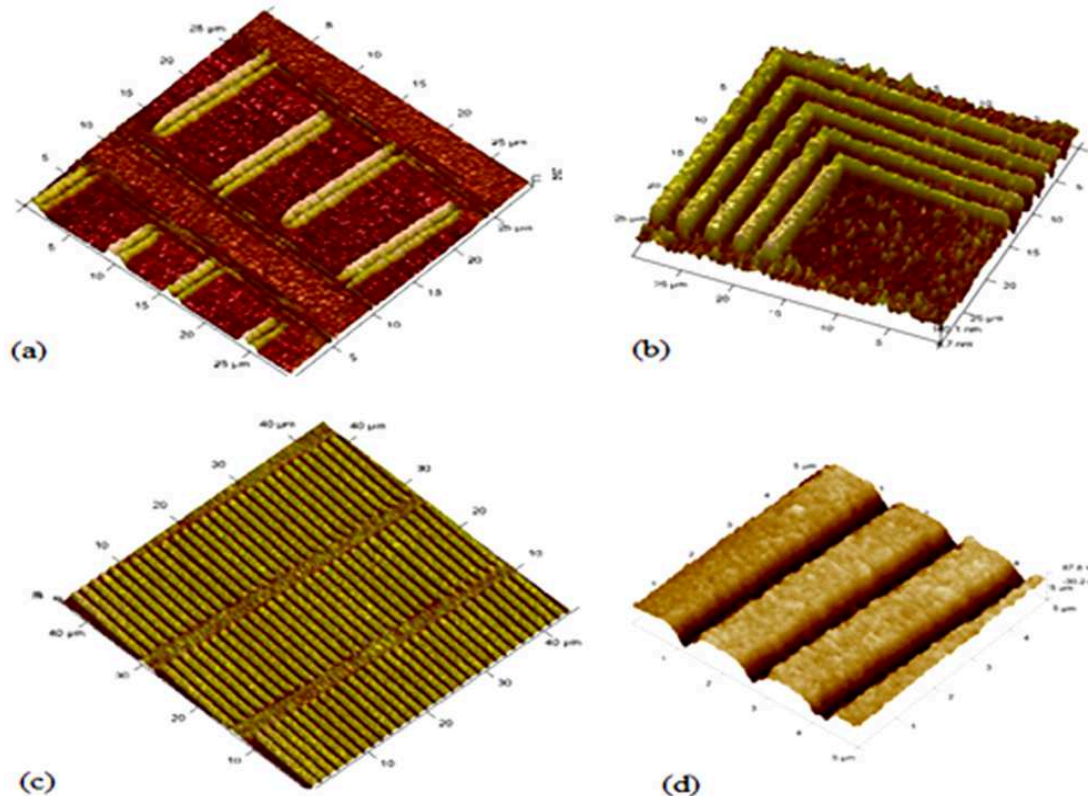


Fig. 2. AFM image (a) Finger pattern shape after developing process. Etch pattern on quartz (b) L-shape (c) Line shape and (d) close up of line shape.

Fig. 2 shows the FESEM image of pattern after etching process (a) finger and L-shape (b) Line shape (c) and (d) close up image on finger pattern shape. As can be seen, there are should be square on the edge. Proximity corrections on design during EBL are required especially a complex pattern where the size and shape the pattern elements are distributed over a wide range. Modifying the square contact on pattern with additional geometry will improve imaging capability [6]. The average vertical sidewall structure, 140 nm are achieved after 10 minutes etching process. As expected, the ICP-RIE process gives higher etching rate compared to conventional etch process. Typically, the amount of the ion created will increase when the ICP power is increased. This will increase the chemical etch rate, both vertically and laterally, increase the milling etch rate, reduce the selectivity by milling the mask away faster, and reduce the effect of passivation by bombarding the sidewalls more due to the ion angular dispersion effect. However, the optimum condition such as the matching power of ICP and forward, temperature, pressure and etchant gases flow rate needed further research because it dependent on the features size of the pattern.

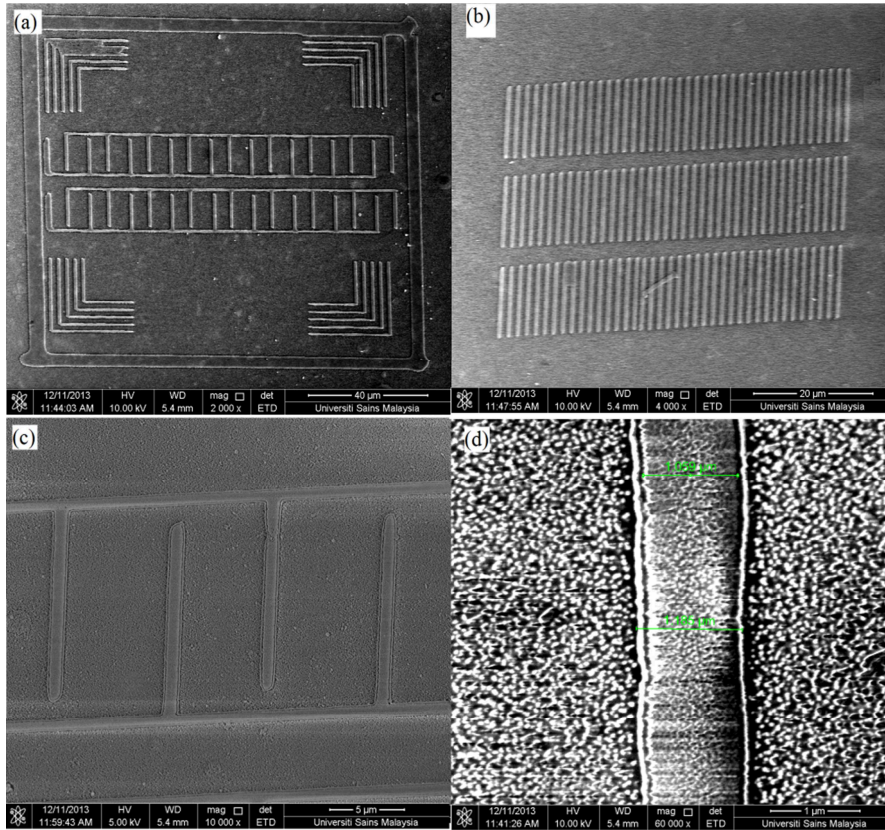


Fig. 3. FESEM image of pattern after etching process (a) Finger and L-shape (b) Line shape (c) and (d) Close up image on finger pattern shape.

From present experiment of quartz etching process using CHF_3 etchant, the etching chemistries were described as follows [7]:

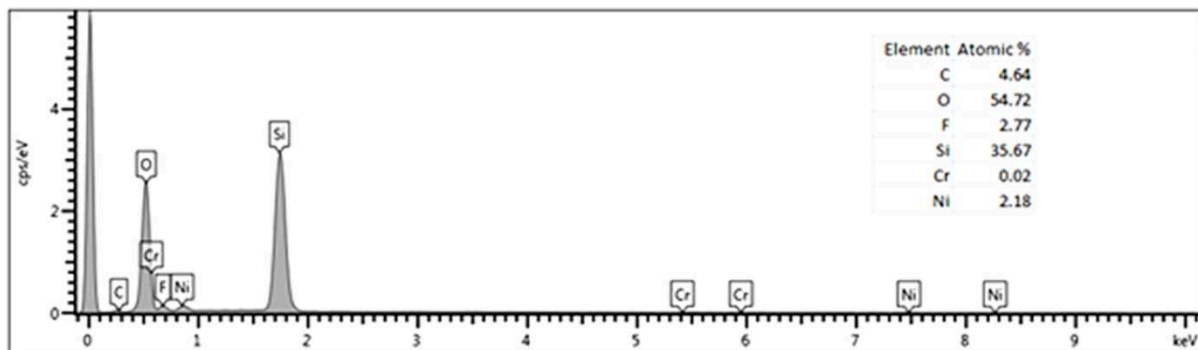
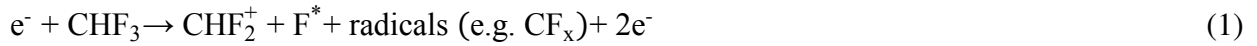


Fig. 4. EDX data of etched pattern.

The free fluorine radicals F^* are created by the RIE plasma from supplied CHF_3 etchant gases (Eq. 1). The etching of quartz consumes the F atom to form SiF_x (Eq. 2). One of the radical created, CF_x tend to deposit polymer films on all surfaces under certain condition, but while the oxygen liberated in the etching of quartz reacts with CF_x radicals to form volatile CO , CO_2 and COF_2 (Eq. 3). The EDX data taken as shown in Fig. 4 which from the finger shape after etching process shows

the presence of silicon, oxygen, nickel, chromium, carbon, fluorine. While in between the shape only silicon, oxygen and fluorine are presence.

Conclusion

This study of micro/nano structures fabrications is baseline knowledge to fabricate high aspect ratio structure and 3D structures on quartz in the future. There are so many factors affect the during pattern definition and pattern transfer processes. It was recommended reduce the scan area of exposure and beam current in order to reduce proximity effect during EBL process and achieve the fine shape. With capability of EBL and ICP-RIE will drive on the designing and fabricating more complex nanostructures. The optimum conditon for quartz micro and nano structures etching using an ICP-RIE system are needed further investigation since the setting parameter dependent on feature size of structures.

Acknowledgements

The authors would like to acknowledge NORLab, School of Physics Universiti Sains Malaysia for the facilities, Malaysian Ministry of Education and School of Mechanical Engineering USM.

Reference

- [1] M. Guo, X. Chou, J. Mu, B. Liu, J. Xiong, Fabrication of Micro-Trench Structures High Aspect Ratio Based on DRIE Process for MEMS Device Applications, *Microsyst, Technol.* 19 (2013) 1097-1103.
- [2] K. Mohamed, M.A. Alkaisi, The Fabrication of High Aspect Ratio Nanostructures on Quartz Substrate. *InTech: Updates in Advanced Lithography* (2013) 211-225.
- [3] W. Kern, *Handbook of semiconductor wafer cleaning technology: science, technology and application*, United States of America, Noyes Publication (1993).
- [4] K. Mohamed, Three-dimensional patterning using ultraviolet curable nanoimprint lithography, *Electrical and Computer Engineering*, Christchurch, New Zealand, University of Canterbury, Doctor of Philosophy (2009).
- [5] T.H.P. Chang, Proximity effect in electron-beam lithography. *J. Vacuum Science and Technology.* 12 (1975) 1271-1275.
- [6] G.S. May, S.M Sze, *Fundamentals of semiconductor fabrication*, United States of America, John Wiley & Sons, Inc. (2004).
- [7] M.A. Alkaisi, K. Mohamed, Three dimensional patterning using ultraviolet nanoimprint lithography. *Intech: Lithography.* (2010) 571-596.
- [8] M.A. Rad, K. Ibrahim, K. Mohamed, Atomic force microscopy investigation of surface roughness generated between SiO₂ Micro-Pits in CHF₃/Ar Plasma, *Superlattices and Micro structure.* 51 (2012) 597-605.

Potential of Clay Deposits in Kelantan for Ceramic Production: A Literature Analysis

Olalere Folasayo Enoch^{1,a}, Ab. Aziz Shuaib^{1,b}, Khairul Azhar bin Mat Daud^{1,c}

¹Faculty of Creative Technology & Heritage, Universiti Malaysia Kelantan
Locked Bag 01, 16300 Bachok, Kelantan, Malaysia

^afolasayoidd@yahoo.com, ^baziz@umk.edu.my, ^cazhar.md@umk.edu.my

Keywords: Ceramics, Clay deposit, Clay properties, Kelantan

Abstract. Kelantan state, regarded as the cradle of Malay culture is not only known for her unique cultural heritage, but also a land blessed with both metallic and non-metallic minerals. These include enormous clay deposits discovered in six (6) districts with estimated total reserve of 29.4 million tonnes of ball clay and 51.5 million tonnes of mottled clay. Hence, this paper investigates the physiochemical and mineralogical properties of the clay deposits. This was achieved by reviewing existing literatures and reports at the Mineral and Geoscience Department, Malaysia. The properties investigated were green and fired clay colour, plasticity, green strength, dry and fired shrinkage, porosity, chemical and mineral composition. The properties of the clay revealed that they have geographical IP potential; particularly, the predominantly off-white fired colour of the ball clay at temperature range of 900-1100⁰C can secure an identity for Kelantan ceramics in the local, national or international market. Based on these properties, the ball clay is applicable for table ware, earthenware and local tile production while the mottled clay has a potential use for vitrified clay pipe, local tile and brick production.

Introduction

Clay is a general term which includes combination of one or more clay mineral with traces of metal oxides or organic matter [1], [2]. These clay minerals are typically formed over long period of time by the gradual chemical weathering of rocks, usually silicate-bearing, by low concentrations of carbonic-acid and other diluted solvents. According to the U.S. Geological Survey [3], the term clay applies both to materials having a particle size of less than 2 micrometres (25,400 micrometres=1inch) and to the family of minerals that has similar chemical compositions and common crystals structural characteristics [4]. Thus, clays may be composed of mixtures of finer grained clay minerals and clay-sized crystals of other minerals such as quartz, carbonate and metal oxides.

Clay is one of the most common ceramic raw materials. It is used widely because it is found in great quantities naturally and it is easily formed. It is used in structural clay products (bricks, pipes, tiles) and whitewares (pottery, tableware, china, sanitary ware); making up the majority of the ceramic body and is primarily composed of hydrated aluminium silicates, $Al_2O_3 \cdot SiO_2 \cdot H_2O$. Most clay products also contain inexpensive filler, often quartz (SiO_2), and a feldspar or flux ($K_2O \cdot Al_2O_3 \cdot 6SiO_2$ or $Na_2O \cdot Al_2O_3 \cdot 6SiO_2$), that forms a glass to bind ceramic particles during heat treatment [5].

Clay minerals are result of the erosion of the earth's crust over spans of time; where the original mineral feldspar in igneous rocks and primarily granite, breaks down overtime and becomes the microscopically fine particle clay. The effects of erosion over enormous time cause igneous rocks to disintegrate and the feldspar content is altered to Kaolinite, which is the identifying substance in clay [6]. Clay deposits which remain at or near site of parent material (granite) are called residual or primary clays. Residual clays are grainy and lack the smoothness necessary for workability; thus, they are said to be non-plastic because they do not shape easily [6]. Those clays which have been transported by water wind, ice and deposited in locations distant from the source materials are called sedimentary or secondary clays [3]. According to [6], sedimentary clays are more plastic, and

the particles are smaller, more uniform, and more mixed with other materials. Under the microscope, clay particles resemble playing cards with flat, hexagonal and thin form. When wet, the particles can slip across each other; this ability gives a clay its workability, called plasticity.

Clay Deposit in Kelantan and Their Properties

There are ten (10) clay deposits discovered in Kelantan with an estimated reserve of 29.4 million tonnes of ball clay and 51.5 million tonnes of mottled clay. The deposits are found within 6 districts in Kelantan state. These include; Pasir Mas, Bachok, Kota Bharu, Tumpat, Pasir Puteh and Machang. The summary of the reserves are shown in Table 1;

Table 1: The summary of the clay deposit in Kelantan

District	Potential Area	Samples No.	Types of Clay	Reserved (Million Tonne)
Pasir Mas	Gual Lemsu & Kampung Cherang Hangus,	PMm ₁	Ball clay	10.3
		PMb ₁	Mottled clay	23.2
Pasir Mas	Kampung Geretak Tiga & Padang Lichin	PMm ₂	Ball clay	1.8
		PMb ₂	Mottled clay	3.9
Pasir Mas	Kampung Bakong Kechik	PMm ₃	Ball clay	2.4
		PMb ₃	Mottled clay	14.4
Pasir Mas	Bukit Pak Junus, Pasir Mas, Kelantan	PMm ₄	Ball clay	4.6
		PMb ₄	Mottled clay	10.0
Pasir Mas	Kg. Bt. Karang; Kg. Gual Tok Cha	PMb ₅	Ball Clay	1.2
Bachok / Kota Bharu	Mukim Sering-Mukim Tawang	B/KB	Ball Clay	0.9
Tumpat	Pengkalan Kubor	T	Ball Clay	1.2
Pasir Puteh	Mukim Mahligai	PP ₁	Ball Clay	2.2
Pasir Puteh	Mukim Bt. Jawa	PP ₂	Ball Clay	2.7
Pasir Puteh / Machang	Kg Nering; Kg. Pangkal Mak Wan	PP/M	Ball Clay	2.1
TOTAL			Ball Clay	29.4
			Mottled Clay	51.5

The Potential of the Clay for Ceramic Production

Clays are major raw materials used in ceramic and pottery industries; their potential use for ceramic production is determined based on the appropriateness of the clay properties. Thus, the potential use of clay deposit in Pasir Mas district of Kelantan State are analysed based on the clay properties which include colour, plasticity, strength, shrinkage, porosity and composition. The analytical result of the clay properties is presented in Table 2, along with six (6) commercial clays.

Fired Colour: The mottled clay discovered at the four locations in Pasir Mas district are red in colour at green state, while the fired colour at 1100^oC ranges from light-pink to reddish-brown. This is as a result of the high percentage of Fe₂O₃ present in the mottled clays [6], this property is similar to some of the clay used for vitrified clay pipe and bricks. Although the green state colour of the ball clays is mainly light-grey, however, six out of the ten deposits discovered have predominantly off-white colour at 1100^oC, while the colour of the other four deposits ranges from Light-pink to Off-white. This can be attributed to the low percent content of Fe₂O₃ present in the clay composition. When compared with six (6) commercial clay samples, it was noticed that at fired temperature of 1100^oC, only one sample shows off-white as fired colour. Thus, if these ball clays are effectively harnessed for ceramic/pottery production in Kelantan, the uncommon property (off-

white) can serve as a geographical IP that can help to secure an identity for Kelantan ceramics both at local, national and international market.

Table 2: Analytical results of some commercial clay and the clays from the potential areas

Source	Product	% Mineral Composition			Plasticity	Dry Strength	% Dry Shrinkage	% Firing Shrinkage (1100°C)	% Water Absorption (1100°C)	Fired Colour (1100°C)
		SiO ₂	Al ₂ O ₃	Fe ₂ O ₃						
Local	Tiles	60.9	25.7	1.33	Medium	Good	4.0	1.7	25.1	Pink White
Local	Sanitary wares	67.4	23.2	0.36	Medium	Medium	5.6	6.7	31.5	White
Import	Porcelain	51.4	31.9	1.12	Medium	Low	5.3	4.7	13.1	Pink White
Local	Tableware	64.6	22.8	0.65	Medium	Good	3.7	3.4	14.2	Pink White
Local	Jewelry	67.9	22.4	0.55	-	Medium	5.4	1.6	17.8	Off white
Local	Brick	60.2	21.7	6.81	-	Medium	3.8	7.3	14.0	Off white
PMm ₁	-	47.5-68.2	21.2-33.2	1.04-6.19	Medium	Medium-Good	4.3-10.1	2.8-13.6	14.5-23.0	L. pink-L. Red
PMB ₁	-	48.0-62.2	24.5-33.6	1.14-2.62	medium	Medium-Good	3.9-8.0	3.1-10.2	10.5-24.5	L. pink-Off white
PMm ₂	-	52.4-62.3	25.1-29.3	1.86-6.2	Medium	Good	6.0-8.2	2.6-6.0	16.1-19.4	L. pink
PMB ₂	-	46.5-56.5	27.9-35.0	1.23-2.26	Medium	Medium-Good	5.4-7.8	2.4-9.0	13.4-25.6	Off White
PMm ₃	-	49.5-59.6	26.3-30.4	3.16-9.42	Medium-Good	Medium-Good	4.6-8.0	3.9-9.0	13.6-19.5	L. Brown-Red
PMB ₃	-	51.6-69.6	21.3-30.7	1.15-2.37	Medium	Good	3.6-6.6	2.0-7.0	13.3-17.9	Off-white
PMm ₄	-	45.8-61.1	22.5-34.1	1.52-9.80	Medium-Good	Medium-Good	5.2-6.7	1.3-1.6	11.7-23.2	P. White-R. Brown
PMB ₄	-	53.0-70.7	17.5-31.0	0.96-2.46	Medium	Good	4.7-7.0	0.0-4.9	11.0-21.9	L. Pink-Off White
PMB ₅	-	48.4-64.2	25.6-28.7	1.56-2.17	Medium-Good	Good	5.0-5.3	1.7-5.5	17.0-24.1	Off white
B/KB	-	57.5	27.2	1.84	Medium-Good	Good	6.4-6.8	2.6-8.4	14.7-16.9	Off white
T	-	53.0-65.2	26.3-27.6	1.32-1.79	Medium-Good	Good	3.9-8.3	5.7-7.1	14.8-18.5	Off white
PP ₁	-	48.4-57.3	28.6-32.7	1.57-2.50	Medium-Good	Good	4.4-7.9	2.7-10.2	13.8-18.1	Off white
PP ₂	-	47.9-59.6	25.4-33.2	2.39-2.84	Good	Good	6.3-7.6	10.0-10.8	13.0-13.9	Off white
PP/M	-	56.3-59.6	31.9-33.2	1.66-2.84	Medium-Good	Good	6.1-7.6	2.6-3.4	13.9-18.1	P. white-Off white

Plasticity and Green Strength: The plasticity and strength test conducted on both the mottled and the ball clays shows that they have medium to good plasticity and medium to good green strength. The commercial ball clay samples in the market analysed by Zainol & Loh (1995a) also revealed medium to good in both plasticity and green strength. Thus, this similarities proves that the mottled and ball clays discovered are appropriate for ceramic production.

Dry and Firing Shrinkage: The analytical result of the shrinkage test revealed that the mottled clay have percentage drying shrinkage range from 4.3-10.1% while drying shrinkage of the ball clay ranges from 3.6-8.3. Also, the fired shrinkage at 1100⁰C for the mottled clay ranges from 1.3-13.6%, while ball clay ranges from 0.0-10.8% (Table 2). Similarly, the percentage shrinkage of six (6) commercial ball clay samples from the local market revealed dry shrinkage ranging from 3.7 to 5.6 % and fired shrinkage range from 1.6 to 7.3% [8]. According to Lakeside Pottery (n.d.), the percentage shrinkage of good clay should not exceed 15%; since the clay deposits falls within this range, it can be concluded that the clays discovered have appropriate dry and fired shrinkage for ceramic production.

Porosity: The percentage of water absorption of the mottled clay at 1100⁰C ranges from 11.7-23.2% while the ball clay ranges from 10.5-25.6. Similarly, Zainol & Loh (1995b) collated the porosity values of six (6) commercial ball clay samples in the market which shows that their porosity at 1100⁰C ranges from 13.1 to 25.1%. This shows that the ten clay deposits discovered in Kelantan have appropriate porosity for ceramic production.

Composition: The analytical result of the chemical composition of the mottled and ball clays reveal that the clays have high percentage of SiO₂, followed by Al₂O₃ while Fe₂O₃ is the lowest percentage

content among the three chemical. However, mottled clays have higher percentage content of Fe_2O_3 (range: 1.04-9.80%) than ball clay (range: 0.96-2.84%). This high Fe_2O_3 content in the mottled clay results in the absence of off-white colour when fired at 1100°C . The analytical result of the commercial clay use in bricks production also revealed a high percentage of Fe_2O_3 (6.81%). Thus, the mottled clay is seen to be most appropriate in brick or vitrified clay pipe production.

Sustainable Clay Volume: According to British Geological Survey (2011), the overall clay to waste ratios for ceramic industry are about 1 to 1.5. Thus, the clay consumption in ceramics industry can be calculated based on this ratio; for example, a ceramic product with an average weight of 0.5kg will be produced from 0.75kg ($0.5\text{kg} \times 1.5$) of raw clay.

Thus; a SMI that produces 10,000 pieces of ceramic wares (with average weight of 500g each) per month will consume;

$$(10,000 \times 0.5 \times 1.5) \text{ kg} = 7,500\text{kg of raw clay per month}$$

In a year, it will be;

$$(7,500 \times 12) \text{ kg} = 90,000\text{kg} = 90 \text{ Tonnes of raw clay per annum}$$

Therefore, if 50 cottage industries operate simultaneously in Kelantan, and each consumes 90 Tonnes of ball clay per year; the total consumption will be 4500 Tonnes per annum. For the estimated total of 29.4 million tonnes of ball clay discovered in Kelantan to be exhausted; it will take:

$$(29,400,000 \div 4500) \approx 6,533 \text{ years}$$

Hence, apart from the good properties of the clay, the volume of the clay deposit guarantees long term sustainability of ceramic industries in Kelantan.

Conclusion

With the enormous and yet untapped clay deposits discovered in six (6) districts in Kelantan state [12]; having estimated total reserve of 29.4 million metric tonnes of ball clay and 51.5 million tonnes of mottled clay; Kelantan is seen as a virgin land for ceramic industries, especially small and medium scale ceramic/pottery industries. This is not only because of the large volume of the deposit which guarantees sustainability; but also the good quality of the clay (mottled and ball clay); and the uncommon property of the ball clay, especially the predominantly off-white colour shown at 900, 1000 & 1100°C which is rarely found among other ball clay samples in the market [13]. This can help to establish a geographical IP which can play a significant role in enhancing and sustaining the heritage values of Kelantan ceramics, by securing identity for Kelantan ceramic wares, in the local, national or international market.

The high product demand over the limited numbers of ceramics industries also proves that ceramic sector have multi-business potential that are yet to be fully explored. Thus, it is important to encourage more entrepreneurs to venture into this sector, focussing not only on decorative pottery wares but also on functional products such as ceramic table and kitchen wares, jewellerys, burnt brick and roof tiles etc (Table 3). These will not only help in job creation (source of income), but also play a significant role in sustaining the heritage values of Kelantan ceramics.

Table 3: Summary of the clay deposits and their potential usage

Clay Deposits	Measured Reserved (Million metric tonnes)	Potential Products
PMm ₁	10.3	Burnt bricks, roof tiles, vitrified clay pipe
PMb ₁	23.2	Table & kitchen wares, Floor & wall tiles,
PMm ₂	1.8	Burnt bricks, roof tiles, vitrified clay pipe
PMb ₂	3.9	Jewellerys, Sanitary wares, tiles
PMm ₃	2.4	Red bricks, roof tiles, vitrified clay pipe
PMb ₃	14.4	Porcelain wares, sanitary wares
PMm ₄	4.6	Burnt bricks, roof tiles, culvert pipe
PMb ₄	10.0	Floor and wall tiles, decorative pottery, Jewellerys
PMb ₅	1.2	Decorative Pottery, table and kitchen wares

B/KB	0.9	Decorative pottery, tiles
T	1.2	Decorative pottery, table and kitchen wares
PP ₁	2.2	Decorative pottery, table and kitchen wares
PP ₂	2.7	Decorative pottery, table and kitchen wares
PP/M	2.1	Decorative pottery, table and kitchen wares, tiles

Although, some of the lands where the clay deposits were discovered are privately owned land; however, larger percentage of the land are owned by the government [7]. Thus, the status of these areas can be converted to non-agricultural land; this will give room for its exploitation for ceramic production and thereby encouraging the growth of the industry in the state of Kelantan.

References

- [1] S. Guggenheim and R. T. Martin, "Definition of clay and clay mineral: Journal report of the AIPEA nomenclature and CMS nomenclature committees," *Clays Clay Miner.*, vol. 43, no. 2, pp. 255–256, 1995.
- [2] P. Justin and E. Daniel, *Clay: Types, Properties and Uses*. Nova publishers, 2011.
- [3] USGS, "Environmental Characteristics of Clays and Clay Mineral Deposits," 1999. [Online]. Available: <http://pubs.usgs.gov/info/clays/>. [Accessed: 22-Jun-2013].
- [4] B. Velde, "Composition and mineralogy of clay minerals, in Velde, B., ed., Origin and mineralogy of clays: New York," *Springer-Verlag*, pp. 8–42, 1995.
- [5] "Traditional Ceramics," *UNSW*. [Online]. Available: <http://www.hsctut.materials.unsw.edu.au/Ceramics/ceramics7b.htm>. [Accessed: 22-Jun-2013].
- [6] GcCeramics, "Clay types, geological origins and working properties of clay." [Online]. Available: <https://sites.google.com/site/meeneecat/educational-materials/clay-types-geological-origins-working-properties-gccceramics>. [Accessed: 22-Jun-2013].
- [7] A. S. Zainol and C. H. Loh, "Follow up study of ball clay in Kampung Bakong Kechik, Pasir Mas, Kelantan.," 1995.
- [8] A. S. Zainol, C. H. Loh, and L. H. Teoh, "Follow up study of ball clay in Bukit Pak Junus, Pasir Mas, Kelantan.," 1994.
- [9] Lakeside Pottery, "Clay, the drying and firing process." [Online]. Available: [http://lakesidepottery.com/HTML Text/Tips/Clay drying and firing process.htm](http://lakesidepottery.com/HTML%20Text/Tips/Clay%20drying%20and%20firing%20process.htm). [Accessed: 05-Feb-2014].
- [10] A. S. Zainol and C. H. Loh, "Follow up study of ball clay in Kampung Cherang Hangu, Pasir Mas, Kelantan.," 1995.
- [11] British Geological Survey, "Mineral planning factsheet: Ball clay," 2011.
- [12] MT-JGSC, "Geology of the Batu Melintang-Sungai Kolok transect area along the Malaysia – Thailand border.," 2006.
- [13] I. Mohd Suhaili, A. Mohd Pauzi, C. H. Loh, and L. H. Teoh, "Ball Clay Reconnaissance Study, Kelantan.," 1993.

CHAPTER 2:

Applied Mechanics and its Applications in Civil Engineering

Finite Element Prediction of Mechanical Behaviour under Bending of Honeycomb Sandwich Panels

Kaoua Sid-Ali ^{1,a}, Mesbah Amar ², Boutaleb Salah ², Azouaoui Krime ²

¹Laboratoire des Sciences et Génie des Matériaux (LSGM), FGMGP, USTHB, Alger, Algeria

²Laboratoire de Mécanique Avancée, FGMGP, USTHB, Alger, Algeria

^a sakaoua@gmail.com

Keywords: sandwich composite, aluminum honeycomb, finite element modelling.

Abstract. This paper outlines a finite element procedure for predicting the mechanical behaviour under bending of sandwich panels consisting of aluminium skins and aluminium honeycomb core. To achieve a rapid and accurate stress analysis, the sandwich panels have been modelled using shell elements for the skins and the core. Sandwich panels were modelled by a three-dimensional finite element model implemented in Abaqus/Standard. By this model the influence of the components on the behaviour of the sandwich panel under bending load was evaluated. Numerical characterization of the sandwich structure, is confronted to both experimental and homogenization technique results.

Introduction

Sandwich structures have long been recognized as one of the most weight-efficient plate or shell constructions for resisting bending loads. The aerospace industry, with its many bending stiffness dominated structures, and its need for low weight, has employed sandwich constructions using aluminum honeycomb cores extensively [1].

The characterization of mechanical properties of sandwich structures poses special challenges due to their heterogeneity and considerable mismatch in properties between core and face sheet [2]. The need to an efficient numerical modeling for predicting the mechanical behavior of the sandwich structures is still an open area of research. Extensive work [3], has been carried out on the development of computational models for studying the response of sandwich panels and shells in an attempt to make their use more widespread. Nowadays, numerical simulations based on the finite element (FE) method have become a standard tool in the development process of the aircraft industry (from the material level over the component level up to the full aircraft).

Analysis of load-deflection behavior of a composite sandwich beam in three-point bending was described by Gdoutos et al. [4]. They found that the effect of material nonlinearity on the deflection of the beam is more pronounced for shear-dominated core failures in the case of short span lengths. The authors thought that it is due to the nonlinear shear stress-strain behavior of the core. For long span lengths, the observed nonlinearity is small and is attributed to the combined effect of the facings nonlinear stress-strain behavior and the large deflections of the beam.

Thereby, numerical models allow for efficient parameter studies or optimizations. In the present work, a numerical model is used to examine the behavior of sandwich panels made of aluminum skins with aluminum honeycomb core under four bend loading.

Finite Element Model

The finite element model used for the simulations of core structures honeycomb requires mesh generation for finite element structure, the allocation of behavior laws and the definition of boundary conditions and loading. The numerical model is based on the introduction of the geometric parameters of the unit cell of a honeycomb, the RVE size (length, width, height, or the number of unit cells), the size of the element and the type and boundary conditions. An elementary cell is generated from the geometric data and duplicated in the two directions of the plane depending on the size of the RVE. For the sandwich structure, the two skins are generated by the

upper and lower faces of the core, on which the loads are applied. The whole model is meshed with shell elements with 4-nodes depending on the size of the element, and the core and the skins are connected by nodes defining solid contact between these two bodies. Then the boundary conditions are applied to the skin of the sandwich structure.

The analysis was performed by imposing known displacements or forces. The opposite side of the applied displacement is clamped and then the forces are obtained. The elastic moduli are obtained by measuring the slope of the linear stress-strain curve. Code Abaqus was used for the finite element calculation.

For the four-point bending test, only a quarter of the panel was modeled due to the symmetry of the problem. A non-homogeneous three-dimensional mesh is used. The adopted mesh contains 88,907 shell elements with 4-nodes reduced integration (S4R in Abaqus).

Mechanical Behavior of Sandwich Panel

In this section, we considerate the mechanical behavior of sandwich panel in function of some geometric parameters; such as: skin thickness, core expanding angle (θ), core wall thickness (t) and core edge length ratio (b/a).

Figure 1. illustrates linear evolution of Young's modulus according to x direction (E_x) in function of skin thickness. This explains the important effect of skins on in-plane properties. However, the expanding angle θ hasn't a great effect on these properties.

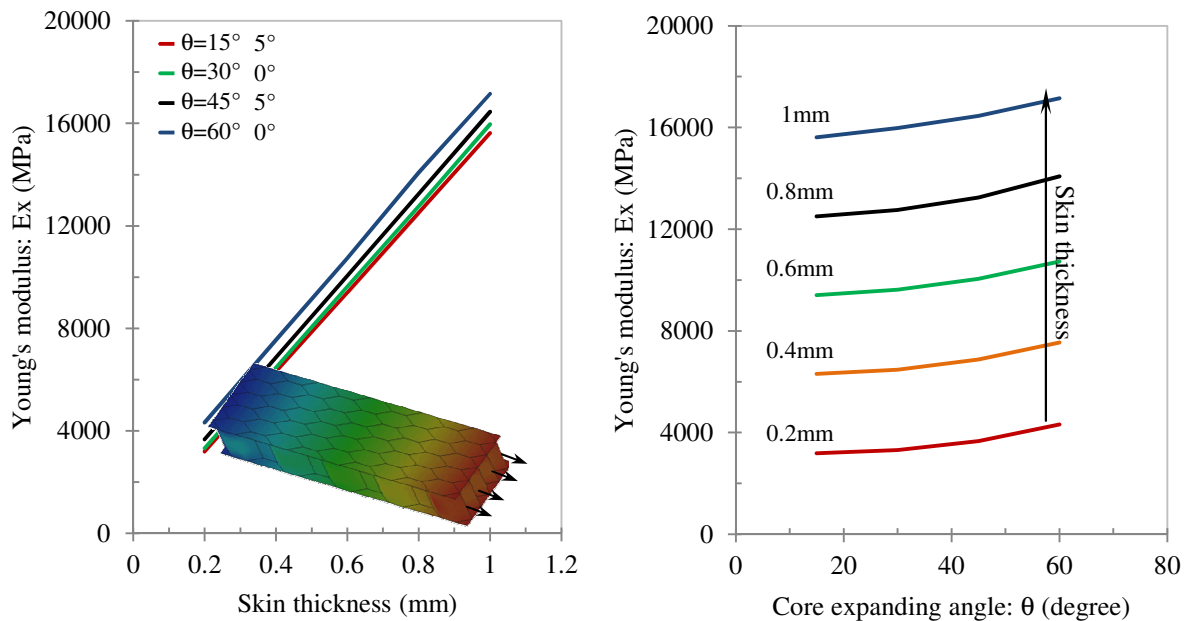


Fig.1 Influence of skin thickness and expandable angle on in-plane Young's modulus (E_x)

Similarly, honeycomb wall thickness has a moderate influence on the in-plane stiffness (Fig.2).

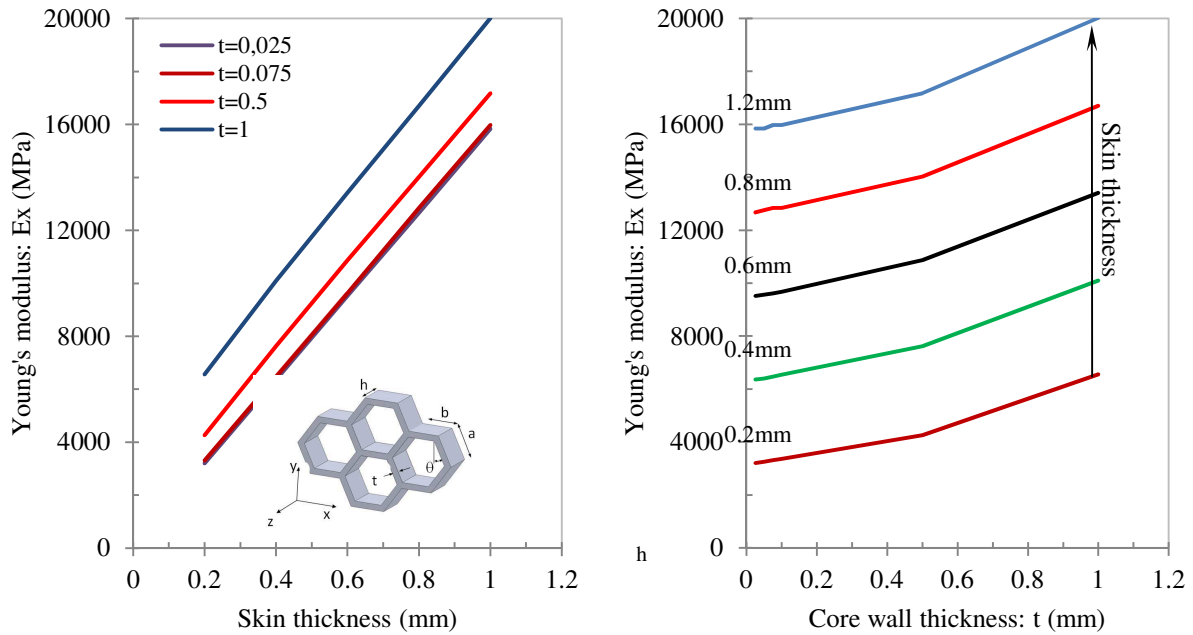


Fig.2 Influence of skin thickness and wall thickness on in-plane Young's modulus (E_x)

The mechanical behavior of panel sandwich is governed mainly by the skins properties. Figure 3. shows clearly this; the core edge ratio hasn't any influence on Young's modulus E_x of the sandwich.

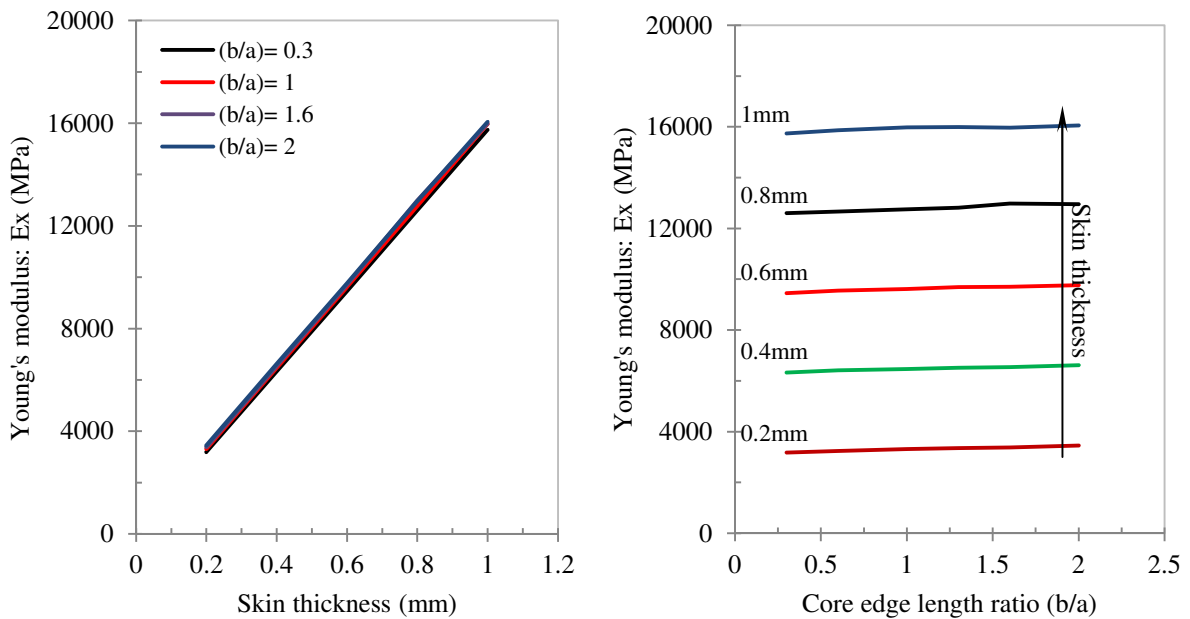


Fig.3 Influence of skin thickness and edge length ratio on in-plane Young's modulus (E_x)

In figure 4 below, we have plotted the in-plane Young's modulus (E_x) for an aluminium plate (skin), a honeycomb core structure and a sandwich panel. It indicates that the skins improve the in-plane properties of honeycomb structures.

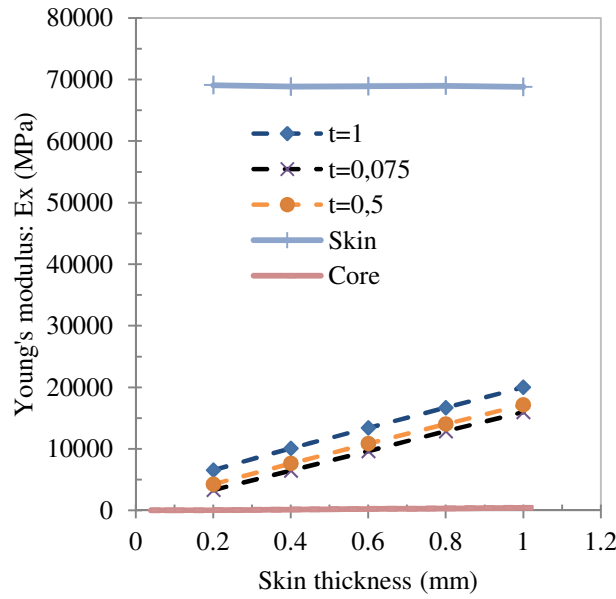


Fig.4 Influence of skin thickness on in-plane Young's modulus (Ex- comparison with those of the skins and core

The virtual simulation of a four point bending test on a sandwich beam shows the deflection of the beam, and a zoom of the central part reveals a cell with the attached skins (Fig.5).



Fig.5 Deflection of beam under four-point bending load

A good agreement can be seen in figure 6, between experimental bending tests (Abbadi, [5]) and the present work based on finite element model.

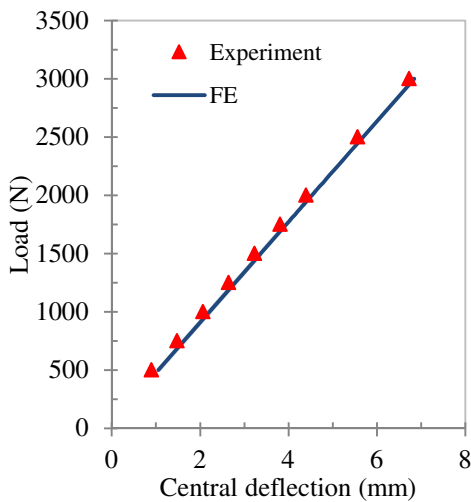


Fig.6 Confrontation diagrammes charge-déplacement under four-point bending (Experiment (Abbadi, 2009) and FE)

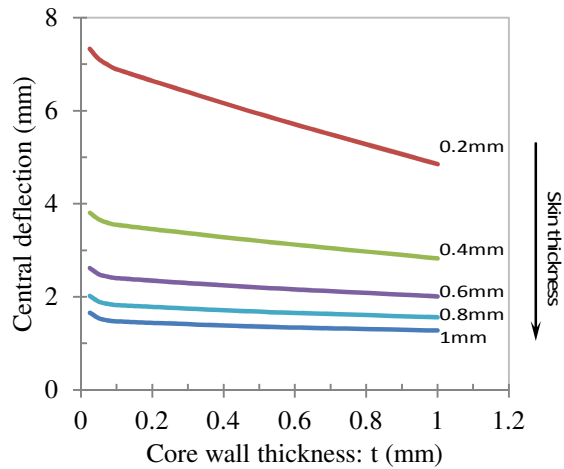


Fig.7 Central deflection vs core wall thickness (four point bending)

The central deflection decreases with cell wall thickness of the honeycomb (Fig.7), which is completely justified. However, the central deflection exhibits growing values when skin thickness decreases. Figure 8 shows iso-values of the displacement at the cell level.

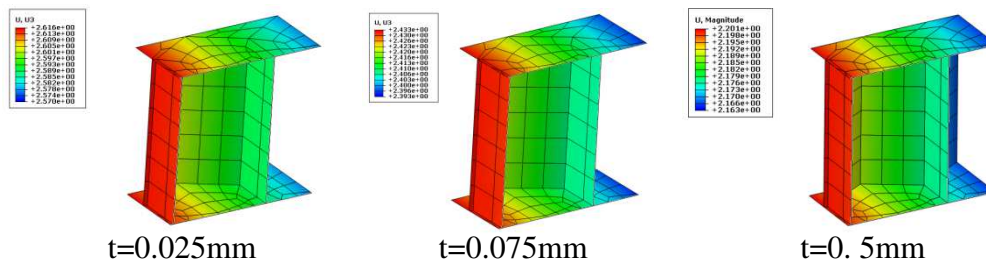


Fig.8 Effect of wall thickness on displacement at the cell level (skin of 0.6mm)

Conclusion

This study shows that there is a good agreement between the mechanical properties of honeycomb sandwich structure with experimental results. Our numerical approach illustrates the linear evolution of Young's modulus according to x direction (E_x) in function of skin thickness and the minimal effect of the expanding angle θ on these properties. Additionally, The central deflection, in the virtual simulation of a four point bending test on a sandwich beam, decreases with cell wall thickness of the honeycomb. However, the central deflection exhibits growing values when skin thickness decreases.

References

- [1] Palazotto AN, Herup EJ, Gummadi LNB. Finite element analysis of low-velocity impact on composite sandwich plates. *Composite Structures*, (2000), 49, p. 209-227.
- [2] Ravichandran G, Rajapakse YDS. Sandwich Structures. *Experimental Mechanics*, 2012, 52, p. 1–2.
- [3] Rahman H, Jamshed R, Hameed H, Raza S. Finite Element Analysis (FEA) of Honeycomb Sandwich Panel for Continuum Properties Evaluation and Core Height Influence on the Dynamic Behavior. *Advanced Materials Research*, (2011), 326, p. 1-10.
- [4] Gdoutos EE, Daniel IM, Wang KA, Abot JL. Nonlinear behavior of composite sandwich beams in three-point bending. *Experimental Mechanics*, (2001), 41(2), p. 182–189.
- [5] Abbadi A, Koutsawa Y, Carmasol A, Belouettar S, Azari Z. Experimental and numerical characterization of honeycomb sandwich composite panels. *Simulation Modelling Practice and Theory*, 2009, 17, p. 1533–1547.

The Effect of Alkali Treatment of OPKS Filler on Mechanical Property of Polyester-Composite

O. Nabinejad^{1a}, D. Sujan^{1b*}, M. E. Rahman^{1c}, M.M. Reddy^{1d},
Willey Y. H. Liew^{2e} and Ian J. Davies^{3f}

¹School of Engineering and Science, Curtin University Sarawak, Malaysia

²School of Engineering & Information Technology, University Malaysia Sabah, Malaysia

³Department of Mechanical Engineering, Curtin University, Perth, Australia

^aomid.nabinejad@gmail.com, ^bd.sujan@curtin.edu.my, ^cmerahman@curtin.edu.my,
^dmohan.m@curtin.edu.my, ^ewyhliw@ums.edu.my, ^fI.Davies@curtin.edu.au

Keywords: Oil Palm Kernel Shell, polyester, composite, alkali treatment, mechanical property.

Abstract. This paper presents a study on the effect of alkali treatment of Oil Palm Kernel Shell (OPKS) on the mechanical properties of polyester composite. The dosage of NaOH in this study is limited to 5wt% concentration. The experiments on mechanical properties investigate the tensile strength, the flexural strength and the flexural modulus of untreated, cold alkali treated and hot alkali treated OPKS reinforced polyester composite. It is found that the alkali treatment improves the mechanical properties of the composite. However, the improvement due to the hot alkali treatment is significant compared to the cold alkali treatment. The morphology of OPKS and the fracture surface of OPKS composites were investigated using scanning electron microscopy (SEM), showing a rough surface and good interfacial adhesion between OPKS as filler and polyester as a matrix.

Introduction

Industry in this era is moving towards environmentally friendly products. The rapid development of technology in construction, automobile, aerospace, transportation and numerous applications has prompted the invention of new composite materials to meet the ever increasing demand of outstanding properties to replace the conventional material. The conventional materials have limitations to possess an excellent combination of mechanical properties such as high strength, high stiffness, and high toughness with low density [1, [2]. Industrial wastes result in negative impacts on our environment and health. The waste management issues, among others, include organic and agro-industrial waste, impacts of waste on surface and groundwater, treatment systems, waste disposal, agro-industrial waste management and recovery of the waste [3].



Fig.1 Oil palm kernel shell (OPKS) as a biomass of Palm Oil industry

Oil palm as the highest yielding edible oil crop in the world is cultivated in 42 countries in 11 million hectares worldwide [4]. Malaysia and Indonesia produce around 80% of the total palm oil of

the world. Nearly 80% of the volume is removed as waste materials from the processing of the fresh fruit bunch[5]. OPKS which presented in Fig.1, is one of the wastes produced during palm oil processing. It is estimated that over 4.56 million tons of OPKS waste are produced annually[6]. It is clearly observed from Fig.1, that the OPKS has a significant surface roughness which has potential to use as filler in polymer composite. The aim of this study is to investigate the effect of alkali treatment of OPKS on mechanical properties of polyester composite.

Physical Properties of OPKS

The Textural characteristics and lignocellulose composition of OPKS are presented in Table 1. These properties lead some researchers to use OPKS as a lightweight aggregate in concrete. Due to the significant amount of porosity, BET surface area and lignocellulose composition, OPKS can be used in polymer composite materials as natural filler.

Table 1 Physical properties and lignocellulose composition of OPKS

Textural characteristics[7]			Lignocellulose composition (%) [8]			
Solid Density (g cm ⁻³)	Total Porosity, ϵ (%)	BET Surface area S_{BET} (m ² g ⁻¹)	Cellulose	Hemicellulose	Lignin	Extractives
1.53	3.9	1.6	32.6	22.1	42.3	3.0

Chemical Treatment

The main limitation of natural fillers reinforced polymer composites is the poor compatibility between the hydrophobic polymer group in the matrix and the hydrophilic group in fiber or filler. Thus, the weak interface as a result of this poor compatibility inhibits the stress transfer at the interface between reinforcement and matrix in composite materials. Subsequently, these materials with natural fiber or filler have a drawback in mechanical strength[9]. In order to overcome the above limitations and to improve the mechanical properties, surface treatments of natural filler are necessary. The Alkali treatment is a kind of chemical surface treatment, which is able to remove some amount of wax, oil and cementing substance such as hemicelluloses and lignin, leading to the growth of rough surface topography and breaking down of the composites fibre bundle into smaller and thinner fibres[10, [11]. The chemical reaction of the alkali treatment is shown in Equ. 1.

(1)

Materials Preparation

Material selection. The isophthalic unsaturated polyester (UP) resin was selected as matrix phase for the composite. Methyl ethyl ketone peroxide (MEKP) and Cobalt Naphthenate (technical grade, 6%) were used as catalyst and promoter respectively. The OPKS material, obtained from Lambir Oil Palm Company in Sarawak, Malaysia, was grounded by ball mill. The flours were sieved and separated by shaker in the sizes less than 300 μ m.

Surface treatments. The alkali treatment in this study was conducted in cold and hot conditions. In cold condition the OPKS were immersed into 5 %wt concentrations of NaOH at room temperature for 48 hours. In hot conditions, the OPKS were immersed in the same concentration of NaOH at room temperature for 38 hours and then heated at 95 °C for 10 hours. Then these samples were washed with distilled water to reduce pH value at 7.0. Finally the all samples were dried in an oven for 24 hours at 80 °C.

Preparation of composite. The unsaturated polyester resin was placed in a beaker. The Cobalt Naphthenate was added to the polyester resin as an accelerator by 0.01 phr (parts per hundred resin) and mixed until a uniform mixture achieved. All composite samples were prepared by using 5 wt% of OPKS. After achieving a uniform mixture, 1.5wt% of MEKP was added to the mixture. The mixture was then cast into the molds to make samples according to ASTM D638 and ASTM D760

for tensile and flexural test respectively. After curing the composites on the mold at room temperature, the samples were placed in an oven at 80°C for 1hour for post curing.

Test Method

Mechanical properties. A universal testing machine was used to measure the tensile strength, flexural strength and flexural modulus. The tensile and flexural test were conducted according to ASTM D638 and ASTM D790 respectively and averages of five specimens for each category were reported.

SEM observation. The untreated, cold and hot treated of OPKS, the fractured surfaces of their composites were investigated by SEM. By means of this observation, it was possible to determine qualitatively the removing impurities from the OPKS particles and the adhesion degree between the reinforcement and the polymer matrix.

Results and Discussion

Mechanical properties. The tensile strength, flexural strength and flexural modulus of the OPKS in untreated, cold alkali and hot alkali treated OPKS/polyester composite are presented in Fig.2. To investigate the effects of alkali treatment, three types of composite were prepared. In this study the pure polyester used as a benchmark. It can be seen from Fig.2 that the tensile strength and flexural strength of the composites increased by the alkali treatment. By cold alkali treatment, the tensile strength increased from 24MPa to 28MPa compared to untreated composite samples. The flexural strength of untreated composite samples increased from 54MPa to 55MPa. Although the mechanical properties of composite improved by cold alkali treatment method; however, these mechanical properties are still slightly lower compared to the value of pure resin. By increasing the temperature of alkali treatment, there were significant improvement in the tensile strength and flexural strength (26% and 28% respectively), which exceeded the value of pure resin.

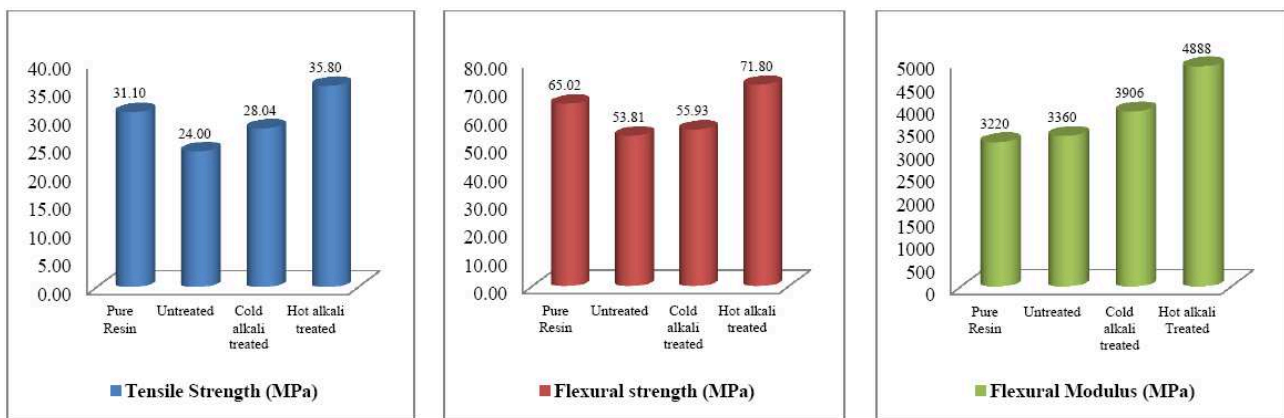


Fig.2 The mechanical properties of OPKS composite

The flexural Young's modulus of the composite also improved by means of alkali treatment. The Young's modulus of the cold alkali treated sample was obtained 3906MPa which is 16 %, higher than untreated sample. The hot alkali treated sample showed the highest Young's modulus value. The Young's modulus of the hot alkali treated composite increased 1.45 times compared to the untreated composite and 1.25 times compared to the cold alkali composite.

SEM observation. The SEM micrographs of the untreated, cold alkali and hot alkali treated OPKS filler are presented in Fig.3. It can be observed from Fig.3(a) that the surface of the untreated OPKS covered with some impurities and there is no evidence or trace of surface roughness on the surface of the OPKS. The cold alkali treated OPKS is presented in Fig.3(b). It can be seen from Fig. 3(b) that the treated OPKS has lots of holes and surface roughness which have a potential for matrix bonding. However, the significant amount of surface roughness can be seen

in Fig. 3(c), which indicates that hot alkali treatment removed most of impurities from the surface of OPKS.

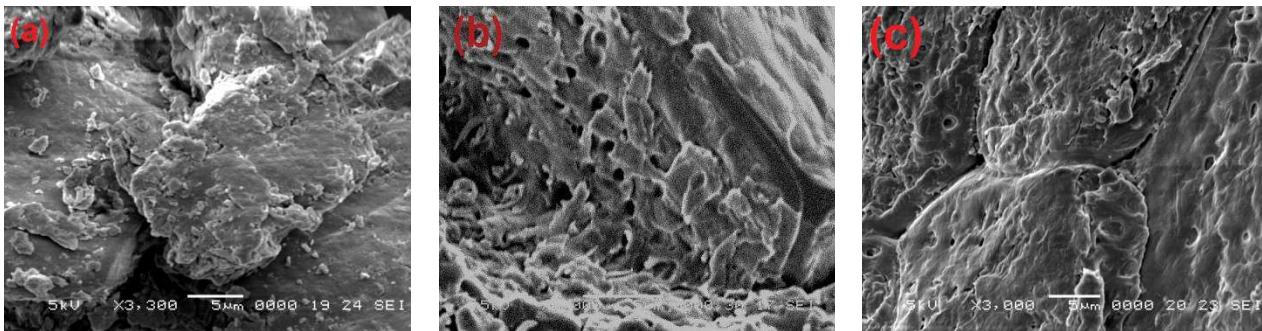


Fig.3. SEM images of (a) Untreated OPKS and (b) Cold alkali treated (c) Hot alkali treated

The SEM micrographs of the fracture surface of OPKS composites are presented in Fig. 4. The Fig. 4(a) shows the fracture surface of the untreated OPKS/polyester composite without any bonding between filler and matrix due to the impurities on the filler surface. SEM micrograph of cold alkali treated OPKS/polyester composite is presented in Fig. 4(b). It can be seen from Fig. 4(b) that there is weak bonding between filler and matrix. The weak bonding between the filler and the matrix is due to the small amount of impurities still remaining on the surface of the filler.

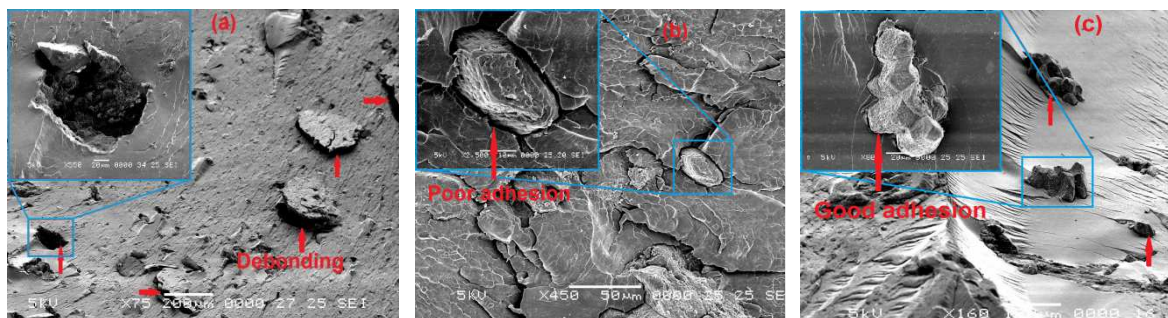


Fig.4. The SEM images of (a) untreated OPKS/polyester composite, (b) Cold Alkali treated OPKS/polyester composite, (c) Hot Alkali treated OPKS/polyester

The SEM micrographs of the fracture surface of hot alkali treated composites are presented in Fig. 4(c). It is clearly indicated that hot alkali treatment ensured the best adhesion between OPKS particles and polyester matrix due to the removal of all impurities and increased the surface roughness. In addition, the significant improvement in mechanical properties in hot alkali compared to the cold alkali is due to the better efficiency of alkali reaction which presented in Equ. 1. In hot alkali condition, probably more Na^+ ion could be replaced instead of OH group compared to the cold alkali condition. As a result, better adhesion occurred between the polymer and filler and the good adhesion leads to a significant improvement in the mechanical properties.

Conclusion

The following observations and conclusions can be made on the basis of the current experimental results:

- The mechanical properties of OPKS/polyester composite with hot alkali treatment samples yielded higher compared to other samples.
- According to the SEM micrograph the quality of cleaning processes of hot alkali treatment was more effective than cold alkali treatment.

- The interfacial bonding between OPKS particles and polyester matrix by hot alkali was better than the cold alkali and the cold alkali were better than untreated samples. As a result, hot alkali treated sample yielded better mechanical properties in composite.

Acknowledgements

The researchers would like to thank the Curtin University Sarawak for providing the research grant that has made this work possible.

References

- [1] Y. R. Loh, D. Sujan, M. E. Rahman, C. A. Das "Sugarcane bagasse - The future composite material: A literature review" *Resources Conservation and Recycling*; vol. 75, 2013, pp.14– 22
- [2] M. E. Rahman, A. Muntohar, Vikram P, Brabha H, & D. Sujan, "Self Compacting Concrete from Waste Materials & Blended Fine Aggregate", *Materials and Design*; vol. 55, 2014, pp. 410–415
- [3] L. Lancaster, M. H. Lung, and D. Sujan "Utilization of Agro-Industrial Waste in Metal Matrix Composites: Towards Sustainability" *World Academy of Science, Engineering and Technology*, vol.73, 2013, pp. 1136-1144
- [4] S. Shinoja, R. Visvanathanb, S. Panigrahi, M. Kochubabua, "Oil palm fiber (OPF) and its composites: A review", *Ind. Crop. Prod.* vol.33,2011; pp. 7–2,
- [5] F.O. Okafor. "Palm kernel shell as a lightweight aggregate for concrete". *CemConcr Res.* vol.18(6), 1988; pp.901–10.
- [6] Teo DCL, Mannan MA, Kurian VJ, Zakaria I. Flexural behaviour of reinforced lightweight OPS concrete beams. In: 9th International conference on concrete, engineering and technology, Malaysia; 2006; pp. 244–52.
- [7] Jia Guo,1 and Aik Chong Lua. Microporous Activated Carbons Prepared from Palm Shell by Thermal Activation and Their Application to Sulfur Dioxide Adsorption. *Journal of Colloid and Interface Science*, vol.251, 2002;pp.242–247
- [8] PooyaLahijania, ZainalAlimuddinZainala, Abdul RahmanMohamedb. Catalytic effect of iron species on CO₂ gasification reactivity of oil palm shell char. *ThermochimicaActa*, vol. 546, 2012; pp. 24– 31
- [9] Suradi, S.S., Younus, R.M. and Beg, M.D.H. "Oil palm bio-fibre-reinforced polypropylene composites: effects of alkali fibre treatment and coupling agent." *Journal of composites materials.*" vol. 45 (18), 2011; pp. 1853-1861.
- [10] Majeed, K., M. Jawaid, A. Hassan, A. Abu Bakar, H. P. S. Abdul Khalil, A. A. Salema, and I. Inuwa. "Potential Materials for Food Packaging from Nanoclay/Natural Fibres Filled Hybrid Composites." *Materials & Design*, vol.46 (0), 2013; 391-410.
- [11] Faruk, Omar, Andrzej K. Bledzki, Hans-Peter Fink, and MohiniSain. "Biocomposites Reinforced with Natural Fibres: 2000–2010." *Progress in Polymer Science*, vol.37(11), 2012;pp. 1552-1596.

Effect of Curing Age on the Compressive Strength of Petrovege Blocks

Johnson O.A.^{1, a}, Madzlan N.^{2, b} and Kamaruddin I.^{3, c}

^{1 2 3} : Department of Civil and Environmental Engineering, Universiti Teknologi PETRONAS
31750 Seri Iskandar, Tronoh, Malaysia

^ajohnsonolufemi02@gmail.com, ^bmadzlan_napiah@petronas.com.my,
^cibrakam@petronas.com.my

Keywords: Petrovege blocks, Curing age, Density, Compressive strength, Porosity.

Abstract. In the recent years there has been an intensification of policies on sustainable construction materials in the construction industry. This environmental policy has brought about development of various sustainable materials in which Petrovege blocks is one of the outstanding products. This paper investigates the effect of curing age on the compressive strength of the product. Block samples were prepared by adding 8%, 9%, 10%, 11%, 12%, and 13% liquid content of the mixture of vegetable oil and crude oil sludge as a binder after the optimum liquid content has been established. The specimens were cured at different period of time of 48hrs, 72hrs, 96hrs, and 120hrs. Mechanical properties of the products were evaluated. Compressive strength of Petrovege samples varies from 5.31 N/mm² to 18.88 N/mm² indicating that the compressive strength increases with increase in curing age, while decrease in porosity leads to increased compressive strength for the stipulated curing ages. All samples satisfied the minimum requirements in terms of compressive strength, in accordance with all available standards.

Introduction

Waste generation both from industrialization and urbanization are creating an environmental concern [1, 2]. In recent years researchers have been focusing attention on ways to reuse, and recycle waste to enhance a sustainable environment. Some of the waste that are have been used in construction industry for the production of building materials includes red mud, fly ash [3, 4], blast furnace slag, industry steel dust [5, 6], and several sewage sludge [7, 8, 9]. Intensive investigations have been done towards encapsulation of sludge toxic metals using wide variety of materials, involving cement, polymers [10, 11]. As a result, researchers and engineers have developed a sustainable alternative construction material [12], which leads to the production of petrovege block.

Petrovege block is a building block manufactured using crude oil sludge with oxidized vegetable oil as binder. This product has helped to reduce the environmental concern of petroleum sludge and also the greater cost involved in its removal and disposal. The good compressive strength of the product has made it inevitably useful in the construction industry.

Building Blocks generally are manufactured from the mixture of cement, sand and water and in special cases with admixture, molded into different sizes. Block can be manufactured in different sizes and shapes in accordance with available standards and design desired. In solid state, block demonstrates a high compressive stress and this strength increase with density.

Abdullahi[13] discovered that the quality of sandcrete blocks depend on some major factors which include but not limited to methods of production and the properties of the materials used. Uzoamaka [14] investigate the compressive strength of sandcrete blocks and found that it increases with decreasing specific surface of sand and that curing of block by water sprinkling enhances their strength.

Afolayan[15] carried out a full investigation on the compressive strength of sandcrete blocks produced by different block industries in Ondo State, Nigeria; the results indicates lower values of compressive strength compared to recommended values in available Codes and Standards. They also recorded high coefficient of variation in the block samples which shows poor quality control in the

production processes. Wenapere [16] discovered that the compressive strength of sandcrete blocks increased with age of curing for all mixes tested at the water-cement ratio of 0.5. The strength at ages 7, 14, and 21 days were 43%, 75%, and 92% of the 28-day strength respectively.

Dhir, [17] in his study discovered that the compressive strength of sandcrete blocks depend on some factors which are; mix proportion, quality of material, method of production and curing age, duration of time, and curing temperature.

The objective of this study is to evaluate the effect of curing age on the compressive strength of Petrovege block in order to establish the optimum curing age for the optimum compressive strength. The impact of binder content percentages and porosity on the compressive strength was also determined.

Materials and Methods

Materials. The crude oil sludge used was collected from PETRONAS Refinery at Melaka, Malaysia. The used vegetable oil is one that is available in Malaysia market. Two types of sand used were both river sand collected from Perak state, Malaysia, the size distribution of the sands were determined in accordance with ASTM C 136-96 and the specific gravity of the sands were also determined using helium ultracycnometer. The summary of the sand characterization is shown in Table 1.

Table 1: Characterization of sand

BS SIEVE SIZE (mm)	SAND 1	SAND 2
3.35	97.5	91.9
2	91.5	81.2
1.18	79.7	66.6
0.6	53.3	47.6
0.425	37.2	36.6
0.3	18.7	21.8
0.212	11.7	8.70
0.15	0.00	0.00
Density	2.65	2.67

Specimen Preparation. 600g of sand was weighed, 300g from each of the sand type and mixed properly together. The binder which is of a mixture of petroleum sludge and vegetable oil was prepared well to obtain a homogeneous 1:1 mixture. The binder content used was 8%, 9%, 10%, 11%, 12%, and 13 %. After thorough mixing, the freshly prepared mixes were placed in cylindrical moulds of 50mm × 100mm in size and compacted with 75 blows in Marshall compacting machine in accordance with BS598 standard. The samples were cured in an oven at temperature of 160°C for 48, 72, 96, and 120 hours.

Testing methods. The mechanical properties of the petrovege blocks samples were determined in triplicate after curing. The testing methods employed were; measurement of the samples mass and bulk density, determination of compressive strength, density and porosity.

Results and Discussions

Sand characterization. The result of the particle size distribution done on the sands used is shown in Figure 1. The particle –size distribution curve shows not only the range of particle sizes present in the sand but also the type of distribution of various size particles. It can be deduced from the graph that the particle –size distribution represents a type of sand in which the particles are distributed over a wide range. It could be observed from the grading curves that the coefficient of uniformity (Cu) and coefficient of curvature (Cc) for the aggregates are 7.3 and 1.1 respectively. Since the Cu is greater

than 6 and the C_c is within 1-3 value, the sand can be said to be well graded [18]. The specific gravity of the sand is 2.66.

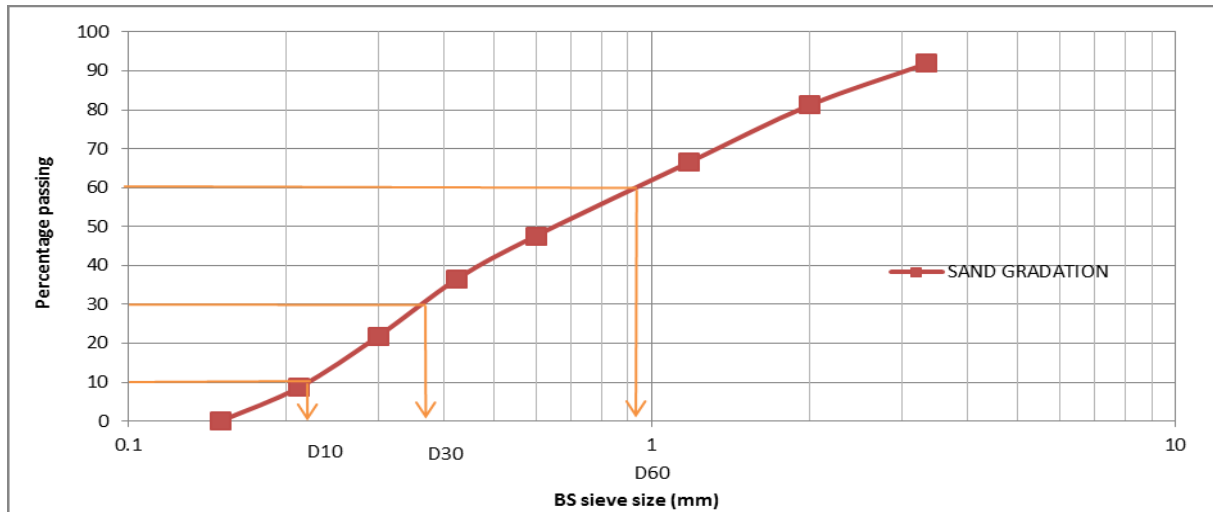


Figure1: Particle size distribution of sand.

Compressive strength. Compressive strength is the most common performance measure used by engineer to design building structures [19]. The compressive strength was measured by breaking cylindrical samples with a diameter of 100 mm and height of 50 mm in a compression- testing machine. The set necessary for one test was formed by three cylinders from every type of mixes. Only intact and unbroken bodies of the prescribed shape were used in the test.

The results of the test were an arithmetic average of the detected values on a set of three test cylinders from every type of mixes. The calculated value of the compression strength is indicated with an accuracy of 0.01 MPa. The results indicate that the optimum compressive strength of the samples is attained at 96 hours curing, where the maximum recorded is 18.88 N/mm². The compressive strength with the curing age is summarized in Table 2.

Table 2: Compressive strength and curing age

BINDER CONTENT (%)	COMPRESSIVE STRENGTH AT 48hr (N/mm ²)	COMPRESSIVE STRENGTH AT 72hr (N/mm ²)	COMPRESSIVE STRENGTH AT 96hr (N/mm ²)	COMPRESSIVE STRENGTH AT 120hr (N/mm ²)
8	7.919	9.484	12.222	9.777
9	7.002	9.421	12.871	9.230
10	7.320	10.388	12.171	16.919
11	7.588	13.113	16.397	16.104
12	5.309	9.115	16.372	17.581
13	5.665	12.018	18.880	18.523

It can also be deduced from the results that the compressive strength increases with increase in the binder content as seen in the figure 2, where sample at 96 hour curing exhibit the highest compressive strength with 13% binder content.

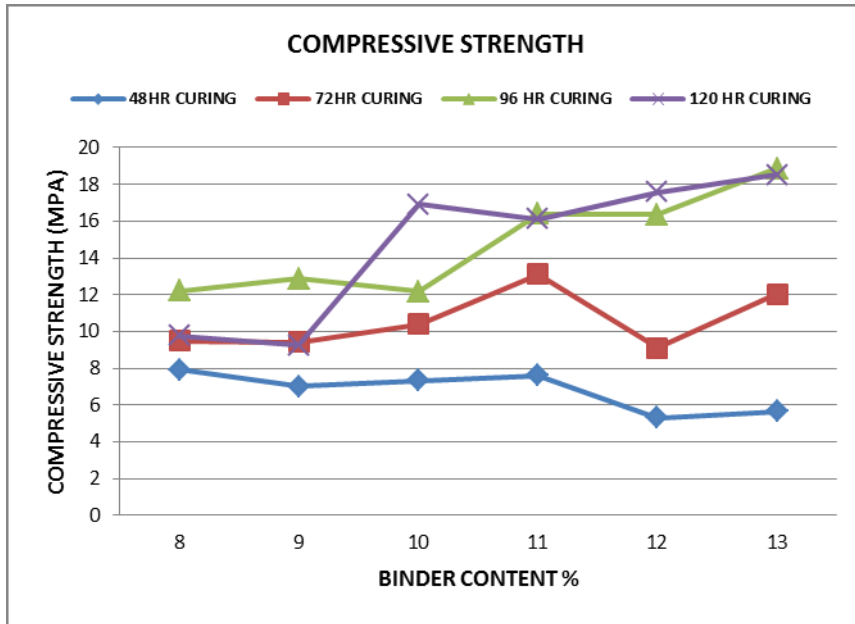


Figure 2: Compressive strength and binder content

Porosity. Porosity is the ratio of pore space and total volume of a material. It is an important factor that determines the movement rate of constituents from a material to the water phase and the environment [20]. High porosity in a material means transport of water is easier in it due to the pores, which always lead to higher release of contaminants from the material if any. The results from the samples show that the porosity decreases with increase in the binder content as indicated in Figure 3, this indicates that the binder content thus affect the porosity, it makes the aggregates binds more as it increases in content. Results also show that the compressive strength increases with the decrease in porosity as shown in Figure 4; the curing age does not have any significant effect on the porosity. It can be deduced from the Figure 4, that a well cured samples exhibit high compressive strength when the porosity is low and the compressive strength decreases as the porosity increases.

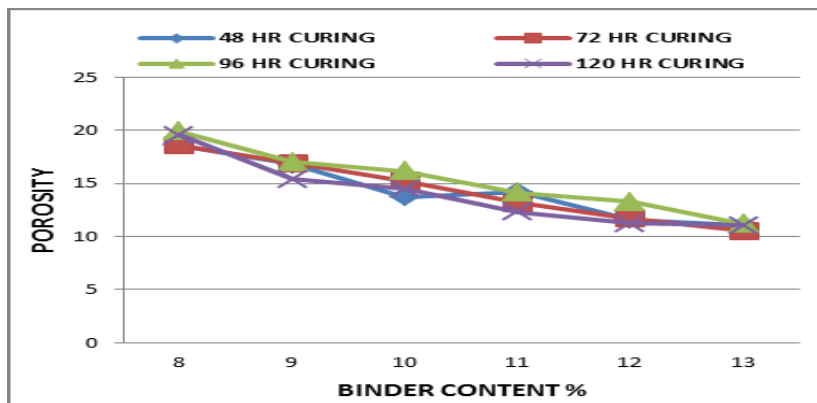


Figure 3: Porosity and binder content

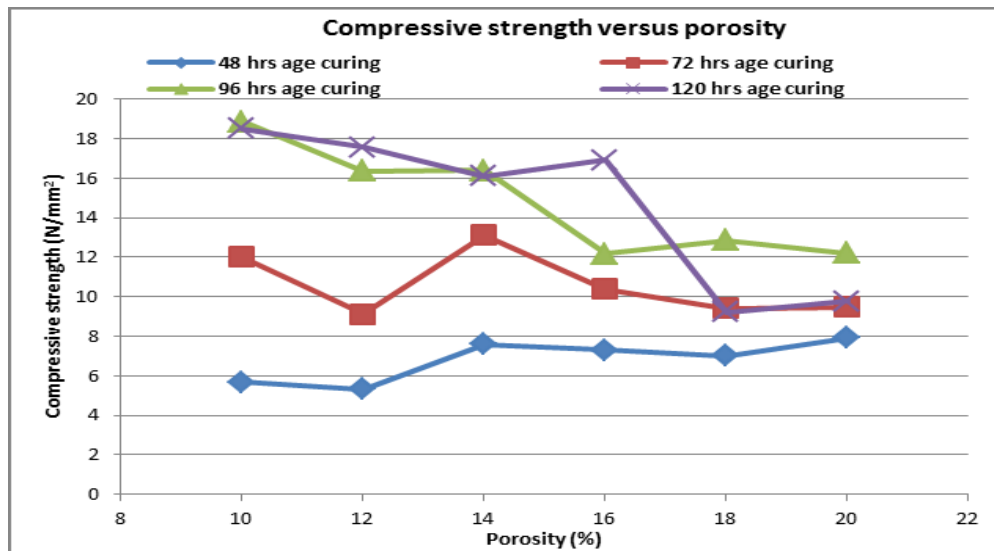


Figure 4: Compressive strength versus Porosity

Conclusion

Based on the results from this study the following conclusions have been drawn:

- The compressive strength increased with increase in curing age;
- The optimum compressive strength of Petrovege block can be obtained at 96 hours curing age with 13% binder content;
- Compressive strength of Petrovege blocks increased with increase in binder content at curing age of 96 hours and above;
- Improper curing of Petrovege block could lead to undesirable effects such as reduced strength, increased porosity, increased shrinkage and internal cracking of the product. However well cured Petroblocks will have a good compressive strength, reduced porosity, cracking and increase durability property.

References

- [1] Y. Tian, W. Zuo, D. Chen, "Crystallization evolution, microstructure and properties of sewage sludge-based glass-ceramics prepared by microwave heating", *Journal of Hazard. Material* 196 (2011) 370–379.
- [2] H. Wang, C. Wang, F. Chen, M. Ma, Z. Lin, W. Wang, Z. Xu, X. Wang, "Modification to degradation of hexazinone in forest soils amended with sewage sludge", *Journal of Hazard. Mater.* 199–200 (2012) 96–104.
- [3] M. Erol, S. Küçükbayrak, A. Ersoy-Mericboyu, "Comparison of the properties of glass, glass-ceramic and ceramic materials produced from coal fly ash". *Journal of Hazard. Mater* 2008;153:418–25.
- [4] G. Cultrone, E. Sebastián, "Fly ash addition in clayey materials to improve the quality of solid bricks". *Journal of Construction and Build Material* 2009;23:1178–84.
- [5] P.H. Shih, Z.Z. Wu, H.L. Chiang. "Characteristics of bricks made from waste steel slag". *Journal of Waste Management* 2004;24:1043–7.
- [6] C.M.F. Vieira, P.M. Andrade, G.S. Maciel, F. Vernilli, S.N. Monteiro. "Incorporation of fine steel sludge waste into red ceramic". *Journal of Material Science Eng A-Struct* 2006;427:142–7.

- [7] S.N. Monteiro, J. Alexandre, J.I. Margem, R. Sánchez, C.M.F. Vieira. "Incorporation of sludge waste from water treatment plant into red ceramic". *Journal of Construction and Building Material* 2008;22:1281-7.
- [8] K.Y. Chiang, P.H.Chou, C.R. Hua K.L.Chien, C. Cheeseman . "Lightweight bricks manufactured from water treatment sludge and rice husks". *Journal of Hazard Material* 2009;171:76-82.
- [9] M.A. Montero,M.M Jordán, M.S. Hernández-Crespo, T. Sanfeliu . "The use of sewage sludge and marble residues in the manufacture of ceramic tile bodies". *Applied Clay Science* 2009;46:404-8.
- [10] P. Randal , S. Chattopadhyay . "Advances in encapsulation technologies for the management of mercury-contaminated hazardous wastes". *Journal of Hazard Material* 2004;B114:211-23.
- [11] J.M. Magalhaes, J.E. Silva, F.P. Castro,J.A. Labrincha. "Effect of experimental variables on the inertization of galvanic sludges in clay-based materials". *Journal of Hazard Material* 2004;106B:139-47.
- [12] A.A Abang, S. Chandra . "Waste materials used in concrete manufacturing". New Jersey (USA): Noyes Publications Westwood; 1977.
- [13] Abdullahi, M. (2005). "Compressive Strength of Sandcrete Blocks in Bosso and Shiroro Areas of Minna, Nigeria", *AUJT*, 9(2), 126-131.
- [14] Uzoamaka, O. J. (1977a). "Some other factors which affects the crushing strength of Sandcrete Blocks". *Materials and Structures*, 10(1), 45-48.
- [15] Afolayan, J. O., Arum, C., and Daramola, C. M. (2008). "Characterization of the Compressive Strength of Sandcrete Blocks in Ondo State, Nigeria". *Journal of Civil Engineering Research and Practice*, 5 (1): 15-28.
- [16] Wenapere, D.A. and Ephraim, M.E. (2009). "Physico- mechanical behaviour of sandcrete block masonry units". *Journal of building*.
- [17] Dhir,J (1980). "Civil Engineering material". Macmillan, London. 5th edition Pp 493-526.
- [18] ASTM C136, "Standard Test Method for Sieve Analysis of Fine and Coarse Aggregates".
- [19] National Ready Mixed Concrete Association (2003). "Concrete in Practice- Testing Compressive Strength of concrete".Silver spring MD, www.nrmca.org.
- [20] Van der Sloot, H.A., Dijkstra, J.J.(2004). "Development of horizontally standardized leaching tests for construction materials: a material based or release based approach. Identical leaching Mechanisms for different materials, <https://www.ecn.nl/docs/society/leaching/C04060.pdf>.

Evaluation of Spur Gear Pair on Tooth Root Bending Stress in Yawing Misalignment Contact Condition

M.R.Lias^a, M.Awang^b, T V V L N Rao^c, M.Fadhil^c

Mechanical Engineering Department, Universiti Teknologi PETRONAS,
Bandar Seri Iskandar, 31750 Tronoh, Perak, Malaysia

^arizal_lias@ptsb.edu.my, ^bmokhtar_awang@petronas.com.my, ^ctadimalla_v@petronas.com.my,
^cfarfiez@yahoo.com

Keywords: Yawing misalignment (Y), Finite-element method (FEM), Tooth root bending stress (TRBS), Yawing misalignment influence factor (YMIF), Assembly errors (AE)

Abstract. This paper evaluates the effects of yawing misalignment contact on the tooth root bending stress values of spur gear pair during the gear meshing cycle. A model based on involute 3D parametric CAD geometry, of spur gear design ISO 6336:2006 is analyzed with worst loading position when yawing misalignment (Y) exist due to assembly error (AE) between 0.2° to 0.4° in degree scale values. Finite-element method (FEM) with dynamics module from ANSYS is used in order to calculate the tooth root bending stress (TRBS) at the critical region with respect to face width of pinion and gear section. A comparison is made between standard high point single tooth contact models (HPSTC) to this model as verification. Further analysis showed a good agreement that these methodologies are adequate in order to conduct a real time dynamics simulation to define the value of TRBS in Y condition due to AE. Yawing misalignment influence factor (YMIF) was introduced as an indication of TRBS values in consideration of Y due to AE shows a higher result for pinion, give a good justification that the pinion is weaker compared to the gear in Y condition.

Introduction

Mechanical design practice that involved with rotating part such as a pinion-gear needs a lot of intentions due to its complicated art of motion. The meshing assembly in between pinion and gear is a very complex task procedure for an engineer in order to get the full efficiencies of loading transferred as a theory state happened in line of action (LOA). For instance, if it is mesh too tight, the assembly will behave on certain characteristics, but if it is too loose, then other function will be happened. Thus, engineer tense to give allowance or called as backlash allowable tolerance in order to ensure that the pinion-gear meshing contact in a smooth correct manner. These nuances sometimes are over really conservative, makes it possible leads to "bad assemblies" or called as assemble errors (AE). These errors will impact the Tooth root bending stress (TRBS) value and distribution along the important plane at 30° angles for each section tooth. The cyclic loading behavior with vibrations, furthermore, will leads bending fatigue failure happened thus, reduce the service life of the gears.

Misalignment in gear meshing contact is described as a small deviation or error in a pinion-gear assembly as theoretical LOA to the actually happened [1]. Yawing misalignment (Y) denotes as the twisting of the pinion or gears in its nominal position due to backlash tolerance given happened from assembly errors (AE) when a pinion is mesh to the gears. This position is described based on the coordinate system such as Fig. 1 in between contact of the pinion-gear as suggested by [2].

In many years of perspectives review in gear design, the effect of misalignments due to AE is found discussed in early 70's. Experiment was conducted by Timmers [3] in order to correlate the effect of AE to TRBS. Their result showed that misalignments weakened the structure and reduce efficiencies of the gear tooth contact and bending strength. Recent advances in computerization make finite-element method (FEM) become a trend to solve the problem related to the gearing. This had leads to the development of a more reliable model in optimization of gearing system. Started late 1980s, Townsend et al. [4] describe a new approach to calculate maximum TRBS with FEM. Their use

single model teeth with asymmetry load allowed calculation of stress distribution in the adjacent teeth. Krambergeretal.[5] applied boundary element method (BEM) analyzing the maximum TRBS of thin-rim spur gear. Shun Li [6] continue the research with quasi-static using a load sharing ratio (LSR)method with tooth modifications. Though, there are many research continues comes out in this recent decade with TRBS as the main subject[7] so far, an effective detail of Y due to AE is still considered sparse in shadowed.

Thus, this paper determines to focus on this problem in detail with a significant FEM methodology using ANSYS tool. A full model of involutes 3D parametric CAD geometry, based on mathematical standard formulation of ISO 6336:2006 spur gear design is develop to analyze Y with worst condition of allowable AE values from 0.2^0 to 0.4^0 . The result is then compared with static high point single tooth contact (HPSTC) model from [8] with no Y. Yawingmisalignment influence factor (YMIF) is introduced as an indication of TRBS in Y condition due to AE.

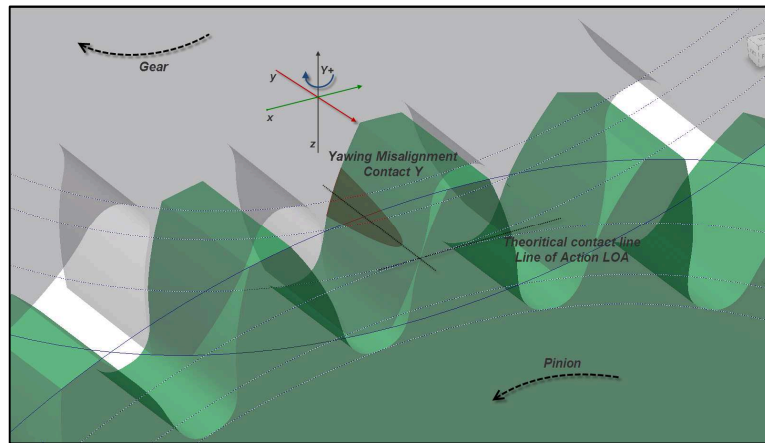


Fig. 1: Illustration of pinion gear meshing in yawing misalignment contact (Y)

Finite Element Model

The physical FEM model is obtained from involutes parametric 3D CAD geometry of spur gear design based on Autodesk Inventor gear generator standard ISO 6336:2006with basic parameter describesas Table 1. It consists of one pinion and one gear in full teeth with material SCM415 [6]. The pinion was subjected to an angular velocity $\omega = 1$ rad/s counter clockwise. A torque $T=10$ Nm is applied to the gearin order to simulate the dynamics load. The displacement of node changes over time during the analysis, which can be described as:

$$\{q\} = q(x, y, z, t) \quad (1)$$

Where, q is the displacement of a node, x, y, z are three coordinates respectively, t is time. For the whole analysis model, elements are under the status of force equilibrium and the displacement of every node is also in equilibrium. When the gear pair is under external load, based on the principle of force equilibrium the relationship between the displacement node and external dynamics load can be expressed as:

$$[K]\{q\} = F_i(t) \quad (2)$$

Where, $\{q\}$ is the displacement node, $[K]$ is a total stiffness matrix of the element, which was the set of blocking stiffness matrix of elements mesh generated from the model. $F_i(t)$ is the matrix of external dynamics load history as function of time.

Both pinion-gears are meshed with symmetrical FEM mapped element as Fig. 2 with 192 part bodies. Joint revolute UZ is applied as constraint on the hollow region for both pinion-gears. Contact element augmented langrage model [9] is use with refine mesh 0.1 mm in between 3 teeth of the model. At first, the model is arranged in perfectly aligned order where TRBS is allowed. Then, AE

value in yawing axis between 0^0 , 0.2^0 , 0.3^0 and 0.4^0 gradually applied as Y simulation. APDL mechanical module in ANSYS is use in order to calculate the value of stress for each node and element. TRBS is then plotted at the critical region [8].

Table 1: Gear Model parameters

Parameter	Symbol	Unit	Pinion	Gear
Geometry				
Normal Module	m	mm	5	
Normal Pressure Angle	α_n	degree	20^0	
Number of Teeth	z		27	27
Center Distance	a_x	mm	135	
Face width	b		12	
Load				
Torque	T	Nm	10	
Speed	N	rad/s	1	
MaterialSCM415				
Modulus of Elasticity	E	GPa	206	
Poisson's Ratio	μ		0.300	
Density	ρ	kg/m ³	7830	

According to Haiba et.al[10] stress of the dynamic mechanical system can be estimated by separated time step using quasi-static stress analysis approach, which:

$$\sigma_x(t) = \sum_{i=1}^n \sigma_{xi}F_i(t), \sigma_y(t) = \sum_{i=1}^n \sigma_{yi}F_i(t), \sigma_z(t) = \sum_{i=1}^n \sigma_{zi}F_i(t) \tag{3}$$

$$\tau_{xyz}(t) = \sum_{i=1}^n \tau_{xyzi}F_i(t) \tag{4}$$

Where n is the number of applied load histories and $\sigma_{xi}(t)$, $\sigma_{yi}(t)$, $\sigma_{zi}(t)$, $\tau_{xyzi}(t)$ are the stress due to a unit load in a function of time. TRBS is then calculated based on von-misses yield criteria σ_{vm} for each specific nodal in normal direction for each load history time $F_i(t)$. It is meant that the analysis is based on certain real time dynamics moment, in this case, is the highest TRBS only.

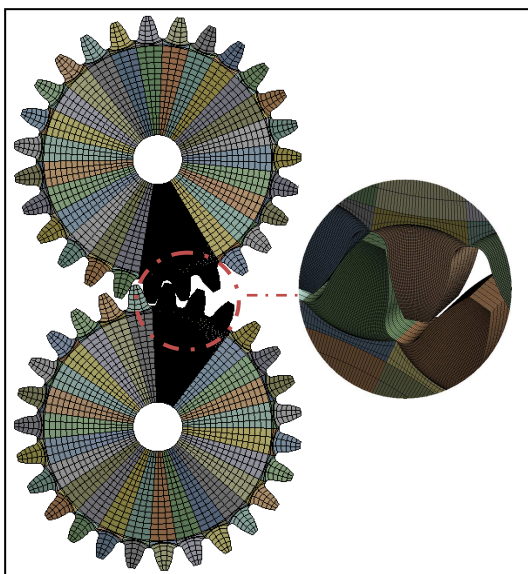


Fig. 2: Element mapping and meshing of FEM model

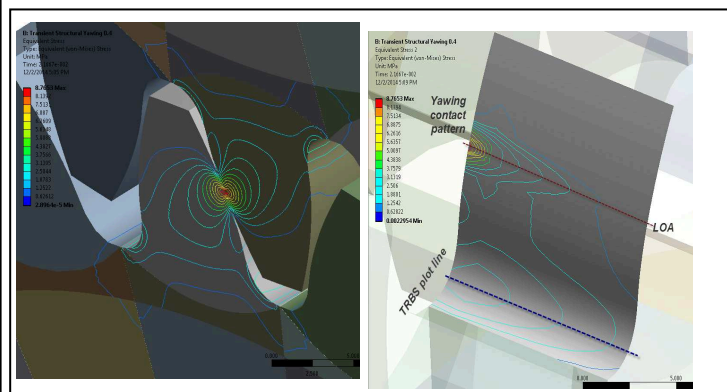


Fig.3: Contour ISO line result of σ_{vm} contact and TRBS value when $AE= 0.4^0$

Results and Discussion

TRBS calculations of Y with effect of AE are performed in dynamics condition with 1rad/s speed of the pinion to the 10 Nm load for the gear. Equivalent Von-misses stress criteria are plotted at critical root region as Fig. 3for each node and element across the face width of the pinion-gears. From Fig. 4 and 5, it is clearly shown that when AE = 0, value of TRBS is much lower compared with static HPSTC model. When value Y gradually increased between 0.2⁰ to 0.4⁰ as Fig.4, the stress becomes greater with a skewed pattern between one sides of misalignment contact to the other side of the face width of the pinion tooth. In Fig. 5, a similar pattern of TRBS was plotted for the gear, the only different is the value of the stress plotted, which was little bit lower for gear. As Fig. 6 and 7, YMIF for pinion-gear was introduced as an indication of the effect Y from AE on TRBS. It is calculated by dividing the maximum value of TRBS when AE existed to the value when the pinion-gear mesh in perfect contact or AE = 0. Relationship between these factors found that the YMIF value is the highest 3.68 when AE = 0.4⁰ for pinion and 3.54 for the gear. The graph of maximum TRBS to YMIF factor showed a similar pattern between each other's values can be described as a good justification as a result from [7] that the pinion is weaker compared to the gear, thus the factor should be more in terms of value.

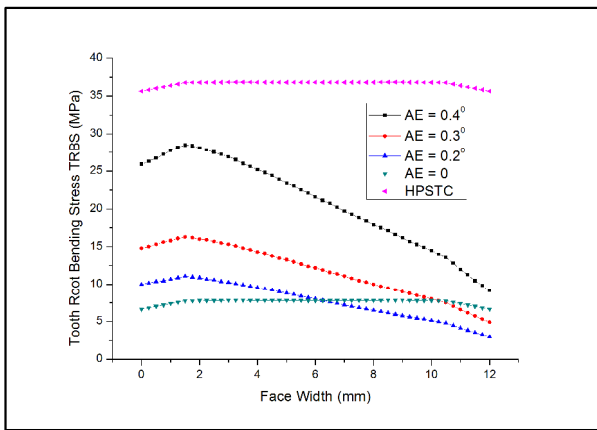


Fig 4: TRBS across critical region for the pinion

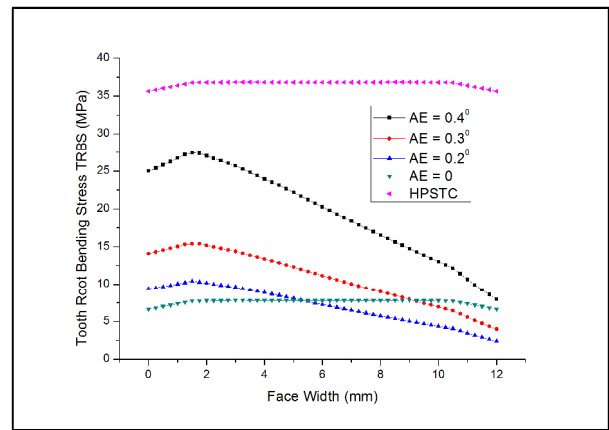


Fig. 5: TRBS across critical region for the gear

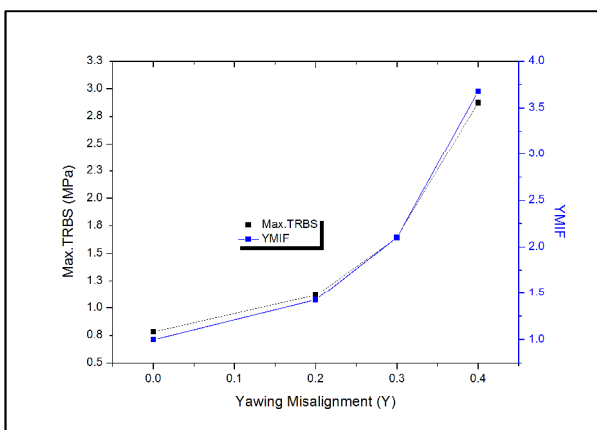


Fig. 6: Maximum TRBS to (Y) with YMIF value for pinion

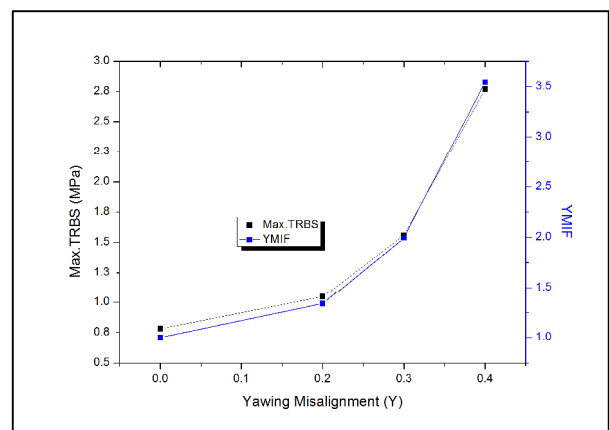


Fig. 7: Maximum TRBS to (Y) with YMIF value for gear

Conclusion

In this paper, FEM model based analysis was conducted to evaluate the effect of yawing misalignment contact (Y), due to assembly error (AE), on the tooth root bending stress (TRBS) values of spur gear pair during gear meshing cycle. Major contribution in this paper can be summarized as:

1. The propose FEM model and methodology are adequate in order to conduct a real time dynamics simulation to define the value of TRBS in Y condition due to AE.
2. YMIF influence factor of Ycondition on TRBS shows the stress valueof the pinion is higher compared to the stress values of gear. These gave a justification that the pinion is weaker compared to the gear in yawing misalignment condition.

Acknowledgements

This research work is funded by Exploratory Research Grant Scheme - Ministry of Higher Education Malaysia (ERGS-MOHE) under grant ERGS 0153AB-I14. The authors greatly appreciate the support provided by MOHE and Universiti Teknologi PETRONAS for the facilities, system support and financial aid for this research.

References

- [1] M.R.Lias, T.V.V.L.N.Rao, M. Awang and M.A. Khan, "The Stress Distribution of Gear Tooth Due to Axial Misalignment Condition," *Journal of Applied Sciences*, vol. 12, pp. 2404-2410, 2012.
- [2] A. Palermo, D. Mundo, R. Hadjit, and W. Desmet, "Multibody element for spur and helical gear meshing based on detailed three-dimensional contact calculations," *Mechanism and Machine Theory*, vol. 62, pp. 13-30, 2013.
- [3] J. Timmers, "Der Einfluss fertigungstechnisch-und lastbedingter Achsversetzungen in Stirnradgetrieben auf die Zahnverformung, English Translation," *Mechanism and Machine Theory*, vol. 87 pp. 1771-1778., 1965.
- [4] J. J. Coy, D. P. Townsend, and H. H. Coe, "Results of NASA/Army transmission research," DTIC Document 1987.
- [5] J. Kramberger, Šraml, M., Potrč, I., and Flašker, J., "Numerical Calculation of Bending Fatigue Life of Thin-Rim Spur Gears," *Eng. Fract. Mech.*, vol. 71 pp. 647-656, 2004.
- [6] S. Li, "Effects of machining errors, assembly errors and tooth modifications on loading capacity, load-sharing ratio and transmission error of a pair of spur gears," *Mechanism and Machine Theory*, vol. 42, pp. 698-726, 2007.
- [7] Y. Z. Xu, Z. X. Wu, S. A. Tian, and Y. J. Hua, "Three-Dimensional Analyses of Spur Gear Bending Stresses by Global-Local Finite Element Technique," *Applied Mechanics and Materials*, vol. 365, pp. 309-313, 2013.
- [8] A. Kawalec, D. Ceglarek, and J. Wiktor, "Comparative Analysis of Tooth-Root Strength Using ISO and AGMA Standards in Spur and Helical Gears With FEM-based Verification," *Journal of Mechanical Design*, vol. 128, pp. 1141-1158, 2005.
- [9] A. W. 11.0, *ANSYS Modeling and Meshing Guide*. USA: ANSYS, Inc., 2006.
- [10] B. Haiba M., DC, Brooks, PC, Levesley, MC "Review of life assessment techniques applied to dynamically loaded automotive components," *Computers and Structures*, vol. 2, pp. 481-494, 2002.

The Effect of Morphing Force on Aerodynamic Performances of TM Wing

N.I. Ismail^{1, a}, A.H. Zulkifli^{1, b}, M.Z. Abdullah^{2, c}, M. Hisyam Basri^{3, d}
and Mahadzir M.M.^{3, e}

¹ Faculty of Mechanical Engineering, Universiti Teknologi MARA (Pulau Pinang), Malaysia

² School of Mechanical Engineering, Universiti Sains Malaysia, Pulau Pinang, Malaysia

³ Automotive Research and Testing Center (ARTEC), Faculty of Mechanical Engineering, Universiti Teknologi MARA (Pulau Pinang), Malaysia

^aiswadi558@ppinang.uitm.edu.my, ^babdulhalim540@ppinang.uitm.edu.my, ^cmezul@eng.usm.my,
^dmhisyam.mbasri@ppinang.uitm.edu.my, ^emohdmahadzir@hotmail.com

Keywords: Micro Air Vehicle (MAV), Fluid-Structure Interaction (FSI), morphing wing, aerodynamics.

Abstract. Twist Morphing (TM) wing is one of biomimetic MAV design that highly depends on morphing force actuation. Despite of vital morphing force influenced, the effect of morphing force variation on the aerodynamic performances of TM wing was not fully comprehended due to high complexity of fluid-structure interaction (FSI) behaviour. To elucidate the effect of morphing force influence, a series of TM wing with different morphing force intensity was used here to elucidate the effect of morphing force on C_L , C_D and C_M distribution. Fully coupled Ansys-FSI method was employed in this study. C_L and C_M results showed that TM wing with higher morphing force configuration had induced better static stability and higher C_L distribution. However, TM wing also promoted earlier AOA_{stall} incidence and higher C_D penalty than the baseline wings. These situations turn out to be greater in the TM wing cases with higher morphing force configurations.

Introduction

Twist Morphing (TM) wing is one of biomimetic MAV design that has been extensively studied to improve fixed MAV wing performances [1–3]. TM wing executed through morphing force actuation to perform the twist motion on the wing, which in turn induced benevolent aerodynamic behaviour over the MAV wing [1]. Despite of vital morphing force influenced, the effect of morphing force variation on the aerodynamic performances of TM wing was not fully comprehended [1,3]. This is probably due to high complexity of fluid-structure interaction (FSI) behaviour between the wing structural and flow surrounding the MAV wing. Thus, this paper demonstrated the effect morphing force intensity on the aerodynamic performance of TM wing. A series of morphing force intensity was imposed on the TM wing to create a distinction and further elucidated its effect on TM wing performances. Ansys-FSI numerical method was fully applied here to alleviate the complexity of FSI study on TM wing.

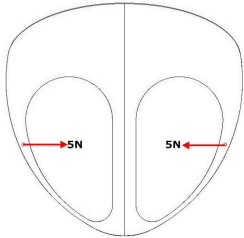
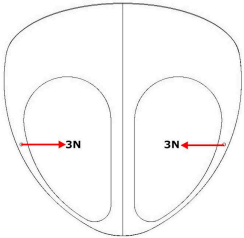
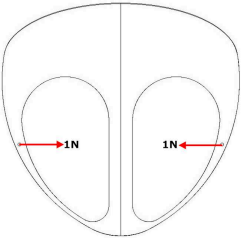
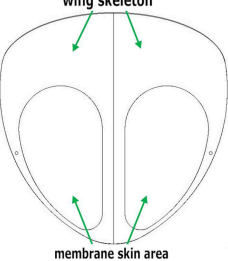
TM Wing Model

TM wing is modeled based on previous research shown in the reference [1]. The details of each TM wing configuration considered in current works are given in Table 1. Each TM wing configuration was named accordingly to its morphing force intensity: TM 5N, TM 3N and TM 1N wing. The following coordinate system adopted for each TM wing models: x is chordwise direction, z is spanwise direction, and y is normal to the wing, origin located at the outermost wing leading edge point. The thickness for all wings models (including the membrane skins) is set at 1.0 mm.

To simplify the FSI modelling, the fuselage, propeller and stabilizers (horizontal and vertical) components are intentionally removed. Technically, the objective function of morphing force is to alter the wing twist characteristics on each TM wing. The physical structure and basic kinematic principle of a TM wing morphing mechanism is illustrated in Figure 1. The morphing force applied at

morphing point located 90mm from the leading edge and directed towards inward-wing at 45° angle from the XZ plane. In order to elucidate TM wing performances, the unmorph TM wing setup was also included in the wing analysis as the baseline wing configuration.

Table 1 The basic configuration for TM 5N, TM 3N, TM 1N and baseline wings.

	TM 5N	TM 3N	TM 1N	Baseline wing
				
Wingspan, b	150mm	150mm	150mm	150mm
Root chord, c	150mm	150mm	150mm	150mm
Aspect ratio, A	1.25	1.25	1.25	1.25
Maximum camber at the root	6.7% of c (at x/c =0.3)	6.7% of c (at x/c =0.3)	6.7% of c (at x/c =0.3)	6.7% of c (at x/c =0.3)
Maximum reflex at the root	1.4% of c (at x/c = 0.86)	1.4% of c (at x/c = 0.86)	1.4% of c (at x/c = 0.86)	1.4% of c (at x/c = 0.86)
Geometric twist , ε	13.0°	8.6°	3.2°	0.6°
Force component	F=5N	F=3N	F=1N	F=0N
Approximate membrane skin location	0.34 ≤ x/c ≤ 0.9 0.10 ≤ 2z/b ≤ 0.83	0.34 ≤ x/c ≤ 0.9 0.10 ≤ 2z/b ≤ 0.83	0.34 ≤ x/c ≤ 0.9 0.10 ≤ 2z/b ≤ 0.83	0.34 ≤ x/c ≤ 0.9 0.10 ≤ 2z/b ≤ 0.83

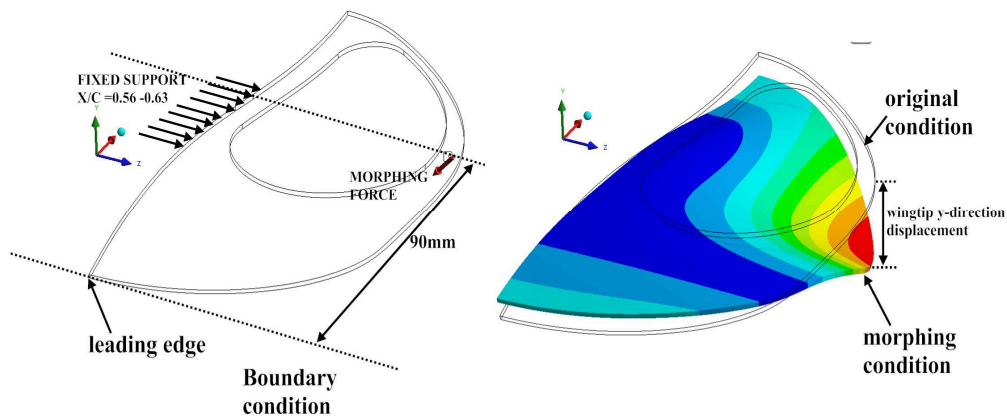


Figure 1 Basic kinematic principle behind TM wing actuation.

Polymethyl methacrylate (also known as Perspex) and silicone rubber is adopted as the material for the wing skeleton and membrane skin, respectively. Perspex and silicone rubber material material is chosen due to its feasibility in actual model development through rapidprototyping process. The material properties of Perspex and silicone rubber are listed in Table 2.

Table 2 Properties of Perspex and Silicone rubber

Material Name	Density (kg/m ³)	Young Modulus (Pa)	Poisson`s Ratio	Bulk Modulus (Pa)	Shear Modulus (Pa)	Tensile Yield Strength (Pa)
Perspex (Polymethyl methacrylate)	1190	2.8x10 ⁹	0.46	1.667x10 ¹⁰	9.589x10 ⁸	70x10 ⁶
Silicone Rubber	1290	6.5x10 ⁶	0.48	5.416x10 ⁷	2.1959x10 ⁶	2.5x10 ⁶

Ansyes-FSI Computational Method

Ansyes-FSI method consist of fully coupled computational fluid dynamic (CFD) and computational structural solver (CSD). The CFD problems over TM wings were solved based on steady and incompressible turbulent flow in Ansyes-CFX solver. Here, the Reynolds Average Navier-Stokes (RANS) equations coupled with SST $k-\omega$ turbulent model is fully utilized in the in Ansyes-CFX solver solver[4]. The CFD analysis over TM wings was set at speed of 15m/s with angle of attack (AOA) range between -5° to 30° (with 2° interval). The automatic wall function is fully employed to solve the flow viscous effect. The CFD study was highly focused on C_L , C_D and C_M distributions on TM wings. The CSD problems on TM wings were solved based on quasi-static structural deformations in Ansyes-Mechanical solver. Arbitrary Lagrangian-Eulerian (ALE) description is employed in Ansyes-FSI computation through the satisfaction of boundary velocity or displacement continuity at fluid and solid boundaries. The details of Ansyes-FSI computation and boundary conditions setups for CFD and CSD solver is found in the references [1,5]. Fully coupled FSI simulation method is summarized in Fig 1.

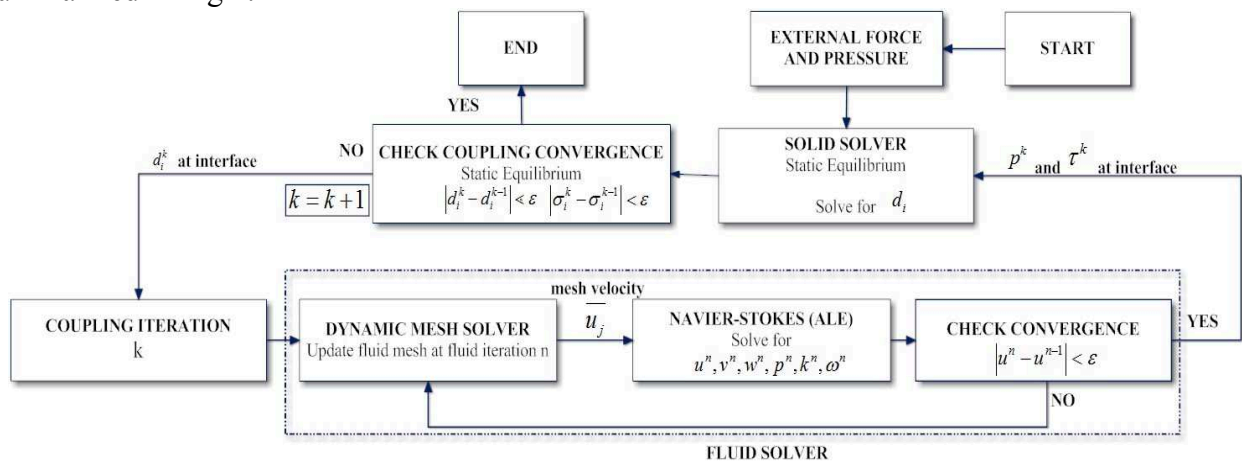


Figure 2 Fully coupled FSI simulation method

Results and Analysis

Lift Coefficient (C_L). C_L distributions for all TM wings are depicted in Figure 3. The results apparently showed that the lift curve for each TM wing (and baseline wing) was almost linearly increased with AOA changes until the stall angle (AOA_{stall}). Each TM wings had produced better lift distribution than the baseline wings. In fact, for a given AOA case at pre-stall angle ($<AOA_{stall}$), TM wing with higher morphing force magnitude had produced higher C_L distribution. Eq. 1 summarized the C_L distribution found on current TM wings.

$$C_L \text{ distribution on TM wings: } \quad TM\ 5N > TM\ 3N > TM\ 1N > \text{Baseline} \quad (1)$$

The C_L results also showed that TM 5N wing had experienced the earliest stall condition at $AOA_{stall} \approx 16^\circ$. This is followed by TM 3N and TM 1N wing at $AOA_{stall} \approx 19^\circ$ and 21° , respectively. The membrane wing stalled at $AOA_{stall} \approx 22^\circ$. From these results, one can presume that TM wings promoted earlier AOA_{stall} incidence than the baseline wings. In fact, TM wing with higher morphing force configuration promotes earlier AOA_{stall} incidence on TM wings.

Drag Coefficient (C_D). The C_D results (Figure 4) showed that TM 5N wing had produced the highest C_D magnitude in certain AOA case. This situation obviously found at the pre-stall AOA region between 0° to AOA_{stall} . At this point, TM 5N wing managed to produce about 150% higher C_D magnitude than the baseline wing. This is followed by TM 3N and TM 1N wings at 70% and 17%. From these C_D results, one can presume that the morphing force intensity highly influenced the C_D generation over TM wing. TM wing with higher morphing force configuration had induced higher C_D distribution. Eq. 2 summarized the C_D distribution found on current TM wings.

C_D distribution on TM wings: TM 5N > TM 3N > TM 1N > Baseline (2)

Moment Coefficient (C_M). The C_M results (Figure 5) showed that for each TM wings experienced a non-linear decrease in C_M magnitude towards the C_L increment. To analyze the C_M curve, a details analysis is conducted on the C_M slope ($\Delta C_M/\Delta C_L$) for every TM wing taken at AOA region between 0° to 15° . In aerodynamic study, steeper C_M slope (negative $\Delta C_M/\Delta C_L$ magnitude) means better static stability for an aircraft. The analysis showed that TM 5N had produced the steepest mean C_M slope at $\Delta C_M/\Delta C_L = -0.300$. TM 3N and TM 1N wing produced $\Delta C_M/\Delta C_L = -0.284$ (TM 3N) and -0.272 (TM 1N), respectively. The C_M slope for the baseline wing is at $\Delta C_M/\Delta C_L = -0.263$. Based on these C_M results, one can concluded that TM wing had produced better C_M slope (better static stability) than the baseline wing. Besides, TM wing with higher morphing force configuration had induced better static stability (C_M slope) distribution. Eq. 3 summarized the magnitude of C_M slope found on current TM wings.

Magnitude of C_M slope (static stability) on TM wings: TM 5N > TM 3N > TM 1N > Baseline (3)

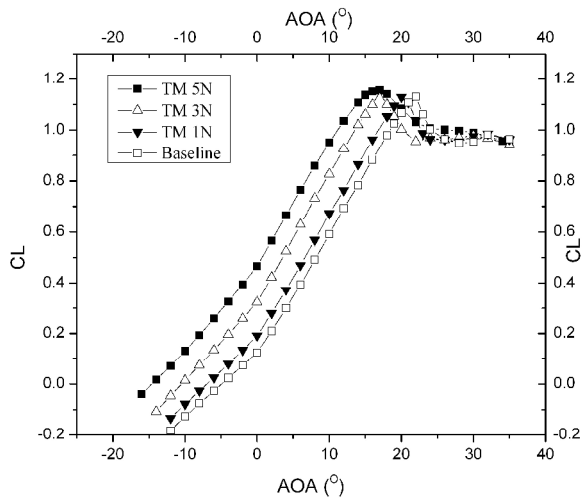


Figure 3 Lift coefficient (C_L) distribution for all TM wings

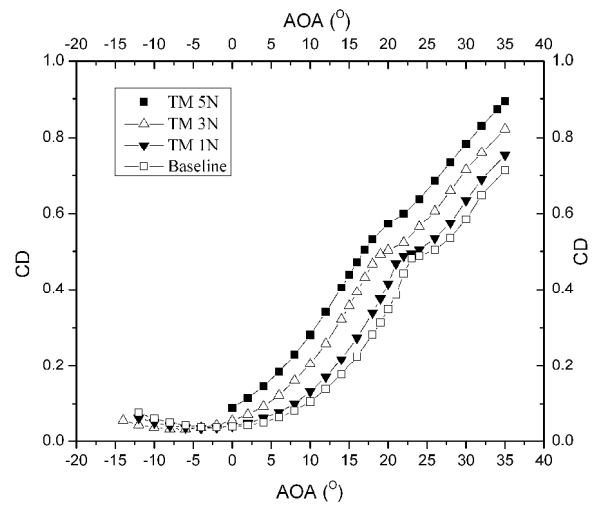


Figure 4 Drag coefficient (C_D) distribution for all TM wings

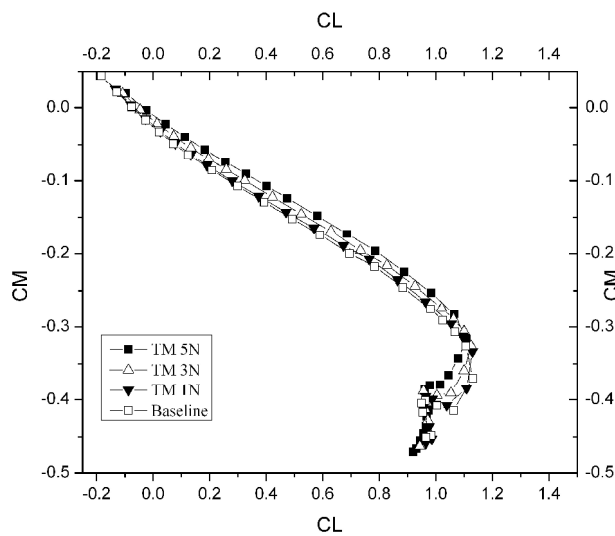


Figure 5 Moment coefficient (C_M) distribution for all TM wings

Summary

A series of TM wing with different morphing force intensity was used to elucidate the effect morphing force on the distribution of C_L , C_D and C_M performances. Fully coupled Ansys-FSI method was applied here to alleviate the complexity of FSI study on TM wing. C_L and C_M results showed that TM wing had produced better C_L and C_M slope performances than the baseline wing. In fact, TM wing with higher morphing force configuration had induced better static stability and higher C_L distribution. Despite of benevolent C_L and C_M slope performances, TM wing also promoted earlier AOA_{stall} incidence than the baseline wings. In fact, higher C_D penalty was induced on TM wings. These situations turn out to be greater in the TM wing cases with higher morphing force configurations.

References

- [1] N.I. Ismail, A.H. Zulkifli, M.Z. Abdullah, M. Hisyam Basri, N. Shah Abdullah, Computational Aerodynamic Analysis On Perimeter Reinforced (PR)-Compliant Wing, Chinese Journal of Aeronautics. 26 (2013) 1093–1105. doi:10.1016/j.cja.2013.09.001.
- [2] N.I. Ismail, A.H. Zulkifli, M.Z. Abdullah, M.H. Basri, N.S. Abdullah, Aerodynamic Performance of Twist Morphing MAV Wing FSI computation method, in: International Conference on Advances in Mechanical and Robotics Engineering (AMRE 2013), Zurich, Switzerland, 2013: pp. 26 – 30. doi:10.3850/978-981-07-7965-8_57.
- [3] N.I. Ismail, A.H. Zulkifli, M.Z. Abdullah, N.S. Abdullah, M.H.M. Basri, Investigation of Structural and Aerodynamic Performance of Twist Morphing Wing MAV ., in: IEEE Symposium on Business, Engineering and Industrial Applications, Kuching, Malaysia, 2013: pp. 142–147.
- [4] ANSYS, ANSYS CFX-Solver Theory Guide, 13.0 ed., ANSYS, Inc., Canonsburg, PA, 2010.
- [5] ANSYS, Ansys Multifield Coupled-Field Analysis Guide, 12.0 ed., Canonsburg, PA, 2009.

Analysis of Concurrent Brake Application for Underbone Motorcycle

M. Hisyam Basri^{1,a}, A.H. Zulkifli^{1,b}, N.I. Ismail^{1,c}, Sharzali Che Mat^{1,d}
and Mahadzir M.M^{1,e}

¹Automotive Research and Testing Center (ARTeC), Faculty of Mechanical Engineering, Universiti Teknologi MARA (Pulau Pinang), 13500 Permatang Pauh, Pulau Pinang, Malaysia.

^amhisyam.mbasri@ppinang.uitm.edu.my, ^babdulhalim540@ppinang.uitm.edu.my,
^ciswadi558@ppinang.uitm.edu.my, ^dsharzali.chemat@ppinang.uitm.edu.my,
^emohdmahadzir@hotmail.

Keywords: Motorcycle Braking, Underbone motorcycle, road friction coefficient.

Abstract. The application of single front wheel brake can yield large deceleration on underbone motorcycle. However, the motorcycle motion potentially exposed to the nosedive effect during this application. Therefore, in order to avoid this issue, the application of concurrent brake are required. Hence, this research was carried out to understand the basic braking performance for underbone motorcycle and elucidate the influenced of concurrent braking application involving the front and rear brake component. A theoretical study was carried out in this work through the derivation of motion equation for underbone motorcycle. The preliminary results showed that the total brake force and the brake force component acting on the front wheel had increased linearly with its deceleration intensity. Further study showed that in order to achieve higher safety range, the brake force applied on the front wheel should be at least 70% higher than the rear brake force intensity. This is probably due to the weight transferred condition during the underbone motorcycle braking.

Introduction

Accident cases in Malaysia are increasing severely. According to the statistic by Road Safety Department, in 2010, there are 120,156 motorcycles involved in accidents, the increment of 24% compared to 2005 [1]. The figure is quite alarming because accident always involves injury and fatality. Therefore, it is very important to prevent the motorcycle from accident. Beside the rider's responsibility to follow all the safety precaution during riding, related industries and academia also have the obligation to study and improve the current design or system to reduce motorcycle accident [2].

Prevention from road accident is known as active safety where brake is the crucial device in this category [3]. Nowadays, the underbone motorcycle (also known as motor-cub [4]) has individual brake system where the front brake controlled by hand lever, while the rear brake controlled by foot pedal. The application of front wheel brake alone can yield large deceleration but the nosedive (possibility of rear wheel to lift or front wheel to lock which can lead to unstable riding or loss of control) is large due to the shift of centre of gravity, while application of rear wheel brake alone has smaller nosedive but yield less deceleration [3,5,6]. Therefore, in order to increase the deceleration with minimal nosedive effect on underbone motorcycle, the application of concurrent brake are required through the single operation of hand lever or foot pedal.

The aim of this paper is to understand the basic braking performance for underbone motorcycle and elucidate the influenced of concurrent braking application involving the front and rear brake component.

The analysis is developed based on the following criteria:

- A braking condition is assumed on a straight line.
- The rider and the underbone motorcycle are modeled as a single rigid body.

Motorcycle Braking

Fig.1 shows the simple underbone motorcycle model moving on a horizontal surface. The system is assumed to be in equilibrium condition during braking. In normal underbone motorcycle application, the brake may apply singularly to the rear wheel or the front wheel. In some cases both are applied simultaneously.

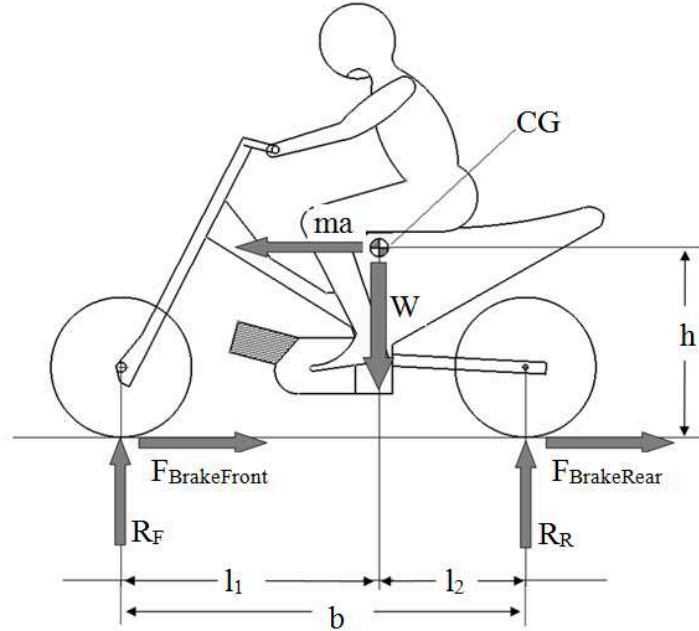


Figure 1. Forces acting on the underbone motorcycle during braking.

When the front and rear brakes are applied concurrently, higher braking force are induced compared to the single operation of front or rear brake. Based on the figure above, the equation of motion can be written as:

$$W = R_F + R_R \quad (1)$$

$$\frac{W}{g} a = \mu R_F + \mu R_R \quad (2)$$

where $F_{Brake} = \mu R$.

In ideal braking condition, the road friction coefficient is assumed to be equal to the motorcycle deceleration over gravity [7,8].

$$\mu = \frac{a}{g} \quad (3)$$

By taking the wheel-ground contact point (for front and rear wheel) as a pivot point, the moment equilibrium is calculated. Hence, the reaction forces acting on front and rear wheel can be written as:

$$R_R = \frac{W}{b} \left(l_2 - \frac{a}{g} h \right) \quad (4)$$

$$R_F = \frac{W}{b} \left(l_1 + \frac{a}{g} h \right) \quad (5)$$

The resulting equation showed that the motorcycle weight has been transferred towards near the front wheel. The weight transferred can be calculated as:

$$W_{transfer} = \mu \frac{(mah)}{b} \quad (6)$$

Instead of applying this weight on rear wheel calculation, the weight now is transferred on front wheel calculation.

Hence, the total brake force of the underbone motorcycle included the force acting on the front and rear wheel as shown in Eq. 7. Each acting force (rear and front) is calculated by multiplying the reaction force with road friction coefficient as shown in Eq. 8 and Eq. 9.

$$F_{BrakeTotal} = F_{BrakeFront} + F_{BrakeRear} \quad (7)$$

$$F_{BrakeFront} = \frac{\mu W}{b} \left(l_1 + \frac{a}{g} h \right) \quad (8)$$

$$F_{BrakeRear} = \frac{\mu W}{b} \left(l_2 - \frac{a}{g} h \right) \quad (9)$$

Analysis of the Motorcycle Ideal Brake

Based on Eq. 8 and Eq. 9, the brake force distribution (acting on front and rear wheel) under the influenced of road friction coefficient is summarized in Fig. 2. In current case study, the total mass of the underbone motorcycle is assumed equal to 98 kg while the ground contact distance (measured from ground to the center of gravity) is equal to 0.48m. The wheelbase length is 1.25m. The l_1 (distance between the center of gravity to front wheel center rotation) and l_2 (the center of gravity and rear wheel center rotation) is assumed equal to 0.78m and 0.47m, respectively.

Based on preliminary analysis (Fig. 2), the results exhibited that the total brake force required for underbone motorcycle is increased linearly with its deceleration intensity. Despite of linear total brake force distribution, there is major discrepancy in the brake force component acting on the front and rear wheel. The brake force component acting on the front wheel increased almost linearly with deceleration magnitude. However, the brake force component acting on the rear wheel had decreased with the deceleration intensity. This is probably due to weight transferred phenomenon during the normal braking condition. Based on this result, one can presumed that if the deceleration is greater than 0.9g the rear wheel of the underbone motorcycle will lift up and cause the rider lose control on the motorcycle [9].

Analysis of the Concurrent Brake Application

Fig.3 presents the analysis of concurrent brake application for underbone motorcycle. The results included the ideal and brake force distributions ratios (front: rear) for underbone motorcycle. The brake force distribution ratios are presented based on the percentage of front brake force to rear brake force. The ratios include 50:50, 60:40, 70:30 and 80:20 braking distribution points.

Based on 50:50 and 60:40 curves (Fig.3), it does not intersect with the ideal braking curve. Thus, these conditions represent the unsafe range for braking condition [10]. However, 70:30 and 80:20 curves had intersect with ideal braking curve. These conditions had signified higher safety braking condition for underbone motorcycle. By comparing 70:30 and 80:20 case study, 80:20 condition is preferred due to the larger safety range [10]. Based on this result (Fig. 3), it apparently showed that in order to achieve higher safety range during braking condition, the brake force applied on the front wheel should be at least 70% higher than the rear brake force intensity. This is due to the weight transferred condition during the underbone motorcycle braking. Thus, the front brake component

posses higher influence to decelerate the motorcycle. Despite of significant front brake influenced, the rear brake application still importance for under-controlled braking condition.

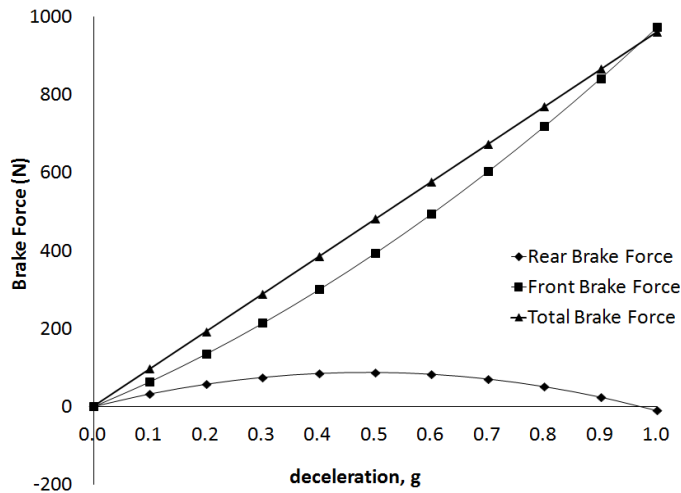


Figure 2. The ideal brake forces analysis.

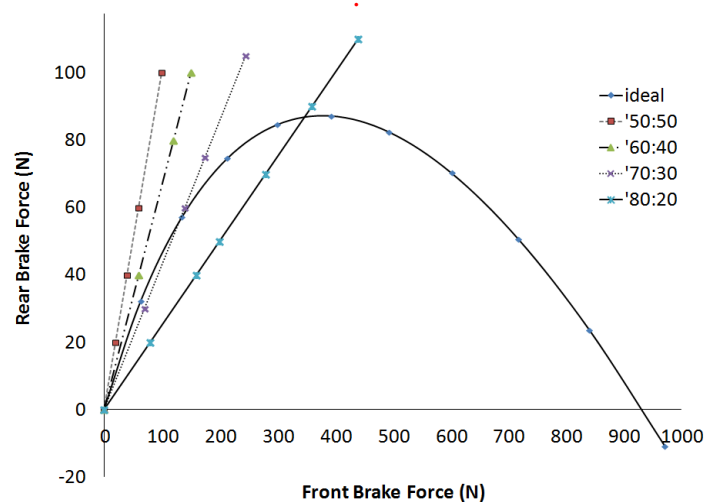


Figure 3. Concurrent brake analysis for underbone motorcycle.

Conclusion

A study on underbone motorcycle braking has been carried out in this research with the main objective to understand the basic braking performance for underbone motorcycle. A set of equation of motion was derived here by considering the road friction conditions for ideal braking condition. Preliminary results showed that the total brake force and the brake force component acting on the front wheel had increased linearly with its deceleration intensity. However, the brake force component acting on the rear wheel had decreased with the deceleration intensity. Based on these results, a theoretical study was conducted to elucidate the influenced of concurrent braking application involving the front and rear brake component. The results showed that in order to achieve higher safety range (during braking condition), the brake force applied on the front wheel should be at least 70% higher than the rear brake force intensity. This is due to the weight transferred condition during the underbone motorcycle braking. Despite of significant front brake influenced, the rear brake components is still importance for under-controlled braking condition.

Acknowledgement

The authors acknowledge financial support from the Universiti Teknologi Mara (UiTM) under UiTM's Excellent Fund to complete this research work.

References

- [1] R. Sarani, A. Roslan, N. Saniran, Statistics and Accident Characteristics Involving Motorcycles in Malaysia, 2011.
- [2] T.R. Jaafar, M.F. Mustafa, S. Kemin, R. Kasiran, Kemalangan Jalan Raya: Analisis Data Membabitkan Pengguna Motosikal, Jurnal Teknologi. 38 (2003) 1–13.
- [3] P. Seiniger, K. Schröter, J. Gail, Perspectives for motorcycle stability control systems., Accident; Analysis and Prevention. 44 (2012) 74–81. doi:10.1016/j.aap.2010.11.018.
- [4] L.A. Rashid, A.J.Alimin, M.F.M. Ali, M.F.M. Batcha, M.F. Hushim, An overview on durability study on a retrofit fuel, in: Postgraduate Seminar Universiti Tun Hussein Onn Malaysia (UTHM), 2010.
- [5] E.R. Teoh, Effectiveness of Antilock Braking Systems in Reducing Motorcycle Fatal Crash Rates, 2010.
- [6] K. Masaie, M. Takushi, T. Keishin, I. Hiroshi, H. Tatsuo, H. Wasaku, Combination of Antilock Brake System (ABS) and Combined Brake System (CBS) for Motorcycle, SAE Technical Paper 960960. (1996) 59–66. doi:10.4271/960960.
- [7] D. Lie, C.-K. Sung, Synchronous brake analysis for a bicycle, Mechanism and Machine Theory. 45 (2010) 543–554. doi:10.1016/j.mechmachtheory.2009.11.006.
- [8] Dr.N.K.Giri, Automotive Mechanics, 8th ed., Khanna Publisher, 2009.
- [9] M. Corno, S.M. Savaresi, M. Tanelli, L. Fabbri, On optimal motorcycle braking, Control Engineering Practice. 16 (2008) 644–657. doi:10.1016/j.conengprac.2007.08.001.
- [10] J.F. Han, J. Tao, H.J. Lu, D.H. Xin, Development and Prospect of Regenerative Braking Technology of Electric Vehicles, Applied Mechanics and Materials. 448-453 (2013) 3164–3171. doi:10.4028/www.scientific.net/AMM.448-453.3164.

The Three-dimensional Unsteady Numerical Analysis of the Internal Flow Field of the New Control Valve

Qu Dongyue^a, Xu Jialei^b, HuangYangyang^c and Xie Xiaozeng^d

College of Mechanical and Electrical Engineering, Harbin Engineering University, Harbin 150001, China

^aqudongyue@hrbeu.edu.cn, ^bxujialei1991@126.com, ^chuangyangyang1314@yeah.net
^dxiexiaozeng@hrbeu.edu.cn

Keywords: control valve; unsteady flow; numerical simulation; pressure fluctuation

Abstract. The medium flow of control valve is a typical complex unsteady flow, the internal flow is very unstable which leads to trim or body with vibration of different amplitude, therefore, control valve has been a failure-prone components in the turbine inlet steam system. This paper take the new valve as the research object, by computational fluid dynamics (CFD) software, the numerical simulation of the internal steam steady state flow field of valve normal work a typical opening in the process of opening is made, and obtain the internal flow field visualization distribution and flow characteristics of control valve. Extract unstable place pressure pulsation of the flow field, get the pulse frequency, and provide the basis for the design, optimization and application of low vibration noise control valve.

Introduction

As an important part of the steam turbine control system, the working reliability and stability of the control valve have a significant impact on operation efficiency, safety and economy of the entire steam turbine unit. The control valve of the steam turbine unit in service in open process will often appear the phenomenon of insufficient lifting force, at the same time with the phenomenon of vibration and noise, often occur the valve rod broken, seat uprooted and other accidents in use process. New control valve (as shown in figure 1) adopts the anticipated valve device, avoids the problem of insufficient lifting force.

The current domestic study of control valve stay in level of conventional engineering imitation and prototype performance, few numerical simulation of unsteady flow in the valve, and abroad for the vibration of the control valve adopted a negative test method to solve, not from the viewpoint of fluid dynamics to study the unstable flow control valve. The steam flow in control valve belongs to supersonic flow, so also brought difficulties for design and optimization of control valve.

In this paper, three-dimensional entity model of the new control valve is created, and extract finite element model of flow channel, and simulate the three dimensional unsteady flow in the valve, obtain the complex internal flow information of control valve, the existing the internal spiral, drafting, tremor, the boundary layer separation and other undesirable phenomenon in the design is predicted, thereby improving design technology.

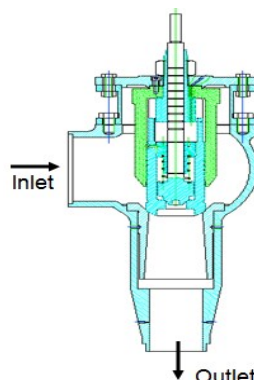


Fig.1 The new control valve structure

The Calculation Model

The control valve is a sleeve-type structure, the internal configure the pre-start valve. Studies ignore the impact of the steam flow is relatively small tiny structures to build a three-dimensional solid model and flow channel model of the control valve, and divide mesh. Figure 2, respectively, when the valve is fully open of the three-dimensional entity model, the flow model and the grid division.

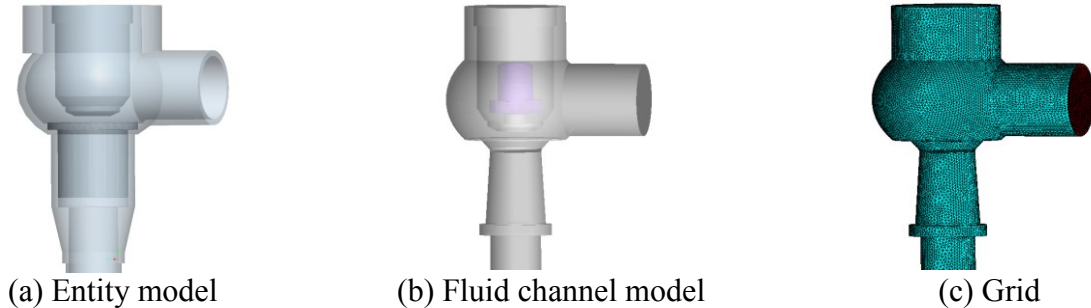


Fig. 2 The control valve related models

Computational fluid dynamics software FLUENT calculate the full three-dimensional N-S equations, turbulence model select Realizable $k - \epsilon$ model. Choice the total pressure and static export as its import and export boundary conditions in the process of numerical simulation. This paper aiming at 100% and 10% open condition of the typical flow field numerical analysis, the import total pressure is 2.9 Mpa and 2.7 Mpa, the corresponding export static pressure is 2.6 Mpa and 1.58 Mpa, namely pressure ratio is 0.9 and 0.585, respectively. The wall adopt adiabatic no-slip boundary condition, the working medium is ideal superheated steam.

The Analysis of Steady State Flow Field

The steady-state analysis of 100% opening, the discrete format of momentum, energy, turbulent kinetic energy and turbulence dissipation rate first use first-order upwind format, after calculation convergence the switch to the second-order upwind format in order to improve the computational efficiency, the results shown in figure 3-4.

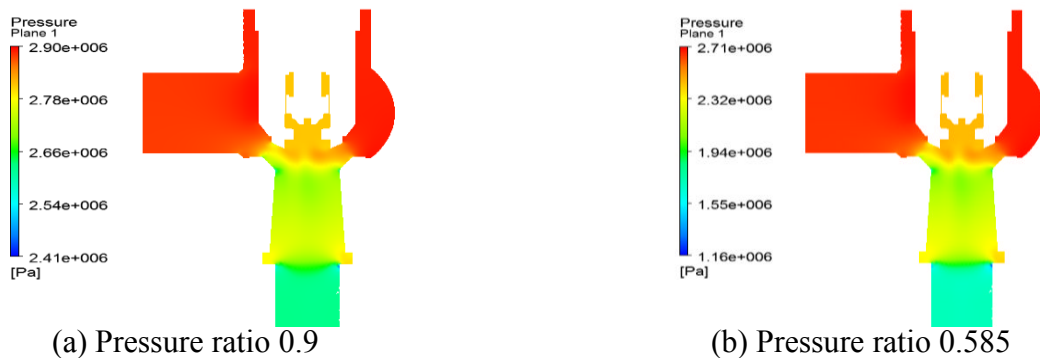


Fig. 3 Pressure field distribution of full open degree

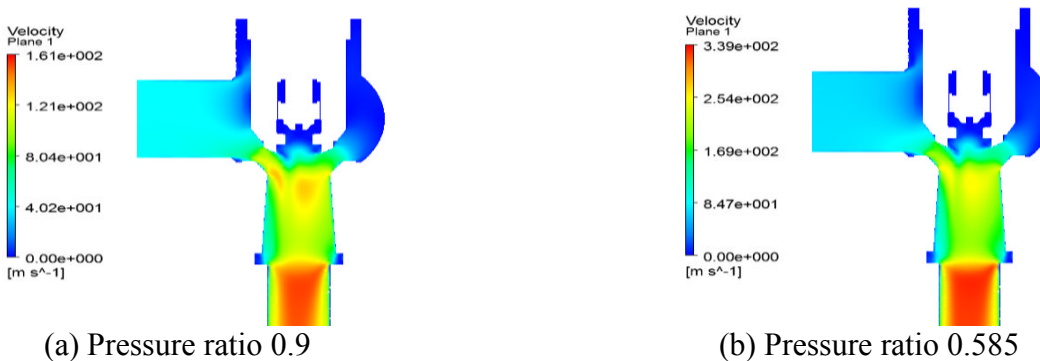


Fig. 4 Velocity field distribution of full open degree

Similarly can get the steady state flow field pressure and velocity distribution of 10% opening, respectively, as shown in figure 5 to figure 6.

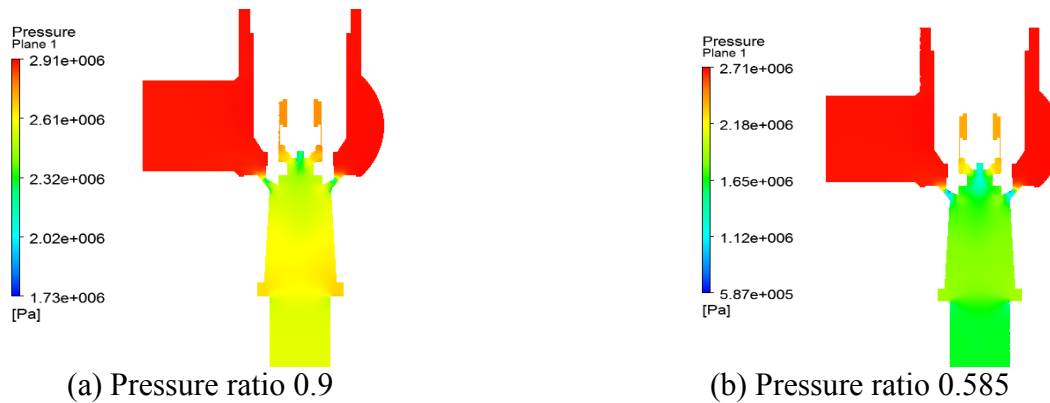


Fig. 5 Pressure field distribution of 10% opening

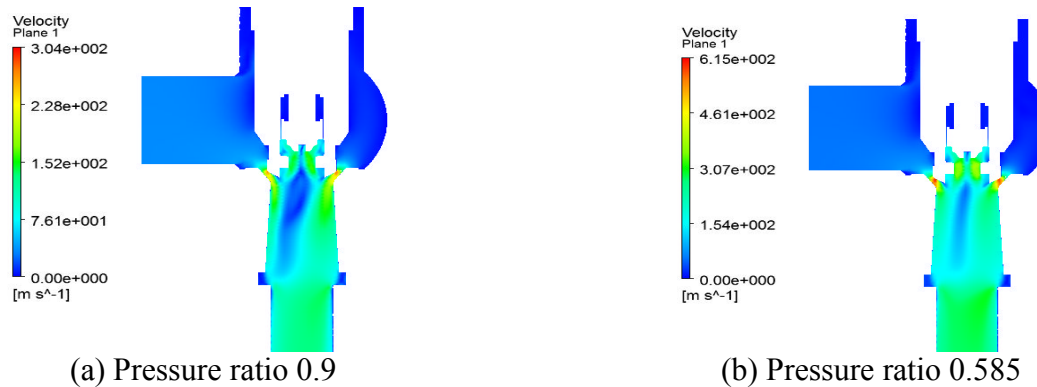


Fig. 6 Velocity field distribution of 10% opening

Calculation results show that, under different working conditions, the common of the stress field distribution is that stress decrease gradually in valve throttle, and the distribution of velocity field and pressure field are opposite, the speed of the steam is in surge after it into the throttle. Both pressure field and velocity field in throttle and diffuser are presented irregular distribution. At the same time, throttling phenomena is observed in all the valves' throats, reflect the stress of valve interior flow field changes is non-monotonicity, but it presents the change is irregular disorder, this change leads to stem parts and others the vibration of pressure pulsation.

The both sides on the center surface of the control valve forms a strong asymmetric jet. In the center of the right air flow through the throat, and then form the valve seat attached to the wall flow; And the left side of center surface of the air flow injects from the throat and form a larger area of influence, the influence of the air flow jet region continues to the exit of the airflow. On both sides of the air mix severely, and interact with each other to form the asymmetric flow hedge, which lead to form void area at the top of the hedge position and make the flow medium flow back and forth in the void area and leave the impact of valve plate and valve stem.

The Analysis of the Unsteady State Flow Field

The steady-state analysis results show that flow of the medium inside the valve has obvious turbulence characteristics, and a pressure fluctuation produce on the inner surface. When pressure pulsation frequency of the inner surface of the valve and natural frequency of the valve structure are close, it is easy to induce resonance structure of the valve. Under different working conditions, compared the different opening pressure field and velocity field distribution, when the opening is 10% and the pressure ratio is 0.585, the flow of the hedge stream medium hedge more intense, the flow of the valve disc at the bottom is more disorder. Pressure distribution is more uneven. So in the next will mainly proceed transient simulation of 10% opening under pressure ratio is 0.585. The information of flow field is shown in figure 7.

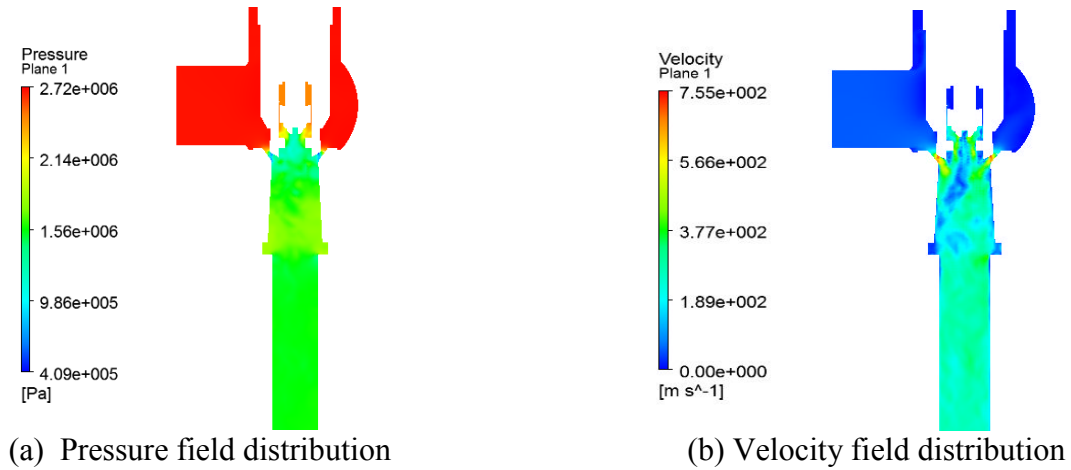


Fig. 7 Unsteady state flow field distribution

As can be seen from the figure 7, the flow field in the period of the entrance of the valve and valve chamber and the steady-state analysis results are basically identical, meanwhile the distribution are more uniform, the pressure field and velocity field distribution of unsteady state flow field brought about major changes than the calculation results of steady flow field. But after throttling segment, the distribution of pressure field is not regular distribution, but the high and low pressure area distribution are on the state of chaos, and the high and low pressure area boundary are disorder, presented the characteristics of turbulence vortex. It can be seen from the velocity profile, Vortex exists mainly in the bottom below the valve stem and valve disc. The forming reason is mainly high-speed collision of hedge jet and reflux of wall.

Through the unsteady state flow field analysis, we can capture more clearly the characteristics of the flow field distribution and vortex in the valve; at the same time, in this work we can get the pressure pulsation of unstable point, the parameters of the pressure pulsation is helpful for valve vibration analysis. This paper extracted velocity and distribution curve of the turbulence intensity from pipeline center line of the flow direction of medium and steam outlet center work as a starting point, in order to determine the most unstable points in the flow field in the valve, as shown in figure 8.

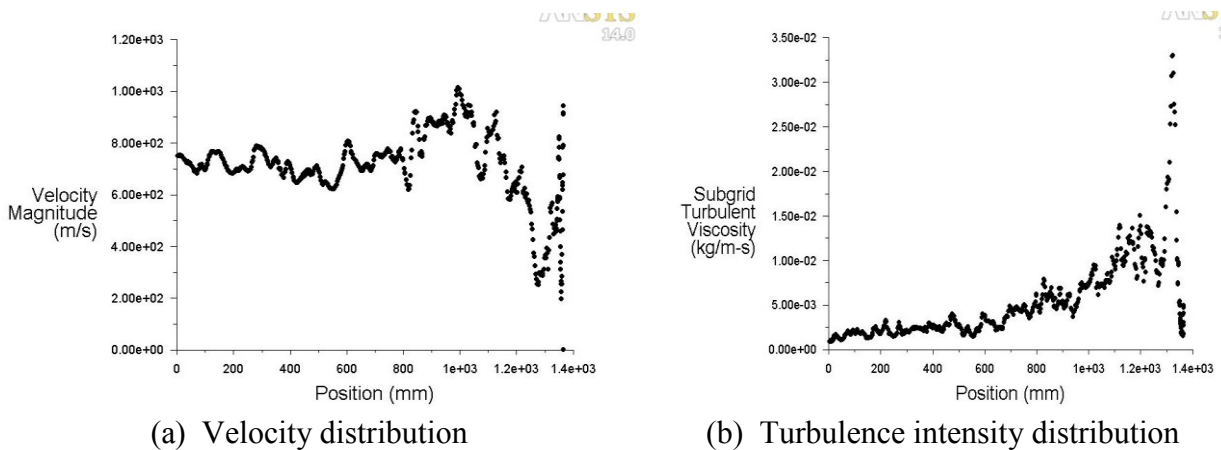


Fig. 8 Graphs of flow field distribution

It can be seen from the figure 8 that the turbulence intensity at point (1300, 0, 0) is the largest, the point on the throat jet valve hedge area, extract time-domain distribution of the pressure pulsation at this point as shown in figure 9, after Fourier transform (FFT), we can get the frequency domain distribution, as shown in figure 10.

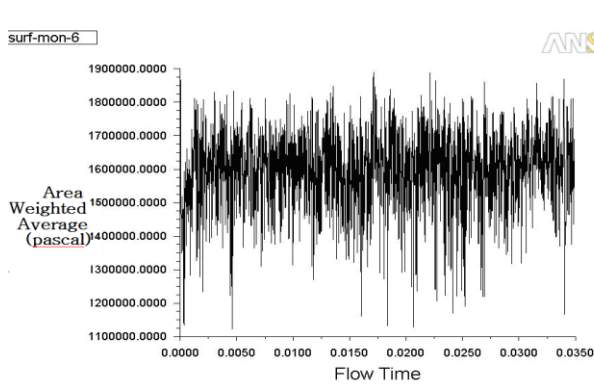


Fig.9 Time-domain distribution

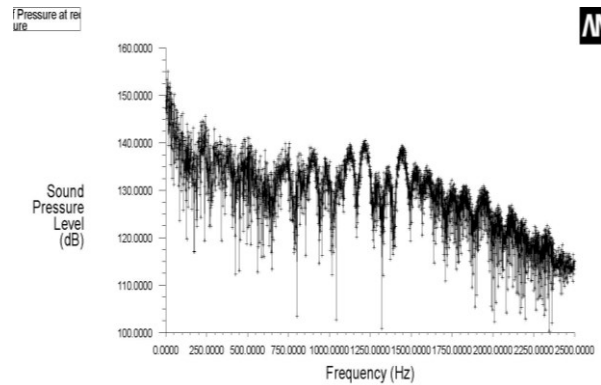


Fig.10 Frequency domain distribution

After getting the frequency distribution of fluctuating pressure, we can get the multiple frequency noise, in the design or choose the valve to avoid this frequency, in case to occur a resonant spoke.

Conclusion

This article through proceeding the three dimensional unsteady numerical simulation of the internal flow field of the new control valve, get the conclusion as follows:

(1) When the steam flows through the control valve's throat, it will appear obvious throttling phenomena, so to improve main control flow capacity, characteristics of the flow field and stability of the control valve, optimize the laryngeal lines is the key.

(2) Under the same pressure ratio, the smaller the opening, the airflow is the more unstable, the pressure pulsation is the more intense, it more easily lead to resonance vibration; Under the same opening, the pressure ratio is the smaller, the chance of vibration is the greater.

(3) The largest reason to affect steam flow stability of the valve is the existence of hedge flow, to improve the stability of the valve should to improve the steam flow lines, so that reduce hedge flow in valve as much as possible, increase flow attached to the wall.

(4) The pressure pulsation is the reason of spoke resonance, if you want to analyze the problem of noise and trims resonance, the pressure fluctuation analysis is the essential factor.

Acknowledge

This paper is supported by the Fundamental Research Funds for the Central Universities(HEUCF 140708).

References

- [1] Xiang Xiaowei, Mao Jingru, Sunbi. The design new ideas of turbine control valve[J]. Journal of Engineering for Thermal Energy and Power, 2006, 03.
- [2] Xu Kepeng, Caihu, Cui Yongqiang, Jiang Hongde. Large steam turbine experiment and numerical analysis of main steam control valve[J]. Power Engineering, 2003(06).
- [3] Joh I, Cofer IV, John K, Reinker, William J. Sumner. Advances in Steam Path Technology. GER-3713D, 1996.

Determination of Nozzle Angle for Flow Performance in Supersonic Subsea Compact Wet Gas Separator

MohdHashim F.M^{1, a*}, Ahmad M.F.A^{2, b}

^{1,2}Department of Mechanical Engineering, Universiti Teknologi PETRONAS, Bandar Seri Iskandar, 31750 Tronoh, Perak, Malaysia

^afakhruldin_mhashim@petronas.com.my, ^bahmadmohdfadzilali@yahoo.com

Keywords: Supersonic Separator, Wet Gas Separation, Nozzle

Abstract. Flow assurances in deep water pipeline have received greater attention in oil and gas industry in order to meet the optimum production of hydrocarbons. However, existence of free water in the gas pipeline decreases production output and increases operational cost and time. Alternatively, a new supersonic subsea compact wet gas separator is design to remove free water from gas transmission pipeline. The key parts of the new design separators is the nozzle. The performance of supersonic flow is highly related on the design of the nozzle. Therefore, the objective of this paper is to find correlation between the angle of the nozzle against separator flow performance, namely velocity. From the analysis done, it can be concluded that a nozzle angle of 15°, maximum velocity is achieved thus producing supersonic flow.

Introduction

The energy demand in Malaysia is increasing due to continuous development of commercial and domestic sector. The highest source of energy is from petroleum products and natural gas which contribute 54% and 24% respectively [1]. In addition, there is a requirement for efficiency improvement in transporting stranded natural gas in remote reservoir to consumer. Gas transmission pipeline is an efficient way in transporting natural gas. However, it is often related to significant traces of water which resulted in decrease efficiency.

In Malaysia, water formation is often found in the form of superheated vapor at the well. Superheated vapor occurs due to the well high temperatures of up to 200°C and high pressure of 10436.48 kPa. Superheated water vapor is influenced by the constant heat coming from the earth crust and the high pressure in the well. The problem of superheated vapor is as it reaches upstream, it began to condensate and become saturated water mixture thus producing free water. Free water exists in the magnitude of few thousand ppm level whereas gas transmission pipeline requirement is in the range of 126-168 ppm level and even lower for deep water pipeline [2].

Supersonic separators have been introduced to treat natural gas for condensing and separating water and hydrocarbon [3-6]. Supersonic separators are smaller, lighter, cheaper and with fewer emissions than conventional dehydration plants [7-9]. In addition, supersonic velocity has short residence time of gas-liquids mixture preventing hydrate problems and eliminates the need for chemical and associated regeneration systems [9-12]. Supersonic separators main part consists of swirl generator, gas throttling, separation chamber and diffuser. Several nozzle designs such as the 3-S and Twister gave different performance rates of their separators since it is dependent on the part performance and assembly of the design.

Literature Review

Separation Technology Evolution. Historically, many options have been considered in removing water from natural gas. The evolution of technologies in designing separators varies with space and weight saving as well as improving efficiency of particle removal. Fig. 1 shows the evolution of technologies for mechanical separators.

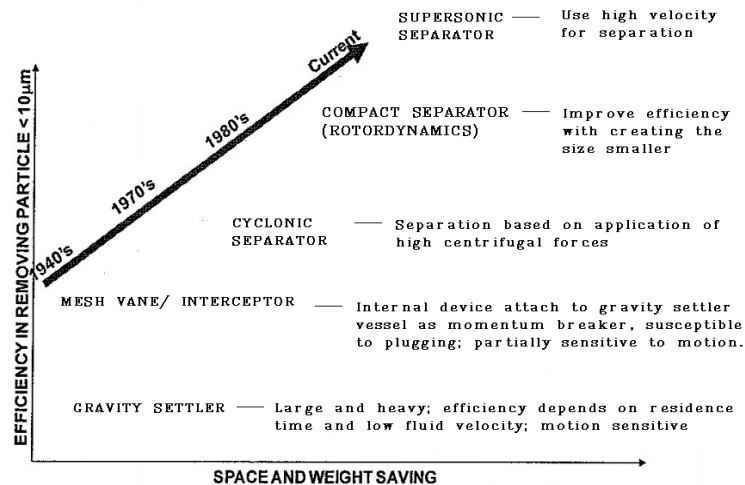


Fig. 1: Separator technology evolution [13].

Gravitational separators such as vertical separators, horizontal separators and spherical low pressure separators use gravity settling principle carried out in large vessels. The design provides sufficient residence time for the phases to separate and also provide adequate volume to contain the fluctuating liquid level. Although gravity separators are reliable and very efficient, it is a very large equipment with associated problems in terms of weight, high capital manufacturing expenditures and operating costs. Cyclonic separators have been developed to remove problem encountered in gravity settler. It has smaller size compared to gravity separator even with separation enhancement features in place [14]. The types of cyclonic separators are gas liquid compact cyclone separators (GLCC), Gasunie Cyclone, Degasser, Deliquidiser, Deoiler and Desander. The rotordynamics separators have been developed in enhancement of cyclonic separators. It has rotating element which is embedded as a part of separators. Comparison of technologies shows that the weight of rotor dynamic separators are less compared to cyclonic separators and gravitational separators [14]. The latest technology that has been developed after rotor dynamic is supersonic separators.

Previous Research Studies. There are many studies related to the flow behaviour of the separators. Anahid Karimi et. al [15] predict the behaviour of high pressure natural gas flowing through supersonic nozzles. Standard $k-\epsilon$ turbulence model is used and result with different parameters such as inlet temperature, inlet pressure and flow rate are discussed. Chuang Wen et. al [16] investigate flow using RNG $k-\epsilon$ turbulence model. The analysis successfully predicts the shock wave location according to fluids behavior. Chuang Wen et. al [17] studied the effects of swirls on natural gas flow in supersonic separators. Natural gas flow were computationally simulated with the Reynolds Stress model (RSM). Chuang Wen et. al [18] analyzed the gas dynamics parameters of natural gas flows in the supersonic separators. Simulation is conducted based on the standard $k-\epsilon$ flow model. Inlet pressures on natural gas characteristics were computationally simulated with ideal gas and Redlich-Kwong equation of states (EoS).

Methodology

Fig.2 shows the research methodology flowchart. The methodology is based on simulation whereby some of the constraint such manufacturing capabilities is applied during the built geometry process. One of the examples of manufacturing constraint is the channel. It is set at 2mm due to known limitation of milling capabilities. The channel is located in between of the throat and the external wall supersonic subsea compact wet gas separator. The process is run for eight times where the angle is varied from 5° to 75° . The converging and diverging section is varied with the same angle. The geometry was developed using program controlled proximity and curvatures and 3402896 elements were generated with orthogonal quality of 0.87 (which is in the good range of

quality). The inlet pressure is taken at 5000kPa with the inlet temperature of 300K. The variation of angle helps to identify what is the optimum design angle to achieve supersonic conditions.

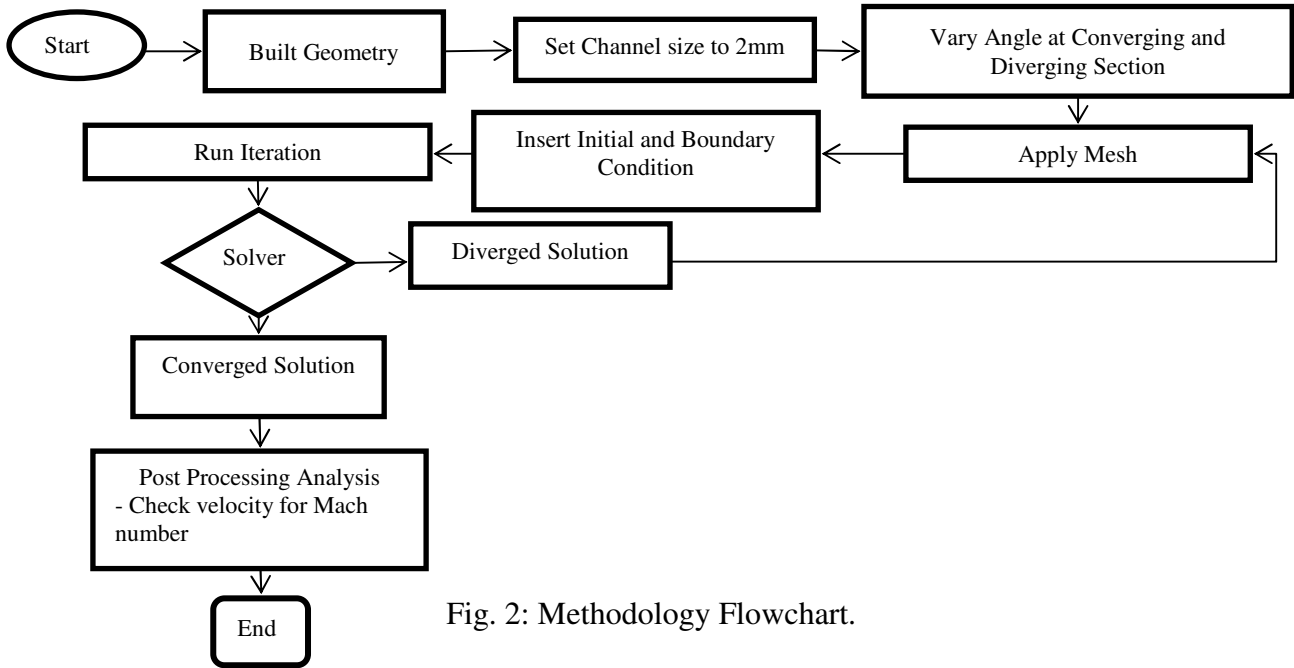


Fig. 2: Methodology Flowchart.

Geometric Model Development. Fig.3 shows the geometrical model of the supersonic subsea compact wet gas separators that have been designed at UniversitiTeknologi PETRONAS Gas Separation Research Center (UTP GSRC). The design was developed using CATIA and analysed using ANSYS v.14. The middle section of the separators is the location of the nozzle. Fig. 4 shows the nozzle profiles. The nozzles comprised of three components which are converging section, throat and diverging section. In this design, the channel (location between the throat and the wall) is kept to minimum in achieving highest flows. The diverging section is where the velocity is the highest.

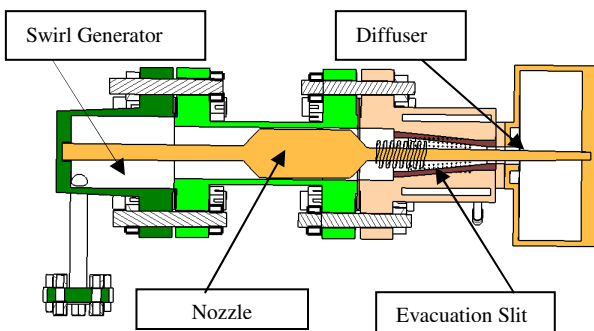


Fig. 3: Geometrical Model.

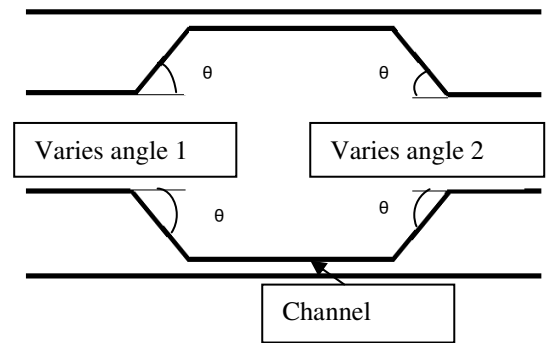


Fig. 4 Nozzle Profile.

Results and Discussion

Fig.5 shows the CFD model with the velocity streamline. From the figure, the increase of velocity started at the middle where the location of angle 1 (shown in green color). It also shows that at the angle 2 (shown in red color) is where the maximum velocity occurs thus producing supersonic flow. Supersonic flow occurs when the velocities exceed the speed of light. Fig. 6 and Table 1 shows the results of the velocities for various angle respectively.

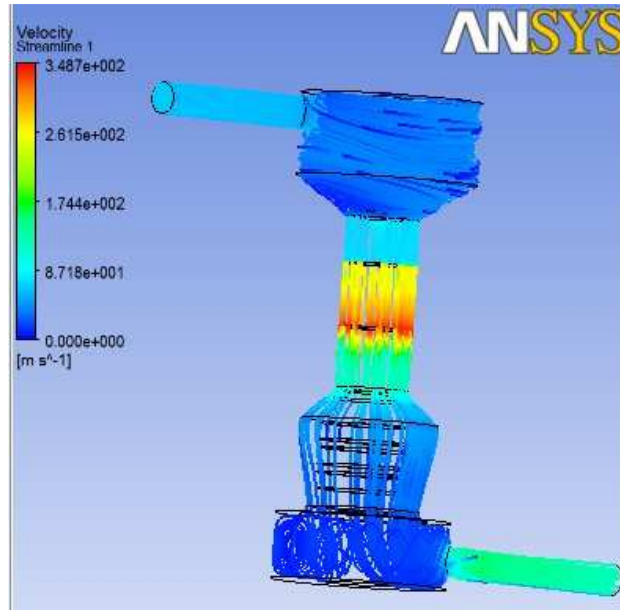


Fig. 5: CFD Velocity Streamline Model.

The results show that at an angle of 15°, the highest velocity occur which is at 348.7 m/s. The lowest velocity is at an angle of 75° which is 201.5 m/s. The angle 45° and above shows that Mach number of 1 cannot be achieved meanwhile at 35° and below shows Mach number of 1 is achievable.

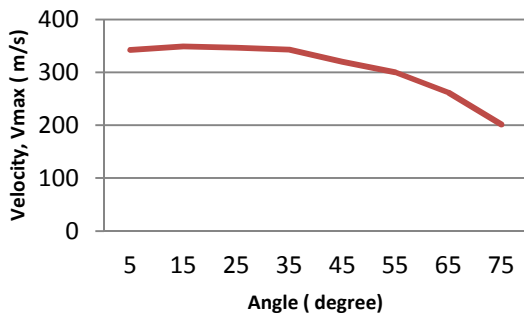


Fig. 6: Nozzle angle vs. velocity.

Table 1: Simulation results of angle vs. Velocity

Angle (Deg.)	Velocity, Vmax (m/s)	Mach Number
5	342.4	1.007058824
15	348.7	1.025588235
25	346.3	1.018529412
35	342.6	1.007647059
45	320	0.941176471
55	299.7	0.881470588
65	261.8	0.77
75	201.5	0.592647059

From the results, it can be concluded that the best angle is 15°. This is because the velocity is directly proportional with the Mach number. It also can be concluded that higher angle would not help in achieving supersonic flow. This result is important as it can give an indication the nozzle design angles in achieving supersonic flows.

Acknowledgement

This research work is funded by the Prototype Research Grant Scheme-Ministry of Higher Education Malaysia (PRGS-MOHE).

Reference

- [1] Information on <http://unitperancangekonomi.blogspot.com/2010/04/malaysias-energy-sector-in-pursuit-of.html>.
- [2] Guo Boyun and Ghalambor Ali, "Natural Gas Engineering Handbook", University of Louisiana at Lafayette: Gulf Publishing Company, vol. 1, 2005.
- [3] M. Betting, H.D. Epsom, Supersonic separator gains market acceptance, *World Oil* 254 (2007) 197-200.
- [4] M. Betting, T. Van Holten, J. Van Veen, US Patent, 6524368, February 25 (2003).
- [5] V.I. Alferov, L.A. Baguirov, V. Feygin, A. Arbatov, S. Imaev, L. Dmitriev, V.I. Rezunenko, US Patent, 6372019, April 16 (2003).
- [6] V.I. Alferov, L.A. Baguirov, L. Dmitriev, V. Feygin, S. Imaev, J.R. Lace, Supersonic nozzle efficiently separates natural gas component, *Oil Gas J.* 103 (2005) 53-58.
- [7] H. Liu, Z. Liu, Y. Feng, K. Gu, T. Yan, Characteristic of a supersonic swirling dehydration system of natural gas, *J. Chem. Eng.* 13 (2005) 9-12.
- [8] W. Jiang, Z. Liu, H. Liu, J. Zhang, X. Zhang, Y. Feng, Two dimensional simulation and analysis of the flow in supersonic separator, *J. Eng. Therm.* 29 (2008) 2119-2121.
- [9] Okimoto D, Brower J. Supersonic gas conditioning. *World Oil* 223 (2002) 89-91.
- [10] Brower J, Epsom H, Twister supersonic gas conditioning for unmanned platforms and subsea gas processing, Proceedings of the offshore Europe Conference, UK: Aberdeen 2-5 (Sept 2003) 219-25.
- [11] Jiang W, Liu H, Zhang J, Zhang X, Numerical simulation of two component mixture in one-dimension supersonic separator, *Acta Pet Sinica Pet Process* 6 (2008) 697-701.
- [12] Mokhatab S, Poe WA, Speight J.G, Handbook of Natural Gas transmission and processing. Burlington: Gulf Professional Publishing, 2006.
- [13] Nurhayati Mellon, "Hydrodynamics and Separation Performance Analysis of Horizontal, Inline, Swirl Tube Separator for Natural Gas-Water Separation for Potential Offshore Application," PhD Thesis, Universiti Teknologi Petronas, Dissertations and Theses, 2011.
- [14] C.H Rawlins, "The case for compact Separation" *Journal of Petroleum Technology*, vol. 55, no. 5, pp 77-79, May 2003.
- [15] Anahid Karimi, Majid Abedinzadegan Abdi, Selective dehydration of high-pressure natural gas using supersonic nozzles, *Chemical Engineering and Processing* 48 (2009) 560-568.
- [16] Chuang Wen, Xuewen Cao, Yan Yang, Wenlong Li, Supersonic Separators for Natural Gas Processing: Real Gas Effects, Twenty-second (2012) International Offshore and Polar Engineering Conference.
- [17] Chuang Wen, Xuewen Cao, Yan Yang, Wenlong Li, Numerical simulation of natural gas flow diffusers for supersonic separators, *Energy* 37 (2012) 195-200.
- [18] Chuang Wen, Xuewen Cao, Yan Yang, Swirling flow of natural gas in supersonic separators, *Chemical Engineering and Processing* 50 (2011) 644-649.

Identification of the Mechanical Properties of High-Strength Steel using Digital Image Correlation

Michaela Štamborská^a, Miroslav Kvíčala^b and Monika Losertová^c

Department of Non-ferrous Metals, Refining and Recycling, Faculty of Metallurgy and Materials Engineering, VŠB-Technical University of Ostrava, Czech Republic

^astamborska.michaela@gmail.com, ^bmiroslav.kvicala@vsb.cz, ^cmonika.losertova@vsb.cz

Keywords: digital image correlation, virtual fields method, notched specimens

Abstract. Identification of the mechanical properties of high-strength steel using digital image correlation. In this paper an experimental procedure to identify the plastic behaviour of sheet metals up to large strains using full field measurement is presented. The tests were conducted on notched specimens. This geometry generates a heterogeneous strain field which was measured during the test using a digital image correlation system. The advantage of using a heterogeneous strain field in the identification procedure is that a complex state of stress-strain can be analyzed at the same time and much more information can be obtained in a single test. On the other hand, the stress field cannot be directly computed from the test and a suitable identification procedure must be developed. Here, the virtual fields method (VFM) adapted for large strains and plasticity was used to identify the hardening behaviour and the anisotropy of the material. The values obtained with the VFM were compared with the results from a standard identification made using uniaxial tensile tests.

Introduction

Identification and quantification of the plastic deformation of materials is important in several respects. On the one hand, industry manufactures many components by cold forming, on the other hand, overloading of supporting structural elements often leads to plastic deformation of materials and to their violation (break). Knowing the size and distribution of plastic deformation allows better use of the properties of materials in the production of parts and in their operation. A typical example of the production of parts by plastic deformation of the material is cold forming of sheet steel. This process is most commonly used in the automotive and consumer industry (and to improve performance moldings in these fields of industry).

Usually, the identification of mechanical properties is tested by using uniaxial tensile tests. However, in recent years, thanks to developments in full-field measurement techniques, more complex specimens which generate heterogeneous stress-strain fields can be used to study the behaviour of material properties during plastic flow. Then the parameters can be identified using, for example, an inverse approach which includes FE updating [1-2].

Digital image correlation is a full-field measurement technique which allows us to evaluate spatial displacement and deformation along the surface of an object. Some of its features are: flexible area of measurement (mm^2 to m^2), applicability to different materials and geometries, and spatial visualization of the measured quantities [3-6].

This contribution deals with the use of digital image correlation in measuring the strain fields on the surface of notched specimens and use of these data to identify the mechanical properties of the material. Digital image correlation was used to evaluate the displacement and strain fields.

The next identification process is the Virtual Fields Method [7] which has been successfully applied in many applications, including elasto-plasticity [8,9] and large-strain plasticity [10,11]. The use of heterogeneous tests allows us to get a lot of information from a single test since different stress-strain conditions are evaluated at the same time. In this article, tests on a notched specimen were carried. The displacement and strain field was measured using digital image correlation. Then the virtual fields method (VFM) was used to identify the hardening behaviour. The stress fields

were calculated from the strain fields using the hardening behaviour obtained with the virtual fields method.

Materials and Methods

Geometry and material parameters of specimens. The analysis was carried out on specimens made of cold-rolled sheet metal used in the automotive and consumer industries. The geometry of the notched specimen and the dimensions in millimetres are shown in Fig. 1.

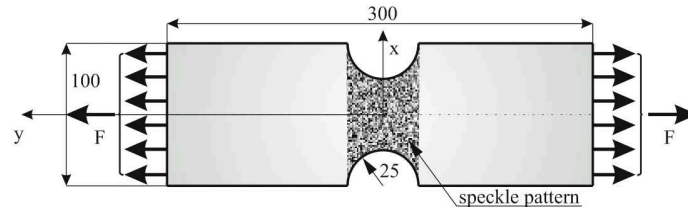


Figure 1. Geometry of specimens

Specimens were produced from hot dip galvanize steel, namely HX220PD steel. This material has high strength stress and rather atypical values of anisotropy. The mechanical properties obtained from standard tensile tests for directions 0° , 45° and 90° are listed in Table 1.

Table 1. Mechanical properties

Dir.	Thickness [mm]	$R_{p0,2}$ [MPa]	R_m [MPa]	A80 [%]	r
0°	0.9	225	387	35	1.1
45°	0.9	235	372	37.5	1.9
90°	0.9	245	388	35	1.8

Diagrams of force - displacement obtained by the tensile test on the INSTRON 880 tensile machine are shown in Fig. 2 for notched specimens.

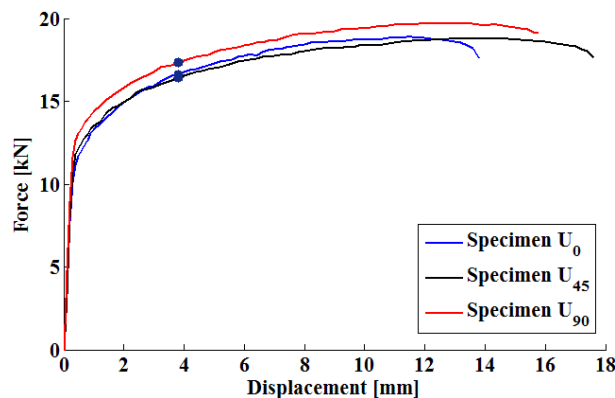


Figure 2. Diagram of force-displacement for notched specimens in all directions

Digital image correlation. The experiment was carried out using an INSTRON 880 tensile machine with hydraulic grips. Measurements were taken using a couple of JAI Pulnix TM - 4000 CL high-speed CCD cameras (fig. 3), which are able to acquire 2048×2048 pixels with 10-bit dynamic range. The displacement and strain fields were measured using VIC 3D. The results are shown for a traverse displacement of 3.2 mm.

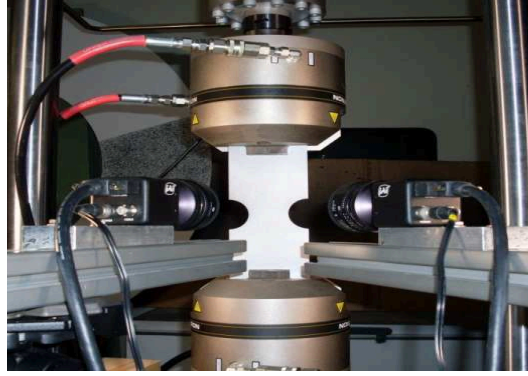


Figure 3. Experimental setup

Figure 4 shows the strain fields ε_x , ε_y , γ_{xy} [-] for a notched specimen along the rolling direction.

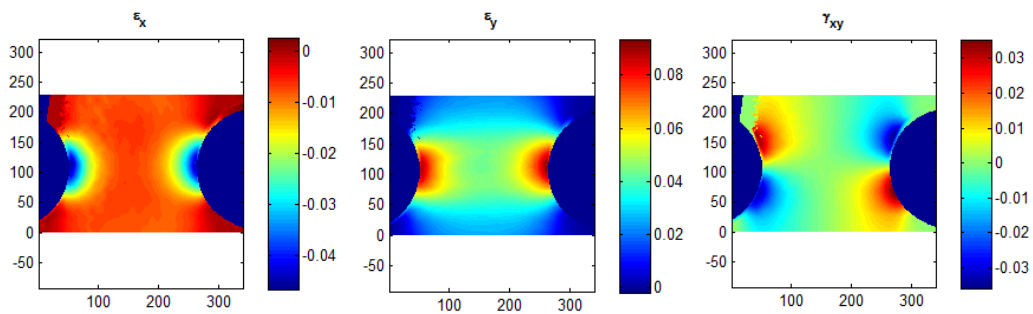


Figure 4. The strain fields ε_x , ε_y and γ_{xy} [-] obtained by Vic 3D for notched specimen along the rolling direction

Identification using VFM. The displacement fields obtained by digital image correlation were imported to Camfit, a Matlab GUI which implements the Virtual Fields Method. The program can identify the isotropic elastic constants and the hardening behaviour using different constitutive laws. In this case, the hardening is described using a Swift law, see equation 1:

$$\sigma_{eq} = K.(\varepsilon_0 + \varepsilon_{eq_{pl}})^n \quad (1)$$

where $\varepsilon_{eq_{pl}}$ is the equivalent accumulated plastic strain, and K , ε_0 , n are the parameters to be identified by Camfit [5]. The parameters obtained by Camfit are listed in Table 2.

Table 2. Identified parameters

Dir.	Elastic range		Elasto-plastic range obtained with Power law			
	Young's modulus [GPa]	Poisson's ratio [-]	X ₁ [MPa]	X ₂	X ₃	Initial yield stress [MPa]
0°	173.6	0.32	1531.7	0.084	0.779	223.2
45°	126.6	0.36	1320.6	0.080	0.683	234.9
90°	223.2	0.27	797.9	0.023	0.313	245.1

The stress fields σ_x , σ_y , τ_{xy} [MPa] obtained in the notched specimen for a traverse displacement of 3.2 mm are illustrated in Fig. 5.

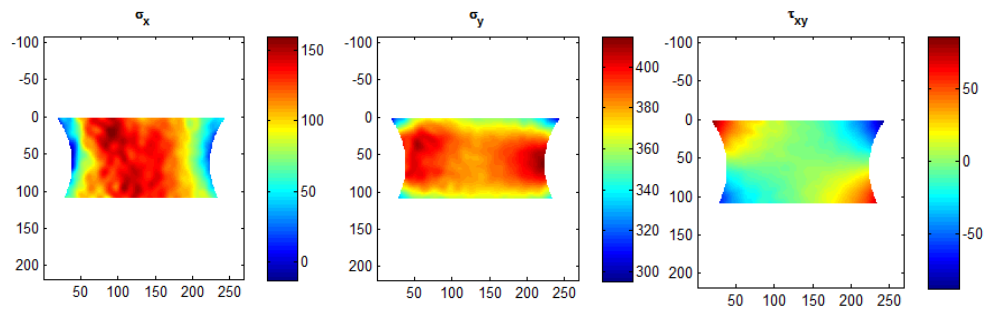


Figure 5. Stress fields σ_x , σ_y , τ_{xy} [MPa] obtained from strain fields for notched specimen

Two tensile tests were realized before the experiment and the results of the yield stress are compared with the results obtained by the virtual fields method and are listed in Table 3.

Table 3. The parameters obtained by Camfit and standard tensile test

Dir.	Strain fields [-]	Stress fields [MPa]	Camfit	Standard tensile test	
			Initial yield stress [MPa]	Test1 [MPa]	Test2 [MPa]
0	0.095	410	223.2	226	225
45	0.093	375	234.9	235	233
90	0.0965	405	245.1	245	246

Conclusion

This article deals with an identification of the mechanical properties of high strength steel using digital image correlation. DIC was used to measure the displacement and strain fields on the surface of specimens. The displacement fields were exported to the Camfit, which implements the virtual fields method, to determine the material parameters for the elastic and plastic range. It was Young's modulus and Poisson's ratio for elastic range and four hardening parameters for plastic range, which are necessary for calculation stress fields from strain fields. One of this hardening parameters was yield stress. Two tensile tests were realized before experiment and the results of yield stress are compared with results obtained by virtual fields method.

The presented results show that applying digital image correlation is a suitable measuring method to analyze plastic strain on the surface of objects and corroborates the fact that the virtual fields method is suitable for determining material properties of metal sheet specimens.

Acknowledgements

This article has been elaborated in the framework of the project Opportunity for young researchers, reg. no. CZ.1.07/2.3.00/30.0016, supported by Operational Programme Education for Competitiveness and co-financed by the European Social Fund and the state budget of the Czech Republic and in the Project No. LO1203 "Regional Materials Science and Technology Centre - Feasibility Program" funded by Ministry of Education, Youth and Sports of the Czech Republic.

References

- [1] M.A. Sutton, X. Deng, J. Liu, L. Yang, Determination of elastic-plastic stresses and strains from measured surface strain data, *Experimental Mechanics* 36 (1996) p. 99–112.
- [2] A. Butz, T. Rist, B. Springub, F. Roters, S. Schultz, Virtual Processing of Dual Phase Steels – A Microstructure Based Simulation Approach. *Proceedings of the Fourth International Conference on Multiscale Materials Modeling* (2008), p. 302-305.
- [3] F. Šimčák, M. Štamborská, R. Huňady, Analysis of Plastic Deformation of Materials by Using Digital Image Correlation, *Chemické listy* 105 (2011) p.564-567.

- [4] M. Rossi, G.B. Broggiato, S. Papalini: Application of digital image correlation to the study of planar anisotropy of sheet metals at large strains. *Mechanica* 43 (2008) p. 185–199
- [5] M. Rossi, F. Pierron, M. Štamborská, F. Šimčák, Identification of the Anisotropic Plastic Behaviour of Sheet Metals at Large Strains. *Experimental and Applied Mechanics* 4 (2013) p. 229-235,
- [6] M. Štamborská, F. Šimčák, M. Kalina, M. Schrötter, Identification of the Stress Fields from the Strain Fields in the Isotropic Materials. *Procedia Engineering* 48 (2012) p. 665-672.
- [7] F. Pierron, M. Grédiac, *The Virtual Fields Method*, Springer New-York, 2012. ISBN 978-1-4614-1823-8.
- [8] M. Grédiac F. Pierron, Applying the virtual fields method to the identification of elasto-plastic constitutive parameters. *International Journal of Plasticity* 22 (2006) p. 602-627.
- [9] M. Grédiac, F. Pierron, S. Avril, E. Toussaint, The virtual fields method for extracting constitutive parameters from full-field measurements: a review. *Strain* 42 (2006) p. 233-253.
- [10] M. Grédiac, E. Toussaint, F. Pierron, Special virtual fields for the direct determination of material parameters with the virtual fields method. Part 1. Principle and definition. *International Journal of Solids Structures* 39 (2002) p. 2691-2705.
- [11] M. Rossi, F. Pierron, Identification of plastic constitutive parameters at large deformations from three dimensional displacement fields, *Computational Mechanics* 49 (2012) p. 53-71.

Comparison of the Stress-Strain Behaviour of Cast TiAl6V4, Porous TiAl6V4 and Cortical Bone during the Mechanical Load Caused by Common Daily Activities

Miroslav Kvíčala^a, Michaela Štamborská^b, Jaromír Drápala^c

Department of Non-ferrous Metals, Refining and Recycling, VŠB-Technical University of Ostrava,
17. Listopadu 15, Poruba, 708 33 Ostrava Czech Republic

^amiroslav.kvicala@vsb.cz, ^bstamborska.michaela@gmail.com, ^cjaromir.drapala@vsb.cz

Keywords: Biocompatibility, FEM, porosity, TiAl6V4, von Mises stress

Abstract. This paper deals with FEM analysis of six models that represents human cortical bone, cast TiAl6V4 alloy and porous TiAl6V4 with different pore diameters. Reliable data for the simulations were achieved by meta-analysis that consisted from 53 scientific works. Strain value was chosen with a respect to the frequent daily activities such as walking. According to the FEM analysis of presented models von Mises stress values and stress concentration factors were similar for human cortical bone and porous TiAl6V4.

Introduction

The most frequently used biocompatible materials are stainless steel, pure titanium [1,2] and titanium alloys, such as TiAl6V4 [2,3,4,5]. Titanium and its alloys are commonly used in traumatology because of its good biocompatibility [6], favourable osteointegration [7,8], excellent mechanical properties and corrosion resistance [9]. However, cast titanium elastic modulus is approximately 100 GPa and frequently used titanium alloy Ti6Al4V is about 115 GPa [7]. Human bones mechanical properties depend on gender, age and health status [10]. The difference between human bones and titanium implants elastic modulus causes so called shielding effect, that may result in the necessity of reoperation [11,12,13]. Porous biocompatible materials are often prepared by powder sintering with pore forming additive. The other perspective method for preparation of the highly porous materials are slip freeze [14], reverse casting [15,16], and/or metal injection molding [17]. Many papers related to the porous biocompatible materials mechanical properties were published in the past. However, results obtained by the authors are very heterogeneous. It is mainly caused by the fact that mechanical properties of the porous titanium and/or titanium alloys are strongly affected by many variables such as compacting pressure [18], powder size and morphology [16,19], pore forming additive [4,15], sintering time and temperature [1,2], porosity [20], pores' shape [16], pores' size distribution and possible pores' interconnections [16,21].

Materials and Methods

Experimental data (mechanical properties of the TiAl6V4 bulk material, porous TiAl6V4 and cortical bone) used in our paper were obtained by meta-analysis of the 53 scientific works published in the journals with an impact factor. All data were analysed using statistical software Minitab 15. Cortical bone models and porous TiAl6V4 models were prepared by Digimat software. FEM calculations were performed by Abaqus software.

Due to the fact that human cortical bone is more sensitive to the failure caused by tensile load than to the load caused by compression, our simulations are focused on tensile stress behaviour of the human cortical bone, cast TiAl6V4 as a commonly used biocompatible material and on a porous TiAl6V4 as a perspective biocompatible material.

Following variables were used in our FEM simulations: ultimate tensile strength, yield strength, porosity, elongation, Young's modulus and Poisson constant. TiAl6V4 with porosity 50 % was chosen because its mechanical properties are similar to those of the cortical bones. Moreover, 50%

porosity can be achieved without problems with pores distribution heterogeneity. FEM simulations were realized for spherical pores with diameter within 200 – 400 μm . These pores' sizes are frequently recommended because of good osteointegration [1,22]. Tetragonal elements with global size 0.05 were used. The studied variables (by means of FEM analysis) were maximal von Mises stress, average von Mises stress and stress concentration factor.

Results and Discussion

Scientific data meta-analysis allowed to define reliable values of the variables that are necessary for FEM simulations of stress distributions for cortical bone, cast TiAl6V4 and porous TiAl6V4, see Tab. 1

Tab. 1 Meta-analysis results for TiAl6V4 and cortical bone; P – porosity, Δl – elongation, UTS – ultimate tensile strength, YS – yield strength, E – elastic modulus, CS – compressive strength ν – Poisson constant, ρ – density.

Material	P (%)	Δl (%)	UTS (MPa)	YS (MPa)	E (GPa)	ν	CS (MPa)	ρ ($\text{kg}\cdot\text{m}^{-3}$)
TiAl6V4	0	12 \pm 0.5	1150 \pm 65	1030 \pm 38	115 \pm 1	0.34 \pm 0.1	1170 \pm 108	4420
TiAl6V4	50	3 \pm 0.4	286 \pm 52	185 \pm 41	26 \pm 2	0.34 \pm 0.1	350 \pm 48	2210
Cortical bone	10 \pm 4	1.7 \pm 0.2	140 \pm 18	130 \pm 15	22 \pm 4	0.4 \pm 0.1	205 \pm 32	3200

First model consisted of cortical bone. The second model represents porous TiAl6V4 and the third model shows cast TiAl6V4 alloy that is commonly used in biomedical applications. Tensile loads were applied on all three models. Tensile strain was fixed to $\epsilon = 2 \cdot 10^{-4}$, this value corresponds to the deformation during common daily activities such as walking [23]. Stress distribution obtained for cortical bone is shown on Fig. 1

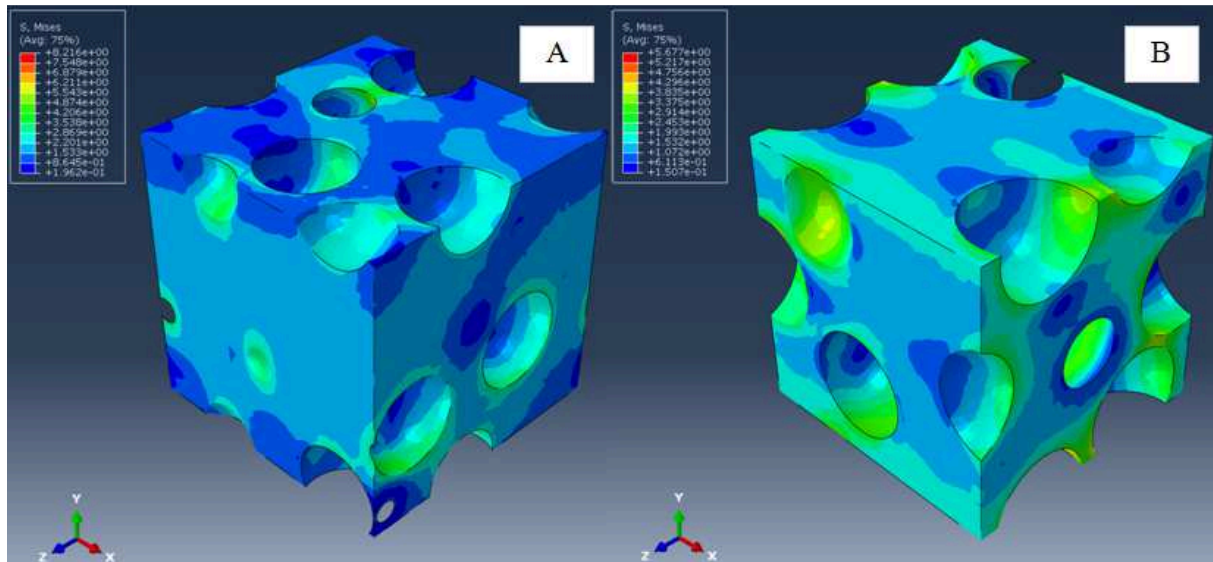


Fig. 1 FEM simulation of the von Mises stress in cortical bone ($\epsilon=2 \cdot 10^{-4}$) with uniform pore size; A – $d=200 \mu\text{m}$, B – $400 \mu\text{m}$.

Simulations revealed that strain value typical for common daily activities such as walking led to low values of the maximal and average von Mises stress for cortical bone with pores with diameter 400 μm than for those with diameter 200 μm . Both maximal values are much lower than typical yield stress of the cortical bones ($\sigma_{YS} = 130 \text{ MPa}$). Spherical pores represented stress concentrators, remaining parts of the cortical bone tissue were almost uniform.

The same strain value applied on TiAl6V4 alloy with 50% porosity exhibited slightly higher values of the von Mises stress in comparison with cortical bone. The differences between both models were marginal (maximal von Mises stress, average von Mises stress and stress concentration factor). The most significant difference among cortical bone models and porous TiAl6V4 models was that in case of low porous cortical bone, maximal von Mises stress was localized inside the pores, meanwhile, highly porous TiAl6V4 exhibited stress concentrators are not only inside the pores but also between them (when pores were close each other), see Fig. 2

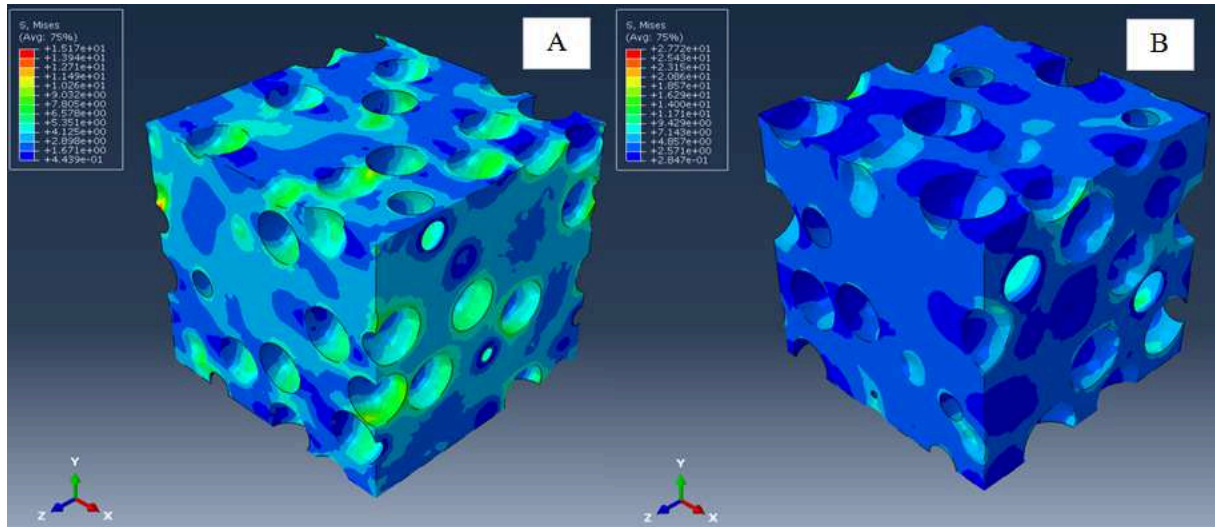


Fig. 2 FEM simulation of the von Mises stress in porous (50%) TiAl6V4 ($\epsilon=2 \cdot 10^{-4}$) with uniform pore size; A – $d=200 \mu\text{m}$, B – $400 \mu\text{m}$.

Simulation focused on cast TiAl6V4 (bulk material) revealed uniform value of the von Mises stress 20.5 MPa, see Fig. 3

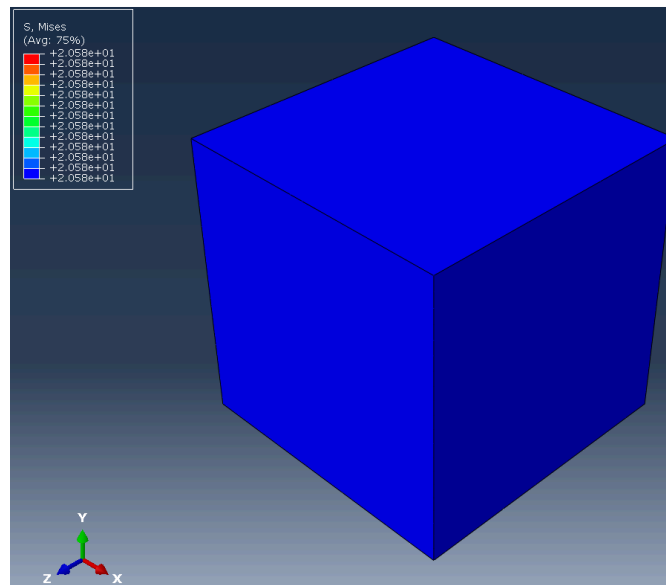


Fig. 3 FEM simulation of the von Mises stress in cast TiAl6V4 alloy ($\epsilon=2 \cdot 10^{-4}$).

Although, even maximal values of the von Mises stress were significantly lower in case of the porous TiAl6V4 than in case of the TiAl6V4 bulk material, the most important factor is the comparison of average values of the von Mises stress, see Tab.2

Tab. 2 Analysed variables summary of the cortical bone, cast a porous TiAl6V4 alloy. σ_{max} - maximal von Mises stress, $\bar{\sigma}$ - average von Mises stress, K – stress concentration factor.

Material	Porosity (%)	σ_{max} (MPa)	$\bar{\sigma}$ (MPa)	K	Pore diameter (μm)
Cortical bone	10	4.8	2.5	1.9	200
Cortical bone	10	4.3	1.9	2.3	400
TiAl6V4	0	20.5	20.5	1	0
TiAl6V4	50	10	4.1	2.4	200
TiAl6V4	50	11	4.5	2.4	400

Although, all values of the von Mises stress mentioned in this study are lower than cortical bone yield stress, porous TiAl6V4 mechanical properties are superior to the cast TiAl6V4. Porous TiAl6V4 alloy represents perspective trend in development of new implants for traumatology due to their beneficial mechanical properties that are close to human cortical bones. Moreover, highly porous TiAl6V4 alloy exhibits excellent osteointegration parameters.

Conclusions

Meta-analysis of the 53 scientific papers published in journals with impact factor revealed mechanical properties of cortical bone and TiAl6V4 alloy (bulk and porous material) that is commonly used as biocompatible material for production of implants used in traumatology. Six models represented cortical bones, cast TiAl6V4 and porous TiAl6V4 with different pores' diameter were tested by FEM analysis with respect to the strains that occur during normal daily activities such as walking. According to the simulations results, TiAl6V4 with 50% porosity is perspective biocompatible material with mechanical properties very similar to those of human cortical bones.

Acknowledgements

This paper has been elaborated in the framework of the project Opportunity for young researchers, reg. no. CZ.1.07/ 2.3.00/30.0016, supported by Operational Programme Education for Competitiveness and cofinanced by the European Social Fund and the state budget of the Czech Republic. This paper has been also elaborated in the framework of the project IT4Innovations Centre of Excellence project, reg. no. CZ.1.05/1.1.00/02.0070, by the Grant Agency of the Czech Republic (P205/11/2137) and by the grant reg.no. SP 2013/51.

This paper was created in the Project No. LO1203 "Regional Materials Science and Technology Centre - Feasibility Program" funded by Ministry of Education, Youth and Sports of the Czech Republic.

References

- [1] A. Barbas, A.S. Bonnet, P. Lipinski, R. Pesci, G. Dubois, Development and mechanical characterization of porous titanium bone substitutes. *Journal of the Mechanical Behavior of Medical Materials* 9 (2012) 34 – 44.
- [2] Z. Esen, E.T. Bor, S. Bor, Characterization of loose powder sintered porous titanium and Ti6Al4V alloy. *Turkish Journal of Engineering Environmental Science* 33 (2009) 207 – 219.
- [3] I. Watanabe, M. McBride, P. Newton, K.S. Kurtz, Laser surface treatment to improve mechanical properties of cast titanium. *Dental Materials* 25 (2009) 629–633.
- [4] J. Parthasarathy, B. Starly, S. Raman, A. Christensen, Mechanical evaluation of porous titanium (Ti6Al4V) structures with electron beam melting (EBM). *Journal of the Mechanical Behavior of Biomedical Materials* 3 (2010) 249 – 259.
- [5] X.Y. Cheng, S.J. Li, L.E. Murr, Z.B. Zhang, Y.L. Hao, R. Yang, F. Medina, R.B Wicker, Compression deformation behavior of Ti–6Al–4V alloy with cellular structures fabricated by electron beam melting. *Journal of the Mechanical Behavior of Biomedical Materials* 16 (2012) 153 – 162.
- [6] M. Niinomi, Fatigue performance and cyto-toxicity of low rigidity titanium alloy, Ti 29Nb 13Ta–4.6Zr. *Biomaterials* 24 (2003) 2673–2683.

- [7] T.,J. Webster, C. Ergun, R.H. Doremus, Enhanced functions of osteoblasts on nanophase ceramics, *Biomaterials* 21 (17) (2000) 1803–1810.
- [8] F. Rupp, L. Scheideler, D. Rehbein, D. Axmann, Geis-Gerstorfer, *Journal of Biomaterials* 25 (2004) 1429–1438.
- [9] S. Bauer, P. Schmuki, K. Mark, J. Park, Engineering biocompatible implant surfaces Part I: Materials and surfaces. *Progress in Materials Science* 58 (2013) 261–326.
- [10] T. Traini, C. Mangano, R.L. Sammons, F. Mangano, A. Macchi, A. Piattelli, Direct laser metal sintering as a new approach to fabrication of an isoelastic functionally graded material for manufacture of porous titanium dental implants. *Dental Materials* 24 (2008)1525–33.
- [11] J. Gallo, J. Losták, K. Langová, Long-term survival of the uncemented Balgrist cup. *International Orthopaedics*, 37(8): 1449-1456, 2013.
- [12] J. Gallo, S.B. Goodman, Y. Konttinen, M. Wimmer, M. Holinka, Osteolysis around total knee arthroplasty. A review of pathogenetic mechanisms. *Acta Biomaterialia* 9 (2013) 8046-8058.
- [13] C. Nich, Y. Takakubo, J. Pajarinen, M. Ainola, A. Salem, T. Sillat, A. Rao, M. Raška, Y. Tamaki, M. Takagi, Y. Konttinen, S.B. Goodman, J. Gallo, Macrophages – Key cells in the response to wear debris from joint replacements. *Journal of Biomedical Materials Research. Part A*, 101 (2013) 3033-3045.
- [14] Q. Xu, B. Gabbitas, S. Matthews, Influence of porosity on mechanical behaviour and gas permeability of Ti compacts prepared by slip casting. *Materials Science & Engineering A* 587 (2013) 123–131.
- [15] H.D. Jung, S.W. Yook, T.S. Jang, Y. Li, H.E. Kim, Y.H. Koh, Dynamic freeze casting for the production of porous titanium (Ti) scaffolds. *Materials Science and Engineering C* 33 (2013) 59–63.
- [16] S.W. Yook, H.D. Jung, C.H. Park, K.H. Shin, Y.H. Koh, Y. Estrin, H.E. Kim, Reverse freeze casting: A new method for fabricating highly porous titanium scaffolds with aligned large pores. *Acta Biomaterialia* 8 (2012) 2401–2410.
- [17] L.J. Chen, T. Li, Y.M. Li, H. He, Y.H. Hu, Porous titanium implants fabricated by metal injection molding. *Transactions of Nonferrous Metallurgical Society China* 19 (2009) 1174 – 1179.
- [18] Y. Torres, J.J. Pavón , I. Nieto, J.A. Rodríguez, Conventional Powder Metallurgy Process and Characterization of Porous Titanium for Biomedical Applications. *Metallurgical and Materials Transactions B* 42 (2011) 891 – 900.
- [19] I.H. Oh, H. Segawa, N. Nomura, S. Hanada, Microstructures and Mechanical Properties of Porosity-Graded Pure Titanium Compacts. *Materials Transactions* 44 (2003) 657 – 660.
- [20] B. Lee, T. Lee, Y. Lee, D.J. Lee, J. Jeong, J. Yuh, S.H. Oh, H.S. Kim, C.S. Lee, Space-holder effect on designing pore structure and determining mechanical properties in porous titanium. *Materials and Design* 57 (2014) 712–718.
- [21] A.M. Hodge, J. Biener, J.R. Hayes, P.M. Bythrow, C.A. Volkert, A.V. Hamza, Scaling equation for yield strength of nanoporous open-cell foams. *Acta Materialia* 55 (2007) 1343–1349.
- [22] Karageorgiou V, Kaplan D. Porosity of 3D biomaterial scaffolds and osteogenesis [J]. *Biomaterials*, 26 (2005) 5474–5491.
- [23] J. Minister, Modeling of viscoelastic deformation of cortical bone tissue. *Acta of Bioengineering and Biomechanics* 5 (2003) 11 – 21.

Development of Splice Connections for Precast Concrete Structures

Ahmad Baharuddin Abd Rahman^{1,,a}, Jen Hua Ling^{2,b}, Zuhairi Abd Hamid^{3,c},
Mohd Hanim Osman^{1,d}, Shahrin Mohammad^{1,e} and A Aziz Saim^{1,f}

¹Faculty of Civil Engineering, Universiti Teknologi Malaysia, 81310 Skudai, Johor, Malaysia

²School of Engineering and Technology, University College of Technology Sarawak,
96000 Sibul, Sarawak, Malaysia

³Construction Research Institute of Malaysia (CREAM), Jalan Chan Sow Lin, Malaysia

^{1,a}baharfka@utm.my

Keywords: splice sleeve, anchorage bond, grouted sleeve, precast concrete connection

Abstract. This paper presents the test results of proposed grouted sleeve connections under increasing tensile load. The objective of this research was to investigate splice connections that could provide tensile strength similar to the full tensile strength of the connected rebars. The parameters varied were splice types, splice length and rebar embedment length. The performance of the splice connection was evaluated based on the load-displacement, ultimate load, displacements and failure modes. The results show that the strength of splice connection depends on the bond strength between sleeve-to-grout and grout-to-rebar; the tensile strength of spliced steel bars and also the tensile strength of sleeve. It is observed that when the grout compressive strength is more than 60N/mm^2 and bar embedded length is at least 10 bar diameter, the splice connection in BS series is able to provide full tensile strength of the connected rebars.

Introduction

A grout-filled splice sleeve connection is a specially designed cylindrical coupler that utilizes non-shrinkage grout as bonding material to splice reinforcement bars and to ensure continuity of load transfer [1] [2] [3]. In order to splice the reinforcement bars, two steel bars are inserted into the sleeve connection from both ends to meet at mid length before high early-strength grout is injected or poured into the sleeve. A splice sleeve connection can be used to join precast concrete wall-to-wall or column-to-column.

The structural performance of the splice sleeve connection is essential in joining loose precast concrete components, by ensuring integrity and continuity of the precast components [4] [5]. Ideally, the connection should not be the weakest point that will affect the performance of the global structural system. Furthermore, the splice sleeve connection that acts as a connection system to join discontinuous steel bars should not fail prior to failures of other structural components [6]. To investigate the adequacy of the splice connection, an experimental tensile test should be carried out.

This paper presents the tensile test results of proposed splice sleeve connections. The performance was evaluated based on their load-displacement curves, ultimate tensile capacities and the corresponding displacements at ultimate states.

Experimental Programs

In this study, the tensile test results of nine specimens were investigated from three different series of splice sleeve connection, namely CS-Series, OS-Series and BS-Series. Their tensile performance and failure modes were studied in order to acquire the factors that govern the tensile strength of a splice sleeve connection. Fig. 1(a) shows the details and dimensions of the test specimens and Fig 1(b) shows the preparation of making the splice connections. High strength Y16 steel bars were spliced using the proposed splice sleeve connections by using non-shrinkage *Sika Grout-215* as the bonding material. The anchorage length of all reinforcement bars embedded in the sleeve was less than 150 mm. Subsequently, the sleeve length for all specimens was limited to 300 mm length.

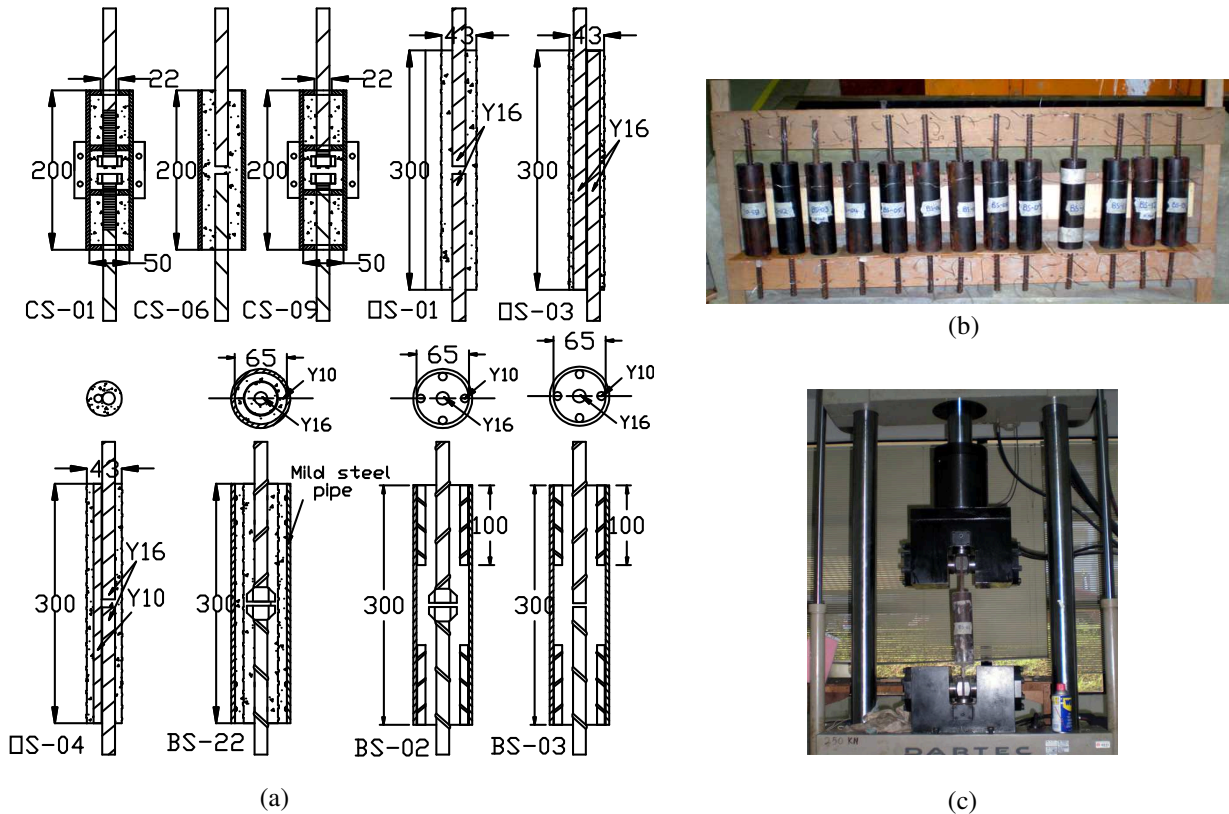


Fig. 1 (a) Details of tested specimens (b) Preparation of specimens (c) Tensile test of specimen

The sleeves of the proposed splice connection were made from mild steel pipes for specimens CS-01, CS-06, CS-09, BS-02, BS-03 and BS-22; and corrugated aluminium sleeve for specimens OS-01, OS-03 and OS-04. The size, thickness and length of the sleeve were varied as shown in Fig. 1(a). Specimen CS-01 was tested to join threaded steel bars, whereas CS-06 and CS-09 were tested to join deformed steel bars. For specimens CS-01 and CS-09, additional middle steel plates were included to act as the interlocking mechanism to resist the nut-headed steel bars from slipping out of the sleeve. Meanwhile, no modification was made to the CS-06 sleeve connection.

Specimens OS-series were made from corrugated aluminium sleeve. The OS-01 had its reinforcement bars spliced at end-to-end position, while the OS-03 had its reinforcement bars lapped adjacently throughout the length of the sleeve connection. As for OS-04, the Y16 reinforcement bars were discontinued at mid-length but were spliced with a Y10 high strength steel bar to bridge the discontinuity.

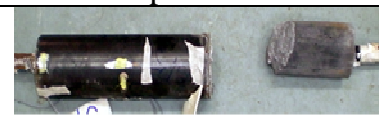
BS-series were developed as an improvement to the OS-series. Mild steel pipes that performed better under direct tensile load were used as the sleeve to overcome the problem of sleeve fracture as seen in OS-series. Specimen BS-22 utilized two sleeves, i.e. mild steel pipe to envelop the OS-01, and eventually to enhance the tensile resistance of the corrugated aluminium sleeve. Meanwhile, BS-02 and BS-03 eliminate the use of corrugated aluminium sleeves by replacing them with mild steel pipe. Then, Y10 steel bars were welded onto the inside wall of mild steel pipe to act as interlocking mechanism between with the grout and splice reinforcement bars.

When the grout hardened and achieved the design strength of 40 N/mm^2 at seven days, all the specimens were tested under increasing tensile load until failure (Fig.1(c)) at the rate of 0.5 kN/s .

Performance of Proposed Specimens

Table 1. Tensile capacities and failure modes of the specimens

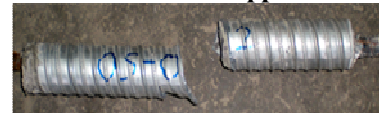
Specimen	Grout f_{cu} (N/mm ²)	P (kN)	ΔL (mm)	Failure modes
Control specimen (Y16 bar)		140.6	57.5	Bar fractured
CS-01	43.32	87.0	8.7	Bar slipped
CS-06	43.32	40.9	1.0	Grout slipped
CS-09	43.32	101.8	5.6	Bar slipped
OS-01	58.1	11.9	2.7	Sleeve fractured
OS-03	58.1	135.6	35.5	Bar slipped
OS-04	58.1	47.5	18.2	Sleeve fractured
BS-02	62.97	119.2	22.4	Bar fractured
BS-03	62.97	141.2	31.0	Bar fractured
BS-22	62.97	123.0	20.9	Bar fractured



CS-06 Grout slipped



OS-03 Bar slipped



OS-04 Sleeve fractured



BS-03 Bar fractured

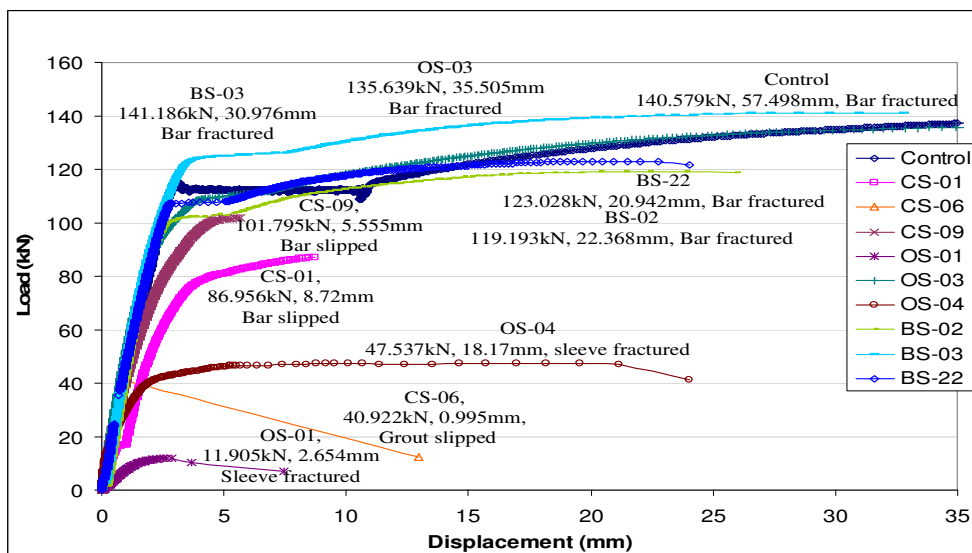


Fig. 2 Response of load versus displacement of splice reinforcement bar

Table 1 shows the connection performance, in terms of grout compressive strength, f_{cu} , ultimate tensile capacity, P (kN), displacement at ultimate state, ΔL (mm), and failure modes. Fig. 2 shows the load-displacement response of all specimens. The proposed specimens were also compared with the control specimen, a Y16 high strength steel bar in order to determine the adequacy of the splice connections. The test results showed that the ultimate tensile capacity of Y16 steel bar was 140.6 kN and the corresponding displacement of 57.5 mm. Hence, a splice sleeve connection can be considered satisfactory when (a) the connection endured up to at least 140.6 kN tensile load, or (b) their spliced steel bars fractured outside the sleeve connection.

The results showed that the tensile strength of the specimens ranged from 119 kN to 141.2 kN, where OS-01 gave the lowest tensile resistance and BS-03 offered the highest. Based on the results, OS-03, BS-02, BS-03 and BS-22 gave satisfactory results as their load-displacement responses were comparable to the control specimen. This is shown by the higher stiffness at initial state as seen from the steep slope of the graph, followed by yielding of steel bars as seen on the drastic decrease of the slope of the load-displacement graph. Eventually the spliced steel bars fractured without any anchorage bond failures. Meanwhile, CS-09, CS-01, OS-04, CS-06 and OS-01 presented unsatisfactory performance because of low tensile capacity, and poor ductility.

The corresponding displacements of the specimens at the ultimate states listed in Table 1 indicate the ductility level of the specimens indirectly. The displacement values ranged between 1.0 mm and 35.5 mm, excluding the displacement of the control specimen. It was recorded that OS-03, OS-04, BS-02, BS-03 and BS-22 had undergone relatively larger displacements as compared to others, which were 35.5 mm, 18.2 mm, 22.4 mm, 31.0 mm and 20.9 mm, respectively. These specimens showed fluctuation response as can be seen in the load-displacement graphs (see Fig. 2), indicating yielding process due to extreme tensile stress per unit area to be resisted by the steel bars. Meanwhile, the specimens that recorded low displacements at ultimate state in Table 1, such as CS-01, CS-06, CS-09 and OS-01 presented premature failure and small displacements. This premature and sudden failure was due to either loss of anchorage bond between rebar and the surrounding grout, or loss of bond between grout and sleeve. As a result the steel bar was unable to achieve the yielding point.

Axial Stress and Bond Stress

The axial stress, σ , and the average bond, U of the spliced steel bars at the sleeve failure state is calculated by using Eq. 1 and Eq. 2, respectively, and the results are listed in Table 2:

$$\text{Axial stress, } \sigma = \frac{4P}{\pi D^2} \tag{1}$$

$$\text{Average bond stress } U = \frac{P}{\pi D L_d} \tag{2}$$

Where: P = failure load, D = nominal diameter of the main bar, L_d = embedded length

Table 2 Axial stress and average bond stress

Specimens	Embedded length, L_d , mm	σ , N/mm ² , Eqn. (1)	U , N/mm ² , Eqn.(2)
CS-01	100	433	17.3
CS-06	100	203	8.1
CS-09	100	506	20.3
OS-01	150	59	1.6
OS-03	300	674	9.0
OS-04	150	236	6.3
BS-02	150	593	15.8
BS-03	150	702	18.7
BS-22	150	612	16.3

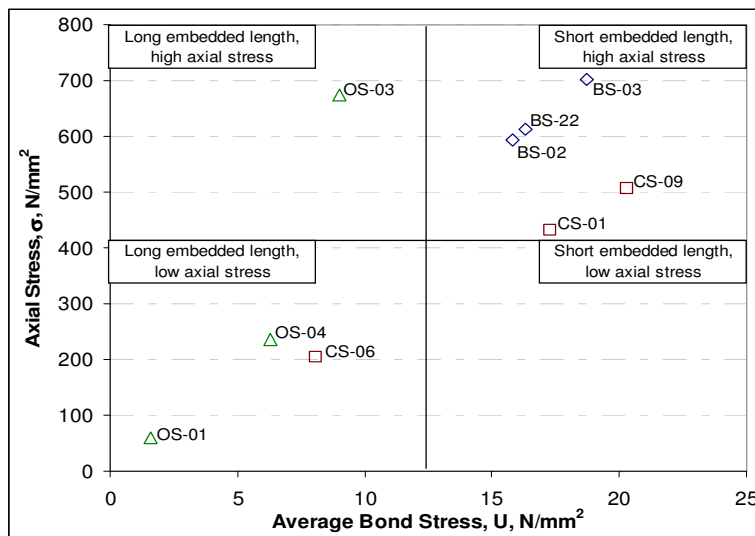


Fig. 3 Axial stress versus bond stress in reinforcement bar

Fig. 3 shows the plot distributions of the equivalent axial stress (axial strength) versus average bond stress (average bond strength) of the spliced steel bars in the specimens, where the specimens were classified in accordance to the interrelationship between embedded length and the axial stress. Specimens BS-03, BS-22, BS-02, CS-09, CS-01 fall in the category of short embedded length with high axial strength, of which these specimens are more preferable as they are able to generate ultimate axial strength of at least higher than the specific bar yielding stress of 410 N/mm^2 at short embedded length. Specimen OS-03 is classified in the category of high axial strength with long embedded length, of which is also acceptable but not economical. The specimens that fall in the other categories are not preferable for construction applications due to low axial strength. From the plot distributions, Specimens BS-series are more preferable as compared to other series because (a) very high axial strength was generated in steel bars, indicating excellent bond between the steel bar and the grout, and (b) the plots of distribution are more concentrated as compared to other series, signifying more consistent and reliable outcomes as compared to other series.

Conclusions

In this study, a total of nine mild steel pipe sleeve connections were experimentally tested under increasing tensile load until failure. In conclusion,

1. specimens BS-02, BS-03 and BS-22 show high potential for their feasibility as connection system in precast load-bearing wall system as they are able to generate sufficient bond that could outperform the tensile resistance of their spliced reinforcement bars.
2. The required anchorage length of Y16 rebar to provide its full tensile strength in specimens BS-02, BS-03 and BS-22 is 150mm, that is equivalent to 10 times bar diameter.
3. The factors that govern the tensile performance of a splice sleeve connection are bond between grout-rebar, bond between grout-sleeve, tensile capacity of the sleeve connection, and tensile capacity of the spliced reinforcement bars.

References

- [1] Lutz, L. A., and Gergely, P., 1967, "Mechanics of bond and slip of deformed bars in concrete," American Concrete Institute Journal, Vol. 64, No. 11.
- [2] Amin Einea, Takashi Yamane, Maher K. Tadros, "Grout-Filled Pipe Splice for Precast Concrete Construction," PCI Journal, Jan-Feb 1995, pp.82-93.
- [3] Untrauer, R. E., and Henry, R. L., "Influence of Normal Pressure on Bond Strength," ACI Journal, V. 62, No. 5, May 1965, pp. 577-585.
- [4] Parvis Soroushian, Ki-Bong Choi, Gill-Hyun Park and Farhang Aslani, "Bond of Deformed Bars to Concrete: Effects of Confinement and Strength of Concrete" ACI Material Journal, May-June 1991.
- [5] Hayashi, Y., Shimizu, R., Nakatsuka, T., Suzuki, K., "Bond stress-slip characteristic of reinforcing bar in grout-filled coupling steel sleeve," Proceedings, Japan Concrete Institute, V. 15, No. 2, 1993, pp. 256-270.
- [6] Ling Jen Hua, Ahmad Baharuddin Abd. Rahman, Abdul Karim Mirasa, Zuhairi Abd. Hamid, 2008, "Performance of CS-Sleeve under Direct Tensile Load: Part I - Failure Modes", Malaysian Journal of Civil Engineering, Vol. 20, No 1, pp 89-106.

Study of Ultra High Performance Fiber Reinforced Concrete with Expansive and Shrinkage Reducing Agents

NARDINOCCHI Alessandro^{1,a}, and CORINALDESI Valeria^{1,b}

¹Dep.t SIMAU. Università Politecnica delle Marche. Via Brecce Bianche. 60131. Ancona.Italy

^aa.nardinocchi@univpm.it, ^bv.corinaldesi@univpm.it.

Keywords: Drying Shrinkage; Expansive Agent; Flexural Strength; Shrinkage-Reducing Admixture; Ultra High Performance Fiber Reinforced Concrete.

Abstract. UltraHigh Performance Fiber Reinforced Concrete (UHPFRC) exhibits remarkable mechanical performance, which can allow to reduce the cross-section of structural members. However, a problem involving UHPFRC is the likely tendency to crack at early age, due to autogenous and plastic shrinkages, caused by the very low water-to-binder ratio adopted. Therefore, this experimental work intends to detect the effectiveness of a possible solution for reducing the risk of shrinkage cracks in UHPFRC, by adding to the mixture a suitable combination of expansive and shrinkage reducing agents. Compression and bending tests were carried out up to 28 days of curing. Free drying shrinkage strains were evaluated up to 56 days of exposure to 50% relative humidity. The experimental results obtained by using expansive and shrinkage reducing agents were extremely encouraging in terms of free drying shrinkage reduction, and even surprising in terms of flexural behaviour.

Introduction

Concrete cracking at early ages is a significant problem for many concrete structures, and in particular for structure in aggressive environment. The presence of cracking can reduce the service life of a concrete structure by allowing aggressive agents to penetrate through it faster in easy ways. This obviously leads to increases in maintenance costs. A possible solution for this problem could be the use of Shrinkage Reducing Admixture (SRA). Concerning the counteraction of concrete cracking, SRA proved to be effective if used alone [1], but especially in combination with expansive agent it showed synergic effect [2].

Ultra High Performance Fibre Reinforced Concrete (UHPFRC) is a superplasticized silica fume concrete, fiber reinforced, with improved homogeneity because traditional aggregates are replaced with very fine sand. According to Richard and Cheyrezy [3], if soft cast and cured at room temperature, its compressive strength can reach 200 MPa.

Nowadays, UHPFRC is regarded as a promising material for special prestressed and precast concrete members [4-5], including those within industrial and nuclear waste storage facilities [6].

Although production costs of UHPFRC are generally high, some economic advantages also exist in UHPFRC applications: in fact, steel reinforcement can be reduced or eliminated by using fibers. Moreover, due to its extraordinary mechanical performances, the thickness of concrete elements can be reduced, which results in materials and cost savings.

In addition, one of the main problems concerning the use of concrete as building material in general arises from the fact that it shows strongly different mechanical behavior under either compressive or tensile stress. This difference rises with increasing concrete strength class, and the ratio between tensile strength and compressive strength may vary from 0.15 to 0.11 for concrete having compressive strength varying between 28 and 63 MPa [7]. Conversely, the difference between concrete compressive and tensile behavior may decrease if concrete is prestressed, because when it will be subjected to loads producing tensile stress, it will show first of all a phase of discharge from the initial compressive prestress, and only later the material will start to undergo tensile stresses.

In this work, the possible onset of a self-prestressing effect due to the presence of both expansive agent and homogeneously dispersed steel fiber reinforcement was investigated.

Experimental Part

Materials and mix proportions. As binder, commercial Portland cement type CEM I 52.5 R according to the European Standards EN-197/1 was used at a dosage of 960 kg/m^3 with a water to cement ratio of 0.25 (corresponding to a water dosage of 240 l/m^3). The Blaine fineness of cement was $0.48 \text{ m}^2/\text{g}$ and its relative specific gravity was 3.15.

As aggregate, well-graded very fine quartz sand was used with particle size up to 1 mm. The specific gravity value was 2710 kg/m^3 while its water absorptions was 1.4%.

As filler, 250 kg/m^3 of silica fume (SF) with grain size smaller than $1 \mu\text{m}$, obtained as industrial by-product of the silicon processing, were used. Silica fume powder had a specific surface area of about $18 \text{ m}^2/\text{g}$, evaluated by means of BET surface method, and a relative specific gravity of 2.20.

As fibers, 192 kg/m^3 of brass-coated steel fibers were added; their main properties are reported in Table 1.

In addition, in two mixtures an expansive agent was added, made of about 99% dead burnt lime (CaO), at the same dosage of 35% by weight of cement. Then, in the third mixture also SRA polyethylene glycol was used to reduce the surface tension of the pore water in order to decrease the drying shrinkage.

Finally, 10% by weight of cement of an acrylic-based superplasticizer was always employed, constituted of a carboxylic acrylic ester polymer in the form of 30% aqueous solution liquid (SP).

The UHPFRC mixture proportions are listed in Table 2. Workability of UHPFRCs at the fresh state was evaluated by means of the flow table according to the procedure described in EN 1015-3, and results obtained in terms of consistency of fresh mortars are in the range 40-50%.

Table 1: Properties of steel fibers.

Density [kg/m^3]	Tensile strength [MPa]	E [GPa]	l_f [mm]	d_f [mm]	Aspect ratio
7850	> 250	190	12	0.16	75

Table 2: UHPFRC mixture proportions [kg/m^3].

Mixture Composition	RPC	RPC+CaO	RPC+CaO+SRA
Portland Cement CEM I 52.5 R	960	960	960
Silica fume	250	250	250
Quartz Sand (0-1 mm)	960	960	925
Superplasticizer	96	96	96
Brass-coated steel fibers	192	192	192
Water	240	240	240
Expansive agent	/	35	35
Shrinkage Reducing Agent (SRA)	/	/	4
Water/Cement	0.25	0.25	0.25

Mechanical Properties of Hardened Concrete

Compressive and bending tests. Nine prismatic specimens (40 by 40 by 160 mm) were cast for each UHPFRC mixture for compression and bending tests. They were soft cast in steel forms (vibrated for 30 seconds after casting), and after one day of wet curing they were stored at constant temperature (20°C), and constant relative humidity ($50 \pm 2\%$) for 28 days. Compressive strength was evaluated according to EN 1015-11 after 1, 3 and 28 days of curing. Results obtained are reported in Figure 1.

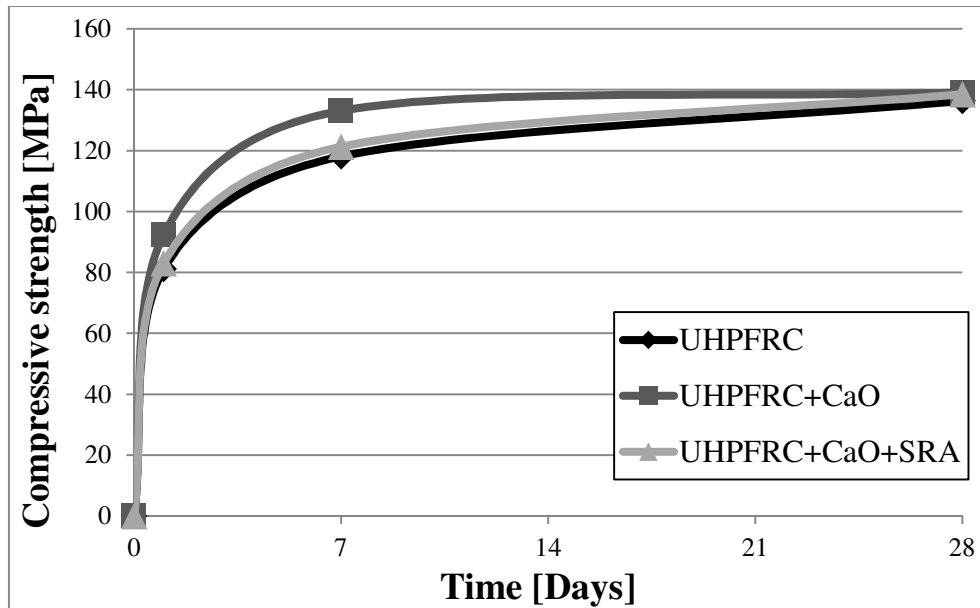


Figure 1: Compressive strength vs. curing time.

It can be noticed that at early ages the addition of expansive agent produces a certain positive effect on compressive strength development. However, when the expansive agent is used together with SRA this effect almost disappears. The slightly negative effect of SRA on mechanical performance is well-known on the basis of data reported in the literature [8, 9], indeed.

Flexural strength was evaluated according to EN 1015-11 after 1, 3 and 28 days of curing. Results obtained are reported in Figure 2.

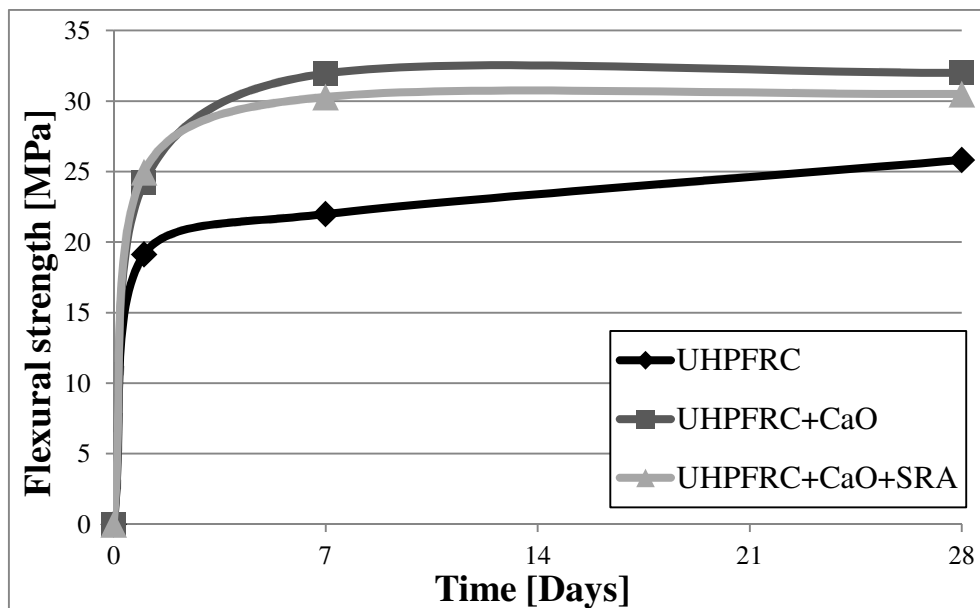


Figure 2: Flexural strength vs. curing time.

With respect to plain UHPFRC the presence of the expansive agent produced a surprising beneficial effect, particularly at early age, with a value of 1-day flexural strength of 25 MPa, and an increase on 7-day flexural strength of about 45%. The reason for this extraordinary performance is likely due to a synergistic effect between expansive agent and homogeneously dispersed fiber reinforcement.

In fact, during the first 24-48 hours since ingredients' mixing, the cementitious matrix thanks to the presence of expansive agent would tend to expand, but its swelling is counteracted and fully (or almost) cancelled by the fiber reinforcement. This phenomenon would produce a mutual interfacial

stress between fibers and matrix, and the resulting effect (if the adherence between cement paste and fiber is maintained) could be an internal homogeneous prestress able to enhance the flexural strength of UHPFRC.

On the other hand, the addition of SRA slightly penalized the flexural strength, as expected also on the basis of the compression stress, as well as on the basis of data reported in the literature [8, 9].

Drying shrinkage tests. For free drying shrinkage strains monitoring, two prismatic specimens (70 by 70 by 280 mm) were prepared for each concrete mixture according to EN 11307. After one day of wet curing, the specimens were stored at constant temperature ($20\pm 2^\circ\text{C}$), and constant relative humidity ($50\pm 2\%$), while measuring drying shrinkage at different curing times up to 56 days of exposure. Results obtained are shown in Figure 3.

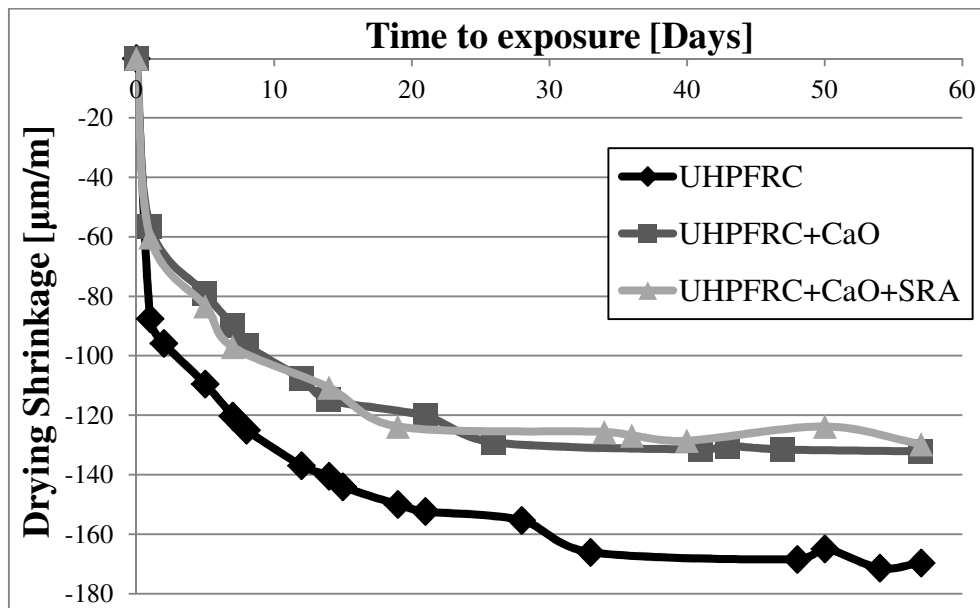


Figure 3: Free drying shrinkage vs. time to exposure.

As you can see in Figure 3, the presence of expansive agent, with or without SRA, allows a reduction of 56-day drying shrinkage strains equal to about 30%. The same positive effect was detected also by [10], which found an even higher reduction of roughly 80%. Usually, when expansive agents are added to concrete mixture, especially together with SRA, an initial expansion can be detected during free drying shrinkage testing, as outlined in previous works [8, 9]. In this case, the expansion (positive strains) has not been observed, because it has likely been counteracted by the short steel fibres. The exchange of stress between expanding cementitious paste and steel fiber produced a certain self-prestress effect, confirming the hypothesis already done before, in order to explain the extraordinary enhancement of flexural strength at early ages.

Conclusions

On the basis of the results obtained the following conclusions can be drawn:

- the addition of expansive agent caused a slight improvement at early age of the compressive strength, while this effect was negligible when also SRA was used;
- concerning flexural strength, at early age the addition of expansive agent, with or without SRA, caused a remarkable improvement of strength (+45% at seven days), likely due to a self-prestress effect developed in the cement matrix thanks to the restrain of the fiber reinforcement;
- concerning the results of free drying shrinkage tests, the addition of expansive agent and SRA produced an evident reduction of the shrinkage strain of about 30% up to 56 days of curing;
- in conclusion, the use of CaO-based expansive agent for producing UHPFRC seems to be extremely advantageous from all viewpoints.

References

- [1] V. Corinaldesi, G. Moriconi, Recycling of rubble from building demolition for low-shrinkage concretes, *Waste Manage* 2010;30(4):655–9.
- [2] M. Collepardi, R. Troli, M. Bressan, F. Liberatore, G. Sforza, Crack-free concrete for outside industrial floors in the absence of wet curing and contraction joints, *CemConcr Compos* 2008;30:887–91.
- [3] P. Richard, M.H. Cheyrezy: *Cem. Concr. Res.* Vol. 25 (1995), p. 1501.
- [4] V. Corinaldesi, The study of using fly ash to produce Ultra High Performance Fibre Reinforced Concrete, *Advanced Materials Research*, Vols. 535-537 (2012) 1889-1892.
- [5] G. Moriconi, V. Corinaldesi, in: *Excellence in Concrete Construction - Through Innovation*, edited by M.C. Limbachiya, H.Y. Kew, Taylor & Francis Group (2009), p. 239.
- [6] M. Collepardi, V. Corinaldesi, S. Monosi, G. Moriconi: *L'Ind. Ital. Cem.* Vol. 777 (2002), p. 540.
- [7] M. Collepardi, *Scienza e tecnologia del calcestruzzo*, Hoepli edizioni, Terza edizione, 463.
- [8] V. Corinaldesi, Combined effect of expansive, shrinkage reducing and hydrophobic admixtures for durable self compacting concrete. *Construction and Building Materials* 2012;36:758-64.
- [9] V. Corinaldesi, S. Monosi, M.L. Ruello, Influence of inorganic pigments' addition on the performance of coloured SCC, *Construction and Building Materials* 2012;30:289-93.
- [10] J.J. Park, S.W. Kim, D.Y. Yoo, Y.S. Yoon, Drying shrinkage cracking characteristics of ultra-high-performance fibre reinforced concrete with expansive and shrinkage reducing agents, *Magazine of Concrete Research* 65(4) (2013) 248-256.

Lightweight Aggregate Mortars for Sustainable and Energy-Efficient Building

CORINALDESI Valeria^{1, a}, NARDINOCCHI Alessandro^{1, b}
and DONNINI Jacopo^{1, c}

¹Dep.t SIMAU, Università Politecnica delle Marche, 60131, Ancona, Italy

^av.corinaldesi@univpm.it, ^ba.nardinocchi@univpm.it, ^cj.donnini@univpm.it

Keywords: Energy Efficient Building, GRP Waste, Polyurethane Waste, Self-Leveling Lightweight Mortars, Sustainable Building, Thermal Conductivity, Wooden Waste.

Abstract. Self-leveling lightweight mortars were developed to attain good workability, sufficient compressive strength (at least 5 MPa after 28 days of wet curing), and low specific weight (less than 1100 kg/m³), as well as low thermal conductivity (lower than 0.3 W/m·K). The attention was also focused on the sustainability of this construction material, which was improved by using in the mixture both glass reinforced plastic (GRP) industrial by-product as filler replacing limestone powder, and recycled aggregates replacing natural sand. GRP is a composite material made of glass fibres dispersed in a resin, usually polyester, widely used in several fields from building to furniture factory to boatyard. The recycled aggregates used were alternatively either wooden waste or polyurethane waste particles. Concerning wooden waste, they are produced by cutting, drilling and milling operations, where wood is removed from a finished product; they are sawdust and offcuts often collected in filter bags or dust collectors. On the other hand, the polyurethane waste particles were obtained as a rejection of a factory producing rubber soles for the footwear industry.

The influence of GRP filler and waste particles on fresh mortar workability, compressive and flexural strength of hardened mortar, as well as on its thermal conductivity was examined. An optimization of the mortar mixture proportions was carried out by suitably varying the dosage of the ingredients. The experimental investigation showed that both the material unit weight and its thermal conductivity resulted strongly reduced, thus indicating a high and promising potential for future developments.

Introduction

The reduction of energy consumption in construction, the production of thermally insulating materials and the solution of environmental problems by recycling industrial and municipal waste are becoming a relevant problem. Therefore, the development of composite construction materials with low thermal conductivity by using either polyurethane (PU) waste particles or wooden waste (WW) could be an interesting alternative that might solve simultaneously energy and environmental issues.

Concerning the reuse of recycled rubber in mortars and concrete, extensive studies have been conducted on used tyre modified concrete and mortars [1-2]. The literature about the use of tyre rubber particles in cement-based materials focuses on the use of tyre rubber as an aggregate in concrete and evaluates only the mechanical properties. Results have indicated that rubberized concrete mixtures show lower density, increased toughness and ductility, higher impact resistance, lower compressive and splitting tensile strength, and more efficient sound insulation. However, there are a few studies about the reuse of other plastic or rubber waste in lightweight aggregate concrete (LWAC) [3-7].

In the present paper an attempt was made to prepare cementitious (lightweight if possible) mortars by adding to the mixtures polyurethane (PU) waste particles, which were supplied by a factory producing rubber soles for the footwear industry. In 2007, the shoes' factory produced about 250 tonnes of polyurethane waste particles at all, amount corresponding to the 18% of the overall production.

A further attempt was that of using wood waste particles replacing sand. In many countries, the wood industries generate a large amount of waste products. Sawdust is generated from cutting, drilling and milling operations where wood is removed from a finished product. Wood dust consists of very fine particles generated during sanding or other machining operations. They are often collected in filter bags or dust collectors. The physical and chemical properties of wood dust vary significantly depending on many factors such as geographical location and industrial processes. On average, the wood sawing results in 5–10% by weight of dust [8]. In some cases, wood waste contain some degree of contamination reducing the net value of the material and requires further processing in order to meet end market specifications. Each of these factors can generally influence the possibility to recycle wood waste. Moreover, the generation of energy from burning wood wastes may give rise to problems related with the greenhouse effect. Some research projects carried out in the past used wood ash wastes as a replacement for cement in concrete or mortar mixtures [9–10], without showing a great improvement in mechanical properties. In this paper, sawdust was used, which came from a company in which wood is worked to produce wood packing. Sawdust is made of fir (the main component) as well as poplar and beech, and it was collected from sawing. Small amounts of paint, insecticide, fungicide are present inside the sawdust and they forbid a safe reuse of this wooden waste as fuel. Consequently, the possibility to reuse sawdust in mortars can be environmentally-friendly.

Among other things, in this work glass reinforced plastic (GRP) by-product was used as filler. GRP is a composite material made of glass fibres dispersed in a resin, usually polyester, widely used in several fields from building to furniture factory to boatyard. Every year, in Western Europe, GRP processing produces 40,000 tons of industrial by-product. In Italy, this by-product is landfilled due to the difficulty of separating the glassy part from the polymeric matrix, its intrinsic thermosetting composite nature, the lack of information relating to its characteristics as well as insufficient knowledge on potential recycling options.

Experimental Part

Materials. A commercial portland-limestone blended cement type CEM II/A-L 42.5 R according to EN-197/1 was used. The Blaine fineness of cement was $0.42 \text{ m}^2/\text{g}$ and its relative specific gravity was 3.05.

As aggregate fraction, polyurethane (PU) waste particles (0–8 mm) derived from rejected rubber-shoe soles were used. The particles were obtained by grinding in an universal cutting mill (Pulverisette 19 by Fritsch) polyurethane soles, reducing them into particles smaller than 8 mm. Their relative specific gravity was 0.55, even if according to Mounanga et al. [5], the estimation of PU foam density, greatly influenced by its high compressibility as well as water absorption, was quite uncertain and makes difficult the mixture proportion.

Alternatively, as aggregate fraction sawdust (0–8 mm) was used. Its value of loss on ignition is 96%, while its relative specific gravity is 0.68. It came from a company in which wood is worked to produce wood packing. Sawdust is made of fir (the main component) as well as poplar and beech, and it was collected from sawing. Small amounts of paint, insecticide, fungicide are present inside the sawdust and they forbid a safe reuse of this wooden waste as fuel. Sawdust was always pre-soaked in water for at least 24 hours, in order to avoid further water absorption while mortar ingredients are mixed.

In order to achieve adequate cohesiveness of the fresh mortar, limestone powder (LP) was used as a filler, obtained as a by-product of quarry activity. In limestone quarries, considerable amount of powders is produced as by-products of stone crushers, whose management is a big problem concerning disposal, environmental pollution and health hazards. Previous studies showed the feasibility of the use of limestone powders as a filler for SCC [11]. The Blaine fineness of limestone powder was $0.58 \text{ m}^2/\text{g}$ and its relative specific gravity was 2.65.

Alternatively to LP, a GRP powder was used, directly coming from a shipyard as an industrial by-product. GRP powder composition was about 20% by volume of glass fibres and 80% by volume of organic material identified by FT-IR spectroscopy as polyester resin. The GRP powder

water absorption and relative specific gravity were 20% and 1.40, respectively. Since the relative specific gravity of LP is 2.65, its replacement with GRP powder can further on reduce the mortar weight.

As water reducing admixture (WRA), 30% aqueous solution of carboxylic acrylic ester polymer was added to the mixtures.

As air entraining admixture (AEA), an alkaline solution of fatty acid salts was used.

Mortar mixture proportions. Mortar mixture proportions are reported in Table 1. The same content of cement was used for each mortar, while the water dosages were adjusted in order to obtain self-levelling ability. Therefore, all the mixtures in the fresh state showed practically the same value of consistency obtained by means of the flow table, according to UNI EN 1015-3. The mortars could be defined as self-levelling, since their consistency value was in the range 140-160%.

Limestone powder was always added to the mixtures in order to obtain the right cohesiveness and, eventually, it was partially replaced by GRP powder (20% in volume), in order to reduce the unit weight of the mortar without compromising its rheological behaviour.

As aggregate, either polyurethane (PU) waste or sawdust (wooden waste, WW) were used, totally replacing sand.

Concerning chemical admixtures, the same dosage of superplasticizer (WRA), equal to 0.8% by weight of cement, and air entraining admixture (AEA), equal to 0.6% by weight of cement were always added. In particular, such high dosage of AEA was used to introduce as many air bubbles as possible in the hardened mortars, in order to lighten them.

The values of the unit weight of the mortars after 28 days of wet curing are also reported in Table 1. It can be noticed that values close to 1100 kg/m^3 were obtained, and even lower when GRP powder was added and wooden waste particles were used.

Table 1: Self-levelling mortar mixture proportions [kg/m^3]

Mixture	PU	PU+GRP	WW	WW+GRP
Water	225	225	170	170
Cement	375	375	375	375
Limestone Powder (LP)	315	252	315	252
GRP waste powder	-	33	-	33
PU waste	210	210	-	-
Wooden waste	-	-	330	330
WRA	3	3	3	3
AEA	2.3	2.3	2.3	2.3
Unit weight (kg/m^3)	1133	1103	1055	1025

Preparation and curing of specimens. Six prismatic specimens were prepared for each mortar mixture, 40x40x160 mm in size, by casting them in steel forms. They were wet cured at 20°C up to 28 days and used for bending and compression tests after 7 and 28 days of curing.

Then, two flat cylindrical specimens (diameter of 200 mm, 20 mm thick) were cast for each mixture in order to perform thermal conductivity tests, after 28 days of wet curing and suitably polishing the cylinder bases (by sanding them).

Results and Discussion

Compression tests. Compressive strength was measured at 7 and 28 days of wet curing according to EN 1015-11. Results obtained are reported in Figure 1.

The target value of 5 MPa after 28 days of curing was achieved in every case.

Bending tests. Flexural strength was also measured at 7 and 28 days of wet curing according to EN 1015-11. Results obtained for the mortars listed in Table 1 are reported in Figure 2.

Values obtained were quite good with respect to the related low compressive strength value. In particular, the effectiveness of the addition of GRP powder can be highlighted, since the reason of this positive effect is the presence of glass fibers (about 20% by weight) within GRP powder, which act as reinforcing material.

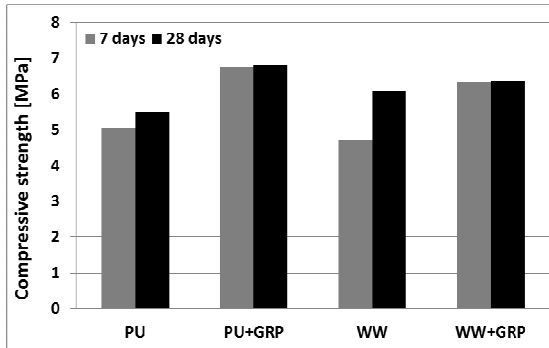


Figure 1: Compressive strength vs. curing time for the different mortar mixtures

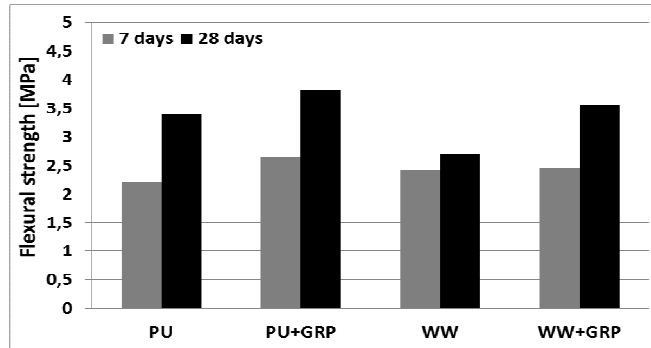


Figure 2: Flexural strength vs. curing time for the different mortar mixtures

Thermal conductivity tests. Thermal conductivity measurements were carried by using the guarded hot plate method, according to UNI 7745 [12].

Specimens were previously dried in the oven at 375-390°K to constant weight (mass loss lower than 1%). The experimental device is made of a heating element (central element for measuring plus an external guarded ring), a cooling element and external thermal insulation. The temperatures of the heating and cooling elements, as well as those of the frontal surfaces of the specimen, were measured by means of thermocouples.

Results obtained are reported in Table 2. With respect to an ordinary mortar, which was tested by the authors in a previous work [13] by using the same experimental equipment, as well as the same experimental procedure, very lower thermal conductivity values were found. In fact, for the ordinary mortar the thermal conductivity was 0.739 W/m·K [20]; consequently, for the studied mixtures it is reduced by a factor ranging from 2.75 to 4.25, depending on the presence of GRP powder and on the use of WW (both rising the factor value).

Table 2: Thermal conductivity of self-levelling mortars

Mixture	PU	PU+GRP	WW	WW+GRP
Thermal conductivity [W/m·K]	0.268	0.217	0.227	0.174

Conclusions

On the basis of the experimental results obtained the following conclusions can be drawn:

- self-levelling mortars can be obtained by using either PU waste or sawdust particles fully replacing sand by suitably optimizing the mortar mixture proportions;
- the use of GRP powder partially replacing limestone powder is strongly positive: in fact, it allows to guarantee self-levelling ability by lowering both unit weight and thermal conductivity of the mortar and by improving its mechanical properties (in particular the flexural strength, thanks to the presence of glass fibers);
- the use of lightweight aggregates (PU and wooden waste particles), lightweight filler (GRP powder), and high dosage of AEA allows to strongly reduce mortar unit weight (under 1100 kg/m³) and mortar thermal conductivity (under 0.3, or even under 0.2 W/m·K) by fulfilling the minimum requirement of 28-day compressive strength of 5 MPa necessary to build lightweight slabs;
- finally, the use of industrial by-products such as PU particles, sawdust particles and GRP powder to manufacture self-levelling mortars allows to produce a construction material

which fully meet the green building issues of energy saving, waste recycling and judicious use of natural resources.

References

- [1] Eldin, N.N., Senouci, A.B., Rubber tires particles as concrete aggregate, *J Mater Civ Eng* 5(4) (1993) 478–496.
- [2] Topçu, I.B., The properties of rubberized concrete, *Cem Concr Res*, 25(2) (1995), 304–310.
- [3] Turatsinze, A., Bonnet, S., Granju, J.L., Potential of rubber aggregates to modify properties of cement, based-mortars, *Constr Build Mater* 21(1) (2007) 176–181.
- [4] Mounanga, P., Gbongbon, W., Poullain, P., Turcry, P., Proportioning and characterization of lightweight concrete mixtures made with rigid polyurethane foam wastes, *Cem Concr Comp*, 30(9) (2008) 806-814.
- [5] Kou, S.C., Lee, G., Poon, C.S., Lai, W.L., Properties of lightweight aggregate concrete prepared with PVC granules derived from scraped PVC pipes, *Waste Manage*, 29(2) (2009) 621-628.
- [6] Akçaözoğlu, S., Atiş, C.D., Akçaözoğlu, K., An investigation on the use of shredded waste PET bottles as aggregate in lightweight concrete”, *Waste Manage*, 30(2) (2010), 285-290.
- [7] Fraj, A.B., Kismi, M., Mounanga, P., Valorization of coarse rigid polyurethane foam waste in lightweight aggregate concrete, *Constr Build Mater* 24(6) (2010) 1069-1077.
- [8] Turgut, P., Algin, H.M., Limestone dust and wood sawdust as brick material, *Building and Environment*, 42(9) (2007) 3399–3403.
- [9] Elinwa, A.U., Mahmood, Y.A., Ash from timber waste as cement replacement material, *Cem Concr Comp*, 24(2) (2002) 219–22.
- [10] Udoeyo, F.F., Dashibil, P.U., Sawdust ash as concrete material, *ASCE*, 0899-1561, 14(2) (2002) 173–176.
- [11] Corinaldesi, V., Moriconi, G., Naik, T.R., Characterization of marble powder for its use in mortar and concrete, *Constr Build Mater*, 24(1) (2010) 113-117.
- [12] UNI 7745, 1977, “Materiali isolanti. Determinazione della conduttività termica con il metodo della piastra calda con anello di guardia”.
- [13] Corinaldesi, V., Mazzoli, A., Moriconi, G., Mechanical behaviour and thermal conductivity of mortars containing waste rubber particles”, *Materials and Design*, 32(3) (2011) 1646-1650.

Study on Damage Modes of a Sandwich Panel Impacted Repeatedly

AZOUAOUI Krime^{1, a} and MOUHOUBI Said^{1, b}

¹ Université des Sciences et de la Technologie Houari Boumediene (USTHB), Alger, Algeria

^a azouaoui@yahoo.com, ^b said.mouhoubi@gmail.com

Keywords: aluminum sandwich panels, honeycomb core, damage, repeated impact, impact energy, impact fatigue life.

Abstract. This paper describes an experimental investigation for determining the damage modes under low energy impact-fatigue of sandwich panels consisting of aluminum skins supported by honeycomb core made of aluminum. Square samples of 125mm by 125mm sides and 10mm thickness (skin of 0.6mm and 8.8mm of core) were subjected to impact fatigue loading using a testing machine at four different energy levels (2J, 3J, 5J and 7J). The square plates are clamped in a fixture system over a 100mm diameter hole. Three different diameters of impactor head (15mm, 25mm and 35mm) are used to study their influence on life duration of the sandwich plates. Results showed that damage area at impacted face and propagation of multi-cracks at rear face are greatly affected by energy level and impactor diameter.

Introduction

Several works were performed to identify the damaging modes in sandwich structures subjected to low energy impact [1,2,3,4]. The damages are generally induced in the impacted skin, and in the core and in the impacted skin-core interface. Moody and Vizzini [5] have demonstrated that under impacts of very low energy levels, the impactor deflects the surface and the skin rebounds. There was no visible damage to the panels; however, the cell walls of the core were crashed. Higher energy impacts cause the skin to have a permanent indentation at the impact site. However, several experimental works, aiming to better understand the different damage mechanisms under impact of sandwich structures, have shown that skin damage develops linearly with incidental energy, until a maximum value is reached [6,7]. The damage of the core, in addition to cracking, fracture can occur by buckling of cell walls (honeycomb core). Finally, the authors [8] reveal that debonding is the main physical mechanism responsible for the rupture of the interface.

Nevertheless, less work has been performed on sandwich panels impacted repeatedly. Then, the aim of this work is to describe an experimental investigation for determining the damage modes under low energy impact-fatigue of sandwich panels consisting of aluminum skins supported by honeycomb core made of aluminum.

Experimental Procedure

Square samples (Fig. 1a) of 125mm by 125mm sides and 10mm thickness (skin of 0.6mm and 8.8mm of honeycomb core) were subjected to impact-fatigue using a testing machine (Fig. 1b) at four different energy levels (2J, 3J, 5J and 7J). For more details refer to reference [9]. The square plates are clamped in a fixture system over a 100mm diameter hole (Fig. 1c). Three different diameters of impactor head (15mm, 25mm and 35mm, with same weight) are used to study their influence on life duration of sandwich plates.

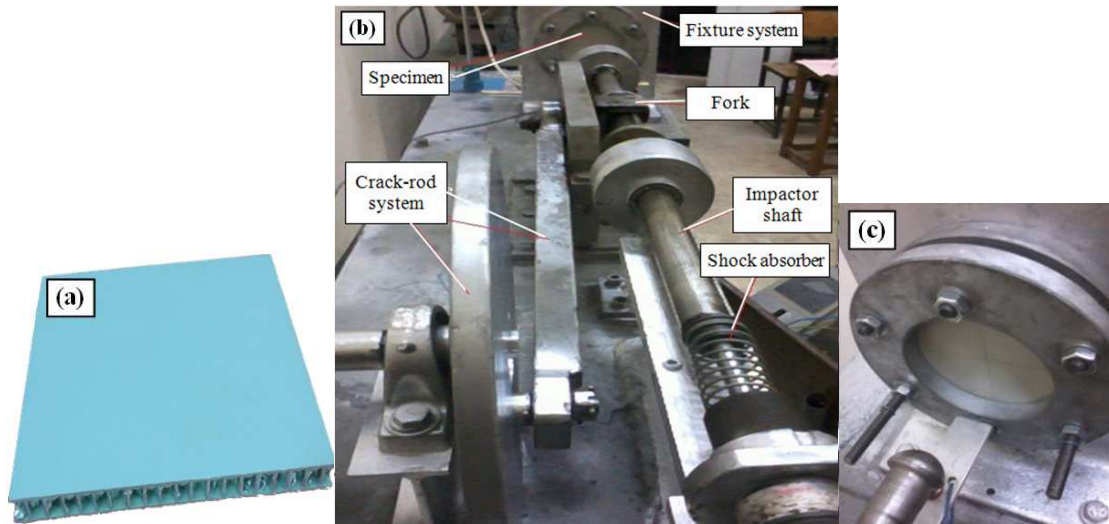


Fig. 1 Specimen (a), impact-fatigue machine (b) and fixture system (c)

The material properties of the skins and core materials are given in tables 1 and 2.

Table 1 Material properties of the core

Property	value
Density [kg/m^3]	82
Through-thickness Shear modulus [MPa]	430
Through-thickness Shear strength [MPa]	2,4
Compression strength [MPa]	4,5

Table 2 Material properties of the skin

Property	value
Young modulus [GPa]	70
Tensile strength [MPa]	367
Elongation to failure [%]	13

Results

The results show that under same impact energy, the number of impacts to failure (perforation) increases with impactor diameter. Fig. 2 shows the damaged area (perforation) on the impacted face, for three impactors of same weight and different diameters (15mm, 25mm and 35mm), relatively to an impact energy of 3J.

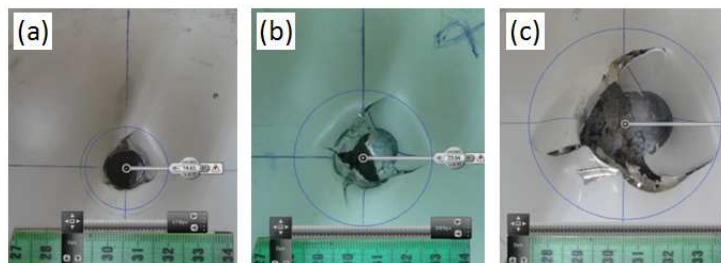


Fig. 2 Estimated damage area for different impactors: (a) 15mm, (b) 25mm, (c) 35mm
The damage area and the number of impacts to failure increase with impactor diameter (Fig. 3).

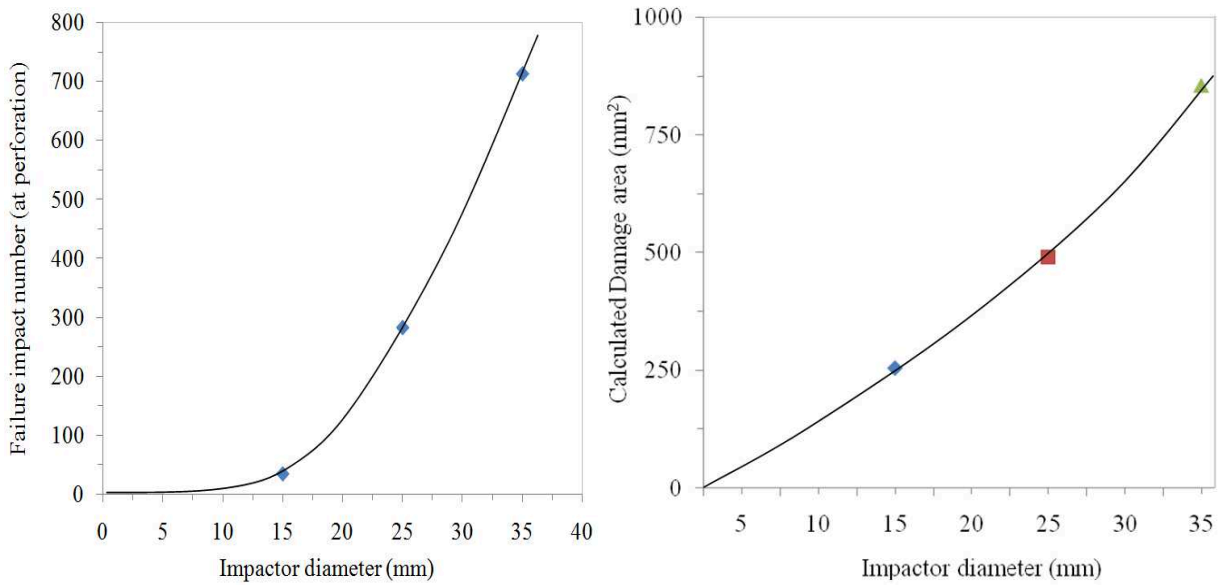


Fig. 3 Failure impact number and calculated damage area vs projectile diameter (2J)

Fig. 4 shows different pictures taken during impact-fatigue tests under impact energy of 2J. A hemispherical indentation clearly visible on the impact face indicates that impact causes a permanent deformation of the skin of the sandwich. Beyond 18,000-20,000 impacts, three cracks initiate in the upper skin from three different sites. When Nida cells cede, under the point of impact, the perforation occurs fairly quickly, tearing the skin below. The damage modes inventoried are: localized buckling of the core, the core cracking, permanent indentation under the point of impact, cracking of the impacted skin, debonding of the skin-core interface.

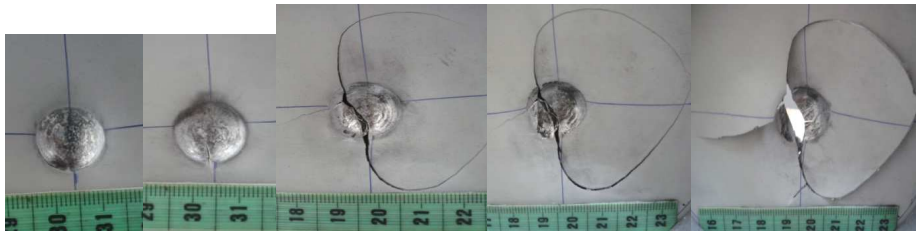


Fig. 4 Front face at 8,000 - 12,000 - 20,000 - 28,000 and 30,986 impacts (2J)

The comparison of damage area, represented by the “footprint” left by the impactor on the impacted face (crater shape), brings up the undeniable effect of impact energy on the damaging of sandwich panels (Fig. 5).

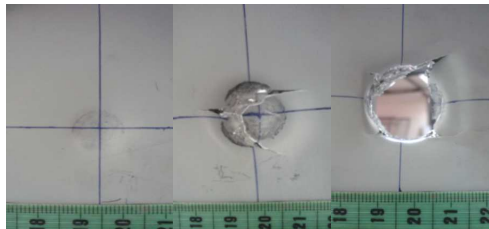


Fig. 5 Impacted face under 3J, 5J and 7J (number of impacts: 10)

The evolution of calculated damage surface based on the number of impact is manifested in two phases: a first zone of acceleration of damage (the early impacts) and a second phase of slower damage, until failure (Fig. 6a). For the lowest energy (2J), this development is in three phases: the two phases listed above, followed by a third phase of accelerated damage until perforation (Fig. 6b).

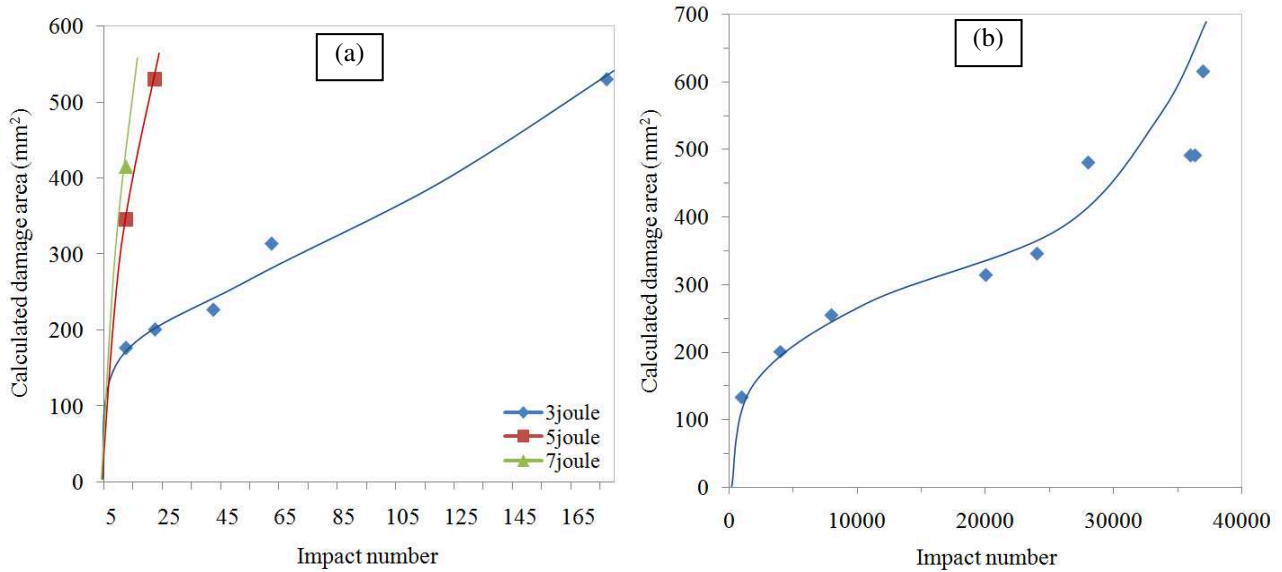


Fig. 6 Calculated damage area with number of impacts: (a). 3J, 5J, 7J, (b). 2J

Damage to the upper skin is manifested by the initiation and growth of three cracks whose lengths increase with the number of impacts, following curve paths (Fig. 7).

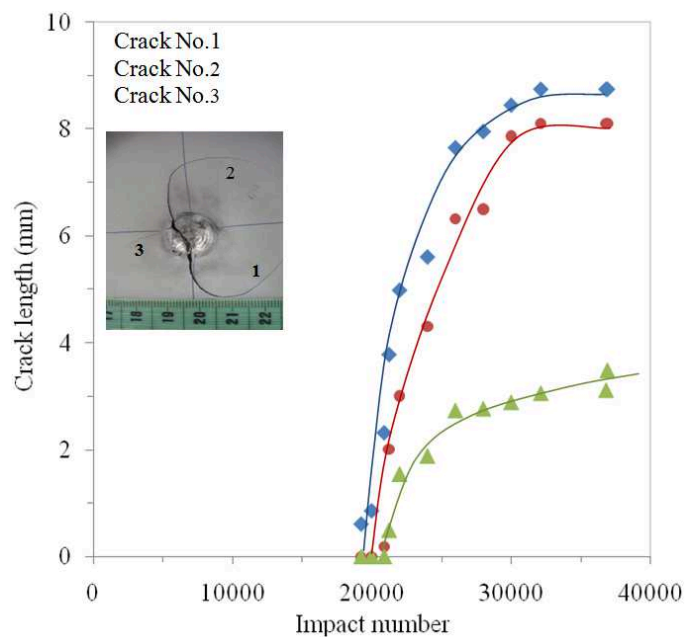


Fig. 7 Crack length (three cracks numbered 1, 2 and 3) vs impact number (2J)

Conclusion

Damage occurs by a slight indentation located at the upper skin, followed by a crater, characteristic of impact-fatigue test using a hemispherical impactor. The dimension of the crater increases with number of impacts and diameter of the impactor. After a number of impact (about 19,000 impacts for energy of 2J), three cracks initiate and propagate rapidly on the upper skin of the sandwich. The influence of the impact energy (2J, 3J, 5J, 7J) is clearly demonstrated. Indeed, the highest energy levels cause earlier the perforation of sandwich plates, at a smaller number of impacts. On the other hand, it was noted that the impact energy has a significant effect on the damage strength of sandwich structures, more impact energy is low and more damage area is high. This is tantamount to a greater

consumption of energy available by damage and not by perforation. This energy balance is reversed when energy becomes more important.

References

- [1] C.C. Foo, L.K. Seah, G.B. Chai, Low-velocity impact failure of aluminium honeycomb sandwich panels, *Composite Structures*. 85(1) (2008) 20-28.
- [2] V. Crupi, G. Epasto, E. Guglielmino, Collapse modes in aluminium honeycomb sandwich panels under bending and impact loading, *International Journal of Impact Engineering*. 43 (2012) 6-15.
- [3] L. Aktay, A.F. Johnson, M. Holzapfel, Prediction of impact damage on sandwich composite panels, *Computational Materials Science*. 32(3-4) (2005) 252-260.
- [4] K.W. Jeon, K.B. Shin, An experimental investigation on low-velocity impact responses of sandwich panels with the changes of impact location and the wall partition angle of honeycomb core, *International Journal of Precision Engineering and Manufacturing*. 13(10) (2012) 1789-1796.
- [5] R.C. Moody, A.J. Vizzini, Test and analysis of composite sandwich panels with impact damage, In: U.S. Federal Aviation Administration, Office of Aviation Research, Washington, 2002, pp. 6.
- [6] T.E. Plam, Impact resistance and residual compression strength of composite sandwich panels, In: Proc 8th Int Conf on Composite Mat. (ICCM/8), Honolulu, 1991, pp. 1-13.
- [7] T. Gottesman, Criticality of impact damage in composite sandwich structures, In: Proc of 6th Int Conf on Comp Mat Combined with the 2nd European Conf on Comp Mat, London, 1987, pp. 3.27-3.35.
- [8] J.S. Tomblin, Impact damage characterization and damage tolerance of composite sandwich airframe structures - Phase II, In: U.S. Federal Aviation Administration, Office of Aviation Research, Washington, 2002, pp. 4-6.
- [9] K. Azouaoui, Z. Azari, G. Pluvinage, Evaluation of impact fatigue damage in glass/epoxy composite laminate, *International Journal of Fatigue*. 32(2) (2010) 443-452.
- [10] X.L. Fan, T.J. Wang, Q. Sun, Damage evolution of sandwich composite structure using a progressive failure analysis methodology, *Procedia Engineering*. 10 (2011) 530-535.

Micromechanical Model Prediction Overall Young Modulus Nanocomposites Polymer-Clay-Silica by Self Consistent Approach

MESBAH Amar^{1,a}, AZOUAOUI Krimo^{1,b}, KAOUA Sid-Ali^{1,c}
and BOUTALEB Salah^{1,d}

¹ Université des Sciences et de la Technologie Houari Boumediene (USTHB), Alger, Algeria

^a ammar_mesbah@yahoo.fr, ^b azouaoui@yahoo.com, ^c sakaoua@gmail.com,

^d salaboutaleb@gmail.com

Keywords: micromechanical formulation, nanocomposites, polymer-clay-silica, self consistent approach, interphase.

Abstract. In order to address the problem of stiffness and mechanical properties, a micromechanical approach for the prediction of the overall modulus of nanocomposites (Nylon-6/nanoclay/silica) using a self-consistent scheme based on the double-inclusion model and taking into account the different morphologies exfoliated or intercalated of the nanoparticles. Self-consistent approach that is used in our calculations was explained after reviewing the inclusion of Eshelby, in particular the double inclusion and while considering also the effect of constrained region, modeled as an interphase around reinforcements. Namely, polyamide 6 reinforced with clay platelets and silica particles. Several parameters on the Young's modulus of the composite were studied to see the effect of having mixed two or three reinforcements in polymer matrix. Finally, we demonstrated the process undertaken for the calculation of elastic constants of the material studied.

Introduction

The main motivation behind the polymer mixture is usually reported as an impact on the modification and enhancement of mechanical properties. Among the more promising composite materials may be nanocomposites polymer/clay or polymer/silica based [1, 2] (see eg the pioneering work of Usuki and Kojima). Predicting the effective behavior of heterogeneous materials from the component properties and microstructure is a critical step in the design of new materials.

In this context, micro-mechanical approaches have been developed for evaluating the effective property of heterogeneous materials and their dependence on the properties of the components and the microstructure. These approaches are mainly based on the theory of Eshelby equivalent inclusion. The most representative are the self-consistent Hill, the scheme Mori-Tanaka, the model of the double inclusion developed by Nemat-Nasser.

Our model assumes the selected particle dispersion is homogeneous and takes into account the morphology of the nanocomposite hierarchical [3, 4]. The main objective is the establishment of a transition model scales to predict the homogenized properties and distributions of mechanical states in a nanocomposite. That is why we must take into account a real microstructure;

Micromechanical Model for Heterogeneous Elastic Materials

Among the micromechanical models, we opted for the self-consistent approach in which physical approximation is enhanced by integrating the interaction between inclusions and inclusion-matrix interaction. Improvements of mechanical properties of nanocomposites comes in part explained by the presence of a constraint region adjacent nano-reinforcement [5]. The constraint region may be defined as an interphase between the nano-reinforcement and the matrix, result to the local interaction between the particle and the matrix.

We assumed that our particle (first inclusion) is included in a medium having the same mechanical properties as the matrix (Young's modulus and Poisson's ratio) even medium is in turn

included in the matrix (second inclusion). From there, we see that our second medium incarnates the interphase, ie to be able to model the effect of the latter we considered a material part, starting from a principle of dual inclusion whose details can be found on the book by Nemat-Nasser. In the case of a multi-phase composite, the expression for giving the stiffness tensor can be written as follows:

$$C = C_0 + \sum_{i=1}^n f_i (C_i - C_0) : \left(I + S_{Esh}^i : \left[(C - C_i)^{-1} : C - S_{Esh}^i \right]^{-1} \right) \tag{1}$$

Where f_i ($i = 1, 2, \dots, n$) is the volume fraction of each Type inclusion.

In our case we considered $n=3$ ie three types of reinforcements are exfoliated silicate, intercalated and spherical silica, S_{Esh}^i is the Eshelby tensor corresponding to the inclusion I and the I term is identity tensor. It is assumed that all inclusions 'i' in the composite multi-phase do not have the same aspect ratio and elasticity. Therefore, the composite material becomes a five-phase formed from the matrix material, to which we give the index '0' and inclusions (reinforcements), to which we give the index '1, 2, 3', respectively exfoliated silicate, silica and intercalated where each inclusion is surrounded by an interphase. From there, reinforced spheroidal particles randomly oriented transversely isotropic composite material and the general formula becomes:

$$C = C_0 + f_1 \{(C_1 - C_0) : A_1\} + f_2 \{(C_2 - C_0) : A_2\} + f_3 \{(C_3 - C_0) : A_3\} \tag{2}$$

Thus global modules compressibility k and shear μ can be written as follows:

$$\begin{cases} k = k_0 + \frac{f_1}{3} \phi_1 + \frac{f_2}{3} \phi_2 + \frac{f_3}{3} \phi_3 \\ \mu = \mu_0 + \frac{f_1}{2} \psi_1 + \frac{f_2}{2} \psi_2 + \frac{f_3}{2} \psi_3 \end{cases} \tag{3}$$

Expressions ϕ and ψ are functions of the rigidity of components.

To deal with the morphology of the equivalent particle, the hierarchical approach [5] is introduced in the model. This approach leads to the estimation of geometrical parameters such as the thickness of the equivalent particle and aspect ratio see the work of our group [5-7].

Results and Discussion

To examine the relative influence of the volume fraction of reinforcement in clay and silica, a parametric study is investigated. We assumed that the matrix polymer, the silicate sheets and the silica particle [6] are all isotropic, their elastic response is simply defined by two constants: Young's modulus and Poisson's ratio. The mechanical properties assigned to polyamide-6 $E_0 = 3$ GPa and $\nu_0 = 0.4$. According to the literature, the Young's modulus assigned to the layer silicate $E_1 = 170$ GPa, $\nu_1 = 0.23$ and the silica $E_{silica} = 88.7$ GPa et $\nu_{silica} = 0.25$ $R_{silica} = 20nm$.

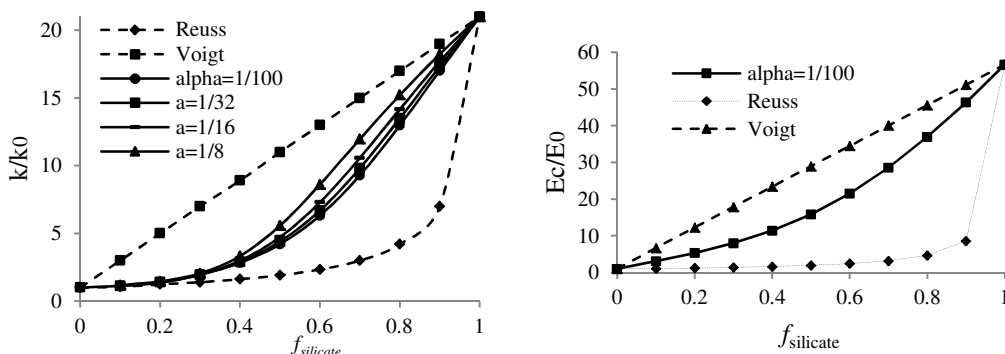


Figure 1: Effect of volume fraction of silicate

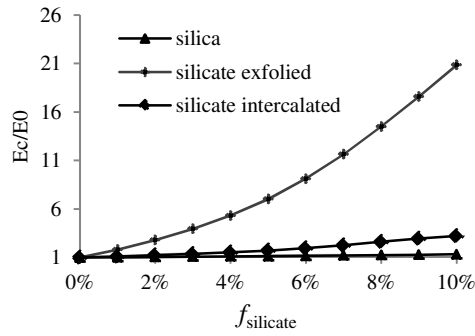


Figure 2: Effect of reinforcements on nanocomposites

Figure (3.a) showed evolution in Young's modulus as a function of the variation of the radius of the silica particle which varies from 10 to 80 nm for the thickness of the interphase ($e_i = 1, 3, 6, 10 \text{ nm}$). As for Figure (3.b) was evolution the Young's modulus as a function of the variation of the interphase thickness for different values of radius. Note that for two figures there is a modulus interphase $E_i = 10 \times E_0$ and a volume fraction of 5%. For a small particle size, the contact surface is larger which gives a high Young's modulus.

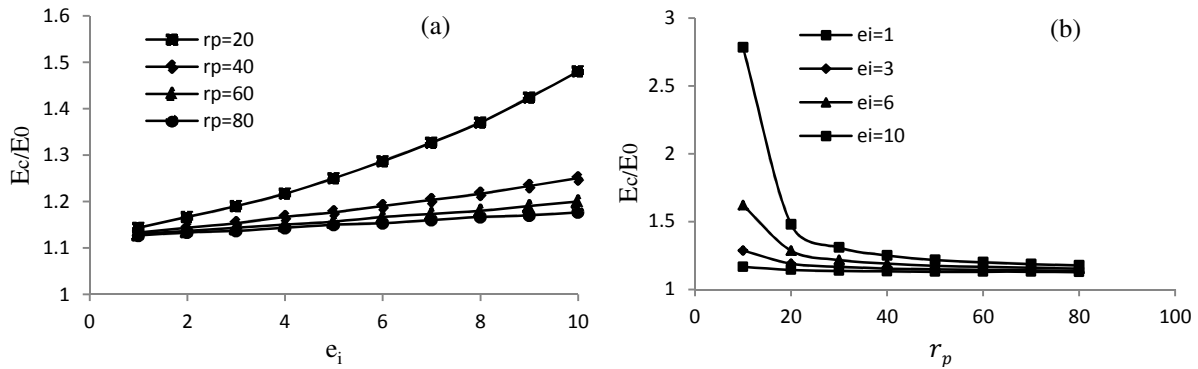


Figure 3: Contribution of dimensional silica particle (a) and interphase (b) the overall Young modulus

In this part of the work, we have proposed to characterize the composite material to a mixture containing two types of nano-fillers immersed in the PA6 polymer matrix. For this, we have three possibilities mixtures containing particles: exfoliated, intercalated, exfoliated spherical, spherical-interleaved. Once defined mixtures, our approach is to arbitrarily fix the volume fraction one of reinforcements 1% and to vary the volume of the remaining fraction of 0% to 5% reinforcement. We did the same operation for each mixture.

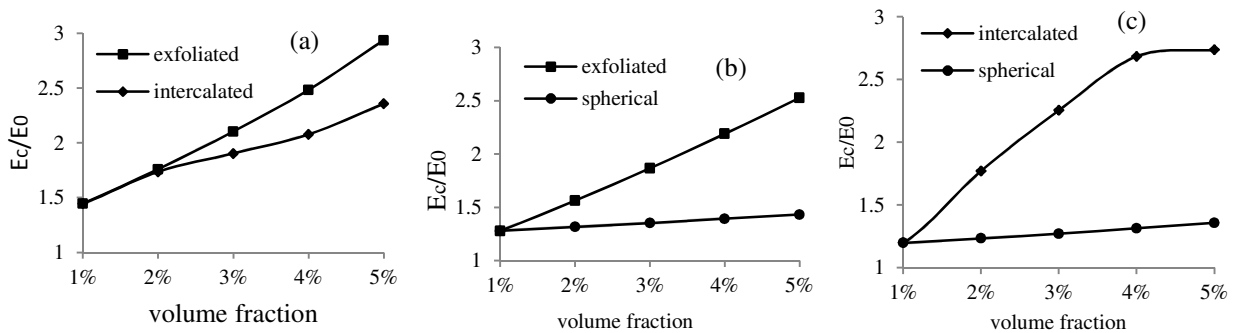


Figure 4: Effect of mixture of reinforcements on the Young's modulus: (a) silicate exfoliated with intercalated, (b) silicate exfoliated-silica, (c) silica-silicate intercalated.

Figures 4 (a, b, c) show the variation of Young's modulus E_c of a nanocomposite composed of two types of reinforcements. We note that the 1% nanocomposite intercalated silicate reinforced exfoliated silicate has a remarkable contribution to the mechanical properties relative to other combinations of reinforcements. In this part, we have proposed to characterize this composite material as mixture having three types of nano-reinforcement PA6 immersed in a polymer matrix $d_s=200\text{nm}$, $d_{001}=4\text{nm}$, $E_f=10E_0$. Subsequently, our approach has been to arbitrarily fix the volume fraction of two reinforcements to 1% and varying the volume fraction of the third reinforcement of 0 to 5% and the same operation is repeated three times for each reinforcement. Figure (5) represents the variation of Young's modulus E_c of the composite according to the variation of the volume fraction of the dominant reinforcement. Note after studying the mixture that gives good results is a mixture where the reinforcement is exfoliated dominant. with $E_c = 9.35\text{ GPa}$, $\nu=0.35$.

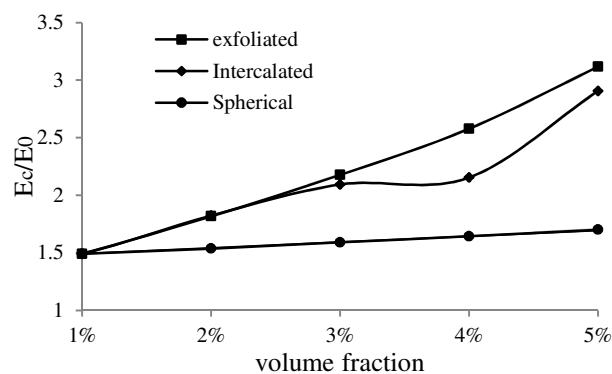


Figure 5: Effect of mixing three types of reinforcements

Conclusion

Whatever the type of reinforcements (platelet-exfoliated, intercalated platelet-spherical) nanocomposites provide for low volume fractions of inclusions, usually less than 10% of high mechanical properties, with a huge difference in weight compared to conventional composites. The main purpose of this work is show that a mixture of nanoparticles is desirable or not! To have good overall mechanical properties of the composite. Namely, the Young's modulus E and Poisson's ratio. And this by studying the variation of modulus of elasticity for the different structural parameters given in the mixture such that the volume fraction of the reinforcement, of the aspect ratio and the effect of the interphase. Analysis of the results showed a mixed nanocomposite reinforcements which presents the largest mechanical properties of nanocomposites is those with a high volume fraction of exfoliated silicate. The silica particles in the presence of silicate (clay) in the polymer matrix is low effect on the mechanical properties of the composite. While the nanocomposites in the presence of silicate or exfoliated silicate intercalated silica reinforced properties are averages. Finally, hoping this work will provide good starting bases for new advance in this field and will open the new perspectives include an experimental study may be implemented as well as analytical development work in our model may be more appropriate and give good results for mixtures of nano-reinforcements has different morphology.

References

- [1] A. Usuki, M. Kawasumi, Y. Kojima, A. Okada, T. Kurauchi, O. Kamigaito, Swelling behavior of montmorillonite cation exchanged for α -amino acid by ϵ -caprolactam. *J. Mater. Res.* 8 (1993) 1174–1178.
- [2] Y. Kojima, A. Usuki, M. Kawasumi, A. Okada, Y. Fukushima, T. Kurauchi, O. Kamigaito, Mechanical properties of nylon-6-clay hybrid. *J. Mater. Res.* 6 (1993) 1185–1189.
- [3] M. Alexandre, P. Dubois, Polymer-layered silicate nanocomposites: preparation, properties and uses of a new class of materials. *Mat. Sci. Eng.* 28 (2000) 1–63.

- [4] T.D. Fornes, D.R. Paul, Modelling properties of nylon6/clay nanocomposites using composite theories. *Polymer* 44 (2003) 4993–5013.
- [5] A. Mesbah, F. Zaïri, S. Boutaleb, J. M. Gloaguen, M. Naït-Abdelaziz, Experimental characterization and modeling stiffness of polymer/clay nanocomposites within a hierarchical multiscale framework, *J Appl Polym Sci.* 114 (2009) 3274–3291.
- [6] S. Boutaleb, F. Zaïri, A. Mesbah, M. Naït-Abdelaziz, J. M. Gloaguen, T. Boukharouba, Micromechanics-based modelling of stiffness and yield stress for silica/polymer nanocomposites, *Int J Solids Struct.* 46 (2009) 1716–1726.
- [7] K. Anoukou, F. Zaïri, M. Naït-Abdelaziz, A. Zaoui, T. Messenger, J. M. Gloaguen, On the overall elastic moduli of polymer–clay nanocomposite materials using a self-consistent approach, Part I: Theory, *Composites Science and Technology.* 71 (2011) 197–205.

CHAPTER 3:

Modern Technologies for Modelling, Simulation and Automation, Instrumentation, Measurement and Control Technologies

A Method of Determining the Direction of Two Dimensional Curves

F. Wang^{1, a}, R.K.F. Abdelmaguid^{2, b} and H.M.A. Hussein^{3, c}

¹Jiangxi College of Solar Energy Technologies, Jiangxi 33800, China

²Beni-Suef University, Production Technology Department, Faculty of Industrial Education,
Beni-Suef, Egypt

³Advanced Manufacturing Institute, King Saud University, 11421, Riyadh, Saudi Arabia

^aWangfengyin@hotmail.com, ^brgab65@gmail.com, ^chhussein@ksu.edu.sa

Keywords: Computer algorithms. Computational geometry. Direction of two-dimensional curves.

Abstract. Two-dimensional curves are represented by a list of vertices and other parameters that control the shape or curvature of the segments. In computer programming to deal with closed two-dimensional curves, it is often required to know the direction of the curve, which is reflected by the sequence of the vertex data. It can be anticlockwise or clockwise. This paper presents a robust, linear algorithm to determine the direction of a closed two-dimensional curve, by computing the total angular change of a tangent vector travelling along the curve for a complete cycle. A new, robust linear algorithm is proposed for the determination of the positional relationship of a point to a two-dimensional curve. For curves that consist of line and arc segments, which are most commonly used in engineering applications in computer aided design, the paper presents algorithms and procedures for solving the above problems.

Introduction

Two-dimensional curves are important entities widely used in computer aided design (CAD) systems and desktop publishing (DTP) systems. Typically, two-dimensional curves are defined as polylines and splines in CAD systems. These are very commonly used by industrial engineers for their amazing properties. Polyline is the most commonly used entity because profiles consisting of lines and arcs are easy to design and manufacture. A closed polyline can be used to define the profile of a part, the shape of a pocket or a hole on a plate, or an AEC column, brace, or beam etc in architectural design.

Normally, a polyline consists of a number of lines and arcs segments. Once defined, those lines and arcs are tied together as one object unless the user purposely "explodes" it. Internally a CAD system defines a polyline entity by recording a number of vertices and bulge factors, which is another form of the included angle of arcs. To automate computer aided design tasks, it is useful to develop necessary computer algorithms of two-dimensional curves. This paper deals within the method of determining the direction of a closed two-dimensional curve. The algorithms are implemented on the AutoCAD platform. It will provide basis for many other geometric algorithms.

Definition of The Problem

The Direction of Two-dimensional Curves. Normally, a two-dimensional curve is created in AutoCAD in an interactive manner. It is observed that the internal records of the vertices of a polyline may be clockwise or anticlockwise. This has caused greater complexity when processing the data of polylines: one always needs to generate two branches of his computer codes to consider two situations, one for clockwise direction and other being for anti-clockwise direction of the profile. It is thus necessary to have a fundamental algorithm to determine the direction of a two-dimensional curve. Once a curve is found to be clockwise (negative direction), the vertices and the bulge factors may be reversed properly so that only curve data of "positive" direction (normally anticlockwise) will

be generated for other applications. In the downstream applications, one then needs to consider only the situation of one direction.

For the definition of the curve direction, see Fig. 1. A two-dimensional curve, C , being smooth for each of its segments, encloses a single region, B . When one travels along the curve, if region B is on his left-hand side, it is said that the direction is positive (+); if the region is on one's right-hand side, the direction is negative (-).

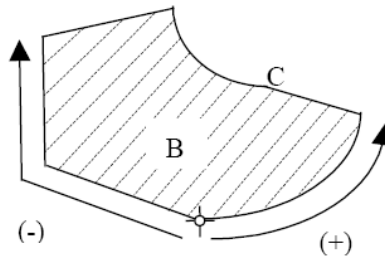


Fig. 1. Direction of a two-dimensional curve.

Related Work

Computational Geometry. Geometry is an ancient science in human history that, together with algebra played important roles to the development of other sciences. Computational geometry is a young science started in the 70s as the use of computers became popular.

Excellent reviews of the field can be found in [3-4]. Shamos [5-6] was a pioneer of this field and his PhD thesis treated a large number of geometric algorithms, which stimulated much of later research. Eventually the book of Preparata and Shamos [7] became the classic reference of the domain. The field is developing quickly. Edelsbrunner [8] describes many results of the 80s. The classic problems include intersections, simple closed path, inclusion of polygons, convex hull, range searching, and closest-point problem. Algorithms of these problems serve the foundation for computer aided design and other computer graphics applications. Boissonnat [9], and Baerentzen [10] describes the recent demand of the new concepts of computational geometry in our life.

Direction of Two-dimensional Curves. Strictly speaking, there is no direction for a closed two-dimensional curve. However, when vertices and other shape parameters are used to represent the curve, there is a sequence issue, and thus there is always a direction issue. It is caused by the sequence of the vertices. No previous work has been found to investigate this problem to the best of the authors.

Algorithm for Determining Curve Direction

Basic Principle of Determining the direction of a Two-Dimensional Curve. Let's consider a generic two-dimensional curve C on a plane. It will meet with the following conditions:

- (1) Being smooth within each segment;
- (2) Not having self-intersections;
- (3) Being closed, i.e., it's first and its last vertices are at the same position.

As a result, the curve encloses a single region, B , on the X - Y plane. If a particle travels along the curve when the enclosed region is on the left-hand side, we call the direction positive or anticlockwise; otherwise, it is negative or clockwise. To determine the direction, we introduce a vector, r , at a point $p(x,y)$ on the curve, see Fig.2. The magnitude of the vector is not of concern. Its direction is along the tangent of the curve at point p . The vector is called Tangent Vector (TGV) of the curve. When p travels along the trace of a curve the tangent vector moves with the point at a direction always following the tangent of the curve at the point p . We denote the variable of the angle of the vector as $\varphi(x,y)$ ($0 \leq \alpha \leq 2\pi$), with zero at the right direction along with the x -axis. When point p moves from $p(x,y)$ to a nearby point $p(x+\Delta x, y+\Delta y)$, there is a change in the angle of the vector,

$$\Delta \varphi = \varphi(x + \Delta x, y + \Delta y) - \varphi(x, y)$$

We call this angle the Swept Angle of the Tangent Vector (SAT) from point $p(x,y)$ to $p(x+\Delta x, y+\Delta y)$. When $\Delta\phi \rightarrow 0$, we use directive notation for the incremental swept angle, $d\phi$. In fact, $\phi = dy/dx$, the directive of the y to x . Then, we perform integration along the closed curve, getting:

$$\Phi = \int_c d\phi \tag{1}$$

Lemma 1: A closed two-dimensional curve, C , forms a single region, B . When a point p travels continuously along the curve with the enclosed region being on the left hand side of the point, from a start point P_0 all the way back to the start point, the integral of the swept angle of the tangent vector, ϕ , will be 2π . Otherwise, when the point p travels continuously along the curve with the region being on its right-hand side, from a start point P_0 all the way back to the start point, the integral value of ϕ will be -2π .

Proof: In the current problem, we do not concern about the position of the vector.

What is important in the calculation is the change in angle of the vector. As such, at any point $p(x, y)$, we can shift the vector to one point P_i inside of the curve, see Fig.3. When the point travels along the curve and the vector moves with the point, the problem is equivalent to a problem of rotating a vector around point P_i

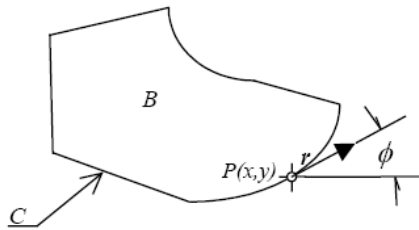


Fig. 2. Tangent Vector of curve C and its angle

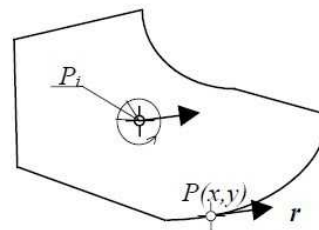


Fig. 3. Total swept angle of tangent vector.

Properties of the Swept Angle for Tangent Vector. Before we present the implementation of the algorithm, we need to show some interesting properties of the swept angle for the tangent vector of a closed curve.

1. For a smooth segment of a curve, as long as it is not self-intersected, the swept angle of tangent vector is the difference between the vector angle at the exit point and that at the entry point, and it is independent of the path of the curve.

This property is obvious. It can be proven in the same way as proving Lemma 1 by considering that the swept angle has nothing to do with position of the vector. Whenever the tangent vector is changing continuously, the total change in angle is only determined by the end and start angles of the vector. With this property, the swept angle of any curves can be easily calculated, being spline, or any other functional form,

$$\phi_g = \phi_e - \phi_s \tag{2}$$

where ϕ_g stands for the swept angle over the current segment, ϕ_s and ϕ_e for vector angles at the start and end of the current segment, respectively.

2. At the common endpoint of two segments, each of which is smooth, the swept angle is calculated by subtracting the tangent angle of 2nd segment at the start point and the tangent angle of first segment at the end point,

$$\phi_v = \phi_v^+ - \phi_v^- \tag{3}$$

where; ϕ_v is the swept angle at the vertex v , ϕ_v^+ the vector angle at the start of next segment, and ϕ_v^- the vector angle at the end of the previous segment. This property is obvious due to the definition of the SAT.

Implementation of the Algorithm Tangent Angle of Arc at Start and End Points.

Let the start point of an arc, A, be P_s , and end point P_e , the tangent angle at the start point is calculated by

$$\varphi_s = \varphi_{se} - \alpha/2 \quad (4)$$

where φ_{se} is the angle from point P_s to P_e , the angle of the chord, in the range of 0 and 2π (see Fig. 4 for its definition).

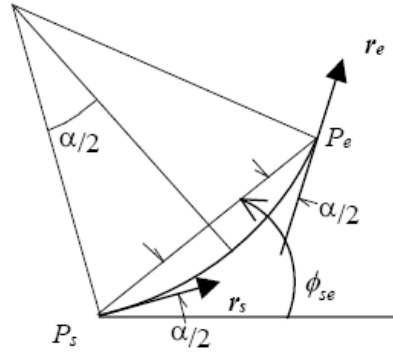


Fig. 4. Start and end angles of tangent vector

The variable α in Eq.(4) is the included angle of the Arc. When bulge factor, β is used in a CAD system internally for the arc's shape, the relationship between the bulge factor and the included angle, α is given by,

$$\alpha = 4 \arctan(\beta) \quad (5)$$

Likewise, the tangent angle at the end point of the arc is calculated from

$$\varphi_e = \varphi_{se} + \alpha/2 \quad (6)$$

It should be noted that when applying property 1 of Swept Angle of a smooth curve, given above, indicating the correctness of these formulae.

In reality, the swept angle of TGV along an arc has no need to compute as it can be obtained directly from the data that defines the arc, for example, from the bulge factor.

$$\varphi_e - \varphi_s = (\varphi_{se} + \alpha/2) - (\varphi_{se} - \alpha/2) \cong \alpha \quad (7)$$

Swept Angle of Tangent Vector at a Vertex. The second property of swept angle of TGV can be followed. Let's consider a vertex at which two segments, Arc A1 and Arc A2, are to be connected. This is the most complicated case. Any one or both of them can be a line. The principle of the computation remains the same.

Let the angle of TGV at the end of A1 be φ_{1e} , and the angle of TGV at the start of A2 be, φ_{2s} , Then, the swept angle of TGV at the this vertex vi will be,

$$\varphi_i = \varphi_{2s} - \varphi_{1e} \quad (8)$$

For a line edge, the angles of TGV at both the start and the end vertices are the same, and are equal to the angle from start to end vertex.

Implementation of the Algorithm. When a curve consists of lines and arcs, the curve can be internally represented by two series of parameters:

$$P_i(x, y) \{i = 0, 1, 2, \dots, N-1\}$$

$$\beta_i \text{ or } \alpha_i \{i = 0, 1, 2, \dots, N-1\}$$

where P_i is a vertex at point i , β_i is the bulge factors of the arc for the i^{th} segment. It can be converted to include angle α_i by Eq. 5.

The total swept angle is calculated using the following procedure

1. Transform the CAD internal data to two series table, P_i and α_i $\{i=1,2,\dots,N-1\}$;
2. Compute the Swept Angle at each vertex ϕ_i $\{i=1,2,\dots,N-1\}$ according to Eq.8.
3. Add all Swept Angles at the vertices together, resulting in Φ_v :

$$\Phi_v = \sum_{i=1}^{N-1} \phi_i \quad (9)$$

4. Add all the included angles together, resulting in Φ_α :

$$\Phi_\alpha = \sum_{i=1}^{N-1} \alpha_i \quad (10)$$

5. Add the swept angle of vertex and that of the arc

$$\Phi = \Phi_v + \Phi_\alpha \quad (11)$$

6. Output the conclusion according to the value of Φ .

Summary

One robust algorithm is presented in this paper for the determination of the direction of a two-dimensional curve. The algorithm helps computer programmers to significantly simplify their application codes for processing two-dimensional curves. With the algorithm, one always simply considers his curve in the positive direction. In order to develop the algorithm, concepts of Tangent Vector of two-dimensional curves and its Swept Angle are introduced. The direction of the curve is judged by the value of the total swept angle of the tangent vector. The second algorithm, which is based on the first algorithm, is used to determine the position of a point in relation to the curve. Concepts of Radial Vector and the Swept Angle of Radial Vector are introduced. Computations are made only on swept angles of tangent vector and radial vector in the algorithms. The first algorithm is a novel one. It uses a simple concept of integral of swept angle of tangent vector to determine the direction of a curve.

Acknowledgment

This work is supported by NSTIP strategic technologies programs, Grant number (12-INF2816-02) in the Kingdom of Saudi Arabia.

References

- [1] F. Wang, SM-Design: SMCAD User's Guide, Published by Gintic Institute of Manufacturing Technology, Singapore. (1998).
- [2] F. Wang, Development of a state-of-the-art CAD for sheet metal progressive dies: SMCAD, Proceedings of CAD/CAM/CAE for Internet & Intranet, Temasek Polytechnic, Singapore. (1998) 28-29.
- [3] P. Zhou, Editor, Algorithm Design and Analysis, Text book for higher education, Mechanical Engineering Publisher, Beijing, (1998).
- [4] R. Sedgewicw, Algorithms in C++, Addison-Wesley Pub. Company, Geometric Algorithms, pp. 347-401.

- [5] M.I. Shamos, D. Hoey, Closest-point problems, presented in 16th, Annual Symposium on Foundations of Computer Sciences, IEEE. (1975).
- [6] M.I. Shamos, D. Hoey, Geometric intersection problems, presented in 17th Ann. Symposium on Foundations of Computer Sciences, IEEE. (1976).
- [7] F.P. Preparata, M.I. Shamos, Computational Geometry: An Introduction, Springer-Verlag. (1985).
- [8] H. Edelsbrunner, Algorithms in Combinatorial Geometry, Springer-Verger. (1987).
- [9] J.D. Boissonnat, M. Teillaud, Effective computational geometry for curves and surfaces, Springer-Verlag, Berlin, Heidelberg. (2006).
- [10] J.A. Baerentzen, J. Gravesen, F. Anton, H. Aanaes, Guide to computational geometry processing, Foundations, Algorithms, and Methods, Springer-Verlag, London. (2012).

Implementation of a Voice-Control System for Issuing Commands in a Virtual Manufacturing Simulation Process

Yun Suen PAI^{1,a}, Hwa Jen YAP^{2,b}, and S. RAMESH^{3,c}

^{1,2,3}Department of Mechanical Engineering, Faculty of Engineering,
University of Malaya, 50603 Kuala Lumpur, Malaysia

^ayspai1412@gmail.com, ^bhyap737@um.edu.my, ^cramesh79@um.edu.my

Key words: Speech Recognition, Voice Control, Virtual Manufacturing, Robotic Work Cell

Abstract: Speech recognition is a technology that attempts to involve audio cues during interaction with machines, instead of being limited to just visual and touch interfaces. However, a keyboard and mouse input is an archaic method of interaction, adding on to the fact that voice control is seemingly more natural. This study aims to implement speech recognition as a form of machine control to perform simple commands in a virtual simulation process. The simulation system is an in-house developed augmented reality robotic work cell which includes a robot arm, a conveyer belt, a computer numerical control (CNC) machine, and a pellet. Issuing commands are performed via the Windows Speech Recognition software built from the Microsoft Speech Application Programming Interface (SAPI). This software is advantageous because it can be fairly accurate once trained properly, is easily modifiable by anyone regardless of the operator's programming knowledge, and is free. A macros tool is used to support the additional features of the recognition software which includes directly programmable Extensible Markup Language (XML) codes.

Introduction

Voice recognition is a technology that plays a part in contributing towards a more efficient, flexible, expressive, and transparent means of human-machine interaction. It pushes the boundaries of interactivity to achieve a sense of immersion unlike any other, which is vital in today's trend of technological approach which favors wearable technology and computing. However, the technology still requires further refinements before it is able to completely replace the more traditional input methods of a keyboard and mouse. Precision is the main source of concern for speech recognition, as the human voice comes in a varying degree of intonation, language, and interpretation. Therefore, the main objective of this study is to apply speech recognition into virtual manufacturing as a form of control by using it as a replacement in issuing fundamental commands, instead of quantifiable functions like inputting depth of cut values, the final coordinate in inverse kinematics, and so on. This limitation ensures that voice control will not interfere with operations that require high precision, yet is able to deliver a higher sense of immersion to the user. Once issuing commands start to feel natural, a simulation operation can reduce the time required to perform them.

Related Studies

The concept of a natural human interface was first coined by Bill Gates, as he predicted that voice recognition would be a key technology in replacing the traditional input methods, alongside touch and vision-based systems [1]. Voice data goes through pretreatment, feature extraction and finally recognition algorithms in its processing cycle. Pretreatment is usually conducted behind the scenes to filter the noise. Algorithms like Mel Frequency Cepstrum Coefficients (MFCC), linear predictive coding (LPC), and Fast Fourier Transformation (FFT) fall under feature extraction. Finally, the Hidden Markov Models (HMM) creates the recognition system by calculating the output probability. Fractional Fourier transform (FrFT) which is based on FFT has been used to extract features for signal processing [2]. In terms of efficiency, it is similar to that of the typical Fourier

transformation. This method showed an improvement when compared to the MFCC at a high signal-to-noise ratio. This means that the FrFT method can be applicable in other areas like synthesis or audio enhancement, though in the case of virtual simulations, the Discrete Fourier method should prove sufficient.

Existing Issues with Speech Recognition. The main limitation present in commercial speech recognizers is the effects of ambient noise that causes recognition errors in the control system [3]. Therefore, it was found that interfacing the recognizer with a hybrid noise suppression filter can enhance the accuracy even under noisy conditions, though it only works for stationary noises. Furthermore, if the microphone comes with a built-in surround noise cancellation, the enhancement would not be too drastic. In a manufacturing environment, ambient noise can be a major concern due to its direct effect on operators in the long term [4]. The Cave Automatic Virtual Environment (CAVE) is a recently developed system that is able to produce a virtual environment to represent the sound level present. Though no speech recognition system was used, the acoustic measurement that was utilized can prove useful in determining the optimum operation position without stalling production or the simulation.

With regards to user interface, consumer electronics is a suitable reference to generate guidelines on interfacing voice control applications so that it remains straightforward and robust [5]. It should give the user the freedom of choice for input, consistency, an appropriate feedback, consideration of the user's expectations, and avoid overloading the channel to maintain precision. These steps are naturally present in this proposed system, making it very accessible to even penetrate the mainstream market.

Microsoft SAPI and SDK. The Microsoft SAPI and software development kit (SDK) proved to be a versatile and efficient tool from numerous research utilizations. A recent study developed a voice control system in a robotized work cell, which is similar to the augmented reality case study for this proposed implementation [6]. Its main focus lies in the specific requirements of a manufacturing cell and considers the mutual influence between the semantic analysis, recognition, syntactic, and spontaneous effects. The underlying rules are that these mutual influences are taken into heavy consideration, the optimal solution for voice variation is by defining a sublanguage, some sort of mechanism for spontaneous speech is required coupled with an immediate reaction to commands, and an easy method for semantic analysis. Microsoft SAPI was used for the online-based aspect of the study as it covers most of the aforementioned factors. ViRbot, a control system for mobile robots that depends on a Microsoft SAPI-powered speech recognition engine, was also developed [7]. A conceptual dependency (CD) primitive is generated with each voice command, which then procedurally generates subtasks to fulfill the command. Since XML notations are supported, the recognition errors were drastically reduced, thus increasing the overall efficiency. Interestingly, command lines which are different but carry the same meaning was able to be recognized by the robot since the CD representation is the same.

Robotic related applications to this software do not end there, as it was implemented for commanding industrial robots as well [8]. It was proven that the technology is suitable for industrial use with reliable results, though it needs to be noted that when it comes to number commands, fixed rules should be avoided to maintain the flexibility. Another issue is that direct voice control on a robotic arm, or any manufacturing tools, must consider ambient noise that is present in the environment that may obstruct the recognition process. Another study combined speech recognition with a web-based control system for a robotic work cell [9]. This allows an operation to be remotely controlled purely through voice that is not limited to pre-defined voice commands. A quasi-natural language system based on the Microsoft SAPI as well allows the system components to be distributed among the client and server. However, since the scope of grammar has been expanded and not limited to voice commands, naturally false recognitions may happen more frequently. This is not to say that an error-free function is impossible, but as of now, if machining is involved, it is best to limit the usage of voice recognition. Therefore, this shows that the Microsoft SAPI has low recognition time and high accuracy. For tele-operated robots, such as the Lego Mindstorm, web-based control via WiFi works in a similar fashion [10]. Limitations of such a system have been

tested with multiple case studies, and since both WLAN and IR are the primary method of communication with the robot, latency that exists in wireless communication needs to be considered.

Multimodal interface adoption that includes both gesture and speech is an interesting aspect as well, when applied in fields that can greatly benefit from them, such as architectural work or interior design [11]. A system dubbed as the Open Gesture Recognition Engine (OGRE) system uses both hand motion and speech recognition and comprises of various in-house developed modules, with Microsoft Speech SDK included for voice synthesizing. Most of the restrictions that exist is due to the gesture module, and as for the speech module, the results show that it is favorable when tested on subjects with minimal experience. Therefore, another study excludes the use of bodily gestures and focuses solely on spoken dialogue [12]. This exclusion negates the previously mentioned limitations, and due to the flexibility of Microsoft SAPI, it is able to couple with any API that is SAPI-compliant and dynamically define grammars with XML that can be understood by the robot. The bridge between language and vision exist due to the common memory structures since both of them use symbols for the robot to understand.

Robotics and design tasks aside, training is a ground that needs to be further analyzed for voice recognition to be implemented successfully into simulation systems. A recent study utilizes the Microsoft SAPI as the speech engine in their system for engineering training [13]. The training includes a virtual engine for system control simulation, which contains some resemblance to the virtual manufacturing in this study. The developed intelligent agent facility (IAF) was able to enable multimodal input such as natural spoken language analysis. In this aspect, the voice commands are able to interpret and provide two-way communication by converting the language into scripts. The data from the scripts are used for animation, arm motion, and facial expression.

Application of Other Speech Recognition Tools. Speech recognition has been used for math equations by having it produce equations in digital form. The main challenge is of course the large dictionary, and a recently developed system called Mathifier, places a limitation by following the characteristics of mathematical equations that requires specific grammar structures [14]. This is similar to limiting the engine into recognizing only machine commands instead of a wide array of operations. Systems like Mathifier has a great support for English language as well, but when it comes to support for other languages or those who do not speak English fluently, certain considerations must be taken. Through studies with the Dragon system, it was found that native speakers produce significantly higher accuracy scores, which concludes that single-speaker dependency still requires constant research [15]. Further use of voice recognition systems is highly encouraged to test these boundaries.

Methodology

The interface of the speech recognition allows the user to code for both speech recognition and text-to-speech, as well as offers two levels of access; high-level objects and low-level objects. For this study, the high-level access is utilized because it is more suited for minimalistic voice commands compared to the latter which is designed for sophisticated orders but runs the risk of lower precision, which is not an option in a machining simulation. Figure 1 shows the high-level API that is able to call low-level objects to perform the tasks.

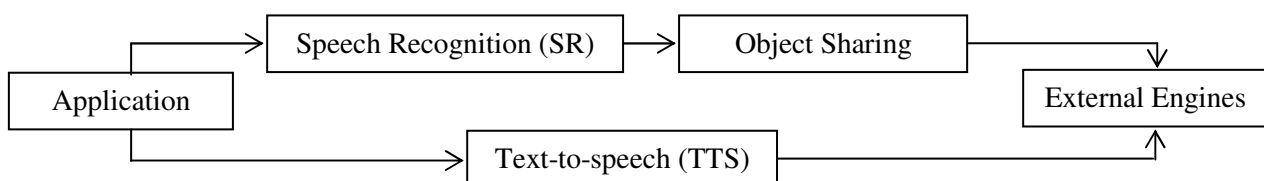


Fig. 1. Architecture of the high-level API

For the speech recognition section, initialization of the Object Linking and Embedding (OLE) is done by calling the “*CoInitialize*” function to create a Voice Command for the application. OLE is

automatically able to launch the specific dynamic-link library (DLL) that corresponds with the application. A notification sink is registered, which is a function used to callback notifications when something happens, and is also required to create a voice menu. Multiple voice menus are possible depending on the number of applications running on the PC. This means that two simultaneous simulations can be performed, or a simulation program coupled with data tabling programs, without any confusion occurring between the voice operations of the running applications. This is done via the “*gpIVoiceCommand*” function. Finally, once all operations are finalized, the OLE is released in the Windows handler. The full sequential functions are detailed in Figure 2, though at this point of time, no actions are taken yet since only recognition is conducted without TTS.

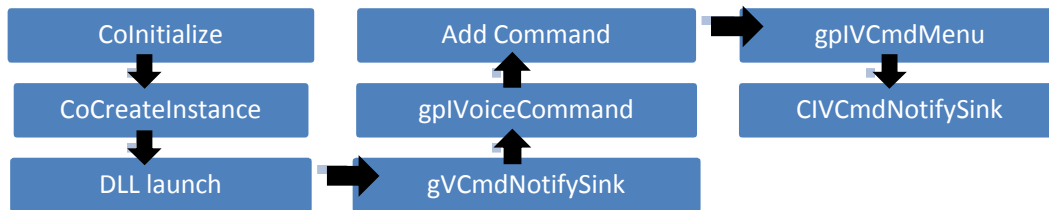


Fig. 2. Program sequence of the speech recognizer

To get the system to actually reply back in English to the operator as a form of feedback to confirm a successful operation, voice text is necessary. The TTS engine is able to output audio depending on the preceding notification sink. Fourier transformation is used to process the voice data, especially when the audio samples are extremely similar. In general, Fourier transformation uses sinusoidal curves to characterize a waveform. It is defined as

$$F(k) = \int_{-\infty}^{\infty} f(x) e^{-2\pi i k x} dx. \quad (1)$$

Since the waveform consists of sample signals, the discrete transformation is then defined as

$$X_k = \sum_{n=0}^{N-1} x_n e^{-\frac{2\pi i}{N} kn} \text{ where } k = 0, \dots, N - 1. \quad (2)$$

The discrete Fourier transformation is able to transform a voice input and sample a continuous function so long as it has a finite duration. The default female cyber voice is embedded into the Microsoft Voice system, but for the general use of manufacturing simulation, it is not necessary to alter this since it will require a low-level API which is needlessly complex in this context.

The Windows Speech Recognition macros further extends the capabilities of the speech recognition tool by utilizing XML codes as shown in the figure below which is able to issue various English language commands triggered by voice commands. This eliminates the need for complex programming because XML grammar is able to interpret English accurately. Figure 3 shows the basic layout of an XML code which immediately allows the system to recognize any English word within the “*listenFor*” function and perform an immediate reply through the “*speak*” function. The priority function on the code tells the system to ensure the macros has maximum importance over any other Windows core functions, and the question mark at the “*?computer*” indicates that the word is optional when issuing the command, which is similar to CD primitives.

```

<?xml version="1.0" encoding="UTF-16"?>
<speechMacros><command priority="100">
<listenFor>Hello ?computer</listenFor>
<speak>Yes, sir?</speak>
</command></speechMacros>
  
```

Fig. 3. Layout of an XML code

This powerful set of macros is able to perform both individual tasks and multiple tasks in series. The virtual simulation processes that will be used runs on the Windows platform, and so it is necessary for the voice recognizer engine to know each keyboard and mouse function that can be dictated, and placed into the XML code in the way where the voice synthesizer can utilize the TTS engine to understand the commands. Additionally, the macros provides two forms of feedback; visual text via the speech widget docked on the screen, and audio confirmation programmed by the operator. Since one of the aims of this study is a higher immersion, audio feedback is favored as it allows the operator to focus on the visualization of the simulation and not the computer screen.

Voice Control in Robotic Work Cell Simulation. The simulation is an augmented reality-based robotic work cell which is created via Visual C++ programming, OpenGL library, and ARToolKit. A graphical user interface (GUI) is not included and the simulation runs purely from compilation of the codes involved in building it. Figure 4 depicts the work cell, which is rendered with OpenGL and tracked with ARToolKit. In this simulation, an offline programming method is implemented to teach the robot arm coordinates in space. The end effector of the arm is manipulated with a marker cube, and mouse operations will save the coordinate of the end effector. Inverse kinematics according to Denavit-Hartenberg's theorem is used to calculate each of the joint angles of the robot. Part of the simulation involves mouse operation to pick and place a virtual object around; if the user clicks the left button and holds it down, the virtual objects is picked, i.e. snaps to the manipulator, and letting it go places the object down, i.e. unsnaps the object. To achieve this in the XML code, the Autohotkey, which is a macro program, gives the additional function of "mousedown" and "mouseup" functions.

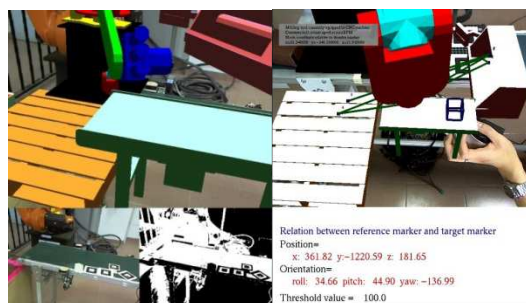


Fig. 4. Augmented reality robotic work cell simulation

The XML code for the simulation process covers the launching of the application until the closing, with a vocal reply assigned to each command, as shown in Table 1. Anytime throughout the simulation, the operator can choose to end the voice recognition simply by saying "stop listening" to pause the system if he or she wishes to switch to keyboard input, and then resume anytime by saying "start listening."

Table 1. List of voice command in the XML code

Voice Command	Function	Computer Reply
Run program	debugs program	initializing robotic work cell simulation
Create work cell	enters key to generate work cell	generating work cell
Save point	saves current coordinate of manipulator into an output file	saving current point
pick	snaps virtual object to manipulator	picking object
place	unsnaps virtual object	placing object
Remove work cell	removes the work cell	removing work cell
End program	ends the program	closing simulation

Discussion

An analysis was conducted on the sound wave of the user to determine the sound clarity and loudness of the input sound which is recorded from the microphone using Audacity, a digital audio

recording software. The user firstly records himself or herself saying “Hello, nice to meet you” in the same intonation, volume, and pronunciation when issuing commands, to collect the sound data in waveforms. Using the FFT algorithm, the region of data is converted into a power spectrum, which represents the energy present in each frequency. A higher vertical or decibel value represents a louder sound. The highest attained decibel is at a frequency of 521Hz which lies between the range of 469Hz to 603Hz. This analysis allows us to inspect the degree of acceptance of sound data for the microphone and how much is being understood by the system. The results in Figure 5 show that each audio input is sufficiently loud and can easily be distinguished from the ambient noise present, boosting the signal-to-noise ratio.

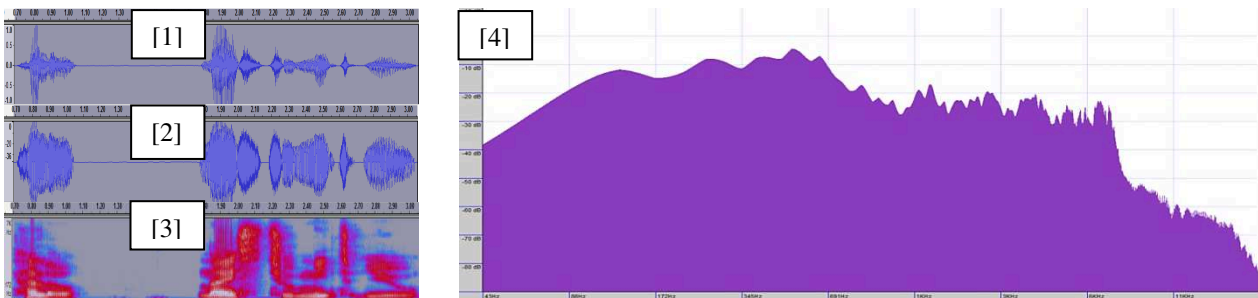


Fig. 5. Waveform of the recorded sound displayed in the unit of (1) Frequency, Hz, (2) Decibel, dB, (3) Spectrum colour, Hz. (4) Graph plotting the Decibel against Log Frequency interpolated using FFT algorithm

The word error rate (WER) method is used to determine the accuracy of the overall system since in general, a higher accuracy indicates a higher level of understanding. WER is calculated with the following equation:

$$WER = \frac{S+D+I}{N} = \frac{\text{Wrong commands}}{\text{Total Commands}} \times 100. \quad (3)$$

Where S is the number of substitution, D is the number of deletion, I is the number of insertion, and N is the total number of words. This equals to the percentage of wrong commands over total commands[14]. The case study is divided into a trained and untrained test for WER, and Table 2 summarizes the results. It is found that when 30 commands were issued, the trained system produces a WER of only 3.3%, while an untrained system produces a WER of 20.0%. This shows that if the SAPI is trained accurately, the voice command is reliable.

Table 2. Comparison result for robotic work cell simulation

	WER (%)	Correct Commands	Wrong Commands
Trained	3.3	29	1
Untrained	20.0	24	6

However, it needs to be understood that a higher degree of understanding a command does not entirely depend on the value of WER where lower WER indicates higher accuracy, since it has been demonstrated before that true understanding depends on more than high recognition accuracy[16]. As long as the experiment conducted matches the optimization objectives or the specific conditions, understanding becomes easier despite having a higher WER. Therefore, the WER value is a rough, though fairly dependable assumption on the degree of which the words are understood by the system, but is not indicative of the true accuracy.

Conclusion

The key point in speech recognition is that currently, it is still almost impossible to make it error-free. Therefore, utilizing the technology is only useful for automating common activities like

issuing commands. Due to the demand of occasional manual intervention, the transition between traditional and voice input needs to be seamless.

Acknowledgements

Thank you to the Department of Mechanical Engineering, Faculty of Engineering, University of Malaya, for providing the necessary facilities to support this study. This work was supported by the Fundamental Research Grant Scheme (FRGS) under Grant Number: FP026-2013A.

References

- [1] Lu, J.-n., et al., *Human-machine Interaction Based on Voice*. AASRI Procedia, 2012. **3**(0): p. 583-588.
- [2] Sarikaya, R., G. Yuqing, and G. Saon. *Fractional Fourier transform features for speech recognition*. in *Acoustics, Speech, and Signal Processing, 2004. Proceedings. (ICASSP '04). IEEE International Conference on*. 2004.
- [3] Chan, K.Y., et al., *A hybrid noise suppression filter for accuracy enhancement of commercial speech recognizers in varying noisy conditions*. Applied Soft Computing, 2014. **14**, Part A(0): p. 132-139.
- [4] Aurich, J.C., et al., *Noise investigation in manufacturing systems: An acoustic simulation and virtual reality enhanced method*. CIRP Journal of Manufacturing Science and Technology, 2012. **5**(4): p. 337-347.
- [5] Gamm, S. and R. Haeb-Umbach, *User interface design of voice controlled consumer electronics*. Philips Journal of Research, 1995. **49**(4): p. 439-454.
- [6] Rogowski, A., *Industrially oriented voice control system*. Robotics and Computer-Integrated Manufacturing, 2012. **28**(3): p. 303-315.
- [7] Savage, J., et al., *ViRbot: A System for the Operation of Mobile Robots*, in *RoboCup 2007: Robot Soccer World Cup XI*, U. Visser, et al., Editors. 2008, Springer Berlin Heidelberg. p. 512-519.
- [8] Pires, J.N., *Robot-by-voice: experiments on commanding an industrial robot using the human voice*. Industrial Robot: An International Journal, 2005. **32**(6): p. 505 - 511.
- [9] Rogowski, A., *Web-based remote voice control of robotized cells*. Robotics and Computer-Integrated Manufacturing, 2013. **29**(4): p. 77-89.
- [10] Ayres, T. and B. Nolan, *Voice activated command and control with speech recognition over WiFi*. Sci. Comput. Program., 2006. **59**(1-2): p. 109-126.
- [11] Sales Dias, M., et al., *Using Hand Gesture and Speech in a Multimodal Augmented Reality Environment*, in *Gesture-Based Human-Computer Interaction and Simulation*, M. Sales Dias, et al., Editors. 2009, Springer Berlin Heidelberg. p. 175-180.
- [12] Kulyukin, V., *Human-Robot Interaction Through Gesture-Free Spoken Dialogue*. Autonomous Robots, 2004. **16**(3): p. 239-257.
- [13] Wasfy, A., T. Wasfy, and A. Noor, *Intelligent virtual environment for process training*. Advances in Engineering Software, 2004. **35**(6): p. 337-355.
- [14] Batlouni, S.N., et al. *Mathifier*; *Speech recognition of math equations*. in *Electronics, Circuits and Systems (ICECS), 2011 18th IEEE International Conference on*. 2011.
- [15] Coniam, D., *Voice recognition software accuracy with second language speakers of English*. System, 1999. **27**(1): p. 49-64.
- [16] Wang, Y., Acero, A., and Chelba, C., *Is Word Error Rate a Good Indicator for Spoken Language Understanding Accuracy*, in *IEEE Workshop on Automatic Speech Recognition and Understanding 2003*: St. Thomas, US Virgin Islands.

Non-Zero Multi-Valued Decision Diagram (NZMDD) based Synthesis of Multi-Valued Logic (MVL) Functions

Adib Kabir Chowdhury^{1, a}, Nikhil Raj^{1, b} and Ashutosh Kumar Singh^{2, c}

¹Dept. of Electrical and Computer Engineering, Curtin University, Miri, Sarawak, Malaysia

²Dept. of Computer Application, National Institute of Technology, Kurukshetra, India

^achowdhury_adib@yahoo.com, ^bnikhilquick@gmail.com, ^cashutosh@mail.nitkkr.ac.in

Keywords: Multi-valued logic, decision diagrams, logic synthesis, logic gate, evolutionary algorithm.

Abstract. In this paper a method for synthesizing Reduced Multi-Valued Logic Networks (RMVLNs) using NZMDD is presented. MVL functions represented as large MVLNs are reduced by RMVLN. The detailed working of NZMDD method is presented elaborately in this paper. It is observed that reduced average Product Term (PT) is achieved in MVL synthesis using NZMDD. Experimental analysis is carried out by examining randomly generated 49998 non-sequential benchmark circuits. An improvement average PT reduction of 12.486% is noted in comparison to evolutionary ACO-MVL algorithm.

Introduction

Over the last two decades, synthesis and simplification of MVL functions has become a major research field of study. MVL is defined as a non-binary logic and involves the switching between more than two states [1-5]. There are several researches of MVL synthesis based on Decision Diagrams (DD). According to Files et.al (1997), the MVL functions can be functionally decomposed using the decision diagrams [6]. DDs can also be used to represent and manipulate MVL functions. The DD packages as discussed in the paper by Dreschler et.al (1999) is based on recursive synthesis operations. According to the author the approach discussed can be easily utilised to prototype the MVL DD packages [7]. Dreschler et.al (2000) utilised the decision diagram for the synthesis of MVL specifically MVL Networks by developing an edge-mapping approach for MVLN. His resulted circuits had linear size with respect to the initial DDs [8]. Miller et.al (2002) examined the constructions of MDDs. The evaluation was achieved by comparing the recursive MIN and MAX as primitive operations in MDD and using the cyclic negations and complements as MDD edge operations to reduce the MDD node count [9]. Jiang et.al(2003) studied the optimum functional evaluation problem for a multi valued relation. The Generalized Cofactoring Diagram(GCD) proposed in this paper was tested on multi valued relations which can be used in logic simulation, software synthesis for embedded control applications and functional decomposition in logic synthesis [10]. It has been observed that many existing algorithm requires more hardware compared to evolutionary algorithms [1]. Thus an effort of reducing the PT for synthesizing MVL functions has been undertaken in this paper.

The represents a tree-like decision diagram NZMDD which is an extension of the existing Multi-Valued Decision Diagram (MDD). Firstly the MVL function is represented as the RMVLN. RMVLN is reduced to only two rows in height. Later RMVLN is mapped to NZMDD for synthesis process. The synthesized compact form of NZMDD is evaluated as MV logic expressions. MVL gates such as, WINDOW LITERAL, EXTENDED AND, MIN and MAX is used to realize the logic expressions. Two sets of randomly generated benchmark circuits are generated to evaluate the experimental results. First set initially consisting of 1 million randomly generated MVL functions, out of which 19600 circuits were used to represent 3-valued MVL synthesis. 4-valued 49998 MVL benchmark circuits were used for synthesis and comparing against ACO-MVL algorithm.

Proposed Methodology

In this section a description of nodal logic gates are presented. A detailed elaboration of RMVLN is introduced and discussed that how NZMDD is used to synthesize from RMVLN. The structure of NZMDD and its working are elaborately discussed. A brief sight of MV logic expression is presented to show how these are used to form the circuits.

Model of Reduced Multi-Valued Logic Network (RMVLN) and its Nodal Logic Gates. Multi-Valued Logic (MVL) functions are represented as a Reduced Multi-Valued Logic Network (RMVLN). RMVLN's are formed as a directed acyclic graph which consists of vertices V and edges E . The graph is represented as $C = (V, E)$. One of the basic cell's which comprises of an Initial Input (II) or Initial Output (IO) is labeled with each of the vertex $v \in V$. There exists a set of fundamental cells in RMVLN which consists of WINDOW LITERAL, EXTENDED AND, MIN and MAX logic gates. If an output of a cell related with u is connected to the input of another cell related with v , then there exists an edge $E = (u, v)$ from vertex u to v . The vertex information about their input and output is embedded in every edge. The first node of the network is labeled as II since it has no incoming edge. Nodes that have no outgoing edges are labeled as IO . The basic cells interact with each other through edge and later help forming logic expressions. The network has a maximum of two rows of nodes. Incoming and Outgoing edge of a node is considered to decide the form of fundamental cell and their inputs.

In a RMVLN the II values are determined from an ordered finite set S , where $S = \{0, \dots, k-1\}$ and k denotes the logic levels. Terminals $T = \{T_0, T_1, \dots, T_l\}$ are available for each of the II . Terminal values are determined by the ordered finite set T_s , where $T_s = \{1, \dots, k-1\}$. The terminal values for initial input x is defined as $T_i(x_i) = \{1, \dots, k-1\}$.

A WINDOW LITERAL consisting of bounds $\{a, b\}$ and $(a, b) \in S$, $[0 \leq a \leq b] < k$ has one input and output. As proposed in [11] for a given input x with bounds $\{a, b\}$ the literal or short literal is defined as:

$${}^a x^b = \begin{cases} b & \text{if } x = a \\ 0 & \text{otherwise} \end{cases} \tag{1}$$

Where $a_1, a_2, \dots, a_n \in R$, $b_1, b_2, \dots, b_n \in R$ and $0 \leq \{a, b\} \leq (k-1)$ and b is called the value of the literal. In an MVL function ${}^a x_1^b$ and ${}^a x_2^b$ represents the value of a minterm. Window literal helps to form the representation of non-zero minterms, with the assistance of coordinate (x_1, x_2) . Considering coordinate $(x_1, x_2) = (2, 1) = 2$ the minterm is retrieved from 3rd column 2nd row of the function. Since the minterm is 2, then $b = 2$. $x_1 = 2$ therefore $a_1 = 2$ and $x_2 = 1$ therefore $a_2 = 1$. Hence the literal could be represented as ${}^2 x_1^2 \bullet {}^1 x_2^2 = 2 \bullet 2 = 2$. Therefore an ideal minterm could be represented as MIN operation of two WINDOW LITERALS as ${}^{a_m} x_1^{b_n} \bullet {}^{a_m} x_2^{b_n}$ where $a_m \neq a_n, b_n = b_n$ and:

$${}^{a_1} x_1^{b_1} = \begin{cases} b_1 & \text{if } x_1 = a_1, \quad \text{where } b_1 = \text{min term value} \\ 0 & \text{otherwise} \end{cases} \tag{2}$$

$${}^{a_2} x_2^{b_2} = \begin{cases} b & \text{if } x_2 = a_2, \quad \text{where } b_2 = \text{min term value} \\ 0 & \text{otherwise} \end{cases} \tag{3}$$

Considering a given input of ${}^a\vec{x}_1^{b_1, b_2}$ and x_2 an EXTENDED AND operator as proposed in [12] is defined as below:

$${}^a\vec{x}_1^{b_1, b_2} \bullet x_2 = \begin{cases} b_1 & \text{if } x_2 = b_1 \text{ and } x_1 = a \\ b_2 & \text{if } x_2 = b_2 \text{ and } x_1 = a \\ 0 & \text{otherwise} \end{cases} \quad (4)$$

Where $0 \leq \{a, b, x_1, x_2\} \leq (k-1)$ and x_2 determines the value of the operator. If there exists an implicant from a MVL function as ${}^0x_1^1 \bullet {}^1x_2^1 + {}^0x_1^2 \bullet {}^2x_2^2$. The implicant can be simplified using EXTENDED AND operator. The simplified implicant can be represented as below ${}^0\vec{x}_1^{1,2} ({}^1x_2^1 + {}^2x_2^2)$. Considering coordinate $x_1 = 0$ and $x_2 = 2$ the implicant achieves ${}^0\vec{x}_1^{1,2} (0 + 2) = {}^0\vec{x}_1^{1,2} \bullet 2$, where $x_2 = 2$ and the output is 2.

Non-Zero Multi-Valued Decision Diagram (NZMDD). Functions ranging in $f : \{1, \dots, k-1\}^n \rightarrow \{1, \dots, k-1\}$ represents a NZMDD. This decision diagram only maps the non-zero minterms in the multi-valued logic network. Hence the edges from a node that are relevant to the non-zero minterms are considered and mapped to the RMVLN. From root to terminal the nodes are defined from a set $N = \{ {}_0N_0, {}_0N_1, \dots, {}_rN_n \}$ where $r = \{0, 1\}$. A node contains the fundamental cells. Based on the incoming and outgoing edges the cell is selected. Each internal node has minimum one outgoing and maximum $k-1$ outgoing edges, where for a particular edge $e_x \rightarrow T_t(x_i) = \{1, \dots, k-1\}$. Each ${}_rN_n$ has an if-else clause to determine the flow of incoming edges. The flow leads to the non-zero terminal of the decision diagram. NZMDD does not contain vertices with isomorphic sub-graphs or with all successors pointing to the same node. On all such paths of this DD the variables are not encountered in the same order. Hence NZMDD is reduced but not ordered. The remaining of this paper focus on reduced NZMDD.

The function $f(x_1, x_2) = [012111000]$ is a two variable three valued vector presented as shown Figure 1. Figure 2 exhibits a diagram of a reduced and ordered MDD of the same function and Figure 3 represents diagram of reduced NZMDD.

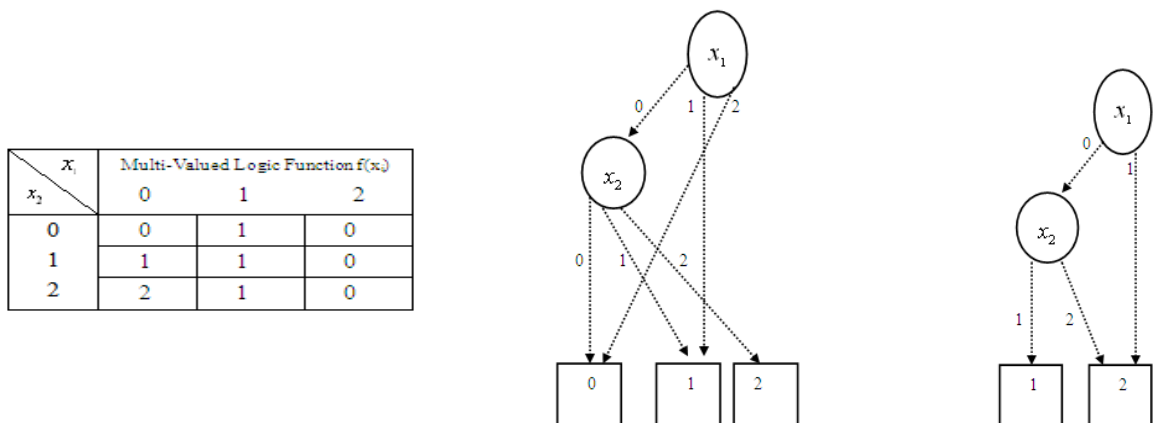


Fig. 1. Matrix of Function $f(x_1, x_2)$ Fig. 2. Ordered-Reduced MDD Fig. 3. Reduced NZMDD

A directed acyclic RMVLN can be constructed based on function $f(x)$ for which a corresponding NZMDD can be generated as below:

- I. Nodes are labeled with II and IO . Terminal nodes ${}_0N_{0,0}N_1, \dots, {}_rN_n$ are created, where the value of N is $N \in T_i(x_i) = \{1, \dots, k-1\}$.
- II. In reduced RMVLN for each of the II a vertex or variable is created in the NZMDD. The node checks all non-zero minterm $\sum_{i=0}^n f(x_1^i, x_2^i)$.
- III. Based on the nodal clause the outgoing edge points to the terminal nodes. The logic gates of the reduced RMVLN are visited in a topological order. Each of the logic gates has its corresponding NZMDD operation which is carried out.

The two rows of reduced RMVLN assure a complete visit of all the nodes in a topological manner. This also ensures that all input edges are known before it is evaluated through logic gate expression. After visiting all the nodes the IO 's of the NZMDD is evaluated.

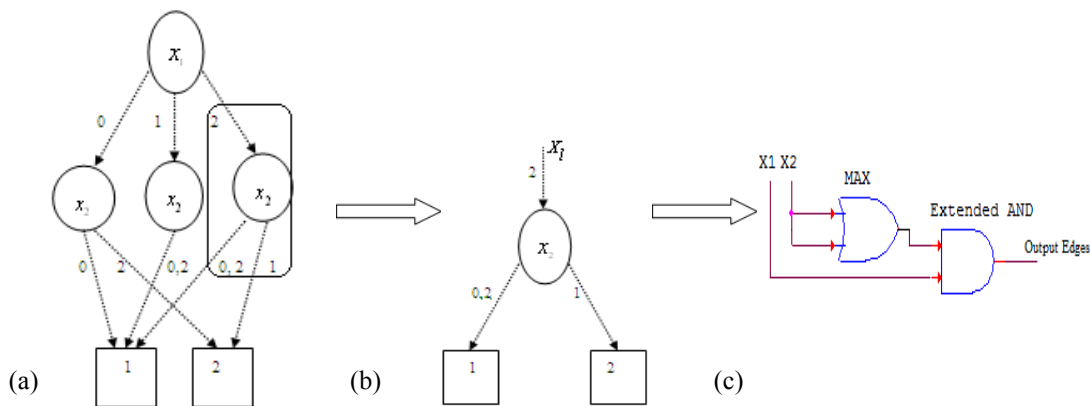


Fig. 4. A Nodal Simulation of NZMDD using MAX and EXTENDED AND

In Figure 4 an example of a nodal simulation of NZMDD is shown through logic gates. The logic gates consists of EXTENDED AND and MVL MAX gate. The input to gate corresponds to the outgoing edge of x_1 and outgoing edge of x_2 . Input to the MAX gate depends on the repeated incident edge of x_2 . The output edges of the gates correspond to the nodal relation that is represented by the NZMDD.

Synthesis of MVL Function using NZMDD

Consider an NZMDD representing a k valued two variable function which is initially provided for the synthesis purpose. The function $f(x)$ is the cumulative set of all sub-functions of the main $f(x) = \{Z_0(x) + Z_1(x) + \dots + Z_n(x)\}$. Each of the sub-function's representing intermediate nodes of NZMDD. Root node and Terminal nodes are not considered as sub-functions of the DD. Each $Z_n(x_2)$ consisting variable x_2 with input edges from x_1 and outgoing edges from the node are mapped to a set of logic gates. The incoming edges and outgoing edges of $Z_n(x_2)$ is represented as $e_{a_0}, e_{a_1}, \dots, e_{a_n}$ and $e_{x_0}, e_{x_1}, \dots, e_{x_n}$. If the function being computed is $f(x)$ then the number of logic

gates require can be represented by $\left(\sum_{i=0}^n Z(x_i) \right) \cdot \left(\sum_{j=0}^m e(x_j) \right)$. All the sub-functional output edges are

input to a MAX gate. The output from the MAX gate is the final output of the function $f(x)$. In order to compute the functions the basic gates which are available are EXTENDED AND, MIN, MAX and WINDOW LITERAL. It is assumed that each intermediate node is referring to a

fundamental logic cell, where the inputs are from incoming edge $e_{a_0}, e_{a_1}, \dots, e_{a_n}$, outgoing edge $e_{x_0}, e_{x_1}, \dots, e_{x_n}$ and output is terminal node $T_i(x_i) = \{1, \dots, k-1\}$.

Each incidental repeating outgoing edge of intermediate node of NZMDD translates into EXTENDED AND and MAX gate. Other outgoing non-incidental edges are translated into MIN gate. As shown in Figure 5 three inputs to the MAX1 gate originate from the repeating outgoing edge of x_2 . The predecessor edge of x_2 and output from MAX1 gate serves as the input to the EXTENDED AND. Non incidental outgoing edge for x_2 and predecessor edge serves as the input for MIN gate. Output edges of EXTENDED AND and MIN serves as the final input for MAX2 gate. The MAX2 gate produces the final value for the specified sub-function.

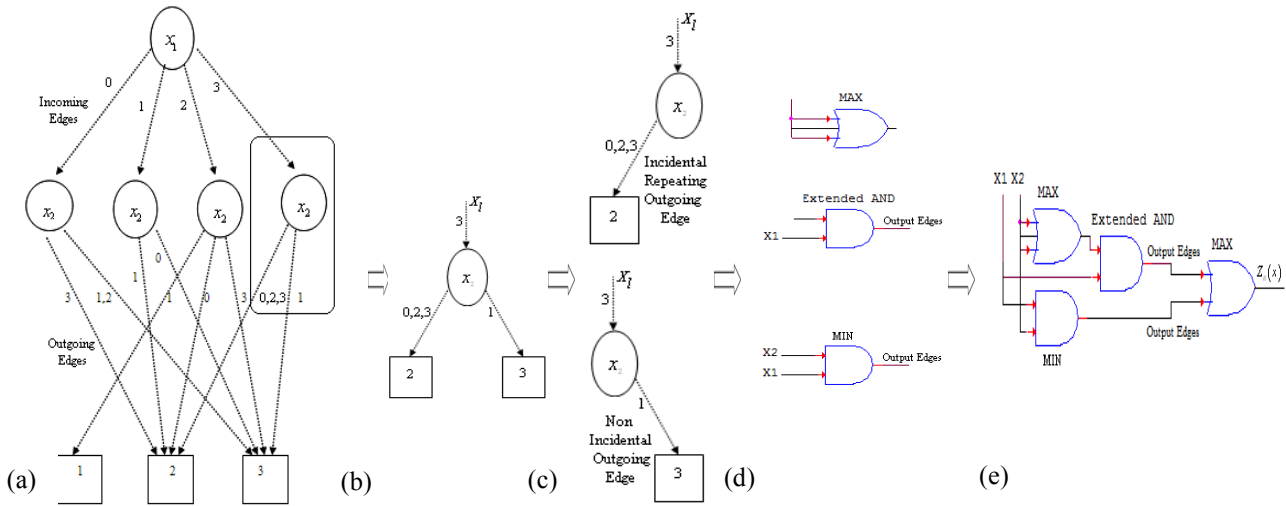


Fig. 5. A 4 valued 2 variable MVLN, its sub-functional synthesis to MVL gates

The circuit portion in Figure 5(d) & 5(e) shows the relevant inputs and gates related to outgoing edge e_{x_2} and e_{x_3} , predecessor edge e_{a_3} and intermediate node $Z_3(x_2)$. Considering the NZMDD in Figure 5 if a realization for node $Z_3(x_2)$ is to be constructed, incoming edge e_{a_3} and outgoing edge e_{x_2}, e_{x_3} are needed. Redundant single input-output WINDOW LITERAL gates can be replaced with a single pass. MAX gates which determine the final output of the function $f(x)$ can be shared across all the output edges of the sub-functional nodes. For a k valued logic level each intermediate node in the NZMDD can accommodate at max $k-1$ outgoing edges, $\frac{k}{2}$ incidental repeating outgoing edges. A worst case scenario may appear when at least one outgoing edge is incidental repeating. In these circumstance the total number of logic gates required to express a sub-functional intermediate node can be observed by $2 \cdot \left(\sum_{i=0}^n e_{x_i}\right)$ and $2 \cdot \left(\sum_{i=0}^n e_{x_i}\right) + 1$. Using EXTENDED AND in all the outgoing edges decreases the number of MIN gates but increases the number of MAX gate. The best outcome has been achieved when at most one of the edge has utilized EXTENDED AND operator.

Experimental Results

An NZMDD analyzer has been constructed to generate experimental results using 19600 and 49998 benchmark circuits. This benchmark generating method was also used in [1], [11] and [12]. Two set of experimental datum was generated using the analyzer. The first and second set consecutively consists of 19600 and 49998 randomly generated MVL functions. The first set benchmarks are 3

valued 2 variable functions, while the second set consists of 4 valued 2 variable MVL functions. The benchmark does not contain any sequential circuits. All measurements were performed on a *Microsoft windows XP*, Intel Core2 duo 2.20GHz CPU, 0.98GB RAM machine. The 3 valued combinational benchmarks were used to observe the average number of product term (PT) needed to synthesize each MVL function provided in Table 1. The number of minterms the function contains is shown in the first column. The proposed NZMDD column denotes the average PT needed to synthesize the group of functions.

Table 1. Average PT used in synthesis of 3-valued MVL benchmarks using NZMDD method.

Minterm	Generated MVL Functions	NZMDD (proposed) Avg. PT
9	799	5.2140
8	3067	4.9680
7	5178	4.6450
6	5319	4.2730
5	3338	3.8230
4	1461	3.2610
3	438	2.6250

In [12] paper the author has experimented on synthesizing MVL functions of 4 valued 2 variable using evolutionary techniques. It can be clearly observed that evolutionary algorithm had outperformed all other previous synthesis techniques. Considering the experimental results shown in Table 2 it is observed that the proposed method synthesizes an average 10.5 minterm 4-valued MVL functions for an average of 4.975 PT. ACO-MVL requires an average of 6.286 PT for the same experiment. For synthesis NZMDD reduces the number of PT by 52.619%, while ACO-MVL reduces PT by 40.133%. Hence our proposed NZMDD synthesis method outperforms ACO-MVL algorithm by 12.486% of improvement. Further reduction in synthesis can be achieved if the NZMDD can be reduced to its optimal size.

Table 2. PT reduction using NZMDD over ACO-MVL for 4-valued MVL functions

Minterm	MVL Functions	ACO-MVL [12]	NZMDD (proposed)
16	500	6.73	6.3160
15	2679	7.054	6.1240
14	6589	7.163	5.8520
13	10585	7.182	5.7195
12	11230	7.086	5.4830
11	9003	6.904	5.2100
10	5434	6.66	4.7820
9	2575	6.356	4.6260
8	1038	5.934	4.4290
7	277	5.48	4.0940
6	75	4.96	3.9870
5	13	3.923	3.0770

Conclusion

In this paper we have presented and evaluated a tree-like decision diagram. NZMDD is considered as an extension to MDD, which synthesizes reduced MVL functional networks. The synthesized MVL functions are realized with MVL gates. The compact form of NZMDD reduces the size of

logic expression, which in turn reduces the size of the circuit. The results obtained using the NZMDD is compared using 49998 benchmark circuits against ACO-MVL evolutionary algorithm. The results achieved have shown that the NZMDD outperforms the existing evolutionary ACO-MVL algorithm in [12]. The result depicts an improvement of 12.486% for reduction in PT for synthesizing 4-valued MVL functions compared to ACO-MVL algorithm.

References

- [1] B.A.B Sarif, M. Abd-El-Barr, Synthesis of MVL functions - part II: The genetic algorithm approach, International Conference on Microelectronics (2006) 154-157.
- [2] F. Sarica, A. Morgul, Basic circuits for multi-valued sequential logic, 7th International Conference on Electrical and Electronics Engineering, (2011) II-66-II-68.
- [3] A.K Jain, R.J. Bolton, M. Abd-El-Barr, CMOS multiple-valued logic design part II: Function realization, IEEE Transactions on Circuits and Systems I: Fundamental Theory and Applications, 40 (1993) 515-522.
- [4] A.K Jain, R.J. Bolton, M. Abd-El-Barr, CMOS multiple-valued logic design part I: Circuit implementation, IEEE Transactions on Circuits and Systems I: Fundamental Theory and Applications, 40 (1993) 503-514.
- [5] A. Gawande, S.A. Ladhake, Constraints in the design of CMOS MVL circuits, 7th WSEAS International Conference on Instrumentation, Measurement, Circuits and Systems, (2008) 108-113.
- [6] C. Files, R. Drechsler, M.A Perkowski, Functional decomposition of MVL functions using multi-valued decision diagrams, 27th International Symposium on Multi-Valued Logic, (1997) 27-32.
- [7] R. Drechsler, D. Jankovic, R.S Stankovic, Generic implementation of DD packages in MVL, EUROMICRO Conference, 1 (1999) 352-359.
- [8] R. Drechsler, M. Thornton, D. Wessels, MDD-based synthesis of multi-valued logic networks, 30th IEEE International Symposium on Multi-Valued Logic, (2000) 41-46.
- [9] D.M. Miller, R. Drechsler, On the construction of multiple-valued decision diagrams, 32nd IEEE International Symposium on Multi-Valued Logic, (2002) 245-253.
- [10] Y. Jiang, S. Matic, R.K Brayton, Generalized cofactoring for logic function evaluation, Design Automation Conference, (2003)155-158.
- [11] M. Abd-El-Barr, B.A.B. Sarif, Synthesis of MVL functions - part II: The ant colony optimization approach, International Conference on Microelectronics, (2006) 158-161.
- [12] A.K Chowdhury, N. Raj, A.K. Singh, A novel high deduction algorithm for synthesizing multiple-valued logic and circuit realization, submitted to Journal of Multi-Valued Logic and Soft Computing (2013).

Developing a Solar Calculator System

Saidalmaruzi Muhammad-Sukki^{1, a}, Mohd Toriq Khan Mohd Niyaz Khan^{1, b},
Akram M. Zeki^{1, c}, Adamu Abubakar^{1, d}, Firdaus Muhammad-Sukki^{2, 3, e}

¹ Department of Information Systems, International Islamic University Malaysia, Selangor, Malaysia

² Faculty of Engineering, Multimedia University, Cyberjaya, Selangor, Malaysia

³ School of Engineering and Built Environment, Glasgow Caledonian University, Glasgow, United Kingdom

^asaidalmaruzi@gmail.com, ^btoriq_bs@hotmail.com, ^cakramzeki@iium.edu.my,
^d100adamu@gmail.com, ^efirdaus.sukki@gmail.com

Keywords: solar energy, solar photovoltaic, solar calculator.

Abstract. There is a rapid increase in global warming over the years. This follows with continues campaign on reducing the energy consumption and protecting the earth against climate change. The Feed-In Tariff (FiT) program was introduced to encourage people to use renewable energy. One of the alternative energies that has shown significant potential is solar energy, which could be harvested using the solar photovoltaic (PV) technology. This project is intended in developing an online application system to help the user in making a decision about installing a solar PV system. This system will help the user to calculate the size of solar panel that a user should install, the amount of electricity generated from the system and the profit that the user will gain after a few years in implement solar PV system in his premise(s) or house(s).

Introduction

Electricity generation in Malaysia is largely produced from fossil fuels, mainly from natural gas and coal, which constitute nearly 90% of the overall generation. However, to sustain this increasing energy demand, while cutting the dependency on the fossil fuels, Malaysia needs to shift its energy generation to alternative energy resources. The government has started to elevate the usage of renewable in delivering its energy need to ensure the country's economy is resilient and sustainable in the long run.

Malaysia is convinced that the Feed-in Tariff (FiT) is the way forward to shift to renewable energy [3,4]. The FiT scheme was introduced in Malaysia by the Parliament passing the Renewable Energy Act 2011 (REA) in April 2011. As mentioned in the preamble to the REA, its creation is with a specific purpose, which is to establish and implement a special tariff system or FiT to catalyze the generation of renewable energy from 2011 onwards. The FiT in Malaysia puts much emphasis on solar PV. Catalyzed by the FiT scheme, renewable energies are expected to play a significant role in Malaysia, with a projected cumulative capacity of 11.5 GW by 2050. From this, close to 9 GW is expected to come from solar PV.

However, despite the lucrative incentives provided by the government, the uptake of solar PV is still considered very low in this country. Some of the major hindrances of implementing solar PV include: (i) lack of knowledge about solar PV technology since it is still considered as a new technology in Malaysia; (ii) financial problem to implement the solar panel, and (iii) the benefit of utilizing solar PV is still not widely spread amongst the citizens in the country.

To persuade the general public, proper planning is needed particularly to see the viability of any solar PV project. Of particular interest will be the cost to implement the solar panel as well as the return generated from the FiT scheme. In order to achieve this, we propose to create a simple solar calculator system. This exciting project aims at producing a small application to monitor any installations of solar PV panel in Malaysia. The system should address these objectives: (i) to give the

bright picture about the benefits of solar energy; (ii) to promote solar energy as the main source of energy in producing electricity; (iii) to create an application that can propose the size of a solar panel based on the electricity requirement/usage of a house; (iv) to project the expected output power generated from the solar panel, and (v) to calculate the total profit generated from the FiT scheme.

This system has its own focus and target. It can be implemented by gaining some information from certain trusted agency that expertise in this field in order to have confidentiality, integrity and accountability (CIA) through the system. The limitation and the scope of this system only can be clearly seen by looking at the community that will use it.

Related Works

To date, there are many existing online solar calculator systems created around the world such as in European countries, United States of America and Australia. These existing systems provide the same basic function such as to calculate cost of electricity, energy data and etc. Some systems also provide suggestions on the size of solar panel needed, the cost of the installation and some financial analysis gain from the installation.

Green Energy Trading 0, for example, created a solar energy calculator that is easy to understand and use. The interface of the design is simple and straightforward, and is considered the best when compared to the selected systems. However, this system is only applicable for installation in Australia. Find Solar 0 is another excellent example of an online solar calculator. Despite only catering for the installations in the USA, this system provides an easy-to-understand interface. The website also provided a detailed description on the left-hand side of the calculation form to guide the user. Based on the electricity consumptions of the users, the system could suggest the most appropriate size of the solar PV system needed by the users.

The Minnesota's Department of Natural Resources 0 produced quite a detailed system or product that enables calculation and calculates the cost used within the predicted life span of the solar PV. A graph is also provided to allow users to clearly view their energy usage which shows greater information when compared to other systems. It would allow users to carefully monitor with their usage of the energy. Again, the disadvantage of this system is that it only works for Minnesota residents only.

Another example of solar calculator is provided by the Energy Groove 0, a company based in the USA. This system is easy to understand and users do not have to register before using the application. However, the system requires some complicated data for the input (e.g. the tilt angle of the solar panel) as well as some technical jargons that might not be understandable by typical people. This system is somewhat slightly difficult to deal with compared to the other systems.

Development Approach

The proposed system is developed using the rapid prototyping development cycle. The system will be divided into administrator's view and customers' point of view. However, both parties will have the same view except the register list and delete functions that can only be viewed and used by an administrator.

System Requirement Specification. The system will be divided into administrator's view and customers' point of view. However, both parties will have the same view except the register list and delete functions that can only be viewed and used by an administrator. Table 1 shows the requirements and the descriptions of the proposed solar calculator system.

Table 1. The requirements specification of the proposed solar calculator system.

Requirements	Descriptions
Administrator	Admin can add, modify and delete the data on the system and change the coding if necessary.
User	User can read all the information stated on the website, use the solar calculator system by add some value on it and view the result.
Calculator	User can enter their electricity usage here and calculate the appropriate size of the solar panel that they have to install, as well as to calculate the profits they can earn from selling the energy and
Calculation Result Form	This page will show the results based on the data provided in the calculator page.

Logical Design. Logical design (Figure 1) shown is concerned with the processes to be performed. It describes what is to be done by the system or the functions required by the system.

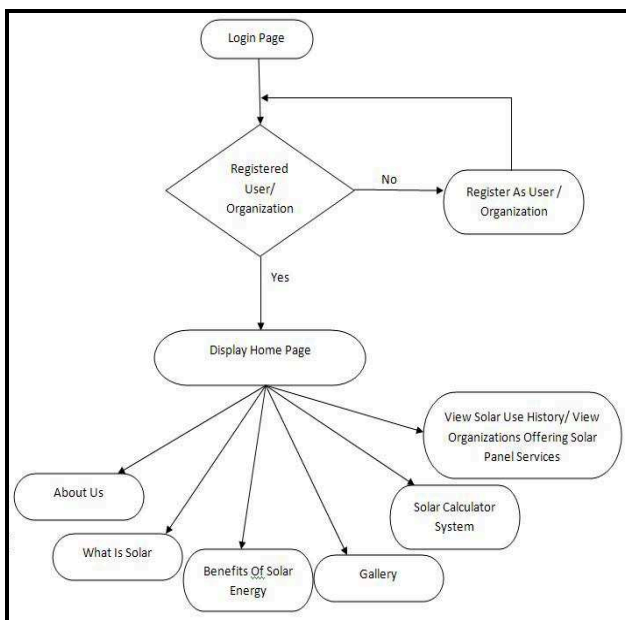


Figure 1 : Logical Design

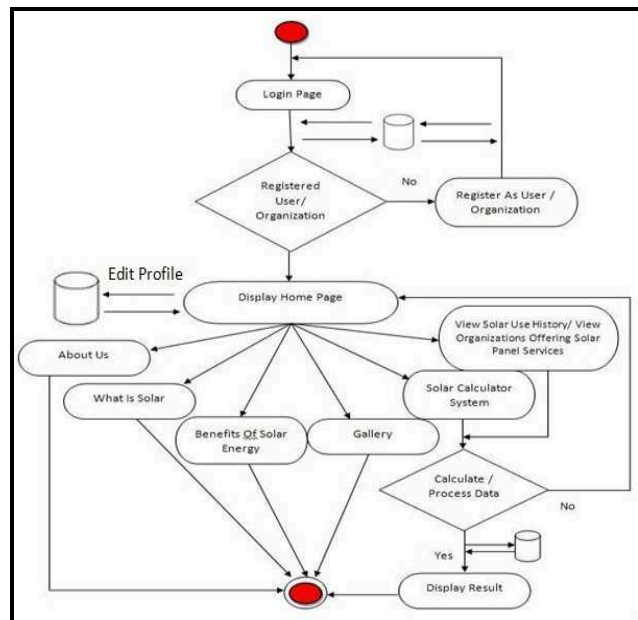


Figure 2 : User activity diagram

Activity Diagram. This is user activity diagram (Figure 2). Activity diagram is a graphical representation of workflows of stepwise activities and actions with support for choice, iteration and concurrency. In the Unified Modelling Language, activity diagrams can be used to describe the business and operational step-by-step workflows of components in a system. It also shows the overall flow of control.

Package Diagram. Figure 3 shows which element of the website is private and public. A public element is denoted by '+' sign and '-' for private.

Sequence Diagram. Figure 4 shows the flow of the website. It indicates that the system begins with 'login' and ends up with 'log out'.

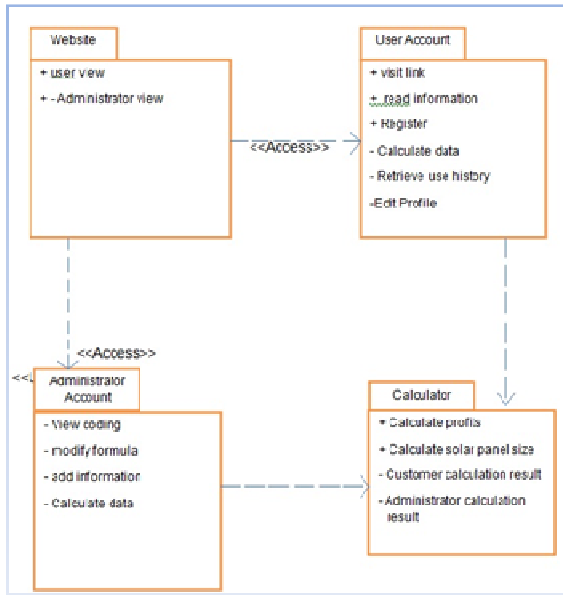


Figure 3 : Package Diagram

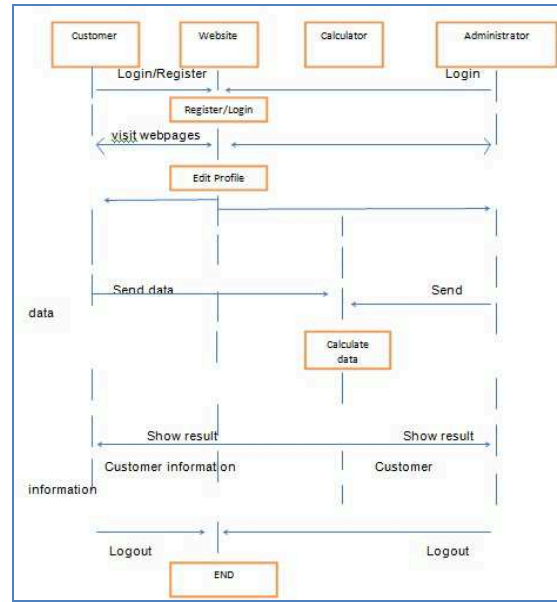


Figure 4 : Sequence Diagram

The outcome of the development yielded a product. The system is implemented and tested. The programming language, database, web designing and content of solar energy are all tested. The components of this system are created by using multimedia flash, php, html and also MySQL database. Figure 5 shows the page where it gives an introduction to solar power, while Figure 6 shows the page where benefits of solar energy are explained. Figure 7 shows the solar calculator page. This is where the main event happens, where users can use the calculator to calculate how big their solar panel should be and also how much they would earn from the FiT initiative. Users can also save their calculations. Figure 8 shows the page where users would choose what table they would want to view.



Figure 5 : What Is Solar Energy Page



Figure 6 : Normal user home page



Figure 7: Solar Calculator Page



Figure 8: Solar Calculator Page

Conclusions and Discussions

This paper presents a solar calculator. The motivation for the project comes from the fact that people still not aware about the benefits of solar energy since there is still lack of information provided in virtual and real world. An online solar calculator has been designed using generic software development process. The system is tested and proved efficient in calculating solar energy. Although some limitations were observed, the system still works very well. In the future, this system could be enhanced by adding some more functions that are related to solar energy. There are some limitations that can be improved in future. Although this current design has some weaknesses, these will not affect the main process. It is hoped that this system can improve the development of solar PV in Malaysia as a whole by providing some knowledge about the technology and potential investment about solar energy.

References

- [1] Economic Planning Unit, Ninth Malaysia Plan 2006-2010, Putrajaya, Malaysia (2006).
- [2] Muhammad-Sukki, F., Abu-Bakar, S.H., Munir, A.B., Mohd Yasin, S.H., Ramirez-Iniguez, R., McMeekin, S.G., Stewart, B.G. & Abdul Rahim, R. Progress of feed-in tariff in Malaysia: A year after. *Energy Policy*. 16 (2014) 618-625.
- [3] Ministry of Energy, Green Technology and Water. Handbook on the Malaysian feed-in tariff for the promotion of renewable energy. Government of Malaysia, Malaysia (2011).
- [4] Muhammad-Sukki, F., Ramirez-Iniguez, R., Abu-Bakar, S.H., McMeekin, S.G. & Stewart, B.G. An evaluation of the installation of solar photovoltaic in residential houses in Malaysia: Past, present and future. *Energy Policy*. 39 (2011) 7975–7987.
- [5] Government of Malaysia, Malaysia. Renewable Energy Act 2011. Government of Malaysia, Malaysia (2011).
- [6] Muhammad-Sukki, F., Munir, A.B., Ramirez-Iniguez, R., Abu-Bakar, S.H., Mohd Yasin, S.H., McMeekin, S.G. & Stewart, B.G. Solar Photovoltaic in Malaysia: The Way Forward. *Renewable and Sustainable Energy Reviews*. 16 (2012) 5232-5244.
- [7] Muhammad-Sukki, F., Ramirez-Iniguez, R., Abu-Bakar, S.H., McMeekin, S.G., Stewart, B.G. & Chilukuri, M.V. Feed-In Tariff for Solar PV in Malaysia: Financial analysis and public perspective”, in Proceedings of 5th IEEE International Power Engineering and Optimization Conference, Shah Alam, Selangor, Malaysia (2011) 221-226.
- [8] Green Energy Trading on <http://greenenergytrading.com.au/>
- [9] Find Solar on <http://www.findsolar.com/>
- [10] Department of Natural Resources Minnesota on <http://www.dnr.state.mn.us/energysmart/why/calculator.html>
- [11] Energy Groove on <http://www.energygroove.net/energycalculator-solarpanels.php>

ISO 6983 Translator for PC Based CNC Systems

Yusri Yusof^a and Kamran Latif^b

Faculty of Mechanical and Manufacturing Engineering, University Tun Hussein Onn Malaysia
Parit Raja, Batu Pahat, 86400, Johor, Malaysia

^ayusri@uthm.edu.my, ^benr.kamranqureshi@gmail.com

Keywords: Interpreter, Open Architecture Controller, CAD/CAM, ISO 6983, Lab view

Abstract. Computer Numerical Control (CNC) controller is an important part of machine, composed of hardware and software models. Software model, usually called an interpreter translates input code as per internal structure of CNC machine. Now a day's traditional controllers of CNC machine are found to be closed in nature, because they are depended of vendor's specifications. Due to that dependence they do not facilitate access to the inner features of machine. In order to overcome these problems open architecture controllers were introduced. In this article a new ISO 6983 translator for open architecture CNC controller is being proposed. The developed software model is able to read commercially available Computer Aided Design (CAD) /Computer Aided Manufacturing (CAM) system generated International Standards Organization (ISO) 6983 file and extracts position, feed rate, spindle speed, tool etc data and translates to OAC machine. At the same time it is also able to generate output in user defined text and EXtensible Markup Language (.xml) formats. Further design of paper includes development of translator, followed by case study experiment and finally ends with conclusion.

Introduction

Over the last 50 years machine tools have evolved from simple machines to highly stylish Computer Numerical Control (CNC) machines. CNC refers to a computer "controller" that drives a machine tool to create objects by selective removal of material. CNC machines were developed in the 1970s with the introduction of minicomputers and CAD drawing software to support the development of on-machine programs to enable machining of different parts [1]. The CNC is a technology that uses microcomputers to generate, parse and execute the sequential control that describes the end effector's behavior [2]. These CNC machines can be classified by a range of different categories including machining process, number of axes, spindle arrangement, number of spindles and kinematics configuration [3, 4]. These machines are operated by ISO 6983 standard formally known as (GM Codes), this standard is based on the representation of the tool path digitized with respect to a tool size and machine command status.

CNC Machines are composed of many parts. Controller is one of the important part of CNC machine which is consists of two modules; hardware and software. The software module usually known as interpreter, translates the processing information such as coordinates, spindle speed, feed rate, tool number etc contained by input G-code into the machine understandable language. The interpretation method of ISO 6983 is simple structure, low in cost, requires less memory and takes less system resources [5]. For over a decade various companies had build interpreters (like NIST [6]) which runs machining centers by interpreting G-code programs. These interpreters are build to be subordinate to machine controllers [7]. The G-code language is line based, where the programs written in this language is intended to be executed line by line [8].

Today's conventional CNC machines programming language is still based on ISO 6983 and there are many CAM tools available to support NC manufacturers. But the problem of portability and interoperability from system to system remain an obstruction, because each machine builder has extended the G-Code to include proprietary functions and alterations. Due to these extensions each machine type and controller requires specific post processor. Most of the today's CNC machine tool

systems are being equipped with CNC controller supplied by controller vendors as a “black box” and this makes it difficult for the machine tool builder to quickly develop and implement the custom control functions[9]. In order to overcome these shortcomings, open architecture controllers need to be developed. Open controller means “Controller independent from the manufactures technology, allowing the user to buy hardware and software from several different manufactures and freely assemble the acquired piece of equipments”[10]. The interpreter is the software model of the CNC machine controller, and due to the closeness of controller the interpreter is also dependent of vendor’s specifications.

This paper presents an ISO 6983 translator for open architecture CNC control system. The developed software system reads commercially available Computer Aided Design (CAD) /Computer Aided Manufacturing (CAM) system generated International Standards Organization (ISO) 6983 file. The system then extracts position, feed rate, spindle speed, tool etc data and translates to OAC machine and at same time it also able to generate output in user defined text and EXtensible Markup Language (.xml) formats.

ISO 6983 Translator

ISO 6983 translator is a software model, specially designed for personal computer based open architecture CNC control systems. The function of this software model is to translate current CAD/CAM system generated ISO 6983 code into open architecture controller CNC system understandable data structure, so that the stepper/servo motors can be moved throughout linear interpolation or circular interpolation. It also interprets the acceleration, deceleration, spindle speed and feed rate for each stepper/servo motor. It is programmed in National Instruments (NI) lab view with some special functions. Overall it extracts data from current CAD/CAM systems generated ISO 6983 file and translates to open architecture CNC controller as per their internal structure to perform machining operations.

Developed software system is composed of three modules; input, data extraction and output [11]. Input data module provides the path for file uploading, data extraction module is based on lexical and syntax analysis which extracts position, feed rate, spindle speed, tool etc data. The function of last, output data module is to organize extracted data as per internal structure of machine and translates to machine or generate output in terms of user defined .txt or .xml file formats as shown in Fig. 1.

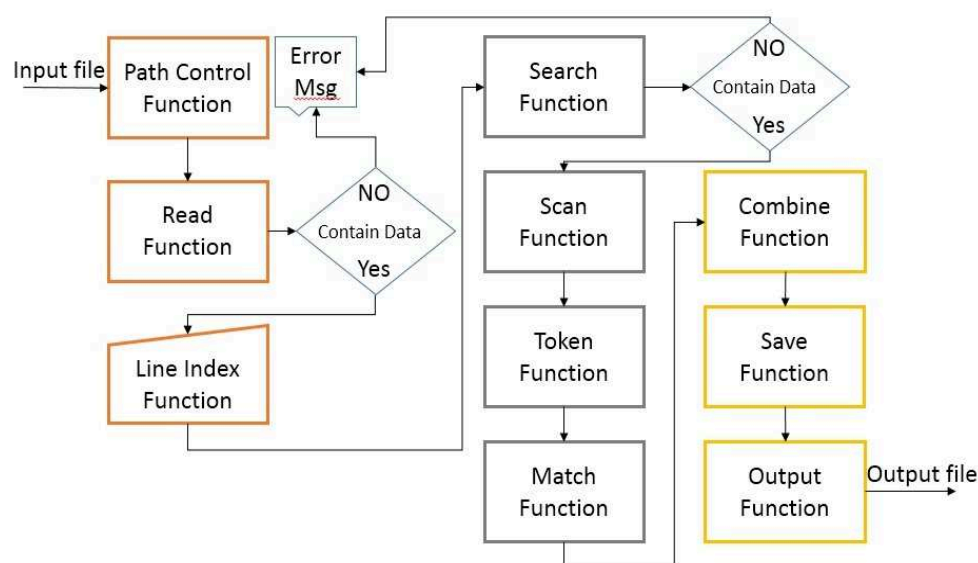


Fig. 1. Internal Structure of ISO 6983 translator

Developed interpreter works with current available CAD/CAM systems. Its working cycle starts with the CAD design, which then utilizes CAM software for the generation of ISO 6983 code. The interpreter takes that machine specific CAM file in .txt format as an input, and extracts the position,

spindle speed, feed rate etc data from input code and gives output in user defined .txt and .XML file. The interpreted data file is then transferred to the open architecture CNC machine, which performs operations and gives output product. The algorithm of translator starts with the reading of ISO 6983 input code generated by using current CAD/CAM system. It is designed in such a way that it reads entire code line by line. While reading the code it searches for patterns position, feed rate, spindle etc data. After search, the software combines all the extracted data, saves and then translates to the OAC machine. ISO 6983 translator is able to generate output file in .txt and .xml with user defined format. Fig. 2. Shows the working principle of developed software module.



Fig. 2. Working principle of developed system algorithm

Experimental Study

In this study various experiments have been performed for the testing and validation of developed interpreter. One of them is discussed in this section. This experiment is carried out to write U, T, H and M letters on a piece of wax material by using current CAD/CAM system, developed interpreter and [12] open architecture CNC machine.

This experiment starts with the design process, in which U, T, H and M letters, were designed by using CAD/CAM software. After designing CAM machine features are given to the design in order to generate ISO 6983 code. Then CAD/CAM generated code is saved in .txt format by using CAM software code editor. After the generation of ISO 6983 code the next step is to upload code in developed interpreter. Before performing interpreting operation the setting of output file has been carried out as per requirements from setting tab of developed interpreter. In this experiment the output code is formatted as floating point number (%f) with comma (,) delimitation. After all settings are done, the code is executed and output file is saved in .txt format. Then finally interpreted code is transferred to open architecture control CNC machine and operations are performed. Figure 3 shows experiment performed by developed interpreter.

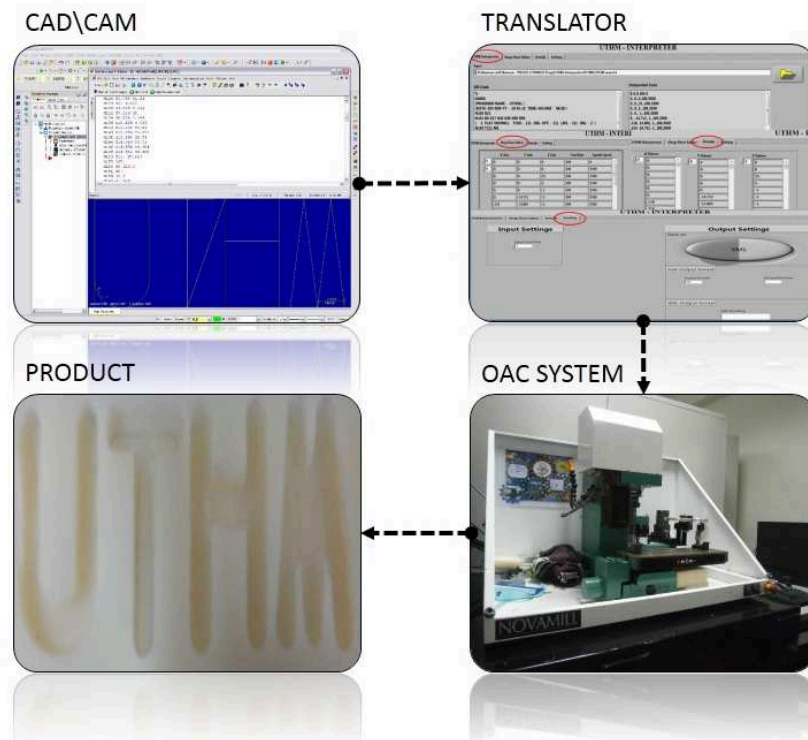


Fig. 3. Experiment performed by ISO 6983 translator

Conclusion

Conventional CNC machines are operated by controllers. Each controller has software model inside known as interpreter. The function of interpreter is to translate input data model code into CNC understandable internal data structure. These conventional CNC controllers are found to be closed in nature and are dependent of vendor specifications. These systems are closed in both aspects hardware and software. In other words they are closed in terms of Human Machine Interface (HMI) platform, input and output functions, connectivity, data interface model etc. In order to overcome these shortcomings, open architecture CNC control systems are introduced. In this work, a software model is developed for open architecture control systems of CNC machine. The developed interpreter is programmed in national instruments lab view and it is independent of vendor's specifications. It's open in nature, HMI platform, input/output function, connectivity etc. It can be used anywhere without any additional hardware requirements.

Developed interpreter works with current CAD/CAM systems. It takes ISO 6983 code generate by currently used CAD/CAM software as an input and gives output as in interpreted code composed of position, feed rate, spindle etc data in user defined .txt and .xml formats.

This study also shows the validation of developed interpreter in experimental works. There are a number of successful experiments that are performed with developed model. The output of experiments shows a good accuracy and performance of developed translator with open architecture control CNC system. In future the model will be updated by enabling new data interface model ISO 14649 interpretations. With the enabling of new standard, developed system will be able to work on both standards and it can be used to update ISO 6983 systems into ISO 14649 data model based systems.

Acknowledgment

This work was supported by the Malaysian Government under Science fund (MOSTI), Malaysian International Scholarship (MIS) under Ministry of Higher Education Malaysia (MOHE) and GIPs Grant, Universiti Tun Hussein Onn Malaysia (UTHM).

References

- [1]. J. Talavage: Flexible Manufacturing Systems in Practice, Design: Analysis and Simulation, Vol. 26. (1987), CRC.
- [2]. M.P. Groover: Automation, production systems, and computer-integrated manufacturing, (2007), Prentice Hall Press.
- [3]. J.S. Stenerson and K. Curran: Computer numerical control: operation and programming, (2005), Prentice-Hall, Inc.
- [4]. P. Vichare, A. Nassehi, S. Kumar, and S.T. Newman: A Unified Manufacturing Resource Model for representing CNC machining systems, Robotics and Computer-Integrated Manufacturing, Vol 25(6), (2009) p. 999-1007.
- [5]. G. Teng, J. Zhifeng, and F. Jianglong: Research of NC Code Interpreter Based on Theory of Finite Automaton, Modern Applied Science, Vol 6(4), (2012) p.38.
- [6]. T.R. Kramer, F.M. Proctor, and E. Messina: The NIST RS274/NGC Interpreter-Version 3, ISD of NIST, Gaithersburg, MD, (2000).
- [7]. F.M. Proctor, T.R. Kramer, and J.L. Michaloski: Canonical machining commands, Intelligent Systems Division National Institute of Standards and Technology Administration, US, Department of Commerce Gaithersburg, Maryland, (1997).
- [8]. T.R. Kramer, F. Proctor, X. Xu, and J. Michaloski: Run-time interpretation of STEP-NC: implementation and performance, International Journal of Computer Integrated Manufacturing, Vol 19(6), (2006), p. 495-507.
- [9]. M. Mori, K. Yamazaki, M. Fujishima, J. Liu, and N. Furukawa: A study on development of an open servo system for intelligent control of a CNC machine tool, CIRP Annals-Manufacturing Technology, Vol 50(1), (2001), p. 247-250.
- [10]. O. Asato, E. Kato, R. Inamasu, and A. Porto: Analysis of open CNC architecture for machine tools, Journal of the Brazilian Society of Mechanical Sciences, Vol 24(3), (2002) p. 208-212.
- [11]. K. Latif and Y. Yusof: Interpreter for Open Architecture CNC System: A Conceptual Model, Applied Mechanics and Materials, Vol 465-466, (2014) p.779-783.
- [12]. Y. Yusof and K. Latif: Frame Work of LV-UTHM: An ISO 14649 Based Open Control System for CNC Milling Machine, Applied Mechanics and Materials, Vol 330, (2013), p. 619-623.

On the Proportionality of Damage Rule in Finite Element Simulations of the Ductile Failure

František Šebek^{1,a}, Jiří Hůlka^{1,b}, Petr Kubík^{1,c} and Jindřich Petruška^{1,d}

¹Brno University of Technology, Brno, Technická 2896/2, 616 69 Brno, Czech Republic

^ay107598@stud.fme.vutbr.cz, ^bhulka@c-box.cz, ^cm3petr@gmail.com, ^dpetruska@fme.vutbr.cz

Keywords: ductile failure, damage rule, uncoupled model, explicit.

Abstract. Extended Mohr–Coulomb criterion which is uncoupled, therefore the plasticity is not influenced by the damage, was selected and calibrated. Experiments on the aluminum alloy 2024-T351 were carried out. Further, the impact of the damage rule proportionality was investigated. The damage exponent was sequentially held 1, 2 and 3, respectively. Therefore, the influence of the damage rate on the damage failure in finite element simulations was examined. Numerical simulations of the tensile test of smooth and notched cylindrical specimens and flat grooved specimen were performed. It is also shown that there is inability to predict slant fracture by uncoupled models for flat grooved specimen and in the final phase of tensile tests of cylindrical specimens.

Introduction

The ductile failure prediction has been still a great challenge not only for mechanical engineers. It also could be important for petroleum or civil engineering. So it really has a considerable impact in many branches of engineering and in many practical industrial applications.

Number of robust failure models and damage approaches has been developed so far. Paper is focused on the empirical criteria which can also be interpreted as phenomenological. The pioneer work in this field was published by Cockroft and Latham [1].

When predicting ductile failure, one has to know the plasticity of examined material. In case of uncoupled failure models, the plasticity is not influenced by the damage process and the plastic flow remains during straining the same as the flow curve identified from standard tensile tests, until the fracture occurs. The other part, when modeling the ductile failure, is to have a reliable ductile failure model. However, this paper does not deal with assessing the reliability or predictive accuracy of such models. This problem has been discussed in number of publications and it is not the aim of this paper. One of the crucial parts of ductile failure model could be its damage rule, so the influence of the damage rate, controlled through damage exponent, is studied hereinafter.

Approach to Ductile Failure Modeling

Wierzbicki et al. [2] carried out fifteen fracture tests including various specimens. They obtained flow curve using tensile tests of smooth specimens. The stress-strain relationship was described by

$$\bar{\sigma} = A \bar{\epsilon}^n, \quad (1)$$

where $\bar{\sigma}$, A , $\bar{\epsilon}$ and n are the equivalent Mises stress, stress amplitude, equivalent total strain and strain hardening exponent, respectively.

Bai and Wierzbicki [3] introduced a new model of metal plasticity with pressure and Lode dependence. By suitable setting of material constants, the model is reduced either to von Mises or Tresca yield criterion. Later, Bai and Wierzbicki [4] modified Mohr–Coulomb failure criterion using the previous plasticity model and introduced Extended Mohr–Coulomb criterion as another uncoupled phenomenological failure model.

Assuming material constants of plasticity model [3] in order to obtain and adopt von Mises yield criterion, the fracture strain of failure model [4] concerning two material constants, c_1 and c_2 , is expressed as

$$\bar{\epsilon}^f = \left\{ \frac{A}{c_2} \left(\sqrt{\frac{1+c_1^2}{3}} \cos\left(\frac{\pi}{6}\bar{\theta}\right) + c_1 \left[\eta + \frac{1}{3} \sin\left(\frac{\pi}{6}\bar{\theta}\right) \right] \right) \right\}^{\frac{1}{n}}, \quad (2)$$

where $\bar{\theta}$ and η are the normalized third invariant of the deviatoric stress tensor and stress triaxiality, respectively.

Calibration constants of the failure model discussed above are obtained through non-linear least square method which can be generally written in vector terms as

$$\min_x \|f(x)\|_2^2 = \min_x (f_1(x)^2 + f_2(x)^2 + \dots + f_k(x)^2), \quad (3)$$

where $f(x)$ and x are a function that returns a vector value and vector, respectively. In our case, k represents the number of fracture tests.

The last part of ductile failure model is the damage rule. Xue [5] derived the damage evolution law as a power function

$$dD = m \left(\frac{\bar{\epsilon}^p}{\bar{\epsilon}^f} \right)^{m-1} \frac{d\bar{\epsilon}^p}{\bar{\epsilon}^f}, \quad (4)$$

where m and $\bar{\epsilon}^p$ are the damage exponent and equivalent plastic strain, respectively.

Calibration of Material Constants

At first, material constants related to plasticity were taken over, $A = 744$ MPa and $n = 0.153$, according to Eq. (1) from [2]. These were not used only in ductile failure model in Eq. (2) but also as input into finite element simulations.

Further, the fracture strains and average values of the stress triaxiality and normalized third invariant of the deviatoric stress tensor were taken over [2]. Average values, used in calibration process, were determined using numerical integration

$$\eta_{av} = \frac{1}{\bar{\epsilon}^f} \int_0^{\bar{\epsilon}^f} \eta d\bar{\epsilon}^p, \quad (5)$$

$$\xi_{av} = \frac{1}{\bar{\epsilon}^f} \int_0^{\bar{\epsilon}^f} \xi d\bar{\epsilon}^p. \quad (6)$$

Following expression was used for conversion from the normalized third invariant of the deviatoric stress tensor to normalized Lode angle

$$\bar{\theta} = 1 - \frac{2}{\pi} \arccos(\xi), \quad (7)$$

where ξ is the normalized third invariant of the deviatoric stress tensor.

The material constants of Extended Mohr–Coulomb criterion, $c_1 = 0.0621$ and $c_2 = 343.845$ in Eq. (2), were obtained through non-linear least square method using Eq. (3). The fracture envelope according to these constants and taken over values of fracture strain is depicted in Fig. 1.

Bai and Wierzbicki [4] obtained similar results. Slight variance is due to slightly different values of the stress amplitude and strain hardening exponent which were used in [4].

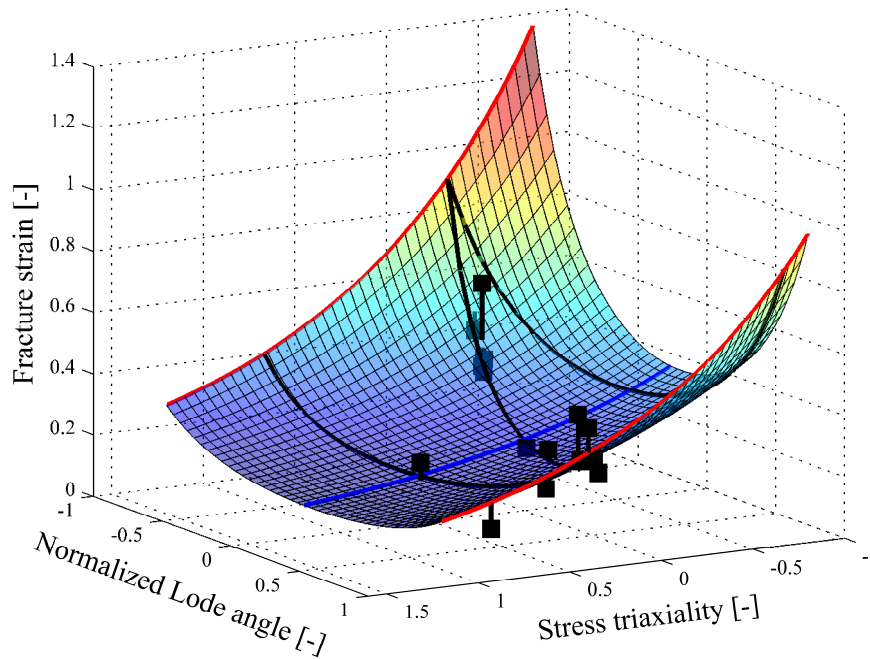


Fig. 1 Fracture envelope of Extended Mohr–Coulomb criterion

Finite Element Simulations

The finite element simulations were realized within Abaqus/Explicit commercial code via the user subroutine VUMAT.

Numerical simulations of tensile tests of smooth and notched cylindrical specimens and flat grooved specimen were conducted (Fig. 2). The axisymmetric condition is generated in cylindrical specimens and plane strain in the flat grooved specimen. Smooth specimens had 9 mm diameter. Two types of notched specimens had notch radii 4 and 12 mm and both 8 mm diameter in minimal cross-section. Flat grooved specimens had thickness 3 mm and width 12.5 mm. The gauge length was 25.4 mm for all specimens [2, 6].

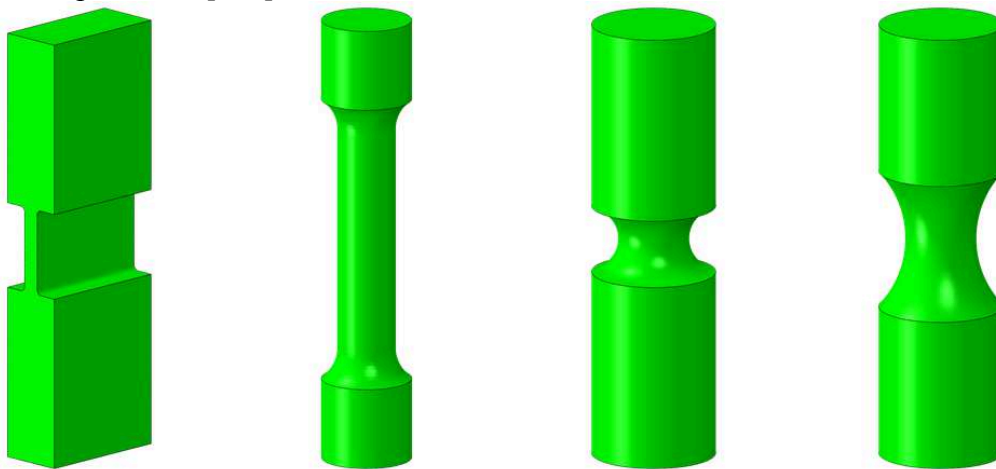


Fig. 2 From left, geometry of flat grooved specimen, smooth specimen and notched specimens

Fields of damage for each specimen, immediately before crack initiation and after separation, and sequentially for damage exponent 1, 2 and 3, in order to gain linear, quadratic and cubic damage evolution, respectively, are depicted in Figs. 3-6.

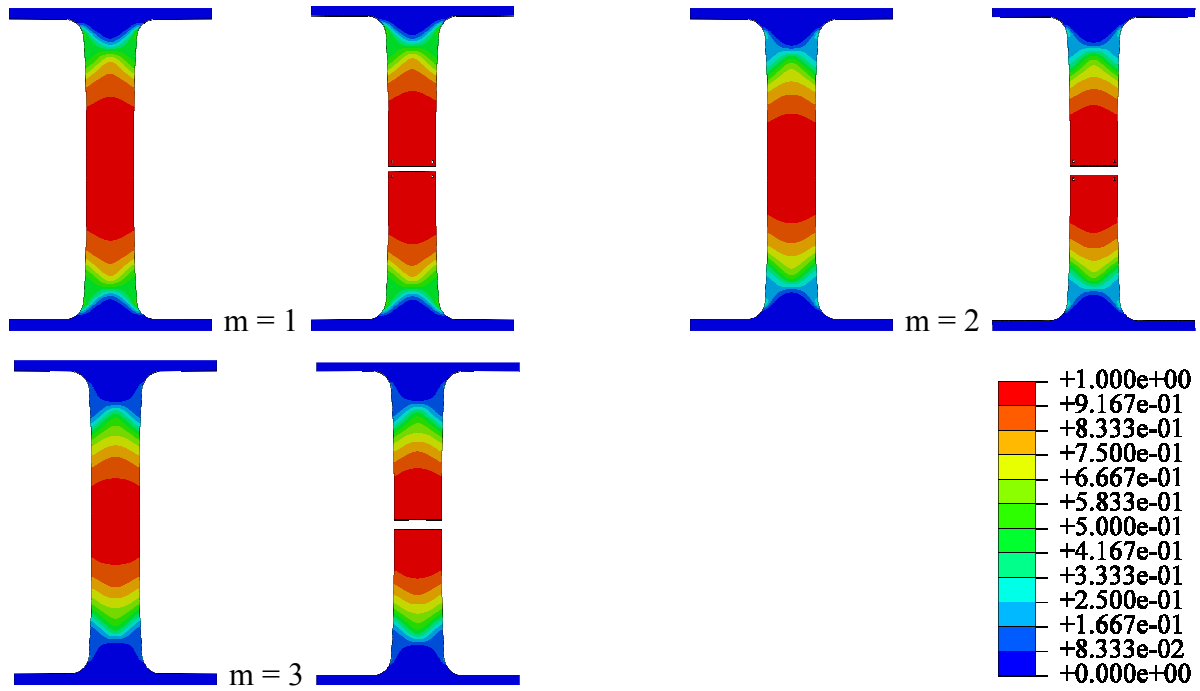


Fig. 3 Fields of damage parameter before initiation and after separation, in pairs, for flat grooved specimen

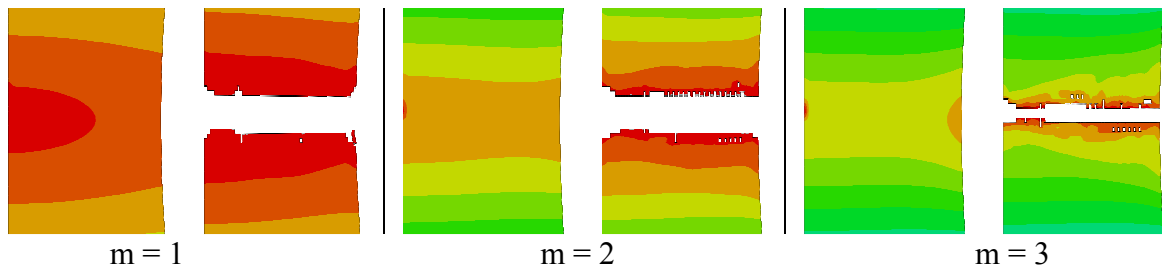


Fig. 4 Fields of damage parameter before initiation and after separation, in pairs, for smooth cylindrical specimen (legend is the same as in Fig. 3)

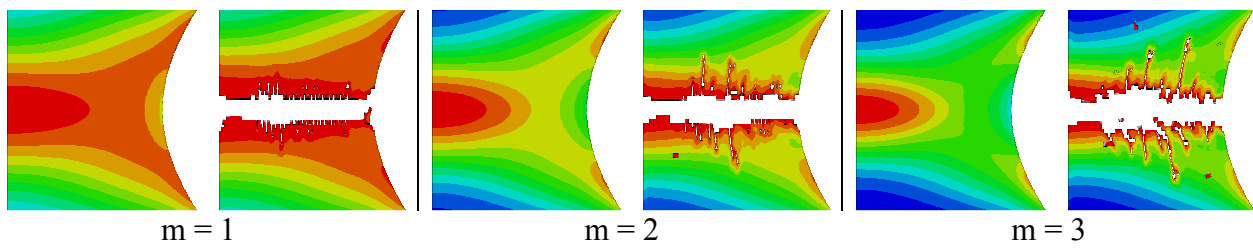


Fig. 5 Fields of damage parameter before initiation and after separation, in pairs, for notched cylindrical specimen with notch radius 4 mm (legend is the same as in Fig. 3)

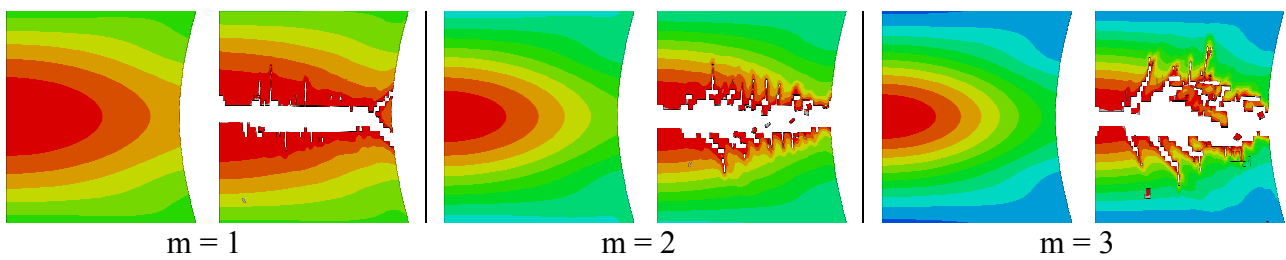


Fig. 6 Fields of damage parameter before initiation and after separation, in pairs, for notched cylindrical specimen with notched radius 12 mm (legend is the same as in Fig. 3)

In Fig. 7 are shown histories of damage evolution and damage rate.

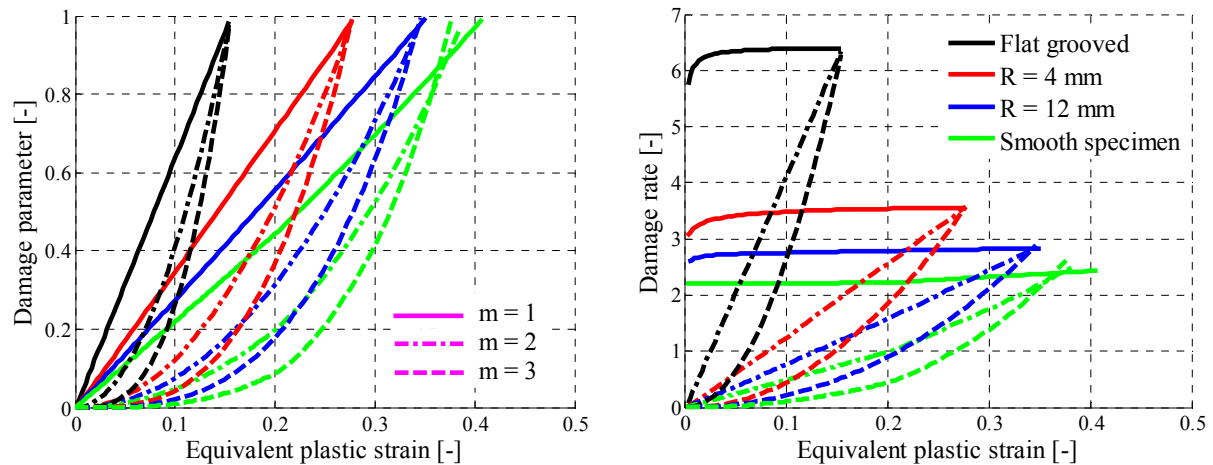


Fig. 7 Histories of damage evolution (left) and damage rate (right)

Summary

The proportionality of damage rule was examined through changing the damage exponent. When the damage exponent equals to unity, the damage parameter is proportional to the equivalent plastic strain and therefore the damage rate is constant. It can be clearly seen that localization problem at flat grooved specimen, when the plane strain condition is generalized, is not distinct. The localization is significant at cylindrical specimens, especially at the smooth one. Slant fracture at final stage is predicted only for notched specimen with notch radius 12 mm. One can see that slant cracks propagated with rising damage exponent, but stopped and the major flat crack grew further until separation. Finally, there was some localization effect but not strong enough to govern the slant fracture where it was observed experimentally.

Acknowledgment

This work is an output of cooperation between grant project FSI-S-14-2311 and NETME Centre, regional R&D centre built with the financial support from the Operational Programme Research and Development for Innovations within the project NETME Centre (New Technologies for Mechanical Engineering), Reg. No. CZ.1.05/2.1.00/01.0002 and, in the follow-up sustainability stage, supported through NETME CENTRE PLUS (LO1202) by financial means from the Ministry of Education, Youth and Sports under the „National Sustainability Programme I“.

References

- [1] M. G. Cockcroft, D. J. Latham, Ductility and the Workability of Metals, *J. Inst. Metall.* 69 (1968) 33-39.
- [2] T. Wierzbicki, Y. Bao, Y.-W. Lee, Y. Bai, Calibration and evaluation of seven fracture models, *Int. J. Mech. Sci.* 47 (2005) 719-743.
- [3] Y. Bai, T. Wierzbicki, A new model of metal plasticity and fracture with pressure and Lode dependence, *Int. J. Plast.* 24 (2008) 1071-1096.
- [4] Y. Bai, T. Wierzbicki, Application of extended Mohr–Coulomb criterion to ductile fracture, *Int. J. Fract.* 161 (2010) 1-20.
- [5] L. Xue, Damage accumulation and fracture initiation in uncracked ductile solids subject to triaxial loading, *Int. J. Solids Struct.* 44 (2007) 5163-5181.
- [6] Y. Bao, Prediction of ductile crack formation in uncracked bodies. Ph.D. thesis, Massachusetts Institute of Technology, 2003.

New Algorithm to Reduce File Size and Bandwidth of Hashed Digital Signature for Image Steganography using LSB

Erfaneh Noroozi^{1, a}, Salwani Mohd Daud^{2, b}, Ali Sabouhi^{3, c}
and MohammadReza Salehnamadi^{4, d}

^{1,2}Advanced Informatics School (AIS), Universiti Teknologi Malaysia
Malaysia, Kuala Lumpur

³Software Engineering of Computer Science, Malaysia, Kuala Lumpur

⁴Doctor of Computer engineering, Tehran Jonob Branch, Tehran, Iran

^anerfaneh2@live.utm.my, ^bsalwani@ic.utm.my, ^cali_sabouhi@yahoo.com, ^dM_saleh@azad.ac.ir

Keywords: Digital signature, encoding, decoding, hash algorithm, image steganography.

Abstract. In computer cryptography, digital signature is one of the best cryptography systems. Public-private keys are used to pass sensitive information however it can also be used to provide authentication on the particulars of a sender. Proposed algorithm is a new design and simple implementation mechanism for producing a digital signature. Some applications such as multi agent systems transferred data with small size and capacity. The new scheme minimizes the size of original file and gives us a dynamic and smaller hashed message output. In this algorithm load the original files then hashed the message and encode it with the private key of sender. Finally modify the established code into a unique digital signature at Base 16. We concentrate on designing and implementation of functions of algorithm.

Introduction

Most of the time, users on the internet have to send, share or receive confidential information. Due to rapid development in both computer technologies and Internet, the security of information is regarded as one of the most important factors of Information Technology and communication. Attacks on confidential data, unauthorized access of data have crossed the limits. Accordingly, we need to take measures which protect the secret information. Steganography has emerged as a powerful and efficient tool which provides high level for security particularly when it is combined with encryption. The general idea of hiding some information in digital content has a wider class of applications that go beyond steganography. The techniques involved in such applications are collectively referred to as information hiding. Two special cases of information hiding include digital watermarking and Fingerprinting. Watermarking can be used to provide copyright protection by extending the cover source with some extra information which can later be extracted and can be used for variety of purposes like copyright protection and control. Digital watermarking has become an active and important area of research, and development and commercialization of watermarking techniques is being deemed essential to help address some of the challenges faced by the rapid proliferation of digital content. In Fingerprinting, different customers are given different and specific marks embedded in the copies of their work. It helps to identify those customers.

Identity Based Cryptography

Cryptography is a branch of applied mathematics concerned with the transformations of data for security (Schneier, 1996). In cryptography, a Sender transforms information (plaintext) into coded text (cipher text). Two fundamental algorithms of cryptography are symmetric key algorithms and asymmetric key algorithms. This classification is based on the number of cryptographic keys used in the algorithm. In a symmetric key algorithm, data is transformed into an unintelligible form that is difficult to undo without the knowledge of a secret key (i.e. symmetric key). If an attacker is able to obtain the key, then the secrecy of a communication will be compromised. The nature of a

symmetric key algorithm that requires a unique key to be known by each Sender and receiver leads to the problem called combinatorial explosion (Skerratt, 2002). For example, three devices need 3 unique keys for the three possible pairs (AB, AC and BC) while four devices need 6 unique keys for all possible pairs (AB, AC, AD, BC, BD and CD). However, a sender might experience difficulties to determine whether a public key is it published by the real owner or an attacker. The authenticity of a public key can be ensured by introducing a trusted thirdParty (TTP) (Mensoret a1., 2001; Schneier, 1996; Skerratt, 2002). In this situation, there is no need for the TTP to store both correspondents to have a prior relationship with the TTP. Instead, a TTP guarantees that the public key originates from the real owner by certifying the public key. A TTP that certifies public keys is also known as a certificate authority (CA). A CA binds the identity of each entity to their public key. This method prevents impersonation by an attacker as well as releasing the burden of the TTP to store multiple keys.

Digital Signature Scheme

The certification process in an asymmetric key algorithm depends on digital signature to provide trust. A digital signature is an electronic method of signing an electronic document that is reliable, convenient and secure (Skerratt, 2002). A digital signature mechanism consists of a digital signature generation and associated digital signature verification. A simplistic model of digital signature schemes involves a sign operation that uses a sender's private key to generate a signature. The receiver retrieves the sender's certified public key from a CA and performs a verify operation on the signature. A successful verification procedure convinces the receiver that the received message is from the actual originator and the contents are not tampered since leaving the originator. Digital signature schemes that are commonly used in practice might vary from this model. The following section provides one of the classifications of digital signature schemes. This study starts with literature review of digital signature and the other hand, importance of image steganography technique to embed the data into the image. Figure 1 shows an overview of these steps.

Image Steganography

An image is a collection of numbers that form different light intensities in different areas of the image. This numeric representation form a grid and the individual points are referred to as pixels. Most images on the Internet consists of a rectangular map of the image's pixels (represented as bits) where each pixel and its color is located. These pixels are shown horizontally row by row. The number of bits in a color scheme, called the bit depth, refers to the number of bits which is used for each pixel (Fridrich and Rui, 2000). The smallest bit depth in current color schemes is 8, which has the meaning that there are 8 bits used to describe the color of each pixel. Monochrome and grayscale images use 8 bits for each pixel and are able to show 256 different colors or shades of gray. Digital color images are normally stored and saved in 24-bit files and they use the RGB color model, also known as true color. All color differences in the pixels of a 24-bit image are driven from three primary colors: red, green and blue, and each primary color are represented by 8 bits. Thus, in one given pixel, there can be 256 different quantities of red, green and blue, which will add up to more than 16-million combinations, and will result in more than 16-million colors. Not surprisingly, the larger the file size, the larger amount of colors can be shown (Fridrich and Long, 2000). An image is an array of numbers that represent light intensities at different points, or pixels. These pixels make up the image raster data. An image size of 640 by 480 pixels, utilizing 256 colors (8 bits per pixel) is fairly common; such an image would contain around 300 kilobytes of data (Tamura, 2011).

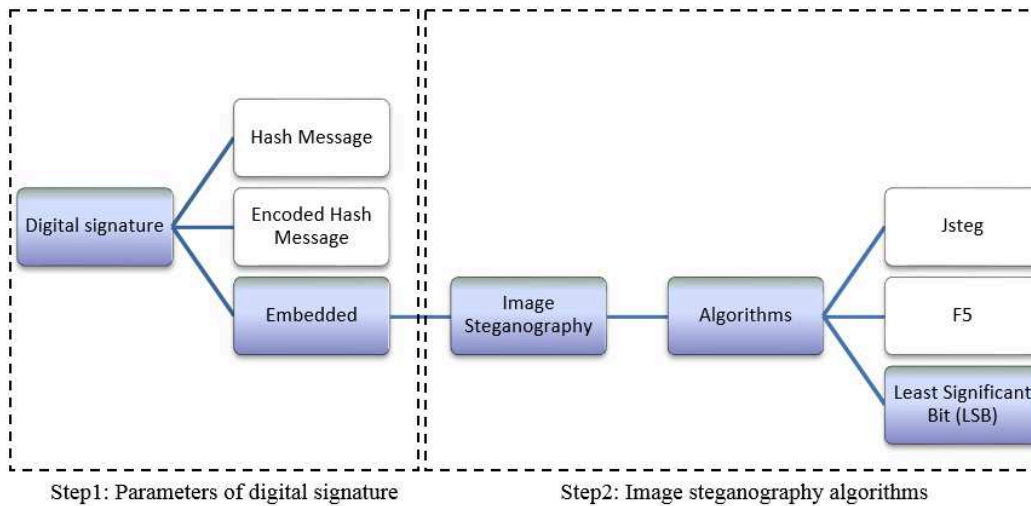


Figure 1: Two Steps of Literature Review

Proposed Algorithm

The overall scheme in proposing a new method to decrease the size and bandwidth needed for digital signature. The procedures of the suggested algorithm are as follows, do a procedure in a package of 100 bytes. Every one of the byte has loaded from file and does the logical operation of OR with a byte of (00000001), after that setting the product passionate to character of the variable (Figure 2). Subsequent to the dealing out of initial 100 bytes, multiply all of the ORed outcome bytes and maintain them in variable of 32 bits. Utilize the 32 of chief bits development of the outcome. Afterward the second 100 bytes will be procedure through the similar action. Accordingly every 100 bytes of information are cutting to hashed information in 32 bits (Figure 3).

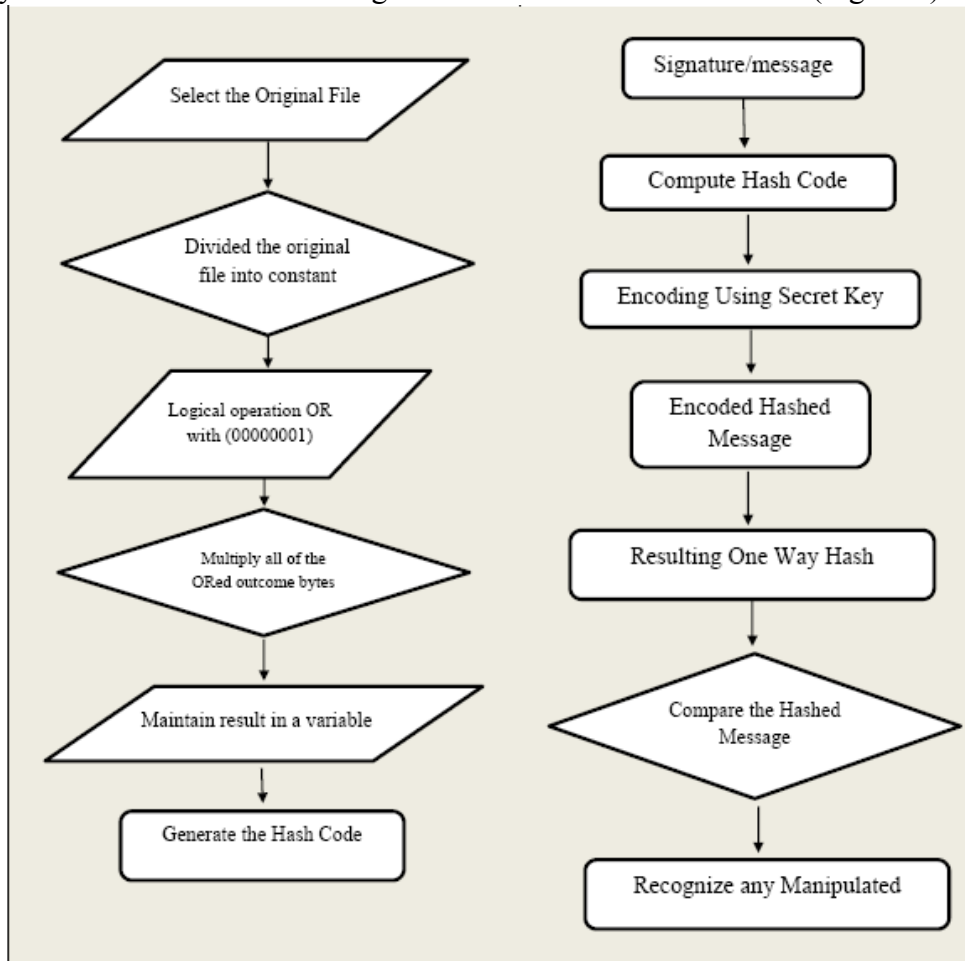


Figure 2: Generating One Way Hash Code

Figure 3: Verification One Way Hash Code

Conclusion

It is often thought that communications may be secured by encrypting the traffic, but this has rarely been adequate in practice. Cryptography deals with the encryption of text to form cipher (encrypted) text using a secret key. However, the transmission of cipher text may easily arouse attacker's suspicion, and the cipher text may thus be intercepted, attacked or decrypted violently. In order to overcome the shortcomings of cryptographic techniques, an important sub-discipline of information hiding, Steganography has been developed as a new covert communication means in recent years. It transfers message secretly by embedding it into a cover medium with the use of information hiding techniques.

Acknowledgment

The authors would like to express greatest appreciation to Ministry of Education (MOE), Malaysia and Universiti Teknologi Malaysia for providing the grant to carry out this research work with vot number R.K130000.7838.4L073. Last but not least, the authors would like to thank Advanced Informatics School, Universiti Teknologi Malaysia for their support of this project.

References

- [1] Fridrich, Jiri, Rui Du. "Secure steganographic methods for paletteimages." Center for Intelligent Systems, Information Hiding, *Proceedings of the Third International Workshop, IH_99 Dresden Germany, Computer Science2000*, pp 47–60.
- [2] Askling, Johan, et al. "Haematopoietic malignancies in rheumatoid arthritis: lymphoma risk and characteristics after exposure to tumour necrosis factor antagonists." *Annals of the rheumatic diseases* 64.10 (2005): 1414-1420.
- [3] Fridrich, Jiri, and M. Long. "Steganalysis of LSB encoding in color images." *Multimedia and Expo, 2000. ICME 2000. 2000 IEEE International Conference on*. Vol. 3. IEEE, 2000.
- [4] Schneier, Bruce. "Applied cryptography. Protocols, Algorithms, and Source Code in C/Bruce Schneier." (1996).
- [5] Mensor, Luciana L., et al. "Screening of Brazilian plant extracts for antioxidant activity by the use of DPPH free radical method." *Phytotherapy research* 15.2 (2001): 127-130.
- [6] Skerratt, Jennifer H., John P. Bowman, and Peter D. Nichols. "Shewanellaolleyana sp. nov., a marine species isolated from a temperate estuary which produces high levels of polyunsaturated fatty acids." *International journal of systematic and evolutionary microbiology* 52.6 (2002): 2101-2106.
- [7] Tamura, Koichiro, et al. "MEGA5: molecular evolutionary genetics analysis using maximum likelihood, evolutionary distance, and maximum parsimony methods." *Molecular biology and evolution* 28.10 (2011): 2731-2739.

Simulation Optimization – Testing Selected Optimization Methods and Their Setting of the Parameters

RASKA, PAVEL^a and ULRYCH, ZDENEK^b

Department of Industrial Engineering - Faculty of Mechanical Engineering, University of West Bohemia, Univerzitni 22, 306 14 Pilsen

^apraska@kpv.zcu.cz, ^bulrychz@kpv.zcu.cz

Keywords: Optimization Methods Parameters Settings, Simulation Optimization, Discrete Event Simulation, Testing Function.

Abstract. The paper deals with testing optimization methods and their setting of the parameters used to search for the global optimum of specified objective functions. The objective functions were specified considering the objectives of the discrete event simulation models. We specified the evaluation methods considering the success of finding the global optimum (or the best found objective function value) in the defined search space. We tested Random Search, Hill Climbing, Tabu Search, Local Search, Downhill Simplex, Simulated Annealing, Differential Evolution and Evolution Strategy. After the testing we proposed some slight modifications of the Downhill Simplex and Differential Evolution optimization methods.

Introduction

Our department focuses on modelling and optimizing production and non-production processes in industrial companies. Most current simulation software – Arena, Witness, Plant Simulation, etc. uses its own black-box simulation optimizers [1]. The user cannot set up the parameters of the optimization method. Another problem is that some integrated simulation optimizers cannot affect all the parameter types of the designed simulation model (e.g. Arena). Hence we have developed our own simulation optimizer using different optimization methods that can affect all the parameter types of the designed simulation model. Many simulation optimizers use similar optimization methods to search for the global optimum of the objective function – Tabu Search, Simulated Annealing, etc. [1]. Hence we selected commonly used optimization methods in discrete event simulation optimization and modified them in such a way that they are applicable for discrete event simulation optimization purposes. These methods are Random Search, Hill Climbing, Tabu Search, Local Search, Downhill Simplex, Simulated Annealing, Differential Evolution and Evolution Strategy. We tested these methods on three discrete event simulation models and four testing functions. After the initial testing and analysis of the behaviour of the implemented optimization method we have proposed some slight modifications to Downhill Simplex and Differential Evolution. We were also interested in how the setting of the optimization method parameters can affect the success of finding the global optimum in the search space where the global optimum is known (we performed all possible – feasible – combinations of simulation model input parameters). We had to perform many optimization experiments (simulation runs) with different optimization method settings to define the appropriate setting of the algorithm. These optimization experiments were replicated to reduce the influence of random behaviour of optimization methods.

Simulation Models and Objective Functions

We tested selected optimization methods on three ARENA discrete event simulation models of production systems of industrial companies. The first simulation model “The Assembly Line” represents an assembly line where products are conveyed by conveyor belt. The objective function reflects the penalty which is affected by the number of defective products and the palletes in the system. The objective function is maximized. The second simulation model “The Penalty” represents a production line which consists of eight workstations where the product is penalized if the product

exceeds the specified production time. The objective function is affected by the total time spent by the product in the manufacturing system. The objective function is minimized. The third discrete event simulation model “The Manufacturing System and Logistics” represents the production of different types of car lights in a complete production system. The objective function is affected by the sum of the average utilization of all assembly lines and average transport utilization. The objective function is maximized. A more detailed description of each simulation model can be found in [2]. We also tested optimization methods on four standard testing functions – De Jong’s, Rosenbrock’s, Michalewicz’s and Ackley’s functions. All testing objective functions were minimized.

Tested Optimization Methods and Proposed Modifications

We selected commonly used optimization methods in discrete event simulation optimization - Random Search, Hill Climbing, Tabu Search, Local Search, Downhill Simplex, Simulated Annealing, Differential Evolution and Evolution Strategy [2] - and modified them in such a way that they are applicable for discrete event simulation optimization purposes. We slightly modified the Downhill Simplex and Differential Evolution methods.

Downhill Simplex. This optimization method uses the idea of the Nelder–Mead Downhill Simplex algorithm [3,4]. This method uses the rounding of coordinates of the point to the nearest feasible coordinates in the search space and this leads to deviation from the original direction in our case. We performed additional optimization experiments with smaller steps to test the success of finding the optimum in this case. The success was higher than the success with the largest steps. Ordinarily this method uses a set of $n + 1$ linearly independent candidate solutions (n denotes search space dimension) - Simplex. We deliberately break the rule of the linearly independent points. The optimization method could generate the same point in the search space. The success of finding the optimum was very small in this case. We proposed a slight modification of the reduction phase. If the same point (same coordinates of the point) is generated in the search space, each point coordinate will be changed with 50 % probability to a value which equals the current value of the coordinates + (+ with 50 % probability and – with 50 % probability) the value of the lowest step in the search space which optimization method can perform. After this modification, this method achieved success comparable to other favourite methods Evolution Strategy and Simulated Annealing in finding global optimum.

Differential Evolution. This optimization method uses selection which is carried out between the parent and its offspring [5]. The optimization method uses General Evolution (copying individuals) and the Ali and Törn adaptive rule [6]. The offspring are created through a crossover between the parent and the new individual. This individual is created through the mutation of four selected individuals and the best one selected from the population – BEST method [7]. To avoid the premature convergence (duplication of a good individual to another population leads to faster finding of the solution but reduces the diversity and converges too early) we proposed the rule: If the difference between the objective function value of the current generated individual and the objective function of the best found individual is less than $1 \cdot 10^{-11}$ the gen of \mathbf{X}_{New} is changed with 30 % probability (\mathbf{X}_{New} denotes the individual to crossover with parent). The gen is changed to a value which equals the current value of the coordinates + (+ with 50 % probability and – with 50 % probability) the value of the lowest step in the search space which optimization method can perform * 10 * random number in the interval 0 (including) and less than 1 using uniform distribution. Both modified methods achieved comparable success in finding the global optimum with other favourite methods Evolution Strategy and Simulated Annealing.

Evaluation of the Setting of the Optimization Method Parameters

After the initial testing of the optimization methods on the simulation models we were surprised how the setting of the optimization method parameters affected the success of finding global optimum in the search space. We performed many optimization experiments with a concrete optimization method setting to find the optimum of objective function to define the appropriate setting of each method. The

number of concrete optimization method settings was affected by the number of optimization methods parameters. If the optimization method contains the same parameter (the same nature of this parameter as the other optimization methods) we performed optimization experiments with the setting of this parameter (same step, lower and higher boundaries). The optimization experiment contains the specified number of simulation runs if the optimum was not found; otherwise the optimization experiment contains simulation runs until the optimum was found. The optimization experiments were replicated (series) to reduce the influence of random behaviour of optimization methods. After finishing all series with different settings we filtered the series where the optimum was found. We proposed different criteria which express the success or the failure of the optimization method in different ways. The first criterion f_1 is the value of not finding the known VTR (value to reach). The criterion value is between [0, 1]. If the failure is 100[%] the criterion equals 1 therefore we try to minimize this value. This value is expressed by:

$$f_1 = \frac{s - n_{succ}}{s} \quad (1)$$

where s denotes the number of performed series, n_{succ} denotes the series where the VTR was found. If there was no series where the optimum was found $f_1 \neq 0$ we proposed other evaluation criterion - the Difference between Optimum and Local Extreme - f_2 (there is no series which contains any optimum). We did not use this criterion, because no such series was performed (there was at least one series – concrete setting of the optimization method parameters - where the success of finding the optimum was 100 %). This success was due to the quite small search space (all possible settings of simulation model input parameters were performed to find the optimum). As mentioned, the number of concrete optimization method settings was affected by the number of optimization methods parameters. We performed 45,490 different settings for each simulation model and approximately 4,112,000,000 simulation runs were performed. The testing was extremely time consuming, hence we used more computers to perform the series. We were especially limited in the number of licences of simulation software. We will focus on the modified Downhill Simplex and Differential Evolution. The success f_s of a concrete setting – series - is expressed by:

$$f_s = \frac{n_{succ}}{s} \quad (2)$$

where n_{succ} denotes the number of concrete series (the concrete setting of the optimization method parameter) where the VTR was found (in our case $f_1 = 0$); s denotes the number of all performed series with concrete setting of the optimization method parameter. The following bar charts represent the success of the concrete setting of the optimization method parameter. If all bars (concrete setting of the optimization method parameter) in the chart reach almost the same value of success, we can say that the setting of the parameter is less sensitive. If the concrete bar reaches a high success value for all the simulation models we can deduce that the value of the parameter has an impact on the method behaviour.

Downhill Simplex Parameters. The following charts –Fig. 1 - contain the performed series and the success of all parameters of the Downhill Simplex method for all simulation models. We can see that the setting of reflection and contraction coefficient affects the method behaviour of finding global optimum more than the expansion and reduction coefficient for our simulation models. The dimension of the search space is quite small.

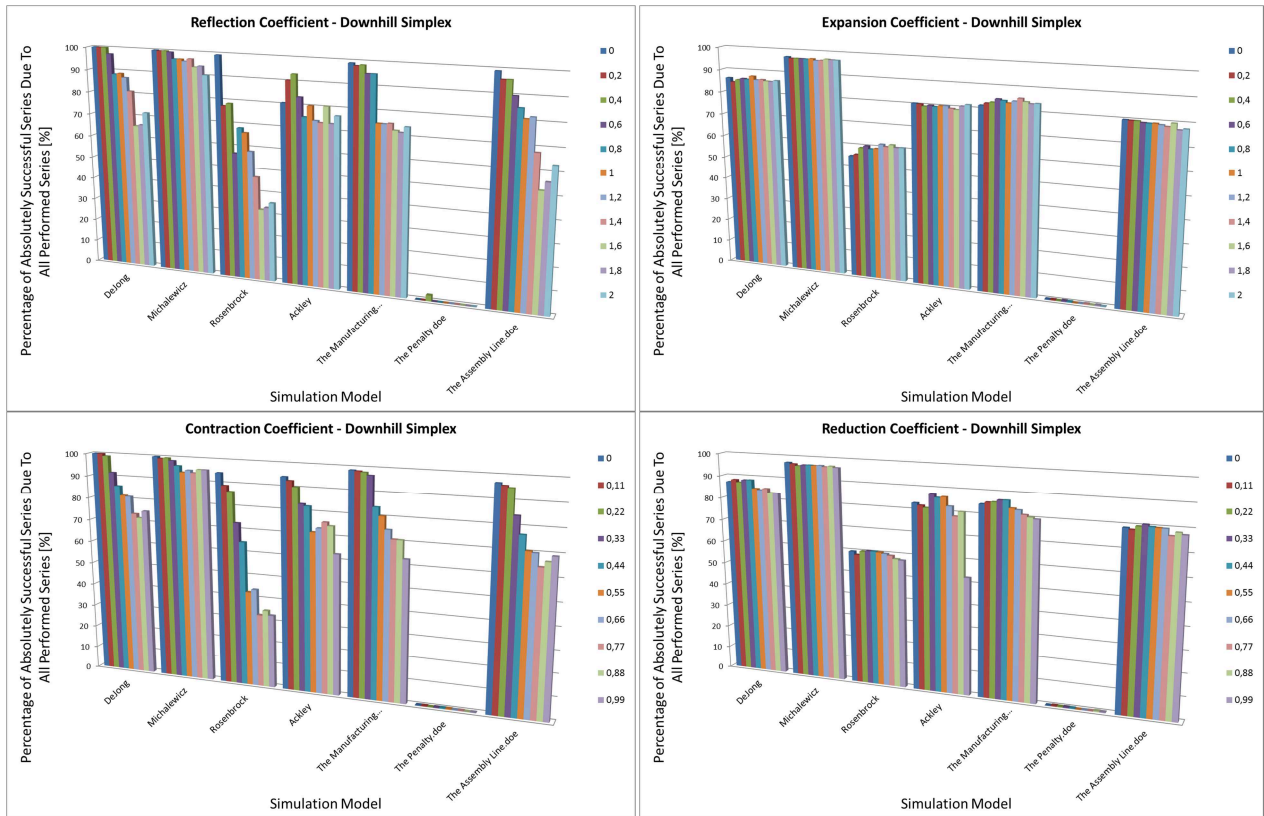


Fig. 1 The Success of Downhill Simplex Series –Maximization of Values

Differential Evolution Parameters. The following charts –Fig. 2 - contain the performed series and the success of all parameters of the Differential Evolution method for all simulation models.

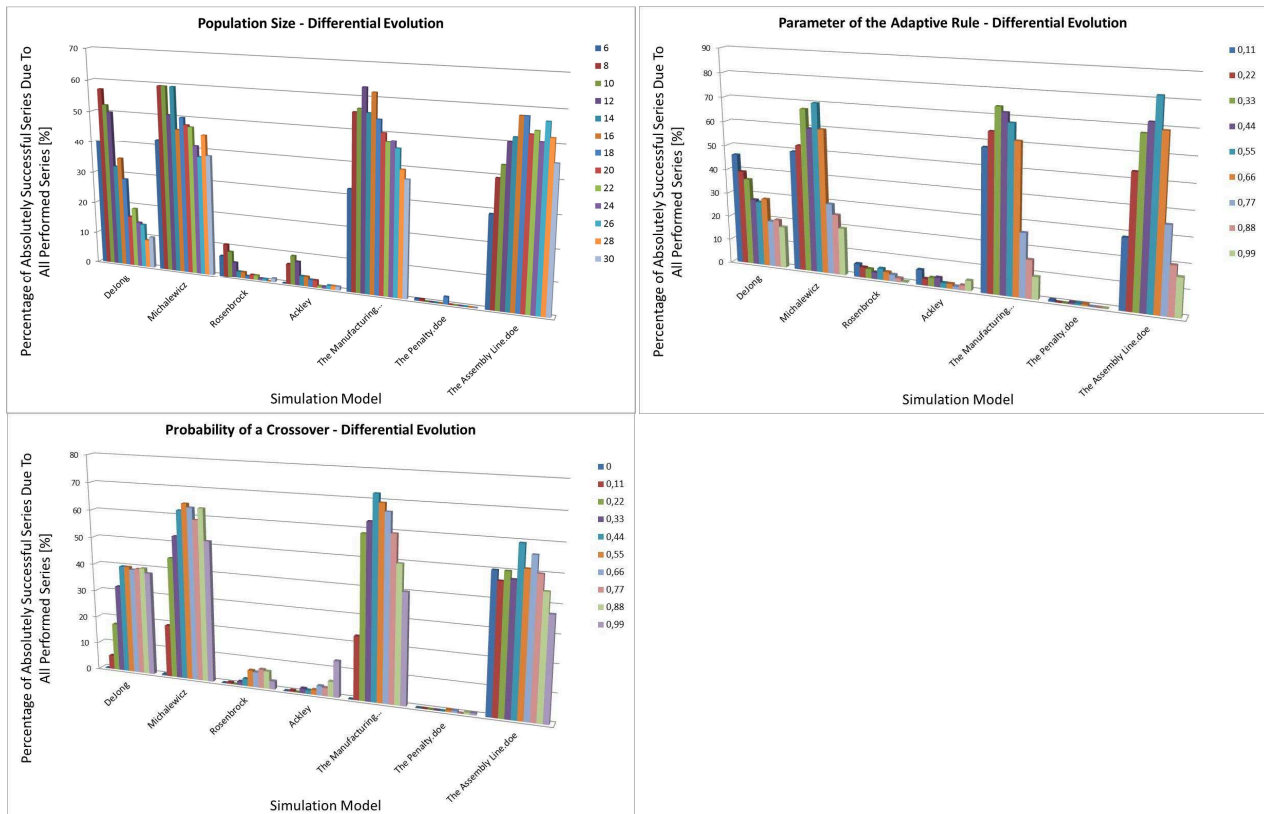


Fig. 2 The Success of Differential Evolution Series–Maximization of Values

Summary

The goal of the research is to test setting the optimization methods parameters of the optimization methods which are used to search for the global optimum of specified objective functions while considering the objectives of the discrete event simulation models. We tested Random Search, Hill Climbing, Tabu Search, Local Search, Downhill Simplex, Simulated Annealing, Differential Evolution and Evolution Strategy in the first phase (we had to specify the evaluation methods considering the success of finding the global optimum in the defined search space). Then we analysed the optimization methods behaviour and proposed some slight modifications of the Downhill Simplex and Differential Evolution methods to increase the success of finding the global optimum in the search space. All optimization methods had a problem with the “Penalty” discrete event simulation model. This simulation model has a complicated objective function landscape. The area around the optimum is straight and the optimization method could not obtain information about rising or decreasing the objective function terrain. The success of heuristic optimization methods depends on the objective function landscape. Downhill Simplex was more successful in finding the optimum than other optimization methods because of the quite small dimension of the search space. We specified quite a small dimension of the search space for evaluation of all possible (feasible) combinations of simulation model input parameters to find the global optimum. Optimization methods were successful in these cases. We can see that the setting of the reflection and contraction coefficient affects Downhill Simplex method behaviour of finding the global optimum more than the expansion and reduction coefficient of our simulation models. All performed settings (series) of the Differential Evolution had a bigger problem to find the optimum with a complicated objective function landscape than the Downhill Simplex. We must conclude that it is very hard to set up the optimization methods parameters. Even the authors of the algorithms are unable to unambiguously determine the appropriate settings of the algorithm. A possible answer to this question is to use another optimization method to set up the parameters of optimization method searching for the optimum of the objective function. We also tested the optimization methods in the cases where the dimensions of the search space were much bigger (44 simulation model input parameters). Optimization methods were weaker at finding the global optimum of these simulation models.

Acknowledgements

This paper was created with the subsidy of the project CZ.1.05/2.1.00/03.0093 “RTI - Regional Technological Institute”. The paper uses the results of the project CZ.1.07/2.3.00/09.0163. Both projects are carried out with the support of Ministry of Education, Youth and Sports.

References

- [1] Information on: <http://www.orms-today.org/surveys/Simulation/Simulation6.html>
- [2] P. Raska and Z. Ulrych, Simulation Optimizer and Optimization Methods Testing On Discrete Event Simulations Models and Testing Functions, Proceedings of the European Modeling and Simulation Symposium (2013)
- [3] Information on: http://prf.osu.cz/doktorske_studium/dokumenty/Evolutionary_Algorithms.pdf
- [4] Information on: <http://www.it-weise.de/projects/book.pdf>
- [5] K. P. Wong and Z. Y. Dong, Differential Evolution, in: Modern Heuristic Optimization Techniques, M. E. El-Hawary, Editor, New Jersey, John Wiley & Sons, 2008, pp. 171–186.
- [6] M. M. Ali and A. Törn, Population set-based global optimization algorithms: some modifications and numerical studies, Computers & Operations Research, vol. 10, (2004) 1703–1725
- [7] R. Storn and P. Price, A Simple and Efficient Heuristic for Global Optimization over Continuous Spaces, Journal of Global Optimization (1997)

Characterization of Diamond Electrodeposited Tool for Vibration Assisted Grinding Diagnostic

Mohd Fauzi Ismail^{1, a}

¹ Faculty of Mechanical Engineering, Universiti Teknologi Mara (Pulau Pinang), 13400 Bukit Mertajam, Pulau Pinang, Malaysia

^a mohdfauzi305@ppinang.uitm.edu.my

Keywords: Surface Topography Characterization, Ultrasonic Vibration Assisted Grinding, Surface Characterization Datum

Abstract. Causal analysis of diamond electrodeposited tools surface topography to the variation of grinding results is required to clarify the variations in grinding results of its application in ultrasonic vibration assisted grinding (UVAG) for steel mirror finishing. On the other hands, reference datum as defined by existing surface topography standard is not suitable and may lead to fruitless conclusion in relation to the DET characterization. This study aims to characterize the DET surface topography in relation to its performance in UVAG for steel mirror finishing. In this paper, samples of DET tool-work pairs are obtained from constant condition UVAG grinding test. The whole surface of DET surface topography is captured in one measurement using con-focal laser microscope and stitching toolbox. Surface Reversal Method is proposed to obtain the reference datum for the identification of active grains (diamond grains which actually involved in the grinding) on the DET working surface based on the most protruded grains from the surface. Based on the protrusion depth, this study found that only small number of grains can be considered as active grains. Then, each DET is characterized based on the distance of active grain to the tool rotational centre (active grain locus R_g). As a result, it is clarified that there is a non-linear relationship between the active grain locus R_g and work surface roughness S_q . There is an optimum size of active grain locus R_g for current grinding condition and for larger or smaller R_g , higher work roughness S_q is observed. Additionally, observation using high magnification white light interferometer on the work surface topography for each sample showed the existence of ultrasonic vibration marks with the marks wavelength consistence to the size of active grain locus R_g of the DET, which also validates the methodology used for DET characterization.

Introduction

The introduction of ultrasonic vibration assisted grinding (UVAG) enabled the utilization of good properties of diamond cutting edge for mirror finish of mould steel through diamond electrodeposited tool (DET) [1]. The UVAG system was built based on NC milling machine with ultrasonic vibrator combined with the main spindle to embed the ultrasonic vibration to the rotating tool. The DET was made of super-hard alloy cylinder and the tool working surface is the flat end surface which covered with #100/120 diamond grains by means of nickel electroplating. Comparing the machining optimization results from the consecutive reports [1,2]; they showed different machining optimum condition and tendency in relation to the roughness of work surface despite of using the same tool. These show variability of the UVAG while the most undefined element of it is the tool-work interaction between the DET working surface and ground surface during grinding, and the analysis on the geometrical properties of the DET working surface topography is necessary to clarify the matter.

The tool-work interaction analysis requires information of the tool working surface topography [3] but characterization based on small sampled area can only provide statistical characterization. The ground surface profile from the UVAG with DET was analyzed [2] and the possibility that only a small number of grains, probably one, are active during the grinding process was highlighted, but it has not yet been known how the 3D grain protrusion parameters were related to the ground surface. Hence, the necessity to measure the whole DET working surface in a lump was proposed, while the

imperfection of the characterization when using least square reference datum was also highlighted [4].

This paper is focused on identifying the active grains and parameterizes the DET working surface based on quantity and distribution of the active grains, and then make clear how these grain protrusion parameters are related to the UVAG performance.

Characterization of DET Working Surface

In this study, topography measurement of the DET working surface is performed using Confocal laser scanning microscope [4]. The objective lens used is 20× with NA 0.6 and the pixel size is 0.747 mm × 0.747 mm. The viewing area of 0.6 mm × 0.6 mm is increased to about 4 mm × 4 mm based on 7 × 7 frames measurement by utilizing the automated positioning and repeating measurement provided in stitching toolbox available in the measuring instrument. Prior to the DET characterization, the problem related to the reference datum is considered. Fig. 2(a) shows the orientation of DET related to the measurement axis during the measurement of the working surface topography $F(x, y)$. The preferred datum for the characterization is plane $C(x, y)$ while the inclination angular α is unknown (Fig. 2). The following procedure is proposed to extract the plane $C(x, y)$ based on reversal method [6, 12].

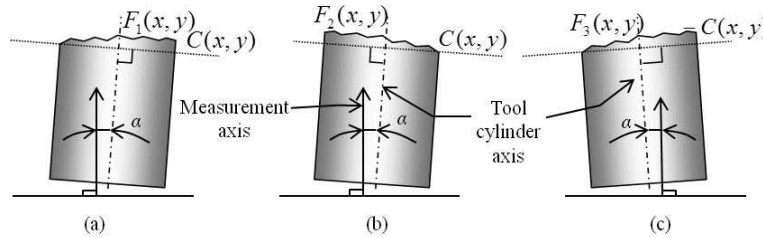


Fig. 1 Angular relationship of tool and measurement axes (a) normal position, (b) tool rotated 180° about the cylinder axis, (c) tool rotated 180° about the measurement axis.

Reversal method based datum extraction. Fig. 1 shows orientation of a cylindrical tool to a measurement axis; Fig. 1(a): normal position, Fig. 1(b): after the tool is rotated 180° about the tool cylinder axis and Fig. 1(c): after the tool is rotated 180° about the measurement axis from (b) position. Referring to Fig 1, 2 sets of primary surface $M_1(x, y)$ and $M_2(x, y)$ are captured from position (a) and (b). Primary surface $M_3(x, y)$ of position (c) is obtained by digitally 180° rotates the primary surface $M_2(x, y)$. Relationship of the primary surfaces to the inclination component $C(x, y)$ are as follows.

$$\begin{aligned} M_1(x, y) &= F_1(x, y) + C(x, y) \\ M_2(x, y) &= F_2(x, y) + C(x, y) \\ M_3(x, y) &= F_3(x, y) - C(x, y) \end{aligned} \quad (1)$$

Since the surface topography $F_1(x, y)$ and $F_3(x, y)$ are ideally same, the inclination component $C(x, y)$ is obtained by subtraction between the primary surface $M_3(x, y)$ and $M_1(x, y)$.

$$C(x, y) = \frac{M_1(x, y) - M_3(x, y)}{2} \quad (2)$$

In this study, the inclination component $C(x, y)$ is the reference datum and by subtracting it from primary surface $M_1(x, y)$ or $M_2(x, y)$, the topography $F(x, y)$ is ready to used for grain height measurement. By keeping the holding jig fixed rigidly to the measuring machine, the inclination component $C(x, y)$ will be constant between measurements. Therefore, in this study, the inclination component $C(x, y)$ is obtained using a reference cylindrical artefact and being used to extract the DET topography $F(x, y)$.

Data pre-processing for DET working surface topography. Data pre-processing for DET working surface topography in this study is as follows.

Down sampling. The down sampling of the primary surface is performed to reduce the number of data points from 5448×5468 to 2033×2041 by changing the pixel size from $0.747\text{mm} \times 0.747\text{mm}$ to $2\text{mm} \times 2\text{mm}$, in order to reduce the computation load.

Inclination removal. The measurement inclination removal of the DET surface topography data was performed by subtracting it with the extracted reference datum $C(x, y)$.

Outliers correction. In this study, an outlier correction procedure reported in [7] is employed with the largest outlier cluster is defined as 5×5 pixels and detection level L is 1.1. The height information of identified outliers is deleted and replaced with an artificial value based on the weighted average of available normal data points on 8 equiangular directions.

Surface filtering. Batwing effect [8] appeared as a spike noise at the edges of diamond grains plateau. The amplitude of batwing effect is relatively small to be detected using the outliers' correction procedure. 9×9 pixels Median filter [10] is employed to reduce the batwing effect.

Motif analysis. Areal motif analysis with Wolf pruning at 5% (i.e., 5% of the peak-to-valley of the data) [9] is applied to the DET surface topography data for diamond grains identification. The feature parameter (i.e., peak height), is used to identify the highly protruded grains as possible active grains.

Experiment

Sample Preparation. In this study, DET-work pair samples are prepared. Machining parameters for all pairs are same to reduce the uncertainty of the machining to cutting edge protrusion on DET working surface topography. The UVAG system is made of Makino NC milling machine V22 equipped with ultrasonic spindle (Takesho). The DET is made of super-hard alloy substrate cylinder with one end coated with diamond grains #100/120 with average diameter of $160\ \mu\text{m}$ by means of nickel electroplating, and the flat end is the working surface of the tool. The DET is fixed to the spindle with thermal chuck and truncated using a rotating truer wheel. During grinding, the rotational speed S of $2000\ \text{min}^{-1}$, vertical ultrasonic vibration frequency f is $60\ \text{kHz}$ with the vibration amplitude around $0.5\ \mu\text{m}$. The depth of cut h is $1\ \mu\text{m}$, the tool feed rate F is $500\ \text{mm/min}$ and the cross feed P is $20\ \mu\text{m}$.

Work Surface Characterization. Work surface topography characterization is performed for two reasons; 1) process assessment, 2) process diagnostic.

Work roughness characterization for process assessment. The topography of work surface is measured at six randomly selected locations on the surface using white light interferometer (WLI) with $10\times$ Mirau objectives which provides $0.8\text{mm} \times 0.65\ \text{mm}$ viewing area and $0.64\ \mu\text{m}$ lateral resolution. The viewing area is used as the evaluation area for the surface topography characterization. Gaussian filtering [5] is performed to suppress the waviness component from the measured topography data with cut-off wavelength λ_c $0.1\ \text{mm}$. Roughness parameter S_q [6] is employed for the process assessment.

UVAG ground surface characterization for process diagnostic. WLI with $50\times$ Mirau objectives is used to capture the ground surface topography to analyze the surface for process diagnostic. The viewing area is $0.18\ \text{mm} \times 0.133\ \text{mm}$ and the pixel size is $0.131\ \mu\text{m} \times 0.131\ \mu\text{m}$.

Result and Discussion

Process diagnostic on work surface topography. Fig. 2 shows isometric view of micro-topography from selected samples with the tool feeding along x axis and the cross feed descending y axis. The effect of ultrasonic vibration has materialized as a consistence waveform pattern on the surface topography. Average Power Spectrum Density (APSD) analysis [10,11] is performed to characterize the wavelength lu observed on the work surface along the tool feeding direction (x axis). As a result, all samples show only one high spectrum for $lu < 7\ \text{mm}$. The significant wavelengths from APSD analysis is used to estimate the distance of the cutting edge from tool rotation centre which is equivalent to the active grain locus radius R_g (Eq. 3).

$$Rg = \frac{60f \times l_u}{2\pi \times 10^3 S} \tag{3}$$

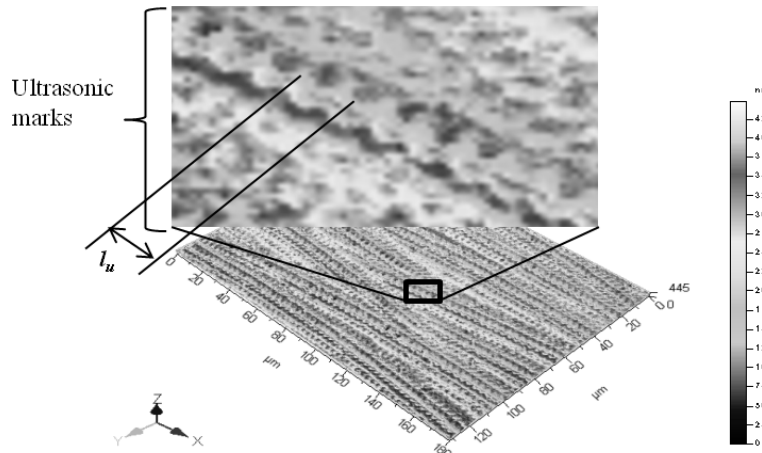


Fig. 2 Measurement result with WLI 50% objective for typical UVAG surface and the ultrasonic vibration marks.

Effect of active grain position on surface roughness. The relation between the locus radius Rg derived from APSD analysis and work roughness Rq is shown in Fig. 8. The smallest value of the roughness occurs when the locus radius Rg is around 1500 mm and the roughness increases as the locus radius distanced from the optimum point (around $Rg=1400$ mm).

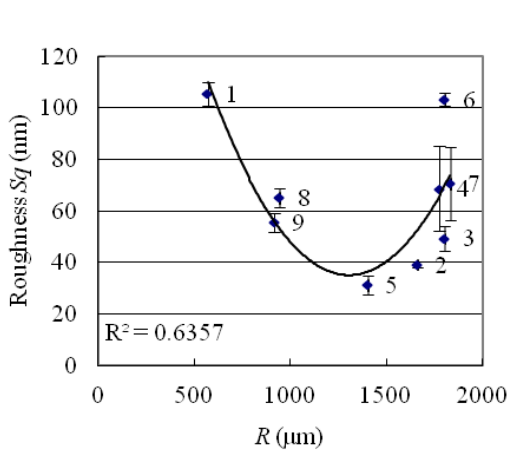


Fig.3 Relation of active grain locus Rg and roughness of ground surface

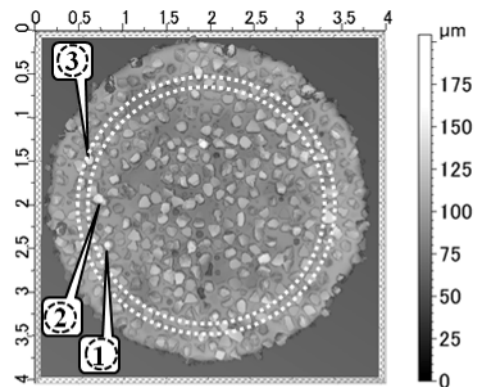


Fig.4 Samples for comparison of possible active grains to estimated cutting edge locus

Identification of possible active grains. As a result of the possible grain identification, only six of the nine samples are successfully characterized. The other three samples faced poor repeatability suspected due to geometrical error on the DET cylinder. Fig. 4 shows typical successful samples for the possible active grains identification where the number bullet shows the highest grains in sequence for the top 5 μm. All successful samples only have a small number of possible active grains while some only have one possible active grain.

The area segmented by the dotted line circles in Fig. 4 is the region of cutting edge locus estimated from the ultrasonic vibration marks on the works surface. All successful samples have some of their possible active grains located within the estimated active grain locus. This is the evidence that the active grains caused the ultrasonic vibration marks and cutting marks on the work surface topography and finally affects the quality of the surface finish.

Conclusion

- 1) Surface topography characterization for process diagnostic may differ from surface topography characterization for process or product evaluation as the production process fingerprint may not be included.
- 2) DET active grain can be identified by finding the highest protruded grain from the reference datum gained from the surface reversal method.
- 3) The position of the active grain contributes to the grinding quality and there is an optimum position for the given grinding conditions.

Acknowledgement

The financial support for this research by Universiti Teknologi MARA (UiTM) and Exploratory Research Grant Scheme (600-RMI/ERGS 5/3 (37/2012)) are greatly appreciated.

References

- [1] K. K. Hara, H. Isobe, H. Yoshihara, A. Kyusojin, K. Yanagi, Ultrasonically assisted machining for mirror finishing of die (1st report). Face grinding of die steel using electroplated diamond tool, *Journal of the Japan Society for Precision Engineering* 72 (9) (2006) 1134–1138.
- [2] H. Isobe, K. Hara, A. Kyusojin, M. Okada, H. Yoshihara, Ultrasonically assisted grinding for mirror surface finishing of dies with electroplated diamond tools, *International Journal of Precision and Manufacturing* 8 (2) (2007) 38–43.
- [3] D.L. Butler, L.A. Blunt, B.K. See, J.A. Webster, K.J. Stout, The characterization of grinding wheels using 3D surface measurement techniques, *Journal of Materials Processing Technology* 127 (2002) 234–237.
- [4] M.F. Ismail, K. Yanagi, H. Isobe, Characterization of geometrical properties of electroplated diamond tools and estimation of its grinding performance, *Wear* (2010), 271 (2011) 559–564
- [5] ISO/DIS 25178-2: 2007 Geometrical product specification (GPS) – Surface texture: Areal – Part2: Terms, definitions and surface texture parameters (International Organization for Standardization).
- [6] M. F. Ismail, K. Yanagi, H. Isobe, Surface Reversal Method for Cylindrical Tool Characterization, 2013, *Applied Mechanics and Materials*, 393, 266-271
- [7] M.F. Ismail, K. Yanagi, A. Fujii, An outlier correction procedure and its application to areal surface data measured by optical instruments, *Measurement Science and Technology* 21 (105105) (2010) 11 pp.
- [8] R. Leach, *Fundamental Principles of Engineering Nanometrology*, Elsevier Inc., Oxford, 2010
- [9] P.J. Scott, Feature parameters, *Wear* 266 (2009) 548–551.
- [10] B. Muralikrishnan, J. Raja, *Computational Surface and Roundness Metrology*, Springer, Meppel, Netherlands, 2009.
- [11] Digital Surf (2010) MountainsMap Premium ver. 5.1.1.5674, [/http://www.digitalsurf.fr/en/index.html](http://www.digitalsurf.fr/en/index.html), (accessed on July 15, 2010).
- [12] M.F. Ismail, K. Yanagi, H. Isobe, Geometrical transcription of diamond electroplated tool in ultrasonic vibration assisted grinding of steel, *International Journal of Machine Tools and Manufacture* (2012) 62, 24-31

If-Then Rules for Selection the Die-Set for Sheet Metal Punching and Blanking Dies

H.M.A. Hussein^{1,a}, J. Abu Qudeiri^{1,b}, U. Umer^{1,c} and R.K. Abdel-Magied^{2,d}

¹Advanced Manufacturing Institute, King Saud University, Riyadh 11421, Saudi Arabia

²Production Technology Dept., Faculty of Industrial Education, Beni-Suef University, Beni-Suef

^ahhussein@ksu.edu.sa, ^buumer@ksu.edu.sa, ^cjqudeiri@ksu.edu.sa, ^drgab65@gmail.com

Keywords: Die-set. Punching die. Blanking die. Computer aided selection. If-Then rules. VBA.

Abstract. Die-set is an essential tool accessory in sheet metal punching and blanking. The selection of the die-set represents an important activity in the die design operation. Time and money consumed in this operation could be saved by using an automated selection system for die-set components. This paper discusses an intelligent die-set selection system using the AutoCAD platform. The developed system is able to work as either standalone or connected with any die design CAD system by using the well-known AutoCAD programming tools. The proposed system is built using IF-THEN rules approach. The system code is developed using AutoCAD with Visual Basic. A data-base of Nasr Automotive Company (NASCO) for die-set was considered, from which suitable size of die-set was selected automatically. The proposed system could reduce the consumed time in the tool room department from hours to minutes and could reduce effort and cost as well.

Introduction

The Punching/Blanking operations are important in mass production systems and they represent the bottleneck for the most sheet metal die design and manufacturing companies. Depending on the type of product, die-sets can be very complex and expensive devices. A breakdown of a die-set, which is caused by the failure of one single punch, results in an enormous loss in production time. Tool life is also an important factor, when production costs are concerned. To solve these problems, Hijink [1] used 2-D finite-element method to establish a relationship between the displacements of the cutters and the dimensions of the press and die-set of the load of the punching process. In addition, a 3-D finite-element analysis has been applied for the die-set considering the analysis of the die deformations which concentrate on the guide post of the die-set plate [2-5]. The results obtained were checked against the practical data on die-set design and experiments. Kumar [6-7] described an intelligent system for selection of die-set of metal stamping press tool. A production rule-based expert system approach has been utilized to develop an intelligent die-set selection system called (IDSS) to assist die designers. The system IDSS was coded in Auto LISP language and loaded into the prompt area of AutoCAD. Kiani [8, 9] presented an analytical model for predicting the variation in the pitch distance between pilot holes stamped in strip layout in progressive die. The model is useful in designing die-sets since it relates pitch variation to die-set parameters such as the quantity of pilot pins, clearance in the stripper plate bearings, clearance about the punch, and clearance about the pilot pins. Rao [10] suggested an expert system to distribute the expertise of a human or group of humans throughout a group of users. A low cost Knowledge Base System (KBS) was proposed for design of deep drawing die.

To the best of the authors' knowledge, there is a limited number of systems developed in the literature for the automated selection of die sets. Evidently, a small number of companies are specialized in the design and manufacturing of die-sets for different purposes. However, there are limited available information of the automated selection programs those companies use to support the designer in die-set selection process.

In this work, rational steps for the selection of the suitable die-set using IF-THEN rules are described, in which the system selects between different sizes of die-sets that are mainly used in punching and blanking operations. The system works as either standalone or a module of the blanking die CAD system in both 2D and 3D. In case of working as a module of a 2D blanking die system, dimensions and factors added to the die-set database to decrease the required number of variables. This paper is one of work series that will be appear elsewhere.

The remainder of this paper is organized as follow. The next section presents the selection of the die-set. Then the proposed system is explained in the following section. The results of the application of the system on the NASCO die-set database are included. The paper ends with a conclusion section that briefly outlines the main conclusions.

Selection of Die-Set

Die-Set. The use of a die-set not only shortens the manufacturing time of the forming die but also assists in the smooth proceeding of the forming process. The selection of proper die-set yields better quality stamped products, better protection while using the press, and better performance of the press and die. Typically, a die-set is composed of a punch holder, a die holder, guide-post and guide bushings.

Two, four or more guide-posts are used for providing good alignment, for maintaining good relative horizontal position between die and press during operation and for case of setting. The number of guide-posts required increases when the size of the die-set increases and the demand on product quality is higher. The guide-posts can be placed at the rear corners, diagonal corners, or every corner at a certain distance from each other.

For manual operation, a die should provide more space for operators to pick and place the workpiece, thus uses lesser number of guide-posts than those used for automatic operations. Generally, ball bearing guides are used for high speed stamping; bearing guides are used when high lateral forces are expected whereas roller bearing guides yield both rigidity and high positional accuracy during stamping operations. In general, ready-made die-sets are used for smaller dies, and larger dies tend to be specially designed according to the requirements of the product and the press available. Die-sets are available commercially in a large variety of sizes and styles. In general, the dimensional accuracy of commercially available die-sets can meet the general demands as well as high precision requirements. Selection of die-sets depends on die type, die size, tonnage, manual or automatic operation and so forth. While round die-sets are normally used for drawing round cups or cylindrical products, rectangular die-sets are employed in connection with the production of most other shapes. Cast iron is used for smaller ready-made die-sets, while the hot-rolled steel is the preferred material for larger type. Cast iron die-sets are lower in cost, easier to machine and have the ability to provide good dampening for vibration, while the hot-rolled steel die-sets have better toughness, rigidity and provide better resistance to shock loads than cast iron ones.

Advantages of Using Ready-Made Available Die-sets. Most of the commercially available ready-made die-sets are manufactured in mass production. Thus, various sizes and types of die-sets are often readily available when needed. The utilization of ready-made die-sets can increase the tool room capacity and speed up the die making process by freeing the die designer from the design of die-set and preparing numerous associated drawings. Maintainability of the die is high since the parts of the ready-made die-set usually offer high interchangeability. Thus, skills required for an artisan and a die designer can be achieved through less training time.

The Proposed System

Since the standardized data and information are usually presented in table format, they can be converted readily as decision tables, which can be used in a data-base for the selection process. To illustrate the proposed system, we consider the case of NASCO company whose die-set data-base includes seven different sizes of die sets. Their dimensions were established by a high level of

experience of NASCO expert engineers and technicians for several years. These databases for the seven die sets were modified further by the authors by adding new dimensions and coordinates that are provided to the software automatically. In the proposed system, and based on the parametric data and dimensions of the die holder, the module selects a suitable die-set number from the NASCO die-set database. The schematic 2D drawing of the NASCO die-sets is shown in Fig. 1, while the 3D shown in Fig. 2.

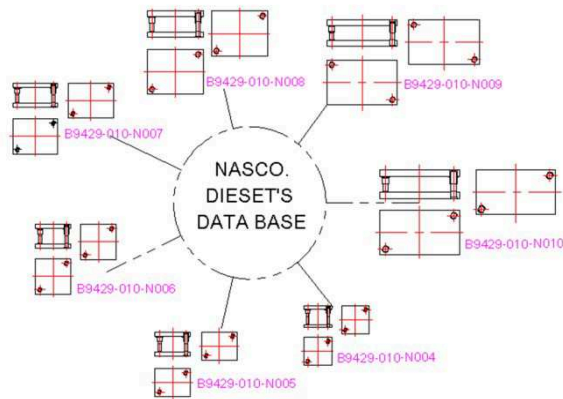


Fig. 1. 2D schematic for Nasco Die-Set DataBase

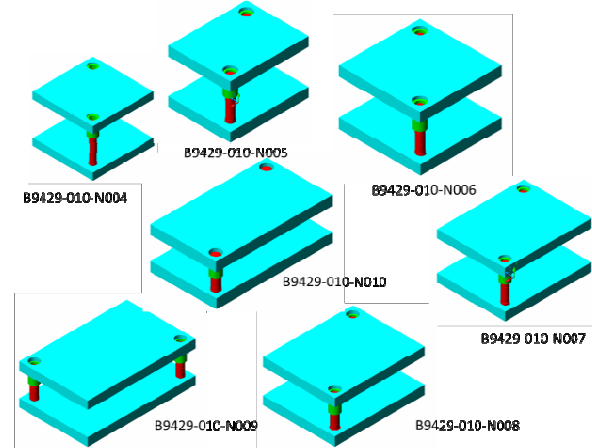


Fig. 2. 3D schematic for Nasco Die-Set

The IF-Then Rules of Selection. The lack of the data about automated selection systems of die sets even from the well-known die-set companies such as FIBRO and HASCO can be explained as follows. When there is no die design CAD system, there is no need for companies to build a die-set module as the die-set is an additive component to the other dies components. In our case, we built a computer-aided blanking die design system in both 2D [11] and 3D [12]. The die-set module is prepared to work as a stand-alone program or to add as an additive module to the above system. The die-set selection system was built in 2 ways, in 2D as in Fig. 1 to suit the 2D blanking die design system, and in 3D as in Fig. 2, to suit the 3D blanking die system. In case of the additive die-set module, to select the suitable size of the NASCO's die-set, a knowledge-based applied in form of IF-then rules, which was coded using Visual Basic with AutoCAD. If a condition is within the required range, then the action will be that the selected die-set drawing will insert automatically in its position in the AutoCAD drawing file with respect to the other items of the blanking die. The seven available die-set are; B9429-010-N004, B9429-010-N005, B9429-010-N006, B9429-010-N007, B9429-010-N008, B9429-010-N009, B9429-010-N010.

The die holder could be represented parametrically in 2D as a square surrounded with 4 points; each point contains X and Y coordinates. The first point is (P1, P2), the second Point (P3, P4), the third Point (P5, P6), and the fourth point (P7, P8). In the same way, the die set is also represented as a square parametrically in 2D as shown in the Fig. 3. Table 1, shows the IF-then rules of the optimum and automated selection of the die set based on the die holder dimensions. K is factor that takes a value related to the die-set size.

Table 1.

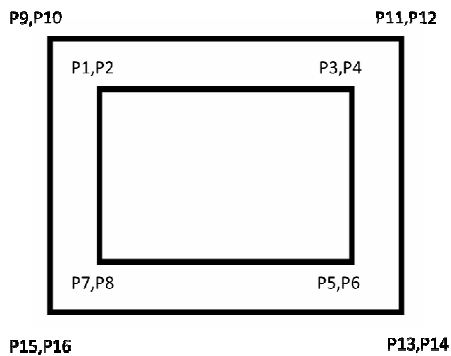


Fig. 3. The parametrical relations between the die holder and the die-set lower plate.

IF	Then
$(P1 - P3) < 531 \& (P4 - P6) < 221$	$K = ((P4 - P6)/2) + 400$ Insert B9429-010-N010
$(P1 - P3) < 479 \& (P4 - P6) < 249$	$K = ((P4 - P6)/2) + 400$ Insert B9429-010-N009
$(P1 - P3) < 349 \& (P4 - P6) < 249$	$K = ((P4 - P6)/2) + 400$ Insert B9429-010-N008
$(P1 - P3) < 269 \& (P4 - P6) < 184$	$K = ((P4 - P6)/2) + 300$ Insert B9429-010-N007
$(P1 - P3) < 184 \& (P4 - P6) < 184$	$K = ((P4 - P6)/2) + 300$ Insert B9429-010-N006
$(P9 - P3) < 184 \& (P4 - P6) < 119$	$K = ((P4 - P6)/2) + 250$ Insert B9429-010-N005
$(P9 - P3) < 138 \& (P4 - P6) < 138$	$K = ((P4 - P6)/2) + 150$ Insert B9429-010-N004

The Die-Set Database Parameters Modification. The NASCO data-base is mainly prepared for the manual selection of die-set. The dimensions were prepared in a form of table as shown in Fig. 4 to help the designer in selection operation. The table data were prepared based on the traditional point of view of the formal die drafting in which the die elevation projection is placed in the left upper side of the drafting paper. The lower group, which includes the lower die shoe, the two guide posts, die block, die holder, stripper, guide plate left hand, guide plate right hand, and bridge plate, is drafted lower than the die elevation projection. The upper group, which includes the upper shoe, the two-guide bushes, punch, punch holder, and thrust plate, is drafted in the right side of the die elevation projection. It is very difficult to simulate this technique of drafting by computer as hundreds of variables are required to achieve the final drafting, which will increase the system run time, make it difficult to fix, maintain and follow any bugs in the system. This problem related to the 2D blanking die program only.

To avoid this problem, we modified the NASCO die-set table to assume more dimensions and factors. The advantage of this modification is to insert the die-set as a block in vertical shape as shown in Fig. 4. The upper shoe is inserted above the elevation, and the elevation above the lower shoe. In this way, we could reduce the number of variables. After finalizing the complete die, the upper shoe group is moved to the right side of the elevation project, and drafting returns back to the formal technique. Fig. 5 shows the die-set before moving as well as the fixed factors K1 and K2 and how they decrease the number of variables in the proposed program and facilitates the drafting operation. While Fig. 6 shows the die set after moving. The proposed factors K, K1 and K2 are considered to control the distances between the 3 projections, and define the insertion position of the shank. The value of the the factor K is related to the die-set size. This value belongs to the shank insertion point in the AutoCAD drawing file. The shank must be inserted in its position in the upper plate of the die-set. Therefore, data bases of shanks were added to the system as shown in Fig. 7. The other factors, K1 and K2 are fixed distances that are used to decrease the number of parameters required of design and drafting of the blanking die.

Summary

Automated selection of suitable die-set size from a NASCO company die-set database has been discussed. The proposed system has been constructed in 2 ways, as a standalone program, and as an additive module for a computer aided blanking die design program. It was prepared in both 2D and 3D systems to serve the blanking die design system in both 2D and 3D die designs. The developed system shows the usefulness of the integration between the computer-aided blanking die design and the

automatic selection of the die-set. The system introduces If-then rules for automated selection of the suitable die-set size between different 7 sizes from the NASCO die-set data base.

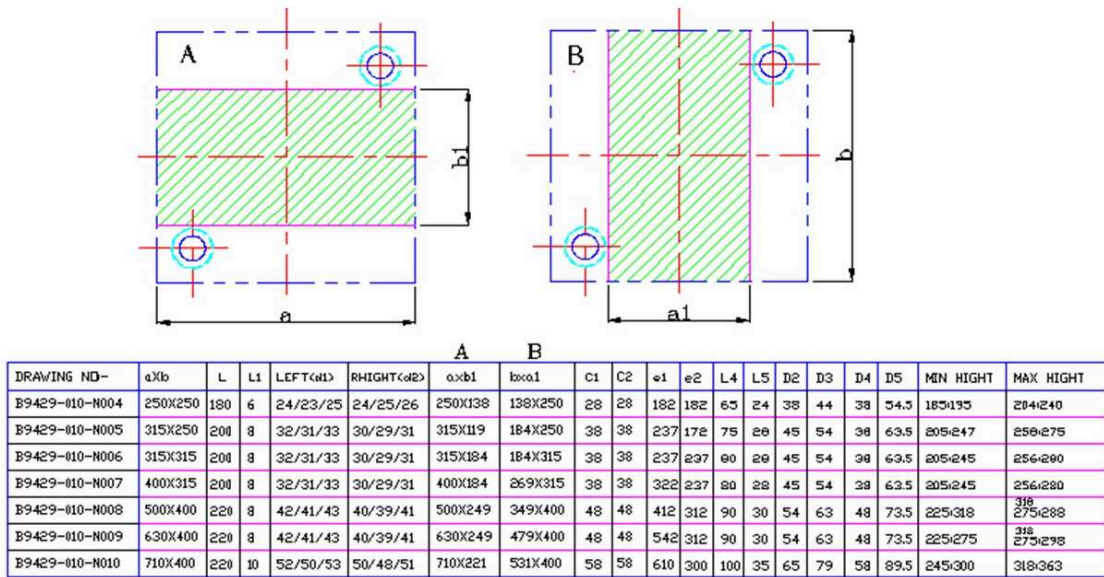


Fig. 4. The main dimensions of NASCO die-set.

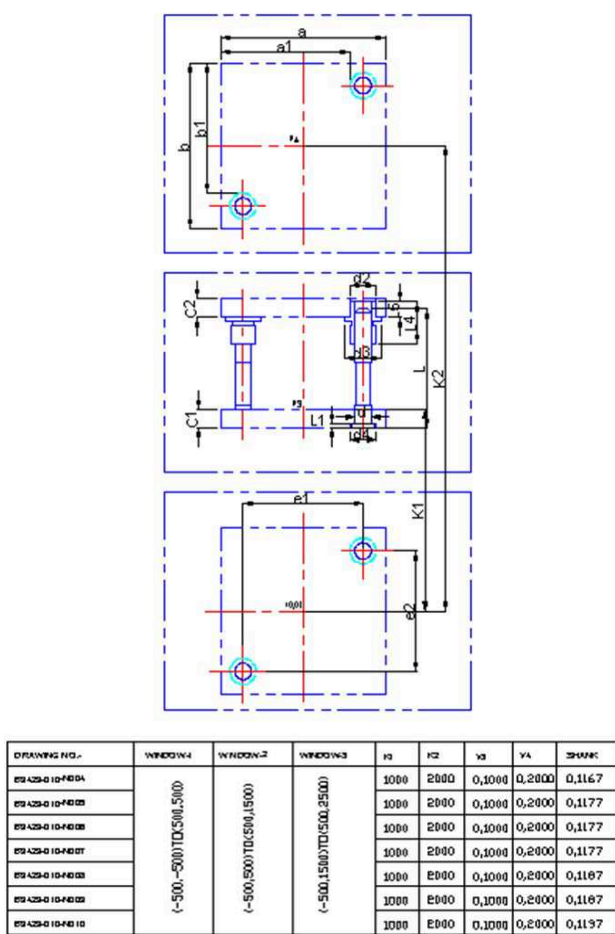


Fig. 5. Die-Set Parameters before movement, showing the k1, and k2 factors.

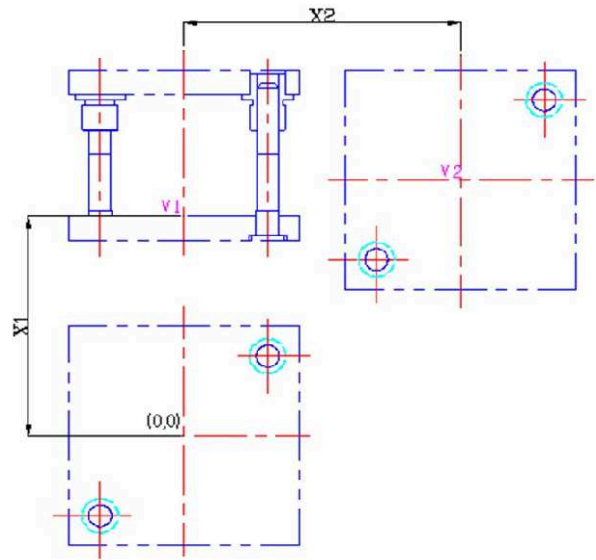


Fig. 6. Die-Set Parameters after movement

Acknowledgment

This work is supported by NSTIP strategic technologies programs, Grant number (12-INF2816-02) in the Kingdom of Saudi Arabia.

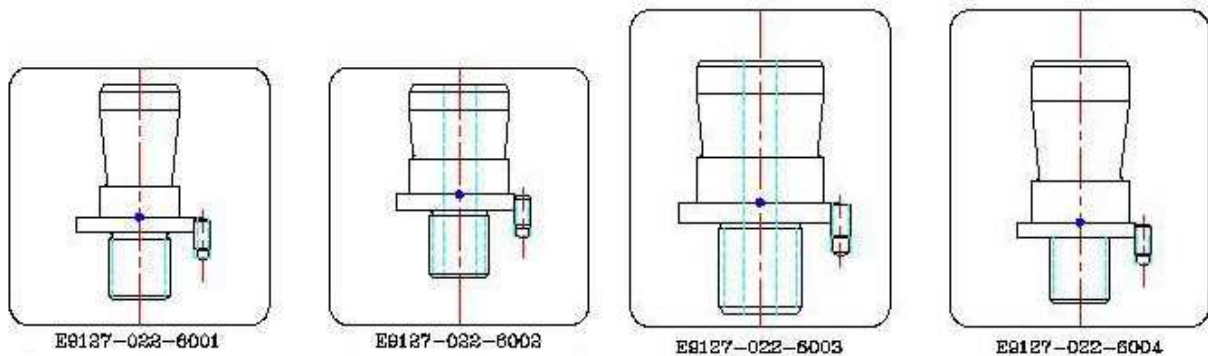


Fig. 7. Shank database

References

- [1] J.A.W. Hijink, A.C.H. van der wolf, On the Design of Die-Sets, *Ann CIRP*. 24 (1975) 357-360.
- [2] U.P. Singh, P.C. Veenstra, J. A. H. Remaekers, J.A.W. Hijink, Numerical analysis of four column under-drive press equipped with 4 guide pillar sub press, *Sheet Metal Industries*. (1976).
- [3] U.P. Singh, P.P. Miller, CAD of die-set, *Proceeding of the 2nd Conference NMC*. (1985).
- [4] U.P. Singh, H.J.J. Kals, A.H. Streppel, Computer aided design of a die-set for punching/blanking, *Proceedings of 28th International MTDR Conference*. (1990) 379-386.
- [5] U.P. Singh, H.J.J. Kals, A.H. Streppel, Design study of a punching/blanking tool geometry, *Proceedings of IMC Conference*. (1990) 806-820.
- [6] S. Kumar, R. Singh, An intelligent system for selection of die-set of metal stamping press tool, *Journal of Materials Processing Technology*, 164-165 (2005) 1395-1401.
- [7] S. Kumar, R. Singh, An intelligent system for selection of die gages of progressive die, *2nd National Conference on Intelligent Systems & Networks (ISN-2005)*.
- [8] S. Kiani, P.R. Vallance, A.H. Slocum, Errors in progressive dies for electronic components, *ASPE annual meeting, Monterey, CA*. (1999).
- [9] R.R. Vallance, S. Kiani, A predictive model for variation in the pitch between stamped pilot holes, *Transactions of the ASME, Journal of Manufacturing Science and Engineering*. 125 (2003) 384-393.
- [10] B.V.S Rao, G.C.M. Reddy, G.K.M. Rao, P. Ranadheer, P.V.R Reddy, Low cost knowledge base system for design of deep drawing die set, *International Journal of Mechanical Engineering and Robotics Research*. 2 (2013).
- [11] M.G. Shebl, M.I. Ghobrial, N.F. Hassan, H.M.A. Hussein, Computer aided design and drafting of sheet metal blanking dies, *Jupiter'99, Ain Shams Univeristy, Scientific Bulletin*. 34 (1999) 611-624.
- [12] H.M.A. Hussein, L.A. Abdeltif, M.I. Etman, A.F. Barakat, An approach to construct an intelligent system in sheet metal cutting die design, *9th Cairo university international conference on mechanical design & production (MDP-9) Cairo, Egypt*, (2008).

Adaptive GA-NN For MDF Prediction Model

FARIDAH Sh Ismail^{1,a} and NORDIN Abu Bakar^{2,b}

¹Malaysian Institute of Information Technology, Universiti Kuala Lumpur, Jalan Sultan Ismail, 50250 Kuala Lumpur, MALAYSIA.

²Faculty of Computer & Mathematical Sciences, Universiti Teknologi MARA, 40450 Shah Alam, MALAYSIA.

^afaridah@unikl.edu.my ^bnordin@tmsk.uitm.edu.my

Keywords: neural network; genetic algorithm; adaptive; prediction; hybrid model; MDF

Abstract. This research presents a hybrid Genetic Algorithm Neural Network (GA-NN) model to replace the physical tests procedures of Medium Density Fiberboard (MDF). Data included in the model is MDF properties and its fiber characteristics. Multilayer Perceptron (MLP) NN model is reliable to learn from seven inputs fed to the network to produce prediction of three targets. In order to avoid result from local optimum scenario, GA optimizes synaptic weights of the network towards reducing prediction error. The research used a fixed probability rates for crossover and mutation for hybrid GA-NN model. GA-NN model is further improved using adaptive mechanism to help identify the best probability rates. The fitness value refers to Sum of Squared Error. Performance comparisons are among three models; namely NN with Back Propagation (BP), hybrid GA-NN and hybrid GA-NN with adaptive mechanism. Results show the hybrid GA-NN model perform much better than NN model used with back propagation optimizer. Adaptive mechanism in GA helps increase capability to converge at zero sooner than the ordinary GA.

Introduction

Medium Density Fiberboard (MDF) is an engineered wood used in furniture industry as an alternative to solid wood. Prior to manufactured, it is compulsory to run for mechanical and physical tests procedures to ensure its mechanical and physical quality. These procedures take as long as 48 hours per sample. The main concern in these test-procedures is the time factor [14][15]. For that, this research aim to replace the lengthy tests with a simulation by a prediction model.

Multilayer Perceptron (MLP) NN is a preferred pattern-learning instrument than decision trees and Naïve Bayes [1]. This method makes predictions in several areas, including in agriculture-based areas. To name a few, weather predictions [2], stock market forecasting [3] and medical diagnosis [4] as well as in the area of agricultural modeling. NN approach has implemented in engineered wood industry such as MDF predictions. Areas of research include moisture resistance by [5] and internal bonding (IB) strength by [6]. Destruction time in laboratory can be reduced through IB prediction based on process parameters ([7] and [8]). Physical properties too were discovered to be able to predict IB [9].

The popular weight optimizer in NN is Back Propagation (BP) algorithm. To overcome the possibility of being stuck in local minima, GA replaces BP algorithm as optimizer; GA has the ability to search for global optimum. Most researchers [10][11][12] have agreed that the performance of GA mainly depend on the operators, the probability of the operators used, and the diversification of the population. The chances of reproduction depend on the operators' probability rate. Therefore setting suitable rates is important. The GA will quickly adapt its parameters to work with the problem at hand [13]. By taking current performance as the index, the values for the parameters will be more reliable. Once the GA is running with optimum parameter values, the time taken to reach global optimum will be reduced considerably.

This paper reports a study on producing an intelligent prediction model, using hybrid GA-NN. Section II draws the methodology, begins with data analysis, techniques used by NN as the main architecture of the model and techniques used by the hybrid GA-NN. Adaptive mechanism

enhances the GA search ability by guiding operators to suit the current population. Section III presents the results of all models and discusses the achievement of each. Finally, the paper ends with a conclusion and recommendation on future work.

Methodology

The main architecture is MLP NN. The NN performance depends very much on the weights and therefore GA with an adaptive mechanism will help increase the model reliability. The multi-output prediction model contains the lengthy test properties, identified as targets; based on other tests, identified as the predictors.

Data. The data analysis was on the experimental tests data obtained from Malaysian Palm Oil Board (MPOB) Research Station. The data were taken from each of the tests done. The mechanical properties are modulus of rupture (MOR), modulus of elasticity (MOE) and internal bonding (IB). The physical properties are thickness swelling (TS), water absorption (WA) and moisture content (MC). All other properties from testing results will be the input. The board density and the mixture percentage of oil palm biomass-rubber wood are two additional variable added to the data compilation. Fiber characteristics are significant and an advantage towards the prediction [16]. Ten variables with 255 observations involved in the compilation and analysis. Each observation is the average value of three test results done on the similar sample. Firstly, missing values and extreme outliers are cleaned by replacing them with the average values. Secondly, rescaling of data is using normalized rescaling technique to reduce data large gap to a range between 0.0 and 1.0.

Neural Network Model. The first model formulates NN prediction using Multilayer Perceptron, which also known as multilayer feed forward. Figure 1 depicts the neural network architecture used by this research containing 7-node input layer, 4-node hidden layer and 3-node output layer. The seven nodes of input layer are the input values. The adjoining lines between layers, called vectors, contain weights. These weights determine the importance of each input towards the prediction of targets. The input layer corresponds to the attributes obtained for each training sample and fed to the hidden layer with the weighted values and consequently forwards results to output layer containing targets. The termination condition is set to 1000 epochs to allow improvements on training session.

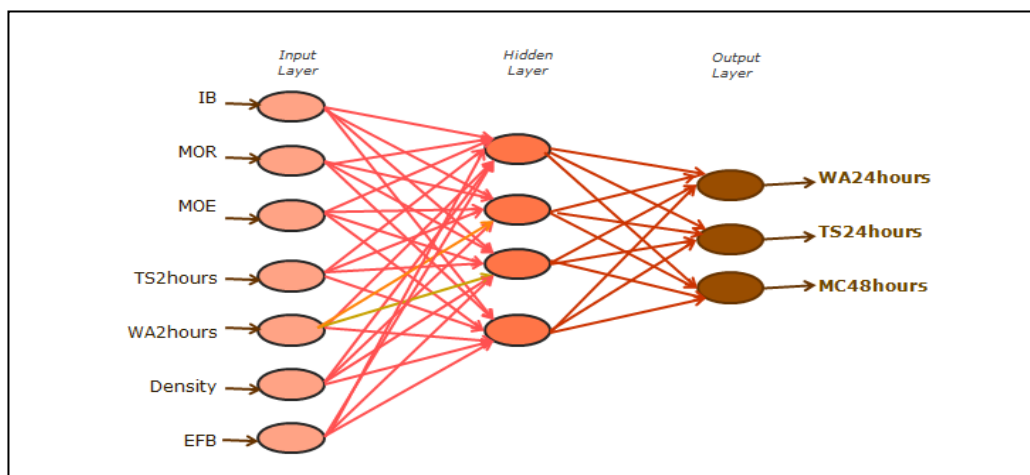


Figure 1. The MLP NN model architecture

Network calculates the output error calculation for each target in each pattern. This error considers the prediction gap as well as the proportion of prediction. Overall evaluation handles negative error by calculating Sum of Squared Error (SSE) for all patterns. Finally, produces Root Mean Squared Error (RMSE) for each epoch by dividing with number of patterns and number of targets in output layer. Among important parameter in BP are learning rate and momentum coefficient. Research is using an inverse value of epoch for learning rate; the higher the iteration, the smaller the learning rate is. Momentum coefficient has constant 0.5. Sigmoid activation function

is suitable for data with positive values. Referring to [16], four hidden nodes are suggested for this network topology.

Hybrid Genetic Algorithm Neural Network Model. Embedding GA in NN will replace BP and optimizes network weights better. Having a 7-4-3 network topology, meaning there are 40 synaptic weights and 7 biases created. Each weight and bias represents an allele in a chromosome. The chromosome contains real valued data in the range of -1.0 to 1.0. Fitness value refers to SSE. After fitness evaluation is done, population is sorted in ascending order, whereby the lowest error is the fittest and placed at the top of array of population. With that, parents are easily determined through rank selection for reproduction task. The probability rates for crossover (P_c) and mutation (P_m) is fixed at 0.3 and 0.01 respectively. Each training sample is iterated for 50 generations in search of best set of weights from 100 populations. All the above steps repeat for 1000 epochs.

Adaptive Genetic Algorithm Neural Network Model. The hybrid model is improved with an adaptive influence on the fitness performance of previous population. The adaptive mechanism is to ensure operators hold the best probability rates for reproduction based on the changes in population. Adaptive measure looks into the mean and median of fitness in current population and suggests on operators' updates significantly. When mean fitness lies smaller than median, increase P_c and decrease P_m . The opposite takes place when the mean value is higher than median.

Results

The prediction models tested on the data are the NN model using BP algorithm and hybrid GA-NN models. Figures 2 through 4 show the RMSE of each model.

Results of Neural Network model. Fig 2 shows model has early convergence at epoch 50 with RMSE of 0.017 and no improvement noticed until end of cycle. This is an acceptable prediction model, however local minima situation is an expected problem and usual scenario when using BP.

Results of Hybrid GA-NN model. Fig. 3 shows that RMSE remain between 0.001 and 0.0 as early as epoch 8 and remain until the end of cycle. This is apparently better than NN model as it.

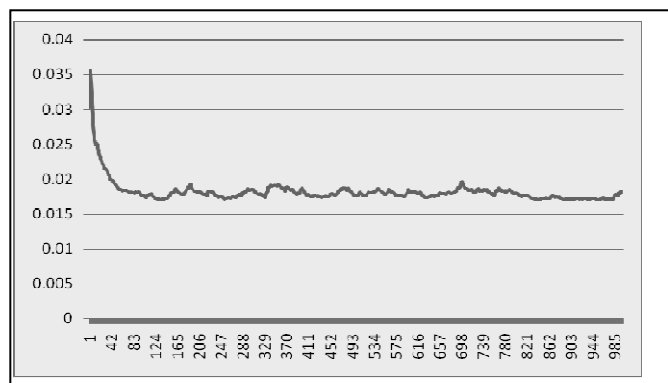


Figure 2. RMSE for NN Model

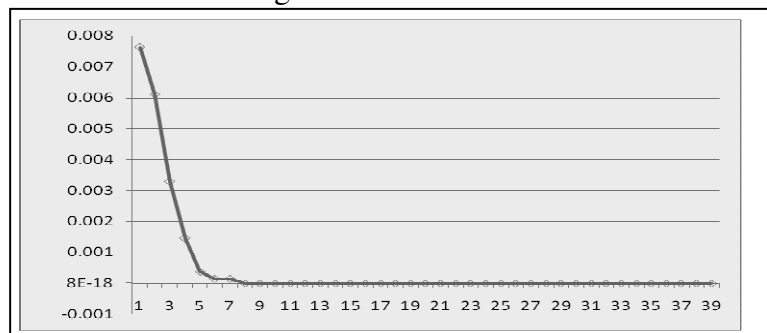


Figure 3. RMSE for GA-NN Model

Results of Adaptive GA-NN model. The final P_m is 0.0145 while P_c remains unchanged at 0.3. Fig. 4 shows that adaptive mechanism works well with this data. The RMSE reached zero

convergence at epoch 10. This model has outperformed the ordinary GA by allowing sooner convergence.

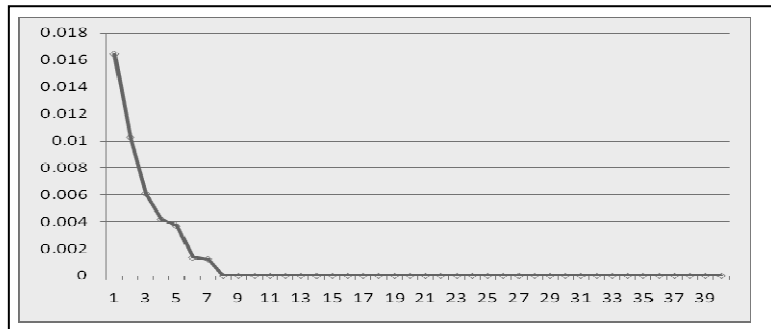


Figure 4. RMSE for Adaptive GANN model

Table 1 summarizes the performance of all models. Both training and testing error reflects that none of the models experience overfitting; results of training explains testing data very well. Therefore, all models are reliable.

Table 1. Error Comparison at Epoch 50

Model	Training RMSE	Testing RMSE
NN with BP	0.017	0.018
Hybrid GA-NN	7.9E-18	0.0
Adaptive Hybrid GA-NN	0.0	0.0

Conclusion

Three prediction models, BP-NN, hybrid GA-NN and adaptive GA-NN were presented and discussed. The targets are MDF testing variables; namely, TS24hrs, WA24hrs and MC48hrs. All models use NN as the main architecture. The results of prototype implementation were drawn. Parameter adjustments and considerations have contributed in producing multi-output from each model. In order to make a reasonable comparison among performance of the models, the same network topology is applied to all models. Obvious improvement was seen when GA replaces BP in the NN model. Different methodologies applied to individual models have shown excellent results.

MDF plants require perfection in quality testing. With the results drawn, manufacturers can reduce testing time by reducing lengthy procedures while maintaining the quality standard set by BS EN. Furthermore, a multi-output model contributes to reduce simulation time. For future research, this problem domain will be tested using other GA adaptive measures.

References

- [1] A.A. Radwan, H.M. El-Bakry, H.M. El-Hadad, A New Expert System for Repository Diseases by Using Neural Networks, *Recent Researches in Applied Informatics WSEAS* (2011) 296-306.
- [2] A.A. Munot and K.K. Kumar, Long range prediction of Indian summer monsoon rainfall, *Journal Earth System Science*, 116-1 (2007) 73–79.
- [3] R. Lawrence, *Using NN to Forecast Stock Market Prices*, Univ of Manitoba (1997).
- [4] H.A. Abbass, An evolutionary artificial neural networks approach for breast cancer diagnosis, *Artificial Intelligence in Medicine*, 25-3 (2002) 265-281

- [5] L.G. Esteban, F.G. Fernandez, P.Palacios and B.G. Rodrigo, Use of ANN as a predictive method to determine moisture resistance of particle and fiber boards under cyclic testing conditions, (UNE-EN 321) Wood and Fiber Science, 42-3 (2010) 1-11.
- [6] D.F. Cook, C.C. Chiu, Predicting Internal Bond Strength of Particleboard utilizing a radial basis function Neural Network, Eng Application of Artificial Intelligence, 10-2 (1997) 171-177.
- [7] T.M. Young, L.B. Shaffer, F.M. Guess, H. Bensmail, R.V. León, A comparison of multiple linear regression and quantile regression for modeling the internal bond of medium density fiberboard, Forest Products Journal 58-4 (2008).
- [8] G. Painter, H. Budman and M. Pritzker, Prediction of oriented strand board properties from mat formation and compression operating conditions. Part 2: MOE prediction and process optimization, Wood Science Technology Springer 40 (2006) 291–307
- [9] F.G. Fernandez, L.G. Esteban, P.D. Palacios, N. Navarro, M. Conde, Prediction of Std Particleboard Mech properties utilizing an ANN & subsequent comparison with a multivariate regression model, Investigacion Agraria: Sistemas y Recursos Forestales, 17-2 (2008) 178-187.
- [10] D.E. Goldberg, Genetic Algorithms in Search, Optimization, and Machine Learning. Reading, Massachusetts: Addison-Wesley (1989).
- [11] K.A. De Jong, Analysis of the behavior of a class of genetic adaptive systems, Ph.D. Dissertation, Dept of Computer and Comm Sciences, Univ of Michigan, Ann Arbor, MI, (1975).
- [12] T. Back, Self Adaption in Genetic Algorithms, Towards a Practice of Autonomous Systems, MIT Press (1992) 263-271.
- [13] L. Davis, Adapting operator probabilities in genetic algorithms, J. David Schaffer ed., Proceedings of the Third International Conference on Genetic Algorithms, San Mateo, CA: Morgan Kaufman Publishers, Inc., (1989) 61-69.
- [14] N. Andre, H.W. Choo, S.Y. Baek, M.K. Jeong, T.M. Young, Prediction of internal bond strength in a medium density fibreboard process using multivariate statistical methods and variable selection, Wood Science Technology, Springer 42 (2008) 521-534.
- [15] T.M. Young, Predictive Of The Physical Properties Of Wood Composites Using Genetic Algo, Wood Utilization Research Project, Univ of Tennessee Forest Product Center, (2004).
- [16] F. Sh Ismail, N. Abu Bakar, N.E. Abdul Khalid and R. Mamat, Optimizing Oil Palm Fiberboard Properties Using Neural Network, IEEE Conference on Data Mining and Optimization, (2011) 271-275.

New Model for Knock Factors Optimization in Internal Combustion Engine (SI)

Azher Razzaq Hadi Witwit^{1,2 a}, Azman Yasin^{1, b}, Horizon Gitano^{3, c},
Tarun Kumar Yadav^{4, d}

¹University Utara Malaysia(UUM), Kedah, Malaysia

²University of Babylon, Babylon, Iraq

³University Kuala Lumpur Malaysian Spanish Institute (UniKL MSI), Kulim, Kedah, Malaysia

⁴University Putra Malaysia (UPM), Kuala Lumpur, Malaysia

^a azherwitwit@yahoo.com , ^b yazman@uum.edu.my , ^c _horizonusm@yahoo.com,
^d 77.tarun@gmail.com

Keywords: Knock, Curve Fitting, Akaike Information Criterion (AIC), Throttle Position sensor (TPS).

Abstract: The main goal of this paper is to construct a new mathematical model and study the behavior of the factors affecting the problem of knocking in internal combustion engines. Curve fitting technique was used in construction of the model, and also Akaike Information Criterion (AIC) was used as a test in choosing the best model. Factors affecting the problem of knocking have been identified through the use of test engine had promised to do so. The mathematical model was built through real data under certain conditions. Three influential factors (Temp., TPS and RPM) have been taken into consideration. Curve fitting models were used in achieving the goal and then studied the effect of one of the factors in the problem of knocking was investigated. Results obtained through the application of the new model is a low level knocking with increasing temperature (Temp) at the same points in Throttle (TPS), the Revolution Per Minute (RPM), which shows the effectiveness of the new model with non-linear behavior of the factors affecting the knock.

Introduction

Knock in gasoline engines is one of the major challenges to achieve higher performance efficiencies. To improve the control systems, the behavior of the knocking and the factors affecting this problem should be studied. It is known that the nature of the factors that influence the behavior of the knocking are non-linear, so the study of the relationships between these factors is critical. Thereby, it is difficult to build a control system on the knocking which works efficiently. One of the techniques that deal with the nature of the data with non-linear technique is a curve fitting.

Curve Fitting

Curve Fitting is used to “connect” observed data to a mathematical model, this operation is very important in finding a rewarding relationship for any system [1]. It is noted that the behavior of the data of the factors is non-linear. For example, when you enter a set of inputs, you will notice that the output takes a set of points are distributed randomly with no specific relationship [2].

Akaike Information Criterion (AIC)

Akaike Information Criterion (AIC) It is a measure of the relative quality of a model for a set of data providing a tool for model selection. AICc deals with trade-off among the complexity and goodness of fit of the model. It provides a relative estimation of the information lost when a model is applied to represent the process that generates the data. AIC does not present a test of a model in the case of examination of a null hypothesis, i.e. AIC may tell nothing about the model quality in an

absolute sense. If all the models fit poorly, AIC will not offer any warning of that. Generally, the AIC is calculated through the following formula:

$$AIC=2R-2\ln(L)$$

Where:

R is the number of parameters in given statistical model.

L is the maximized value of the likelihood function of the estimated model.

Many researchers have used different types of appropriate curve fitting solutions in resolving different kinds of problems in many areas. One approach that deals with appropriate curve fitting is in the field of image processing (image segmentation) by [3] and others, where an effective method has been developed for the study of cervical vertebra maturation (CVM) for bone age evaluation. The researchers applied a curve fitting method based on rotating and overlapping parabolic curves to derive the final segments of the cervical vertebra. Another study by researchers [4], dealt with a programme verification problem of the positively invariant sets of a class of nonlinear loops and discussed the relation between these sets and the attractors of the loops. In this study researcher suggested a numerical method based on curve fitting determined by an algebraic polynomial of degree 5 to find a positively invariant set containing the strange attractor for the H' enon map. Researcher L. Shen conducted a number of studies related to the same issue, but with a linear behaviour [5,6,7,8,9]. Another researcher established an engine dynamic model based upon a theoretical approach and supplemented the acquired engine experimental data using a dynamometer setup. Experimental data was employed to obtain the relation between the throttle valve opening, injected fuel amount, ignition timing, air/fuel ratio, engine speed and generated torque using curve fitting techniques. Accordingly, the gathered experimental input-output relations for coexisting physical quantities were curve-fitted to acquire interpolated functions with the purpose of achieving a complete model for simulations of that particular engine [10]. In addition, some professionals set up fuel injection systems on certain motorcycle engines with the aim of investigating the influence of fuel injection pressure, fuel injection width, and fuel injection timing on engine combustion performance under different load and speed operating conditions [11,12]. In 2006 researchers Yongping, H., et al. developed a steady state power model of a fuel cell stack based on a polarization curve. On the basis of the experimental results, a parasitic system power model was developed by fitting the experimental data with a quadratic polynomial [13].

Achievement of This Study

The aim of the current study is mainly to choosing the best model from a group of nonlinear models applied to real data for a variety of nonlinear factors that affect the accuracy in internal combustion engines. These data were obtained from test engines at the Proton company in Malaysia. The tests were applied through the execution of an applications set to find the appropriate curve fitting for the data, like (Curve Expert Professional v2.0.0).

Experimental Aspect of the Study

The experimental aspect of the study was done through the application of the data obtained for the influential factor TPS, regarding the set of functions to get the best possible model that fits the data, as given in Fig.(1):

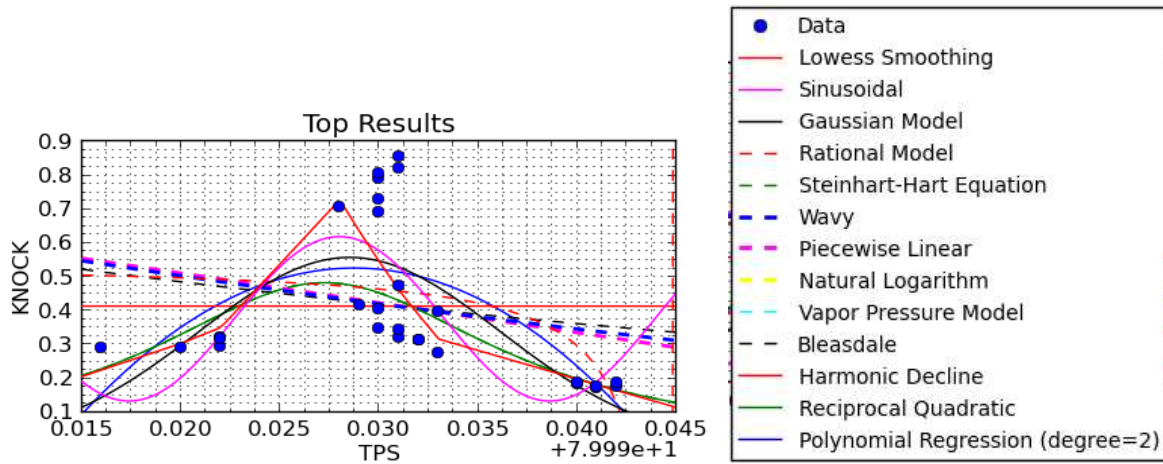


Figure (1): Curve fitting models for Tps factor.

After doing a series of the calculations on a group of models in order to assess and determine the best model of them the following results were obtained, as shown in table (1):

Table (1): Best Model for Tps factor

Name	Kind	Family	Score	R	R ²	Std_Err	AICC
Sinusoidal	Regression	Miscellaneous	525	0.733239	0.537640	0.162446	-99.0911
Gaussian Model	Regression	Miscellaneous	489	0.690112	0.476255	0.169400	-98.1200
Polynomial Regression (degree=2)	Regression	Linear Regressions	461	0.653337	0.426849	0.177210	-95.5960
Steinhart-Hart Equation	Regression	Miscellaneous	438	0.619208	0.383419	0.183802	-93.5510
Reciprocal Quadratic	Regression	Yield-Density Mod...	438	0.619214	0.383426	0.183801	-93.5510
Rational Model	Regression	Miscellaneous	377	0.494487	0.244517	0.207649	-85.3420
Natural Logarithm	Regression	Exponential Models	339	0.262106	0.068700	0.221504	-84.3300
Wavy	Regression	Custom	337	0.233177	0.054372	0.223202	-83.9030
Piecewise Linear	Regression	Custom	333	0.262139	0.068717	0.230547	-79.4850
Bleasdale	Regression	Yield-Density Mod...	333	0.219354	0.048116	0.228374	-81.3920
Harmonic Decline	Regression	Imported	331	0.008189	0.000067	0.229521	-82.3390
Vapor Pressure Model	Regression	Exponential Models	157	0.000000	0.000000	0.467316	-41.2950

Table above shows the value (-99.0911) of the AICc for the first model (sinusoidal), as well as the value of the standard error as less as possible, and the R² which is the best of all. Therefore, it has been chosen as the best (model sinusoidal) which model can represent data for influential factor TPS, seen in Fig (2).

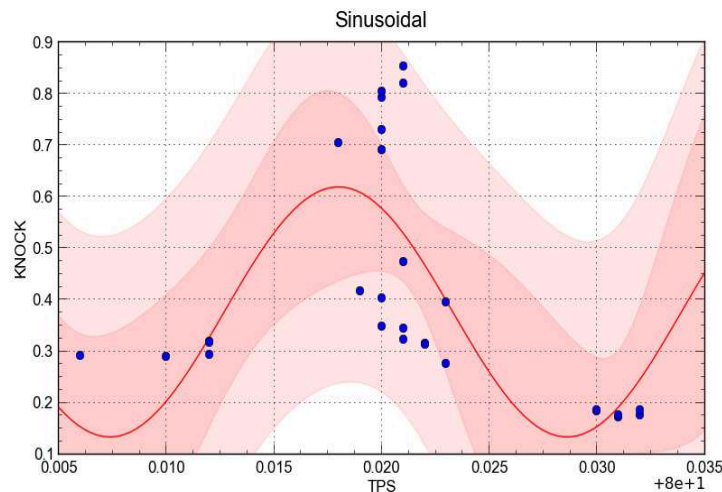


Figure (2): Sinusoidal model for Tps.

After that we can obtain the formula and its parameters as it showing below:

Overview			
Name	Sinusoidal		
Kind	Regression		
Family	Miscellaneous		
Equation	$y = a + b \cdot \cos(c \cdot x + d)$		
# of Indep. Vars	1		
Standard Error	0.162446		
Correlation Coeff. (r)	0.733239		
Coeff. of Determination (r ²)	0.537640		
DOF	24		
AICC	-99.091172		
Parameters			
Value	Std Err	Range (95% confidence)	
a	0.376553	0.031781	0.310959 to 0.442146
b	0.243041	0.088041	0.061334 to 0.424749
c	295.873652	28.390305	237.278942 to 354.468361
d	-14005.390028	2271.759927	-18694.072074 to -9316.707983

The same procedure was carried out on other factors alone (RPM, TEMP). In this study the partial effect of each of the factors, affecting the process of the knocking, and thus find the sum of these effects on those factors in creating the overall effect of the factors on the knocking was found. At the beginning, a better model was taken for one factor that affects knocking, and then find the first derivative of the model in order to find the partial effect of the factor after applying real data considering fixed values of other factors. The proposed model, which consists of three factors with non-linear behavior, was used for the first derivative to reduce the complexity of the model assumed.

$$knock = a + b \cdot \cos(cTps + d), \quad dk = \left(\frac{\partial k}{\partial Tps} dTps \right)_{Rpm, Temp}, \quad \frac{\partial k}{\partial Tps} = -bc \sin(cTps + d) \quad (1)$$

Where k denoted to $knock$. Also take (Rpm) factor:

$$knock = p + qRpm + sRpm^2, \quad dk = \left(\frac{\partial k}{\partial Rpm} dRpm \right)_{Temp, Tps}, \quad \frac{\partial k}{\partial Rpm} = q + 2sRpm \quad (2)$$

Also take ($Temp.$) factor:

$$knock = m + n \cdot \cos(oTemp + e), \quad dk = \left(\frac{\partial k}{\partial Temp} dTemp \right)_{Rpm, Tps}, \quad \frac{\partial k}{\partial Temp} = -no \sin(oTemp + e) \quad (3)$$

So, we can get an overall model, which can be used in the analysis of the effect of factors on knocking, since the knocking depends upon the Rpm, temperature and Tps, Thus, we can have the following formula:

$$k = k(Rpm, Temp, Tps)$$

To get the relation among RPM, TEMP and TPS, we used partial deferential

$$dk = \left(\frac{\partial k}{\partial Rpm} dRpm \right)_{Temp, Tps} + \left(\frac{\partial k}{\partial Temp} dTemp \right)_{Rpm, Tps} + \left(\frac{\partial k}{\partial Tps} dTps \right)_{Rpm, Temp} \quad (4)$$

Substituting the value of (1),(2),(3) from above eqns in eqn (4) we get:

$$dk = (q + 2sRpm)_{Temp, Tps} dRpm + [-on \sin(oTemp + e)]_{Rpm, Tps} dTemp + [-bc \sin(cTps + d)]_{Rpm, Temp} dTps$$

$$Knock = -0.24304 * 292.873 * \sin(292.873 * tps - 14005.39002) - 2.08452 + 2 * 0.00117 * rpm - 0.09226 * 38.29344 * \sin(38.29344 * temp + 32.15755)$$

For example, if take the factor TPS, with the consideration of the fixed values of the other factors, and apply the overall in formula in many situations to investigate its effect on knocking, the following results are obtained, as the shown in fig. (3). The behavior of knock appeared in different (RPM) like 2000,4000,5000.

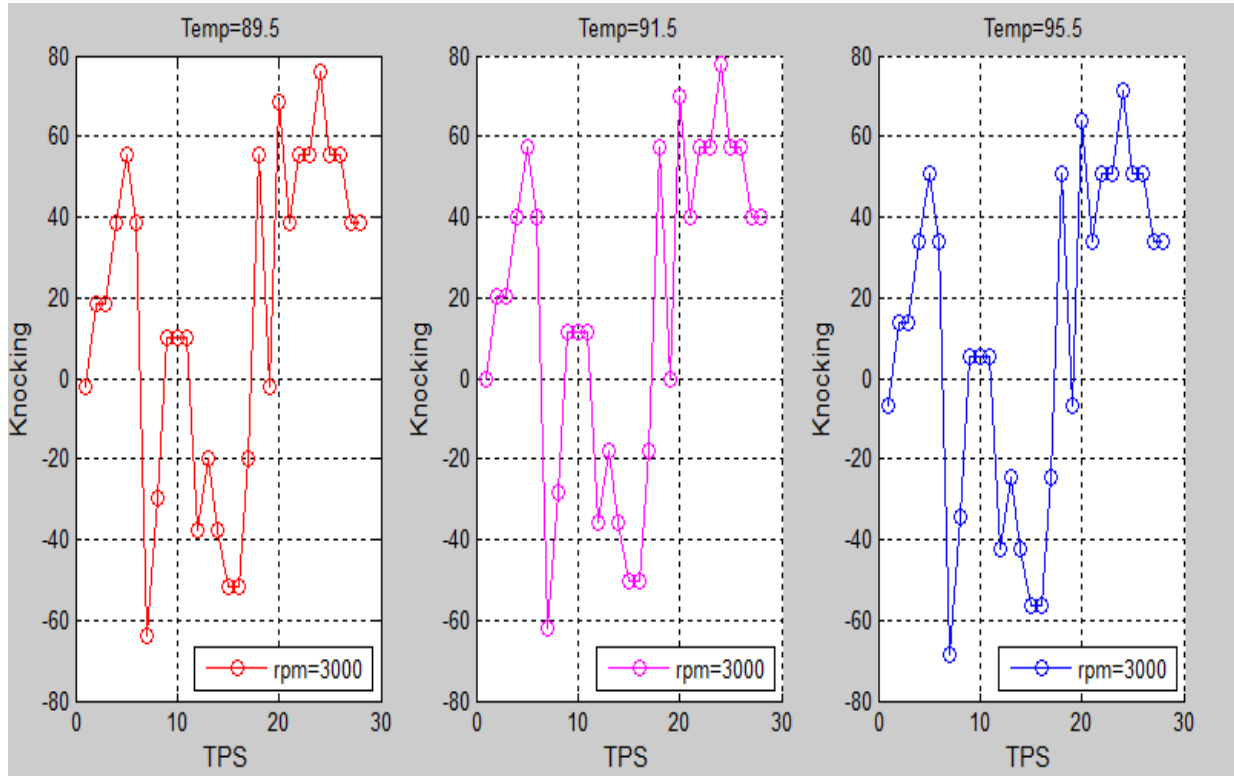


Figure (3): Effect TPS in defferent (Temp.) on knocking

Summary

By observing the figure above (3), you will note the change in knocking when the values of TPS changes, with fixed temperature (Temp.) in the value of 89.5, and engine cycle (RPM) equals 5000, the value of the knocking will be equal 80. After increasing the (Temp) to 91.5, it is observed that the knocking is also increased, but when the (Temp) is continues rising, knock starts to decrease. Results obtained through the application of the new model is a low level knocking with increasing temperature (Temp) at the same points in Throttle (TPS), the Revolution Per Minute (RPM), which shows the effectiveness of the new model with non-linear behavior of the factors affecting the knock.

Reference

- [1] N. A. Azli and A. H. M. Yatim, "Curve fitting technique for optimal pulse width modulation (PWM) online control of a voltage source inverter (VSI)," in TENCON 2000. Proceedings, 2000, pp. 419-422.
- [2] P. Howard, "Modeling Basics," 2009.
- [3] H. Hu, H. Liu, C. Lili., H. Chih.-Cheng., X. Xiangyang, & L. Zhicong, Image segmentation of cervical vertebra in X-ray radiographs using the curve fitting strategy. Paper presented at the Proceedings of the 2011 ACM Symposium on Applied Computing, 2011, pp. 853-858.

- [4] S. Liyong, W. Min, Y. Zhengfeng, & Z. Zhenbing, Finding positively invariant sets of a class of nonlinear loops via curve fitting. Paper presented at the Proceedings of the 2009 conference on Symbolic numeric computation, 2009, pp. 185-190.
- [5] C. Mechil, Finding invariant assertions for proving programs. Paper presented at the ACM SIGPLAN Notices, 1975, pp. 165-171.
- [6] S. M. German and B. Wegbreit, A synthesizer of inductive assertions. Software Engineering, IEEE Transactions on(1), 1975, 68-75.
- [7] M. Karr, Affine relationships among variables of a program. Acta Informatica, 6(2), 1976, 133-151.
- [8] S. Katz and Z. Manna, Logical analysis of programs. Communications of the ACM, 19(4), 1976, 188-206.
- [9] B. Wegbreit, The synthesis of loop predicates. Communications of the ACM, 17(2), 1974, 102-113.
- [10] L. Fu-Shin., T. Shao-Chin, T. Chung-Chih, & W. Jhen-Cheng. Fuel injection motorcycle engine model development. Paper presented at the Networking, Sensing and Control, 2004 IEEE International Conference on, 2004, pp. 1259-1264.
- [11] G. S. Lin, Four-stroke fuel injection motorcycle engine combustion characteristics, Master's thesis, Mechanical Eng. Inst, National Cheng-Kung University, 1994.
- [12] U. L. Tsai, Fuel injection timing influence on exhaust compositions for a four-stroke engine running at idle speed with valves overlap;, Master's thesis, Mechanical Eng. Inst, National Cheng-Kung University, 1997.
- [13] Y. Hou, G. Wan, W. Jiang., & M. Zhuang, Steady State Performance Modeling of a Fuel Cell Engine. Paper presented at the Vehicular Electronics and Safety, 2006. ICVES 2006. IEEE International Conference on, 2006, pp. 424-427.

RFID Secure Protocol Based on Time-Based Hash Chain

Chen Lin^{1,a}, Shufeng Zhao^{2,b}, Shiping Chen^{3,c}

^{1,2,3}Postbox 247, No.516 Jungong Rd., Yangpu District, Shanghai, China

^alc@usst.edu.cn, ^bzhaosf@usst.edu.cn, ^cchensp@usst.edu.cn,

Keywords: RFID. Secure privacy. Hash function. Hash chain. Timeline.

Abstract. This paper describes several typical RFID privacy protection protocol security methods. To improve the security of RFID protocols, which proposed in the literature and some deficiencies, propose a new time-based hash chain function. The program can be effective against security issues, such as unauthorized reading, location tracking, eavesdropping, spoofing, replay and etc. The program applies to a higher number of tags and readers, with better security and efficiency.

Introduction

Radio frequency identification (RFID) systems aim to identify tags to readers in an open environment where neither visual nor physical contact is needed for communication. Because it is through radio waves to propagate signals, so there will be many security privacy issues. For example: unauthorized reading, location tracking, eavesdropping, spoofing, replay and etc. As low-cost RFID tag design needs, it can not implement complex high-security encryption algorithm, People have to improve security through authentication protocol [1-5]. Where a representative is Hash-lock [2,3], Hash-chain [4] and distributed asking - response protocol [5], the shared key system, AES password authentication system and etc. This paper presents a time-based hash chain function for RFID authentication protocol, an effective solution to protect the privacy and security of the tags.

Analysis of RFID Security Authentication Protocols

Overview of RFID-related security agreements

The most important security issue of RFID system is to achieve confidentiality and untraceable. Present day, there are already a lot of literature suggests a variety of RFID authentication protocols. There are two authentication methods: Unidirectional authentication and Mutual Authentication. Unidirectional authentication only verifies the legitimacy of tags, mainly used Hash Lock Agreement, randomized Hash Lock agreements and so on. Those agreements sacrificed some security, used to increase the speed and reduce the cost of tags. Mutual authentication is a Unidirectional authentication improvements, it is also legally verified the tags in the communication by increasing the cost of tags.

The tag authentication can be roughly divided into two categories: static and dynamic ID mechanisms. Static ID mechanism is the identification tag identifying the authentication process to maintain the same, but the back-end server computing amount is too large; Dynamic ID mechanism the tag identifies certified identification in every session change, the problem is to bring the refresh ID synchronization. Most RFID security protocols exist a variety of defects, the following will describe and analyze two typical RFID security protocols.

Analysis of RFID security protocols

Hash chain. The tag in Hash chain algorithm [4] uses two Hash function H and G. In the system, tag and database has an initial value of $S_{t,1}$, while the database also stores all tag's ID. The jth authentication of tag and reader executes as follows: 1. The reader requests, the tag according to its cryptographic value $S_{t,j}$ and calculating $a_{t,j} = G(S_{t,j})$; 2. then update the cryptographic value $S_{t,j+1} = H(S_{t,j})$, and $a_{t,j}$ is sent to the reader; 3. Reader sent $a_{t,j}$ to the database, Database find all the

records and calculate whether there is a equation: $a_{t,j} = G(H^{j-1}(S_{t,1}))$; 4.If the equation established, the authentication passed, ID_k will be sent to the reader, shows in Fig. 1.

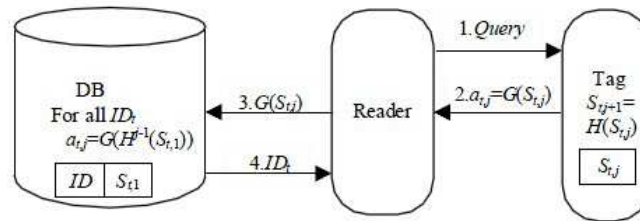


Fig. 1. Hashchain

The agreement with independent ability to update the tag, the tag is positioned to avoid the leakage of private information. Also, because the one-way Hash function, it is impossible to get from $S_{t,j+1}$ to $S_{t,j}$, with forward security. But it only certificated the tag, that usceptible to retransmission and spoofing attacks. Each tag requires two different Hash modules, increasing the cost of the tags. During each verification, the database have to do j times computing for each tag, computing costs are increasing. Therefore, the agreement is not suitable for a large number of tags systems.

David digital library protocol. In David's digital library RFID protocol [6], before the database and each tag is running, system require pre-shared a secret value s, f_s said cryptographic security bys pseudo-random function. During the execution of the protocol are as follows: 1. Reader sends an authentication request and the generation of random numbers R_r to the tag; 2. Tag generates a random number R_t , uses their ID and cryptographic values computing $\sigma = ID \oplus f_s(0, R_r, R_t)$, and sends (R_t, σ) to the reader; 3. Reader forwards (R_t, σ) to the database; 4. Database checks if there is an ID_j , makes $ID_j = \sigma \oplus f_s(0, R_r, R_t)$ established, and if so, the tag is certified, sends $\beta = ID_j \oplus f_s(1, R_r, R_t)$ to reader; 5. Reader forwards β to the tag; 6. Tag verifies if $ID = \beta \oplus f_s(1, R_r, R_t)$ is established that makes reader certified. The protocol is no obvious security vulnerabilities, but 2 function modules must be included in the tag circuit to achieve a random number generation and secure pseudo-random function. Therefore, this method does not apply to low-cost RFID systems.

Time-Based RFID secure protocol

When we have a large number of electronic tags, lower cost is an important consideration factor. In ensuring the safety of the premise, as far as possible to simplify the tag design. Advantages and disadvantages of the above agreement, the paper designs a new RFID secure protocol. The protocol uses static ID mechanisms and mutual authentication, and simplify tag circuit, without the random number generation modules. Each tag and reader share a secret. Reader receives the tag information, according to the certification arrival time, based on time-chain algorithm, calculate all previous keys in order to protect data against replay attack.

Traditional methods [7] are based on a symmetric key system request-response authentication protocol. The protocol shared between tag and reader with the same key, once a key is compromised, it will destroy the entire system. Therefore, set the time slice during the communication parameters, use the time chain to determine whether the tag is forgery and tampering, that can improve system safety.

Time-Based hash chain fundamentals

Assume various tags and readers to share a secret key, but actually it is difficult to implement. Because the certification requirements essentially asymmetric (All tags to verify the authenticity, but can not identify forged keys). Therefore, the new method disclosed in the delay using the key to achieve this asymmetry.

Tags generate a time-based key chain $K_{t,i}$, key $K_{t,i}$ as an argument of the hash chain. Use one-way hash function G randomly selects seeds $K_{t_n,i}$, so there can be a key chain $K_{t_n,i} = G(K_{t_{n+1},i})$. Since G is a one-way function can be calculated forward (backward in time), but not backward (forward in time) as Fig. 2. For example, given $K_{t,i}$, it can be calculated $K_{0,i} \dots K_{t-1,i}$, can not be calculated $K_{t+1,i}$.

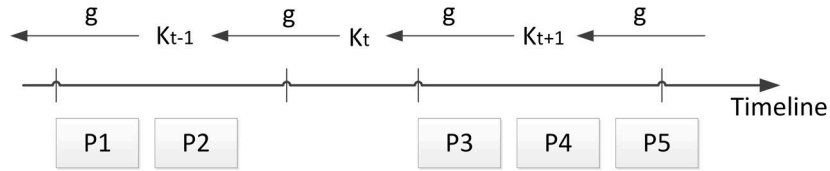


Fig. 2. Time-Based chain

Protocol certification process

Initialization: First, select a suitable key encryption algorithm [8] for the system. Commitment reader through a standard agreement for each tag key chain as promised. For example, with its first private key K_0 signature (assuming each tag has a certified public key), and published the commitment on the server.

Authentication process: 1. Reader generates a random number S , sending Query S to tag for a certification; 2. Tag receives a request, uses the key K_0 and its own ID to calculate $R_i = H(K_0 \parallel R_{i-1} \parallel S)$, and sends $R_i, H(ID \parallel S \parallel R_i)$ to reader; 3. Reader forwards $R_i, H(ID \parallel S \parallel R_i), S$ to the database; 4. Database uses the key K_0 to decrypt and obtain ID' , determine whether it meets $H(ID' \parallel S \parallel R_i) = H(ID \parallel S \parallel R_i)$, otherwise, the authentication fails, discarding; 5. Database sends $H(ID' \parallel R_i)$ to the reader; 6. Reader forwards $H(ID' \parallel R_i)$ to the tag; 7. Tag uses the key K_0 to decrypt and obtain ID , then determine whether it is equal to the local ID that makes the authentication succeed, otherwise, the authentication fails, discard. Above the system complete the authentication process as Fig. 3. The authentication algorithm needs each tag circuitry includes only one random number generation function module.

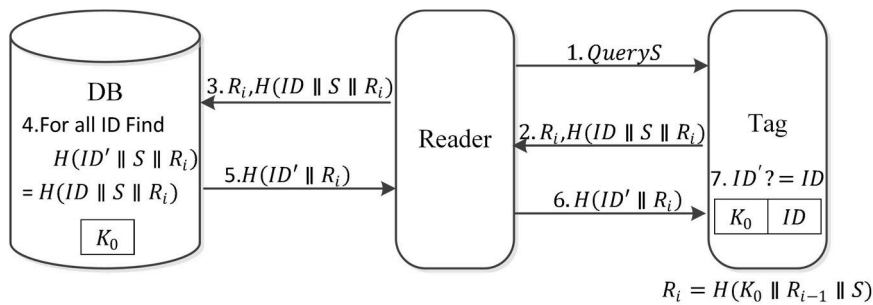


Fig. 3. Time-Based hash chain

Security and Performance

Security

Indistinguishability. For tags response output, because of one-way hash function [8] and the use of a random number, even if an attacker gained multiple tags output, can not distinguish the output of the tags, means $H(ID' \parallel S \parallel R_i) \neq H(ID \parallel S \parallel R_i)$; Even with the same output of a tag cannot distinguish a certain time of the tags output, means $H(ID \parallel S \parallel R_i) \neq H(ID \parallel S \parallel R_j)$.

Forward Security. Assuming the attacker got a particular tag output $H(ID \parallel S \parallel R_i), R_i$, but depends on the one-way hash function, who can not get the tag historical data, shows in Fig. 4.

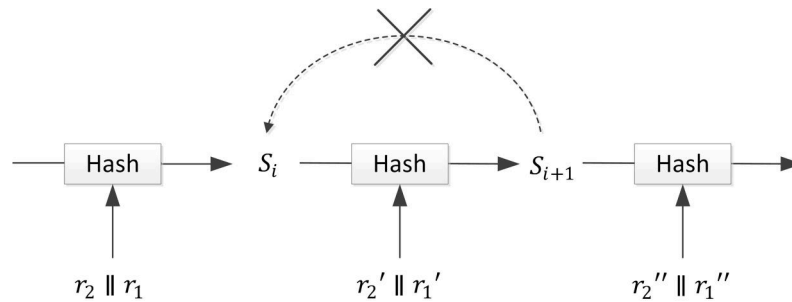


Fig. 4 Forward Security

Replay Attack. Attacker perform the following operations: Readers send QueryS authentication request, Attacker listens to obtain tag output $H(\text{ID} \parallel S \parallel R_i)$, R_i ; When the reader send QueryS authentication request again, tag will monitor the data obtained and send to the reader, to disguise legitimate tag. However, because of $H(\text{ID} \parallel S \parallel R_i)$ anti-collision resistance and randomness from time-based chain encryption R_i , tag output $H(\text{ID} \parallel S \parallel R_i) \neq H(\text{ID} \parallel S \parallel R_j)$, $R_i \neq R_j$, wherein $i \neq j$. Therefore, the protocol is able to withstand the replay attack.

Spoofing Attack. The attacker masquerading as legitimate reader sends QueryS' to the tag, tag responds the output $H(\text{ID} \parallel S \parallel R_i)$, R_i . When a legitimate reader request an authentication, the attacker sends a faked response to deceive the reader. However, during each authentication reader will generate a random number S, based on $H(\text{ID} \parallel S' \parallel R_i) \neq H(\text{ID} \parallel S \parallel R_i)$, therefore, an attacker can not produce a correct tag response.

Traffic Analysis. In order to get a response, the attacker masquerading as reader send QueryS' to the tag, resulting tag output. Attacker tries to analyze the $H(\text{ID} \parallel S' \parallel R_i)$, R_i to obtain specific tags which output. However, collision resistance and randomness of Hash Function avoid the attacker's traffic analysis attacks, an attacker can not trace the traffics.

Key Update. As a result of time-based hash chain, all tag and reader no longer share the same key, once a tag's key is compromised, the entire system is not affected, at the same time key chain K_i keep updating. Therefore, the key in the communication process can not be forged and tampered, it is improving the safety.

Performance

Computation and Efficiency. If there are N number of tags, in this method, database needs to search up to 2N records, performed for N times Hash operation and XOR operation. Some methods, such as hash chain functions required to execute 2N plus 2N records search. The protocol has improved calculation speed, with lower computation and efficiency

Number of Tags and Readers. Tags and readers do not need to store each other's ID information. Finding the records and most of calculations performed by the database. With the number of tags and readers increased, the database computing time increases slowly. Thus, the protocol should be suitable for a larger number of tags and readers.

Conclusion

In this paper, proposed a new RFID encryption method, which is based on the time-based hash chain function. In ensuring the safety of the premise tag privacy, it reduced the frequency of hash function usage, in order to improve the efficiency of certification. The randomness of time-based chain increases the reliability of encryption key. Reduce the random module on the tag certification application that reduces system costs. This method has a high practical value.

Acknowledgement

This research was financially supported by the National Science Foundation (61170277), Shanghai Municipal Education Commission Focus on research and innovation projects(12zz137), and Construction Project of Shanghai-class disciplines(S1201YLXK).

References

- [1] K. Finkenzeller, RFID handbook: fundamentals and applications in contactless smart cards and identification, John Wiley & Sons, Inc., 2003.
- [2] S.E. Sarma, S.A. Weis, D.W. Engels, RFID systems and security and privacy implications. Proceedings of the 4th International Workshop on Cryptographic Hardware and Embedded Systems(CHES 2002). Lectures Notes in Computer Science 2523. Springer-Verlag, Berlin. (2003) 454-469.
- [3] S.E. Sarma, S.A. Weis, D.W. Engels, Radio frequency identification: Secure risks and challenges, RSA Laboratories Cryptobytes. 6 (2003) 2-9.
- [4] M. Ohkubo, K. Suzuki, S. Kinoshita, Hash-chain based forward secure privacy protection scheme for low-cost RFID, Proceedings of the 2004 Symposium on Cryptography and Information Security (SCIS 2004), Sendai. (2004) 719-724.
- [5] K. Rhee, J. Kwak, S. Kim, Challenge-response based RFID authentication protocol for distributed database environment. Proceedings of the 2nd International Conference on Security in Pervasive Computing (SPC 2005). Lectures Notes in Computer Science 3450, Springer-Verlag, Berlin. (2005) 70-84.
- [6] G. Lin, Y. Wang, Y. Zhan, RFID Secure Protocol Based on Random Sequence, Computer Engineering, 20 (2008) 151-153.
- [7] Z. Ding, L. Guo, Y. Wang, An authentication protocol based on key array for RFID, Journal of Electronics & Information Technology. 31 (2009) 722-726.
- [8] S. Yuan, H. Dai, S. Lai, Hash-based RFID Authentication Protocol, Computer Engineering. 34 (2008) 141-143.

A Novel Manufacturing Chain for Low Cost 3D Textile Reinforced Polymer Composites

ALMANSA Ana^{1,a}, FAZELI Monireh^{2,b}, LAURENT Benoit^{3,c}, PADROS Pere^{4,d}
and HÖRLESBERGER Marianne^{5,e}

¹Xedera e.U, Halbgasse 15/2, 1070 Vienna, Austria

²ITM, TU Dresden, Hohe Str. 6, 01069 Dresden, Germany

³Federal Mogul Systems Protection, 69, Rue Henri Laroche, 60800 Crépy en Valois, France

⁴Promaut, Carrer Andorra 22, 08830 St. Boi de Llobregat, Spain

⁵Austrian Institute of Technology, Donau-City-Strasse 1, A-1220 Vienna, Austria

^aaam@xedera.eu, ^bMonireh.Fazeli_Zoghalchali@tu-dresden.de,

^cbenoit.laurent@federalmogul.com, ^dppadros@promaut.com, ^emarianne.hoerlesberger@ait.ac.at

Keywords: manufacturing chain, 3D textiles, textile reinforced composites, hybrid yarn.

Abstract. The project 3D-LightTrans aims to create a highly flexible manufacturing chain for the low cost production of integral large scale 3D textile reinforced polymer composite parts. In a novel approach, multi-material semi-finished fabrics made of hybrid yarn are formed to deep draped pre-fixed multi-layered and multifunctional 3D-textile pre-forms. These are then efficiently processed into the final composite part by thermoforming. This paper presents the results achieved by the project consortium during the last three years, including the development and optimization of the individual processes for prototype production, with a focus on two selected automotive end products, and the adaption of equipment for industrial scale manufacturing.

Introduction

Polymer composites combine the lightweight and low cost of polymers with the superior properties of the reinforcing material, while woven fabric reinforcement leads to higher performance, controllability of properties and flexibility for customization. However, commercial applications of textile reinforced polymer composites (TRPCs) are still restricted to few cost intensive and small series niche markets as a consequence of the difficulty in processing the constituents, the too slow, inflexible and expensive production processes (such as draping and lay-up), and the lack of flexibility in the realization of complex pre-forms with 3D geometry. The project 3D-LightTrans (www.3d-lighttrans.com) was launched in the spring of 2011 to overcome these barriers, developing novel promising research level methods to a stage of industrial maturity for low-cost mass manufacturing.

In a novel approach, multi-material semi-finished fabrics made of hybrid yarn is formed to deep draped prefixed multi-layered and multifunctional 3D-textile pre-forms, which is then processed into the final composite part by an efficient thermoforming process (see Fig. 1).

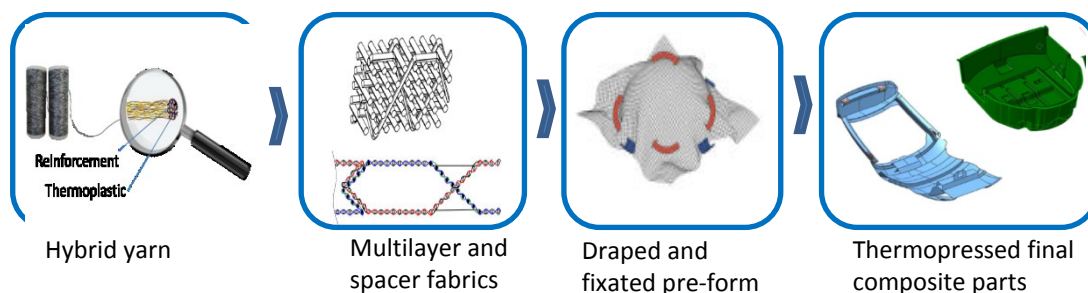


Figure 1. 3D-LightTrans manufacturing approach for high performance composites

The Consortium of 3D-LightTrans merges highly experienced partners in machine tooling and automation (Promaut), the textile machinery manufacturers Michel Van de Wiele (Van de Wiele) and Lindauer Dornier, and the industrial partners P-D Glasseiden Oschatz (PD-GO), Coatema Coating Machinery GmbH (Coatema) and Federal Mogul Systems Protection (FM-SP), as well as the end users from the automotive sector, Centro Ricerche Fiat SCPA (CRF) and Bentley Motors Ltd. (Bentley). The project also profits from the participation of the following well-known specialists in the area of manufacturing and materials research: Xedera, AIT Austrian Institute of Technology (AIT) with LKR Leichtmetallkompetenzzentrum Ranshofen (LKR), Technical University of Dresden (TU Dresden), Onera, Universite d'Orleans (UOrleans), University of Ghent (UGent), Grado Zero Espace (GZE), Leitlat, SVUM and North West Textiles Network Ltd.

Methods

Modelling, simulation and *testing* techniques are extensively used to provide a better understanding of the materials and structures. This involves analysis at different scales, from the macro-scale modelling, where the composite material is modelled as a homogeneous anisotropic material, through the meso-scale modelling, taking into account the fabric architecture and yarn shapes, down to the micro-scale properties of the glass and thermoplastic fibre in the hybrid yarn. With a view to create a knowledge-based manufacturing approach, also the production process steps, from weaving to draping and pressing, as well as the complete manufacturing chain, have been adequately modelled and simulated. A large number of experimental tests have been conducted, both to feed the models with input parameters, and to validate the results of simulations.

Extensive *research on processes and materials* is also necessary, addressing the challenges in the individual processing steps (yarn damage caused during weaving, the difficulty of draping multilayer fabric with increased rigidity, the need for improved local pre-fixation and final fixation processes, etc.). Although the technology will be flexible enough to be applicable to a general case (distinct geometries, alternative yarn composition and different weave architectures), the 3D-LightTrans project focuses on two specific demonstration cases in the automotive sector (a tailgate and a spare wheel well, designed by CRF and Bentley, respectively). This has influenced the choice of the benchmark material used to demonstrate the 3D-LightTrans technology, glass fibre (GF) reinforcement with polyethylene terephthalate (PET) matrix [1].

To ensure the real future industrial deployment of the 3D-LightTrans technology, the *adaption of industrial equipment* is also addressed. A holistic approach to the complete manufacturing chain is taken, comprising multifunctional product design and modelling, automation, quality control, and application specific finishing processes. Furthermore, the project partners will explore the scale-up for mass production and other relevant aspects, such as the product life cycle.

Results

Modelling and simulation toolbox. A comprehensive simulation toolbox with four major modules has been implemented by UGent, CRF, Onera, UOrleans and TU-Dresden. The four modules cover the following aspects: a) meso-scale modelling of the dry fabric architecture, b) draping of the dry fabric architecture and fixation of certain areas of the dry fabric, c) thermoforming of the fabric, and d) micro-, meso- and macro-scale modelling of the final composite part. Finally, the modelling of the complete process chain is addressed by GZE using the Arena, a simulation software by Rockwell Automation which allows to model discrete processes.

The modelling and simulation tools developed have been validated and tested through experimental data with yarns, test fabrics and thermoformed plates, with key contribution of Leitlat and SVUM. The analysis performed include, among others, single fibre and yarn tensile tests and yarn friction tests; uniaxial, biaxial and shear testing of fabrics; friction, compaction, bending and forming tests on fabrics, ultrasonic inspection of the impact of moisture absorption on the thermoformed plates, impact test and micro-CT scans [2,3,4].

Manufacturing of hybrid yarn and 3D textiles. *Hybrid yarn* combines glass reinforcement with thermoplastic matrix filaments in a single yarn. Among the different available technologies commingled hybrid yarns produced by air texturing display a particularly high potential for continuous-fibre-reinforced thermoplastics, due to their great impregnation quality. In air texturing, the hybrid yarn is produced by the pneumatic opening of the filament yarn by cold or hot pressurized air, and the subsequent reallocation of the initial filaments in a special air nozzle. PD-GO, TU-Dresden and UGent have optimized the process to produce highest yarn quality with increased reproducibility and productivity (approx. 500 m/min) in a variety of materials (including PP and PET) with different fibre-matrix ratios. This has been achieved by tuning the fibre yarn count, yarn feeding speed, air pressure and adjustment of the flyer, and by optimizing the yarn sizing, in order to improve the adhesion of the glass fibre to the matrix. The abrasion and hairiness could be also reduced without compromising the final mechanical properties severely.

Concerning the *weaving of 3D textiles*, TU-Dresden has produced fabrics with different multilayer patterns, both with z-reinforcement (in different orientations) and without. The four electronic warp let-offs systems and 20 head frames at the new Dornier loom (modified for 3D-LightTrans) allow to produce multilayer fabric link in Fig. 2 (left), based on commingling hybrid yarn (GF/PET 840 tex) with high warp density, an optimized shedding operation and more structural variety, keeping highest fabric quality and reducing fibre damages. On the other hand, Van de Wiele has developed industrial equipment to manufacture 3D shaped reinforcement textile pre-forms with customized multifunctional structure. In contrast to the conventional spacer fabrics (pile weaves) connected by additional pile yarns, the 3D woven spacer fabrics are constructed of woven outer layers connected by crosslink fabrics (Fig. 2, right), possess superior mechanical properties and can be produced -using Van de Wiele equipment- in just one process step [1].

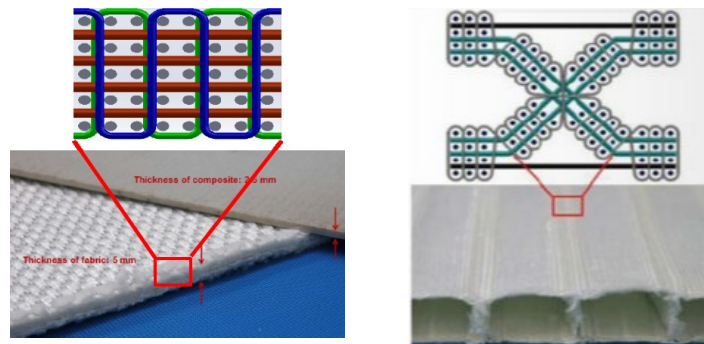


Figure 2. Multilayer fabric before and after thermoforming (left); 3D woven spacer fabric (right)

Manufacturing of the consolidated final composite part. The state-of-the-art technology provides neither standard tools, nor automated procedures with sufficient flexibility to perform in a satisfactory way the draping of complex geometries with thick multilayer fabrics. Nowadays customary manual draping is not only inferior in terms of accuracy and repetitiveness, but also involves a prolonged tool occupation time of the thermoforming tool. 3D-LightTrans approach to solve this consists in decomposing the procedure in several parts: pre-fixation, automated draping in a dummy tool, fixation, and final consolidation by thermoforming.

In order to decrease the fabric handling and draping effort, the fabric is *pre-fixed*, which creates a local increase of mechanical stiffness in well-defined areas previous to the draping. In a novel approach, special fibres with modified characteristics are integrated in the fabric by TU-Dresden, and subsequently processed by Coatema using alternative heating methods. The optical analyses, tensile and bending tests show satisfactory results with increased stiffness in the pre-fixed zones.

As a result of the pre-fixation, draping becomes easier, the flow of forces is better balanced and the number of wrinkles is reduced. In spite of this, the *automated draping* still constitutes a challenge, addressed by Promaut and Leitat. To handle the fabric, experimental tests have been done with suction cups and needle claws, while performed analytical studies show the influence of relevant parameters, such as the air leakage in vacuum grippers as a consequence of the fabric porosity and

roughness. To give the desired 3D form to the dry fabric, a special draping device is attached as end-effector to a robot system, which is subsequently programmed to follow a given trajectory (Fig.3). The implemented force control system makes path programming easier and ensures a constant draping force of the fabric against the tool. While the simulation performed by TU-Dresden provides a first estimation of the effectiveness of a given draping strategy, RobotStudio simulation allows a quick verification of the robot path reachability and draping tool placement [2].



Figure 3: Automatic draping with self-developed tools (left) and robot simulation (right)

One of the key advantages of the 3D-LightTrans technology is the processing to 3D fixed pre-forms, previous to the final consolidation (*fixation*). The pre-forms with fixed 3D geometry can be easily stored and transported without altering their geometry. This can be useful for supply chain and logistic requirements, as well as in distributed manufacturing. The earlier fixation of the draped form allows for final consolidation with decreased tool occupation time, since the 3D fixed pre-form does not need to be draped again in the forming tool. To enable this, different methods are being explored by Coatema, such as thermal activation and the use of additional binders.

To achieve good results of the final composite part, the *thermoforming* process has to be adapted to the needs of the 3D-LightTrans technology. Flat multilayer textile reinforced composite plates have been consolidated by thermoforming at FM-SP varying the pressure applied, time and temperature, for a number 3D-LightTrans fabrics of different characteristics. The resulting thermoformed plates have been visually inspected and analysed by CT-scans, micrographs, and measurements of thickness, impact behaviour [4] and other mechanical properties (tensile stiffness, tensile strength, flexural modulus and bending strength). In parallel to the investigations on flat plates, a small complex tool is used by LKR, combining long plane areas on the bottom and side walls, with both long and tight curvature areas, to investigate the process stability to manufacture parts with close concave-convex geometry curvatures.

The 3D-LightTrans manufacturing chain. The 3D-LightTrans project integrates the novel process steps described with a knowledge-based manufacturing approach and full automation, providing a totally new concept for the design, manufacture and application of high-tech composites for low cost mass products. While the modified air-texturing machine can produce hybrid yarn with high repeatability in a variety of materials (such as glass/PET and glass/PP) in different fibre/matrix ratios, the weaving equipment enables an increased flexibility in the realization of high-performance 3D fabrics. Storage and transport of the fixed pre-forms (if required) do not need refrigeration requirements, as customary with thermoset prepegs. Further, not only is the final consolidation by thermoforming process much more efficient than traditional composite consolidation processes like Resin Transfer Moulding (RTM), but also possible with shorter tool-occupation time, since the draping takes place in an automated way and can be performed out of the thermoforming tool. The consolidated composite part is then ready for any required application specific finishing processes. In the case of the automotive components selected as demonstrators in the 3D-LightTrans project, this includes fastening, bonding, achievement of class A quality and painting (tasks addressed by and FM-SP, LKR, UGent, Coatema, CRF and Bentley).

The manufacturing chain is very flexible and can also be adapted to different production configurations (Fig.4). GZE has defined and tested a framework for the production line design, using modelling and simulation techniques, which has been tested in a specific test case. Test, reliability and quality assurance aspects over the whole manufacturing chain are addressed by Leitat und SVUM. In

order to ensure the real deployment of the 3D-LightTrans technology, in a holistic approach, relevant aspects such as an impact study (realized by Xedera), business cases (AIT), product life cycle (CRF, AIT, GZE), and scale-up for mass production are also considered.

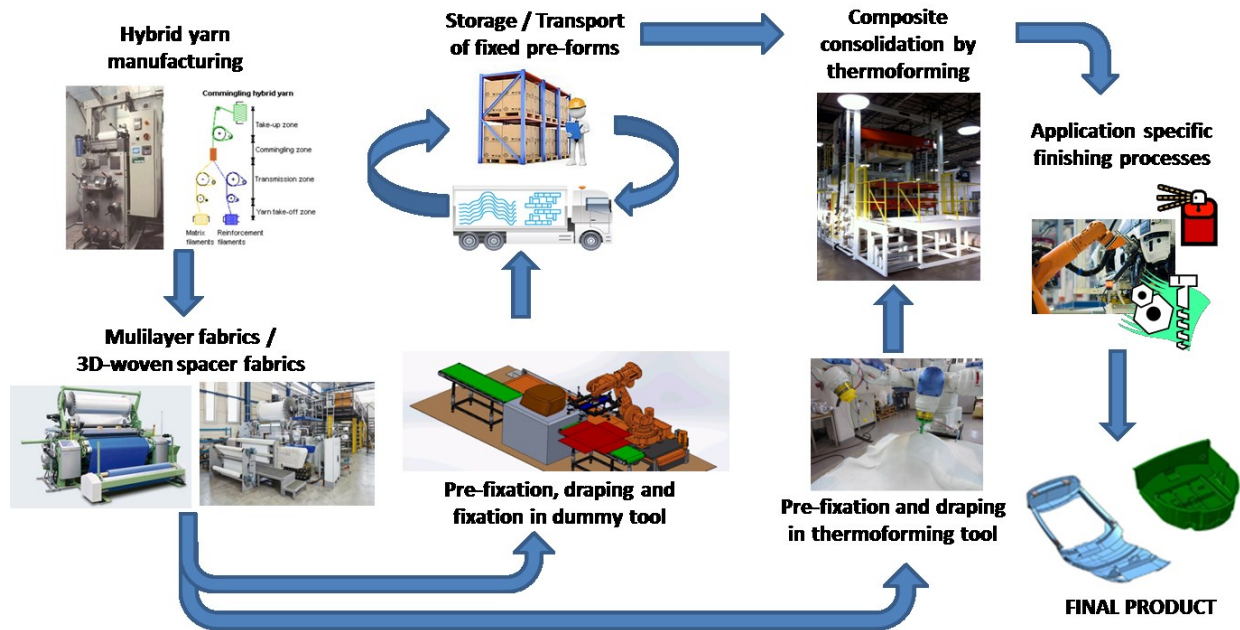


Figure 4: The 3D-LightTrans manufacturing chain

Summary

The project 3D-LightTrans has succeeded to develop most of the technologies and components required for the cost efficient manufacturing of 3D textile reinforced composites, based on hybrid yarn with thermoplastic matrix. A comprehensive modelling and simulation toolbox has been developed. Equipment and processes have been adapted for the manufacturing of hybrid yarn, the weaving of high performance 3D-shaped and multilayer fabrics and the pre-fixation of the fabrics. Significant progress was also achieved with regard to the draping process and tools, as well as in the thermoforming process, which are expected to be finalized and demonstrated in the next months.

Acknowledgment

The research leading to these results has received funding from the European Union Seventh Framework Programme (FP7/2007-2013) under grant agreement n° 263223.

References

- [1] M. Fazeli, A. Mountasir, G. Hoffmann, Ch. Cherif, 3D-shaped multilayer fabrics for high-performance multifunctional composites, JEC Composites Magazine, N° 81(2013), pp 54-55.
- [2] A. Almansa, S. Menegazzi, W. Van Paepegem, L. Bateup, Large scale manufacturing of lightweight 3D multifunctional components, accepted in 16th European Conf. on composite materials, (June 2014, Sevilla, Spain).
- [3] J.E. Rocher, S. Allaoui G. Hivet, E. Blond, Experimental testing of two three-dimensions (3D)-non crimp fabrics of commingled yarns. In AUTEX-13th World Textile Conference, v1 (2013)
- [4] S. Jacques, M. Fazeli, M. de la Fuente, M. Dierick, W. Van Paepegem, Experimental and numerical study of the impact behavior of 3D woven thermoplastic composites for automotive applications, TexComp-11 Conference, volume v1, 2013.

CHAPTER 4:

Product Design and Development, Industrial Engineering

Multi-Echelon Production System Planning: Case study at a Steel Company in Indonesia

GOVINDARAJU Rajesri ^a, HARIADI Rizka Aisha Rahmi ^b

Industrial Engineering and Management Department
Faculty of Industrial Technology, Bandung Institute of Technology
Jl. Ganesha No. 10, Bandung 40132

^arajesri_g@yahoo.com, ^brizka.aisha@gmail.com

Keywords: Production Planning, Make or buy decision, Multi-echelon Production System

Abstract. This paper discusses mathematical modeling process of “make or buy” decision based on a real case in a steel company in Indonesia. The company has a multi-echelon production system that consists of many plants. The plants are connected by a given predecessor-successor relation [4,8]. Each plant needs materials that can be obtained through two alternatives, namely produced internally or imported from supplier [6,10]. The objective of the model discussed in this paper is to determine optimum number of produced material and imported material that can maximize profit gained by the company. To validate the developed model, real data is collected and the model is run using Lingo software.

Introduction

The increasing global competition makes companies vying to boost its competitive strategy in order to survive [3,6]. Price is often seen as an important factor that influences customers' procurement decision. Therefore, companies compete to reduce the cost of their products by making their production process more efficient [1,6].

To provide materials needed in the production systems, there are two alternatives that can be planned by company: 1) stop production process of the materials and purchase materials from external supplier (import the materials) or 2) run of the predecessor plant to produce these materials [3,10]. Importing materials from outside is sometimes cheaper but on the other hand the company still has to bear production fixed cost, although the plants are not in operation. Thus, the total cost must be spent by the company can also be high. Similarly, if the company produces its own material, the costs incurred will be cheap if the number of products manufactured is very large. But each plant has a production capacity limit [7].

This paper discusses a proposed mathematical model based on a case study in SteelCo, a steel company in Indonesia. SteelCo as one of the steel producer in Indonesia currently faces considerable challenges. SteelCo has 7 plants whose production processes related to other processes in different plants within the company. The purpose of this paper is to determine an optimum number of produced and imported products that can maximize profit obtained by the company. In the first part of this paper, we describe the need for this study. In the next section, the model of development is discussed. In this section, previous relevant studies are also described. In the third section, the simulation of the proposed model using real data from the company is presented. In the last section, conclusion made in this study is presented.

Model Development

In its production system, SteelCo has 7 plants, namely Plant A, B, C, D, E, F, and G. Each plant can produce one type of product. Materials required to produce each product are different from each other. For the upstream production process (Plant A and B), the entire materials are imported from outside. Materials required for producing semi-finished and finished goods (Plant C, D, E, F and G) can be produced by previous production processes (other plants within the company) or imported. In other words, for the downstream production processes there are two possible way of providing the materials for the plants: self-producing or importing.

Not all products of the plants are sold to external customer (market). SteelCo just sells HR, CR, Billets, and WR. To meet quality and demand of the market, SteelCo has a policy not sell purchased material directly to the customer. In other words, SteelCo only sells products manufactured by the company. The production flow of SteelCo can be seen in Figure 1.

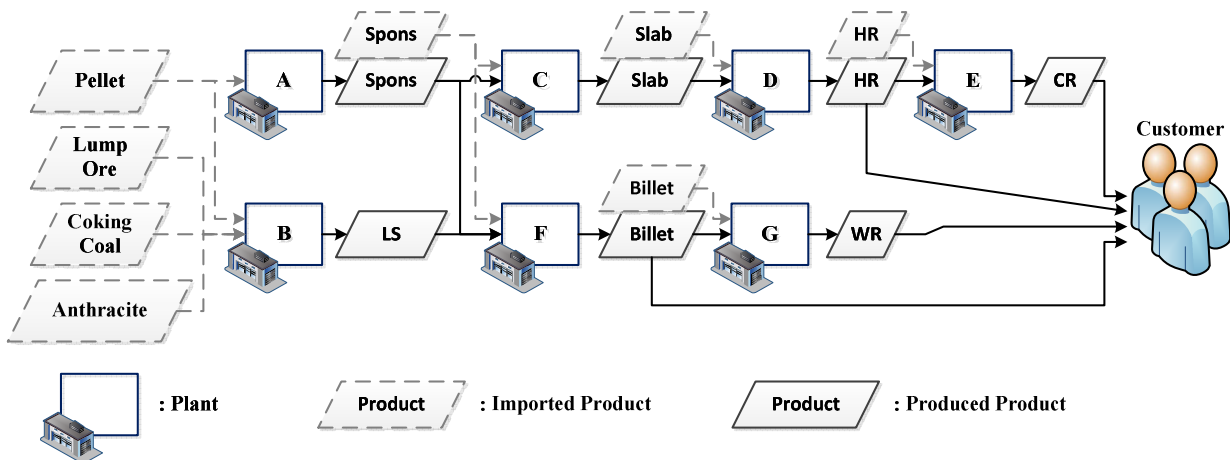


Figure 1. Production Flow in SteelCo

To develop a model that can be used to optimize SteelCo production system, we study relevant literature from previous studies. Among other studies related to make or buy decision, [10] develops an expert system called MOBY, which is a generic customizable make or buy decision advisor. This study proposed a number of focus control block (FCB) to guide the decision making process. The FCBs for *make* decision: cost, capacity, technology, and additional personnel. The FCBs for *buy* decision: sourcing reference and other general info. The influence of production capacity is also discussed in [7].

[9] also develops a make or buy framework. In the framework, make or buy decision is modeled as a decision that needs to be made considering the following aspects: technology and manufacturing process, cost, supply chain management and logistics, and support system. Technology and manufacturing process part consists of technology and equipment, skills to perform the process, technical skills, ownership of the process, ability to cope with volume change, and quality measures factor. Cost is divided into production cost and acquisition cost factor. Supply chain management and logistics aspect consists of supplier selection, cost reduction activities with supplier, collaboration with suppliers, delivery, and inventory control factor. Finally, the support system consists of quality system, information system, engineering changes system, training schemes, continuous improvement program, and technical support factor.

Model Building. Make or buy decision is actually developed from transaction cost economies (TCE) and the resource based view (RBV) theory [2]. TCE theory describes about how to minimize the cost [2] because most make or buy decision is influenced by cost factor [1,5,6,9,10]. However, cost factor is not the only factor that determines the benefits obtained by the company. Revenue factor also affects the decision of make or buy products [5]. Thus, profit which is determined by the value of both factors is used as the objective function in this mathematical model.

Generally, profit earned by company is affected by revenue (sales) and production costs. For the case of SteelCo, overall production cost is composed by 5 types of costs, namely:

1. *Fixed Cost (FC)*, a definite cost incurred by the company although production is not running.
2. *SGA Cost (SGAC)*, is the marketing cost of products sold to customers. This cost will always be spent by the company although no product being sold. Additional personnel factor in [9] model is included in FC and SGAC. Thus, these variables influence *make* decision.
3. *Material Cost (MC)*, is procurement/import cost of material used by each plant which depends on sourcing reference and general info of supplier. This variable influences *buy* decision in the model [6]. The material cost is calculated by looking at the system as a whole.
4. *Conversion Cost (CC)*, a cost of additional materials needed to produce the product.

5. *Energy Cost (EC)*, is cost of using gas and electricity which are the source of energy to run production activities at each plant. SteelCo gets gas supply from 2 suppliers, GS1 and GS2. The usage of gas from both suppliers follows a same supply policy, so the calculation of gas energy costs can be generalized. For electricity, SteelCo use the supply from its subsidiary and two other external suppliers. Both of suppliers have different policies so the generalization of electric energy cost calculation cannot be done. Both CC and EC influences *make* decision.

Different with TCE theory, RBV theory discuss about capability of the system to make the products [2]. This theory is the base theory to develop capacity constrains for production, material, energy and other resources.

Notation Used. In SteelCo's production model, we use the following decision variables: production quantities of product i , import quantities of product i , and suggested external demand (selling) quantities of product i which are represented by $Q_i, I_i, & De'_i$ sequentially. Other variables and parameters used are shown in Table 1.

Table 1. Variable used in the Developed Research Model

Notasi	Definisi	Notasi	Definisi
De_i	External demand fore cast(sales plan) quantities of product i	N_{ji}	Material j needed to produce 1 unit product i
Di_i	Internal demand quantities of product i	ES1	Cost of electricity supplied by Electricity supplier 1 (ES1)
Pi_i	Import price per unit product i	ES2	Cost of electricity supplied by Electricity supplier 2 (ES2)
Ps_i	Selling price per unit product i	PP_{ES1}	Premium price per unit electricity supplied by ES1
y_i	Yield of product i	PR_{ES1}	Regular price per unit electricity supplied by ES1
FC_i	Fixed cost of product i	SP_{ES1}	Number of premium electricity supplied by ES1
SGA_i	SGA cost of product i	SR_{ES1}	Number of regular electricity supplied by ES1
$Alloy_i$	Alloy material cost of product i	Max_{ES1}	Maximum electricity supplied by ES1
Con_i	Conversion cost per unit product i	$MaxR_{ES1}$	Maximum regular electricity supplied by ES1
Gas_i	Amount of gas needed to produce 1 unit product i	Min_{ES1}	Minimum electricity supplied by ES1
El_i	Amount of electricity needed to produce 1 unit product i	K_{ES2}	Multiplier factor (included tax) of Electricity Supplier 2 (ES2) cost
$MaxI_i$	Maximum import of product i	FC_{ES2}	Fixed cost of ES2
$MinI_i$	Minimum import of product i	S_{ES2}	Number of electricity supplied by ES2
$MaxP_i$	Maximum production of product i	P_{ES2}	Price per unit electricity supplied ES2
$MinP_i$	Minimum production of product i	Max_{ES2}	Maximum electricity supplied by ES2
P_k	Supply price per unit gas k	Min_{ES2}	Minimum electricity supplied by ES2
Max_k	Maximum supply of gas k		
Min_k	Minimum supply of gas k		

With i is index for products, j is index for materials, and k is index for gas suppliers.

Developed Model. A detailed mathematical model developed in this study is presented below. Objective function of the mathematical model is as follows:

$$\text{Maximize Profit} = \sum_i De'_i \times Ps_i - (FC + SGAC + CC + MC + EC) \quad (1)$$

$$\bullet FC = \sum_i FC_i \quad (2)$$

$$\bullet SGAC = \sum_i SGA_i Q_{\text{produkt,t}}^P \times K_{\text{produkt,t}} \quad (3)$$

$$\bullet CC = \sum_i (\text{Con}_i + \text{Alloy}_i) \times Q_i \quad (4)$$

$$\bullet MC = \sum_i IP_i \times I_i \quad (5)$$

$$\bullet EC = \text{GasC} + \text{ElC} \quad (6)$$

$$\text{GasC} = \sum_k P_k \times S_k \quad (7)$$

$$\text{ElC} = \text{ES1} + \text{ES2} = [\text{PP}_{\text{ES1}} \times (\text{Min}_{\text{ES1}} + \text{SP}_{\text{ES1}}) + \text{PR}_{\text{ES1}} \times \text{SR}_{\text{ES1}}] + K_{\text{ES2}} \times [\text{S}_{\text{ES2}} \times \text{S}_{\text{ES2}} + \text{FC}_{\text{ES2}}] \quad (8)$$

Based on [9], make or buy decision is not only influenced by cost. The following other aspects also influence make or buy decision: Technology & Manufacturing Process (TMP), Supply Chain Management & Logistics (SCML), and Support System (SS). In this developed model, TMP aspect is translated into production capacity constrain (Eq. 9) that influences *make* decision [2,7,10] as below:

$$\text{Min}P_i \leq \sum_i Q_i \leq \text{Max}P_i \quad (9)$$

And SCML aspect is translated as import capacity (Eq. 10), gas supply capacity (Eq. 11), ES1 (Eq. 12) and ES2 supply capacity (Eq. 13) constraints [2].

$$\text{Min}I_i \leq I_i \leq \text{Max}I_i \quad (10)$$

$$\text{Min}_k \leq S_k \leq \text{Max}I_k \quad (11)$$

$$\text{Min}_{\text{ES1}} \leq S_{\text{ES1}} \leq \text{Max}_{\text{ES1}} \quad (12)$$

$$\text{Min}_{\text{ES2}} \leq S_{\text{ES2}} \leq \text{Max}_{\text{ES2}} \quad (13)$$

SS aspect is beyond the scope of system, so it is not discussed in this paper. In addition to production, import, and energy supply constraints discussed above, the model developed also considers product-material balance constraint (Eq. 14-16) and energy supply balance constraint (Eq. 17 and Eq. 18):

$$Q_i = Di_i + De_i \quad (14)$$

$$De'_i \leq De_i \quad (15)$$

$$Di_j + I_j = \sum_i \frac{N_{ji} \times Q_i}{y_i} \quad (16)$$

$$\sum_i El_i \times Q_i \leq (\text{Min}_{\text{ES1}} + \text{SR}_{\text{ES1}} + \text{SP}_{\text{ES1}}) + S_{\text{ES2}} \quad (17)$$

$$\sum_i \text{Gas}_i \times Q_i \leq \sum_k S_k \quad (18)$$

Numerical Example. When the data was taken, Plant B had not operated yet due to installation process, so there is no use of lump ore, coking coal, and anthracite materials. Besides, hot metal is also not produced. Those real data can be classified into:

- *System parameter:* Data needed to run the model that usually does not change if there is no change in the production system, such as production capacity and yield of each plant and bill of material (BOM).
- *Input variable:* Input data that consists of marketing plan and procurement data (price of material in the market). These data usually changes over time. In this numerical example we use 2 sets of input variable to see differences in the output due to differences in input variable (see Table 2).

Table 2. Input variable for the Simulasi using LINGO

<i>i</i>		PELLET	SPONGE	SCRAP	MJIS	Slab	HR	CR	Billet	WR
Set 1	De_i (10^3 ton)	-	-	-	-	-	145	47	0	20
	Pi_i (\$)	167.55	423	400.30	349.00	497.00	-	-	542.50	-
	Ps_i (\$)	-	-	-	-	-	649.00	752.00	508.00	622.00
Set 2	De_i (10^3 ton)	-	-	-	-	-	145	53	0	20
	Pi_i (\$)	167.55	423	400.30	349.00	487.00	-	-	532.50	-
	Ps_i (\$)	-	-	-	-	-	669.00	775.00	518.00	641.00

The model is run with real data from the company as presented in Table 2 using LINGO 14 (student version). The optimal solution produced is presented in Table 3.

Table 3. Optimal Solution for the Simulation

<i>i</i>		PELLET	SPONS	SCRAP	MJIS	Slab	HR	CR	Billet	WR	Profit
Set 1	Q_i (10^3 ton)	-	0	-	-	0	195.54	47	0	20	-7,319 thousand USD
	I_i (10^3 ton)	0	0	0	0	200.35	0	0	20.58	0	
	De'_i (10^3 ton)	-	-	-	-	-	145	47	0	20	
Set 2	Q_i (10^3 ton)	-	0	-	-	-	200	51.15	0	20	892 thousand USD
	I_i (10^3 ton)	0	0	0	0	204.92	0	0	20.58	0	
	De'_i (10^3 ton)	-	-	-	-	-	145	51.15	0	20	

Based on the output presented in Table 3, we can analyze that importing slab gives more profit than producing it; consequently, the plants in upstream production process are off for both data set. By comparing the two data sets, we can conclude that as the import price of materials (slab) decreasing and selling price of the downstream products (HR, CR, Billet, WR) increasing, the profit will increase. And in data set 2, not all CR's sales plan can be met to get the maximum profit. The model recommends that company sell 51.15 ton CR instead of 53 ton CR as set in the company's marketing plan, in order to get a higher profit.

Conclusion

In this paper, we develop a mathematical model for multi-echelon production plants based on a real production system in a steel company in Indonesia. The objective of this model is to determine optimum numbers of produced material and imported material for each plant that maximize the

profit earned by the company. Besides, this model can also provide a suggested volume of product sales to obtain that optimal solution.

References

- [1] H. Bouchriha, S. D'Amours, P. Ladet, A "make or buy" decision model with economies of scale. International Conference on Systems, Man and Cybernetics, Hammamet, 2002, pp. 1-6.
- [2] M. Dabhilkar, Trade-offs in make-buy decisions. Journal of Purchasing & Supply Management. 17 (2011) 158-166.
- [3] L. Doukas, T. Sirnatupang, Systems engineering approach in make-or-buy technology. Portland International Conference on Management of Engineering and Technology, Portland, 2001, pp. 1.
- [4] G. V. Houtum, Multi-echelon production/inventory systems: optimal policies, heuristics, and algorithms, 2006, pp. 1-43.
- [5] S. Kurokawa, Make-or-buy decisions in R&D: small technology based firms in the united states and japan. Journal of Transactions on Engineering Management 44 (1997) 124-134.
- [6] N. D. Minh, Empirical make-or-buy decision making model in the japanese automobile industry. Winter Simulation Conference, Phoenix, 2011, pp. 647-658.
- [7] M. P. Neghab, S. Poormoaid, Optimum quantities of make and buy in multi-Item manufacturing firms with restriction in production capacity. International Conference on Industrial Engineering and Engineering Management, Singapore, 2011, pp. 313-317.
- [8] I. Peshkova, D. Santalova, On an optimal inventory problem for multi-echelon production system. International Conference of Reliability and Statistics in Transportation and Communication, Riga, 2011, pp. 249-254.
- [9] D. R. Probert, L. E. Chfiez, K. W. Platts, Technology transfer and succession planning: the relevance of make-or-buy analysis. Portland International Conference on Management of Engineering and Technology, Portland, 2001, pp. 253-254.
- [10] B. Wu, R. Stillman, MOBY: A semi-custom make or buy decision advisor. International Workshop on Artificial Intelligence for Industrial Application, 1988, pp. 91-93.

Research – Design & Development of Fast Customized Manufacturing for Prostheses TKR Based on Rapid Prototyping

Agri Suwandi^{1,4,a}, Gandjar Kiswanto^{2,b}, Widjajalaksmi Kusumaningsih^{3,c}
and Tresna P. Soemardi^{1,d}

¹Laboratory of Mechanical Design, Department Mechanical Engineering, Universitas Indonesia, Indonesia

²Laboratory of Manufacturing Technology & Automation, Department Mechanical Engineering Universitas Indonesia, Indonesia

³Department of Rehabilitation Medicine, Faculty of Medicine, Universitas Indonesia, Indonesia

⁴Department Mechanical Engineering, Engineering Faculty, Universitas Pancasila, Indonesia

^aagrisuwandi@yahoo.com, ^bgandjar_kiswanto@eng.ui.ac.id, ^cdokterwida@yahoo.com, ^dtresna.p.soemardi@gmail.com

Keywords: TKR, Customized, Fast Manufacturing, Rapid Prototyping.

Abstract. The challenge for engineer's orthopedic prosthetic rehabilitation is to find a state of the art in the field, technical or otherwise, that will help their clients who have disabilities. Organ replacement with prostheses is one of the most successful procedures until now. However prostheses are still using standard geometry that has been determined by the manufacturer of the prostheses and it becomes a problem. In addition to the design size that does not fit, long manufacturing process takes time and is expensive also being a problem. Suitability of the prostheses with the patient's body anthropometry and speed of production in the manufacture of the prostheses is very important. In manufacturing, precision and speed of manufacture of the product is something that is possible but requires a high cost, especially in the manufacture of prostheses. By using rapid prototyping technology are available, this research try to develop the customized and rapid manufacturing systems for the manufacture of prostheses, especially for Total Knee Replacement (TKR).

Introduction

Human have two knee joint, the right and the left. From spine through to the hip, knee and ankle must work together harmoniously to ensure stability. Any movement of the lower extremity, walking, running and other daily activities knee joint function is very important. The knee joint is the largest joint in the body that serves to accommodate the weight of the body while maintaining a level of mobility and stability [1]. This joint is one of the weight bearing joints are most vulnerable and have a fatal impact on accident.

Prostheses used to replace parts of the body lost due by trauma or disabilities. Total Knee Replacement (TKR) is the most successful orthopedic reconstructive procedures until recently [2,3,4]. TKR have been proven relieving pain due to knee joint disease, osteoarthritis (OA) or rheumatoid arthritis [4,5,6].

There are several critical success factors TKR, i.e.: patient, surgery technique and design of prostheses [4,7,8]. Patient factors influenced by many factors, for example: there are some ligaments and meniscus that must take into account. Also the cardiovascular and pulmonary system must be in good condition, when there is a replacement of the knee joint. While surgical technique depends on the skill or experience of the medical team who performed the surgery, the patient factor is difficult to do optimization as well as operating techniques [9]. Of these three factors, the design of the prostheses is a factor that is easy to do optimization [10,11].

According Soemardi [12], the design including size and shape of prostheses is still using standard geometry prostheses set by the manufacturer. Prostheses size produced commercially with the

standard sizes are categorized by size S (small), M (medium) and L (large) with anthropometric reference Caucasian obviously different gait cycle steps and long steps with Indonesian people (mostly Mongoloid race). As a result of the size that does not match the patient's bone anthropometry (customized), some patients complain of pain after TKR surgery, especially on the bone that is connected to the prostheses. Not only is the problem, in the process of operation and adjustment of prostheses takes quite a long time due to the size of the prostheses is not customized.

To create a customized prostheses required precision manufacturing processes. As we know that in the manufacture of customized prostheses is expensive and requires a long time, then it takes a rapid manufacturing technology at an affordable cost. Rapid prototyping technology is an alternative technology which the application can save production time and costs. In this research we are try to develop the customized and rapid manufacturing system to manufacture prostheses, especially for TKR.

Design and Development Approach

Using the engineering design principles described by Pahl & Beitz [13], that engineering design is a closed cycle as shown in Fig. 1. Starting from the analysis of consumer demand for the product, then the design which developed and implemented and released to the market, then back to the analysis of customer satisfaction for products that have been manufactured to be developed.

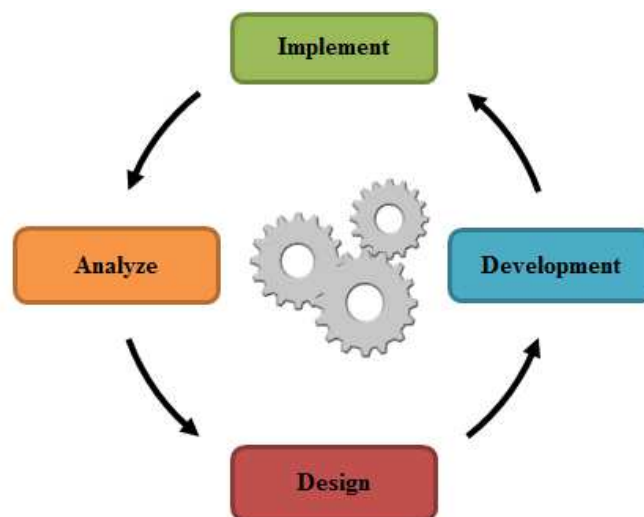


Fig. 1 Cycle of engineering product design

There are some important things to be taken into account in the design and development of products prostheses knee joint, i.e.:

1. The use of current technology for digital imaging such as CT-Scan, MRI , f-MRI etc., which will give you high definition digital output 3D visuals of cracked or broken or problematic bone. The result will be important information to facilitate the design and development prostheses in providing compatibility between digital imaging and process output of CAD / CAE / CAM will then become very important to create an efficient and effective research, design and development.
2. The use of high performance computing with high capacity and speed an adequate,
3. Use of Rapid Prototyping technology to define the function and geometry of artificial organs are developed through the creation of physical prototypes quickly with precision micro,
4. The use of metal or non - metal materials, in accordance with the standards of the implant material and is not sensitive to the human body,
5. The use of precision manufacturing technology such as investment casting, micro - fabrication, injection molding, etc.

Customizing and Manufacturing Prostheses

Digital Imaging and Solid Modeling. In modern orthopedic prostheses, digital imaging technology is a state of the art technology used to obtain the geometry of parts or organs of the patient body. Digital imaging from CT-Scan or MRI (Fig. 2) will be intensively use and more precision, the image quality and facilitate the fast design, prototyping and development of the prostheses and its components. From CT –Scan or MRI imaging results can be transferred from the image DICOM data then converted into STL data. By using CAD software STL data can be analyzed and reverse engineering (RE).

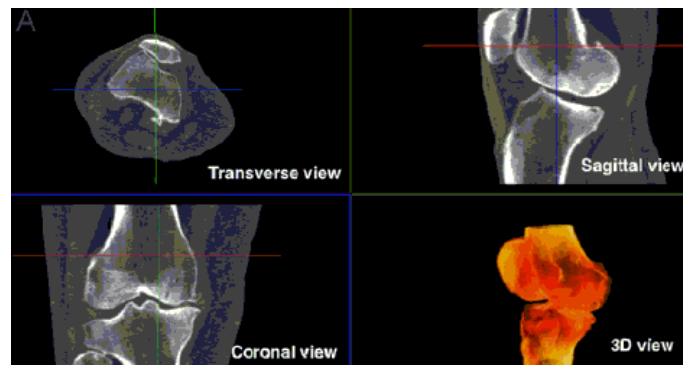


Fig. 2 MRI image of knee joint

Knee joint designed to be analyzed further, based on the power and torque when running normally or even in conditions more severe or extreme as running or playing soccer. In extreme conditions we can multiply the force or torque with a constant. In this case, the calculation and analysis of the strength of the material has been previously calculated to obtain a standard or reference that is used, resulting in a redesign process that is required is the basic geometry of each component of the TKR, i.e.: femoral, tibia and patellar components.

Rapid Prototyping. Rapid Prototyping (RP) technology is a way to realize the concept of a design. The use of RP technology can save production time and costs [14]. RP or layered manufacturing is the process of fabricating a product layer by layer, or the addition of a row of raw material in layers to form a product that conforms to the model. Principle different from the principle of rapid prototyping machining, rapid prototyping is a process where the addition of material, while the machining is a process of removing material. Nevertheless, both have similarities in the determination of the contact point chisel (cc-point) on the facet models. By using rapid prototyping control parameters, such as layer thickness, hatch space, and product orientation, development can use the laser trajectory control of these parameters [15]. Fig. 3 shows the data flow processing of Rapid Prototyping Machine (RPM) [16].

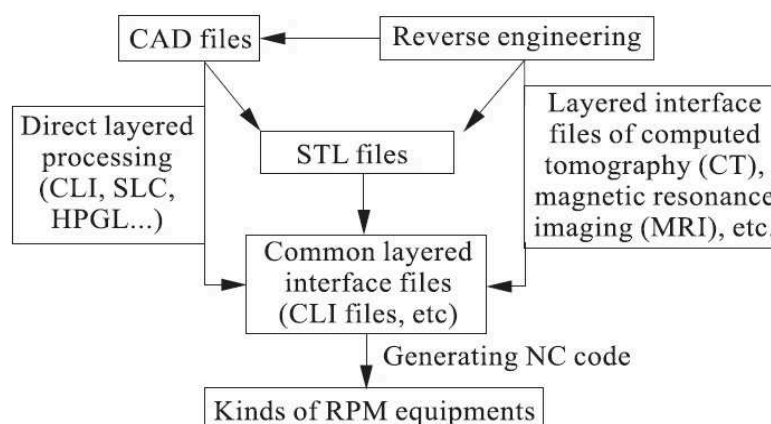


Fig. 3 Data processing in RPM process [16]

After the redesign of the TKR models, the pattern can be created by using RPM that is Three-Dimensional Printer (3D Printing). The patterns are categorized into two types of material components, i.e.: metal materials that will be made using the investment casting process and non-metal materials which will be made by injection molding process.

Manufacturing Prostheses. A manufacturing system was developed to simplify and shorten the time of manufacture of a product. This research has the main objective to be able to produce a fast manufacturing system by targeting one-day services in the manufacture of customized artificial knee joint prostheses. The rapid manufacturing systems that will be developed can be seen in Fig. 4.

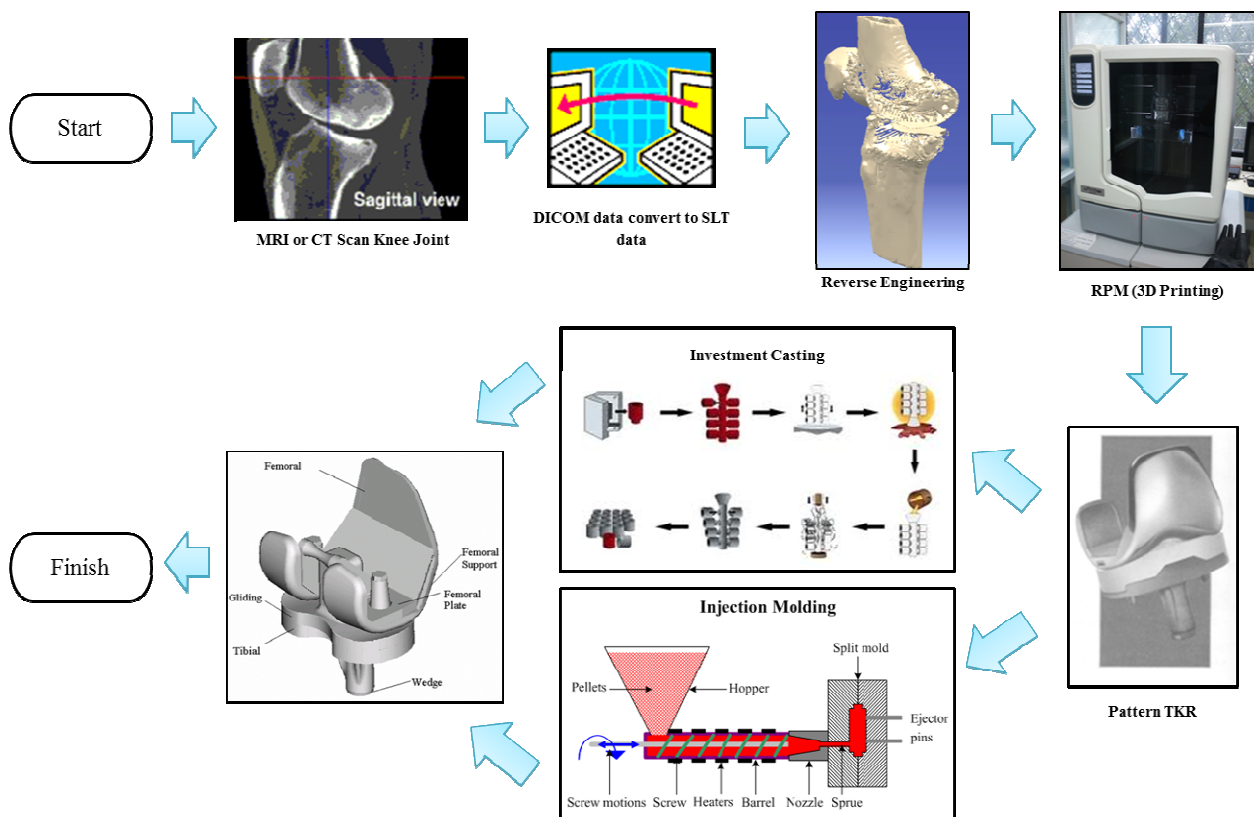


Fig. 4 Flow development of manufacturing systems for TKR prostheses

The data obtained from the results of MRI or CT scan imaging with DICOM data format and then the DICOM data converted into STL files to do RE with CAD software and ready to print. After a model or pattern of the prosthesis according to the patient's body geometry made using RPM, then do investment casting process to make a wax mold is given a ceramic coating. Do the casting process by entering the liquid metal into the ceramic mold, the metal component of the TKR (tibia stem and femoral) have been completed in print. Continue polishing process to make it look smoother. For plastic components TKR (patellar and tibia) were made using the injection mold with a pattern based on that was created before mold can be made. Components are then sterilized free of dirt and bacteria that arise when making processes.

Summary

This paper highlights research in the manufacturing system to be developed customized and fast manufacturing prostheses TKR based on rapid prototyping. And the system is not just for TKR prosthesis products but has the potential to be applied to another product. Further work will be tested on a laboratory scale production floor.

References

- [1]. R. Shenoy, P.S. Pastides, D. Nathwani, (iii) Biomechanics of the knee and TKR. *Orthopaedics and Trauma*, 27 (6), (2013) 364-371.
- [2]. J. Bellemans, H. Vandenuecker, J. Vanlauwe, Total knee replacement. *Current Orthopaedics*, 19 (2005) 446–452.
- [3]. Sharon E. Hohler, Total Knee Arthroplasty: Past Successes and Current Improvements. *AORN Journal*, (2008) 143-158.
- [4]. Alexander D. Liddle, Elise C. Pegg, Hemant Pandit, Knee replacement for osteoarthritis. *Maturitas*, 75 (2013) 131– 136
- [5]. J.M. Wilkinson, P. Haslamb, C.J.M. Getty. Hip and knee reconstruction in the rheumatoid patient. *Current Orthopaedics*, 21 (2007) 330-339.
- [6]. Merrill A. Ritter, Joseph D. Lutgring, Kenneth E. Davis, Philip M. Faris, Michael E. Berend, Total knee arthroplasty effectiveness in patients 55 years old and younger: Osteoarthritis vs. rheumatoid arthritis. *The Knee*, 14 (2007) 9-11.
- [7]. Clare K. Fitzpatrick, Chadd W. Clary, Paul J. Rullkoetter,. The role of patient, surgical, and implant design variations in TKR performance. *Journal of Biomechanics*, 45(1), (2012) S395.
- [8]. William C. Schroer, Keith R. Berend, Adolph V. Lombardi, C. Lowry Barnes, Michael P. Bolognesi, Michael E. Berend, Merrill A. Ritter, Ryan M. Nunley, Why Are Total Knees Failing Today? Etiology of Total Knee Revision in 2010 and 2011. *The Journal of Arthroplasty*, 28(1), (2013) 116-119.
- [9]. A. Wajsfisz, D. Biau, P. Boisrenoult, P. Beaufils,. Comparative study of intraoperative knee flexion. *Orthopaedics & Traumatology: Surgery & Research*, 26 (2010) 242-248.
- [10]. Brandi C. Carr, Tarun Goswami, Knee implants – Review of models and biomechanics. *Materials and Design*, 30 (2009) 398-413.
- [11]. Farid Amirouche, Giovanni F. Solitro, Challenges in modeling total knee arthroplasty and total hip replacement. *Procedia IUTAM*, 2, (2011) 18-25.
- [12]. Soemardi, T. P., Toward Customized and Fast Manufacturing Prostheses. *Proceedings Asialink International Conference on Biomedical Engineering and Technology 2007*, (2007) 217-222.
- [13]. Pahl. G and W. Beitz, *Engineering Design: a systematic approach - English edition*, The Design Council, London, 1984.
- [14]. Yucheng Ding, Hongbo Lan, Jun Hong, Dianliang Wu, An integrated manufacturing system for rapid tooling based on rapid prototyping, *Robotics and Computer-Integrated Manufacturing*, 20 (2004) 281–288.
- [15]. Gandjar Kiswanto, Ario S. B, Rendi K, Andry S, Srijanto, Hadi M, Pengembangan Mesin Rapid Prototyping Berbasis FDM (Fused Deposition Modeling) untuk Produk Berkontur dan Prismatic. *Prosiding Seminar Nasional Tahunan Teknik Mesin (SNTTM) ke-9*, (2010) 123-129.
- [16]. Yan Yongnian, Li Shengjie, Zhang Renji, Lin Feng, Wu Rendong, Lu Qingping, Xiong Zhuo, Wang Xiaohong, *Rapid Prototyping and Manufacturing Technology: Principle, Representative Technics, Applications, and Development Trends*, Tsinghua Science and Technology, 14 (1), (2009) 1-12.

Manufacturing Execution System Design using ISA-95

GOVINDARAJU Rajesri^{1, a}, LUKMANKristianto^{1, b}, CHANDRA Dissa R.^{1, c}

¹Industrial Engineering and Management Department
Faculty of Industrial Technology, Bandung Institute of Technology
Jl. Ganesha No. 10, Bandung 40132

^arajesri_g@ti.itb.ac.id, ^bnitrosakti@yahoo.co.id, ^cdissarc@gmail.com

Keywords: manufacturing execution system (MES), ISA-95, design methodology

Abstract. Manufacturing execution system is information systems (IS) that bridges the gap between IS at the top level, namely enterprise resource planning (ERP) and IS at the lower levels, namely the automation systems. MES has been reported to increase productivity, maintain product quality, and reduce production time. However, the advantage is obtained if MES is integrated smoothly with the other systems. Currently there is an industry standard, ISA-95, which can be used as a reference model in the process of integrating MES with ERP and automation systems. This study was undertaken to propose a methodology for MES design utilizing ISA-95 standard. The methodology is designed considering the objectives of MES development from a point of view manufacturing system and also from the point of view of information systems. Thus, challenges from two domains, namely business (manufacturing) domain and technology (IS domain) are both considered in the development of the methodology.

Introduction

MES is an information system that bridges the gap between top level information systems namely Enterprise Resource Planning (ERP) with the information system at the lower levels namely shop floor information systems (Deuel, 1994). MES provides an electronic and real-time media to optimize the manufacturing process as a whole. MES implementation may support a company in providing updated and complete information to help the production department to produce quality products in a shorter time, and with lower cost (McClellan, 2004).

In implementing MES, functional integration is the most difficult challenge --making all the components of the manufacturing system able to work well together. Before a manufacturing company can integrate its processes, functional boundaries for each system component must be specified. Without a standard to follow, manufacturing companies need a lot of effort to determine the functional requirements that meet their needs. Currently, there has been an industry standard that defines the boundaries between ERP systems and MES. The standard is known as ANSA/ISA-95.00.01-2000 (ISA-95). ISA-95 defines the terminology and models that can be used to perform the integration of the ERP system at a business level with the production automation systems (Fuchs & Thiel, 2009). The standard is very helpful in determining the requirements in the process of integration and implementation of manufacturing execution systems.

There have been studies on the design of MES such as studies by Hadjimichael (2004), Cao (2008), and Waldron (2011). These studies have not specifically discussed how ISA-95 can be used in the design of the MES. Scholten & Schneider (2010) have used the ISA-95 as a guide in determining the requirement of MES, but the requirement definition process proposed in this study can still be improved and steps related to the new manufacturing IS design has not been specifically addressed in the study. Therefore, the purpose of this study is to determine a more comprehensive methodology for MES design that specifically describes the use of ISA-95 standard as a reference model.

Model Development

The conceptual model that describes the methodology (the steps) for designing MES was developed after a synthesis of some methodology developed in previous studies (Hadjimichael, 2004; Cao, 2008; Scholten & Schneider, 2010; Waldron, 2011). In addition to this, the development of the model is also based on IS design methodology developed by Whitten & Bentley (2007).

Synthesis of Previous Models. Of the studies that were examined, only one of which discusses the use of ISA-95, i.e. a study by Scholten & Schneider (2010). Previous studies use different tools in supporting the MES design process, such as the use of IDEF-0 to model the business processes of manufacturing system by Hadjimichael (2004) and the use of UML diagrams for modeling MES logical design by Cao (2008). Majority of these studies focus more on either solving manufacturing problems (e.g. Scholten and Schneider, 2010; Waldron, 2011) or solving information systems problems (e.g. Chao, 2008). A comprehensive study assessing the needs of the system from both points of view are still rarely found.

Model Building. The stages of MES design proposed in this study are discussed below:

- MES development planning. There are 3 activities performed at this level:
 - Identify initial problems and opportunities. At this stage the activity is to determine the problems, opportunities, or directives that triggered the initial development of MES. Document 1 of ISA-95 contains information about the business driving factors of MES implementation. Such information can be used as a guide to determine the problems and opportunities for improvement from the standpoint of manufacturing process. Whitten & Bentley (2007) proposes a framework called PIECES to help identify and categorize problems related to IS. Both perspectives (manufacturing systems and information systems) need to be assessed in determining the priority of solving problems in the implementation of MES.
 - Determine the initial scope of the implementation. Determination of system boundaries is done based on a list of issues and opportunities that exist, current system conditions, and consideration of the budget funds available. Hierarchical model systems contained in the ISA-95 indicates that there are 5 levels of system in manufacturing activities (process). This model can be used as a guide to determine the boundary of each system level (Scholten & Schneider, 2010). MES (level 3) interact with the ERP system and the otomation systems. Figure 1 shows the model of the system hierarchy.

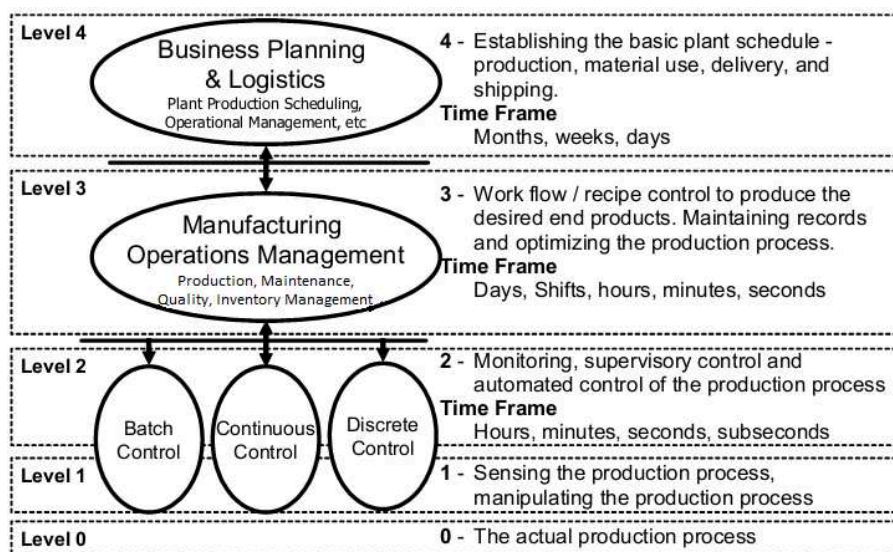


Figure 1. System hierarchy model (ANSI/ISA-95.00.03–2005, 2005, p. 20)

Hierarchical models of equipment in ISA-95 show the hierarchy of the physical assets of the enterprises engaged in manufacturing activities. Equipment hierarchy model can be used to

determine the physical boundary of the MES system (Scholten & Schneider, 2010). Figure 2 shows the hierarchical model of equipment.

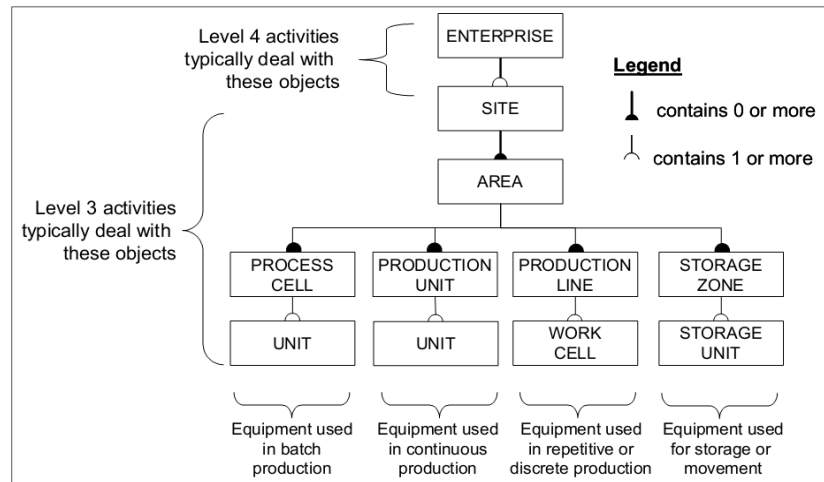


Figure 2. Equipment hierarchy model (ANSI/ISA-95.00.03–2005, 2005, p. 26)

- Develop baseline schedule and resources. At this stage the activity is to determine the schedule of the project activities and the parties involved. Information on the ISA-95 manufacturing operations management can help to determine the complexity of activities to be carried out in several stages of the process, such as the system requirements analysis, business process analysis, and design of MES logical model, which can be used to estimate the duration of the activities.
- Analysis of current system. There are two activities that are carried out at this stage:
 - Business process analysis. Activities undertaken at this stage is to analyze the business processes of manufacturing companies. Generic activity model of ISA-95 defines MES activities and grouped the activities into 4 main sections, namely the production, quality, maintenance, and supplies. Each piece consists of the activities described in the model of a generic activity. These activities are: detailed scheduling, resource management, activity tracking, work order dispatch, definition management, data collection, analysis of operation results, and execution management. Figure 3 shows all the generic activities in ISA-95. Furthermore, using ISA-95 as a reference, IDEF-0 is used to model the business processes. IDEF-0 can describe the flow of information among the modeled business processes, with information about controls and mechanisms for each process being exposed.



Figure 3. Generic activity model (ANSI/ISA-95.00.03–2005, 2005, p. 24)

- Analysis of current manufacturing information systems. Activities undertaken is analyzing the functional aspects and data requirements of the production management systems. The analysis is performed based on previous IS blueprint. If there is not a complete IS blueprint, analysis is

performed directly on concurrent production management IS. Use case diagram and ERD can be used in analyzing current manufacturing IS (Whitten & Bentley, 2007; Pressman, 2010). Use case diagram is used to model the functional aspects of IS and the interaction of the system with external entities such as users of the system and other related IS. Entity Relationship Diagram (ERD) is one model that is widely used to model databases.

- Determine system improvement objectives. Improvement goals are defined along with the identification of criteria that measures the achievement of these goals. Goal setting is done based on the results of problems and opportunities analysis. The list of problems and opportunities that have been generated at the earlier stage may still be a symptom and not the root of the real problem. The symptoms of problems and opportunities that exist should be verified with the actual condition of the system so as to know the root of the real problems. Fishbone diagram can be used to perform root causes and opportunities analysis (Whitten & Bentley, 2007). Information about MES KPIs in ISA - 95 part 3 and standard KPIs for manufacturing operations which is available on the ISO/WD 22400-2 can be used as a guide in determining the criteria for measuring the achievement of MES implementation (Dufort, 2006; Fukuda & Patzke, 2010).
- Analysis of system requirements. Activities undertaken at this stage is to determine MES functional and non-functional requirements. Information on the manufacturing operations management (MOM) contained in the document ISA-95 part 3 can be used as a guide to analyze the system functional requirements (Scholten & Schneider, 2010). MOM Model contains a description of the functional aspects of MES. Diagrams can be used to analyze the functional requirements of the system is use case diagram (Grassle et al., 2004; Eriksson et al., 2004; Whitten & Bentley, 2007; Pressman, 2010). To conduct the analysis of non-functional requirements of the system, Whitten & Bentley (2007) suggested the use of PIECES.
- Designing MES logical model. Activities undertaken at this stage is to design a model that describes an IS logical model that describes objects, workflow processes, and databased on the functional requirements. The model made yet contain technical solution, but more conceptual. Logic models are generally complemented by detailed specifications that contain data attributes, rules, and business policies. Based on Whitten & Bentley (2007), Cao (2008), and Eriksson et al (2004) it is proposed the use of multiple UML (Unified Modeling Language) diagrams i.e. class diagrams, object diagrams, sequence diagrams, activity diagrams, and state diagrams to design the logic model of MES. Class diagram illustrates the structure of the objects, however, class diagram does not define these objects in detail, but in the form of classes (Grassle et al., 2004). Object diagram illustrates the structure of the object involved in a system (Grassle et al., 2004). Circuit diagram is used to model the interaction between classes by considering the time in which the interaction process is done (Grassle et al., 2004). Activity diagrams are used to model activities that occur in each process as parts of the overall process of interaction between classes (Grassle et al., 2004). The information contained in the activity diagram has similarities with the circuit diagram, but in the activity diagram there is no data classes so that it is relatively easy to understand. Activity diagram is a tool used in the validation process of MES logical design by system users. State diagram is used to model the system behavior associated with the process of reading and modification of objects (Grassle et al., 2004). Information about the object model contained in ISA-95 part 1 section 2 can be used as a guide in designing MES logical design, specifically design a the class diagrams. ISA-95 object model contains descriptions of all class descriptions contained in MES. The object model contains information about the relationship between class and the attributes of each class, but information about the methods in each class is not provided in ISA-95.

Conclusion

In this paper a methodology to design MES for a manufacturing company, utilising the support ISA-95 standard is presented. The methodology is designed considering the objectives of MES

development from the perspectives of manufacturing system and information systems. Thus, challenges from two domains, business (manufacturing) domain and technology (IS domain) were considered in the development of the methodology.

References

- [1] ANSI/ISA-95.00.01-2000. (2000). *Enterprise-Control System Integration Part 1: Models and Terminology*.
- [2] ANSI/ISA-95.00.02-2001. (2001). *Enterprise-Control System Integration Part 2: Object Model Attributes*.
- [3] ANSI/ISA-95.00.03–2005. (2005). *Enterprise-Control System Integration Part 3: Activity Models of Manufacturing*.
- [4] Cao, W.-q., Jing, S.-h., & Wang, X.-h. (2008). Research on Manufacturing Execution System for Cement Industry. *Industrial Electronics and Applications, 2008. ICIEA 2008. 3rd IEEE Conference on*, (pp. 1614-1618).
- [5] Deuel, A. (1994). The benefits of a manufacturing execution system for plantwide automation. *ISA Transactions*, 113-124.
- [6] Dufort, Y. (2006). ISA-95-Based Operations and KPI Metrics Assessment and Analysis. *MESA White Paper 24*.
- [7] Fuchs, F., & Thiel, K. (2009). *Manufacturing Execution Systems: Optimal Design, Planning, and Deployment*. New York: McGraw-Hill.
- [8] Fukuda, Y., & Patzke, R. (2010). Standardization of Key Performance Indicator for Manufacturing Execution System. *SICE Annual Conference 2010*, (pp. 263-265).
- [9] Grässle, P., Baumann, H., & Baumann, P. (2004). *UML 2.0 in Action A Project-Based Tutorial*. Birmingham: Packt Publishing Ltd.
- [10] Hadjimichael, B. (2004). *Manufacturing Execution Systems Integration and Intelligence*. Master Thesis, McGill University, Department of Electrical and Computer Engineering, Montreal.
- [11] McClellan, M. (2004). The Collaborative Effect. *Intelligent Enterprises*, 7(16), 35.
- [12] Presley, A., & Liles, D. (1995). The Use Of IDEF0 For The Design and Specification of Methodologies. *4th Industrial Engineering Research Conference*, (pp. 442-448). Nashville.
- [13] Pressman, R. (2010). *Software Engineering: A Practitioner's Approach* (7th ed.). New York: McGraw-Hill.
- [14] Qiu, R., & Mengchu, Z. (2004). Mighty MESs: state-of-the-art and future manufacturing execution systems. *Robotics & Automation Magazine, IEEE*, 11, 19-25.
- [15] Scholten, B., & Schneider, M. (2010). ISA-95 As-Is / To-Be Study. *MESA White Paper 23*.
- [16] Waldron, T. A. (2011). *Strategic Development of a Manufacturing Execution System (MES) for Cold Chain Management Using Information Product Mapping*. Master Thesis, Massachusetts Institute of Technology, Department of Chemical Engineering.
- [17] Whitten, J., & Bentley, L. (2007). *Systems Analysis and Design Methods* (7th ed.). New York: McGraw-Hill.

A Vide Survey on Product Development and Commercialization Process

ROBA RADI SALMAN, YASER A. A. HAMMOUDA, SANAZ MONSEF,
MOHAMMAD SADEGHI

Postgraduate Center of Study (PGC), Limkokwing University of Creative Technology
Cyberjaya, Malaysia

sanaz.monsef@limkokwing.edu.my

Keywords: Product development, commercialization, supply-chain, universities, construction industry

Abstract: The purpose of this paper is to focus on new Product Development (NPD) and Commercialization Process based on previous researches since 1963. We intend the articles to serve two major goals. Firstly, we hope that it will be useful for researchers and postgraduate students who are interesting in understanding of commercialization process for NPD. Secondly, this article is useful for R&D managers to understand how can commercialize a new product. Finally the practical implementations of each article along with its findings as major factors for impacting on NPD process are presented in a table on discussion and result part.

Introduction

Industries and firms all the time try to make new products that cope with the needs and requirements of the communities which vary in many fields from construction and weight loss products; however they come across many problems and challenges when sending a new product to the market as it can be kept on shelves for a long time.

For example, today user authentication stands out as one of the most essential areas in information security which has several ways of being implemented. Dr. Lashkari and his group after doing a wide research and survey on the graphical user authentication or graphical password [5], they have designed and implemented many new graphical passwords such as “a new algorithm on Graphical User Authentication (GUA) based on multi-line grids” [7] and “A Secure Recognition Based Graphical Password by Watermarking” [6]. Now a day, they are trying to commercialize the product and send it out as a product on mobile and tablets. In comparing with other product, they are in a competition with other products for promoting and sail their new product which is a big challenge today.

The issue they face that the firms depend only on their ideas without looking for successful ways for marketing and advertising for their novel products. This causes losses instead of benefits and revenues for the firms. The previous twenty years have observed a surplus of studies regarding the business novel products. The companies’ work environment is the total of all aspects which are beyond the power of the firm and affect the processes trades, revenues, markets, and survival war. Also, this environment involves two markets: capital to produce its inventions and patrons to buy its inventions. If a company can’t contest successfully, it will not practice a reply from the market for its produces and therefore with time passing won’t be profitable [3]. No assurance of accomplishment despite market entrance level or stage is reached; as pointed out by the high frequencies of novel product deterioration [1]. Whatever the case may be, the disappointment figures emphasize the necessity for executive concentration on the procedure of progressing and advertising for innovative products [15]. The objective behind this paper is to summarize the techniques and solutions proposed to solve the problem with commercialization of new products. This paper emphasizes on the successful process when a firm wants to make a new model and send it to the market, papers have been written on this topic since 1950 and yet researchers are still writing on it.

Related Works

Cooper made a research in 1983 and suggested six lessons that he has learnt it. Firstly, for business innovative products a greatly powerful market positioning is required. Second, new products accomplishment is mainly responsive to managing activities. Third, there is no easy method to determine the success of a new product. Forth, a key factor for the success of the product is the uniqueness of the product with real customer advantage. Fifth, a main reason for accomplishing achievement is a good comprehended accurately performed takeoff. Lastly, a good communication and cooperation between involved parties is a great raise for positive innovation process [2].

Also researchers suggested a new product development process, which splits it into seven consecutive phases; innovative product scheme progress, idea creation, inspection and assessment, commerce investigation, progress, examination, and commercialization. In addition, new products failure sources were illustrated in this research, failure in marketplaces, time interval, monetary, practical, managerial, and ecological. Risk traditional aspect is also as a part of new product development failure [1].

Many products fail in the market after the launching, 50% to 67 % of them actually fail in the commercialization process [12]. In 2001 a research argued the lack of relations and connections between the private and public sectors in the process of developing new products, i.e. no association between the academic researches done in the public sector (university) and private sector (companies) [14]. In this research the mistakes practiced in the stages of new products commercialization are discussed to find the reasons behind such failure. The process for achieving the proposed solution is to follow certain criteria of tables and graphs. First is to use the 13 new product development stages where the initiation, testing, and launching take place. Then going through matching development process to product type stage where this represents a graph of opportunity cost vs. development risk. The proposed solution is to make coordination between the managers along with the team members by following a strategy to avoid such mistakes from occurring. Some products are sent to the market and after one year they are still there and haven't made any success, just complete waste of time and resources. The analysis includes using all the identified products and then reducing them by eliminating them to the most desirable product [13]. Four mistakes were found in previous research; mistake one is the absolute shortage of sensitivity to the variations in the managing responsibilities needed of incremental versus breakthrough projects. Mistake two is the propensity to suppose that breakthrough jobs compare with high outline actions requiring supplies and pinnacle management support. Mistake three is when managers adapt the same industrialized-sale system for new products rather than coming up with new ones. Mistake four is when such dealer missed insight guides to flawed product allocating [4].

Some researchers discussed about factors of the supply chain and their relation in the product progress and commercialization procedure. Also, by decreasing the product lifetime, the accurate products must be advanced and strongly sent to market in shortest time frameworks so as to keep the competition among others and attain segregation and power in the market. By applying the effective supply chain process, and integrate both customer and suppliers into the process, the time can be reduced. Also, by decreasing the product lifetime, the accurate products must be advanced and strongly sent to market in shortest time frameworks so as to keep the competition among others [10].

In 2008 McCoy, research about the big and wide history of disappointments in capitalist business projects in the commercialization of structure products. The research points to concentrating on the developer/builder risk along the whole supply chain are one means part to a winning commercialization plan and understanding the role of developer/builders in the concurrent commercialization of product innovation [9].

Other problem that suggested 2009 for having some obstacles and difficulties that stand in the way of the process of commercialization of new products which are connoted to the simultaneous technical and market experimentation and the energetic harmonization of a composite evolving structure of hardware, software, and functions offered by self-sufficient companies. The findings were as follows, first, the use of studies and researches is to decide how various community-based

managerial conceptualizations cause product improvement and marketing in special types of businesses and with unlike mutual benefits. Second, they require more information and background about directing joint societies of companies particularly with regards to progressing the needed business procedures and abilities. Third there exists a necessity for research and study on the capitalist consequences of societies and their insinuations for laws and instructions. Lastly, to show the uniting of characteristics of societies with further associational designs, directors can employ the shared-benefits society of companies' representation as the foundation for giving ideas regarding beginning, collaborating, and running communities that are successful for invention growth and marketing [11].

Chen Li and Glenn Morgan (2010) published a research about the problem of no assessment of the relationship between institutional modification and marketing of university research in China. Also, to know the degree to which the organizational changes have influenced the act of university's research, and to realize how various universities have reacted to such out sourced change. In addition to that, the intellectual property right must be established and accredited to the right people and to test and analyze the possible relations between the governmental change and commercialization of the research performed [8].

Analysis and Findings

The analysis performed here is review of previews researches that is presented in table 1. As you can see most of the articles are focusing on concurrent commercialization, commercializing intellectual property and understanding the role of development /builders in concurrent commercialization. In addition the table shows that culture, competitive market, value procedure and capability of this process effect on commercialization of NPD process more than other factors. Another important finding is the role of supply chain that has more effect on winning of commercialization process.

Conclusion

In conclusion, this review paper made its purpose where it discussed and compared eight published papers along with their analysis and findings. All the papers had something in common which is talking about the new products development and commercialization process in the collaboration between the public and private sectors. Also, some argued the interference of higher education institutions as researches should be performed and applied in the real life, and maintaining the intellectual property. Based on this research there are five major factors namely culture, competitive market, value procedure, capability of the process and role of supply chain will affect the commercialization process of NPD.

Table 1: The comparison performed from all references

No	Paper name	Description of analysis	Results
1	Concurrent commercialization and new-product adoption for construction products	13 products were tested for equilibrium, the percentage of Concurrent Commercialization included, and the CC steps which are presented and missed	When some steps of CC is removed from the process the products don't reach equilibrium and have low CC %, on the other hand when no steps are skipped equilibrium is reach and a 100% CC is obtained
2	Commercializing intellectual property: a university-industry alliance for new product development	An official procedure for planning university intellectual property for commercialization consisted of 3 phases and 6 steps. After completing phase 3 and step 6 the repayment goes back to the university and the revenue is reinvested in further projects or products.	The process has showed to be successful and can be implemented, however several challenges can rise from both the public and private sector such as : culture, competitive market entry, value procedure, sustaining strong solid ground, and capability of working together
3	From Knowledge to product Institutional change and commercialization of university research in China	The analysis focused on gathering the data from the offices and uses them. The tables and statistics were utilized to perform the comparison as a form of graphs where the horizontal axis shows the years from 1986 till 2006 and vertical axis shows the number of copyright applications and granting in both universities. Also, the number of applied patents in each university vs. the duration from (1986-2006) was introduced by using a graph. A number of interviews with chief office managers (CEOs) and intellectual property managers (IP) were made as well.	By comparing both universities, it showed a huge difference between the number of patents and the giving way in each year. For example, in university A the number of patents was approximately 340 while the number of applicants who gained the patents was approximately 155. Despite that there is a change in the last 20 years but a big difference was still present till late 2006. There still exists an issue in China regarding this topic, where as China is considered such a developed country with big number of brilliant thinkers and developers with a very strong economy
4	New Product Commercialization: Common mistakes	A framework is established initially which includes the supplier's insights vs. the customer's insights, and it includes a mismatch, breakthrough, and incremental factors. After deciding whether it is a breakthrough or an incremental product, another figure is used which explains the nature of marketing tasks which includes both the technology and customer voices.	Trades and industrialized actions have a critical position to occupy in improving and commercializing incremental novel products. This is due to the sales/distribution control is frequently the one that is nearest to the client and the best place to interpret customer response. The engineering and manufacturing authority could repeatedly be in a point to make these improvements without going to a extreme try. Sales and
5	Organizing Continuous Product Development and Commercialization: The Collaborative Community of Firms Models	For making the analysis the Blade.org case study is used in this research, by using server examples such as network servers, electronic mail servers, records server, and folder servers. In this case, it occupy the role of Analyzer	The study designates that companies can preserve the profits connected with their self-governing position whereas improving their novelty abilities through inter-firm teamwork. Also, the use of studies and researches is to decide how various community-based managerial conceptualizations cause product improvement and marketing, they require more information and background about directing joint societies of companies particularly, they require more information and background about directing joint societies of companies particularly, there exists a necessity for research and study on the capitalist consequences of societies and their insinuations for laws and instructions, and, to show the uniting of characteristics of societies with further associational designs, directors can employ the shared-benefits society of companies
6	The Product Development and Commercialization Process	To make the analysis and get the findings, 2 sub processes are used. The tactical sub-processes are used as the outline for the execution and contain six steps. The operational sub-procedures are a pattern for the harmonization and management of product expansion and contain eight steps. Also, to analyze the product progress and advertising impact the Economic Added Value in a positive way or in a negative way,	By applying the supply chain management processes successfully, the expenditures can be condensed the returns can be enhanced and increased. Also, it affects the Economic Value Added in a positive way. By touching on the information experience, and abilities of other supply chain elements, a company can enlarge its information possessions and achieve entrance ways to thoughts for product growth or improved growth effectiveness.
7	Towards establishing a domain specific commercialization model for innovation in residential construction	Previous models that were identified such as Rourke (USDOC) model breakdown and Goldsmith model utilized to develop the new standard model. The generic commercialization model presented includes functional areas, definition, concept, feasibility, planning, phase review planning, early production, review early production, standardization, and maturation. Also an example case study for the practical implementation is used that provides the sequence of the process for the product	The model proposed by this paper is applicable and can be introduced for the commercialization of construction industry. A commercialization matrix accepts various inputs that later on enhance its structure. The model's goals is to take advantage of business ventures in marketing of building products.
8	Understanding the role of development/builders in the concurrent commercialization of product innovation	A four step analysis based on Maxwell is used. First to set up a research affiliation with those you will make the study on. Second is to choose the places and members that you will talk to and study to get information. Third is to assemble the data and create a case study for you. Forth is to examine the data and adapt all the facts to practical information. The Delphi method is basically like an algorithm which contains steps. Start by defining the questions then choosing the section and designing the survey. Perform the survey and make the consensus if ok make conclusions if no go back to survey design. Risk management is included and applied in defending, emergency planning and prewarning.	Booming and effective synchronized commercialization needs risk allocation among all constituents of a project's supply chain. The novelists sponsor concurrent management marketing, which involves data division and information transmit amongst supply-chain associates in the early stages in a commercialization project and an unusual type of parallel engineering for manufacture products, which is called concurrent commercialization (CC). The research points to concentrating on the developer/builder risk along the whole supply chain are one means part to a winning commercialization plan. It as well specifies that commercialization engages more than just technological product drawing; commercialization cuts crossways all serviceable fields.

Acknowledgement

We would like to thank Dr. Arash Habibi Lashkari for his encouragement, kind advice and great lecturing in research methodology module. Also we would like to express our appreciation to all respondents who participated in our survey for their valuable contribution.

References

- [1] Booz. Allenand Hamilton (1982), "New Product Management for the 1980s", Booz Allen & Hamilton Inc.
- [2] Cooper, G. R. (1983), "A Process Model for Industrial New Product Development", IEEE TRANSACTIONS ON ENGINEERING MANAGEMENT, 2-11
- [3] Devries, M. G. (1963), " A Dynamic Model for Product Strategy Selection", Industrial Development Research Program
- [4] Harvard Business School (1995), "New Product Commercialization: Common Mistakes", Harvard Business School. Boston: Harvard Business School Publishing

-
- [5] Lashkari AH., Farmand S. (2009),” A survey on usability and security features in graphical user authentication algorithms”, International journal of computer science and network security (IJCSNS), Vol 9, P 195-204
- [6] Lashkari A.H., Manaf AA., Masrom M. (2011) ,” A Secure Recognition Based Graphical Password by Watermarking”, International conference of computer and information technology (CIT), P 164-170, IEEE
- [7] Lashkari A.H., Gani A., Sabet LG., Farmand S. (2010),”A New Algorithm on Graphical User Authentication (GUA) Based on Multi-line Grids”, Scientific Research and Essays journal, Vol. 5 (24), December 2010
- [8] Li, C., & Morgann, G. (2010),”From Knowledge to product Institutional change and commercialization of university research in China”, Journal of Science and Technology, I (3), 254-274
- [9] McCoy, A. P., Thabet, W., & Badinelli, R. (2009),”Understanding the role of developer/builders in the concurrent commercialization of product innovation”, European Journal of Innovative Management, 12 (1), 102-128
- [10] Rogers, D. S., Lambert, D. M., & Knemeyer, A. M. (2004) ,”The Product Development and Commercialization Process”, The International Journal of Logistics Management , Volume 15 (1), 43-56
- [11] Snow, C. C., Fjeldstad, O. D., Lettl, C., & Miles, R. E. (2009, September) ,”Organizing Continuous Development and Commercialization: The Collaborative Community of Firms Model”, Journal of Product Innovation Management
- [12] Song, X. M.andPerry, M. E. (1997) ,”A cross national comparative study of new product development processes: Japan and the United States”, *Journal of Marketing*. 61, 1-18
- [13] Swink, M.andSong, M. (2007) ,”Effects of marketing-manufacturing integration on new product development time and competitive advantage”, *Journal of Operations Management*. 25, 203-217.
- [14] Tatikonda, M. V.andMontoya-Weiss, M. M. (2001) ,”Integrating operations and marketing perspectives of product innovation: The influence of organizational process factors and capabilities on development performance”, *Management Science*. 151-172.
- [15] V. Kasturi Rangan and Kevin Bartus. (1995) ,”New Product Commercialization: Common Mistakes”, Harvard Business School, 1-13.

Basic Approaches to Green Production of Board Wood Composite Materials

TISHCHENKO V.P.^a, MAYOROVA L.P.^b and MORINA O.M.^c

Pacific State University, 136, Tikhookeanskaya str, Khabarovsk, 680035, Russia

^aVtishenko@mail.khstu.ru, ^bmayorova@mail.khb.ru, ^co.morina@mail.ru

Keywords: green production, wood, composite materials, timber processing

Abstract. Deep processing of wood raw materials is the main field of its use. The forecast of timber industry development provides deep chemical processing and start-up of board materials production. In the available forest reserves the share of pulpwood and forestry engineering raw materials is up to 13 per cent. Some measures will contribute to settle the problems of increasing wood raw material complex use and green production of board wood composite materials. They include the improvement of existing technologies and implementation of progressive technologies and systems increasing the volume and quality of board output. One of the main directions will be the maximum possible use of all components of raw materials, when some production wastes are the raw material for the manufacture of new products. This will provide the balance in efficient environmental management. The priority will be given to creation of a relatively closed cycle of wood resources use. Particularly promising in achieving a balance of economic and environmental interests of society will be obtaining of cheap boards capable to be not worse than solid wood with minimum cost of natural resources and preservation of individual properties of each component.

Introduction

Despite the fact that the timber processing complex (TPC) traditionally is one of the key complexes in social-economic development of the region, the wood resources in Khabarovsk Krai (territory) are used extremely irrationally. In Khabarovsk Krai about 3.4 million m³ of wood wastes formed annually at the modern technological level of wood production and mechanical processing, but the revenue is half as much as the average in Russia. In this connection it is necessary to work out technical processes of cheap board wood composite materials (BWCM) production capable to become the alternative to solid wood with minimum costs of natural resources.

Problem Definition

Wood is a universal natural composite, its resources are annually replenished for 7000-9000 million m³ in the process of solar energy biosynthesis. It plays a significant role in the social-economic development of more than 40 entities of the Russian Federation, including the Far Eastern Federal District and Khabarovsk Krai .

Loggers choose high-quality softwoods and hardwoods, leaving timber thinning and firewood alongside with waste. Wood production of every 3 m³ is accompanied with 1-1.5 m³ average loss, and at the subsequent stages 1 m³ more is lost for every 2 m³ of used or recycled wood. Thus, up to 50% of the original stock of wood remains at the cutting area as "normative" waste, being less valuable, but industrial recyclable material [1].

Therefore, rational consumption of wood raw materials is a priority for the country and forest industry complex (FIC) and is defined as follows:

1. Man-made nature, increased technical power and material production scale, which became "the largest geological force."
2. Constantly increasing complication and intensification of the society and nature interaction.
3. Environmental impact on the development of society and the need to consider the ecological factor as the most important for assessment of production conditions and efficiency.

4. Constantly increasing consumption of the relatively limited wood resources and approach of the biosphere ecosystems resource intensity to the threshold limits.

5. Sharp increase of costs for elimination of man-made production activities on ecosystems and the environmental improvement, as an essential element of human welfare [2].

The following approaches are the basis of FIC greening in Russia and Khabarovsk Krai in particular:

1. Creation of a relatively closed cycle of wood resources use at the regional level by combined and compact location of interlinked flexible operations of different capacity, producing a wide range of products as provided by public demands.

2. Maximum possible use of all raw material components when the wastes of some production are the raw material for manufacture of new products that will provide a balance in environmental management.

3. Improvement of existing products and development of new production types and technologies, which occur under pressure, temperature and environment reactions close to the ecosystem (biotechnology). It would eliminate the causes and sources of change of physical, chemical and biological parameters of ecosystems in present and future.

4. Environmental restriction of the material production expansion and preventing the violations of the biosphere natural development.

One of the perspectives of FIC greening is the development of new and improvement of existing board wood composite materials (BWCM) promoting:

1. Increasing of the FIC effectiveness by full use of waste, low-value and low-merchantable wood, which are 90-95 per cent of the timber-cutting volume.

2. Combined and compact spatial location of subsequently related different productions using relatively closed waste-free technologies, when the wastes of some processes are the raw material for the manufacture of new products.

3. Cheap BWCM that are not worse than wood with least costs of natural resources and preservation of individual characteristics of each component.

4. The balance of economic and environmental public interest.

BWCM quality according to ISO 8402 international standard, is defined by a set of artistic and aesthetic, operational, environmental and other criteria, the potential level of which is laid at the envisioning stage in accordance with the market requirements and the achievements of basic science. The criteria level is specified during the research and development of design variants of concept realization. Their real level is forming in the process of design and engineering research and depends on the compliance of quality and structure of raw materials, equipment and personnel qualification and the process procedure parameters to the requirements of operation procedure. This level determines the possibility of BWCM to meet the planned market requirements since manufactured until the loss of the ability to keep the characteristics under the influence of changing environmental parameters, i.e. the efficiency of production and consumption, as well as the level of the market value [2].

Then the concept is corrected and changed during the analysis of operational experience, BWCM exploitation and utilization, i.e., a new life cycle begins that allows to achieve more acceptable quality, but reduces the production efficiency. Therefore, decrease of time and money to achieve an acceptable level of quality is defined by comprehensive and reliable information about the behavior and changes of initial materials, intermediate products and the BWCM at the life cycle stages - a hierarchical set of different complex natural and artificial systems (fig. 1).

At its various stages, these systems are combined into new multi-level systems subjected to a great influence both from each other and from other systems, their borders and characteristics are difficult to determine (a single whole has characteristics its parts lacking).

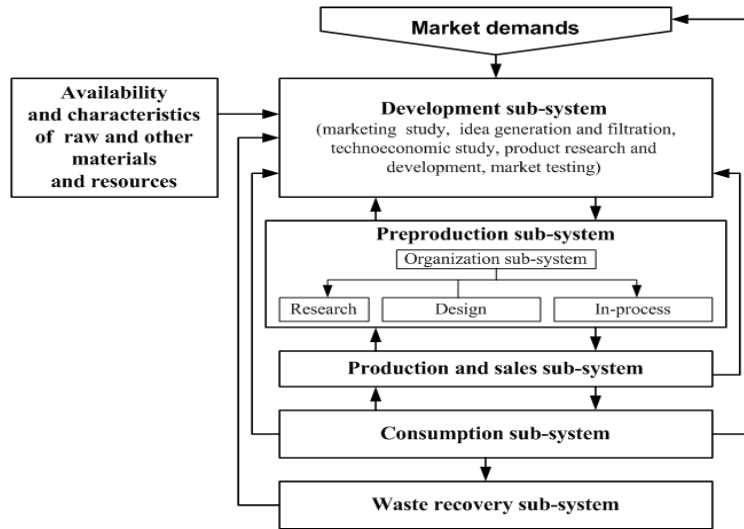


Fig. 1. Life cycle stages [3]

Therefore, a comprehensive analysis of each stage and each part of the BWCM design and manufacturing technology is necessary. Only after identifying the causes, sources and factors influencing the level of anthropogenic impact on the environment and environmental properties it is necessary to develop new and improve the existing BWCM ensuring minimum raw material consumption and acceptable environmental results.

Earlier theoretical and analytical data, information behaviour and changes of BWCM and their individual elements during mechanical, physical-chemical, chemical and other processes at different stages of the life cycle do not allow:

- to get vivid (transparent) models of manufacture process;
- to identify the sources and mechanisms of toxicity level.

Despite the progress achieved in the field of BWCM manufacture greening, the toxicity problem at different stages of their life cycle is far from a complete resolution.

The analysis of conditions of BWCM ecological safety formation is simplified by a decomposition of this system into subsystems and their description by blocks and arcs that form the space [4] which is compressed at the upper and expanded at the lower levels of a hierarchical model (fig.2).

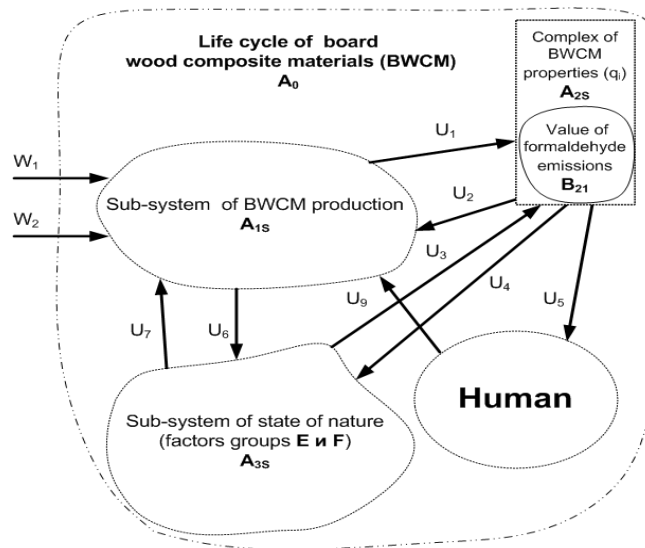


Fig. 2. Subsystems interaction pattern at different stages of BWCM life cycle

The blocks display subsystems: A_{1S} – BWCM production, A_{2S} – a complex of BWCM characteristics (formaldehyde emission amount), A_{3S} – the state of nature. The arcs show their relationship, characterized by phase variables: W_i – input variables; U_i – represent the variables describing the apparent state of subsystems.

The next level of decomposition (by narrowing the field of attributive description, specification and space) facilitates the analysis of the structure of the "BWCM Production" subsystem and the interrelations between the elements (fig. 3). It is marked by a solid line, and is a system for this level [5].

The blocks show subsystems (elements) of the "BWCM Production" multistage system: B_{1S} – preparation of raw materials, B_{2S} – wood sandwich formation, B_{3S} – pressing, B_{4S} – processing of finished material which at the next level of decomposition will split into elements.

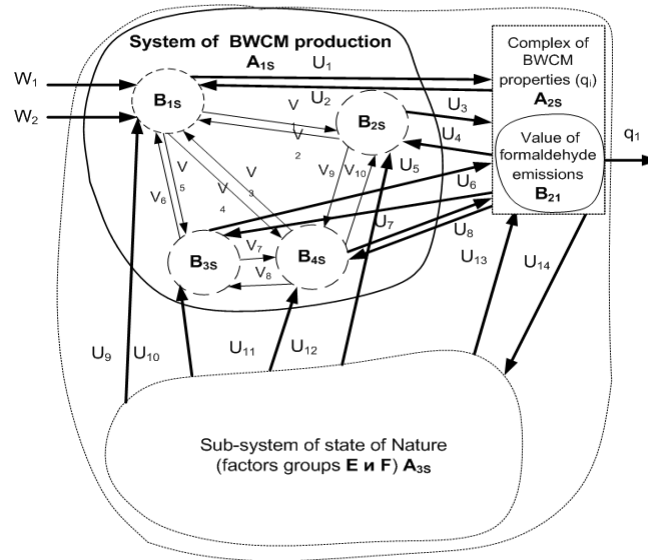


Fig.3. Structure diagram of "BWCM Production" system, interrelation and interaction between its elements

Arcs show their interrelations: W_i – are the input variables that characterize the state of input components; U_i – represent the variables describing the apparent condition of the subsystems; V_i – show the variables describing the internal state of subsystems or outer state of the elements ; q_i – displays performance indicators (formaldehyde emission). This description of BWCM life cycle shows the need to study, identify and evaluate the limits of existence and development of the whole complex of systems and subsystems that make up a unified whole of "BWCM environmental safety" system considering the groups of factors (table 1) determining the processes and changes in its certain elements.

A, B and C group factors are controlled constants, preparing formation of totally new material and influencing formaldehyde emission rate at different stages of its life cycle. Group E-factors are controlled unguided, their characteristics are slowly changing during production process that leads to the drift of material complex properties.

Table 1-Factors determinants of environmental safety plates

Groups	Factors
A	Quality and characteristics of wood particles and binding agent
B	Operation factors of the equipment (chippers, a blender, forming machines, a press, etc.
C	Wood sandwich characteristics (number of layers and their relationship, binding agent concentration and consumption, layers humidity, conditions of wood particles binding, fraction composition of wooden particles by layers and their orientation, etc).
D	Main physico-chemical process regimes, determining formation of break-through material from primary components.
E	Impact of disturbances on the production process, which cannot be quantitatively measured (uncontrolled impurities in resin materials, tree growing conditions, equipment operation, workers health condition and skill, atmosphere factor, etc)
F	Operation conditions – temperature, humidity, oxygen, acid and alkali impact, influence of UVR, ozone, radioactive emission, geomagnetic field, mechanical effect, etc, determining the most important criteria of material quality - strength, durability and environmental safety

Certainly, Group D factors are the most important because their impact determines the intensity of changes in the original material components, the degree of completeness of processes gomopolymerization and gomopolicondensation of polymer matrix and its grafted copolymerization with ligno-carbohydrate matrix of wood particles, proceeding with different speed and on different mechanisms with formaldehyde formation [6].

Conclusion

Thus, one of the prospective trends of TPC is the development of new and improvement of existing board wood composite materials (BWCM) production based on their life-cycle analysis. Comprehensive analysis of each stage and each part, design and production technology of BWCM is based on decomposition of the system into subsystems reflecting BWCM production, complex of BWCM properties (formaldehyde emission amount), state of nature. From the above groups of factors determining the environment safety of BWCM production Group D factors are the most important determining regimes of main physico-chemical processes determining formation of break-through material from primary components. In whole, BWCM production includes the creation of limited in space artificial environments and means of production within these environments operating on bionic principles and is a partial, but necessary form of optimization of human - environment interaction.

References

- [1] L. P. Mayorova. Wood resources conservation as ecological basis of timber processing complex operation. Pacific State University, Khabarovsk (2009).
- [2] L.P Mayorova, A.M. Derbentseva. Ecological safety of timber-processing complex. Pacific State University, Khabarovsk, (2013), 137p.
- [3] V. P. Tischenko, K.S Ryabukhina, P.V. Shugurov. Methodological approaches to improvement of wood-polymeric composite materials technology in: *Natural Resources and Ecology of the Far Eastern Region.*, Pacific State University, Khabarovsk (2013)
- [4] A.V. Oleinik, V.P. Tischenko. On the problem of structural-blocked modeling of processes and systems. Regional Technological-Research Conference on "Russian Far East Program". Pacific State University, Khabarovsk (1995). p.47
- [5] I.S Shamrova, V.P. Tischenko. Construction of target function of formaldehyde emission minimization from wood-chip boards during their production in: *Problems of training process safety and upgrading.* edited by L.P. Mayorova, L.F. Yurasova et al, Pacific State University, Khabarovsk (2001) pp. 159-163
- [6] V.P. Tischenko, S.P. Isaev, et.al. Estimation of technological factors influence of wood boards formation on formaldehyde emission in: *Vestnik TOGU*, Pacific State University, Khabarovsk (2008), pp.189-198

Design and Analysis of Automotive Instrument Panel

Nur Akmal Haniffah^{1, a}, Mohamad Fazrul Zakaria^{1, a}, Tan Kean Sheng^{1, b}

¹National Defence University of Malaysia, Sungai Besi Camp, 57000 Kuala Lumpur, Malaysia.

^anurakmal@upnm.edu.my, ^bkeansheng@upnm.edu.my

Keywords: Instrument Panel (IP), Head Impact Simulation, Head Injury Criterion (HIC), ABS polymer.

Abstract. This study presents the automotive instrument panel (IP) design in order to improve the quality, cost, and safety of the existing design. A few conceptual designs were generated based on safety aspect and ergonomic design. The most suitable design was selected using concepts scoring. The IP head impact simulation was conducted using finite element analysis (FEA) to predict the head injury criterion (HIC) value of the front passenger in vehicle according to ECE-R21 regulation. The finite element (FE) model, which consist of upper IP, lower IP, carrier structure and head-form, was built-up to carry out head impact analysis of the IP assembly. The optimum IP design was proposed by analysis of different materials, which are 20% talc filled rubber modified polypropylene (PP+EPDM-TD20), acrylonitrile butadiene styrene (ABS) polymer, and polypropylene (PP) copolymer. The HIC value for all IP was compared using simulation result and theoretical calculation. The lowest HIC value will reduce the head occupant injury. In this study, only the raw material cost was considered in cost evaluation. The IP from ABS polymer performed the lowest HIC value, which were 179.7 but very costly compare to other materials.

Introduction

Automotive instrument panel (IP) is one of the most important parts in vehicle interior parts. Automotive manufacturer need to consider the quality, cost, and safety of the product when study the conceptual design of automotive parts.

In this vehicle design era, ergonomics design criteria is considered during design process. Ergonomics is the applied science which aims to match the demands of products and equipment, jobs and places of work, with the characteristics of the people who use them [1]. In the context of the IP, ergonomic design will ensure the display in the instrument cluster can be easily seen and the vehicle control system can be easily reached by the driver.

Law related with passenger protection against car crash was taken seriously by manufacturer. The most common sources of head and face injury in frontal crashes were from contact with the IP, driver steering and windscreen [2]. Therefore, the developed IP must fulfil the government regulation and standards, such as Federal Motor Vehicle Safety Standards Regulations 201 (FMVSS 201) for North America, and United Nations Economic Commission Regulations 21 (ECE-R 21) for Europe. These regulations describe the requirement for IP head impact. By using Computer Aided Engineering (CAE) technique for IP head impact, prototype use for physical test will be reduced.

The objectives of this study are to design and modelling the automotive IP in order to improve the quality, cost and safety of the existing design and to determine the head injury criterion (HIC) of front passenger occupant using different materials. Besides, to compare the value of HIC based on simulation and theoretical calculation.

Methodology

The solution or idea of IP design can be illustrated in a few conceptual designs. To choose final design, the best design selected using the concept scoring. The CAD modeling of final design was performed by using CATIA P3 V5R20 software. Besides, head impact simulation was conducted by using LS-DYNA V971 software.

Concept Selection. The assessments show the comparison between the concept designs. The most suitable design was selected using concepts scoring. The maximum point was selected as the final design. Figures (refer with: Fig. 1, Fig.2 and Fig.3) show the each concept.

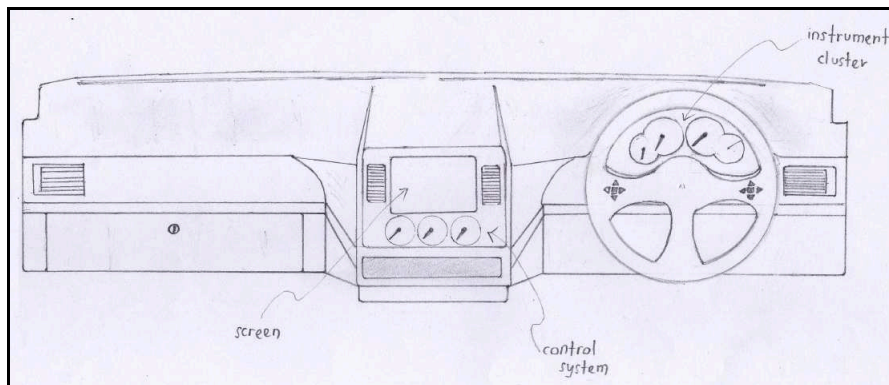


Fig 1 Concept 1

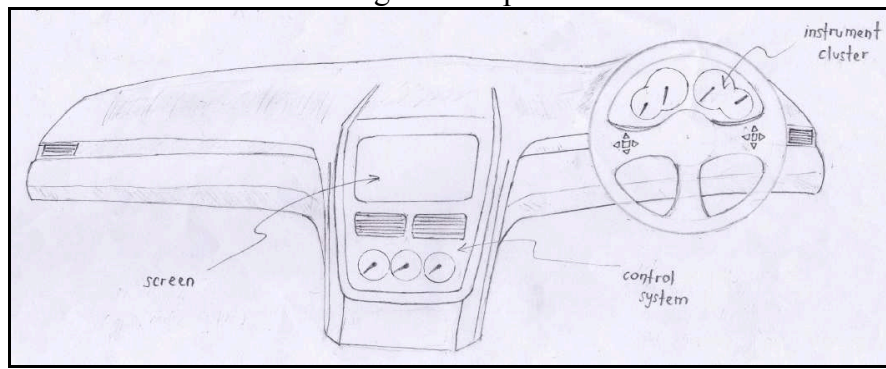


Fig 2 Concept 2

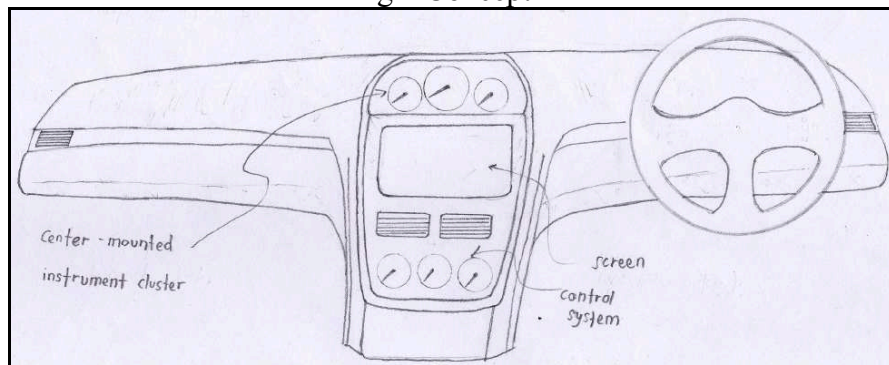


Fig 3 Concept 3

By comparing all the concepts, concept 1 was the highest point. Based on the concept scoring, concept 1 had the criteria such as ergonomic design, aesthetics, safety aspect, high quality and satisfies the regulations. Therefore, concept 1 was considered the best concept to be developed.

Preliminary Selection of Material. The raw of material for IP should be good mobility, excellent mold-ability and dimensional stability because of the large size and long cavity-filing distance of large plastic parts [4]. In this study, three resin materials were considered which are PP+EPDM-TD20, ABS polymer, and PP copolymer.

CAD Modeling. The 3D modeling was generated by using CATIA software. Figure (refer to: Fig. 4) shows the IP model of concept 1. This model also will be used in the CAE analysis. The thickness of this instrument panel was a 4 [mm].

FE Model and Impact Analysis. Both FMVSS 201 and ECE-R 21 regulations describe the requirements for IP head impact. The FMVSS 201 regulations stated that when that area of the IP that is within the head impact area is impacted by a 6.8 [kg], 165 [mm] diameter head form at 19 [km/hr], the deceleration of the head form shall not exceed 80 [g] continuously for more than 3 [ms]. This

requirement is for vehicles with dual airbag; but if vehicle without airbag, the impact speed is 24.1 [km/hr]. Besides, the ECE-R 21 regulation stated virtually the same requirement except that the impact speed is 24 [km/hr] [5]. Figure (refer with: Fig. 5) shows FE model for IP head impact simulation. The spherical shape in was assumed as the head of the vehicle passenger. It was applied the head-form diameter 165 [mm] and weight 6.8 [kg] to the FE model modeling. It was assumed as a rigid body, which means it didn't affect the analysis result. Each part in impact simulation has 4 nodes and 3 nodes shell elements, but mostly was a 4 nodes shell elements. Areas for each element were set up to 4 [mm²].

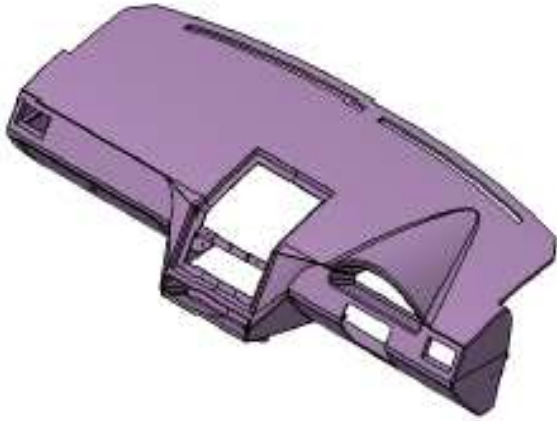


Fig. 4 The IP model

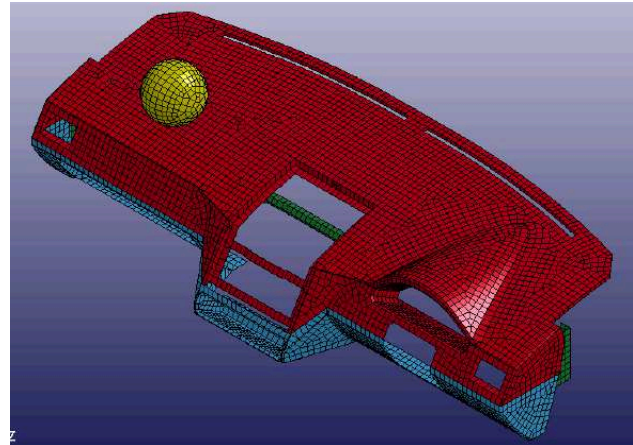


Fig. 5 The FE model for impact simulation

HIC Calculation. For most applications, the parameter that reflects the structure's performance is head injury criterion (HIC). A value of HIC below than 1000 units means that the structure provides satisfactory protection for passenger. Using data from the simulation, HIC can be calculated theoretically by using Eq.1.

$$HIC = \left[\frac{1}{t_2 - t_1} \times \int_{t_1}^{t_2} a \, dt \right]^{2.5} \times (t_2 - t_1) \quad (1)$$

The value for HIC was calculated by using head impact simulation data, times for head impact (t_1 and t_2) and acceleration of head (a). Notes that HIC from calculation need to divide by 1000 because the gravitational constant in simulation was a 0.00981 [mm/ms²]. The percentage of error was calculated by using Eq. (2).

$$\%error = \left| \frac{HIC_{calculation} - HIC_{simulataion}}{HIC_{calculation}} \right| \times 100 \quad (2)$$

Cost Evaluation. In cost evaluation for IP design, only raw material cost was considered. Cost for manufacturing process, labor, and other cost was not considered in this study. Table (refer with: Table 2) shows the cost for a raw plastic in Feb 2012 markets. The value of mass can be calculated from the density-volume relationship. The IP volume can be obtained in the CATIA software.

Table 2 Costs for a raw plastic [6]

Raw plastic Material	PP+EPDM-TD 20	ABS Polymer	PP Copolymer
Price (RM/kg)	3.70	5.87	2.45

Results

Figures (refer with: Fig. 6, Fig 7 and Fig. 8) shows the head impact simulation at a specific time and variation of acceleration at top of the head-form part in IP assembly for each material. For PP+EPDM-TD20, maximum deflection of IP was an approximately 58.29 [mm] between 19 and 26 [ms] and the HIC was 194.8. Besides for ABS polymer, maximum deflection of IP was an approximately 52.58 [mm] between 15 and 18 [ms] and the HIC was 179.9. For PP Copolymer, maximum deflection of IP was an approximately 58.29 [mm] between 19 and 26 [ms] and the HIC was 201.3.

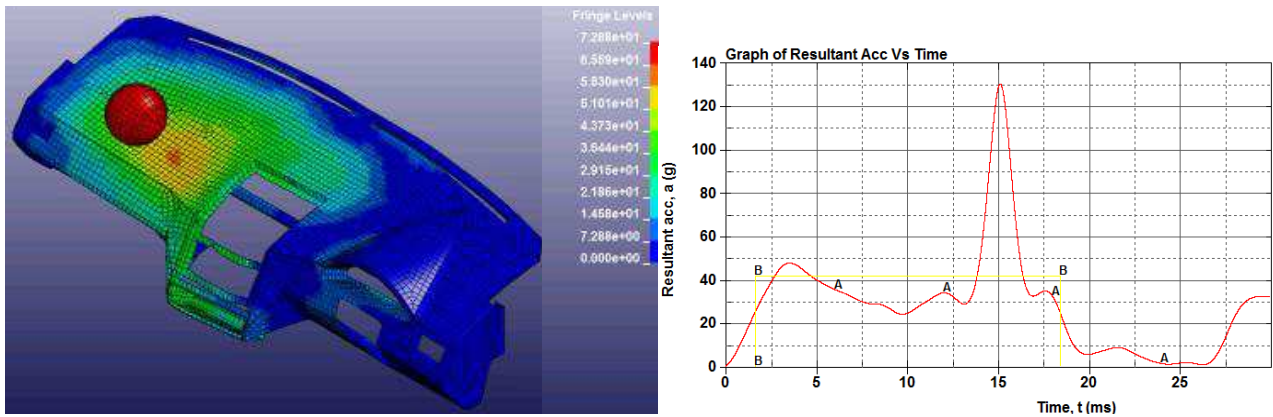


Fig. 6 Analysis results for PP+EPDM-TD20

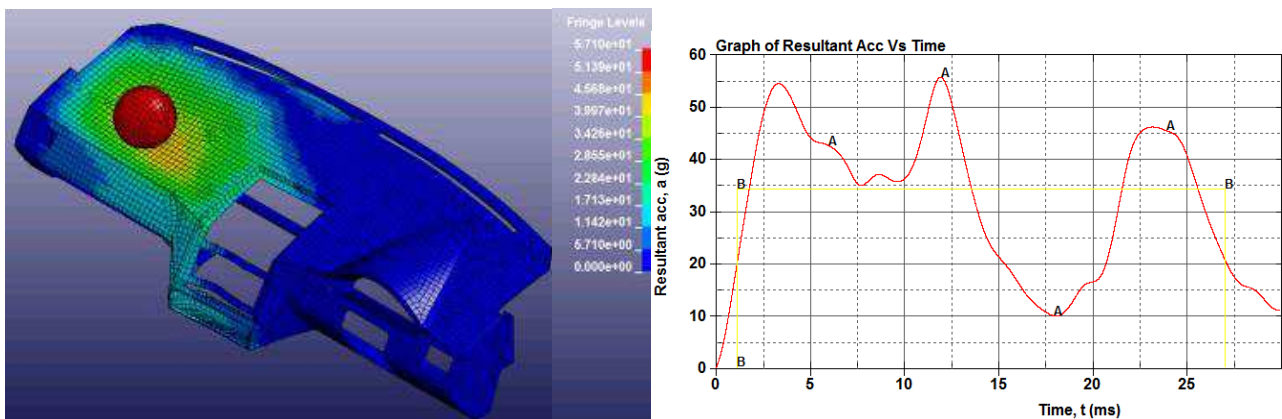


Fig. 7 Analysis results for ABS polymer

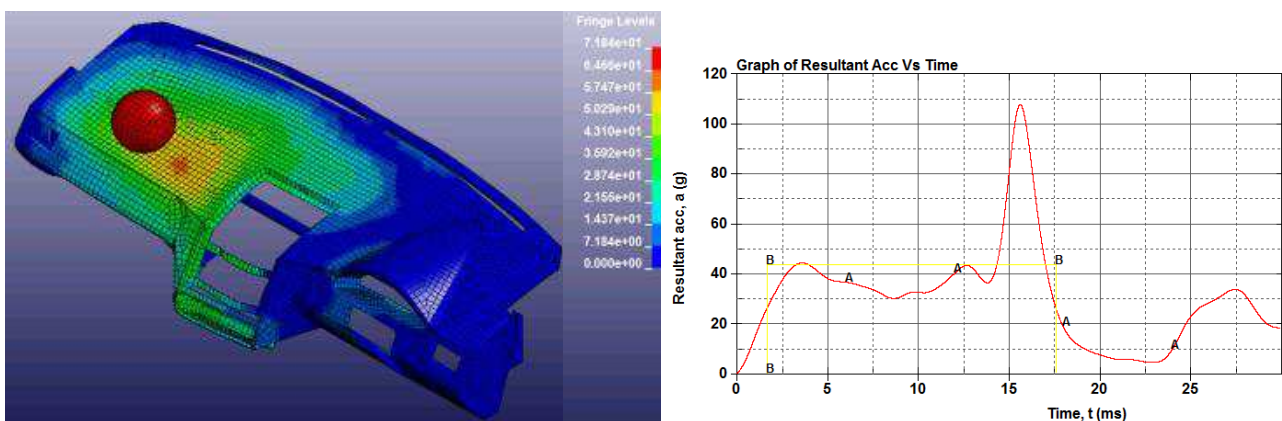


Fig. 8 Analysis results for PP Copolymer

Table (refer with: Table 3) shows the comparison of HIC value resulted from the simulation and calculation. The percentage of error was too small, it value was less than 3%.

Table 3 The comparison of HIC value

Material	t1 [ms]	t2 [ms]	a [g]	HIC simulation	HIC calculation	Percentage of error (%)
PP+EPDM-TD20	1.601	18.4	42	194.8	192.046	1.43
ABS polymer	1.133	27.1	34	179.9	174.830	2.90
PP Copolymer	1.654	17.6	44	201.3	204.778	1.70

Table (refer with: Table 4) shows the raw plastic material price of each material to produce the IP. The ABS polymer was the most expensive compare to other materials.

Table 4 The raw plastic material price of each material

Material	Volume, V [mm ³]	Density, ρ [kg/ mm ³]	Mass, M [kg]	Raw plastic price [RM/kg]	Price [RM]
PP+EPDM-TD 20	6E+6	1.04E-6	6.24	3.70	23.09
ABS Polymer	6E+6	1.04E-6	6.24	5.87	36.63
PP Copolymer	6E+6	0.93E-6	5.59	2.45	13.67

Summary

There were many factors which should be considered while designing automotive IP. Apart from the producing attractive designs, this study also focusing on ergonomic and safety design. This study was trying to simulate the real event for front passenger head when impacting the IP due to frontal crashes. Three different materials for IP model were analysed based on head impact simulation, which are PP+EPDM-TD20, ABS polymer, and PP copolymer.

The HIC value for head impact on IP that use all these three materials were less than 1000 units. It was also satisfying the FMVSS 201 and ECE-R21 regulations requirement. Design model from ABS polymer performed the lowest HIC value compared to the PP+EPDM-TD20 and PP copolymer. The HIC value for different IP material, PP+EPDM-TD20, ABS polymer, and PP copolymer was 194.8, 179.9, and 201.3, respectively.

Based on dynamics analysis, IP model that using ABS polymer as product material, will prevent occupant head impacting or stuck with carrier structure. This material was able to reduce head acceleration and capable to absorb energy due to impact.

Therefore, ABS polymer material was the most suitable for this IP design although the raw material cost was expensive.

References

- [1] M.D. Galer, The Application of Ergonomics in the Design of Automotive Displays, Butterworth & Co (Publishers) Ltd., 1984.
- [2] AJ McLean, BN Fildes, CN Kloeden, KH Digges, Prevention of head Injuries to Car Occupants: An Investigation of Interior Padding Options, NHMRC Road Accident Research Unit, University of Adelaide and Monash University Research Centre, 1997.
- [3] Fatih Arslan, User-centered Design Criteria in Auto Design with a Case Study of Auto Dashboard Design, Master of Science in Industrial Design, Izmir Institute of Technology, 2006.
- [4] Lin Sun & XiaoMing Liu, Control Analysis of Production and Apparent Quality of Automobile Large Plastic Parts, Elsevier Ltd., 2010.
- [5] Mike Keranen, Srikanth Krishnaraj, Kumar Kulkarni, Li Lu and Ravi Thyagarajan, Automating Instrument Panel Head Impact Simulation, Visteon Corporation, 2005.
- [6] Market Report Plastics - March 2012 from http://plasticker.de/index_en.php website.

3D Textiles	230	Curing Age	91
A		Curve Fitting	219
ABS Polymer	263	Customized	243
Adaptive	214	D	
Aerodynamics	102	Damage	147
Akaike Information Criterion (AIC)	219	Damage Rule	189
Alkali Treatment	86	Decision Diagrams	172
Aluminum	62	Decoding	194
Aluminum Honeycomb	81	Density	91
Aluminum Sandwich Panels	147	Design Methodology	248
Anchorage Bond	132	Development Process	69
Apatite	13	Die-Set	208
Assembly Errors (AE)	97	Digital Image Correlation	122
Austenitic Stainless Steel	46	Digital Signature	194
Austenizing Time	46	Dimensional Stability	28
Automotive	33	Direction of Two-Dimensional Curves	159
B		Discrete Event Simulation	198
Bioactivity	13	Drying Shrinkage	137
Bioceramics	13	Ductile Failure	189
Biocompatibility	127	E	
Blanking Die	208	Electron Beam Lithography	69
C		Encoding	194
CaCO ₃	57	Energy Efficient Building	142
CAD/CAM	184	Engine Block	33
Carbon Fiber	8	Epoxy	23
Carbonation	57	Evolutionary Algorithm	172
Cement	57	Expansive Agent	137
Ceramic	33, 74	Explicit	189
Clay Deposit	74	F	
Clay Properties	74	Fast Manufacturing	243
CO ₂ Uptake	57	FEA	52
Commercialization	253	FEM	127
Composite	28, 86	Finger-Like	3
Composite Material	23, 258	Finite Element Method (FEM)	97
Compressive Strength	91	Finite Element Modeling (FEM)	81
Computational Geometry	159	Flexural Strength	137
Computer Aided Selection	208	Fluid Structure Interaction (FSI)	102
Computer Algorithms	159	G	
Construction Industry	253	Gallium Nitride	41
Control Valve	112		
Corrosion Rate	46		

Genetic Algorithm (GA)	214	Manufacturing Chain	230
Glass Fiber	8	Manufacturing Execution System (MES)	248
Green Production	258	Materials	33
Grouted Sleeve	132	MDF	214
GRP Waste	142	Mechanical Property	8, 86
H		Metal Matrix Composite (MMC)	62
Hardness	3	Micro Air Vehicle (MAV)	102
Hash Algorithm	194	Micromechanical Formulation	152
Hash Chain	225	Microstructure	41
Hash Function	225	Morphing Wing	102
Head Impact Simulation	263	Mortar	57
Head Injury Criterion (HIC)	263	Motorcycle Braking	107
Honeycomb Core	147	Multi-Echelon Production System	237
Hot Dipped Aluminizing	3	Multi-Valued Logic	172
Hybrid Composite	8	N	
Hybrid Model	214	Nano Silicon Carbide	23
Hybrid Yarn	230	Nanocomposite	152
Hydrogel Composite	18	Neural Network	214
I		Notched Specimens	122
If-Then Rules	208	Nozzle	117
Image Steganography	194	Numerical Simulation	112
Impact Energy	147	O	
Impact Fatigue Life	147	Oil Palm Empty Fruit Bunch Fiber	18
<i>In Situ</i> Polymerization	18	Oil Palm Fibre	23
Inductively Coupled Plasma Reactive Ion Etching	69	Oil Palm Kernel Shell	86
Instrument Panel (IP)	263	Open Architecture Controlle	184
Interphase	152	Optical Characterizations	41
Interpreter	184	Optimization Methods Parameters Settings	198
ISA-95	248	Organo-Montmorillonite	28
ISO 6983	184	Oxalic Acid	46
K		P	
Kelantan	74	Petrovege Blocks	91
Keratin Fiber	28	PMMA	69
Knock	219	Polyester	86
L		Polymer-Clay-Silica	152
Lab View	184	Polyurethane Waste	142
Lime	57	Porosity	91, 127
Logic Gate	172	Powder Metallurgy	62
Logic Synthesis	172	Precast Concrete Connection	132
M		Prediction	214
Machinability	62	Pressure Fluctuation	112
Make or Buy Decision	237	Product Development	253
		Production	33
		Production Planning	237

Punching Die	208	TKR	243
		Tooth Root Bending Stress (TRBS)	97
R			
Raith ELPHY Quantum	69	U	
Rapid Prototyping	243	Ultra High Performance Fiber Reinforced Concrete	137
Refractive Index	41	Ultrasonic Vibration Assisted Grinding	203
Repeated Impact	147	Uncoupled Model	189
RFID	225	Underbone Motorcycle	107
Road Friction Coefficient	107	Unsaturated Polyester	28
Robotic Work Cell	165	Unsteady Flow	112
S			
Sandwich Composite	81	V	
Scanning Electron Microscopy (SEM)	18	Vacuum-Assisted Resin Transfer Moulding	8
Secure Privacy	225	VBA	208
Self-Consistent Approach	152	Virtual Fields Method	122
Self-Leveling Lightweight Mortars	142	Virtual Manufacturing	165
Shrinkage-Reducing Admixture	137	Voice Control	165
Silicon	41	Von Mises Stress	127
Simulated Body Fluid	13	W	
Simulation Optimization	198	Warm Deep Drawing	52
Solar Calculator	179	Water Absorbency Properties	18
Solar Energy	179	Weaknesses	33
Solar Photovoltaic	179	Wet Gas Separation	117
Speech Recognition	165	Wood	258
Splice Sleeve	132	Wooden Waste	142
Strengths	33	Y	
Supersonic Separator	117	Yawing Misalignment (Y)	97
Supply-Chain	253	Yawing Misalignment Influence Factor (YMIF)	97
Surface Characterization Datum	203		
Surface Topography Characterization	203		
Survey	33		
Sustainable Building	142		
T			
Tempering	46		
Tensile Strength	23		
Testing Function	198		
Textile Reinforced Composites	230		
Thermal Conductivity	142		
Thickness Strain	52		
Throttle Position Sensor (TPS)	219		
Ti-6Al-4V	52		
TiAl6V4	127		
Timber Processing	258		
Timeline	225		
Titanium Carbide	62		

A

Abdel-Magied, R.K.	208
Abdelmaguid, R.K.F.	159
Abdullah, M.Z.	102
Abubakar, A.	179
Adzali, N.M.S.	13
Ahmad, M.F.A.	117
Aldlemey, M.S.	46
Ali, N.	46
Almansa, A.	230
Amar, M.	81
Awang, M.	97
Azmi, A.I.	8
Azouaoui, K.	81, 147, 152

B

Balletto, G.	57
Basri, M.H.	102, 107
Boutaleb, S.	81, 152

C

Chandra, D.R.	248
Che Mat, S.	107
Chen, S.P.	225
Chowdhury, A.K.	172
Corinaldesi, V.	137, 142

D

Daud, A.R.	3
Daud, K.A.B.M.	74
Daud, M.	3
Daud, S.B.M.	194
Davies, I.J.	86
Decoster, D.	41
Deole, A.D.	52
Desai, D.	33
Dogheche, E.	41
Donnini, J.	142
Drápala, J.	127

E

Enoch, O.F.	74
-------------	----

F

Fadhil, M.	97
Faridah, S.I.	214
Fazeli, M.	230
Furcas, C.	57

G

Gebril, M.A.	46
Gitano, H.	219
Govindaraju, R.	237, 248
Gupta, A.K.	52

H

Haider, F.I.	46
Hamdan, S.	28
Hameed, M.	28
Hamid, Z.A.	132
Hammouda, Y.A.A.	253
Haniffah, N.A.	263
Hariadi, R.A.R.	237
Hashim, S.	18
Heng, S.K.	28
Hörlesberger, M.	230
Huang, Y.Y.	112
Hülka, J.	189
Hussein, H.M.A.	159, 208

I

Ismail, M.F.	203
Ismail, N.I.	102, 107

J

Jamiru, T.	33
Johnson, O.A.	91
Josyula, S.K.	62

K

Kakar, A.	28
Kamaruddin, I.B.	91
Kaoua, S.A.	152
Khan, M.T.K.M.N.	179
Kiswanto, G.	243

Ko, S.	41		
Kotkunde, N.	52		
Kubík, P.	189		
Kusumaningsih, W.	243		
Kvičala, M.	122, 127		
L			
Latif, K.	184		
Laurent, B.	230		
Lias, M.R.	97		
Liew, W.Y.H.	86		
Lin, C.	225		
Ling, J.H.	132		
Liyana, M.R.N.	13		
Losertová, M.	122		
Lukman, K.	248		
M			
Madzlan, N.	91		
Mahadzir, M.M.	102, 107		
Majid, R.A.	18		
Maryam, A.R.	69		
Mayorova, L.P.	258		
Mazzella, A.	57		
Mesbah, A.	152		
Mogaji, P.B.	33		
Mohamad, N.	8		
Mohamed, K.	69		
Mohammad, S.	132		
Mohd Hashim, F.M.	117		
Mohsin, M.	28		
Monsef, S.	253		
Morina, O.M.	258		
Mouhoubi, S.	147		
Muhammad-Sukki, F.	179		
Muhammad-Sukki, S.	179		
N			
Nabinejad, O.	23, 86		
Naitza, S.	57		
Nardinocchi, A.	137, 142		
Nordin, A.B.	214		
Noroozi, E.	194		
O			
Osman, M.H.	132		
Othman, N.K.	3		
P			
Padros, P.		230	
Pai, Y.S.		165	
Petruška, J.		189	
Poespawati, N.R.		41	
Q			
Qu, D.Y.		112	
Qudeiri, J.A.		208	
R			
Rabat, N.E.		18	
Rahman, A.B.A.		132	
Rahman, M.E.		23, 86	
Raj, N.		172	
Ramesh, S.		165	
Rao, T.V.V.L.N.		97	
Raska, P.		198	
Reddy, M.M.		23, 86	
Reddy, N.S.K.		62	
S			
Sabouhi, A.		194	
Sadeghi, M.		253	
Sadiku, R.		33	
Saim, A.A.		132	
Salehnamadi, M.R.		194	
Salman, R.R.		253	
Samsu, Z.		3	
Samuel, N.		23	
Saraswati, I.		41	
Šebek, F.		189	
Shamsuddin, L.		69	
Sheng, T.K.		263	
Shuaib, A.A.		74	
Sid-Ali, K.		81	
Singh, A.K.		172	
Singh, S.K.		52	
Siong, K.K.		28	
Soemardi, T.P.		243	
Štamborská, M.		122, 127	
Stolz, A.		41	
Sujan, D.		23, 86	
Suwandi, A.		243	

T

Tan, C.L.	8
Tishchenko, V.P.	258

U

Umer, U.	208
----------	-----

W

Wang, F.	159
Wigajatri, R.	41
Witwit, A.R.H.	219

X

Xie, X.Z.	112
Xu, J.L.	112

Y

Yadav, T.K.	219
Yap, H.J.	165
Yasin, A.	219
Yusof, Y.	184

Z

Zakaria, M.F.	263
Zamzuri, M.Z.M.	13
Zdenek, U.	198
Zeki, A.M.	179
Zhao, S.F.	225
Zulkifli, A.H.	102, 107